

Sol-Gel Coatings for the Protection of Ferrous Heritage Metal

Diana Kuzova Cini

Thesis submitted to the University of Malta in fulfilment of the requirements for the degree of Doctoral of Philosophy in Engineering.

Department of Metallurgy and Materials Engineering,
Faculty of Engineering, University of Malta.

March, 2019



L-Universit`
ta' Malta

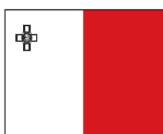
University of Malta Library – Electronic Thesis & Dissertations (ETD) Repository

The copyright of this thesis/dissertation belongs to the author. The author's rights in respect of this work are as defined by the Copyright Act (Chapter 415) of the Laws of Malta or as modified by any successive legislation.

Users may access this full-text thesis/dissertation and can make use of the information contained in accordance with the Copyright Act provided that the author must be properly acknowledged. Further distribution or reproduction in any format is prohibited without the prior permission of the copyright holder.



The research work disclosed in this publication is partially funded by the Endeavour Scholarship Scheme. The scholarship is part-financed by the European Union – European Social Fund.



European Union - European Structural and Investment Funds
Operational Programme II - Cohesion Policy 2014 - 2020
Investing in human capital to create more opportunities and promote the well being of society
Scholarships part-financed by the European Union European Social Fund (ESF)
Co-financing rate: 80% EU Funds; 20% National Funds





UNIVERSITY OF MALTA
FACULTY OF ENGINEERING

Declaration

Student I.D. no.: 0146405(L)
Student's Name: Diana Kuzova Cini
Course: Ph.D.
Title of Thesis: Sol Gel Coatings for the Protection of
Ferrous Heritage Metal

I, hereby declare that I am the legitimate author of this thesis and that it is my original work.

No portion of this work has been submitted in support of an application of another degree or qualification of this or any other university/institution of learning.

Signature of Student

31st March, 2019

ABSTRACT

Ferrous Iron corrodes when exposed to indoor uncontrolled climates as is the case with Heritage Metal (HM) being showcased openly in a museum. One way of protecting metals from corrosion is by applying protective coatings. This work proposes a novel way of protecting HM through the application of organic-inorganic hybrid (OIH) silica coatings produced through the sol-gel method as opposed to more conventionally used coatings such as acrylates or nitrocellulose-based lacquers.

Several precursors ($X-Si(OR)_3$) were studied for their anti-corrosion properties, namely $X=$ methyl, n-propyl-, n-hexyl-, n-octyl- and phenyl-triethoxysilane with tetraethyl orthosilicate (TEOS) in various mol% ratios ($X-Si(OR)_3:TEOS$). Coating systems involving mixtures of $X-Si(OR)_3:TEOS$ displayed similar trends in their corrosion behaviour: the corrosion resistance of the coatings improves with increasing organic content reaching a maximum, the corrosion resistance is then observed to drop again with further organic loading. These observations have been explained through their mechanical properties. Higher silica content leads to harder, more well-adhered coatings; however, if the silica content is too high then brittle coatings form. On the other hand, if the coating contains a large portion of organics, then coatings will be softer and show poor adhesion, even though hydrophobicity is improved.OTES:TEOS 20:80 mol% and MTES:TEOS 60:40 mol% were further considered and applied onto corroded surfaces and their extent of corrosion protection on such a surface was also evaluated. Crack formation was visibly reduced by increasing the silica concentration, thus resulting in thicker coatings and though the increase in XTES:TEOS ratio, both leading to an improvement in corrosion protection.

OIH alkoxy silane coatings impregnated with silica nanoparticles and in/organic chemical inhibitors have been considered in this work. Nanoparticles having a diameter of 10-20 nm purchased commercially (Commercial Nanoparticles, CNPs) produced a slight improvement in corrosion protection. Nanoparticles developed through a bottom up approach, the Stöber method (Stöber

nanoparticles, SNPs) did not bring about an improvement in corrosion protection. More protective coatings were obtained on clean metal with in/organic inhibitor molecules when added to MTES sols, at a given concentration of inhibitor for all six inhibitors studied. This was not the case with OTES coatings for which only one of the six molecules produced an improvement over the blank coating.

A comparative study was drawn between OIH silane coatings and conventionally used lacquers for HM namely, Paraloid B-48, B-72 and Ercalene. Electrochemical testing carried out on dip-coated clean metal coupons revealed OIH silane coatings to be more protective than the lacquers. This was not the case on corroded surfaces where OIH coating were found to be less protective than the lacquers which has been attributed to the thickness of coatings. For accelerated corrosion testing, thicker coatings were applied using both dip and brush application, the latter being a frequently used mode of application by conservators. OIH alkoxy silane coatings were significantly more protective than lacquers using both applications. Finally, a reversibility study on all OIH silane coatings was conducted where it was determined that all coatings can be removed using a mixture of sodium hydroxide solution with isopropyl alcohol solvent. This thesis proves the suitability of OIH silanes as coatings for HM since they are transparent and do not affect the aesthetics of the object, are applied without affecting the microstructure of the metal, provide significant corrosion protection which exceed that offered by conventional lacquers, and can be removed with relative ease.

ACKNOWLEDGEMENTS

I would like to firstly thank my principal supervisor Dr Daniel Vella for his continuous guidance, help and patience throughout the course of my studies. I immensely appreciate the time and effort he spent to assist me during my work. I would also like to thank my co-supervisor Prof. Emmanuel Sinagra who so kindly allowed me to make use of Physical chemistry lab within the Chemistry department and also helped me with challenges that arose. His knowledge and experience helped me gain confidence necessary for my progress.

I would like to thank Prof. Claude Farrugia for allowing me to carry out particle size measurements on Malvern ZetaSizer Nano ZS Dynamic Light Scattering (DLS) instrument whenever needed.

Thanks goes to all staff at the Chemistry Department, namely Jonathan Spiteri, Marie-Stella Grima, Alison Ellul, Joseph Grech, Mark Zerafa and Tony Buttigieg. Special thanks goes to staff at the Department of Metallurgy and Materials Engineering, namely Noel Tonna, Daniel Dimech, Mary Grace Micallef, James Camilleri, Nicky Gingell and Andrew Agius. They have not only helped me with my work but also became dearest friends of mine. I have to mention a few fellow students that I was lucky enough to have met during the course of my studies that have made the experience worth enduring and entertaining thanks to their friendship: Malcolm Caligari Conti, Michael Fiott, Clayton Farrugia, Duncan Micallef, Antonino Mazzonello, Anthea Agius Anastasi, Eleanor Saliba, Christabelle Tonna, Mark Bonello, Matthias Debono, Roberto Migneco, Niki Brincat and Elise Ann Mifsud.

Finally, I would like to thank my family for their continuous support, love and encouragement. I dedicate this work to Ivan.

TABLE OF CONTENTS

DECLARATION.....	iii
ABSTRACT.....	iv
ACKNOWLEDGEMENTS.....	vi
TABLE OF CONTENTS.....	vii
LIST OF FIGURES.....	xvi
LIST OF TABLES.....	xxvi
LIST OF SYMBOLS AND ABBREVIATIONS.....	xxviii
Chapter 1: Introduction	
1.1 Protecting Heritage Metal against corrosion.....	1
1.2 Suitability of OIH alkoxy silane coatings for corrosion protection of HM.....	2
1.3 Thesis Structure.....	3
1.4 Aims and objectives.....	4
Chapter 2: Literature Review	
2.1 Introduction to corrosion and prevention strategies.....	7
2.2 Formation of protective coating through the sol-gel process.....	8
2.3 Sol-gel process.....	10
2.3.1 Main stages of the sol-gel process.....	10
2.3.2 Reaction parameters affecting the hydrolysis process.....	12
2.3.3 The effect of pH on condensation process.....	14
2.4 Organic- inorganic hybrid sol-gels.....	16
2.4.1 Influence of ratio of inorganic : organic precursor molecules on corrosion protection	18

2.4.2 Influence on chain length on coating properties.....	19
2.5 Sol-Gel OIH coatings on steel.....	21
2.6 Incorporation of inhibiting species within OIH coatings	21
2.6.1 Incorporation of Nanoparticles.....	22
2.6.1.1 Commercial Nanoparticles	22
2.6.1.2 Nanoparticles produced through bottom-up approach.....	25
2.6.2 Incorporation of inorganic and organic inhibitor molecules.....	27
2.6.2.1 Inorganic inhibitors.....	27
2.6.2.2 Organic inhibitors.....	29
2.7 Reversibility of OIH alkoxy silane coatings.....	32
2.8 Preservation of HM.....	33
2.8.1 Current modes of corrosion prevention	33
2.8.2 General conservation work guidelines when applying coatings on HM.....	33
2.8.3 Research in Conservation of HM.....	34
2.8.4 OIH alkoxy silane coatings for protection of heritage metals.....	41
Chapter 3: Methodology	
3.1 Introduction	44
3.2 Metal substrate	45
3.2.1 Metal substrate preparation	45
3.2.1.1 Preparation of polished coupons.....	45
3.2.1.2 Preparation of corroded iron coupons.....	46
3.2.2 Characterisation of iron surfaces	48
3.2.2.1 Etching of polished iron surface.....	48
3.2.2.2 Scanning Electron Microscopy (SEM).....	48
3.2.2.3 X-Ray Diffraction (XRD).....	48
3.3 Protective Coating lacquers	49
3.3.1 Materials	49

3.3.1.1 Sol preparation.....	49
3.3.1.2 Lacquer preparation.....	50
3.3.2 Procedure for sol and lacquer preparations.....	50
3.3.2.1 OIH alkoxy silane sols.....	50
3.3.2.2 Preparation of nanoparticles by the Stöber Method.....	52
3.3.2.3 Commercial nanoparticles.....	54
3.3.2.4 Inorganic and organic inhibitors	55
3.3.2.5 Acrylate and nitrocellulose lacquers	57
3.3.3 Coating deposition and curing.....	57
3.3.4 Sol characterisation	58
3.3.4.1 Particle sizing.....	58
3.3.5 Coating characterisation.....	59
3.3.5.1 Infra-red spectroscopy.....	59
3.3.5.2 UV-Vis Spectroscopy	63
3.3.5.3 Contact angle.....	64
3.3.5.4 Optical microscopy.....	64
3.3.5.5 Scanning Electron Microscopy.....	64
3.3.6 Mechanical testing.....	65
3.3.6.1 Nano-indentation.....	65
3.3.6.1.1 Hardness and Young's Modulus determination.....	65
3.3.6.1.2 Nano-scratch testing.....	66
3.3.6.2 Adhesion testing	66
3.3.6.3 Surface roughness.....	69
3.3.6.4 Corrosion testing.....	69
3.4 Accelerated corrosion (salt-spray) testing of coated coupons.....	71
3.5 OIH silica coatings' reversibility.....	73
3.5.1 Preparation of coated coupons.....	73
3.5.2 Immersion testing.....	73

3.5.3 Manual cleaning	75
-----------------------------	----

Chapter 4: Method development and optimisation of OIH alkoxy silane coatings

4.1 Introduction.....	76
4.2. Method development	77
4.2.1 Effect of sol pH on Particle Size measurements	77
4.2.2 Two-step versus one-step method for sol development.....	79
4.2.3 Effect of sol development time and temperature on particle size.....	84
4.2.4 Effect of time allowed for sol development on corrosion protection.....	87
4.2.5 Effect of curing on corrosion protection.....	88
4.2.6 Effect of number of coatings and silica concentration on corrosion protection.....	91
4.2.7 Highly protective coatings and irreproducibility issues.....	98
4.2.8 Surface pre-treatment using sodium hydroxide solution.....	100
4.2.9 Effect of silica:water ratio (SiO ₂ :H ₂ O).....	100
4.3 Method alterations for OTES:TEOS sol development.....	103
4.4 Conclusion.....	104

Chapter 5: Results

5.1 The effect of alkyl/aryl functional groups on the mechanical and anti-corrosion properties of OIH alkoxy silane coatings.....	105
5.1.1 Sol characterisation.....	105
5.1.1.1 Particle sizing.....	105
5.1.2 Coating characterisation.....	108
5.1.2.1 Infra-red spectroscopy	108
5.1.2.2 UV-visible spectroscopy.....	114
5.1.2.3 Coating morphology.....	116
5.1.2.4 Coating thickness.....	116

5.1.2.5 Contact angle.....	119
5.1.3 Mechanical testing of coatings.....	121
5.1.3.1 Nano-indentation.....	121
5.1.3.1.1 Hardness and Young's Modulus determination.....	121
5.1.3.1.2 Nano-scratch.....	125
5.1.3.2 Pull-out test for the study of adhesion of OIH alkoxy silane coatings.....	129
5.1.4 Electrochemical Evaluation Results.....	132
5.2 The corroded iron surface.....	143
5.2.1 Iron microstructure.....	143
5.2.2 Clean and corroded iron surface morphology.....	143
5.2.3 X-ray Diffraction of iron surface.....	145
5.2.4 Electrochemical study on uncoated metal surfaces.....	147
5.2.5 Coated corroded iron surface morphology.....	149
5.2.6 Surface roughness of un/coated iron surfaces.....	150
5.2.7 MTES and OTES-coated corroded metal surfaces.....	151
5.2.7.1 Effect of increasing SiO ₂ concentration.....	151
5.2.7.2 Effect of dip-coating speed on crack formation.....	156
5.2.7.3 Effect of increase in X-Si(OR) ₃	158
5.2.7.4 Effect of Drying Control Chemical Additives	159
5.3 Addition of silica nanoparticles for the improvement of corrosion protection of OIH alkoxy silane coatings.....	172
5.3.1 Addition of Commercial Nanoparticles (CNPs) to OIH alkoxy silane coatings.....	172
5.3.1.1 Dispersion of CNPs studied through PS	172
5.3.1.2 Electrochemical testing on CNP-doped MTES coatings.....	174
5.3.1.3 Surface morphology of CNP-doped MTES coatings.....	177
5.3.2 Addition of Stöber Nanoparticles to MTES coatings	178

5.3.2.1 SNP Sol characterisation through Particle size measurements	178
5.3.2.2 Electrochemical evaluation of SNP-doped MTES coatings.....	181
5.3.3 The origin of SiO ₂ in final sol and its effect on deposited coating.....	181
5.3.3.1 Coating topography.....	183
5.3.3.2 Electrochemical testing.....	184
5.3.4 Effect of 26 nm SNP concentration on corrosion protection of MTES coatings.....	186
5.3.5 Application of MTES-CNP and MTES-SNP coatings to corroded surfaces	189
5.4 Addition of inorganic and organic inhibitor molecules to OIH alkoxysilane coatings for enhanced corrosion protection.....	193
5.4.1 Particle size measurements of inhibitor-doped MTES/OTES sols.....	193
5.4.2 IR spectra of inhibitor-doped MTES/OTES sols	200
5.4.3 Scanning Electron Microscopy.....	206
5.4.3.1 Surface Coating morphology.....	206
5.4.3.2 EDS analysis.....	206
5.4.4 Electrochemical testing.....	207
5.4.4.1 Clean metal surface coated with in/organic inhibitor-doped MTES and OTES coatings.	207
5.4.4.2 Corroded surfaces coated with in/organic inhibitor-doped MTES:TEOS 60:40 mol% coatings	224
5.5 Performance of OIH coatings relative to Paraloid and Ercalene lacquers.....	226
5.5.1 Optical and Scanning Electron Microscopy.....	226
5.5.1.1 Coating morphology and thickness on clean metal surfaces.....	226
5.5.1.2 Coating morphology of lacquer coatings on corroded-cleaned iron surfaces.....	228
5.5.1.3 Coating morphology under different modes of application of coatings onto clean surfaces.....	230

5.5.1.4 Coating thickness determination by fine brush application.....	232
5.5.2 Mechanical testing of lacquers	234
5.5.2.1 Nano-scratch.....	234
5.5.2.2 Pull-out testing.....	236
5.5.3 Electrochemical Tests.....	237
5.5.3.1 Lacquer coatings on clean polished iron surface	237
5.5.3.2 Lacquer coatings on corroded-cleaned iron surfaces.....	241
5.5.4 Accelerated corrosion (salt spray) testing	245
5.5.4.1 OIH alkoxy silane coatings applied through dip, fine brush, coarse brush and sponge applications.....	245
5.5.4.2 Paraloid and Ercalene lacquers applied through dip and fine brush applications.....	251
5.6 Reversibility of OIH alkoxy silane coatings.....	253
5.6.1 Immersion tests.....	253
5.6.2 Removal of coatings by manual cleaning.....	256
 Chapter 6: The effect of alkyl/aryl functional groups on the mechanical and anti- corrosion properties of OIH alkoxy silane coatings	
6.1 Introduction.....	258
6.2. Sol characterisation.....	258
6.3 Coating characterisation.....	259
6.3.1. Infra-red spectroscopy	259
6.3.2 Coating thickness.....	261
6.3.3 Contact angle.....	261
6.4 Mechanical testing.....	262
6.4.1 Hardness and elastic modulus measurement using Nano-Indentation.....	262
6.4.2 Pull-out test for the study of adhesion of OIH alkoxy silane coatings	263
6.4.3 Nano-scratch	266

6.5 Electrochemical Evaluation.....	266
6.6 General discussion.....	267
Chapter 7: The corroded iron surface	
7.1 Introduction.....	271
7.2 Characterisation of uncoated iron surfaces	272
7.3 The variation of surface roughness on polished, corroded and coated surfaces.....	273
7.4 Corrosion protection on corroded surface using MTES:TEOS and OTES:TEOS coatings	274
Chapter 8: Addition of silica nanoparticles for the improvement of corrosion protection of OIH alkoxy silane coatings	
8.1 Introduction.....	281
8.2 Addition of commercial nanoparticles (CNPs).....	282
8.3 Addition of Stöber nanoparticles (SNPs).....	282
8.4 Application of CNP and SNP-doped MTES:TEOS coatings to corroded surfaces	284
Chapter 9: Addition of inorganic and organic inhibitor molecules to OIH alkoxy silane coatings for enhanced corrosion protection	
9.1 Introduction.....	286
9.2 Effect of inhibitor molecules on OIH alkoxy silane sols.....	287
9.3 Inhibitor-doped MTES/OTES coating characterisation.....	287
9.4 Effect of inhibitor molecules on corrosion protection of OIH alkoxy silane coatings	287
9.4.1 Inhibitor-doped 60:40 mol% MTES:TEOS coatings.....	288
9.4.2 Inhibitor-doped 20:80 mol% OTES:TEOS coatings.....	292
9.4.3 Inhibitor-doped MTES coatings on corroded surfaces.....	292

9.5 General Discussion.....	292
Chapter 10: Performance of OIH alkoxy silane coatings relative to Paraloid and Ercalene lacquers	
10.1 Introduction.....	297
10.2 Coating morphology and thicknesses of OIH alkoxy silanes in comparison with Paraloid and Ercalene coatings	298
10.3 Electrochemical testing	299
10.4 Accelerated corrosion (salt-spray) tests.....	303
10.4.1 OIH alkoxy silane coatings deposited through dip, fine brush, coarse brush and sponge application	303
10.4.2 Comparison of OIH alkoxy silane coatings to Paraloid and Ercalene coatings deposited through dip and fine brush applications.....	306
Chapter 11: Reversibility of OIH alkoxy silane coatings	
11.1 Introduction.....	311
11.2 immersion testing versus manual cleaning.....	312
11.3 Further work.....	316
Chapter 12: Conclusion	
12.1 Effect of alkyl/aryl functional groups on anti-corrosion properties of OIH alkoxy silane coatings.....	317
12.2 Application of OIH alkoxy silane coatings onto corroded surfaces.....	318
12.3 Addition of inhibitors to OIH alkoxy silane coatings	319
12.3.1 Silica nanoparticles.....	319
12.3.2 Organic and inorganic inhibitor molecules	320
12.4 Comparative study of OIH alkoxy silane coatings with acrylate/nitrocellulose lacquers.....	321

12.5 Reversibility of OIH alkoxy silane coatings.....	322
12.6 General conclusion	323
REFERENCES.....	324

LIST OF FIGURES

Figure 2.1: Hydrolysis mechanism for a silicon alkoxide under a) acidic and b) basic conditions.....	13
Figure 2.2: Condensation mechanism in a) acidic and b) basic medium.....	15
Figure 2.3: Bonding mechanism for silanol groups present in alkoxy silane sols and metal interface.....	17
Figure 2.4: Anodic and cathodic reactions occurring that bring about the formation of corrosion products on iron surfaces when exposed to an aqueous medium.	21
Figure 2.5: Bode plots obtained from specimen without coating and with specimens 1, 2, 2a and 2b (set 1) (a, b).....	37
Figure 2.6: Bode plots obtained from specimen without coating and with specimens 3, 3a, 3b and 3c (set 1) (a, b).....	37
Figure 2.7: Equivalent electrical circuit used to fit EIS data.....	38
Figure 2.8: Bode plots obtained from pre-corroded specimens coated by immersion (set 2) without artificial ageing (a, b).....	39
Figure 3.1: a) Temperature and b) Relative Humidity measurements taken during wet-dry cycles performed on iron coupons to accelerate the corrosion process.....	47
Figure 3.2: a) 20:80 mol% MTES:TEOS IR plot of wavenumber versus transmittance for smoothed raw data in the 3500-500 cm^{-1} region b) Spectrum of (a) having been translated into wavenumber versus absorbance and applying baseline correction where the software sets baseline shown in red c) spectrum (b) following baseline subtraction, application of normalisation process and conversion back to transmittance. This figure also includes the assigned 8 peaks of interest from which the peak areas are calculated through the software	62
Figure 3.3: Image of home-built contact angle measurement set-up.....	64
Figure 3.4: Set up for pull-off testing carried out on an INSTRON 8802 tensile testing machine.....	67
Figure 3.5: Depiction of the set up used to carry out electrochemical and potentiodynamic testing on bare and coated coupons.	71
Figure 3.6: Set up for immersion testing.....	74

Figure 4.1: Particle size distribution versus a) intensity (%) and b) volume for MTES:TEOS 60:40 mol%.....	78
Figure 4.2: Particle sizing for 2.5% SiO ₂ MTES:TEOS 60:40 mol% at pH 2 (prior to sol neutralisation) and pH 7 (after neutralisation of sol)	78
Figure 4.3: Particle sizing results for 2.5% SiO ₂ MTES:TEOS 60:40 mol% prepared using one-step and two-step methods.	79
Figure 4.4: Electrochemical evaluation for MTES:TEOS 60:40mol% double coating showing repeatability in results presented as a) Bode impedance b) Bode phase angle c) Nyquist and d) Potentiodynamic plots. Plots include bare metal for comparative purposes.	81
Figure 4.5: Electrical circuit model for (a) coated corroding surface (b) uncoated corroding surface.....	82
Figure 4.6: Electrochemical data for 2.5% SiO ₂ 60:40% MTES:TEOS coated iron surfaces, for which coatings were derived from one-step and two-step sol development. Bare metal plots are included to indicate the extent of corrosion protection offered by coatings.....	85
Figure 4.7: Particle sizing for MTES:TEOS 60:40 mol% when a) varying time of sol development at 40 °C and b) varying temperature during sol development.....	86
Figure 4.8: Electrochemical evaluation for MTES:TEOS 60:40mol% double coatings originating from sols that have been allowed different development times a) Bode impedance b) Bode phase angle c) Nyquist and d) Potentiodynamic plot.....	89
Figure 4.9: Electrochemical evaluation for MTES:TEOS 60:40mol% double coatings that have been cured at 150 °C for 1 hr and without curing (left to dry at room temperature overnight) a) Bode impedance b) Bode phase angle c) Nyquist and d) Potentiodynamic plots.....	90
Figure 4.10: Electron micrograph showing the surface and a cross-section through MTES:TEOS 60:40 mol% coatings having an SiO ₂ concentration of a) 2.5%; b) 5%; c) 10% in a i) single coat ii) double coat and triple coating application. Images were captured using a 10k magnification.....	91
Figure 4.11: Electrochemical plots for MTES:TEOS 60:40 mol% having 2.5% (left) and 5% (right) silica concentrations for single, double and triple coated coupons a) Bode impedance b) Bode phase angle c) Nyquist and d) Potentiodynamic plots.	95
Figure 4.12: Electrochemical plots for MTES:TEOS 60:40 mol% upon increasing SiO ₂ concentration for single coatings a) Bode impedance b) Bode phase angle c) Nyquist and d) Potentiodynamic plots....	96
Figure 4.13: a) Bode impedance b) Bode phase angle c) Nyquist and d) Potentiodynamic plots for double-coated MTES:TEOS 60:40 mol% having 2.5% and 10% SiO ₂ concentration, the latter do not fail in a regular manner and lead to irreproducibility in results.....	99
Figure 4.14: a) Bode impedance b) Bode phase angle c) Nyquist and d) Potentiodynamic plots for double coated MTES:TEOS 60:40 mol% having 1:2, 1:4 and 1:10 SiO ₂ :H ₂ O ratios for a final silica concentration of 2.5%. Plots include bare metal for comparative purposes.....	101
Figure 4.15: Particle size versus Intensity plot for MTES sols having different silica:water ratios.....	102
Figure 4.16: Plot of Size versus Intensity for OTES:TEOS 60:40mol% sols allowed to develop at 20 °C. Particle sizing was obtained at various times during the sol development stage.....	104

Figure 5.1: Particle sizing for 2.5% SiO ₂ sols in ethanol following neutralization of sol for a) MTES:TEOS b) PrTES:TEOS c) HTES:TEOS d) OTES:TEOS and e) PhTES:TEOS in various XTES concentrations considered in this work.....	106
Figure 5.2: Mean particle size and standard deviation (nm) for sols investigated in this work. Data points have been connected with lines for better readability.	108
Figure 5.3: Infra-red spectra showing IR window at a) 4000-400 cm ⁻¹ and b) 3500-2500 cm ⁻¹ region for 20:80 mol% organic-inorganic alkoxy silane mixtures i) MTES:TEOS ii) PrTES:TEOS iii) HTES:TEOS iv) OTES:TEOS and v) PhTES:TEOS.....	109
Figure 5.4: Plot of MTES:TEOS hybrid precursor mol% versus percentage area of Peaks (1 to 8) considered. Peak 1 (600 cm ⁻¹) is due to the rocking motion Si-OH /Si-O ⁻ groups, Peak 2 (793 cm ⁻¹) due to the symmetric stretching of the O along the bisector of the Si-O-Si bridging angle, Peak 3 (951 cm ⁻¹) due to stretching vibrations of Si-OH /Si-O ⁻ groups, Peak 4&5 (1067 cm ⁻¹) due to asymmetric stretches of O in Si-O-Si bonds, and Peaks 6-8 due to the asymmetric and symmetric stretches of the -CH ₃ group/s.....	112
Figure 5.5: Plot of five hybrid precursors in 20:80 mol% versus percentage area for Peaks 1-8 considered. Peak 1 (600 cm ⁻¹) is due to the rocking motion Si-OH /Si-O ⁻ groups, Peak 2 (793 cm ⁻¹) due to the symmetric stretching of the O along the bisector of the Si-O-Si bridging angle, Peak 3 (951 cm ⁻¹) due to stretching vibrations of Si-OH /Si-O ⁻ groups, Peak 4&5 (1067 cm ⁻¹) due to asymmetric stretches of O in Si-O-Si bonds, and Peaks 6-8 due to the asymmetric and symmetric stretches of the -CH ₃ group/s.....	114
Figure 5.6: Transmission spectra for a) MTES:TEOS, b) PrTES:TEOS, c) HTES:TEOS, d) OTES:TEOS, e) PhTES:TEOS, in several XTES:TEOS mol% ratios. Plots include blank measurement (uncoated glass slide) for comparative reasons.....	115
Figure 5.7: Electron micrographs of all OIH alkoxy silane coatings considered (mag ×2000). Double coating application was carried out through dip-coating and a 2.5% SiO ₂ concentration was employed: a) MTES:TEOS i) 20:80 ii) 40:60 iii) 60:40 and iv) 80:20 mol%; b) PrTES:TEOS i) 20:80 ii) 40:60 iii) 50:50 and iv) 60:40 mol%; c) HTES:TEOS i) 20:80 ii) 30:70 iii) 40:60 and iv) 60:40 mol%; d) OTES:TEOS i) 10:90 ii) 20:80 iii) 40:60 and iv) 60:40 mol%; and e) PhTES:TEOS i) 20:80 ii) 40:60 iii) 60:40 and iv) 80:20 mol%.....	117
Figure 5.8: Electron micrograph showing the surface and a cross-section through 20:80 mol% coatings of a) MTES:TEOS (mag ×30 k) b) PrTES:TEOS (mag ×5 k) c) HTES:TEOS (mag ×30 k) d) OTES:TEOS (mag ×30 k) and e) PhTES:TEOS (mag ×30 k).....	118
Figure 5.9: Average double-layer coating thicknesses and their respective standard error (nm) for different coatings investigated in this work.....	119
Figure 5.10: Photo-micrographs of sessile water droplets on a) bare metal with the lowest contact angle (left) and b) OTES:TEOS 40:60 mol% having the highest contact angle.....	120
Figure 5.11: Mean contact angle measurements for different organic-inorganic silane coatings. Bare metal contact angle (56°) is represented by dashed line for comparative purposes.....	120
Figure 5.12: Plot of displacement versus load for one of the harder coatings, PrTES:TEOS 20:80 mol% (H= 0.44 GPa, left plot) together with the representative for least hard coatings, OTES:TEOS 60:40 mol% coating (H= 0.02 GPa, right plot) showing loading-unloading cycle during measurement.	122

Figure 5.13: Plot of displacement versus load for OIH alkoxysilane coatings considered in this work showing loading-unloading cycle during measurement a) MTES:TEOS b) PrTES:TEOS c) HTES:TEOS d) OTES:TEOS and e) PhTES:TEOS coatings, each plot in several mol% concentrations of precursor molecule.	124
Figure 5.14: a) Calculated Young's Moduli (GPa) and b) Hardness measurements (GPa) for silica-based coatings considered in this work as obtained using nano-indentation.	125
Figure 5.15: Images of scars inflicted onto iron coupons coated with MTES:TEOS 20:80 mol% and OTES:TEOS 60:40 mol%. Plots of scan distance versus penetration depth for during scratch and scratch profile after scratch for two coatings also featured in Figure.....	126
Figure 5.16: Plot of the average loads from the beginning of the scratch at which point the indenter reaches the underlying metal surface for all silica coatings studied.....	129
Figure 5.17: Images of coated coupons after pull-out testing where coatings have remained completely intact in all cases. Dolly was pulled away from each of the coated coupons where adhesive was left behind on the coupon (as seen in PrTES;TEOS coatings), fully detached from the surface of the coated coupon (such as PhTES:TEOS 80:20 mol%) or partially detached from the surface of the coupon (such as PhTES:TEOS 20:80 mol%).....	130
Figure 5.18: Plot of pull-out force required to detach the dolly from the coated coupons.....	131
Figure 5.19: a) Bode impedance b) Bode phase angle c) Nyquist and d) Potentiodynamic plots for MTES:TEOS double coatings. The data for bare metal is not visually perceivable in Nyquist plot as it is negligible compared to coated coupon data.....	133
Figure 5.20: a) Bode impedance b) Bode phase angle c) Nyquist and d) Potentiodynamic plots for PrTES:TEOS double coatings. Bare metal data is included for comparative purposes.....	134
Figure 5.21: a) Bode impedance b) Bode phase angle c) Nyquist and d) Potentiodynamic plots for HTES:TEOS double coatings. Bare metal data is included for comparative purposes.....	135
Figure 5.22: a) Bode impedance b) Bode phase angle c) Nyquist and d) Potentiodynamic plots for OTES:TEOS double coatings. Bare metal data is included for comparative purposes.....	136
Figure 5.23: a) Bode impedance b) Bode phase angle c) Nyquist and d) Potentiodynamic plots for PhTES:TEOS double coatings. Bare metal data is included for comparative purposes.....	137
Figure 5.24: Plot showing comparison of a) Total Impedance (Z_{tot}) and b) corrosion current density (I_{corr}) for the five types of OIH silane coatings. Bare polished metal featured as grey dotted line..	140
Figure 5.25: Optical micrograph showing pitting formed on (a) 60:40 mol% MTES:TEOS, (b) 50:50 mol% PrTES:TEOS, (c) 30:70 mol% HTES:TEOS, (d) 20:80 mol% OTES:TEOS, (e) 40:60 mol% PhTES:TEOS coated coupons and (f) uncoated (bare) coupon following the potentiodynamic polarisation test at $\times 5$ magnification.	142
Figure 5.26: Microstructure of iron substrate revealed using Nital solution at a mag x50 taken using a metallographic microscope. Arrows indicate faint grain boundaries.....	143
Figure 5.27: Images obtained using stereo microscope using x5 magnification of (a) clean mirror-polished coupon, (b) corroded uncleaned coupon and (c) corroded cleaned coupon.....	144
Figure 5.28: Electron micrograph showing a) cross-sections of i) uncleaned and ii) cleaned corroded coupon; b) surface of i) uncleaned and ii) cleaned corroded coupon. All images were taken using x500 magnification.....	145

Figure 5.29: X-ray diffraction pattern taken from clean and corroded iron surfaces together with superimposed ICCP cards: a) clean polished iron surface and Fe card (00-001-1267), b) uncleaned corroded iron surface with beta-Iron (III) oxide card (00-005-0480) and c) cleaned corroded surface with magnetite card (01-082-3510).....	146
Figure 5.30: a) Bode Impedance b) Bode phase angle c) Nyquist and d) potentiodynamic plots obtained for uncoated polished, ground clean metal and corroded clean metal.	148
Figure 5.31: Electron micrograph showing (a) corroded-cleaned metal surface that has been coated with MTES:TEOS 60:40 mol% having SiO ₂ concentration of (i) 2.5% and (ii) 20% (mag ×500) and (b) cross-section of (i) 2.5% SiO ₂ coated coupon and (ii) 20% SiO ₂ coated coupon (mag ×10k). Coatings are indicated using arrows.	150
Figure 5.32: Surface roughness plot (R _a (nm)) for several coated and uncoated iron surfaces namely: clean polished metal (CM), corroded uncleaned metal (CUM), corroded-cleaned metal (CCM), 2.5% and 20% SiO ₂ MTES:TEOS 60:40 mol%-coated CCM.....	151
Figure 5.33: a) Bode Impedance b) Bode phase angle c) Nyquist and d) potentiodynamic plots obtained for clean-corroded metal coated with 60:40 mol% MTES:TEOS at several silica concentrations	153
Figure 5.34: a) Bode Impedance b) Bode phase angle c) Nyquist and d) potentiodynamic plots obtained for clean-corroded metal coated with 20:80 mol% OTES:TEOS at several silica concentrations.	154
Figure 5.35: a) Electron micrographs (x500 mag) of corroded-cleaned coupon coated with 5% SiO ₂ 20:80 mol% OTES:TEOS uncured coatings b) coating cross sections of 5% SiO ₂ 20:80 mol% OTES:TEOS deposited using i) 280 mm/min (mag × 10k) and ii) 40 mm/min (mag × 20k) dip-speed.....	157
Figure 5.36: electron-micrograph showing (a) surface of coated corroded samples of i) 10% SiO ₂ 80:20 mol% MTES:TEOS and ii) 10% SiO ₂ 40:60 mol% OTES:TEOS (mag ×500) and (b) cross-section of i) 10% SiO ₂ 80:20 mol% MTES:TEOS and ii) 10% SiO ₂ 40:60 mol% OTES:TEOS (mag ×10k). Arrows highlight cracks present in Figure (a i) whereas arrows indicate OIH alkoxysilane coatings in Figure b).....	160
Figure 5.37: electron-micrograph showing 10% SiO ₂ double coating applications of (a) MTES:TEOS i) 60:40 mol% ii) 80:20 mol%; b) OTES:TEOS i) 20:80 mol% ii) 40:60 mol%. Images were captured under x10k magnification.	161
Figure 5.38: a) Bode Impedance b) Bode phase angle c) Nyquist and d) potentiodynamic plots obtained for corroded iron metal coated with 10% SiO ₂ 20:80 mol% OTES:TEOS, 40:60 mol% OTES:TEOS, 60:40 mol% MTES:TEOS and 80:20 mol% MTES:TEOS.....	162
Figure 5.39: Particle size measurements for a) 2.5% SiO ₂ 60:40 mol% MTES:TEOS sols b) 2.5% SiO ₂ 20:80 mol% OTES:TEOS sols developed in EtOH, FMA:EtOH 1:4 (v/v), FMA:EtOH 1:1 (v/v) and EGBE solvent	163
Figure 5.40: Electron-micrograph showing 2.5% SiO ₂ double coating applications of a) MTES:TEOS 60:40 mol% b) OTES:TEOS 20:80 mol% in solvent (i) ethanol; ii) 20% (vol/vol) FMA in ethanol; iii) 50% (vol/vol) FMA in ethanol; and iv) EGBE. Images were captured under x10k magnification.	165

Figure 5.41: Electron micrograph of 10% SiO ₂ 60:40 mol% MTES:TEOS coated corroded surface where solvent used as diluent was a) ethanol at mag x500 and b) ethylene glycol butyl ether at mag x1000. Cracks are indicated with arrows.....	166
Figure 5.42: Electron micrograph of 10% SiO ₂ 20:80 mol% OTES:TEOS coated corroded surface using EGBE as diluent at mag x500.....	167
Figure 5.43: Electron micrograph of 10% SiO ₂ 60:40 mol% MTES:TEOS coated corroded surface using mixture of FMA:EtOH a) 1:1 and b) 1:4 (v/v). images generated at x500 magnification.....	168
Figure 5.44 a) Bode Impedance b) Bode phase angle c) Nyquist and d) potentiodynamic plots obtained for corroded metal coated with 10% SiO ₂ 60:40 mol% MTES:TEOS and 20:80 mol% OTES:TEOS originating from sols that have been dispersed in EtOH, FMA in EtOH, and EGBE solvent.....	170
Figure 5.45: Plot of intensity versus particle size (nm) for 0.01, 0.1 and 1 % (w/v) CNP in ethanol dispersion.	172
Figure 5.46: Plots of intensity versus particle size (nm) for 1% (wt/vol) CNP in water dispersion having CTAB surfactant added in 0.5, 1.0 and 3% (wt/vol) concentrations.....	173
Figure 5.47: Plot of intensity versus particle size (nm) for 100, 300 and 500 ppm CNP in ethanol dispersion.....	174
Figure 5.48: a) Bode impedance b) Bode phase angle c) Nyquist and d) Potentiodynamic plots of 2.5% SiO ₂ MTES:TEOS 60:40 mol% with CNP in various concentrations. Plots include a blank coating (0 ppm CNP) and bare metal for comparative purposes.....	175
Figure 5.49: Electron micrographs of surface of double coated 2.5% MTES:TEOS 60:40 mol% + 100 ppm CNP at a) high magnification (×20,000) b) low magnification (×200).....	177
Figure 5.50: EDS analysis on surface of double coated 2.5% MTES:TEOS 60:40 mol% + 100 ppm CNP at magnification x2000 showing microparticle deposit, cross indicating the points of EDS analysis A and B. Figure features EDX analysis at points A and B together with Wt % table of elements of sampled spots A and B.....	178
Figure 5.51: PS plots of intensity versus particle size for a) 1 M TEOS SNP at various times during sol development and b) SNP from different TEOS concentrations, conducted after 24hr sol development.....	179
Figure 5.52: Particle size measurements obtained for 2.5% 60:40 mol% MTES:TEOS sol, 1M TEOS SNP sol (26 nm SNP), mixture of 2.5% 60:40 mol% MTES:TEOS with 0.025% SNP and 2.5% 60:40 mol% MTES:TEOS with 0.0025% SNP. Results are represented as a) % intensity and b) % volume versus size plots.....	180
Figure 5.53: a) Bode impedance b) Bode phase angle c) Nyquist and d) Potentiodynamic plots for different sized SNP added to MTES:TEOS 60:40 mol% coatings. SNP sols were then introduced into the 2.5% SiO ₂ acidic sol at a concentration of 1% SiO ₂ . Plots include a blank coating (0 M SNP) and bare metal for comparative purposes.....	182
Figure 5.54: Electron micrographs of (a) (i) 5% SiO ₂ MTES:TEOS 60:40 mol% ii) 5% SiO ₂ MTES:TEOS 60:40 mol% + 1% SiO ₂ 26 nm SNP and (b) MTES:TEOS:SNP 60:20:20 mol% (5% SiO ₂ total). Images were obtained using a ×2000 magnification.....	183

Figure 5.55: a) Bode impedance b) Bode phase angle c) Nyquist and d) Potentiodynamic plots for 5% SiO ₂ MTES:TEOS 60:40 mol%, 5% SiO ₂ MTES:TEOS 60:40 mol% + 1% 26 nm SNP and MTES:TEOS:SNP 60:20:20 mol% (5% SiO ₂ total).	185
Figure 5.56: a) Bode impedance b) Bode phase angle c) Nyquist and d) Potentiodynamic plots for 5% SiO ₂ MTES:TEOS 60:40 mol% with various concentrations of 26 nm SNPs.....	187
Figure 5.57: Electron micrograph of corroded coupons coated with 10% SiO ₂ MTES:TEOS 60:40 mol% double coating including a) 100 ppm CNP and b) 1% SNP. Images were obtained at a ×500 magnification, arrow highlights crack formation.....	190
Figure 5.58 a) Bode impedance b) Bode phase angle c) Nyquist and d) Potentiodynamic plots for 10% SiO ₂ 60:40 mol% MTES:TEOS (blank) together with 100 ppm CNP and 1% SNP on cleaned corroded surface.	191
Figure 5.59: Particle size measurements for 2.5% SiO ₂ MTES:TEOS 60:40 mol% sols doped with a) cerium (iii) nitrate hexahydrate (Ce), b) pyrrolidine (Pyr), c) 1-naphthol (1-N), d) 1,4-naphthoquinone (1,4-N), e) 2-hydroxypyridine (2-H), f) phenylbenzoate (PhB) in 0.0001, 0.001 and 0.01 M concentrations. The measurements have been taken just after the addition of inhibitor to developed sols. Plots also feature 0 M inhibitor concentrations (blank MTES:TEOS 60:40 mol%) for comparative reasons.....	195
Figure 5.60: Particle size measurements for 2.5% SiO ₂ OTES:TEOS 20:80 mol% sols doped with a) cerium (iii) nitrate hexahydrate (Ce), b) pyrrolidine (Pyr), c) 1-naphthol (1-N), d) 1,4-naphthoquinone (1,4-N), e) 2-hydroxypyridine (2-H), f) phenylbenzoate (PhB) in 0.0001, 0.001 and 0.01 M concentrations. The measurements have been taken just after the addition of inhibitor to developed sols. Plots also feature 0 M inhibitor concentrations (blank OTES:TEOS 20:80 mol%) for comparative reasons.....	196
Figure 5.61: Particle size measurements obtained for various concentrations of phenylbenzoate in a) MTES:TEOS 60:40 mol% sol and b) OTES:TEOS 20:80 mol% sol i) just after the addition of inhibitor to developed sols (T=0) and ii) 24 hrs after the addition of inhibitor to developed sols (T= 24 hrs).....	199
Figure 5.62: Infra-red spectra showing IR window at 4000-400 cm ⁻¹ region for a) 2.5% SiO ₂ 60:40 mol% MTES:TEOS and b) 2.5% SiO ₂ 20:80 mol% OTES:TEOS doped with inhibitors: i) blank coatings, ii) cerium (iii) nitrate hexahydrate (Ce), iii) pyrrolidine (Pyr), iv) 1-naphthol (1-N)	203
Figure 5.63: Infra-red spectra showing IR window at 4000-400 cm ⁻¹ region for a) 2.5% SiO ₂ 60:40 mol% MTES:TEOS and b) 2.5% SiO ₂ 20:80 mol% OTES:TEOS doped with inhibitors: i) blank coatings, ii) 1,4-naphthoquinone (1,4-N), iii) 2-hydroxypyridine (2-H), iv) phenylbenzoate (PhB).....	204
Figure 5.64: Infra-red spectra showing IR window at 4000-400 cm ⁻¹ region for i) cerium (iii) nitrate hexahydrate, ii) pyrrolidine (Pyr), iii) 1-naphthol (1-N) iv) 1,4-naphthoquinone (1,4-N), v) 2-hydroxypyridine (2-H), vi) phenylbenzoate (PhB).....	205
Figure 5.65: a) Bode Impedance, b) Bode Phase angle, c) Nyquist, and d) Potentiodynamic plots for various concentrations of cerium (iii) nitrate hexahydrate (Ce) inhibitor in 2.5% SiO ₂ 60:40 mol% MTES:TEOS coatings. Plots include bare metal for comparative purposes.....	211

Figure 5.66: a) Bode Impedance, b) Bode Phase angle, c) Nyquist, and d) Potentiodynamic plots for various concentrations of 1-naphthol (1-N) inhibitor in 2.5% SiO ₂ 60:40 mol% MTES:TEOS coatings.....	212
Figure 5.67: a) Bode Impedance, b) Bode Phase angle, c) Nyquist, and d) Potentiodynamic plots for various concentrations of 1,4-naphthoquinone (1,4-N) inhibitor in 2.5% SiO ₂ 60:40 mol% MTES:TEOS coatings.....	213
Figure 5.68: a) Bode Impedance, b) Bode Phase angle, c) Nyquist, and d) Potentiodynamic plots for various concentrations of phenylbenzoate (PhB) inhibitor in 2.5% SiO ₂ 60:40 mol% MTES:TEOS coatings.....	214
Figure 5.69: a) Bode Impedance, b) Bode Phase angle, c) Nyquist, and d) Potentiodynamic plots for various concentrations of 2-hydroxypyridine (2-H) inhibitor in 2.5% SiO ₂ 60:40 mol% MTES:TEOS coatings.....	215
Figure 5.70: a) Bode Impedance, b) Bode Phase angle, c) Nyquist, and d) Potentiodynamic plots for various concentrations of pyrrolidine (Pyr) inhibitor in 2.5% SiO ₂ 60:40 mol% MTES:TEOS coatings.....	216
Figure 5.71: a) Bode Impedance, b) Bode Phase angle, c) Nyquist, and d) Potentiodynamic plots for various concentrations of cerium (iii) nitrate hexahydrate (Ce) inhibitor in 2.5% SiO ₂ 20:80 mol% OTES:TEOS coatings.	217
Figure 5.72: a) Bode Impedance, b) Bode Phase angle, c) Nyquist, and d) Potentiodynamic plots for various concentrations of 1-naphthol (1-N) inhibitor in 2.5% SiO ₂ 20:80 mol% OTES:TEOS coatings.	218
Figure 5.73: a) Bode Impedance, b) Bode Phase angle, c) Nyquist, and d) Potentiodynamic plots for various concentrations of 1,4-naphthoquinone (1,4-N) inhibitor in 2.5% SiO ₂ 20:80 mol% OTES:TEOS coatings.	219
Figure 5.74: a) Bode Impedance, b) Bode Phase angle, c) Nyquist, and d) Potentiodynamic plots for various concentrations of phenylbenzoate (PhB) inhibitor in 2.5% SiO ₂ 20:80 mol% OTES:TEOS coatings.	220
Figure 5.75: a) Bode Impedance, b) Bode Phase angle, c) Nyquist, and d) Potentiodynamic plots for various concentrations of 2-hydroxypyridine (2-H) inhibitor in 2.5% SiO ₂ 20:80 mol% OTES:TEOS coatings.	221
Figure 5.76: a) Bode Impedance, b) Bode Phase angle, c) Nyquist, and d) Potentiodynamic plots for various concentrations of pyrrolidine (Pyr) inhibitor in 2.5% SiO ₂ 20:80 mol% OTES:TEOS coatings.	222
Figure 5.77: EIS results for 2.5% SiO ₂ 60:40 mol% MTES:TEOS coating taken at different times from start of OCP doped with a) 0.001 M Ce and b) 0.01 M PhB where i) Bode Impedance, ii) Bode Phase angle and iii) Nyquist plots.....	223
Figure 5.78: a) Bode Impedance, b) Bode Phase angle, c) Nyquist, and d) Potentiodynamic plots for various concentrations of Ce inhibitor in 10% SiO ₂ 60:40 mol% MTES:TEOS coatings on corroded surface.....	225
Figure 5.79: Scanning electron micrograph showing cross-section of double layered coatings consisting of (a) Paraloid B-48 i) 2.5% (×20k mag) ii) 5% (×20k mag) iii) 10% (×10k mag) iv) 15% (×5k mag); (b) 15% Paraloid B-72 i) 2.5% (×20k mag) ii) 5% (×10k mag) iii) 10% (×10k mag) iv) 15% (×5k mag); (c) 75% Ercalene (×5k mag), d) 20% SiO ₂ MTES:TEOS 60:40 mol% (×10k mag)....	227

Figure 5.80: Scanning electron micrographs for corroded iron surfaces double coated with a) 15% Paraloid B-48 b) 15% Paraloid B-72 and c) 75% Ercalene at i) $\times 500$ mag and ii) $\times 2000$ mag.....	229
Figure 5.81: Micrographs showing 10% SiO ₂ MTES:TEOS 60:40 mol% coated coupons that have been deposited by a) dip coating using i) $\times 5$ and ii) $\times 20$ mag b) fine brush i) $\times 5$ and ii) $\times 20$ mag c) coarse brush i) $\times 2.5$ and ii) $\times 5$ mag and d) sponge application i) $\times 2.5$ and ii) $\times 5$ mag.....	231
Figure 5.82: Electron micrograph showing the surface and a cross-section through double coatings a) 10% SiO ₂ of i) MTES:TEOS 60:40 mol% (mag $\times 10k$) ii) PrTES:TEOS 50:50 mol% (mag $\times 10k$) iii) HTES:TEOS 30:70 mol% (mag $\times 10k$) iv) OTES:TEOS 20:80 mol% (mag $\times 5k$) v) PhTES:TEOS 40:60 mol% (mag $\times 10k$); b) 15% Paraloid B-48 (mag $\times 5k$) c) 15% Paraloid B-72 (mag $\times 5k$) and c) 75% Ercalene (mag $\times 5k$). Coatings were applied using a fine brush.....	233
Figure 5.83: Images of scars inflicted onto iron coupons coated with 2.5% Paraloid B48, B72 and 75% Ercalene. Plots of scan distance versus penetration depth for ‘during scratch’ and scratch profile after scratch for the three coatings also feature in this Figure.....	235
Figure 5.84: Electrochemical data obtained for Paraloid B-48 double-coated clean polished surface where a) Bode Impedance b) Bode Phase angle c) Nyquist and d) Potentiodynamic plots at various acrylate concentrations.....	238
Figure 5.85: Electrochemical data obtained for Paraloid B-72 double-coated clean polished surface where a) Bode Impedance b) Bode Phase angle c) Nyquist and d) Potentiodynamic plots at various acrylate concentrations.....	239
Figure 5.86: Electrochemical data obtained for 75% Ercalene double-coated clean polished surface where a) Bode Impedance b) Bode Phase angle c) Nyquist and d) Potentiodynamic plots.....	240
Figure 5.87: Electrochemical data obtained for Paraloid B-48 double-coated corroded surface where a) Bode Impedance b) Bode Phase angle c) Nyquist and d) Potentiodynamic plots at various acrylate concentrations.....	242
Figure 5.88: Electrochemical data obtained for Paraloid B-72 double-coated corroded surface where a) Bode Impedance b) Bode Phase angle c) Nyquist and d) Potentiodynamic plots at various acrylate concentrations.....	243
Figure 5.89: Electrochemical data obtained for 75% Ercalene lacquer double-coated corroded surface where a) Bode Impedance b) Bode Phase angle c) Nyquist and d) Potentiodynamic plots.....	244
Accelerated corrosion (salt spray) testing	244
Figure 5.90: Photographs of clean iron coupons before (cycle 0) and after several cycles (cycle 1-10) in 0.6% (wt/wt) NaCl solution for polished iron coupons (bare metal) as comparison for coated coupons. Coupons have been double-coated with 10% SiO ₂ MTES:TEOS 60:40 mol% and deposited via dip coating (D), fine-brush (FB), coarse-brush (CB) and sponge application (S).	246
Figure 5.91: Photographs of clean iron coupons before (cycle 0) and after several cycles (cycle 1-10) in 0.6% (wt/wt) NaCl solution for polished iron coupons (bare metal) as comparison for coated coupons. Coupons have been double coated with 10% SiO ₂ PrTES:TEOS 60:40 mol% and deposited through dip coating (D), fine brush (FB), coarse brush (CB) and sponge application (S).....	247
Figure 5.92: Photographs of clean iron coupons before (cycle 0) and after several cycles (cycle 1-10) in 0.6% (wt/wt) NaCl solution for polished iron coupons (bare metal) as comparison for coated coupons. Coupons have been double coated with 10% SiO ₂ HTES:TEOS 60:40 mol% and deposited through dip coating (D), fine brush (FB), coarse brush (CB) and sponge application (S).....	248

Figure 5.93: Photographs of clean iron coupons before (cycle 0) and after several cycles (cycle 1-10) in 0.6% (wt/wt) NaCl solution for polished iron coupons (bare metal) as comparison for coated coupons. Coupons have been double coated with 10% SiO ₂ OTES:TEOS 60:40 mol% and deposited through dip coating (D), fine brush (FB), coarse brush (CB) and sponge application (S).....	249
Figure 5.94: Photographs of clean iron coupons before (cycle 0) and after several cycles (cycle 1-10) in 0.6% (wt/wt) NaCl solution for polished iron coupons (bare metal) as comparison for coated coupons. Coupons have been double coated with 10% SiO ₂ PhTES:TEOS 60:40 mol% and deposited through dip coating (D), fine brush (FB), coarse brush (CB) and sponge application (S).....	250
Figure 5.95: Photograph of HTES:TEOS 30:70 mol% coated coupon following first cycle (left image). Right image shows the covering of corrosion spots in red when the brightness of the image is adjusted accordingly using image J.	251
Figure 5.96: Photographs of clean iron coupons before (cycle 0) and after several cycles (cycle 1-10) in 0.6% (wt/wt) NaCl solution for polished iron coupons (bare metal) as comparison for coated coupons. Coated coupons shown have been double coated with 15% Paraloid B-48, Paraloid B-72 and 75% Ercalene lacquer by dip-coating (D) and fine brush (FB) application.....	252
Figure 5.97: Plot showing immersion time (hrs) required to remove coatings. Coatings that remained intact beyond 240 hrs are marked with (*). Immersion liquids featured in this testing are IPA, NaOH solutions at pH12,13 and 14.....	254
Figure 5.98: Optical micrograph of polished iron coupon that has been coated with 2.5% SiO ₂ 10:90 mol% OTES:TEOS and immersed in pH 14 solution.	255
Figure 5.99: Optical micrograph of polished iron coupon that has been coated with 2.5% SiO ₂ 60:40 mol% PhTES:TEOS and immersed in pH 12 solution which required 96 hrs for removal of coating. Image was acquired after 48hrs from beginning of immersion testing and showing formation of corrosion spots over exposed metallic surface.....	255
Figure 5.100: Number of strokes required to remove coating from the metal surface for all five precursors investigated. The solutions used were pH 14 NaOH solution (100% N), IPA pure solvent (100% I) and mixtures of the two (25:75% N/I, 50:50% N/I, 75:20% N/I).....	257
Figure 7.1: Schema presenting cross-section through coated corroded metal surface. Cracks tend to form where thicker coating deposition occurs.....	275
Figure 9.1: Inhibitor concentration for the six inhibitors studied versus total Impedance (Z_{tot}) for a) MTES:TEOS 60:40 mol% and b) OTES:TEOS 20:80 mol% coatings. Bare metal values indicated through grey line.....	289
Figure 10.1: Plot of lacquer concentration (%) versus total Impedance (Z_{tot}) for 15% Paraloid B-48, B-72, 75% Ercalene and 10% MTES:TEOS 60:40 mol% (labelled as SiO ₂) on a) clean polished iron surface and b) corroded cleaned iron surface applied through dip-coating.....	300
Figure 10.2: Corroded area percentage coverage of coupon surface for the five alkyl alkoxysilane-based coatings considered for salt spray testing conducted over 10 cycles. Each coating system was applied using four methods: dip-coating, fine-brush, coarse-brush and sponge application. Plots include bare metal results for comparative reasons.	305
Figure 10.3: Corroded area percentage coverage of coupon surface calculated through ImageJ software for the five alkyl alkoxysilane-based coatings together with Paraloid and Ercalene lacquers. Each alkyl trialkoxysilane/lacquer was applied through a) dip-coating and b) fine brush. Plots include bare metal results for comparative reasons.	307

LIST OF TABLES

Table 3.1: Chemical composition of high purity Remko iron.....	35
Table 3.2: Mole percent ratio (mol %) of alkyltrialkoxysilane precursor mixtures investigated in this work are marked with an asterisk (*).....	51
Table 3.3: (a) Volumes required for the preparation of 2.5% SiO ₂ exemplary sols listed. X-TES stands for alkyltriethoxysilane where X = methyl, propyl, hexyl, phenyl and octyl and (b) Volumes required for the preparation of 2.5, 5, 10 and 15% SiO ₂ MTES:TEOS 80:20 mol% exemplary sols.	52
Table 3.4: Amounts of chemicals (shown in moles and volume) required to produce several TEOS concentrations of Stöber sol.....	53
Table 3.5: Volumes used to create a final sol consisting of MTES:TEOS 60:40 mol% (5% SiO ₂) loaded with 20, 26 and 56 nm Stober NP (1% SNP) using various starting TEOS concentrations.....	54
Table 3.6: Amounts of CNPs of size 10-20 nm required to produce 100, 300 and 500 ppm CNP-containing 60-40 mol% MTES:TEOS (5% SiO ₂ wt/v).....	55
Table 3.7: Table showing inorganic and organic inhibitors used in this work, chemical name, chemical structure, RMM and melting/boiling point in °C.....	56
Table 3.8: Sols featured in IR Peak Area Analysis.....	60
Table 3.9: Parameters employed for baseline correction of IR spectra using Origin.....	60
Table 3.10: Parameters employed to carry out hardness testing on coated glass slides.....	66
Table 3.11: Scanning parameters employed to carry out surface roughness on clean, corroded and coated coupons.	69
Table 4.1: EEC parameters for runs 1-3 of MTES:TEOS coatings and bare metal where R _{sol} = uncompensated solution resistance, R _{po} = pore resistance of coating, CPE _c = constant phase element of coating, R _t = charge transfer resistance and CPE _{dl} = constant phase element of the double layer formed at the metal-coating interface.....	83
Table 4.2: Measured thickness of silica coatings that have been deposited in this work. Three silica concentrations were considered and deposited in single, double and triple coatings.....	92
Table 4.3: EIS parameters and corrosion current values obtained through electrochemical testing of the various coated surfaces investigated. Bare metal values included for comparative purposes.....	97
Table 5.1: Mean particle size values for peaks obtained for XTES:TEOS sols investigated, Table also includes their corresponding values of polydispersity index (PDI).....	107
Table 5.2: Area% for Peaks 1-8 for MTES, PrTES, HTES, OTES and PhTES in concentrations that allowed for IR testing.....	111
Table 5.3: Elemental analysis along the scratch produced onto MTES:TEOS 60:40 mol% coated iron sample.....	128
Table 5.4: EEC parameters for MTES:TEOS coatings where R _{sol} = uncompensated solution resistance, R _{po} = pore resistance of coating, C _c = coating capacitance, R _t = charge transfer resistance and C _{dl} =	

capacitance of the double layer formed at the metal-coating interface and goodness of fit (GOF).....	138
Table 5.5: EIS parameters modelled using EEC 1 and 2 and I_{corr} values for surfaces studied in Figure 5.30.....	149
Table 5.6: EIS parameters modelled using EEC 1 and 2 and I_{corr} values for coated corroded-cleaned surfaces studied in Figures 5.33 and Figure 5.34.....	156
Table 5.7: Thickness measurements obtained from electron micrographs for double coated 2.5% SiO ₂ 60:40 mol% MTES:TEOS and OTES:TEOS 20:80 mol% dispersed in different solvents.....	164
Table 5.8: EIS parameters modelled using EEC 1 and 2 and I_{corr} values for un/coated corroded surfaces studied in Figure 5.44.....	171
Table 5.9: EIS parameters modelled using EEC 1 and 2 and I_{corr} values for CNP-doped MTES coated surfaces studied in Figure 5.48.....	176
Table 5.10: EIS parameters modelled using EEC 1 and 2 and I_{corr} values for MTES:TEOS coatings with and without the addition of SNPs as obtained from results presented in Figure 5.55.....	186
Table 5.11: EIS parameters modelled using EEC 1 and 2 and I_{corr} values for 5% SiO ₂ 60:40 mol% MTES:TEOS coatings with various concentrations of 26 nm of SNPs as obtained from results presented in Figure 5.56.....	188
Table 5.12: EIS parameters modelled using EEC 1 and 2 and I_{corr} values for 10% SiO ₂ 60:40 mol% MTES:TEOS coatings with 1% SNP and 100 ppm CNP obtained from results presented in Figure 5.58.....	192
Table 5.13: Particle size measurements for 2.5% SiO ₂ MTES:TEOS 60:40 mol% sols doped with cerium (iii) nitrate hexahydrate (Ce), pyrrolidine (Pyr), 1-naphthol (1-N), 1,4-naphthoquinone (1,4-N), 2-hydroxypyridine (2-H), phenylbenzoate (PhB) in 0.0001, 0.001 and 0.01 M concentrations. The measurements have been taken just after the addition of inhibitor to developed sols. Plots also feature 0 M inhibitor concentrations (blank MTES:TEOS 60:40 mol%) for comparative reasons.....	197
Table 5.14: Particle size measurements for 2.5% SiO ₂ OTES:TEOS 20:80 mol% sols doped with cerium (iii) nitrate hexahydrate (Ce), pyrrolidine (Pyr), 1-naphthol (1-N), 1,4-naphthoquinone (1,4-N), 2-hydroxypyridine (2-H), phenylbenzoate (PhB) in 0.0001, 0.001 and 0.01 M concentrations. The measurements have been taken just after the addition of inhibitor to developed sols. Plots also feature 0 M inhibitor concentrations (blank OTES:TEOS 20:80 mol%) for comparative reasons.....	198
Table 5.15: Mean particle size measurements obtained for various concentrations of phenylbenzoate in MTES:TEOS 60:40 mol% and OTES:TEOS 20:80 mol% sols just after the addition of inhibitor to developed sols (T=0) and 24 hrs after the addition of inhibitor to developed sols (T= 24 hrs).....	200
Table 5.16: Elemental analysis of 0.01 M Ce-doped MTES:TEOS 60:40 mol% and 20:80 mol% OTES:TEOS coated iron sample.....	207
Table 5.17: Coating thicknesses for various concentrations of lacquers in their corresponding solvents as applied through dip-coating (280 mm/min). Table features thicknesses for MTES:TEOS 60:40 mol% at several SiO ₂ concentrations (* are taken from Table 4.2).....	228
Table 5.18: Thickness determination of double coatings applied using a fine brush.....	232

Table 5.19: Pull-out force measured when pull-out test is conducted on Paraloid B-48, B-72 and Ercalene. Data for OIH silane coatings marked using (*) is taken from Figure 5.18 is included for comparison purposes.....	236
Table 6.1: Percentage organic content (wt%) calculated for coatings investigated.....	260
Table 6.2: Percentage organic content (wt%) calculated for the five precursors investigated.....	269
Table 7.1: Mean total Impedance, Z_{tot} ($R_{sol}+R_t+R_{po}$) and I_{corr} values for un/coated corroded surfaces considered in Figure 5.38. Table includes weight % organics present in coatings.....	277
Table 7.2: Solvents employed and their physical properties.....	278
Table 7.3: Thickness measurements obtained from electron micrographs for double coated 2.5% SiO ₂ 60:40 mol% MTES:TEOS dispersed in different solvents and their respective vapour pressure in Pa. Values for FMA:EtOH were calculated using Raoult's law.....	279
Table 9.1: List of inhibitors used in this study and their solubilities in water (g/L) at 25 °C.....	291
Table 9.2: Z_{tot} values for six inhibitor molecules that produce the most protective coatings in MTES and OTES and in their respective concentrations	295
Table 11.1: List of mixtures of NaOH and IPA (N/I v/v) that lead to the quickest removal (least strokes) of most protective coatings	315

LIST OF SYMBOLS AND ABBREVIATIONS

HM	Heritage Metal	IPA	isopropyl alcohol
TEOS	tetraethyl orthosilicate	NaOH	Sodium hydroxide
MTES	methyl triethoxysilane	EGBE	ethylene glycol butyl ether
PrTES	propyl triethoxysilane	FMA	Formamide
HTES	n-hexyl triethoxysilane	Ce	Cerium (III) nitrate hexahydrate
OTES	n-octyl triethoxysilane	1-N	1-Naphthol
PhTES	phenyl triethoxysilane	1,4-N	1,4-Naphthoquinone
OIH	organic-inorganic hybrid	PhB	Phenyl benzoate
CNPs	Commercial Nanoparticles	Pyr	Pyrrolidine
SNPs	Stöber Nanoparticles	2-H	2-Hydroxypyridine
SEM	Scanning Electron Microscopy	EtOH	Ethanol
EDS	Energy-Dispersive Spectrometry	H ₂ O	Water

XRD	X-Ray Diffraction	SiO ₂	Silica
PDF	Powder Diffraction Files	HNO ₃	Nitric acid
ICDD	International Centre of Diffraction DATA	NH ₄ OH	Ammonia
DN	Dilute Nitro	KBr	Potassium bromide
DLS	Dynamic Light Scattering	d	Diameter
NNLS	Non-Negative Least Squares	Area %	area percentage
IR	Infra Red	SS strips	Stainless steel strips
UV-vis	Ultraviolet-visible	Hg/Hg ₂ Cl ₂	Mercury/mercury chloride
PS	Particle size	(Z)	impedance modulus
FWHM	Full Width at Half Maximum	(Z)	real impedance
OCP	Open Circuit Potential	(-Z')	imaginary impedance
EIS	Electrochemical Impedance Spectroscopy	R _t	charge transfer resistance
PD	Potentiodynamic	C _{dl}	double layer capacitance
SCE	saturated calomel reference electrode	R _{po}	pore resistance
SHE	Standard Hydrogen Electrode	C _c	coating capacitance
RE	reference electrode	R _{sol}	Solution resistance
CE	counter electrode	<i>I</i> _{corr}	corrosion current density
WE	working electrode	H	Hardness value
NaCl	Sodium chloride	P _{max}	maximum force
RH	Relative humidity	P	Force
PTFE	Polytetrafluoroethylene	h	Depth
r.p.m.	Revolutions per minute	<i>h</i> _{max}	Maximum depth
EEC	equivalent electrical circuit	S	Stiffness
CM	clean polished metal	E _s	elastic modulus of the coating material
CUM	corroded uncleaned metal	E _r	reduced elastic modulus
CCM	corroded-cleaned metal	E _i	Elastic Modulus of the diamond Berkovich indenter
CTAB	cetyltrimethylammonium bromide	<i>v</i> _i	Poisson's ratio of indenter
		R _a	Absolute roughness values

CHAPTER 1:

Introduction

1.1 Protecting Heritage Metal against corrosion

The body of work featured in this thesis was inspired by the need to protect historical irons and low carbon steel artefacts such as the extensive collection of arms and armour hosted at the Palace Armoury, within Grandmaster's Palace in Valletta, Malta. It is a well-known fact that iron and steel corrode when exposed to indoor uncontrolled climates as is the case at the Palace Armoury. One way of protecting metals from corrosion is by applying protective coatings [1].

Nowadays, conservation work practice guidelines have been established and implemented by conservator-restorers *vis-a-vis* coating application for Heritage Metal (HM) protection against corrosion which require that (i) coatings are reversible and can be removed with relative ease, (ii) the entire coating procedure must not change the aesthetics of the object, (iii) coatings have to offer suitable corrosion protection where a guaranteed protection for a minimum of 5 years before the removal and re-application is expected, and (iv) that relatively low temperatures are employed in the process of curing of the coating so as not to alter the metal microstructure [2]. Typically, conservators employ acrylate-based coatings such as Paraloid B-72, nitrocellulose-based formulations such as Frigilene (both of which have been used in the past by conservator-restorers at the Palace Armoury, Valletta) or polycrystalline waxes such as Renaissance wax [1].

1.2 Suitability of OIH alkoxy silane coatings for corrosion protection of HM

This work proposes a novel way of protecting HM through the application of organic-inorganic hybrid (OIH) silica coatings produced through the sol-gel method. Sol-gel materials cover a vast range of inorganic and organic-inorganic (hybrid) materials which share a common preparation strategy: production begins with the generation of a colloidal suspension termed a 'sol' which is then converted into a viscous gel that finally converts into a solid material. This work features silica-based coatings which are applied onto the metal surface whilst still in the sol stage and form a gel as the solvent (dispersing medium) evaporates. Solid protective coatings form once the coatings are cured at elevated temperature (150°C).

HM artefacts are cleaned and polished prior to coating application; however, HM surfaces are generally allowed to be left with black corrosion products after cleaning which are stubborn and difficult to remove compared to the superficial, easily dislodged red corrosion products. The applied coating must therefore be protective on both clean and corroded surfaces. There are several valid reasons for employing OIH alkoxy silane coatings on cultural heritage metals as protective barriers: (i) they form transparent films on surfaces; (ii) they can be designed to have good water repellence, and (iii) they are capable of bonding to corrosion products. Although OIH silica coatings have been extensively studied and well-documented for their good corrosion protection on various clean surfaces of metals, very little work has been done concerning the corroded surface. This work features corrosion testing of coated clean/polished iron surfaces as well as coated corroded iron surfaces so as to capture the extent of corrosion protection offered by these coatings on both kinds of surfaces that are representative of HM surfaces.

1.3 Thesis Structure

This thesis comprises of an Introductory Chapter 1 followed by a Literature Review (Chapter 2) that features relevant and recent literature in the topics featured in the thesis (follows sequence of topics relevant to sections 5.1 to 5.6 described below). Chapter 3 includes a detailed description of the methodology employed in this work. Chapter 4 deals with the method development for achieving the most protective coatings which will feature in the remaining work. The Results of this study are compiled in Chapter 5. This chapter consists of number of sub-sections listed below. The corresponding Discussion chapters are also included for ease of reference:

5.1 ‘The effect of alkyl/aryl functional groups on the mechanical and anti-corrosion properties of OIH alkoxy silane coatings’. The discussion of the results of this section is presented in Chapter 6.

5.2 ‘The corroded iron surface’, The discussion of the results of this section is presented in Chapter 7.

5.3 ‘Addition of silica nanoparticles for the improvement of corrosion protection of OIH alkoxy silane coatings’. The results presented in this Section are discussed in Chapter 8.

5.4 ‘Addition of inorganic and organic inhibitor molecules to OIH alkoxy silane coatings for enhanced corrosion protection’. The results of this Section are discussed in Chapter 9.

5.5 ‘Performance of OIH coatings relative to Paraloid and Ercalene lacquers’. The results of this Section are discussed in in Chapter 10.

5.6 ‘Reversibility of OIH alkoxy silane coatings’. Results discussed in Chapter 11.

The final wrapup conclusions for this thesis are presented in Chapter 12.

1.4 Aims and objectives

The scope of this project is to protect clean and corroded iron surfaces through the application of sol-gel coatings. OIH alkoxy silane coating systems featured in this work were prepared via an acid-catalysed sol-gel route where the precursors consisted of binary mixtures of an alkyl/aryl hybrid precursor of the type $X-Si(OR)_3$ with tetraethoxysilane (TEOS) in various mol% ratios $X-Si(OR)_3$: TEOS. The work has been built sequentially as follows:

- The starting point featured the precursor methyltriethoxysilane in the creation of MTES:TEOS coatings in a 60:40 mol% to which the method for producing the most protective coatings was established. The sample coupons were coated through dip-coating and thinner coatings were initially investigated through the use of low silica concentrations (2.5% SiO_2).
- Based on the initial method optimisation conducted using MTES-based coatings, several other precursors were applied and studied namely, n-propyl-, n-hexyl-, n-octyl- and phenyl-triethoxysilane with TEOS in various mol% ratios. The coatings were characterised using Scanning Electron Microscopy – Energy-Dispersive Spectrometry (SEM-EDS), X-Ray Diffraction, and mechanically tested (pull-out/adhesion testing, nano-scratch and nano-hardness). The coatings' extent of corrosion protection was determined through Electrochemical Impedance Spectroscopy, and potentiodynamic polarisation.
- It was deemed important to establish the mol% ratios $X-Si(OR)_3$: TEOS that would lead to the most protective coatings (where X=methyl, n-propyl-, n-hexyl-, n-octyl- and phenyl-triethoxysilanes). Several ratios were studied for each precursor employed in this work, the most protective coating from the five organic groups studied were then selected and compared. The most and least protective coatings of these five were further considered and applied onto corroded surfaces and their extent of corrosion protection was also evaluated.

- Several attempts were made to enhance the coating's protective properties on corroded surfaces which proved to be difficult and problematic due to cracking issues that arose on such rough surfaces.
- OIH coatings offer a passive mode of protection since they act as a physical barrier that hinders the penetration of aggressive species (chlorides, water) towards the underlying metal. This behaviour can be enhanced through the inclusion of controlled amounts of chemicals possessing the ability to actively retard the corrosion process from occurring when the coating is damaged with time. Silica nanoparticles and in/organic chemical inhibitors have been reported to improve corrosion resistance upon their inclusion in sol-gel OIH coatings and were therefore considered in this work. The effects of inhibitors on the OIH alkoxysilane coatings were studied on both clean and corroded surfaces.
- The commercially available acrylates Paraloid B-72 and Paraloid B-48, together with the nitrocellulose lacquer Ercalene, were included in the study since they are commonly used by conservators to protect Heritage Metals and have been proven to provide a satisfactory corrosion protection, are transparent and easy to apply/remove. These coatings were also assessed through electrochemical testing on both clean and corroded surfaces. It was then possible to compare the performance of these lacquers to previously studied OIH alkoxysilane coatings, thus predicting their suitability for application onto HM.
- The extent of corrosion protection attainable by acrylate-, nitrocellulose- and OIH alkoxysilane-coatings was also assessed and compared through accelerated corrosion (salt-spray) testing. For this study, an increase in silica/acrylate/nitrocellulose concentration was made in order to deposit thicker coatings which were applied using both dip and brush application, the latter being a frequently used mode of application by conservators. Electrochemical and salt spray testing were

used to assess the extent of corrosion protection of coatings which allow for a secure comparative discussion of coatings. However, it was deemed necessary to include salt spray testing so as to provide a richer discussion on coatings' performance.

- The final Section of the work features a reversibility study on all OIH alkoxy silane coatings studied. The concept of reversibility is important in conservation since an effective coating will gradually fail after a number of years and no longer perform its protective function, therefore its removal must be conducted with relative ease prior to the re-application of a fresh coat. Conventional coatings such as Paraloid B-72 are typically dissolved in acetone solvent, but in our case, this is problematic due to the strong silica network formed in OIH coatings which is very well adhered to the metal. The strong bond formed between the silica and metal can be reversed using a 1.0 M solution of sodium hydroxide pH ~ 14; however, practically speaking this is not ideal since it requires caution when handling in high concentrations of alkalis. Since coatings differ not only in their organic group identity (X in X-Si(OR)₃) but in their proportion to TEOS (mol% X-Si(OR)₃ : TEOS) it was postulated that the more organic-containing coatings would be removed using isopropyl alcohol (IPA) or by a mixture of IPA and NaOH, thus forming a safer cleaning fluid for the removal of OIH silane coating.

CHAPTER 2:

Literature review

2.1 Introduction to corrosion and prevention strategies

Steel was historically used in a myriad of applications including structural, marine, military and aerospace. While this metal is exploited for its physical characteristics, such as stiffness and high strength-to-weight ratio, it is unfortunately susceptible to corrosion in aggressive environments [3]. Corrosion causes energy and material losses and has been documented as being one of the largest single expense in the US economy which has been estimated to cost over \$1.1 trillion in 2016 [4], this figure being applicable to the US alone. One common way of protecting metals from corrosion is to apply coatings. There are several techniques for the deposition of coatings on metals, including physical vapour deposition, chemical vapour deposition, electrochemical deposition, plasma spray and sol-gel [5]; the latter will be discussed in detail in the following section as it is the mode of application in this work.

2.2 Formation of protective coating through the sol-gel process

Sol-gel materials encompass a wide range of inorganic and organic-inorganic hybrid (OIH) materials which share a common preparation strategy. The sol-gel process can be described as the generation of colloidal suspensions (sols), which are subsequently converted into viscous gels and finally into solid materials [6]. Over the past three decades or so, soaring interest in research into OIHs via the sol-gel process has occurred due to their impressive range of applications, including controlled release of proteins [7], protective coatings [8], adsorption [9], chromatography [10], biotechnology [11], energy conservation [12], cultural heritage conservation and restoration [13], environmental remediation [14], and many other fields of contemporary technology [15]. In 1997, Guglielmi [16] discussed the potential of sol-gel coatings as a corrosion inhibiting system for metal substrates. Since then, a large amount of research into sol-gel based coatings for metal protection has been conducted which is reflected in the number of review papers [17-20,16,21-23,5,24,25] published on the topic. Sol-gel has been used as surface protection on a variety of metals such as zinc [26], copper [27], steel [28] and aluminium [29]; the latter of which has been well studied due to its aerospace application [5].

Sol-gel coatings can be prepared via two main methods, using purely inorganic precursors or using organic or hybrid precursors. The inorganic route involves the growth and expansion of networks through the formation of a colloidal suspension, typically oxides such as titanium dioxide nanosols from titanium (III) chloride [30] and gelation of the sol to form a solid network in continuous liquid phase. The more widely used method is the organic approach, which generally starts with a solution of monomeric metal or metalloid alkoxide precursors $M(OR)_n$ in an alcohol or other low-molecular weight organic solvent where M represents a network-forming species, such as Si, Ti, Zr, Al, Fe, B, etc. and R is typically an alkyl group ($C_xH_{(2x+1)}$) [5].

A lot of early work was conducted using non-silicate sol-gels through the organic method which have proven to be effective as corrosion protection namely, metal alkoxides of titanium [31-34],

zirconium [35-38], tin [39], cerium [39,40] and aluminium [41,42]. These metal alkoxides are much more reactive towards water than alkoxysilanes due to the lower electronegativity and higher Lewis acidity [5] which brings forward an advantage in that silica-based alkoxides undergo milder and more stable reactions which has led alkoxysilanes to become the most extensively studied in the formation of sol-gel coatings.

This work focuses on the application of trialkoxysilanes as the basic precursor molecules for formation of sol-gel-based coatings. These molecules have a general formula of $X-Si(OR)_3$ where X denotes a non-hydrolysable organic functionality, and OR indicates hydrolysable alkoxy- groups commonly methoxy ($-OCH_3$) or ethoxy ($-OC_2H_5$) groups. These precursor materials have been widely used as adhesion promoters in paints, fillers, and binders in the industry of glass/polymer composites [43]. OIH materials play an important part in research and development activities and technology portfolio in companies such as Bayer, Boeing GE, BASF, Dow Corning; and also feature in more specialised enterprises such as Henkel, Procter and Gamble, Wacker, Nissan Chemicals, Mitsubishi Chemicals and Merck [20].

OIH coating application through sol-gel method confers several advantages over other modes of coating application; for instance, the sol-gel processing temperature is generally low, frequently close to room temperature which translates to minimal volatilisation and degradation of organics and entrapped species such as organic inhibitors [6]. Liquid sols allow for casting of coatings into complex shapes and to produce thin films without the need for machining or melting. Sol-gel film formation is an environmentally friendly technology since the method is waste-free and excludes the stage of washing [5]. Moreover, non-toxic solvents are typically utilised, such as ethanol and isopropyl alcohol. Steel surface substrates have been conventionally passivated through a chromating processes. The scope of this treatment is to generate a passivation layer which is capable of resisting further corrosion. However, due to the high environmental toxicity associated with the use of chromates, efforts have been made to find alternatives which do not pose such risks. OIHs obtained through the sol-gel method have been considered as such suitable alternatives [20]. Another

advantage of using OIH as protective coatings is that during the sol development stage, mild chemical conditions are employed as hydrolysis/condensation reactions are acid or base-catalysed but extreme pH conditions are normally avoided. This allows for the inclusion of pH sensitive organic species such as dyes, biological species including enzymes which can still retain their function [44].

Despite their exploitation over the past decades due to their effectiveness and ease of use, sol-gel materials are not without limitations; for instance, the precursors are often expensive and moisture-sensitive [6]. The process is also time-consuming since several hours are required to develop the sol. Depositing a uniform layer on the substrate and the curing process are crucial factors to ensure the quality of anti-corrosive coatings [6]. Delamination, cracking, adhesion, and thickness limits are issues frequently requiring attention when coating metals through sol-gel process [20].

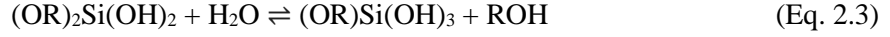
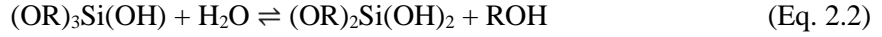
2.3 Sol-gel process

2.3.1 Main stages of the sol-gel process

The sol-gel process comprises of four stages: i) hydrolysis of precursor molecules, ii) polycondensation of monomers to form chains and/or particles, iii) polymer particle growth and iv) agglomeration of the polymer particles to form networks extending through the liquid medium resulting in thickening and the eventual formation of a gel [5]. Typically, the sol is applied to the metal surface prior to the gelation stage. The most common application techniques include electrochemical deposition [45], spray [46], dip- [47] or spin- [48] coating. The sol-gel process enables user-friendly coating deposition on substrates with a large surface area involving simple and inexpensive equipment [20]. In order for the deposited sol to form a durable coating, further subsequent development, drying and densification is required through curing in an oven, to form a dense ceramic coat.

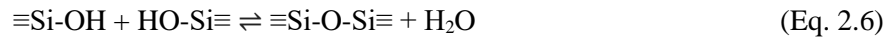
For tetraalkoxysilanes, the sol-gel process can be represented through the following six stages [49]:

i) Hydrolysis:



If $\text{R} = \text{CH}_3$, the precursor molecule is tetramethoxysilane (TMES). If $\text{R} = \text{CH}_2\text{CH}_3$ the precursor is tetraethoxysilane (TEOS). The latter precursor is the more frequently used.

ii) Condensation and polymerisation of monomers to form chains and particles:



iii) Growth of the particles [50]:

The growth of particles can be one-dimensional, leading to the formation of long-shaped particles when polycondensation takes place immediately after hydrolysis of one or two $-\text{OR}$ groups of a molecule (Eq 2.1-2.2). The growth may be three-dimensional, leading to the formation round particles when polycondensation does not take place until all of the $-\text{OR}$ groups of a molecules are hydrolysed to OH groups (Eq. 2.4).

iv) Gelation:

Gelation involves the agglomeration of the polymeric particles followed by the formation of networks that extend throughout the liquid medium resulting in thickening to the point where the liquid no longer flows freely, thus forming a gel. Although the mixture has a high viscosity, many sol particles remain entrapped in the spanning cluster. Once gelation has occurred, further cross-linking of the isolated sol particles into the spanning cluster follows [49].

v) Drying of the resulting gel:

The gel will shrink by an amount equal to the volume of liquid (water, alcohol or a mixture of both) which has evaporated and is termed the constant rate period, can only occur in gels which remain flexible and compliant, and able to adjust to the reduced volume. As the gel continues to dry and shrink it becomes more compact and further cross-linking lead to increased stiffness. The critical point is reached when liquid evaporation does not lead to further shrinkage but instead, the gel becomes sufficiently stiff to resist further shrinkage. At this stage, the liquid begins to recede into the porous structure of the gel. Since the gel pores are small, large pressures are generated across the curved interfaces of the liquid menisci within the pores. Such capillary stresses could lead to cracking of the sample, unless the gel has been very carefully prepared to have optimum cross-linking [6].

vi) Densification through heat treatment.

Although there are several applications of silica gels prepared and dried at or close to room temperature, heat treatment is often required for the production of dense glasses from gels. At low temperatures ($< 200\text{ }^{\circ}\text{C}$) weight loss occurs as pore surface water/alcohol evaporates, but little further shrinkage takes place. At higher temperatures ($200\text{-}500\text{ }^{\circ}\text{C}$), samples generally show both weight loss but little shrinkage due to a loss in organics (pyrolysis). The glass transition temperature is reached when temperature is increased beyond $500\text{ }^{\circ}\text{C}$ where viscous flow occurs leading to rapid densification as thermal energy allows for an extended structural re-organisation.

2.3.2 Reaction parameters affecting the hydrolysis process

- *Effect of pH*

The isoelectric point of silica (i.e. point of zero charge for the silica species) occurs at around pH 2.2 and it is at this acidic pH that the rate of gelation will be the slowest and is represented by the longest gel times. Rates of reaction (hydrolysis and polycondensation) increase as the pH is shifted away from pH 2.2 by making it more acidic or basic [49]. The first step during hydrolysis of a silicon alkoxide can be initiated in both acidic and basic conditions and the mechanism is shown in **Figure 2.1**.

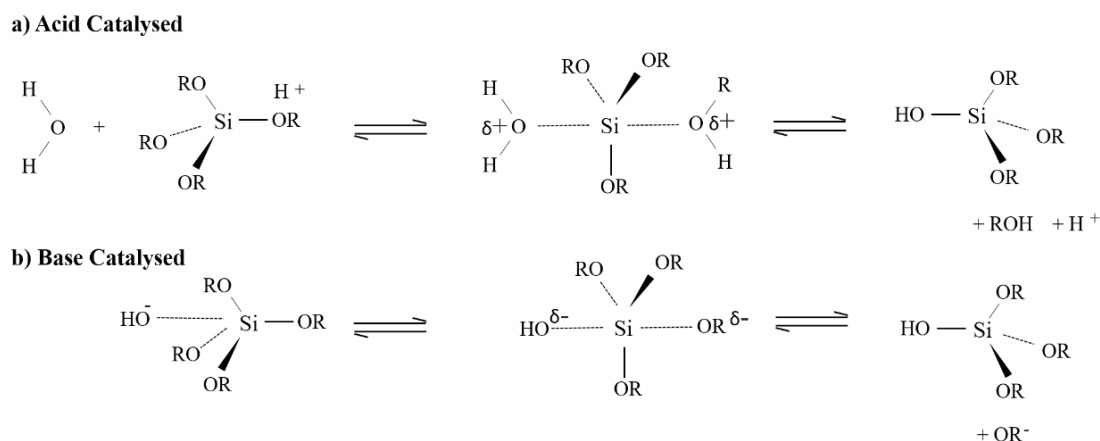


Figure 2.1: Hydrolysis mechanism for a silicon alkoxy under a) acidic and b) basic conditions (adapted from [6]).

- *Precursor substituent effects*

The rate trends in acid and base catalysed processes for the successive hydrolysis of the four alkyl (R) groups (as seen in Eq. 2.1 - 2.4 hydrolysis steps) around silicon can be appreciated in terms of electronic effects. Alkoxy groups are relatively more electron donating than hydroxyl groups and therefore for the positively charged transition state of the acid-catalysed reaction (Figure 2.1 (a)), the more alkoxy groups are replaced by hydroxyl groups results in a less and less stabilised transition state, translating in a decrease in the rate of reaction. Conversely, for the negatively charged transition state of the base-catalysed reaction (Figure 2.1 (b)), more OH group substitution on the silica species leads to a more stabilised transition state and faster reaction [6]. The size of the alkoxy group exerts a large influence on the rates of hydrolysis where larger alkoxy groups lead to more steric hindrance and overcrowding of the transition state, thus resulting in slower rates of reaction. For instance, the methoxy- (-OCH₃) bearing tetramethoxysilane (TMOS) hydrolyses faster than the ethoxy(-OCH₂CH₃) bearing tetraethoxysilane (TEOS).

- *Hydrophobic effects and co-solvents*

Apart for electronic and steric effects of the substituents explained above, the hydrophobic/hydrophilic character of the precursor must also be taken into consideration. Due to the hydrophobic nature of the ethoxy groups, TEOS and water are immiscible in all proportions and it

is therefore necessary to add a co-solvent. However, since alcohol is a by-product of the hydrolysis reaction, if the precursor and water can be mechanically mixed and induced to react e.g. through ultrasonic probe or stirring, eventually a single-phase mixture can be achieved. If larger, thus more hydrophobic, alkyl/aryl organic substituents replace the ethyl groups in TEOS, the miscibility issue aggravates. If mixtures of two or more different precursor silanes are used, such effects may lead to phase separation in the final gels.

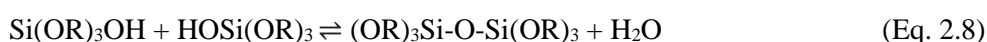
Different co-solvents have been utilised; including alcohols, formaldehyde, dimethylformamide, 1,4-dioxane and tetrahydrofuran. The identity of the chosen co-solvent/s is important, since use of a different alcohol from that produced as a by-product of the hydrolysis step can lead to transesterification of the two kinds of alcohols which may significantly affect the whole hydrolysis and condensation reactions [6].

- *Effect of water:alkoxide ratio*

For the complete hydrolysis of the alkoxide groups, the water:alkoxide molar ratio is required to be 4 [50]:



In practice, less water can be introduced since the condensation reaction itself generates water:



If the amount of water becomes very small, however, the hydrolysis rate slows down due to the reduced reactant concentration, whereas if excessive amounts of water are used, the alkoxide is effectively diluted.

2.3.3 The effect of pH on condensation process

Condensation reaction can either generate alcohol (Eq. 2.5) or water (Eq. 2.6) [6]. As with initial hydrolysis, the reaction proceeds via the rapid formation of a charged intermediate by reaction with a proton or hydroxide ion depending on the set pH, followed by slow attack of a second neutral silicon species on this intermediate (**Figure 2.2**):

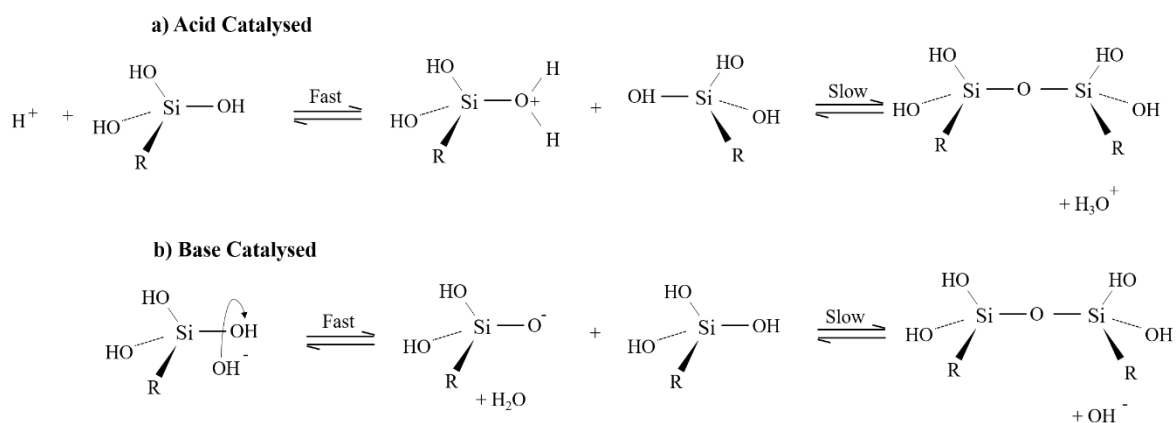


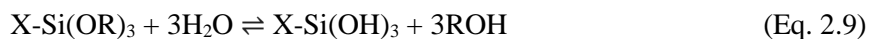
Figure 2.2: Condensation mechanism in a) acidic and b) basic medium adapted from [6].

As with hydrolysis, the rates of reaction of these two species depends on steric effects and the charge on the transition state: for acid hydrolysis producing a positively charged transition state stabilised by electron donating groups, the HO-Si(OR)₃ species condenses faster than the (HO)₂Si(OR)₂, which in turn condenses faster than the RO-Si(OH)₃ i.e. during acid catalysed reactions, the first step also undergoes the fastest condensation (Figure 2.2 (a)). This creates an open network structure initially, followed by further hydrolysis and cross-condensation reactions [6]. In base-catalysed conditions the negatively charged transition state increasingly becomes more stable as the hydroxyl groups replace the electron donating alkoxy groups which lead to the successive hydrolysis steps occurring increasingly faster where finally the fully hydrolysed species undergoes the fastest condensation reactions (Figure 2.2 (b)). This translates to the formation of a highly cross-linked large sol particles initially obtained and will eventually link to form gels with large pores between the interconnected particles. Therefore, the choice of acid or base catalyst impacts the nature of the gel which is formed. Practically speaking, the hydrolysis/condensation reactions are such that for real systems, where hydrolysis and condensation proceed concurrently, the overall reaction kinetics rapidly become complex and difficult to predict.

2.4 Organic- inorganic hybrid sol-gels

Organic-inorganic hybrid (OIHs) sol-gel coatings are more popular for corrosion protection of metal substrates than pure inorganic oxide layers since OIH coatings can form micrometer thick coatings without the risk of cracking and generally require lower curing temperature (< 150 °C) compared to > 400 °C for pure oxide layers [5]. For purposes of this work, only the silicon-based OIH coatings will follow in the discussion.

OIHs coatings consist of an inorganic part which is formed from the hydrolysis of a silicon alkoxysilane such as TEOS (previously described in Eq. 2.1-2.4), while also including an organic group-containing silicon alkoxysilane which remains after hydrolysis step [20] (see Eq. 2.9 below). The introduction of a non-hydrolysable substituent on the silicon atom of a precursor molecule (X-Si(OR)₃), such as methyl triethoxysilane (MTES) has a dramatic effect on the material obtained after polycondensation of the hydrolysed monomers.



Different OIH gels possessing different properties [6] can be produced depending on the functional groups (X in X-Si(OR)₃) present in the starting precursor reagents following the same steps involved in the sol-gel process described previously. Moreover, in order to fine-tune their properties, sol-gel materials have been prepared using mixtures of tetra-functional precursors (such as TMOS, TEOS) and organotrialkoxysilanes in various relative ratios. The presence of the “dead ends” created by the non-hydrolysable organic moieties will impact the chemistry of the pore surface, thus affecting the properties of the resulting material [49]. OIH are effective for corrosion protection since they combine the properties of organic polymeric materials with those of ceramics.

The inorganic components contribute to scratch resistance, durability and adhesion to the metallic substrate while the organic components increase the flexibility of the coating which leads to the formation of homogeneous and defect-free coatings. Such coatings are achievable through a single

coating application thus reducing the need to deposit multiple layers to obtain a final desired thickness [3].

The bonding mechanism of alkoxy silanes to metal surfaces is described in **Figure 2.3**. Silanols (-SiOH) spontaneously adsorb onto the metallic surface through hydrogen bonds. Since the metallic surface possesses M-OH groups, a condensation reaction occurs upon drying with the silanol groups and results in the formation of covalent metallo-siloxane bonds (M-O-Si) at the coating-metal interface [5,20]. The creation of such hydrolyzable stable Si-O-M chemical bonds accounts for the strong interaction and good adhesion performance of the coating with the metal surface [25].

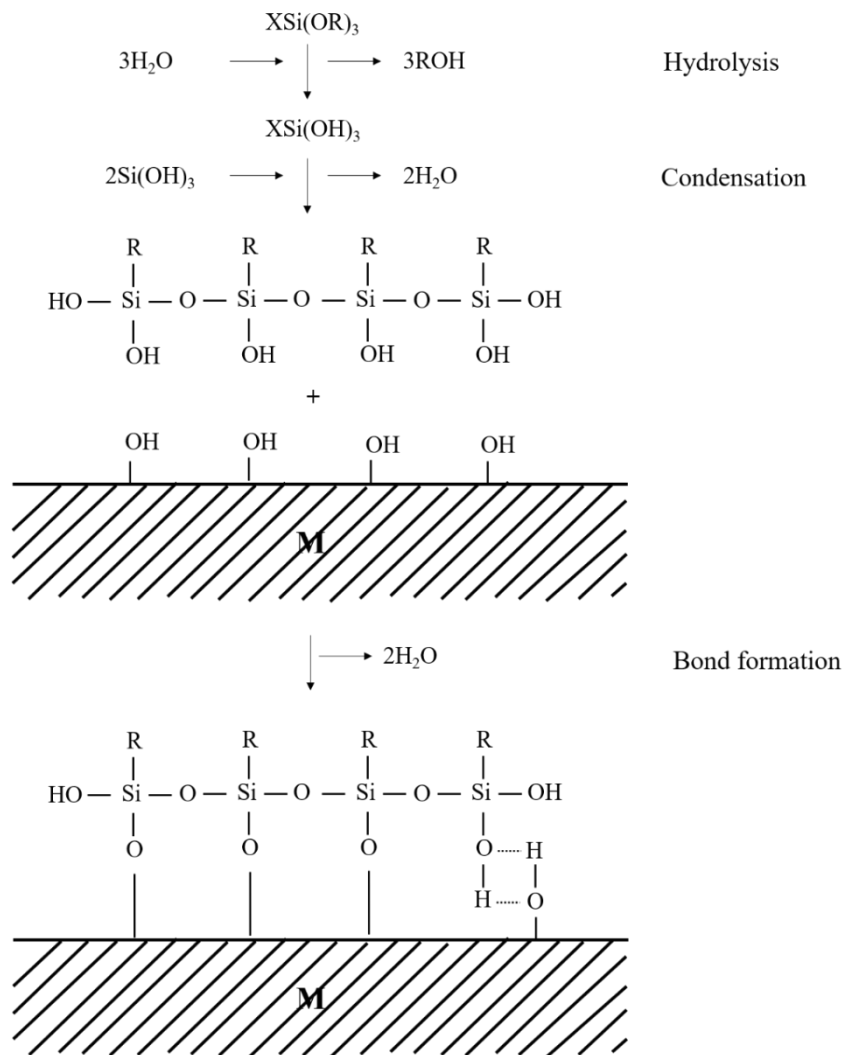


Figure 2.3: Bonding mechanism for silanol groups present in alkoxy silane sols and metal interface (adapted from [20]) .

2.4.1 Influence of ratio of inorganic : organic precursor molecules on corrosion protection

An increase in organic component concentration is expected to promote the formation of thicker films which in turn limits further the diffusion of corrosion species to the coating/metal interface [51]. However, a high concentration of the organic component decreases the effect of adhesion and reinforcement of the coating [52]; on the other hand, if the concentration of the organic component is too low then the coating becomes brittle due to the high concentration of silica derived from TEOS. The appropriate ratio of inorganic–organic components ought to be determined which corresponds to the maximum corrosion resistance of the metals [52].

Seok *et al* [52] studied inorganic–organic hybrid precursors for corrosion protective coatings on galvanised iron, which were prepared by adding GPTMS to an aqueous nano-sized alumina (in the crystalline form boehmite) solution. The electrochemical properties were evaluated by anodic polarisation of the coated surfaces using 0.5 M aqueous NaCl solution exposed to air. The authors observed that the corrosion current shifted towards lower values with increasing GPTMS-content. A gradual increase in corrosion current was then recorded with increase in the GPTMS loading up to 0.7 molar ratio of GPTMS:boehmite.

Vella [53] studied TEOS:PhTES and TEOS:MTES systems using electrochemical polarisation tests. A three electrode cell was used where calomel electrode was used as the reference electrode, 6mm Platinum disk as the counter electrode and a 0.754 cm² area of exposure of un/coated specimen was employed as the working electrode. Polarisation tests were carried out after an hour of soaking in aerated 0.1 N sodium chloride solution during which the open circuit potential was recorded. The potential was scanned from -200 mV from E_{corr} to +500 mV from E_{ref} at a scan rate of 1 mV/s. Vella [53] determined that the optimal corrosion resistance of the coatings are in a 60:40 mol% ratio for MTES:TEOS and 40:60 mol% ratio for PhTES:TEOS coatings for 10% SiO₂ concentration employed.

2.4.2 Influence on chain length on coating properties

Metroke *et al* studied the effect of chain length of the aliphatic alkyl group on corrosion protection of aluminium surface through salt spray techniques and EIS [54]. The silica-based precursor molecules studied were methyltrimethoxysilane, dimethyldiethoxysilane, *n*-propyltrimethoxysilane, *n*-butyltrimethoxysilane, *i*-butyltrimethoxysilane, *n*-hexyltrimethoxysilane, *n*-octyltriethoxysilane, and *i*-octyltrimethoxysilane. Each of these alkyl-silica precursor molecules was mixed with 3-(trimethoxysilyl)propylmethacrylate (MEMO) and vinyl trimethoxysilane (VTMOS) and applied by spray-coating technique. Coating thicknesses were measured to be in the 6–16 μm range, the thickest coatings being observed for the highest concentrations of alkyl-trialkoxysilane. Contact angle measurements showed an enhancement in hydrophobicity of the coatings with increasing size and concentration of the alkyl-groups embedded in the coating.

EIS was used to evaluate the protective properties of the investigated coatings which was performed on a Gamry PC3/300 potentiostat using a Gamry Corrosion Measurement System CMS100 and CMS300 software. Measurements were collected in a two-electrode cell equipped with a platinum reference electrode and a coated 2024-T3 AA panel as the working electrode. An exposed area of 0.36 cm^2 was used and all measurements were conducted in 0.05% NaCl or 0.5 M K_2SO_4 at 25 ± 1 °C. EIS spectra were acquired in the frequency range from 10 kHz to 1 mHz with 10 mV applied AC (versus Eoc). Overall it was concluded that the corrosion resistance characteristics were found to increase with the alkyl chain length [54]. Ni *et al* have also studied the effect of aliphatic alkyl groups on contact angle measurements for aluminium substrate using *n*-butyl-, *n*-octyl-, *n*-dodecyl-, and *n*-hexadecyl- trimethoxysilane [55] where contact angle measurements were found to increase with alkyl chain length.

Numerous studies have involved the use of methyltriethoxysilane (MTES) as a precursor molecule for the development of coatings and metal protection whereas such studies involving phenyltriethoxysilane (PhTES) [53,56-58] and OTES [54,55,59-62] are less frequent. Sheffer *et al* investigated the effect of electrodeposited PhTES and MTES where both coatings proved to protect

the surface of the steel from corrosion when compared to bare steel [57]. Contact angle measurements showed that the hydrophobicity increased from TEOS < MTES < PhTES where PhTES coatings were determined to offer better corrosion protection than MTES coatings based on EIS data. For the Impedance measurements, a three-electrode electrochemical cell was used consisting of Teflon coated aluminium rod as the working electrode, a large surface area platinum wire as the counter electrode and an Ag/AgCl wire was used as the reference electrode. The electrodes were left in a 0.1 M NaCl solution under the open circuit potential for at least 30 mins before each spectrum. Spectra were recorded in the frequency range of 1 to 50 kHz using a 5 mV rms perturbation.

A similar study by Kumar was conducted using these precursor molecules to produce coatings for aluminium [56]. The durability of coatings with respect to hydrophobicity was evaluated on the basis of contact angle measurements, after immersion of the coated substrate in water for 40 days. Electrochemical tests were carried out using a Solatron electrochemical interface SI 1287. Polarisation studies of the coated SS 316 substrate was carried out at 25 °C in a N₂ purged 3.5 % NaCl solution with an exposure time of 1 hr and 24 hrs. Potentiodynamic scans were recorded by applying potentials from -1 V to + 0.6 V with a scan rate of 1 mV/s. In this study however, MTES performed better than PhTES. The reason was attributed to the higher rate of hydrolysis and condensation reaction in case of MTES that allowed formation of a denser silica network [56]. Studies on *n*-octyltriethoxysilane (OTES) derived coatings do not employ TEOS and OTES as the precursor molecules but also include other alkoxy-silane precursors such as vinyl-silanes [54] and acrylate-silanes [59], epoxy-silanes [63], organic resin [61] and zeolites [62]. Although a few studies have been conducted using *n*-propyltrimethoxysilane as precursor molecule and coating formation [54,62,64] no data has been found for the *n*-propyltriethoxysilane precursor molecule employed in this work.

2.5 Sol-Gel OIH coatings on steel

The corrosion resistance behaviour of OIHs sol-gel coatings deposited onto steel substrate has been extensively studied. The publications for steel from 2001 onwards have been found to focus mainly on the use of TEOS [5,56,64-95], (3-Glycidioxypropyl)trimethoxysilane (GPTMS) [70,73,85,88,92,93,96-100], 3-(Trimethoxysilyl)propyl methacrylate (MAPTS) [28,65,71,75-79,81,87,90,96,101] and MTES [56,67-69,72-74,84,102-106]. Generally, the reported studies showed that that the named OIH coatings exhibited promising anti-corrosion properties on iron-based alloys.

2.6 Incorporation of inhibiting species within OIH coatings

The corrosion process is an electrochemical reaction since a material is oxidised in an aqueous environment to form metal oxides/hydroxides. The metal's surface has active anodic and cathodic sites as shown in **Figure 2.4**. The anodic region of the metal surface is oxidised and loses its electrons to the cathodic region. At the cathodic region, the oxygen is reduced and reacts with the oxidised metal (Fe^{2+}) to form the iron (III) oxide (Fe_2O_3) which appears as the formation of rust sets in [107].

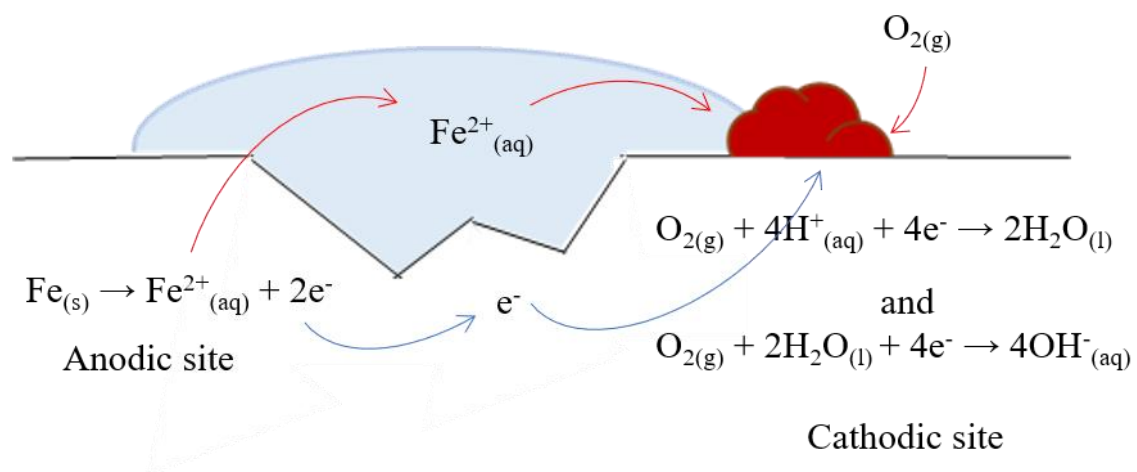


Figure 2.4: Anodic and cathodic reactions occurring that bring about the formation of corrosion products on iron surfaces when exposed to an aqueous medium adapted from [107].

OIH coatings are passive coatings, since they only act as a physical barrier that hinder the penetration of aggressive species towards the underlying metal. The anti-corrosion properties can be further enhanced by the inclusion of controlled amounts of chemicals possessing corrosion inhibiting properties. This section features silica nanoparticles and in/organic chemical inhibitors which have been reported to improve corrosion resistance upon their inclusion in sol-gel OIH coatings.

2.6.1 Incorporation of Nanoparticles

Several researchers have stated that a possible way of improving an OIH coating's mechanical properties and depositing thicker coatings through the incorporation of silica particles [43,108-110]. Silica nanoparticles can be produced through two main methods namely, a top-down or bottom-up approach. Top-down is characterised by reducing the dimension of the particles by utilising size reduction techniques such as milling to a desired particle size. The bottom-up approach involves a chemical synthesis to produce silica nanoparticles starting with molecular building blocks. The sol-gel process is a clear example of a bottom-up approach of nanoparticle production and has been used to produce pure silica particles due to its ability to control the particle size and their distribution, together with the particle morphology through the systematic monitoring and controllability of the reaction parameters [111]. Stöber *et al* have conducted pioneering work on the synthesis of spherical and monodispersed silica particles through the sol-gel method (bottom-up approach) [112]. Stöber reported the formation of silica particles having a size ranging from 5 nm to 2000 nm which have been prepared through an alkoxysilane precursor developed in aqueous alcohol solution in the presence of ammonia as catalyst; the basic conditions distinguish this method from the acidic sols used to prepare OIH coatings.

2.6.1.1 Commercial Nanoparticles

This section discusses the work of several authors that have reported on the effects of adding commercial nanoparticles (CNPs) produced through top-down method to OIH coatings and any improvement towards anti-corrosion properties. Castro *et al* reported the NPs in aiding OIH coatings with a lower shrinkage rate, thus reducing the final internal stresses [113] together with an increase

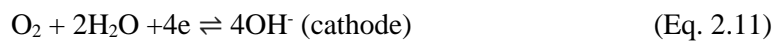
in coating thickness. Sol-gel coatings were deposited via electrophoretic deposition (EPD) onto AISI-304 stainless steel substrates. CNPs (Levasil 200A) were suspended and stabilised using tetramethylammonium hydroxide (TMAH). This suspension was then added to an acid-catalysed MTES:TEOS sol where the total silica concentration was that of 340 g/L for which 109 g/L is CNP with a particle size of 20 nm.

Suegama *et al* studied the effect of NPs that were added to an amino-containing coating where bis-(trimethoxysilylpropyl)amine (BTSPA) was used as the starting precursor alkoxy silane molecule [110]. Electrochemical testing was carried out to evaluate the extent of corrosion protection through EIS and Potentiodynamic testing. Corrosion resistance of the coated steel was evaluated by means of electrochemical measurements of the samples in 0.1 M NaCl solution. The EIS data were obtained by applying 10 mV rms to the E_{oc} value, starting from 50 kHz to 0.001 Hz with seven measurements per frequency decade after 30 mins and 80 mins of immersion. Polarisation curves were recorded for all samples in a potential range from -250 to +250 mV versus $E_{oc}/Ag/AgCl/KCl_{sat}$ at 0.5 mV/s. CAB-O-SIL® TS-610-treated fumed silica nanoparticles (large particle size silica which has been treated with dimethyldichlorosilane) which are CNP that have been treated so as to replace many of the surface hydroxyl groups on the silica with methyl groups, which renders the surface of the nanoparticles more hydrophobic. The particles, having a size of around 10 nm, were dispersed in the ethanol/water solvent using an ultrasonic bath for 30 mins prior to addition to the alkoxy silane and further sol development. A range of CNP concentrations were studied: 100, 200, 300, 400 and 500 ppm [110]. The addition of CNP was found to improve surface hardness and increase film thickness. Both these were found to contribute to an improvement in the barrier properties of the coating.

Palanivel *et al* suggested that apart from the improved barrier properties imparted by NPs when incorporated into OIH coatings, the presence of NPs in the coating actively inhibits (delays) chemical reactions that bring about corrosion of metal surface once the coating has been penetrated by the corrosive medium [43]. Electrochemical impedance spectroscopy (EIS) measurements were employed to evaluate the corrosion performance of the silane-treated AA 2024-T3 systems in a 0.6

M NaCl solution (pH 6.5). The measured frequency range was from 10^{-2} to 10^5 Hz, with an ac excitation amplitude of 10 mV. SCE was used as the reference electrode and coupled with a graphite counter electrode. The surface area exposed to the electrolyte was 5.16 cm^2 . This group of researchers has studied the role of NPs on bis-[3-(triethoxysilyl)-propyl]tetrasulfide (BTESPT) films deposited onto aluminium alloys. The concentration of NPs was varied to include 0, 5, 15 and 50 ppm. This work reports that the corrosion performance depends on the amount of silica (NPs) and that excess of SiO_2 from NPs begin to protrude out of the coating's surface which then facilitates water uptake through pores on the surface of the film, causing premature deterioration.

Nevertheless, the addition of controlled amounts of silica to bis-sulphur alkoxy silane films seems to increase corrosion resistance of the AA-2024 substrates [43]. Corrosion reactions begin to set as the aqueous solution penetrates through the coating and reaches the metal forming anodic and cathodic sites at exposed surface regions. The chemical reactions for this process are shown in Equations 2.10 and 2.11 for aluminium [43]:



When the alkoxy silane film is loaded with small amounts of silica NP, the silica suppresses the cathodic reaction (Eq. 2.11) by reacting with the cathodically generated OH^- ions as follows:



The SiO_3^{2-} ions react with Al^{3+} ions that are being generated at the anodes, thus forming a passive silicate film which prevents further anodic reactions from occurring in that region.

Other authors have also reported on the improvement in mechanical properties and corrosion protection through the inclusion of NPs with OIH coatings. Montemor *et al* have studied the effect of adding 4% (v/v) Bis-[3-(triethoxysilyl)propyl]tetrasulfide (BTESPT) and have included 50 ppm of NP (Hi-Sil T-700 particle size of $2 \mu\text{m}$) which was used to coat hot dip galvanised steel [108]. EIS measurements were performed using a three-electrode electrochemical cell consisting of the working electrode (3.15 cm^2 of exposed area), the saturated calomel electrode as reference and

platinum as counter electrode. The measuring frequency ranged from 100,000 down to 0.001 Hz. The electrochemical experiments were performed under immersion in 0.03 % NaCl solution. The results obtained show that the addition of 50 ppm of silica generated an increase in the impedance relative to coatings containing no NPs. This was attributed to an increased film thickness and decreased porosity due to incorporation of silica [108].

Phanasgaonkar *et al* studied the effect of NP on MTES:TEOS in various molar ratios[74]. The final silica concentration was set to 266 g/L where nanoparticle-modified coatings have 123 g/L of NP added to the MTES:TEOS sol for which the authors report crack-free coatings. A three-electrode cell set up was used with coated specimen as a working electrode, saturated calomel electrode as reference electrode and platinum sheet as a counter electrode. An area of 2 cm² at the centre of each specimen was exposed to the electrolyte. The tests were performed at ambient temperature without stirring or purging the cell. EIS was performed immediately after immersing specimens for 30mins (OCP) in 3.5 wt% NaCl solution sweeping frequencies from 100,000 to 0.01 Hz. Impedance tests demonstrated a half-order of magnitude improvement when NPs are present in the OIH coating compared to coatings that do not contain NPs.

2.6.1.2 Nanoparticles produced through bottom-up approach

Stöber *et al* [112] demonstrated the ability to synthesise silica NP with control over particle size through varying the reaction parameters for which particle mean diameters obtained by these researchers ranged from 0.05 to 2 µm. The method developed by Stöber required the addition of a saturated ammonia solution to the mixture while quantifying the volume of water incorporated into the reaction. To this ammonia solution, an alkoxy silane such as TEOS is added under agitation. Clouding of the reactant mixture was observed within the first five minutes of the alkoxy silane addition. This was attributed to the formation of silica and a total of two hours of reaction time was allowed for all experiments conducted [112]. Stöber kept the concentration of alkoxy silane constant at 0.28 mol/L for all sol developed.

The work by Bogush *et al* [114] defines the reactant concentration ranges required to produce a monodisperse silica which was previously difficult to obtain. Bogush *et al* systematically studied the effect of reagent concentrations, namely the concentration of water, ammonia, and TEOS on particle size and distribution. Upon maintaining a constant concentration of TEOS, variations in water and ammonia concentration revealed that the largest particles obtained (800 nm) are produced with a 7 M water concentration and 2 M ammonia concentration [114]. There have been continued efforts for more efficient modes of synthesis together with better control over material properties. Wang *et al* examined systems with a high TEOS (0.22 – 1.24 M) and low ammonia concentration (0.81 M) to produce silica with a particle size of 30–1000 nm for the purpose of increasing the particle yield [115]. Ibrahim and co-workers investigated the effect of TEOS and ammonia concentrations on the nucleation and growth processes of the Stöber method [116]. The authors report that upon increasing the TEOS or NH₃ concentration a faster/shorter nucleation period is obtained together with an increased growth rate, both increases resulting in a larger particle size [116].

Plumeré *et al* discussed the preparation of silica particles in the size range 50 - 800 nm with desired particle shape, size, polydispersity, porosity and which were free from aggregation [117]. Characterisation of these particles was done using Scanning Electron Microscopy (SEM), Dynamic Light Scattering (DLS), nitrogen sorption isotherms, Gay-Lussac pycnometry and Diffuse Reflectance Infra red Fourier Spectroscopy [117]. The particle diameter was maintained by managing the temperature and ammonia concentration and it was found that at higher temperatures ~ 75 °C, particles of sizes less than 100 nm were produced. Sato-Berru and co-authors developed a simple method for the controlled growth of silica NP ranging from 10nm to 600nm [118]. The method of synthesis was carried out by changing the ethanol : water ratio during the sol development. The characterisation of silica particles was done using Transmission Emission Microscopy (TEM) and Dynamic Light scattering (DLS) [118]. Singh *et al* [119] reported on the preparation of spherical and uniform sized silica NP by the hydrolysis reaction of TEOS in ethanol and ammonia whilst acquiring control of the size of particles using the cationic surfactants dodecyl trimethylammoniumbromide (particle size ~ 140 nm), tetradecyl trimethylammoniumbromide (particle size ~

95 nm), cetyltrimethylammonium bromide (particle size ~ 55 nm). Results obtained displayed a decrease in particle size as the chain length of the surfactants is increased [119].

2.6.2 Incorporation of inorganic and organic inhibitor molecules

A sol-gel coating acts as a physical barrier between a corrosive external environment and the metal surface. A more protective anti-corrosive sol-gel coating can be achieved if corrosion inhibitors are incorporated into the coating materials. In general, the inorganic inhibitors affect reactions occurring at the cathodic or anodic sites on the metal surface [107] whereas the organics inhibitors affect both reactions occurring at the cathodic and anodic sites. Chromate conversion coatings have been used as pre-treatments in the past due to their adhesion properties as well as corrosion inhibiting effects but have been banned as they are deemed environmental and health hazards [120]. Therefore, interest in green inorganic and organic corrosion inhibitors has increased as an alternative to chromate-based applications for industrial protective applications [121].

2.6.2.1 Inorganic inhibitors

Anodic inhibitors (also known as passivation inhibitors) act by reducing the anodic reaction, i.e. by blocking the anode reaction (see Figure 2.4) and supports the natural reaction of passivating the metal surface by the formation of a film adsorbed on the metal. The anodic inhibitors reacts with metallic ions (Me^{n+}) produced at the anode, leading to the formation/precipitation of insoluble hydroxides which are deposited on the metal surface as an insoluble film and are impermeable to metallic ions [107]. Examples of such inhibitor ions include chromate, molybdate, nitrite and orthophosphate ions [122].

The cathodic corrosion inhibitors prevent the occurrence of the cathodic reaction of the metal. These inhibitors have metal ions able to produce a cathodic reaction due to alkalinity, thus producing insoluble compounds that precipitate selectively on cathodic sites. They deposit over the metal a compact and adherent film, restricting the diffusion of reducible species (oxygen diffusion and electrons, see Figure 2.4) in these areas. The cathodic inhibitors form a barrier of insoluble

precipitates which limits the metal contact with the environment, thus preventing the occurrence of the corrosion reaction [107]. Examples of inorganic cathodic inhibitors are cerium, magnesium, zinc, and nickel ions that react with the hydroxyl (OH⁻) ions generated at cathodic sites to form the insoluble hydroxides (Ce(OH)₃, Mg(OH)₂, Zn(OH)₂ and Ni(OH)₂). These hydroxides deposit on the cathodic sites of the metal surface, protecting it from further reaction [107].

Several inorganic inhibitors which possess a low toxicity such as lanthanum salts [123-125], vanadates [126] and the more researched cerium salts [79,85,120,127-134] have been used to create more protective hybrid alkoxysilane films. Improvement in corrosion protection is attributed to the precipitation of insoluble cerium oxide/hydroxide at defects where, in addition to the active corrosion inhibiting effect, the precipitated hydroxide species can act as a diffusion barrier hindering further corrosion processes in active zones [130]. Working with cerium, Montemor *et al* [124,130] brought forward two hypothesis for the interaction between the inhibitor and the silica matrix: the first theory suggests that cerium ions are trapped in the silica network in the form of an oxide or hydroxide whereas the second proposes that cerium ions substitute H⁺ originating from Si-OH functions which would therefore suggest that cerium is covalently bound and incorporated to the silica network i.e. cerium ions substituting some of the silica atoms in the Si-O-Si network [124,130].

Cambon *et al* featured OIH coatings doped with different cerium concentrations deposited onto martensitic stainless steel through the sol-gel method [85]. The OIH coating was obtained through a mixture of the precursors glycidoxypropyl-trimethoxysilane (GPTMS) and aluminum *sec*-butoxide Al(OBu)₃. The extent of the coating's corrosion protection was evaluated through EIS in a 0.05 M NaCl static solution (pH 6.0). A three-electrode electrochemical cell was used, consisting of a platinum counter electrode, a saturated calomel reference electrode and the sample was used as a working electrode, with an exposed area equal to 15 cm². EIS measurements were performed in potentiostatic mode at the OCP, obtained after an hour stabilisation of the potential in the electrolyte. The amplitude of the EIS perturbation signal was 10 mV, and the frequency studied ranged from

100,000 to 0.01 Hz. EIS results revealed that a cerium concentration of 0.01 M into hybrid coating was an optimal concentration leading to the most protective coatings [85].

Cambon and co-workers employed liquid ^{29}Si NMR spectroscopy to investigate the hydrolysis and condensation reactions of the sol-gel process through which it was demonstrated that for the higher cerium concentration (> 0.01 M) there is a modification of the chemical structure of the sol-gel network. When cerium was added in the coating up to 0.01 M, an increase in impedance values was recorded, i.e. the anti-corrosion properties were gradually improved with the lower cerium content from 0 up to 0.01 M. However, upon further increasing the cerium concentration another behaviour begins to take shape where a drop in anti-corrosion property occurs which was not due to a decrease of the coating thickness but because the sols with cerium content of 0.05 M and 0.1 M experienced a higher viscosity. The degradation of the film's anti-corrosion properties have been attributed to the modification in the hybrid network by an excess of cerium ions. The same authors also report similar results obtained when the coatings were deposited onto an aluminium surface. Crack free organic-inorganic coatings were deposited onto AA 2024-T3 aluminium alloy from sols prepared by mixing GPTMS and $\text{Al}(\text{O}i\text{Bu})_3$ with different cerium concentrations, 0–0.1 M [128].

2.6.2.2 Organic inhibitors

Corrosion inhibition is typically brought about by the adsorption of inhibitor molecules at anodic and/or cathodic sites and/or through the formation of a protective barrier film that covers both anodic and cathodic sites as described in inorganic inhibitors Section 2.6.2.1. Factors that contribute to the effectiveness of inhibitors are the molecule's size, presence of aromatic/conjugate groups leading to electron delocalisation, strength of bonding to the substrate, its cross-linking ability and the inhibitor solubility in the particular corrosive environment [121]. Organic inhibitor molecules generally incorporate heteroatoms such as O, N, and S which possess high basicity and electron density; O, N, and S are the active centres for the process of adsorption on a metal surface [121].

Organic inhibitors adsorb onto the metal surface by displacing water molecules and aggressive species such as Cl^- ions present on the surface. Lone pairs from heteroatoms and π -electrons in aryl molecules facilitate electron transfer from the inhibitor to the metal. A coordinate covalent bond involving transfer of electrons from inhibitor to the metal surface may be formed for which the strength of the chemisorbed bond depends upon the electron density on the donor atom of the functional group and also the polarisability of the group [4]. The electron density in the metal at the point of attachment is therefore altered and leads to the retardation of the cathodic or anodic reactions [121].

Many N-heterocyclic compounds such as pyridine derivatives [135], pyrimidine derivatives [136,137], triazole derivatives [138,139], tetrazole derivatives [140], pyrazole derivative [141], bipyrazole derivatives [142,143], indole derivatives [144], pyridazine derivatives [145,146], and benzimidazole derivatives [147,148] have been used for the corrosion inhibition of iron and steel in acidic media. Naphthol derivatives [149-151], quinoline derivatives [152,153] and quinone derivatives [154] have also featured in corrosion protection of steel substrates in acidic media. However, less literature has been found that deals with the incorporation of these inhibitors in a sol-gel coating applied onto metals for their improved protection [131,134,155-161].

The review paper by Rani and Basu [121] dealing with green corrosion inhibitors mentions pyrrolidine as an inhibitor in aqueous media. The authors state that the pyrrolidine undergoes ionisation where the nitrogen atom acquires a negative charge and the free electrons resulting in a strong bond formation between the metal and the nitrogen of pyrrolidine molecule [121]. However, no experimental detail or further references are provided. A literature survey reveals that several pyridine derivatives were used as corrosion inhibitors in acidic medium [162-166], however, no data was found for 2-hydroxypyridine except for a patent [167] which reports the use of 2-hydroxypyridine incorporated within an amine-reactive vinyl polymer and a polyfunctional amine crosslinker cured into coatings that generates superior corrosion resistance.

Although no work has been found which features the incorporation of 1,4-naphthoquinone as a corrosion inhibitor as part of a protective coating, Sherif and co-workers [168] have investigated 1,4-naphthoquinone for its corrosion inhibiting effect on aluminium in aerated and deaerated solutions. Results indicate that 1,4-naphthoquinone is an efficient corrosion inhibitor, shifting the corrosion and pitting potentials in positive directions. Quartz crystal analyzer experiments present evidence that the inhibitor molecules are strongly adsorbed on the aluminium surface where the passive layer is successfully protected by the strong adsorption of the inhibitor molecules [168].

8-hydroxyquinoline (8-H) has been studied for its corrosion inhibiting effects in solution, but less so when incorporated into a coating. Relevant work was carried out by Galio *et al* whom presented 8-H doped anticorrosive sol-gel coatings for the AZ31 magnesium alloy where the sol-gel coatings were prepared by copolymerisation of GPTMA and zirconium (IV) tetrapropoxide [157]. The study featured the incorporation of the inhibitor molecules 8-H (0.26 wt.% of 8-H) at two different stages of sol synthesis, either before or after hydrolysis of the sol-gel precursors [157]. EIS technique was employed to evaluate the corrosion protection performance of the developed hybrid sol-gel films on AZ31B during 2 weeks immersion in 0.005 M NaCl solution. EIS measurements were carried out by applying a 10 mV sinusoidal amplitude in the 100,000 to 0.01 Hz frequency range. A conventional three-electrode cell was used, consisting of a SCE reference electrode, a platinum foil as counter electrode and sol-gel coated AZ31B substrate as working electrode with surface area of 3.3 cm². Low concentration of electrolyte (0.005 M NaCl) was chosen to EIS measurements in order to decrease the corrosion rate of the electrochemically active magnesium alloy. Positive effect of the inhibitor on corrosion performance of AZ31 coated with the sol-gel films has been attributed to the formation of insoluble and stable complexes Mg(8-H)₂ that block the propagation of corrosion by closing the micropores and microdefects in the sol-gel film [157].

The addition of inhibitor after sol development led to the formation of more protective coatings than when inhibitor was added at sol start stage, the author speculating that this result is due to the different interaction of 8-H with the components of the sol–gel formulation where such an interaction can partly deactivate the inhibitor [157]. Galio explains that the addition of 8-hydroxyquinoline after hydrolysis of the sol was complete, at which point the alkoxy silane-based network was already formed, caused less interaction of sol–gel components with the inhibitor molecules and led to a better anticorrosion performance of this sol–gel formulation [157].

2.7 Reversibility of OIH alkoxy silane coatings

A relevant reversibility study of alkoxy silane coatings has been conducted by Kachurina *et al* on aerospace aluminium alloys [169]. The alkoxy silane coatings were based on a mixture of TEOS, vinyltrimethoxy silane (VTMOS) and 3-(trimethoxysilyl)propyl methacrylate (MEMO). Sols were applied onto cleaned aluminium samples through spray coating. Coated samples were immersed in a number of solvents; namely methanol, ethanol, isopropanol, acetone, methyl ethyl ketone, and hexane. Several acids and alkalis having a 5 M concentration were also studied for their effects on coatings; namely, nitric acid, sulfuric acid, citric acid, ammonium hydroxide, sodium hydroxide.

The alcohols and ketones, which are polar organic solvents, were found to affect the integrity of the coatings through the solvents' ability to solubilise the organic portions of the coating thus degrading the integrity of the coating. Hexane, which is a non-polar organic solvent, did not affect the integrity of the deposited films. Acidic solutions did not remove the alkoxy silane coatings whereas basic solutions were found to degrade the coatings considered. This is due to hydroxyl (OH^-) ions in solution which reverse condensation reactions that have occurred during silica network formation (Eq. 2.5-2.6 above).

2.8 Preservation of HM

2.8.1 Current modes of corrosion prevention

Conservation of metals can be categorised into **interventive** methods, which involve the addition or removal of parts of an object in order to preserve it, and **preventive** techniques that are set to control the environment of the object in such a way that slows/stops the corrosion process. Both approaches require a deep understanding of the physical and chemical structure of the metal being conserved, the interaction with environmental variables and the formation process of the corrosion products [1].

Heritage metals are found in both outdoor and indoor environments and may have decorative or artistic significance such as sculptures, can be functional artefacts, or large industrial items. HM kept indoors which have been in good condition since their placement in a museum, such as armoury collections, may have very little corrosion and retain their original surface finish. Conservators aim to retain such a state of finish which is typically done through the monitoring of the indoor environment, simple good housekeeping and environmental control in relation to corrosion threshold values for the metal such as displaying of HM in temperature and humidity-controlled chambers. This minimalist approach to preservation is much favoured in conservation practice. However, such environmental control would imply significant capital outlay and ongoing energy consumption is expected which may go beyond the financial means of many museums. Another way around this problem is temporary protection by application of protective coatings. Conservation coatings are normally applied onto HM as barriers to gaseous, aqueous, or particulate agencies of decay.

2.8.2 General conservation work practice guidelines when applying coatings on HM

Nowadays there are general accepted conservation work practice guidelines. In the case of metal protection coatings, the important requirements are that *(i)* coatings are reversible, *(ii)* the entire coating procedure must not change the aesthetics of the object, *(iii)* coatings have to offer suitable corrosion protection (guaranteed protection for a minimum of 5 years), and *(iv)* that relatively low

temperatures are employed in the process of curing of the coating [1]. Typically, the conservation of corroded metal involves the selective removal of the more friable rust layers, followed by an application of a coating layer of acrylic resin or wax or both [170].

Surface preparation of HM typically involves mechanically removing corrosion products to reveal the original surface. The context of the object is important and the nature of a corrosion patina can be deemed as having an important aesthetic value as it forms part of the artefacts' life history [1]. A coating applied to a metal must not alter its visual aspect and it must therefore inflict no/very little colour change. Since sometimes corroded areas are left purposefully uncleaned, coatings must often perform well on porous, uneven oxidised metal surfaces that may contain friable and chemically unstable material. No coating is perfect and this type of surface will result in a number of coating imperfections such as cracks or pinholes which makes corrosion protection on corroded surfaces much more difficult than on a clean surface and would therefore require more frequent attention [1].

2.8.3 Research in Conservation of HM

Literature sources within conservation is mostly available through conference proceedings and research project publications that support discussion forums for developing, interpreting, and documenting the metallic corrosion and the conservation process applied. Metals conferences are led and published by several national conservation groups, museums, universities, and the International Council for Museums Committee for Conservation Metals Working Group (ICOM-CC Metals WG). These entities develop significant research into the corrosion and conservation of historic and archaeological metals through the contribution of several dedicated specialists and through the funding of large collaborative research programs that have a specific focus such as Architech, PROMET, POINT which will be discussed in the following sections.

The expected role of a coating, environment in which it must be effective and the nature of the metal surface dictate coating choice. In the past, a lack of standardised procedures for testing a coating's effectiveness on HM hindered the ability to comparatively identify the most suitable coating for use

in a specific context which lead to conservators employing coatings that were popularly used and known to provide corrosion protection in a satisfactory manner. While some popular coatings still have qualitative data to support their use, there is now a much-awaited shift toward the availability of quantitative data and standardised testing within conservation literature. Both qualitative and quantitative determination of coating performance now uses electrochemistry and modern methods of instrumentation together with an influx of corrosion scientists has improved the conservation methodology [171-177].

Cano *et al* have published a review paper on the use of EIS for the evaluation of protective properties of coatings for metallic cultural heritage [178]. Cano *et al* [170] have also evaluated the performance of several coatings for historic steel artefacts using Electrochemical Impedance Spectroscopy, this reference ([170]) being most relevant to work presented in this thesis (for a beginner's guide into the theory of EIS, refer to S. Tait's *Introduction into Electrochemical Testing for Practicing Engineers and Scientists* [179]). The composition of the steel was determined using glow discharge-optical emission spectroscopy; 0.13% C, <0.10% Si, 0.53% Mn, 0.010% P, 0.015% S, and balance Fe (by weight). Carbon steel samples were prepared through a climatic cycling process so as to simulate the surface composition and morphology of historic steel objects. The process involved exposing the sample coupons to a 3-day cycle consisting of 100% relative humidity (RH) at a set temperature of 30 °C for 24 h followed by 24 h in a laboratory environment conditions of 55–60% RH at a temperature of 25–30 °C. Finally, a further 24 h exposure at 100% RH and at 30 °C. The coupons were then coated following common application practices.

The organic coating featured in the study [170] are the two commercial coatings commonly used in conservation-restoration treatments, namely Renaissance™ wax (a microcrystalline wax) and Paraloid™ B-72 (a methyl acrylate/ethyl methacrylate copolymer) together with a new (in conservation treatments) organic coating, Poligen™ ES91009, which is a ready-to-use liquid wax (ethylene copolymer wax emulsion in water). The work also features the study of the corrosion inhibiting effects of four types of commercial inhibitors to the Paraloid™ B-72 resin and Poligen™

ES-91009 wax. The additives were commercially purchased (Alkaterge-T™) with known active agents comprising of a blend of triazoles (M435), an ammonium salt of tricarboxylic acid (M370), calcium sulphonate (M109) and bis-oxazoline. Coatings have been applied by a conservator–restorer by hand, as they would be applied in real treatments. Coatings for *Set 1* were applied by brushing in two criss-cross layers, allowing 24 h for drying between layers [170]. Coatings for *Set 2* were applied by immersion and artificially aged in a climate cabinet as described in previous paragraph. To investigate the effect of the coating procedure, clean samples were coated by immersion with the three coatings without additives and were labelled as *Set 3*.

Figures 2.5-2.6 show the Bode plots obtained using EIS data for the steel specimens with and without organic coatings [170]. It can be seen that, on specimens 1 and 2 (Renaissance wax and Poligen respectively), the coatings do not provide significant protection to the base steel since the impedance ($|Z|$) values seen in the lower frequency range of Bode plot (Figure 2.5 (a)) are similar to those of the uncoated specimens. On the other hand, on specimens 2a (Poligen +M435) and 2b (Poligen +M370), the coatings yield an increase of two to three orders of magnitude in the $|Z|$ values. Figure 2.6 presents results obtained for coatings on specimens 3 (Paraloid B-72 without inhibitor), 3b (Paraloid B-72 + M109) and 3c (Paraloid B-72 + Alkaterge-T) which show good protective properties with a two order of magnitude improvement in impedance for Specimen 3, but the addition of corrosion inhibitor additives decreases their protective properties [170].

In the case of specimens 2, 2a and 2b, the appearance of two-time constants in the EIS spectra shown in Figure 2.5 (b) indicates that the electrolyte reaches the surface of the metal through microscopic pores or defects of the coatings [170]. The electrical parameters of the different elements used to fit the EIS data obtained, according to the equivalent electrical circuit (EEC) as schematised in **Figure 2.7**. The circuit comprises of a resistor (R_s) representing the resistance of the electrolyte, which is in series with a constant phase element (CPE_1) in parallel with resistor (R_1) that model the properties of the coating; CPE_1 and R_1 are in series with a circuit constituted circuit (EEC) as schematised

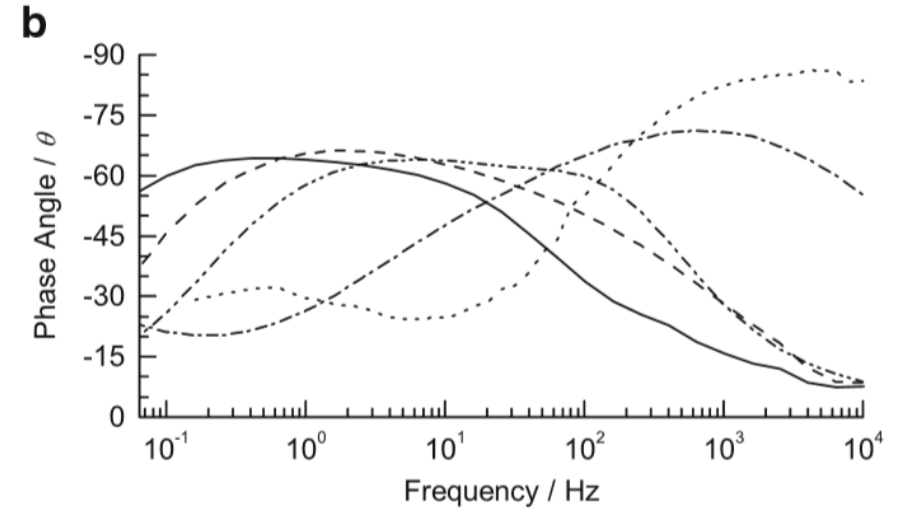
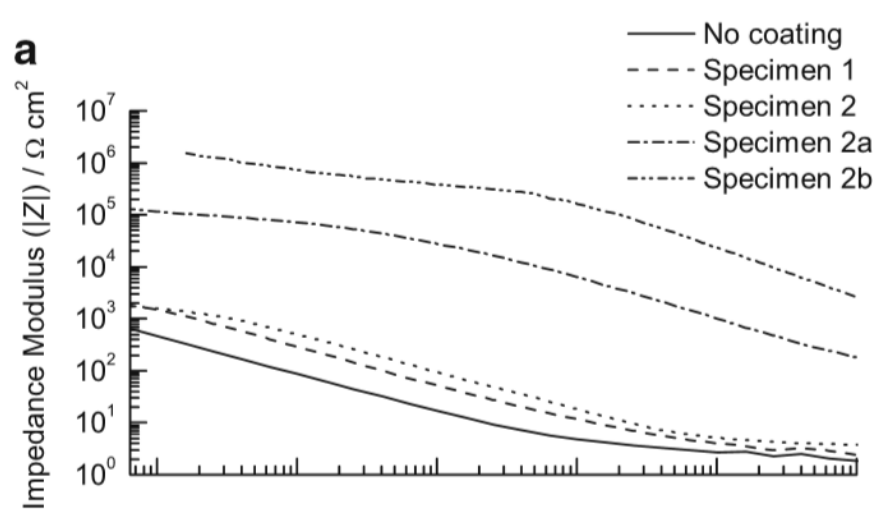


Figure 2.5: Bode plots obtained from specimen without coating and with specimens 1, 2, 2a and 2b (set 1) (a, b) Taken from [170]

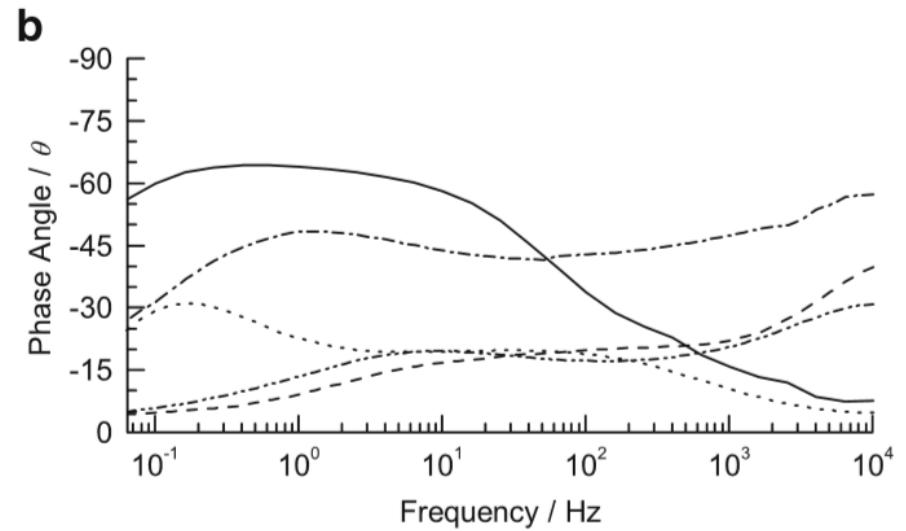
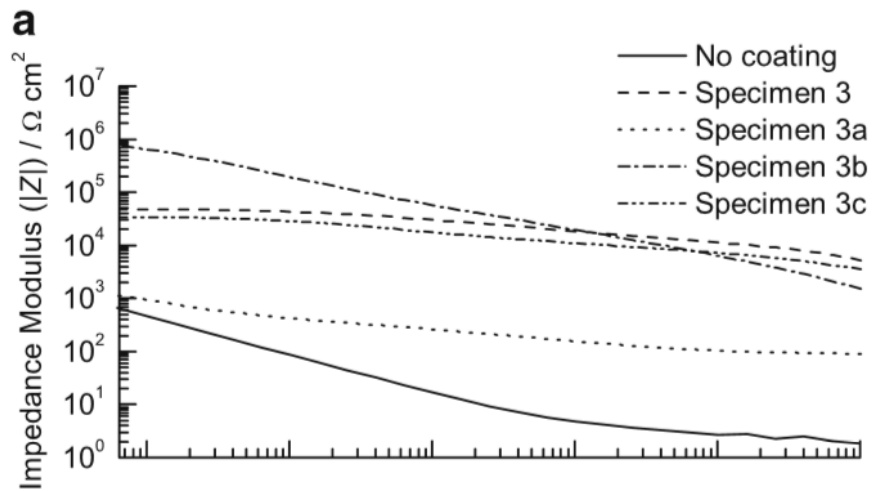


Figure 2.6: Bode plots obtained from specimen without coating and with specimens 3, 3a, 3b and 3c (set 1) (a, b) Taken from [170]

in **Figure 2.7**. The circuit comprises of a resistor (R_s) representing the resistance of the electrolyte, which is in series with a constant phase element (CPE_1) in parallel with resistor (R_1) that model the properties of the coating; CPE_1 and R_1 are in series with a circuit constituted by CPE_2 and R_2 elements in parallel which model the double-layer capacitance and the charge transfer resistance, respectively [170].

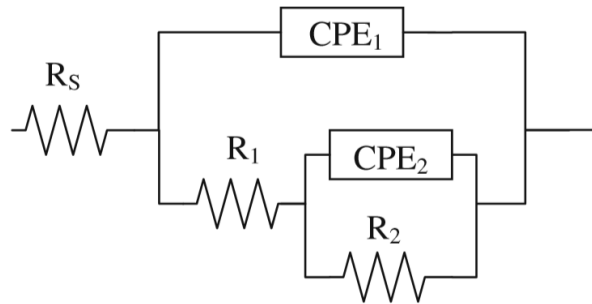


Figure 2.7: Equivalent electrical circuit used to fit EIS data. Taken from [170].

Figure 2.8 shows Bode plots obtained using EIS data for the pre-corroded steel specimens with and without organic coatings (Set 2) without ageing [170]. EIS spectra have also been modelled using EEC shown in Figure 2.7 since the behaviour of these specimens is similar to that of Set 1, The main difference appears in the bare metal sample C0, where two processes can be observed. In this case, the second process, which does not appear in specimen C0 of Set 1, can be attributed to the effect of the corrosion products on localised areas of the surface. The effect of those corrosion products is not visible in the coated samples, where only the response of the coating (R_1 - CPE_1) and the dissolution of the metal (R_2 - CPE_2) can be observed.

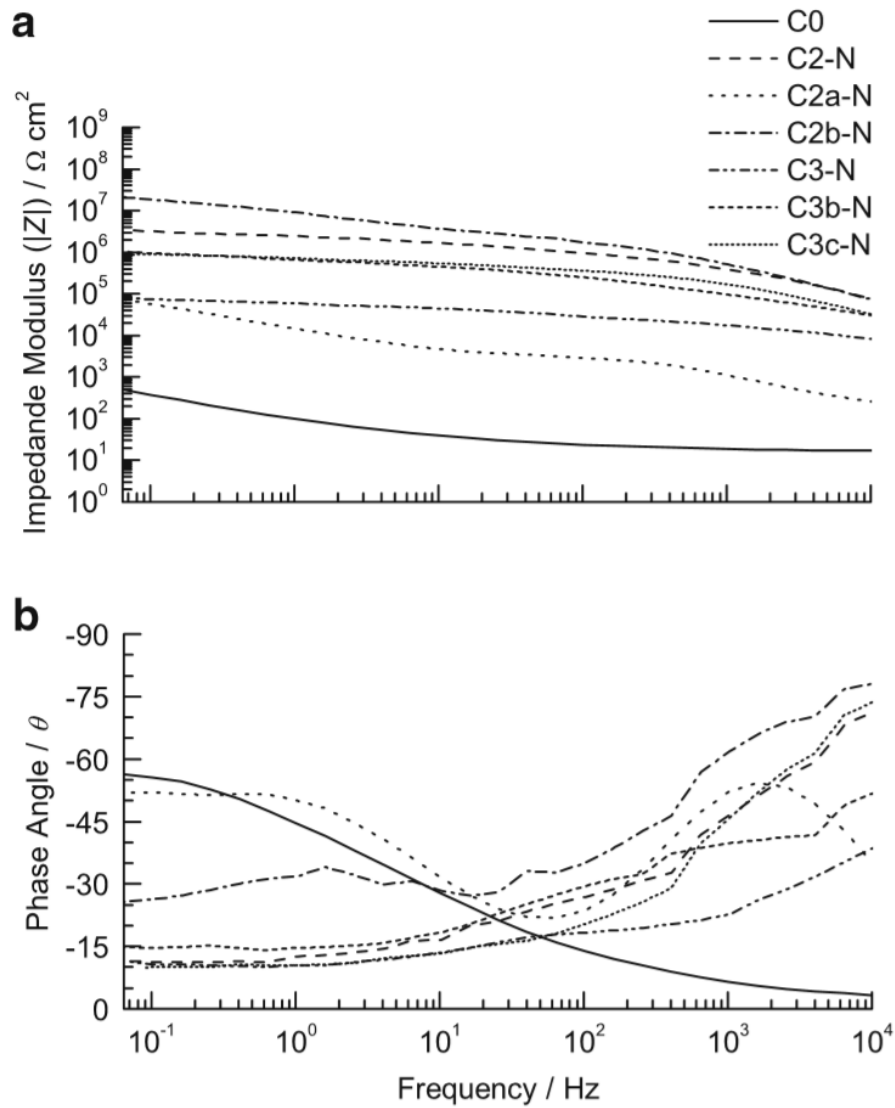


Figure 2.8: Bode plots obtained from pre-corroded specimens coated by immersion (set 2) without artificial ageing (a, b), taken from [170].

Curkovic *et al* [172,180] studied the extent of protection offered by coatings onto clean and patinated bronze which was examined using EIS. Bronze sculptures undergo various corrosion processes when exposed to an outdoor environment due to harsh conditions including humidity, rain and various pollutants such as SO_2 , NO_x and CO_2 . When sculptures are exposed to such conditions the patina (corrosion layer) formed is prone to dissolution and can therefore offer little protection to the underlying bronze (unlike the passive layer formed by aluminium [172,180]). Because of the

archaeological and artistic aspect of the formed patina, usually both the bronze and its green-colored patina are often preserved.

The corrosion inhibitors benzotriazole (BTAH) and 4-methyl-1-(p-tolyl) imidazole (TMI) were considered for their protective effect either by themselves or incorporated in Paraloid B-44 lacquer or Carnauba wax [172]. Patina resembling closely the chemical composition of historic artefacts were produced through electrochemical means by exposing the surface to solution of sodium salts (Na_2SO_4 , NaHCO_3 , NaNO_3) and whilst alternating between OCP and an applied voltage [172]. Interestingly, EIS results revealed that TMI provided better protection of the patina, whereas BTA was better for the protection of the bronze substrate. For all surfaces considered, BTA/Paraloid B-44 coating exhibited better corrosion protection than TMI/Paraloid B-44 coatings [172].

Extensive *in-situ* work on bronze was also carried out by Letardi [177,181] as part of a project commencing in 2001 as a cooperation between a CNR research laboratory and the ICR conservation institution. The bronze statue *Monumento ai Mille* chosen for this study is located in Genoa, Italy. The aim of such a project was to compare the behaviour of several coating systems upon natural weathering, both on polished bronze samples and on selected areas of the above-mentioned bronze monument. Six protective coating systems which are widely used in conservation practice were chosen: (i) Soter 201 LC which is a commercial product consisting of 20-24 wt% crystalline wax, BTA and synthetic organic polymer (ii) R21 which consists of 22 wt% microcrystalline wax dispersed in white spirit (iii) Tromm TeCe 3534F which consists of 33 wt% microcrystalline wax dispersed in white spirit (iv) Incralac which is an acrylic resin containing Paraloid B-44 (v) mixture of Incralac/Soter LC and (vi) mixture of Incralac/0000 R21.

Samples both of un-coated test coupons of bronze and coated with the coating systems (i-vi), were placed on a rack and exposed to the urban marine environment at a site inside the Genoa Harbour. The conservator-restorer also treated test areas on the *Monumento ai Mille* using these coatings through

assigning specified testing zones which were outlined with scotch tape and cleaned by rotating brush, washed with water and acetone and allowed to dry. The coatings were brush-applied following the standard methodology used in conservation, both on test coupons and on the monument test zones.

Unfortunately, EIS results were fairly wide scattered which rendered the data analysis and conclusions difficult to reach [177,181]. This was attributed to the uncontrollable nature of the field conditions where measurements on the monument were rather noisy, and further improvement on the data acquisition method was deemed necessary to solidify the results obtained [177,181]. Nevertheless, Letardi states that after only one year, the acrylate-based Incralac coating offers no advantage with respect to the waxy coatings Soter 201 LC , R21 and Tromm TeCe 3534F (contain microcrystalline waxes). These waxes have the advantage of a better accepted aesthetic appearance and are known to give fewer problems with respect to removal and re-coating.

2.8.4 OIH alkoxy silane coatings for protection of heritage metals

While alkoxy silane compounds have been extensively studied for corrosion protection on clean metal for industrial applications, they have received limited attention in the conservation practice. Sol-gel materials have been considered for the protection of several heritage materials such as wood [182], glass [183-187] and stone [188-191]. Coatings produced through the sol-gel method have also been applied to heritage metals which feature in a number of research projects. However, Sol-gel coatings have yet to be well researched on corroded surfaces. This is exemplified through the few papers published for copper and its alloys (brass, bronze) [192-194], iron and steel [195], which is likely due to the fact that conservators tend to avoid altering conservation practices, especially once conventional coatings are deemed to preserve the artefacts well enough and for several years. Nevertheless, OIH coatings have featured in larger multi-national projects as discussed below.

The CONSIST project produced a series of comprehensive studies made on the use of transparent coating materials termed “Corrosion protection for environmentally endangered industrial heritage

made of iron and steel” which ran between 1996 – 1999 [195] and was continued and extended to “A comparison of conservation materials and strategies for sustainable exploitation of industrial heritage made of iron and steel” in the years 2005 – 2008 [195]. Standard commercial organic coatings (oils, waxes, transparent paints) were featured together with the new group of materials OIH polymer coatings which had been developed and tested at the Fraunhofer Institute for Silicate Research in Würzburg [13]. The formula of these so-called Ormocer™ (Organically Modified CERamic) include a heteropolycondensate of diphenylsilanediol and 3-glycidoxypropyl-trimethoxysilane.

Both time accelerated laboratory tests and field trials were applied on selected objects. Clean and artificially corroded sheet-metal samples were treated with diverse transparent protective coatings which were then deliberately exposed to simulate industrial and condensation atmospheres in climate chambers [195]. Routine evaluation was carried out to assess the coating integrity, any changes in appearance and transparency together with the amount of new corrosion products [195].

These projects have shown that one of the most important factors in coating iron and steel surfaces is the thickness of the layers of the coating. Seipelt *et al* stated that an increase in the amount of the material deposited, achievable through a higher concentration of the lacquer combined with several applications, leads to more effective protection [195]. Glass tinsel which is a transparent glass filler has proven to increase coating thicknesses, and thereby the effectiveness of the protection [195]. The 3 waxes tested, which are known as Huls, Tromm and Cosmoid, were found to be just as effective in protecting metals as the ORMOCER-based coatings. Furthermore, Seipelt *et al* stated that the optical appearance of the waxes, which were deemed matt and unobtrusive, is superior to the ORMOCER lacquer [195].

Another project that has evaluated alkoxysilanes for the protection of HM was the PROMET project which featured “Silane A” comprising of a mixture of 5% g-mercaptopropyl-trimethoxysilane, 2% bis-(trimethoxysilylpropyl)amine, 1% hydrated TEOS in ethanol solvent. The scope of the project was to identify suitable coatings for use on metals within museums surrounding the Mediterranean basin

and aimed to identify a methodology for developing and testing the coatings' performance on iron and copper alloys in museum environments.

Tested protection systems were first applied and assessed on artificial coupons and finally assessed on real artefacts from the collections of the Swiss Army Historical Material Foundation (HAM foundation) [196]. It was found that the alkoxy silane-based lacquer Silane A outperformed the Paraloid B-72™ lacquer which had been impregnated with corrosion inhibitors on bronze in the long-term real-time testing [196]. Such a result is significant since the acrylate Paraloid B-72 is used worldwide by conservators for the protection of HM, and was shown to be inadequate in this experiment due to the frequently forming filiform corrosion developing under the film [196]. Similarly, microcrystalline waxes offered poor protection during the cycling process whereas Poligen ES 91009 polyethylene wax gave promising results for long term protection [196].

There is much scope for employing OIH alkoxy silane compounds on cultural heritage metals as hydrophobic barriers since they form transparent films on surfaces, they can be designed to have good water repellence, and are capable of bonding to corrosion products [1]. While alkoxy silane compounds are extensively used in industry as a means of preventing the corrosion of clean metallic surfaces, they have received limited attention in conservation practice of historic artefacts [1]. The age and use of a metallic objects of historical, archaeological, industrial or artistic importance are often corroded and prone to further deterioration [1]. Metals conservation comprises the preservation of cultural artefacts by conservators whose goal is to preserve objects whilst retaining evidence of their cultural context and integrity. Minimum change to an object should be done while achieving the restoration to the former state, however, this often proves to be difficult.

CHAPTER 3:

Methodology

3.1 Introduction

This Chapter is divided in the following sub-sections:

- Section 3.2 describes surface preparation of the iron coupons used in this work, namely iron that has been polished to a mirror finish (referred to as clean), iron that has been corroded artificially until the surface is covered with a thin corrosion layer (referred to as corroded) and corroded coupons that have been carefully cleaned of the more friable corrosion products (corroded-cleaned).
- Section 3.3 describes the method used for the development and preparation of several OIH alkoxysilane sols and their coatings, including the incorporation of additives such as nanoparticles and inorganic and organic inhibitors. Coating lacquers accepted and used by Conservators-Restorers have also been employed in this study for comparative purposes, and their preparation is also presented in this Section. Details of the mechanical and electrochemical tests carried out to evaluate the mechanical and anti-corrosion properties of the coatings are also presented.
- Section 3.4 describes methodology used in the comparative study of OIH silica coatings and the conventional lacquers conducted through accelerated corrosion (salt-spray) testing.
- Lastly, the procedure for determining the reversibility of the silica coatings is described in Section 3.5.

3.2 Metal substrate

3.2.1 Metal substrate preparation

The aim of this work is to produce coatings that are suitable for application onto Heritage Metals (HM) made out of iron (armour collection, Palace Armoury). Vella *et al* [197] observed that Palace Armoury armour consisted of both steel and iron (completely ferritic) pieces. Because the surfaces of 400 year old armour pieces are often partly corroded, the developed coatings must offer protection on both uncorroded and corroded iron surfaces. This Section describes the steps taken to prepare clean and corroded test coupons.

3.2.1.1 Preparation of polished coupons

Stock iron was supplied in the form of flat bars of size 6.35 mm × 38.1 mm × 1.35 m by Uddeholm, UK. Such low-carbon content was required to represent composition of historic ferritic iron artefacts which have a lower carbon-content than that of steel artefacts (0.02-0.77 wt% carbon content)[198]. The chemical composition of the iron is presented in **Table 3.1**:

Table 3.1: Chemical composition of high purity Remko iron.

Element	C	Si	Mn	P	S	Cr	Mo
wt%	0.022	0.010	0.190	0.004	0.014	0.100	0.020
Element	Ni	V	Al	Cu	Sn	Balance Fe	
wt%	0.040	0.002	0.012	0.050	0.006	(>99 wt%)	

Iron bars were metallurgically sectioned into square-shaped coupons of dimensions 6.35 mm × 38 mm × 38 mm. The coupon surfaces were then ground successively using 120-180-240-400-600-800-1200-2500 SiC abrasive paper purchased from Metprep. The final mirror finish of the surface was obtained using 6 µm polycrystalline diamond paste (Metprep, UK). Once polished, the coupons were cleaned from any surface particles using liquid soap and running tap water, and immediately rinsed with de-

ionised water followed by isopropyl alcohol (IPA). The solvent was removed using a heat gun. Coupons were then wrapped in cotton pads and stored in air-tight plastic containers over a bed of silica gel until use. Coupons were then re-polished prior to coating application.

3.2.1.2 Preparation of corroded iron coupons

In order to simulate the corroded areas on iron Heritage artefacts, polished iron coupons were subject to an artificial corrosive atmosphere maintained in an Aster CNS/500 accelerated corrosion test chamber. Iron coupons were subjected to a number of wet-dry cycles as follows:

- i) Wet-cycle: 16 hours at $40\text{ }^{\circ}\text{C} \pm 2\text{ }^{\circ}\text{C}$ with $90\% \pm 5\%$ relative humidity;
- ii) Dry-cycle: 8 hrs $25\text{ }^{\circ}\text{C} \pm 2\text{ }^{\circ}\text{C}$ with $25\% \pm 5\%$ relative humidity

A 90% relative humidity was achieved by following the ASTM D5032-97 (2003) standard practice through the use of an aqueous glycerol solution (4.15 mol/L refractive index 1.377) purchased from Sigma-Aldrich (95% purity, USA). The humidity was maintained through the use of an air-tight container (500 x 300 x 300 mm³) in which coupons were placed and supported on a Perspex rack specifically designed for this purpose. The dry cycle relative humidity was obtained by replacing the glycerol solution with silica gel (c. 30% RH, refer to Figure 3.1).

The container was placed in the ASTER chamber since the required temperature (40 °C) can be easily regulated in such a chamber, but less so in a regular oven. The wet-dry cycle was carried out for a total of 30 cycles in order to achieve an overall corroded surface on the coupons. Apart from clean surface, surfaces having such a homogeneous layer of surface corrosion were investigated to determine the minimum extent of corrosion protection offered by coatings on such surfaces. Temperature and humidity measurements were recorded using a Hobo® data-logger (see **Figure 3.1**). The scope for applying milder conditions to produce corroded surfaces as opposed to applying harsher conditions such as salt-spray, is to better simulate the gradual formation of corrosion products as occurs under indoor environments. Salt-spray treatment would lead to the fast production of a rather friable bright red/orange corrosion product layer over a thin layer of black rust.

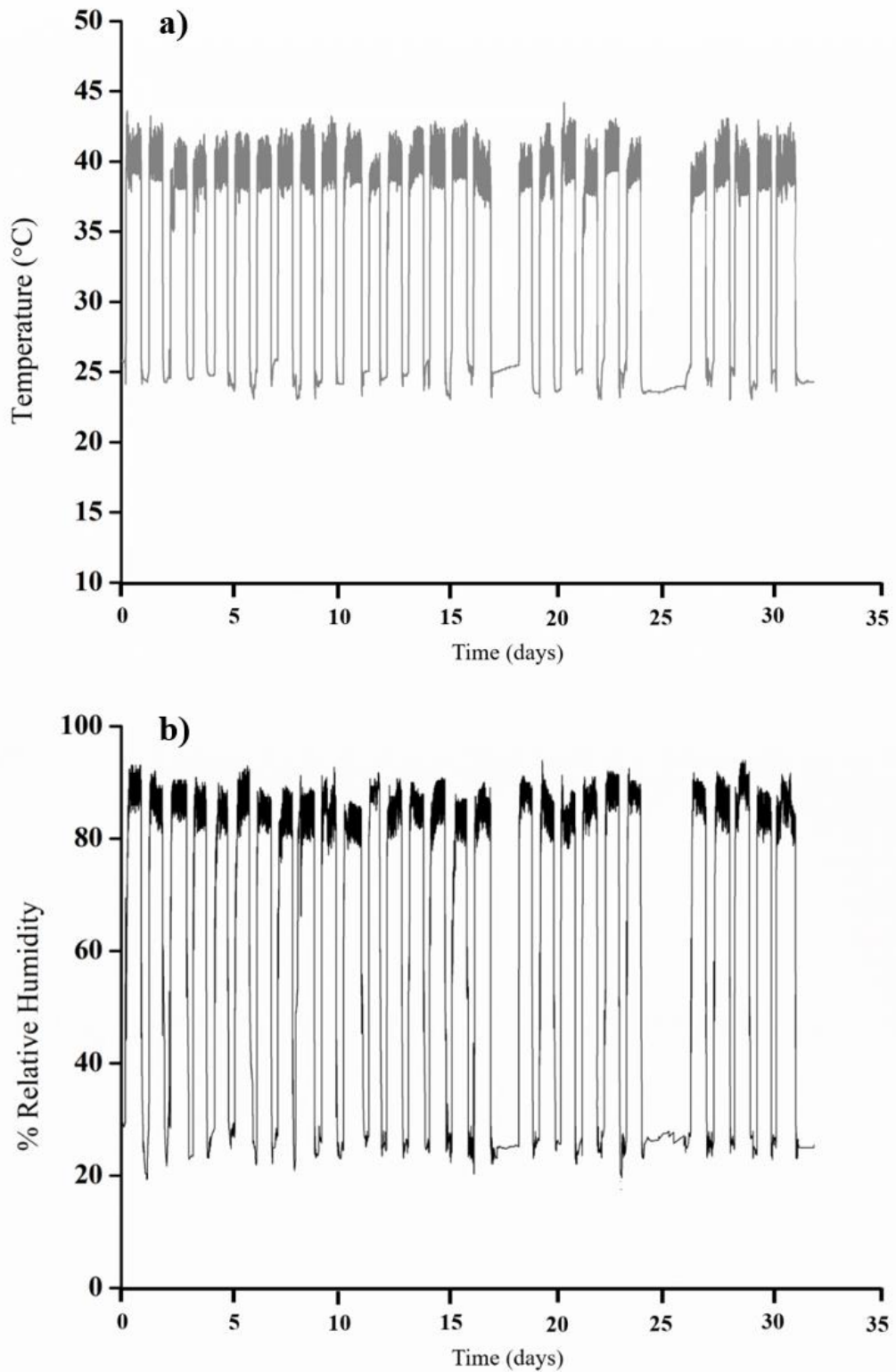


Figure 3.1: a) Temperature and b) Relative Humidity measurements taken during wet-dry cycles performed on iron coupons to accelerate the corrosion process.

Following accelerated corrosion, the coupons were cleaned to remove loosely attached corrosion products using a handheld Dremel® 3000 multi-tool with stainless steel brush attachment used by conservators to clean corroded areas. The lowest operating speed was employed (10,000 rpm) to gently clean the corroded surface. The cleaned surface was then rinsed with acetone to remove dislodged corrosion products from the surface of the coupon.

3.2.2 Characterisation of iron surfaces

3.2.2.1 Etching of polished iron surface

Etching was carried out to reveal the microstructure of the iron under investigation. A few drops of 2% Nital solution (2% v/v concentrated nitric acid in ethanol) were pipetted onto a polished iron coupon for a couple of seconds followed by a quick rinse under running water, so as to remove the Nital solution followed by isopropyl alcohol and drying using a heatgun. The etched surface was then observed using optical microscope (see Section 3.3.8.4).

3.2.2.2 Scanning Electron Microscopy (SEM)

A Carl-Zeiss FE SEM Gemini scanning electron microscope was employed to examine cross-sections of the corroded and corroded-cleaned iron samples (see Section 3.3.8.5). Coupons were cut in half, carefully mounted in Struers PolyFast conductive Bakelite using a Remet IPA 30 Bakelite mounting machine. The mounted cross-sections were then ground and polished as per previous discussion, see Section 3.2.1.1.

3.2.2.3 X-Ray Diffraction (XRD)

The surface of cleaned coupons, together with uncleaned and cleaned corroded surfaces were characterised using a Rigaku Ultima IV diffractometer equipped with a CuK_α source. Glancing angle XRD was used, for which a small angle of incidence (3°) ensures that the depth of analysis is controlled by the angle of incidence and does not vary during the sweeping. The detector arm was moved at a scan speed of 1° per minute, sampling data for every 0.02° in the range between 20° to 85° . The

accelerating voltage and current of the tube were set at 45 kV and 40 mA respectively. The surface crystalline phases of the samples investigated were then determined by comparing the X-ray diffraction patterns obtained with those found in the Powder Diffraction Files (PDF) from the International Centre of Diffraction Data (ICDD).

3.3 Protective Coating lacquers

3.3.1 Materials

3.3.1.1 Sol preparation

Tetraethoxysilane (98%), methyltriethoxysilane (98%), propyl-triethoxysilane (97%) and phenyl-triethoxysilane (98%) were purchased from Alfa Aesar, USA ; hexyltriethoxysilane (96%) purchased from Gelest Inc., USA and octyltriethoxysilane (97.5%) from Sigma-Aldrich, USA. These were used as purchased without further purification. Concentrated nitric acid (64-66% Sigma-Aldrich, USA) was diluted to form a 1 N nitric acid solution to act as the catalyst during the sol development whereas deionised water ($< 0.1 \mu\text{S}/\text{cm}$) was employed for the hydrolysis of the organoalkoxysilane precursors. A 10% (v/v) triethanolamine (98% BDA, Japan) in ethanol (99.99% Sigma-Aldrich, USA) solution was used for sol neutralisation. 99.99% pure ethanol (Sigma-Aldrich, USA) was used as the diluent to obtain the final sol volumes.

Solvents other than ethanol were also used as diluents. These were ethylene glycol butyl ether ($\geq 99.5\%$ Sigma-Aldrich, USA) and formamide ($\geq 99.5\%$ Sigma-Aldrich, USA) in a 1:1 and 1:5 (v/v) mixture with ethanol. 33% ammonia solution (Sigma-Aldrich, USA) was employed as a catalyst in the Stöber process for manufacturing silica nanoparticles. Commercial silica nano-particles (99.5% trace metal basis, Sigma-Aldrich, USA) with an average particle size of 10-20 nm was used as an additive to bulk the prepared acid-sols. Cerium (III) nitrate hexahydrate (99.99%), 1-Naphthol ($\geq 99.0\%$), 1,4-Naphthoquinone (97%), Phenyl benzoate (99%), Pyrrolidine (99%) and 2-Hydroxypyridine (97%) all purchased from Sigma-Aldrich, USA were employed as corrosion inhibitors.

3.3.1.2 Lacquer preparation

The Paraloid B-48 and Paraloid B-72 acrylic resins were supplied by Dow Chemicals, USA. Various coating lacquer concentrations (wt/vol) were obtained by dissolving Paraloid pellets in acetone (99.9% Sigma-Aldrich, USA) respectively. The nitrocellulose lacquer Ercalene (H. S. Walsh, UK) was diluted with lacquer thinner Diluente Nitro 416 (Fidea, Italy) which is a mixture containing mainly the solvents toluene (35-40%), acetone (27-30%), methyl acetate (20-23%), methanol (7-10%) and *n*-butyl acetate (5-6%). Waxes such as Renaissance microcrystalline wax were not considered since this was determined to not offer significant corrosion protection on both clean and corroded metal substrate by Cano *et al* [170].

3.3.2 Procedure for sol and lacquer preparations

3.3.2.1 OIH alkoxy silane sols

Prepared sols consisted of a mixture of TEOS with either methyltriethoxysilane (MTES), *n*-propyltriethoxysilane (PrTES), *n*-hexyltriethoxysilane HTES, phenyltriethoxysilane PhTES or *n*-octyltriethoxysilane OTES in the mole ratios described in **Table 3.2**. The final silica concentration was set to either 25, 50, 100 or a 150g/L.

To ensure stoichiometric hydrolyses of the alkoxy silane precursors, an H₂O : SiO₂ : HNO₃ molar ratio of 4:1:0.00025 was employed. Sols were prepared by transferring known measured volumes of the alkoxy silane precursor into a 250 mL three-necked round bottomed flask which was fitted with a reflux condenser and placed on a water-bath on top of a heating/stirring mantle. The temperature inside the flask and that of the water-bath was monitored using glass thermometers. Measured amounts of water and mineral acid were then added to the precursor mixture kept at a temperature of 20 °C and allowed 4 hours of continuous stirring at a rate of 500 r.p.m.

Table 3.2: Mole percent ratio (mol %) of alkyltrialkoxysilane precursor mixtures investigated in this work are marked with an asterisk (*).

Mixture	mol%						
	10:90	20:80	30:70	40:60	50:50	60:40	80:20
MTES:TEOS		*		*		*	*
PrTES:TEOS		*		*	*	*	
HTES:TEOS		*	*	*		*	
OTES:TEOS	*	*		*		*	
PhTES:TEOS		*		*		*	*

In OTES:TEOS sols, a precipitation of fine silica particles was observed early on in the hydrolyses-polycondensation step. In order to eliminate this problem of precipitation, sol preparation was modified as follows: a 4:1:5 H₂O:SiO₂:EtOH ratio was employed, with ethanol being added to the mixture of OTES and TEOS before the addition of water. Following this, the sols were diluted with ethanol to achieve the required final silica concentration.

Table 3.3 (a) presents volumes of chemicals used to prepare **2.5%** (wt/v) SiO₂ sols of the five alkyltrialkoxysilane precursor mixtures tested in this work. Note that the total SiO₂ amounts to 0.041 mole for all five precursors (2.5 g/60 g SiO₂= 0.041 mole SiO₂). The addition of water comes partially from the small volume of nitric acid added which is also considered as contributing to the total volume of water i.e. 0.25 mL HNO₃ + 2.75 mL H₂O = 3 mL H₂O total (0.166 mole). Higher silica concentrations were prepared as follows exemplified though MTES:TEOS 80:20 mol% sol as shown in Table 3.3 (b).

Prepared sols were stored inside well-sealed polypropylene containers at -25 °C in a chest freezer. Prepared acidified sols were neutralised prior to dip-coating of the metal using 10% (v/v) solution of triethanolamine in ethanol to a final pH of between 6-7. The pH was monitored using universal indicator pH strips range 0-14 (Carolina).

Table 3.3: (a) Volumes required for the preparation of 2.5% SiO₂ exemplary sols listed. X-TES stands for alkyltriethoxysilane where X = methyl, propyl, hexyl, phenyl and octyl and (b) Volumes required for the preparation of 2.5, 5, 10 and 15% SiO₂ MTES:TEOS 80:20 mol% exemplary sols.

(a)								
		X-TES	TEOS	Total SiO ₂	H ₂ O	HNO ₃	Total Water	EtOH
MTES:TEOS 80:20 mol%	moles	0.033	0.0083	0.041	(0.166)	0.00025	0.166	-
	vol (ml)	6.64	1.86	8.50	2.75	0.25	3	-
PrTES:TEOS 60:40 mol%	moles	0.025	0.016	0.041	(0.166)	0.00025	0.166	-
	vol (ml)	5.78	3.72	9.50	2.75	0.25	3	-
HTES:TEOS 40:60 mol%	moles	0.016	0.025	0.041	(0.166)	0.00025	0.166	-
	vol (ml)	4.81	5.58	10.39	2.75	0.25	3	-
PhTES:TEOS 20:80 mol%	moles	0.0083	0.033	0.041	(0.166)	0.00025	0.166	-
	vol (ml)	2.01	7.44	9.45	2.75	0.25	3	-
OTES:TEOS 10:90 mol%	moles	0.0041	0.037	0.041	(0.166)	0.00025	0.166	0.21
	vol (ml)	1.30	8.37	9.67	2.75	0.25	3	9.43
Table 3.3 (b)								
MTES:TEOS 80:20 mol%		X-TES	TEOS	Total SiO ₂	H ₂ O	HNO ₃	Total Water	
2.5%	moles	0.033	0.0083	0.041	(0.166)	0.00025	0.166	
	vol (ml)	6.64	1.86	8.50	2.75	0.25	3	
5%	moles	0.066	0.0166	0.0826	(0.332)	0.0005	0.332	
	vol (ml)	13.28	3.72	17.0	5.50	0.50	6	
10%	moles	0.132	0.0332	0.1652	(0.664)	0.001	0.664	
	vol (ml)	26.56	7.44	34.0	11.0	1.00	12	
15%	moles	0.198	0.0498	0.2478	(0.996)	0.0015	0.996	
	vol (ml)	39.84	11.16	51.0	16.5	1.50	18	

3.3.2.2 Preparation of nanoparticles by the Stöber Method.

The preparation of the Stöber nanoparticles was carried out in a two-necked round bottomed flask fixed over a stirring mantle set inside a fume hood as described in [112]. Varying the TEOS concentration at the start of sol allows the average size of the particles to be varied [112]. Three Stöber sols were investigated based on the initial concentration of TEOS used: 0.2 M, 1 M and 2 M TEOS which are listed in **Table 3.4**. Alkaline Stöber sols of particle size range ~20-60 nm were prepared by

measuring out the appropriate volume of TEOS into the flask at a stirring rate of 500 r.p.m. and room temperature conditions. Unlike the organic-inorganic silica sols described previously, the solvent was added to the TEOS before the addition of ammonia and water so as to avoid forming large sol particles possible gelation. The water : ammonia ratios were kept constant whilst varying the initial concentration of TEOS (see Table 3.4). The sols were prepared in 100 mL batches where the appropriate amount of ethanol was calculated and included prior to the addition of aqueous solution.

Table 3.4: Amounts of chemicals (shown in moles and volume) required to produce several TEOS concentrations of Stöber sol.

TEOS conc.		TEOS	water	ammonia	Total H ₂ O	EtOH	Total sol volume
0.22 M (20 nm)	moles	0.22	1.1968	0.1782	1.375		
	vol (ml)	4.91	1.20	2.12	3.32	86.33	100
1 M (26 nm)	moles	1	1.1968	0.1782	1.375		
	vol (ml)	22.32	1.20	2.12	3.32	68.92	100
2 M (56 nm)	moles	2	1.1968	0.1782	1.375		
	vol (ml)	44.65	1.20	2.12	3.32	46.59	100

OIH silica sols containing /loaded with Stober nanoparticles were prepared as follows:

Freshly prepared Stober nanoparticles (1 wt % silica) were folded into 60:40 mol % MTES:TEOS sol containing 5% SiO₂ to furnish a final sol containing 6% silica. MTES-TEOS sols were prepared having different nanoparticle sizes, namely 20 nm, 26 nm and 56 nm as described in **Table 3.5**. The problem encountered when adding SNPs originating from 0.22 M concentration of TEOS having particle size of 20 nm, is that the silica concentration of this sol is of 1.32g/100ml; thus in order to obtain 1g/100ml (1% SNP) in the final sol, most of this alkaline solution must be added to the acidic MTES:TEOS 60:40 5% SiO₂ sol (see Table 3.5).

Table 3.5: Volumes used to create a final sol consisting of MTES:TEOS 60:40 mol% (5% SiO₂) loaded with 20, 26 and 56 nm Stober NP (1% SNP) using various starting TEOS concentrations.

Stöber sol			Acidic sol (ml)	Vol. EtOH (ml)	Final sol Vol. (ml)
TEOS conc.	SiO ₂ conc. of Stöber sol	Vol. sol required to create 1% SNP	Vol. 5% SiO ₂ MTES:TEOS 60:40 sol		
0.22 M (20 nm)	1.32 g /100ml	75.75	20.00	4.25	100
1 M (26 nm)	6 g/100 ml	16.66	20.00	63.34	100
2 M (56 nm)	12 g/100ml	8.33	20.00	71.67	100

When attempting to lower the pH of the Stöber sol, coagulation was immediately observed. A weaker acid cannot be used since a large volume of water would also be introduced which will affect the particle size and overall integrity of the sol. A higher concentration of TEOS was thus attempted whilst keeping ratios of water:ammonia as for 0.22 M TEOS (TEOS : NH₄OH : H₂O ratio of 1 : 0.1782 : 1.375 M). By increasing the initial TEOS concentration, less of a volume of alkaline sol is required to achieve the desired concentration of SNP in the final sol. The final sol mixture was carried out by firstly adding the required volume of ethanol to the alkaline sol, followed by the dropwise addition of the acidic sol to the diluted alkaline sol, for which coagulation was avoided with both 1 M (26 nm) and 2 M (56 nm) TEOS sols.

3.3.2.3 Commercial nanoparticles

Commercially-purchased nanoparticles (henceforth CNPs) of size 10-20 nm were studied as another source of NP for inclusion/incorporation into OIH alkyl trialkoxysilane coatings. CNPs were incorporated in various amounts to furnish the following final sols as presented in **Table 3.6** below.

Table 3.6: Amounts of CNPs of size 10-20 nm required to produce 100, 300 and 500 ppm CNP-containing 60:40 mol% MTES:TEOS (5% SiO₂ wt/v).

CNP (ppm)	Mass NP (g)	Vol of 60:40 mol% MTES:TEOS mL	ethanol (mL)	Final sol volume (mL)
100	0.01	20.00	80.00	100
300	0.03	20.00	80.00	100
500	0.05	20.00	80.00	100

The weighed amount of CNPs were added to the volume of ethanol and sonicated using a Kerry Pulsatron Sonicator for 20 minutes in order to disperse the particles. The CNP-containing ethanol was then used to dilute the MTES:TEOS sol to a final volume of 100 mL as carried out for sols in the previous section. Therefore, considering 100ppm CNP as an example, the concentration of CNPs present in the final sol is 0.01g per 100mL (or 0.1g/L which is equivalent to 100 ppm).

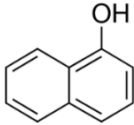
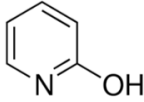
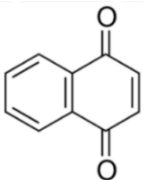
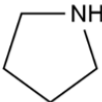
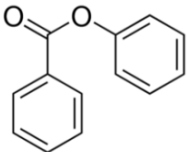
3.3.2.4 Inorganic and organic inhibitors

Each of the five organic inhibitor molecules and inorganic inhibitor (see **Table 3.7**) were added individually to sols consisting 60:40 mol% MTES:TEOS and 20:80 mol%.OTES:TEOS. Mechanism of inhibition of corrosion process and choice of inhibitors featured in this work is explained in Section 2.6.2. The final SiO₂ concentration in these sols was set to 2.5% wt/v. The inhibitors were dissolved in the solvent that was used in the dilution of sols. Inhibitors were prepared in the following concentrations 0.01, 0.001 and 0.0001 M. For example, a 100 mL MTES:TEOS sol having a 0.01 M cerium (III) nitrate hexahydrate concentration would require the dissolution of 0.434 g Ce in ethanol solvent, which is then added to produce 60:40 mol% MTES:TEOS sol (see Table 3.7 for RMM of Ce).

In this study cerium nitrate hexahydrate inhibitor was used for comparative purposes as it a well-researched inorganic inhibitor [85,128-132,79,127,120,133,134] known to impart anti-corrosion properties to sol-gel coatings. Thus, it has been included to determine the extent of improvement in corrosion protection in our OIH alkoxy silane coatings; the extent can then be used as a reference point to other less popular inhibitors namely pyrrolidine [121], 2-hydroxypyridine [162-166] which have

been studied as inhibitors in aqueous solution but not incorporated into coatings *per se*. 1-naphthol and phenyl benzoate are not featured in any known work for their use as corrosion inhibitors. Therefore, these organic molecules have been included in this work since little data could be found on their inhibiting abilities when incorporated in OIH alkoxysilane coatings. The smaller molecules 2-hydroxypyridine and pyrrolidine were incorporated to determine whether inhibition can be related to the size of the molecule.

Table 3.7: Table showing inorganic and organic inhibitors used in this work, chemical name, chemical structure, RMM and melting/boiling point in °C.

Chemical name	Chemical formula/Structure	RMM (g/mol)	MP/BP (°C)
Cerium (III) nitrate hexahydrate	$Ce(NO_3)_3 \cdot 6H_2O$	434.23	96/200
1-Naphthol		144.17	96.1/280
2-Hydroxypyridine		95.10	107.8/280
1,4-Naphthoquinone		158.15	126 (sublimation)
Pyrrolidine		71.12	-57.79/ 86.56
Phenyl benzoate		198.22	68/298

3.3.2.5 Acrylate and nitrocellulose lacquers

Ercalene, Paraloid B-48 and B-72 were used to draw a comparative study with the OIH alkyltrialkoxysilane coatings. The Paraloid coatings were prepared by dissolving various amounts of Paraloid pellets in 100 mL of acetone at room temperature. The concentrations considered in % wt/v were 2.5, 5, 10 and 15%. Nitrocellulose lacquer Ercalene was diluted with lacquer thinner Diluente Nitro 416 (DN) solvent to a ratio of 75:25 Ercalene : DN.

3.3.3 Coating deposition and curing

For the purposes of coating consistency and repeatability, coatings applied to clean and corroded surfaces were primarily deposited by dip-coating. The author is aware however that conservators-restorers typically apply their coatings by brushing or spray [13]. The advantages of dip-coating are consistency and repeatability of coating thickness, even when coatings are deposited over a period of time. An added benefit of using dip-coating is that it is relatively inexpensive, and fast.

After neutralisation of the alkyltrialkoxysilane sols, dip-coating of polished and corroded iron coupons was carried out using a home-built dip coater. The coupons were attached to a holder and the dip/retrieval speed was set to 280 mm/min with a sample immersion time of 60 s for all coatings investigated. In this work, single, double and triple-layered coatings were applied to sample coupons. The coated coupons were then dried in a Memmert UF160 drying oven for 1 hr at 150 °C and allowed to cool down slowly in the oven. Coatings prepared to a silica loading of 10% wt/v were dried and cured between multi-layer coating applications so as to assure a dry underlying coating prior to a top coat application. Coatings with lower silica loading (< 5 % wt/v) were only subject to drying between multiple coating applications without curing in oven. Once cooled to room temperature, coated coupons were stored in polyethylene bags until further testing.

Coatings loaded with inorganic and organic inhibitor molecules were subject to a maximum curing T of 60 °C for 4 hrs since the boiling temperatures of the organic inhibitors 1,4-naphthoquinone and pyrrolidine were < 150 °C (refer to Table 3.7). Control coatings (coatings without inhibitor) for these experiments were also subject to the same curing conditions.

Paraloid and Ercalene coatings were also applied by dip-coating procedure. These coatings were however not cured, but allowed to air-dry in a dry laboratory environment. Both clean and corroded iron coupons were coated with these lacquers. The preparation and handling of sols, their deposition into coating films and curing, was carried out in as much as possible clean, dust-free environment.

3.3.4 Sol characterisation

3.3.4.1 Particle sizing

Particle size measurements were conducted on 1 mL sol samples using a Malvern ZetaSizer Nano ZS Dynamic Light Scattering (DLS) instrument which employs 173° backscatter detection optics. Size distribution analysis was performed using a general-purpose algorithm which employs non-negative least squares (NNLS) analysis which is a suitable model for dispersions and emulsions. Refractive index (RI) for silica nanoparticles was set to 1.48, solvents ethanol and IPA used for sol development are considered as dispersants of SiO₂ nanoparticles, their refractive indices and viscosities were also required for measurements: RI= 1.361 and viscosity= 1.0780 cP [199] for absolute ethanol, RI=1.377 and viscosity 1.9600 cP [199] for Isopropyl alcohol. For each sample, three measurements were recorded by the instrument and for the purpose of reproducibility, three samples were tested i.e. 9 readings were considered when calculating and presenting mean and standard deviation of particle size of a sol as seen in Tabulated PS data (for example, Table 5.1). Plots of PS featured in this work show one representative from the 9 measurements taken for that particular sol (as presented in ex. Figure 5.1).

DLS relies on the interaction of light with the electric field of a small particle which results in the scattering of light equally in all directions (for full explanation, see Section 4.2.1). The intensity of light that the particles produce is proportional to d^6 where d is the particle diameter ($I \propto d^6$) which translates to larger particles producing a higher intensity signal than smaller particles. Results for DLS measurements are presented as plots of either intensity or particle volume versus particle diameter (nm). The distributions presented in terms of intensity distribution or calculated and presented in terms of volume intensities often produce differing results in terms of their mean values and the appearance of the distributions even though they represent the same physical characteristics of a sample.

3.3.5 Coating characterisation

3.3.5.1 Infra-red spectroscopy

IR spectroscopy of powders obtained from alkyl/aryltriethoxysilane:TEOS sols (see Section 3.3.5.1) was performed on a Shimadzu IR-Affinity spectrometer. The powders were cured under the same conditions as for the coated metal coupons (150 °C for 1 hr) following which they were mixed with potassium bromide (KBr) and pressed into transparent discs. KBr was mixed with dried sol-gel derived powders so as to obtain an approximately 5% (wt/wt) silica in KBr which generated the best spectra. Characterisation of 20:80 mol% sols was performed in transmission mode within the range 4000-400 cm^{-1} at a 4 cm^{-1} resolution or between 3500-2500 cm^{-1} region at 1 cm^{-1} resolution.

Specific infrared spectral bands generated for the sol-gel coatings and of interest in this work were subject to area analysis to determine how they alter when the length of the alkyl groups are increased. Peak Area Analysis of a number of cured sols was problematic due to the formation of tacky solid or gel (high organics concentration) rather than powder which renders the task of creating a KBr disk impossible. The identities of the silica powders that formed usable KBr disks and were therefore further subject to peak analysis are marked with asterisk in **Table 3.8**.

Table 3.8: Sols featured in IR Peak Area Analysis.

Mixture	XTES:TEOS mol%						
	10:90	20:80	30:70	40:60	50:50	60:40	80:20
MTES:TEOS		*		*		*	*
PrTES:TEOS		*		*			
HTES:TEOS		*					
OTES:TEOS	*	*					
PhTES:TEOS		*		*			

The procedure for peak area analysis was carried out in the following way and is described by the example presented in **Figure 3.2** (a-b). The raw IR data file was imported into Origin Pro (2017) which is a software dedicated to data processing and to graphic analysis and a 5-point parameter smoothing procedure was applied so as to minimise noise, mostly present in the higher and lower regions of the spectrum. As seen in Figure 3.2 (a), the baseline shifts to a lower transmittance value as the wavenumber increases. This is attributed to the presence of inorganic silica network as reported by [200]. The shift is caused by scattering of IR light at the sample surface, this effect being greater at shorter wavelengths, i.e. higher wavenumbers. Therefore, baseline correction was carried out to minimise this effect. The baseline subtraction was carried out on each spectrum using Peak Analyser function within Origin using the method of asymmetric least square smoothing and having set parameters as listed in **Table 3.9**. Figure 3.2 (a) shows the assigned baseline (red line) onto the transmittance spectrum and Figure 3.2 (b) shows the resultant spectrum, once the baseline has been subtracted to reveal a number of peaks having the same minimum point.

Table 3.9: Parameters employed for baseline correction of IR spectra using Origin.

Parameter	Value
Asymmetric factor	0.001
Threshold	0.005
Smoothing factor	4
Number of iterations	10

The resulting spectrum in Figure 3.2 (b) was also subject to a normalisation process where minimum and maximum points are set and these values are set for all other spectra within the group of spectra. In this work, 20:80mol% MTES:TEOS was arbitrarily chosen as the benchmark spectrum for which the maximum point occurs at wavenumber 1067 cm^{-1} and minimum point being already fixed by the baseline. All other points along the spectrum were set relative to the maximum and minimum points of the original spectrum.

After baseline correction and normalisation, the area under the peaks determined for each spectrum. The 'Integrate' tool was used to calculate the begin/end of a peak, the maximum height, the mathematical area, the centroid and the Full Width at Half Maximum (FWHM), for which each peak was assigned and selected manually.

- Eight absorption bands occurred between $3500\text{-}500\text{ cm}^{-1}$ for all sol-gel derived powders studied (see Figure 3.2 (b) for 20:80 mol% MTES:TEOS): The absorption band at 600 cm^{-1} , (labelled Peak 1) due to the rocking motion Si-OH or Si-O⁻ groups [201]
- The absorption band at 951 cm^{-1} (labelled Peak 3) attributed to the stretching vibrations of the Si-OH or Si-O⁻ groups
- The absorption band at 793 cm^{-1} (labelled Peak 2) is due to the symmetric stretching of the oxygen atoms along the bisector of the Si-O-Si bridging angle [201]
- The absorption band at 1067 cm^{-1} and the shoulder at 1200 cm^{-1} , respectively labelled Peaks 4 and 5 are due to the asymmetric stretch of the oxygen atom within the siloxane -Si-O-Si bond
- Peaks 6-8 have been attributed to the un-hydrolysable organic portion of the silica-network.

Peak at 1035 cm^{-1} falls within a region attributed to primary and secondary alcohols, which may be present in small amounts since sols are dispersed in ethanol and as a by-product of the hydrolysis/condensation reactions during silica-network formation, and will therefore not be considered further.

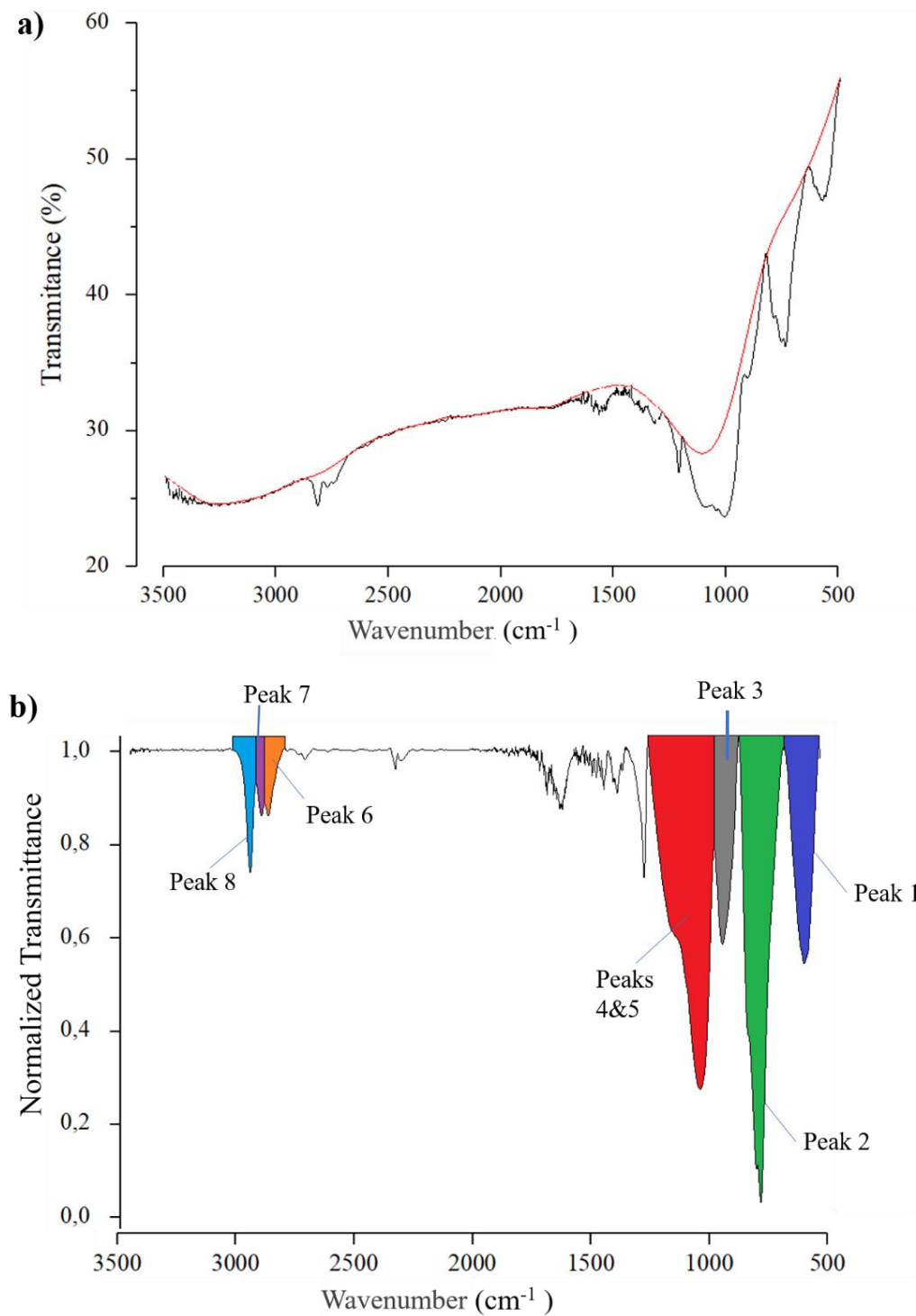


Figure 3.2: a) 20:80 mol% MTES:TEOS IR plot of wavenumber versus transmittance for smoothed raw data in the 3500-500 cm⁻¹ region featuring baseline correction where the software sets baseline shown in red; b) spectrum (a) following baseline subtraction and the application of normalisation process. This figure also includes the assigned 8 peaks of interest from which the peak areas are calculated through the software

For each spectrum analysed, the areas of the eight assigned peaks were added up and expressed as an area percentage (Area %) for each peak; these percentages were then used to draw a comparative study involving all of the systems considered.

An attempt was made to separate the two absorption bands Peak 4 (1067 cm^{-1}) and 5 (1200 cm^{-1}) through a process known as deconvolution. These absorption bands produce the most intense and broad absorption bands in all spectra examined where the dominant band at 1070 cm^{-1} is due to the transverse optical (TO) component of the asymmetric stretching of Si-O-Si bonding, whereas the shoulder at 1200 cm^{-1} is related to the longitudinal optical (LO) component of the same vibration [202]. However, even though the process of deconvolution was well within the capability of the software, this was not possible in this study as the shoulder of the main absorption band was too small for the software to process.

IR spectroscopy was also employed to characterise sol-gel coatings loaded with inorganic and organic corrosion inhibitors. Inhibitors were incorporated into 20:80 mol% OTES:TEOS and 60:40 mol% MTES:TEOS coatings at concentrations of 0.01 M. Lower concentrations of inhibitors were not considered since these molecules produced weak signals even at a higher concentration of 0.01 M.

3.3.5.2 UV-Vis Spectroscopy

The optical transparency of the OIH alkoxy silane coatings prepared as described in Section 3.3.5.1 was determined from optical transmission measurements using single-face coated soda lime glass slides having dimensions 75 mm x 26 mm. During dip coating of the glass slides, the uncoated face was masked with Scotch® Solvent Resistant Masking Tape 226. After coating deposition, the masking tape was peeled off gently to expose a clean uncoated surface and the coated slides were cured as described in Section 3.3.6. The transmission spectra were recorded on a Jasco V-650 UV-visible spectrophotometer between 200-800 nm in transmission mode with a 0.5 nm spectral resolution.

3.3.5.3 Contact angle

Static contact angle measurements were carried out on a home-built contact angle device consisting of an all aligned back light source, sample stage and digital camera, set-up is shown in **Figure 3.3**. A 10 μL drop of distilled water was micro-pipetted onto the coated surfaces and a still image of the droplet was shot using Aveo UVC PC Camera software. The contact angle was obtained by processing the drop images using Image J (Image Processing and Analysis in Java developed by [203]). Average contact angle values were generated over 5 repeat measurements.

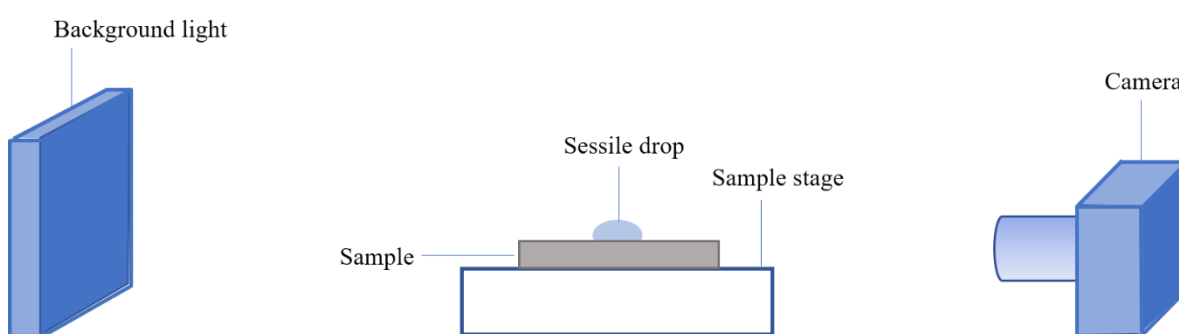


Figure 3.3: Image of home-built contact angle measurement set-up.

3.3.5.4 Optical microscopy

Optical microscopy observations of the uncoated and coated coupons were carried out on a Nikon Optihot 100 microscope using magnifications between $\times 5$ to $\times 50$. Optical micrographs were captured through the microscope optics using a Leica DFC290 digital camera and the digital images were processed using Leica IM500 software.

3.3.5.5 Scanning Electron Microscopy

The surfaces of coupons were observed at high magnification using a Carl-Zeiss Merlin Field Emission Scanning Electron Microscope (SEM) using a voltage setting of 15 kV, 1.0 nA current and variable working distance. Electron microscopy was employed to determine coating thicknesses and to examine the surface topography of un/coated coupon surfaces. Surface topographical imaging was conducted

on iron sample coupons whereas coating thickness was carried out on stainless steel strips dip-coated with double layers of coatings. Stainless steel (SS) strips of 0.5 mm thickness were double dip-coated and cured depending on the coating being studied as described earlier in Section 3.3. Coated SS strips were then bent to form a wedge shape and mounted onto aluminium stubs via double-sided carbon tape. Thickness measurements were carried out at the wedge zone where the coatings were observed to fracture and delaminate exposing their cross-sectional thicknesses.

X-ray elemental analysis of the sol-gel coatings prepared in this work and the underlying substrate was carried out using Energy Dispersive X-ray Spectrometer attached to the electron microscope (SDD Apollo 10 detector by EDAX). The conditions of analysis were as follows: an accelerating voltage of 15 keV, a current of 1 nA and a fixed working distance of 6 mm. EDS was used to determine whether defects in the coatings led to the exposure of the underlying metal substrate; for instance, it was employed to confirm results obtained for nano-scratch testing of the coatings. EDAX analysis was also employed to confirm the presence of inorganic and organic inhibitors after their incorporation into MTES/OTES coatings.

3.3.6 Mechanical testing

3.3.6.1 Nano-indentation

3.3.6.1.1 Hardness and Young's Modulus determination

Coating hardness was determined using a MicroMaterials Nano Test instrument equipped with a Berkovich indenter which has a three-sided pyramidal-shaped diamond tip [204]. The test was carried out on 2.5% SiO₂ sol-gel double coated microscope glass slides. The indenter was loaded onto the coated glass using the parameters presented in **Table 3.10**. Glass was used as underlying substrate since it is harder than Iron and therefore any influence from underlying substrate would be more clearly observable in results obtained. Glass is also more planar and scratch free compared to polished metal surface.

Table 3.10: Parameters employed to carry out hardness testing on coated glass slides.

Initial load:	0.01 mN	No. of indentations:	30
Loading rate:	0.01 mN/s	Maximum load:	0.15 mN
Unloading rate:	0.01 mN/s	Minimum load:	0.15 mN

3.3.6.1.2 Nano-scratch testing

Nano-scratch tests were performed on 2.5% SiO₂ sol-gel double coated polished metal coupons to investigate the coating adhesion to the substrate. 2.5% Paraloid B-48, B-74 and Ercalene (50%) double coated metal coupons were also considered and compared to Silica coated metal coupons. A MicroMaterials Nano Testing machine was employed to carry out the scratch tests. Scratch marks were drawn into the coated surface with a 10 µm radius tip conical indenter. For each scratch generated three scans were carried out: i) a preliminary topography scan having a constant load of 0.8 mN over a total length of 350 µm at a speed of 2.00 µms⁻¹, ii) a scratch scan where the load was initially kept constant at 0.8 mN along 50 µm and then ramped at a constant load rate of 1.33 mNs⁻¹ up to a maximum load of 200 mN and a total scan length of 350 µm; and iii) a second topography scan conducted at a constant load of 0.8 mN. The latter was conducted so as to profile the surface after scratching. A total of five scratches were generated and distanced apart by 150 µm. The final topographic scan was used to investigate the elastic recovery of the material. The scratches carried out by the indenter were also studied using an optical microscope to visually understand changes in depth profile of the scratch test results.

3.3.6.2 Adhesion testing

The Pull-Off test determines the level of adhesion of a coating and was carried out in accordance to the ASTM D4541-17 “Standard Test Method for Pull-Off Strength of Coatings Using Portable Adhesion Testers”. The latter standard consists of two test protocols i) “a test to fracture” which determines the greatest perpendicular force, in the form of an applied tension, that a known surface area can bear before a plug of material is detached and ii) “a Pass/Fail test” that specifies whether

tested coating remains intact following detachment. The pull-off test was performed by securing a loading fixture (known as a dolly) perpendicular to the surface of the coated metal coupons (**Figure 3.4**) using Araldite adhesive glue, which is an epoxy-based fast drying two-part adhesive frequently employed in such tests (ASTM D4541-17).

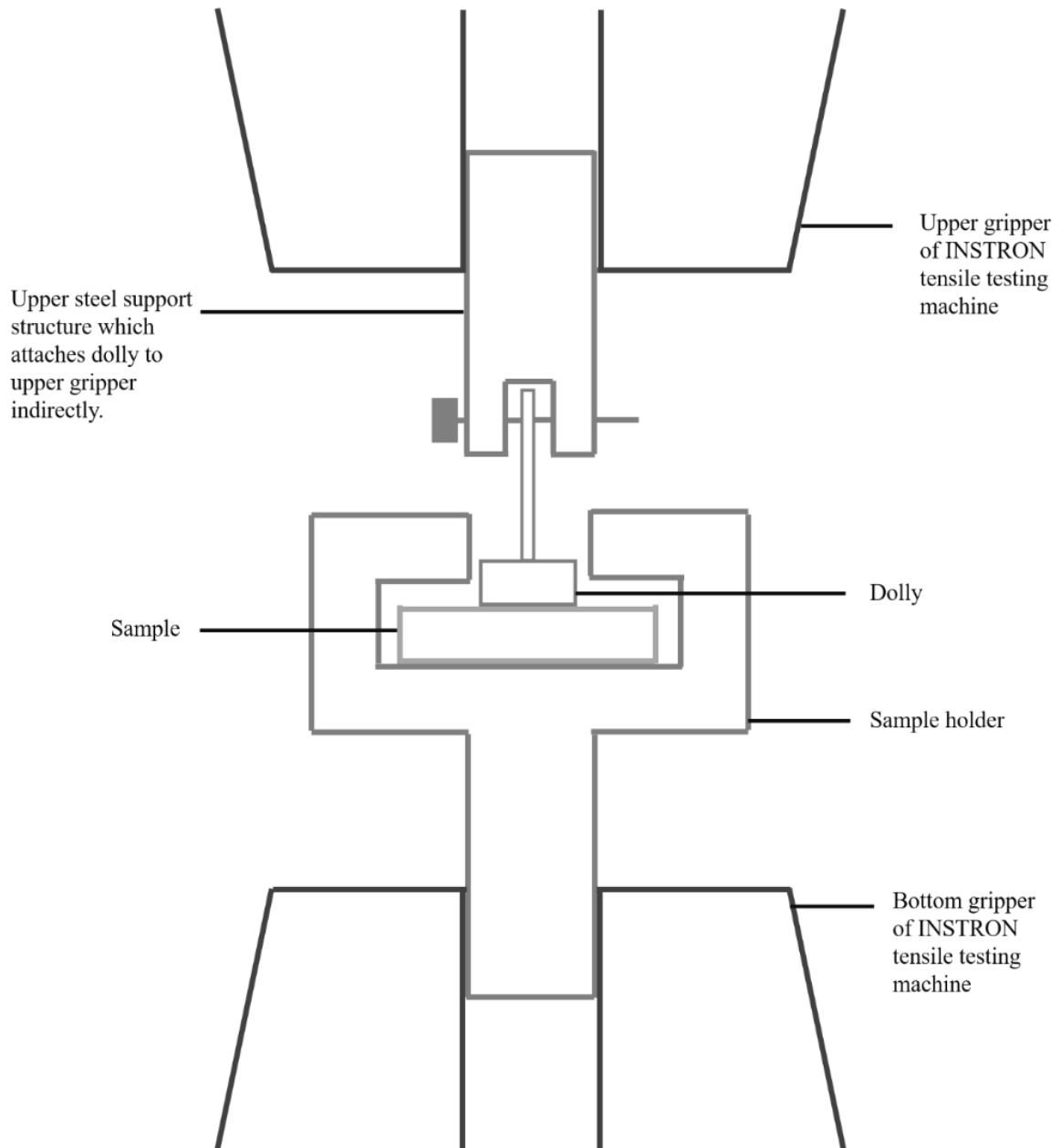


Figure 3.4: Set up for pull-off testing carried out on an INSTRON 8802 tensile testing machine.

Epoxy glue was applied thinly and evenly over the area of the stainless steel dolly (SS 316 dolly diameter = 20 mm) which was then attached the surface of the coated coupon and allowed to air-dry overnight. An INSTRON 8802 tensile testing machine was utilised to determine the load required to detach the dolly. The sample holder was clamped to the bottom gripper of the machine as shown in Figure 3.4. The dolly with the test coupon attached was inserted into the coupon holder, while the dolly was clamped to the top gripper of the tensile tester. The Instron machine was programmed to apply a constant separation speed of 0.05 mm/sec while measuring the resultant load which increases with time, and at a steeper rate just before detachment (see Appendix F for resultant plots). The point of detachment is seen as a sharp drop in load after which the recording of load was halted. The maximum load in kN was generated for each coating tested and compared. The coupon surface post-test was examined visually and photographed to document the mode of failure.

For this test, iron coupons were polished to a mirror finish and coated using sols listed in Table 3.2 having silica concentration of 2.5%. Coating adhesion tests were also performed on coupons coated with the acrylic coatings Paraloid B-48 and Paraloid B-72 (2.5% w/v) and with the nitrocellulose (Ercalene, 75% v/v) coating. Tested coatings were deposited by dip-coating and were conducted on single coats to avoid film delamination between top and bottom coat layers. Three tests were carried out on three separate coated coupons so that the average applied force and standard deviation can be obtained.

Apart from the epoxy- adhesive used in this test, other glues were initially considered for this study namely i) Loctite® Glass Glue which is a hydroxypropyl methacrylate-containing glue specifically formulated for bonding glass and ii) Evobond E-496 which is a cyanoacrylate-based industrial adhesive. Preliminary tensile testing was conducted as explained above to determine which of the three adhesives will adhere best to the OIH alkoxysilane coatings for which MTES:TEOS 20:80 mol% (low organic content) and OTES:TEOS 60:40 mol% (high organic content) were considered as good representatives. It is the epoxy-based adhesive that was selected since it withstood greater tensile forces for both types of coatings tested, thus indicating the best adhesion to the coatings.

3.3.6.3 Surface roughness

The surface roughness of polished clean coupons, uncleaned and corroded-cleaned coupons together with coated 60:40 mol% MTES:TEOS corroded-cleaned coupons were evaluated with an AEP technology NanoMap-500LS profilometer. The roughness of six scan lines was measured in two directions perpendicular to one another (for a total of 6 scans per sample) using a 1 μm diameter stylus so as to obtain the average surface roughness for the surfaces studied. The repeats were taken near the centre of the coupon so as to avoid any edge effects. **Table 3.11** lists the instrument parameters used to carry out the surface roughness tests. Surface roughness was outputted as the absolute roughness value (R_a).

Table 3.11: Scanning parameters employed to carry out surface roughness measurements on clean polished metal surface, cleaned corroded metal surface and silica coated corroded metal surfaces.

Profilometry Parameters	
Vertical range	500 μm
Scan distance	2500 μm
Scan speed	25 $\mu\text{m/s}$
Contact force	25 mN
Sample frequency	50 Hz

3.3.6.4 Corrosion testing

A Gamry Instrument Reference 600 potentiostat/Galvanostat/ZRA system was used to perform the corrosion tests. Corrosion testing was carried out sequentially by first determining the Open Circuit Potential (OCP), followed by non-destructive Electrochemical Impedance Spectroscopy (EIS) and finally Potentiodynamic Polarisation. This sequence of tests was applied to both coated and bare (uncoated, control) iron coupons.

The electrochemical cell set up is presented in **Figure 3.5**. A saturated calomel reference electrode (SCE) ($\text{Hg}/\text{Hg}_2\text{Cl}_2$, $E_{\text{ref}} = +241 \text{ mV}$ versus S.H.E.) was employed as a reference electrode (RE), a 6 mm platinum disc electrode served as a counter electrode (CE) while the test sample coupon served as the working electrode (WE). The exposed surface of the test coupons was fixed to 1 cm^2 using PortHoles Electrochemical Sample Masks that also served to reduce crevice corrosion along the edges. A 0.1 M (or 0.6% wt/vol) sodium chloride solution was used to simulate the indoor museum environment as opposed to 3.5% wt/v, which is typically used to simulate harsher outdoor conditions. The RE was placed in a Luggin tube filled with saturated potassium chloride solution so that the tip of the Luggin tube reached close to the sample surface and thus minimising noise caused from the electrolyte solution. The glass container housing the electrolyte solution and electrodes was water-jacketed so as to maintain a constant temperature of $25 \text{ }^\circ\text{C}$. The sequence of the procedure together with the relevant parameters was programmed through the Gamry Framework software.

The corrosion test sequence was set up as follows:

- i) OCP is conducted to determine when a test electrode has reached steady state. An OCP duration of 1 hour of soaking of the sample surface in 0.1 M NaCl solution was sufficient to obtain a steady state;
- ii) Impedance measurements were recorded for a set range of frequencies from 64,000 Hz to 0.064 Hz [170] (resistance and capacitance values provide information on corrosion behaviour, corrosion rates, diffusion, and coating properties at different frequency ranges) with 5 points per decade of frequency; and using an AC signal of 10 mV [170], such a low signal is required to render a linear system i.e. sum of individual input signals is equal to the sum of the individual responses. Following OCP, Impedance measurements were obtained within 20 mins ensuring stability of system was not altered during long exposure time which could significantly affect the coating integrity and therefore the stability of the system.
- iii) Potentiodynamic sweep was carried out for which the initial potential was set at -0.2 V versus OCP to obtain the anodic branch of the plot, up to a final potential of 0.5 V versus the reference

SCE for the acquisition of the cathodic branch of the corrosion reaction. The scan rate was set to 1 mV/s and a sample period of 1 s as per work by Vella [53].

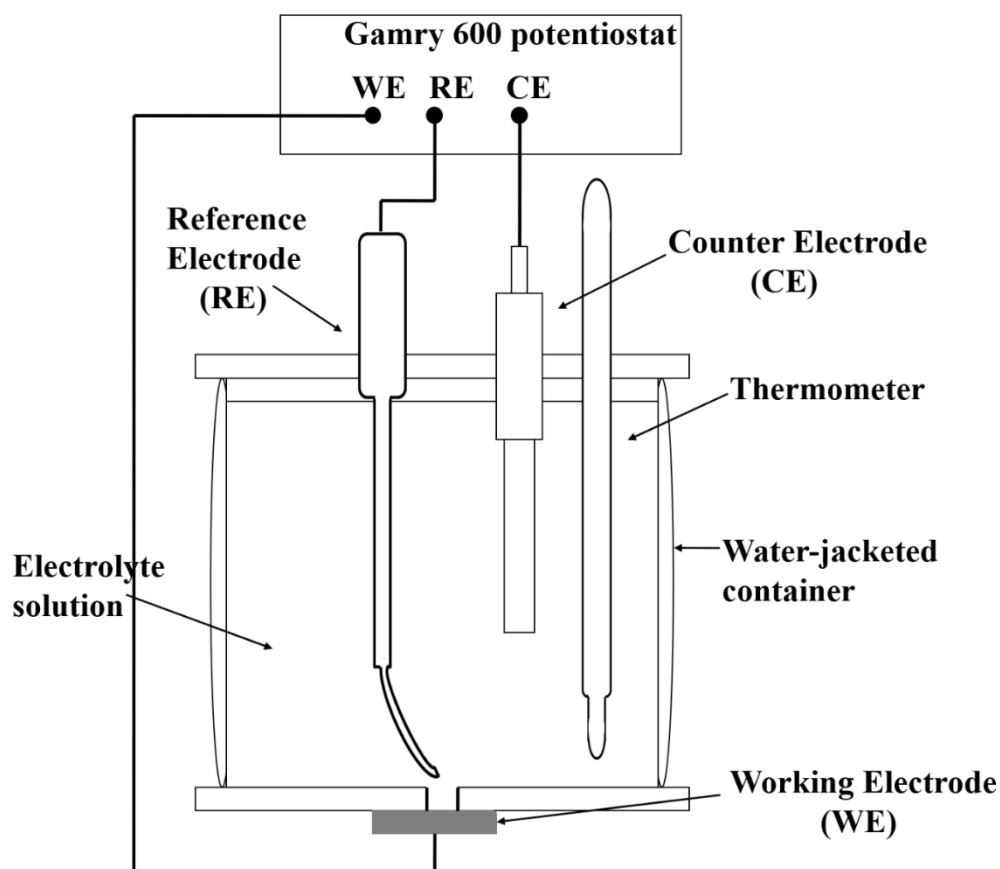


Figure 3.5: Depiction of the set up used to carry out electrochemical and potentiodynamic testing on bare and coated coupons.

3.4 Accelerated corrosion (salt-spray) testing of coated coupons

Accelerated corrosion testing was carried out on double film coated alkyl/aryl trialkoxysilanes (10% wt/v SiO₂) 60:40 mol% MTES:TEOS, 50:50 mol% PrTES:TEOS, 30:70 mol% HTES:TEOS, 20:80 mol% OTES:TEOS and 40:60 mol% PhTES:TEOS coated iron surfaces. For this particular test, coupon edges were rounded off to limit as much as possible the edge effect. Coupon surfaces were then ground and polished to a mirror finish as described previously in Section 3.2.1.1. Coatings were applied via four methods: i) dip-coating (Section 3.3.3), brush coating using a ii) fine-bristle brush (Marabu-Universal Brush no. 12), iii) coarse brush (Harris Classic 25 mm), and iv) sponge (Ecco Verde).

For brush applications, the brush was dipped in the sol and drained slightly so as to remove excess liquid, thus preventing the formation of very thick and uneven coating films. Sols were deposited using single strokes along the coupon length where a newly created stroke overlapped slightly with previous stroke. The second brush application was applied perpendicularly to the first application to ensure coverage of any defects and troughs left behind by brush bristles on the first coating. For sponge application of sols, a fine-pored natural sponge was used which was drained gently prior to the application of sol onto the coupon surface. The sol was deposited by dabbing the sponge along the coupon surface until entirely covered with sol. Alkyl/aryl trialkoxysilane coatings were cured in an oven for 1 hr at 150 °C after application of both coatings. To avoid edge effects, coupon edges and back-surfaces were treated with Wurth® Lacquer Spray Special which is a nitro alkyd spray. The latter was employed to impart weather resistance to areas not undergoing the test. Uncoated mirror polished coupons were also included in the salt-spray test for comparison.

The salt spray test was carried out according to ASTM G85-02 “Standard Practice for Modified Salt Spray (Fog) Testing” using an Aster CNS/500 accelerated corrosion test chamber. The salt-fog was applied using a low concentration salt solution of 0.6% w/w (0.1 M) NaCl to simulate a less aggressive indoor environment. The coated coupons were subjected to a wet cycle consisting of 8 hrs at 100% RH and 35 ± 3 °C followed by the dry cycle consisting of 16 hrs of laboratory climatic conditions (20-25 °C at 50-60% RH). All of the coated and uncoated coupons were placed onto the same Perspex rack as used in Section 3.2.1.2 on which coupons are inclined at an angle of around 30° to the vertical. The rack was placed onto a plastic container housed in the chamber so as to be elevated by 50 cm from the base of the chamber. After every wet cycle, the rack was removed from the chamber and each coupon was washed with distilled water, gently dried and photographed.

The second set of accelerated corrosion tests featured coupons that were double coated with 15% Paraloid B-72 (% w/v in acetone), 15% B-48 (% w/v in acetone) and 75% Ercalene (v/v in diluente nitro) through dip and fine brush applications for which lacquers were allowed to air dry over night

without curing. These set of coupons were subject to the same cycling process and recorded similarly. All photographs taken were imported into image J and individually analysed so as to obtain the total corroded area coverage.

3.5 OIH silica coatings' reversibility

3.5.1 Preparation of coated coupons

Coated polished iron coupons were used for this test. Sols with a total silica content of 2.5% were prepared as described in Section 3.3.1.1 and coating application and curing was conducted as described in Section 3.3.3.

3.5.2 Immersion testing

Coated coupons were stacked in several PTFE racks (**Figure 3.6**) which have been specifically designed and constructed for this test. The racks are flexible so as not to break when coupons are inserted and removed, and are also solvent-resistant, which is a crucial aspect of the set-up given that immersion test was intended to last for several weeks. The immersion liquids considered in this work were isopropyl alcohol (99.9%, Carlo Erba) and the following aqueous NaOH solutions: 0.01 M (pH 12), 0.1 M (pH 13) and 1 M (pH 14). The scope of conducting immersion tests with a range of NaOH concentrations was to avoid as much as possible using the more concentrated NaOH solution given that these cleaning solutions will eventually be recommended for use by conservators.

The coupon-containing racks were then placed in glass trough and filled to approximately 1 cm above the bottom of the coupon with solution/solvent. The troughs were sealed using Parafilm so as to prevent the evaporation of solution/solvent over the test period. Immersing a portion of the coated surface allows for the viewing of the changes occurring between un/immersed surfaces as the coatings begin to degrade with time.

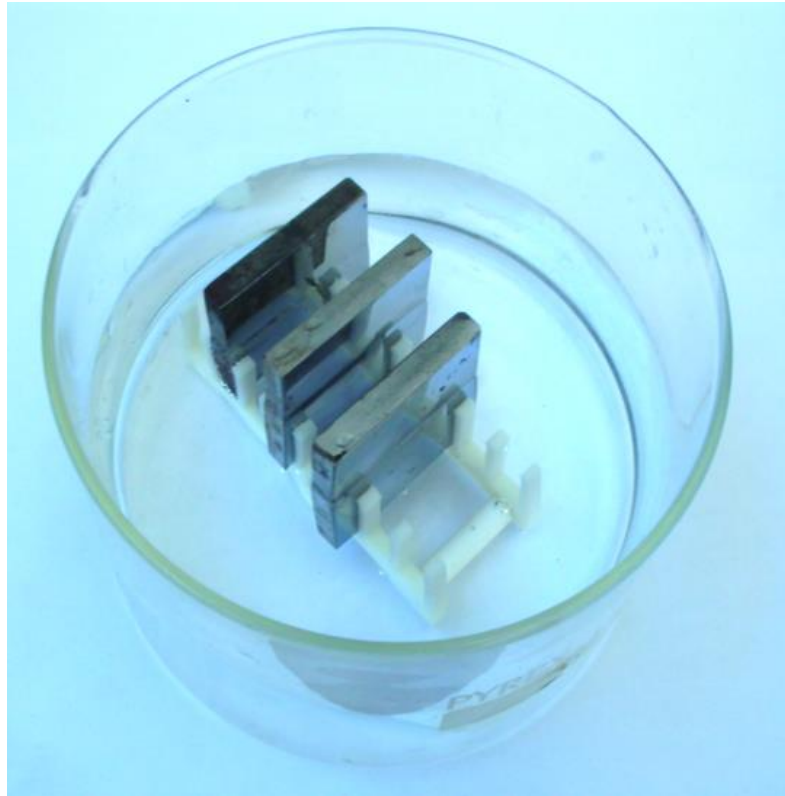


Figure 3.6: Set up for immersion testing

At the start of the test, the coupons were carefully removed from the rack after one hour of immersion, gently wiped using cotton pad and examined under the optical microscope. Coupons that had no remaining coating on the immersed area were put aside and the test for these coupons stopped. The remaining coupons were placed back on the rack to soak for a further hour (2 h from start) and the immersed coatings were re-examined for intactness. The process was conducted after 4 h, 8 h and 24 h from the initial immersion time after which the coupons were examined on a daily basis. The immersion time required to completely dislodge the coating was recorded. The immersion test was halted after 10 days (240 h) from the beginning of the test.

3.5.3 Manual cleaning

A more practical approach to reversing a coating application was carried out as follows: a cotton swab was dipped in the cleaning agent of interest, lightly drained onto a tissue paper to avoid excessive liquid, and gently pressed into a circular pattern over the coated surface where it was ensured that the circular pattern was performed over the same area using approximately 2 revolutions per second. The number of circles (strokes) required to remove the coating was recorded and tabulated. This process was aided using the optical microscope where the integrity of the coating was assessed periodically, typically after 50 strokes and every 100 strokes for more difficult coatings. 1 M NaOH (pH 14 solution) and IPA were considered for the reversibility test together with volume mixtures of the two: 25:75% (v/v) NaOH:IPA (25:75% N/I), 50:50% (v/v) NaOH:IPA (50:50% N/I) and 75:25% (v/v) NaOH:IPA (75:25% N/I). The scope of investigating such mixtures of NaOH:IPA is to identify whether coatings can be removed efficiently using the least amount of 1 M NaOH possible for safety reasons.

CHAPTER 4:

Method development and optimisation of OIH alkoxysilane coatings

4.1 Introduction

This chapter includes the method development for achieving the most protective coatings which will then feature in the rest of the work. The scope of this chapter is to determine which experimental parameters affect the coating's protective properties and factors that do not impact the coating's integrity, thus leading to a simpler coating preparation. Due to this, the discussion is presented with the presentation of results obtained (only for this chapter).

The coating material consisting of a 60:40 molar ratio of MTES:TEOS was used as a starting point in this work since the anti-corrosion properties were well documented [67,69,74,53]. The sol was prepared as specified by Vella [53]. MTES and TEOS precursors were mixed in a 60:40 molar ratio; the ratio of silica: water was set to 1:2 and the pH of the sol was adjusted to \approx pH 2 using 1 N nitric acid solution. Half of the water was added immediately after sol precursors were added and the rest was added after two hours so as to avoid sol clouding. The temperature was set to 40 °C and the stirring rate set to 500 r.p.m. The sol was diluted using ethanol to its final concentration of 10% (100 g/L) as carried out by Vella. Additionally, 2.5% (25 g/L) and 5% (50 g/L) silica concentrations were utilised in this work.

Following dip-coating, coated coupons were placed in an oven and allowed to cure for 1 hr at 150 °C. Coupons that are intended for multiple coatings using either 2.5% or 5% SiO₂ sols were allowed to air dry for 5 minutes in between coatings without the need for curing; curing is typically carried out to initially evaporate solvent thus prevent the re-dissolution of some of the deposited silica. In the case of 2.5% and 5% single silica applications which produced thin coatings, solvent evaporated in a matter of seconds, thus curing was done after the final coating application. In the case of 10% SiO₂ coated coupons, this procedure led to improperly deposited and cured coatings and as a result, the curing process was enforced following each layer of applied coating.

4.2. Method development

4.2.1 Effect of sol pH on Particle Size measurements

Particle size measurements were conducted on three separate samples procured from the sol under investigation to ensure reproducibility of the results as illustrated through measurements conducted on MTES:TEOS 60:40 mol% sol shown in **Figure 4.1**. The intensity distribution plot emphasises the larger particles in the distribution since a small number of larger particles are able to offset the intensity generated by the smaller yet larger population of particles (see Figure 4.1 (a)). On the other hand, volume distribution plots emphasise the smaller particles in the distribution since the majority of particle volume is due to the smaller particles (Figure 4.1 (b)).

In this work particle size distribution plots were presented as intensity versus particle diameter. Particle volume vs. particle diameter plots were only used to ensure that the larger sized particle populations were indeed of insignificant numbers compared to the smaller sized populations. Particle number vs. particle diameter plots were not considered in this work. Particle size is a powerful tool to monitor changes to the sol for which a shift to larger average particle diameters was found to influence the mechanical and corrosion protective properties of the resulting coatings.

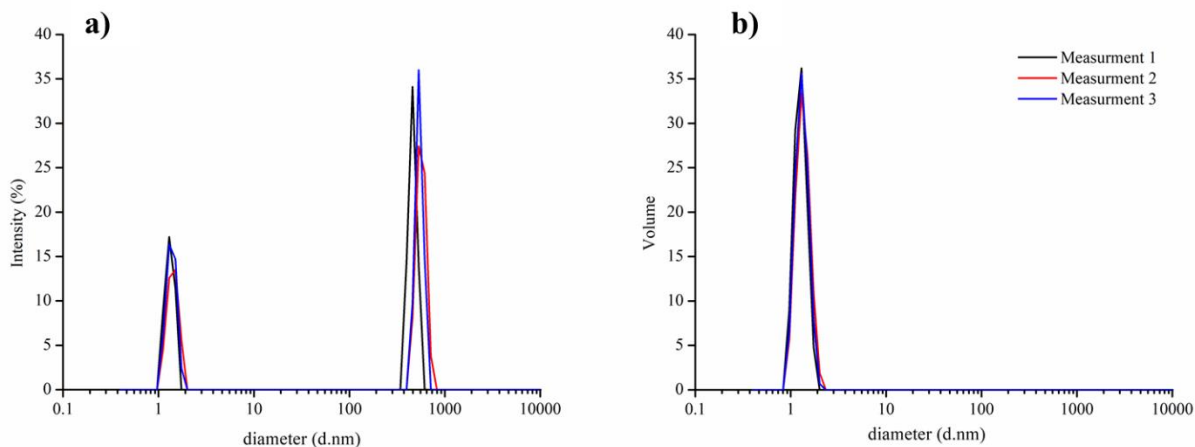


Figure 4.1: Particle size distribution versus a) intensity (%) and b) volume for MTES:TEOS 60:40 mol%.

Particle sizing (PS) was carried out on the two-step MTES:TEOS 60:40 mol% developed sol prior to and after the neutralisation step (pH 2 and 7 respectively, see **Figure 4.2**) to ensure that the nanoparticles do not undergo significant variation in size, which would be an indication of loss of stability with a shift to a higher pH either due to growth or agglomeration of particles.

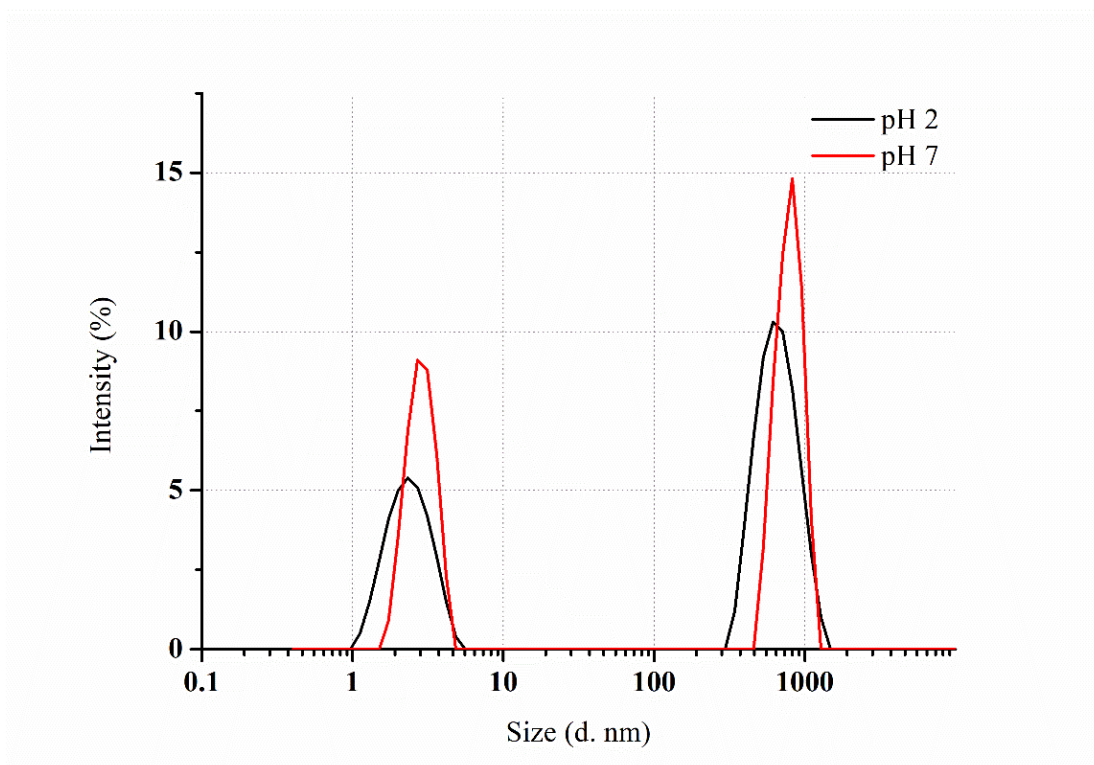


Figure 4.2: Particle sizing for 2.5% SiO₂ MTES:TEOS 60:40 mol% at pH 2 (prior to sol neutralisation) and pH 7 (after neutralisation of sol).

4.2.2 Two-step versus one-step method for sol development

The initial method followed [205] consisted of a two-step process so as to avoid observed clouding of sol that occurs at the early stages of the development. The sol eventually becomes transparent with time. However, Particle size measurements of a one-step sol, where the total volume of water was added following the alkoxy silane precursors, demonstrated no significant changes in PS compared to a sol that has been prepared in a two-step manner (See Figure 4.3), before and after neutralisation indicating that the sol remains stable. To assure this, electrochemical testing was conducted on coatings that have been prepared through a one-step and two-step process.

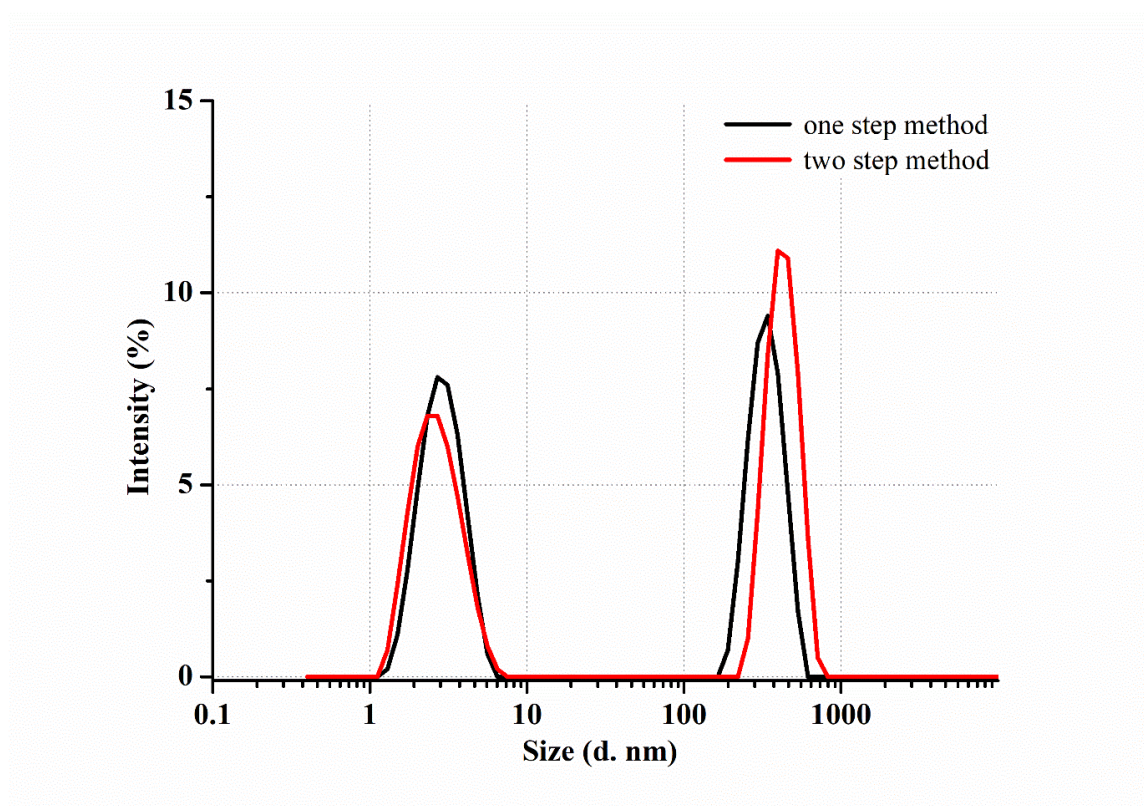


Figure 4.3: Particle sizing results for 2.5% SiO₂ MTES:TEOS 60:40 mol% prepared using one-step and two-step methods.

The extent of protection offered by a coating was evaluated using EIS and potentiodynamic testing. Electrochemical data is outputted in the form of four plots as shown in **Figure 4.4**: (a) and (b) respectively illustrate the Bode and Phase angle Impedance (c) Nyquist and (d) Potentiodynamic plots for double-coated MTES:TEOS 60:40 mol%. Electrochemical testing typically includes testing carried out on bare metal specimen so as to compare and evaluate the extent of improvement in corrosion

protection provided by the coating. For each coating tested, reproducibility was assured by conducting several runs (Runs 1-3 in Figure 4.4) on any given coating where, in each case, a fresh new area was exposed for testing and values reported are the average of the closest three separate measurements.

The Bode plot can be represented as either a plot of the impedance modulus ($|Z|$) in Ωcm^2 versus frequency range in Hz, Figure 4.4 (a), or as the phase angle versus frequency range, Figure 4.4 (b). Two distinct regions (time constants) or maxima can be observed in the phase angle plots (Figure 4.4 (b)). The maximum occurring at high frequencies contains information about the coating; the maximum occurring at lower frequencies is related to the corrosion occurring at the metal surface under the coating [170]. Bare polished metal plot therefore only contain a single-phase angle maximum. The two distinct steps as theoretically expected (see S. Tait's *Introduction into Electrochemical Testing for Practicing Engineers and Scientists* [179]) is not clear through the Bode Impedance plot in Figure 4.4 for which coated systems appear to be similar to the bare metal, and simply occur at higher impedance in the lower frequency range of the Bode Impedance plot.

The impedance modulus ($|Z|$) is significantly higher (approximately two orders of magnitude for MTES:TEOS 60:40 mol%, seen in the lower frequency range) for the coated specimen than for the uncoated bare specimen suggesting that the coatings offer significant barrier protection, see Figure 4.4 (a). Figure 4.4 (c) shows the same data represented as a Nyquist plot. The Nyquist plot for these sets of coatings appears as a capacitive arc whose width increases with increased corrosion protection, in fact, the arc for bare metal cannot be visualised since it is much smaller than that for coated specimens. The Nyquist plot reveals any differences in $|Z|$ more clearly than the Bode Impedance plot and this is due to the fact that it is in linear form rather than logarithmic (Bode impedance). For instance, run 3 has an impedance value that is slightly higher than that of run no. 1 which is difficult to determine through the Bode Impedance plot.

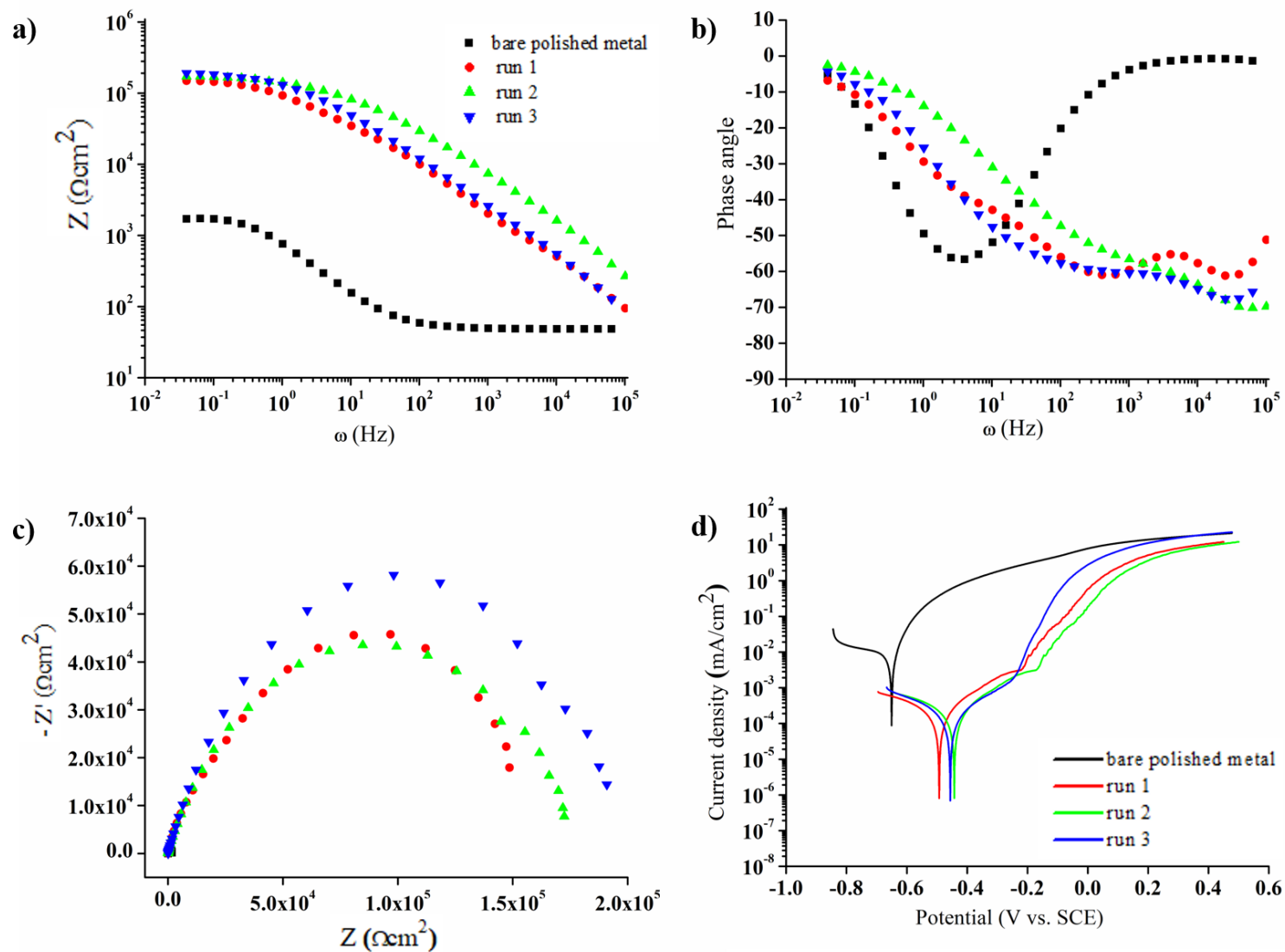


Figure 4.4: Electrochemical evaluation for 2.5% SiO₂ MTES:TEOS 60:40mol% double coating showing repeatability in results presented as a) Bode impedance b) Bode phase angle c) Nyquist d) Potentiodynamic plots. Plots include bare polished metal for comparative purposes.

Both coated and uncoated results as shown in Figure 4.4 have been modelled using the equivalent circuits through Echem Analyst software by means of the Simplex mathematical algorithm. The EIS data obtained for coated metal was modelled using the equivalent electrical circuit (EEC) as depicted in **Figure 4.5** (a) whereas the best fit for bare metal was achieved using EEC 2 in Figure 4.5 (b). An EEC is a representation of the physical/electrical properties of the metal/coating interface, refer to S. Tait's *Introduction into Electrochemical Testing for Practicing Engineers and Scientists* [179] for more detail. The scope of modelling is to numerically quantify the outputted EIS data obtained i.e. quantitative comparison of the coatings' performance is possible. These models were found to have remained relevant even for other organic coatings tested in this work (coatings not based on sol-gels).

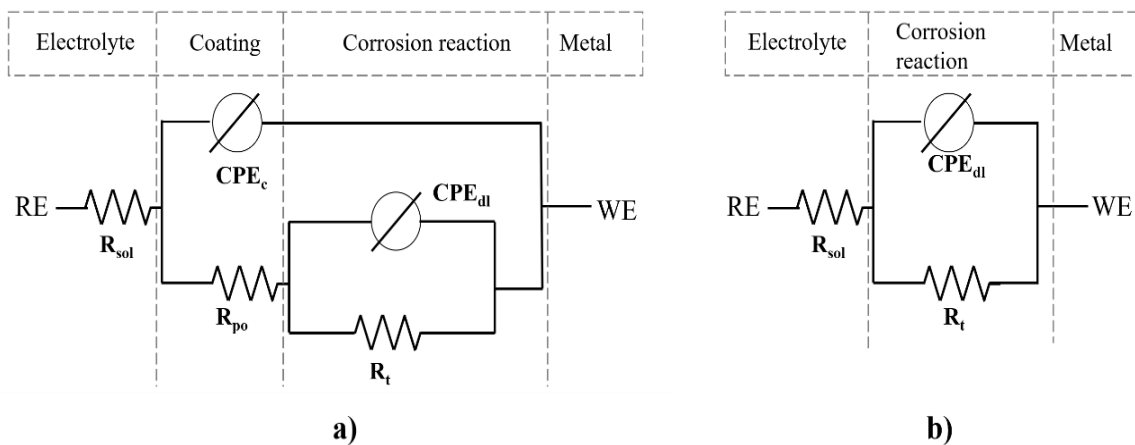


Figure 4.5: Electrical circuit model for (a) coated corroding surface (b) uncoated corroding surface.

Table 4.1 presents the circuit parameters obtained when modelling data obtained in Figure 4.4 for MTES:TEOS repeat runs and bare metal. Upon application of coatings to bare metal, the improvement in anticorrosion properties was quantitatively observed through the tabulated parameters for which the charge transfer resistance (R_t) increases, for example, for Run 3 $R_t = 2.01 \times 10^5 \Omega \text{ cm}^2$ which is almost 2 orders of magnitude higher than that measured for bare metal $\sim 1.50 \times 10^3 \Omega \text{ cm}^2$. On the contrary, the value of double layer capacitance at the metal-coating interface (Y_{dl}) decreases when a coating is applied to the bare metal ($Y_{dl} \text{ bare metal} = 1.45 \times 10^{-4} \Omega^{-1} \text{ cm}^{-2} \text{ s}^\alpha$ whereas for Run 3 $Y_{dl} < 1.15 \times 10^{-6} \Omega^{-1} \text{ cm}^{-2} \text{ s}^\alpha$).

Parameters such as the pore resistance (R_{po}) and coating's capacitance (C_c) are attributed to the coating and therefore do not feature in the bare metal parameters; and as expected, values for R_{po} and Y_c are similar for Runs 1-3. Out of the three resistances (R_t , R_{po} and R_{sol}), R_t is the greatest contributor to impedance as seen in the Bode plot at lowest frequency where impedance $\approx R_t$. Solution resistance R_{sol} contributes minimally while R_{po} values are normally an order of magnitude smaller than the R_t values (see Table 4.1).

Table 4.1: EEC parameters for runs 1-3 of MTES:TEOS coatings and bare metal where R_{sol} = uncompensated solution resistance, R_{po} = pore resistance of coating, CPE_c = constant phase element of coating featuring the exponent α_c and Y_c of CPE_c , R_t = charge transfer resistance and CPE_{dl} = constant phase element of the double layer formed at the metal-coating interface featuring the exponent α_{dl} and Y_c of CPE_{dl} and goodness of fit (GOF).

	R_{sol} (Ω cm^2)	R_{po} (Ω cm^2)	CPE_c		R_t (Ω cm^2)	CPE_{dl}		GOF
			Y_c (Ω^{-1} $cm^{-2}s^\alpha$)	α_c		Y_{dl} (Ω^{-1} $cm^{-2}s^\alpha$)	α_{dl}	
Run 1	32.84	8.3×10^3	8.96×10^{-7}	0.83	1.16×10^5	2.05×10^{-6}	0.76	2.36×10^{-5}
Run 2	29.55	2.5×10^3	2.92×10^{-8}	0.71	1.78×10^5	7.54×10^{-7}	0.63	5.86×10^{-4}
Run 3	33.66	5.77×10^2	1.97×10^{-8}	0.75	2.01×10^5	1.15×10^{-6}	0.68	7.46×10^{-4}
bare metal	51.14	-	-		1.50×10^3	1.45×10^{-4}	0.77	1.02×10^{-4}

A potentiodynamic scan, which in this work was carried out after Impedance testing, is a plot of log current density ($mA\ cm^{-2}$) versus potential (V) for which repeatable results obtained are plotted in Figure 4.4 (d). Corrosion protection is evident by the shift to a lower current density and to a more positive (noble) voltage for coated coupons versus bare metal. The corrosion potential of bare metal occurs at around -650 mV whereas for coated metal the corrosion potential shifts to more positive values of approximately -500 mV (Figure 4.4 (d)). Corrosion protection comparison between coatings was based on the corrosion current density (I_{corr}) value and was estimated manually from the polarisation plots using the Tafel region of the cathodic and anodic polarisation curve having

values of $9 \times 10^{-3} \text{ mAcM}^{-2}$ for bare metal, Run 1 = $3 \times 10^{-5} \text{ mAcM}^{-2}$, Run 2 = $4 \times 10^{-5} \text{ mAcM}^{-2}$ and Run 3 = $4 \times 10^{-5} \text{ mAcM}^{-2}$. The total Impedance (Z_{tot}) is defined as sum of R_t , R_{po} and R_{sol} parameters ($Z_{\text{tot}} = R_t + R_{po} + R_{sol}$) at lower frequency range. It should be noted that there is a two order of magnitude improvement in Z_{tot} for the coated metal sample was due to the presence of a coating on the metallic surface. Indeed a two order of magnitude drop in current density from uncoated to coated specimen was likewise reported in the potentiodynamic scan ($V=IR$).

Figure 4.6 compared electrochemical test results conducted on coated metal samples using one- and two-step sols for which representative plot is shown for each coating (minimum of three runs carried out to assure reproducibility). There appears to be no significant variation in data is obtained to suggest that the two-step sol development produces better coatings. The method was therefore adjusted to include the addition of the total volume of water in the beginning of the sol development.

4.2.3 Effect of sol development time and temperature on particle size

The effects of sol development time and temperature were of interest and investigated through PS. **Figure 4.7** (a) shows the particle size distribution of a MTES:TEOS 60:40 mol% sol at 20 °C when obtaining samples during the course of the four hour reaction. The first sample was obtained immediately after the MTES and OTES precursors became fully miscible (20 minutes). An immiscible system is formed upon addition of water to the organic silica precursors. With time and with the aid of stirring, the silica precursor molecules hydrolyse to form ethanol as a by-product. This solvent, once produced in sufficient amounts, will render the organic and inorganics miscible. During this time frame, condensation reactions are also taking place and thus particle formation is initiated. Particle size increases significantly after one hour of stirring and changes minimally as more time is allowed. It is interesting to note the intensity of the larger peak (>100 nm) for measurements taken at 20 minutes versus the other three time durations. The higher large particle intensity could be a remnant of the clouding at the early stages of the reaction which disappears as the reaction proceeds.

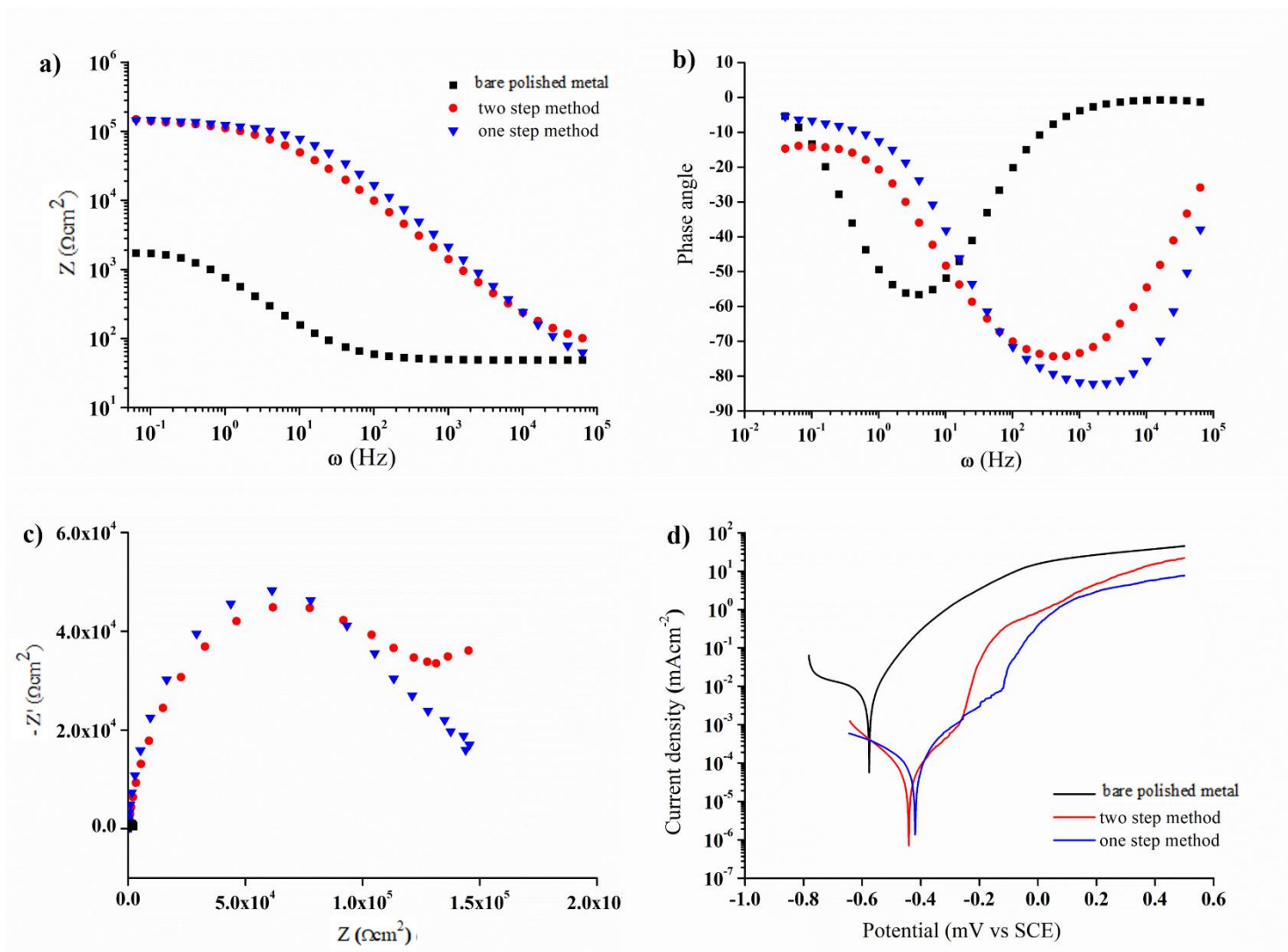


Figure 4.6: Electrochemical data for 2.5% SiO₂ 60:40% MTES:TEOS coated iron surfaces, for which coatings were derived from one-step and two-step sol development. Bare metal plots are included to indicate the extent of corrosion protection offered by coatings.

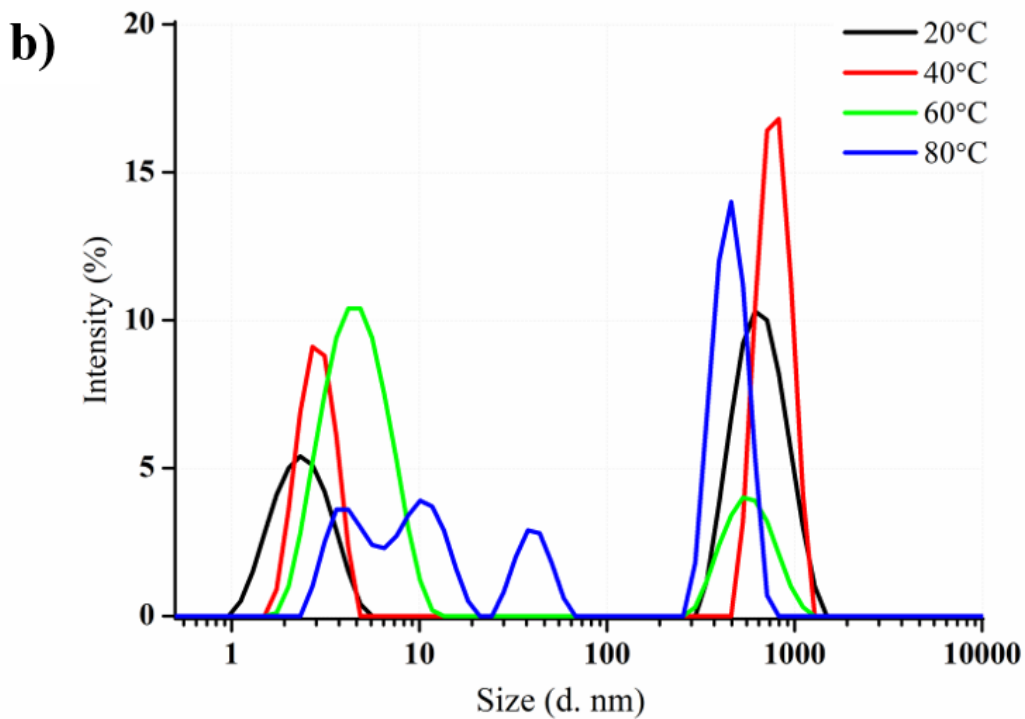
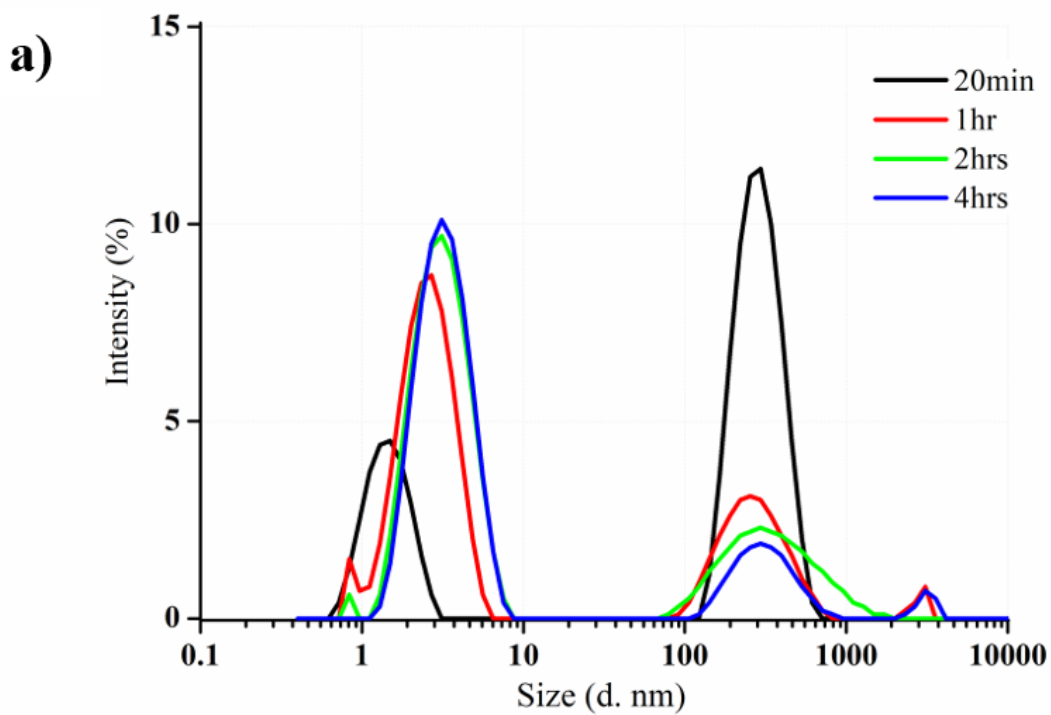


Figure 4.7: Particle sizing for MTES:TEOS 60:40 mol% a) with increasing time of sol preparation at fixed T of 40 °C and b) with increasing T for a fixed sol preparation time of 4 hrs.

The temperature at which MTES:TEOS 60:40 mol% sol was developed was also investigated and is shown in Figure 4.7 (b) where sols were allowed to develop for 4 hours. There is a notable increase in particle size with an increase in temperature during sol development. Additionally, at 80 °C more peaks emerge having a 5-50 nm range and is most likely to have occurred due to accelerated agglomeration of the smaller particles. The differently sized particles could potentially be problematic during coating deposition because larger particles present can pack less efficiently when compared to smaller particles, thus resulting in a less even and smooth coating. Smallest particle size was obtained at 20 °C i.e. the sol can be developed even at room temperature without the need of heating. Following PS results obtained, the method of sol development was adjusted to a temperature of 20 °C whereas a development time of 4 hrs was maintained to assure sufficient development of particles.

4.2.4 Effect of time allowed for sol development on corrosion protection

Through PS results in Figure 4.7 it is clear that higher temperatures lead to the instability of the system, thus temperature during sol development be kept low (20 °C). Zhang *et al* explain the clouding produced at early stages of sol development to be due to the formation of ‘cage’-like structures composed of polyhedral-shaped octamethylsilsesquioxane ($C_8H_{24}Si_8O_{12}$) that form fine crystalline precipitates dispersed in sol [206]. It was determined that a shorter sol development time results in a system that is still unstable due to the formation of such structures, especially when measured after just 20 mins from the start of reaction. Zhang *et al* also specify that these structures eventually form a single compound, that point can be noticed when sol becomes clear again when allowed to develop further.

PS results for 2hr duration of sol development were similar to those obtained for 4hrs. Therefore, it was necessary to determine whether a shorter sol development time (2hrs) would lead to coatings that are just as protective as coatings originating from sols that have been allowed to develop for longer (4hrs), in the hope of reducing the development time if corrosion protection is not affected negatively. As stated previously, when precursors are mixed with water and nitric acid into the flask, a two-phase system is formed due to the initial immiscibility of the precursors with water in the absence of solvent.

After just 20 minutes of mixing a single phase is formed and it is due to the formation of sufficient ethanol. However, more time is necessary to completely hydrolyse the MTES and TEOS precursors which can be observed through a significant improvement in corrosion resistance seen as an increase in impedance through the Bode Impedance and Nyquist plots together with a decrease in I_{corr} presented in Potentiodynamic plot, see **Figure 4.8**. This is most notable when increasing sol development time from 20 mins to 2 hrs. Therefore, the sol can be allowed to develop for only 2 hrs rather than 4 hrs. However, if time is not an issue, the sols should be allowed to develop for 4 hrs since better results in terms of higher total impedance (at low frequency range) were obtained for 4 hr systems, which was maintained for the rest of the work with MTES:TEOS coatings.

4.2.5 Effect of curing on corrosion protection

A significant improvement in corrosion protection is observed with a double coat of 2.5% SiO_2 sol when compared to bare metal (**Figure 4.9** '1 hr at 150 °C'). The two-coat system was also applied without the one hour curing at 150 °C, instead the coupons were allowed to air-dry overnight. The scope of this trial was to determine whether or not curing in an oven was necessary, thus avoiding the heat treatment which can be problematic if such coatings were to be applied in the field of conservation. The application of a single coating that is allowed to dry overnight followed by the re-application of a second coating may prove simpler than having to apply a curing process onto artefacts, especially over larger ones. However, EIS data indicated a half order of magnitude lower impedance values when coated coupons were not cured (see Figure 4.9) as seen through Bode Impedance plot (a), wider arc in Nyquist plots for cured sample (c), and lower I_{corr} for cured versus uncured samples in plot (d); thus proving that curing process is necessary for obtaining optimum coatings.

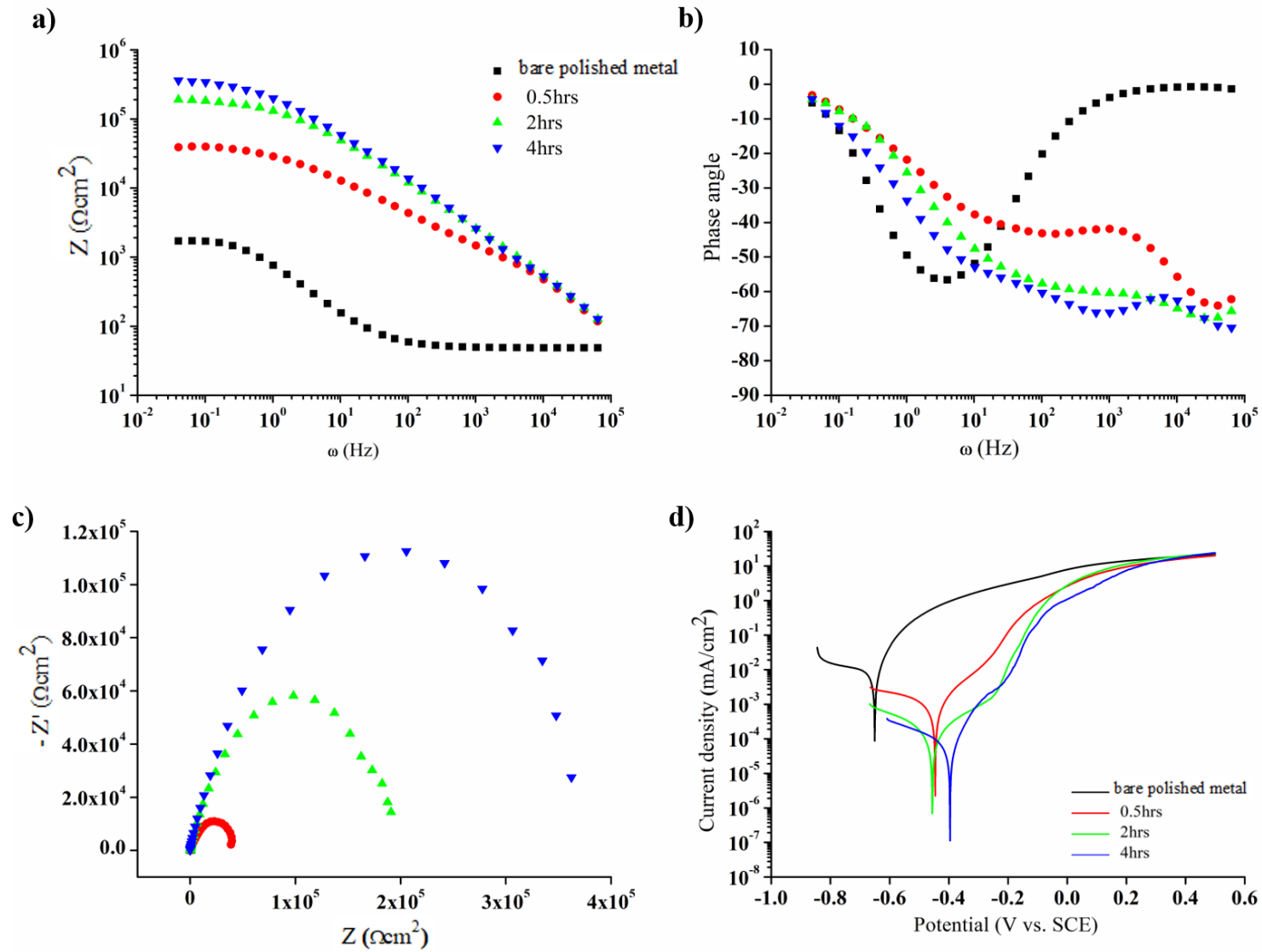


Figure 4.8: Electrochemical evaluation for MTES:TEOS 60:40mol% double coatings originating from sols that have been allowed different development times a) Bode impedance b) Bode phase angle c) Nyquist and d) Potentiodynamic plot

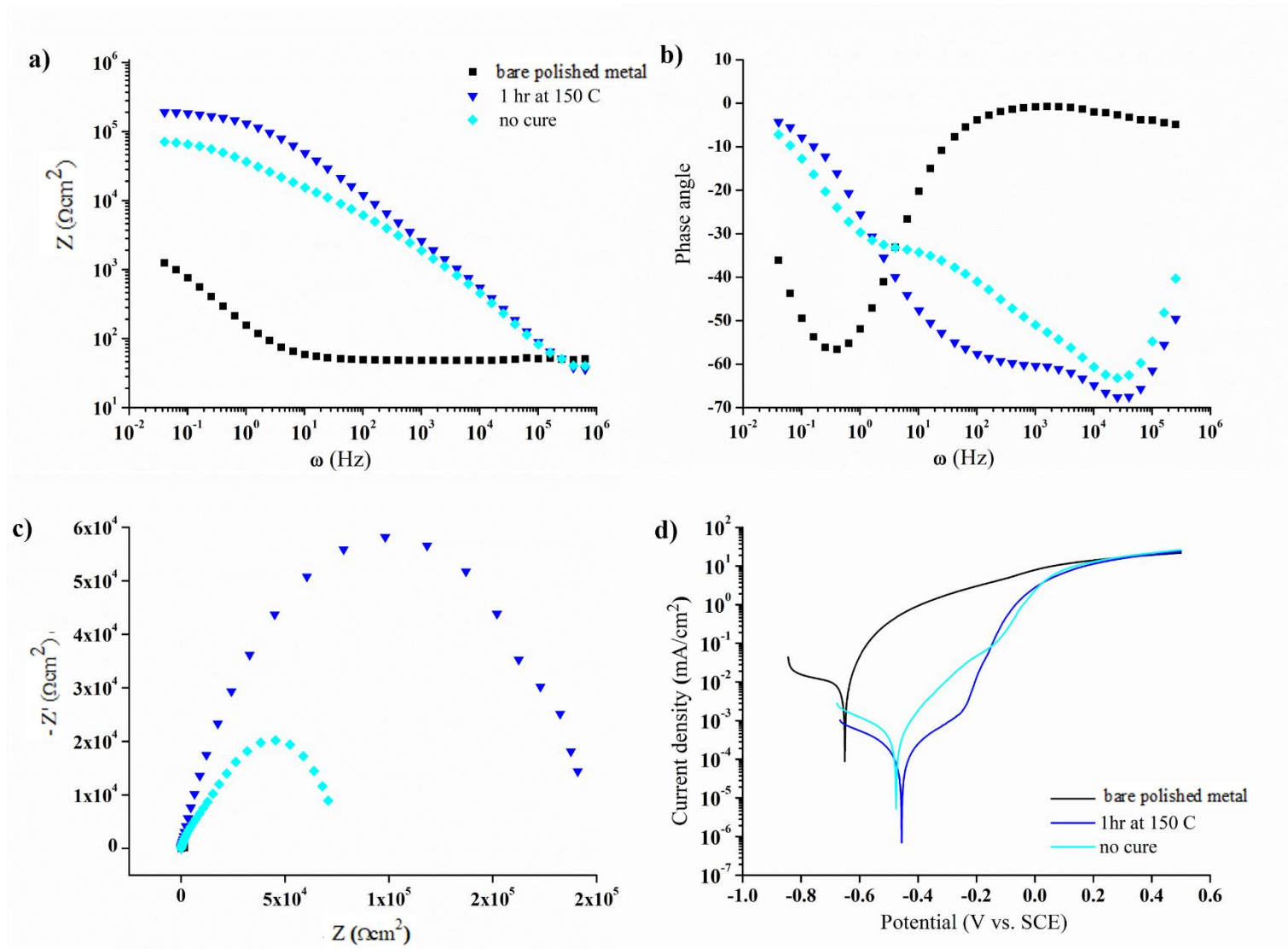


Figure 4.9: Electrochemical evaluation for MTES:TEOS 60:40mol% double coatings that have been cured at 150 °C for 1 hr and without curing (left to dry at room temperature overnight) a) Bode impedance b) Bode phase angle c) Nyquist and d) Potentiodynamic plots

4.2.6 Effect of number of coatings and silica concentration on corrosion protection

Since defects and porosity in the coatings are the main causes of degradation, applying multilayers eliminates/reduces diffusion paths for corrosive species to reach the metal surface, thereby limiting the incidence of localised attack [207]. Therefore, it is safe to assume that more protective coating will be obtained when multiple layered coatings are applied onto a metal surface and that an increase in silica concentration will also lead to better corrosion protection due to the deposition of thicker coatings. Thickness determination of coatings was carried out using SEM for which **Figure 4.10** shows coatings that have been purposefully cracked (bending of coated SS strips) to reveal a cross section of the coatings. Thickness values are presented in **Table 4.2**. For 2.5 and 5% SiO₂ coatings curing was applied after the final coating application whereas for 10% SiO₂ coatings, curing was carried out after every coating application.

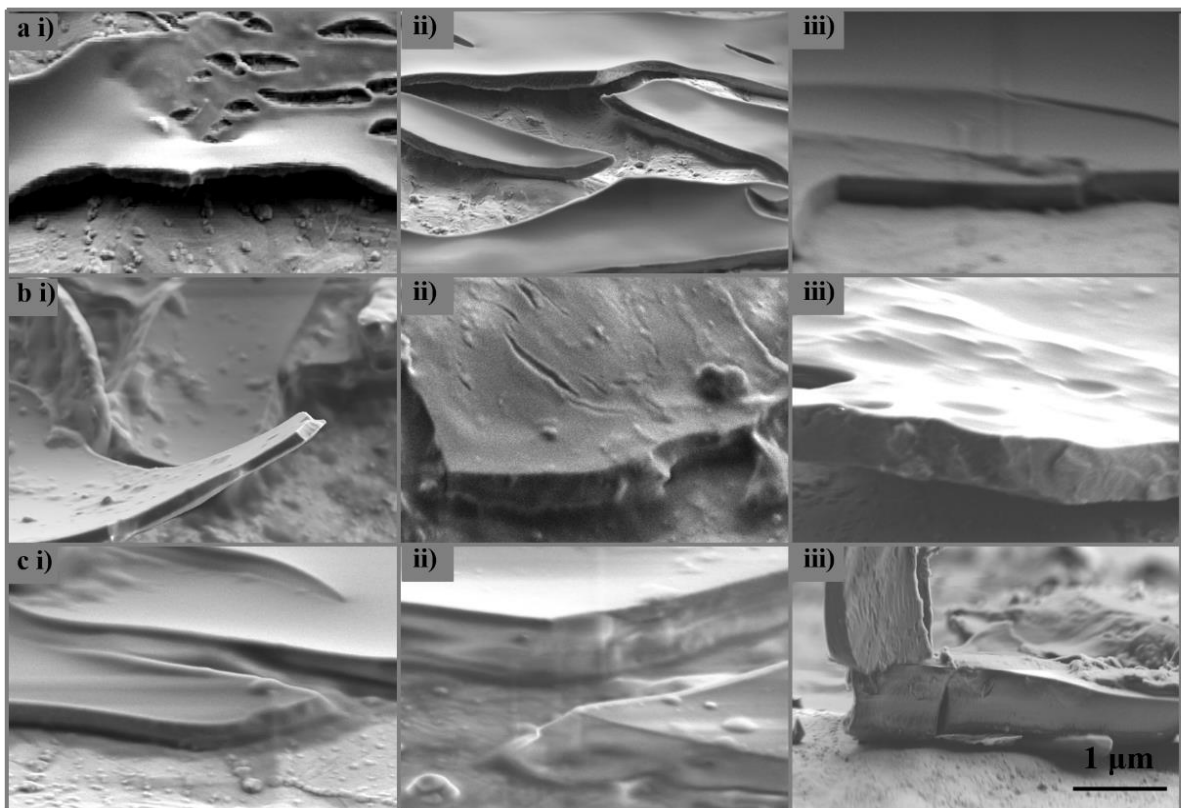


Figure 4.10: Electron micrograph showing the surface and a cross-section through MTES:TEOS 60:40 mol% coatings having an SiO₂ concentration of a) 2.5%; b) 5%; c) 10% in a i) single coat ii) double coat and triple coating application. Images were captured using a 10k magnification.

Table 4.2: Measured thickness of silica coatings that have been deposited in this work. Three silica concentrations were considered and deposited in single, double and triple coatings.

SiO ₂ concentration	No. of coatings	Mean thickness ± Standard error (nm)
2.5%	1	369 ± 14
	2	600 ± 21
	3	755 ± 26
5.0%	1	383 ± 11
	2	632 ± 23
	3	899 ± 16
10%	1	503 ± 32
	2	979 ± 85
	3	1312 ± 142

An increase in SiO₂ concentration and increasing in the number of applied coating leads to an increase in coating thicknesses, as confirmed by electron microscopy observation (Figure 4.10), measurements are presented in Table 4.2. Thickness increases proportionally upon increasing the number of coatings applied to the metal surface. For instance, for a 2.5% SiO₂ concentration, the thicknesses were measured to be 369, 600, 755 nm for single-, double- and triple-coated metal. Less significant increase in thickness was noticed upon increasing the silica concentration (369, 383 and 503 nm for single coats of 2.5%, 5% and 10% SiO₂ concentrations) which was also reported by Franquet *et al* [208]. Some redissolution of silica upon application of second and third coating during dip-coating process is possible and could explain the less than additive figures obtained in Table 4.2 (e.g. for 2.5% SiO₂ concentration single application of coating = 369 ± 14 nm, two-coating application = 600 ± 21 nm, triple coating application = 755 ± 26 nm).

Electrochemical tests were performed on coatings listed in Table 4.2. Electrochemical data is presented in **Figure 4.11**, which includes increasing number of coatings for both 2.5% and 5% SiO₂ systems, a comparison of EIS parameters and I_{corr} values of the featured systems follows in **Table 4.3**. EIS data was modelled using EEC 1 in Figure 4.5 due to two phase system appearing in Bode

phase angle plots shown through two drops in phase angle versus single drop for bare metal (modelled using EEC 2 of Figure 4.5). The two-phase system is also evident in Figure 4.11 a i) for 1 coat plot (not observed for 2 and 3 coat systems) where two slopes are observed as expected (refer to S. Tait's *Introduction into Electrochemical Testing for Practicing Engineers and Scientists* [179]). For both 2.5 and 5% SiO₂ systems (single, double or triple coated), an increase in Z is observed compared to bare metal plots seen as higher Z values in low frequency range of the bode impedance plot (Figure 4.11 (a)), wider arc in Nyquist plot (Figure 4.11 (c)) and drop in I_{corr} in PD scan (Figure 4.11 (d)).

Such enhancement in corrosion protection is further enhanced upon increasing the number of coatings of 2.5% and 5% SiO₂ systems. EIS and I_{corr} values are presented in Table 4.3 for a more quantitative approach to corrosion protection discussion, rather than relying on the electrochemical data outputted and presented in Figure 4.11. For 2.5% and 5% SiO₂ coating systems it can be said that an improvement in corrosion protection is observed when a double-coating is applied versus when only one coating is applied since following first coating, remaining surface imperfections and exposed areas are covered by the second coating. Additional coating applications only make the coating thicker which seems to have minimal effect on the coating's anti-corrosion properties. Although Impedance values for 3-coated systems are slightly better than that of 2-coat systems, such an insignificant improvement outweighs the practicality of preparing three-layered coatings and it is more likely that, for example, foreign particles deposit between the layers.

Figure 4.12 presents electrochemical data for single-coated systems having 2.5%, 5% and 10% SiO₂ concentrations, a comparison of EIS and I_{corr} values is also included in Table 4.3. The significant improvement in corrosion protection of 10% SiO₂ coatings relative to 2.5 and 5% SiO₂ systems can be observed best through the Nyquist plot (Figure 4.12 (c)) where a wider impedance arc is observed. This is also visible in the Bode impedance plot though less noticeable (Figure 4.12 (a)) together with drop in I_{corr} in PD plot (Figure 4.12 (d)). Results obtained clearly show that a significant improvement in corrosion protection occurs when the SiO₂ concentration is increased to 10%, whereas results for 2.5% and 5% concentration appear to present similar results: single coated 2.5% SiO₂ total

Impedance ($Z_{tot} = R_t + R_{po} + R_{sol}$ at lower frequency range) value = $1.44 \times 10^5 \pm 1.58 \times 10^4 \Omega \text{ cm}^2$, 5% SiO₂ Z_{tot} value = $1.27 \times 10^5 \pm 1.10 \times 10^4 \Omega \text{ cm}^2$ and 10% SiO₂ Z_{tot} value = $6.39 \times 10^5 \pm 2.52 \times 10^4 \Omega \text{ cm}^2$ (values for R_t , R_{po} and R_{sol} taken from Table 4.3).

A CPE is commonly used instead of a capacitor to model the behaviour of many electrochemical systems showing depressed semicircles in the Nyquist plot. The impedance of a CPE is defined by the equation: $Z_{CPE} = 1 / Y(j\omega)^\alpha$, for which Y is a constant for the system, $j = (-1)^{1/2}$ and $\omega = 2\pi f$. The exponent α can vary from $-1 \leq \alpha \leq +1$ and for values of $\alpha = 0$ then the CPE is a resistor, $\alpha = 1$ and the CPE is a capacitor, when $\alpha = -1$ the CPE is an inductor. In addition, if $\alpha = 0.5$ then the CPE is the Warburg impedance, i.e. it models a diffusion process [170]. The use of a CPE instead of an “ideal” capacitor is attributed to different reasons, such as surface roughness, inhomogeneous distribution of the reaction rates or the current, or varying thickness or properties of a coating [170].

For coated metal, the Y constant of CPE_c is typically smaller than that of CPE_{dl} (see Table 4.3; for example, $Y_c = 1.93 \times 10^{-7} \pm 2.31 \times 10^{-8} \Omega^{-1} \text{ cm}^{-2} \text{ s}^\alpha$ versus $Y_{dl} = 6.36 \times 10^{-6} \pm 7.63 \times 10^{-7} \Omega^{-1} \text{ cm}^{-2} \text{ s}^\alpha$ for single coated 2.5% SiO₂ system), as is the case with R_{po} for coating being smaller than R_t ($R_{po} = 1.26 \times 10^4 \pm 3.79 \times 10^3 \Omega \text{ cm}^2$ and $R_t = 1.32 \times 10^5 \pm 1.58 \times 10^4 \Omega \text{ cm}^2$). Both Y_c and Y_{dl} decrease in value as the resistance of the system increases i.e. as the coating becomes more protective, in case of Table 4.3 this occurs with an increase in silica concentration. Table 4.3 presents values for α_c are typically higher than α_{dl} due to the highly polished and thus even surface of the metal compared to that of the deposited coating. GOF values are significantly small indicating a good fit of EEC to EIS data obtained (refer to S. Tait's *Introduction into Electrochemical Testing for Practicing Engineers and Scientists* [179] for brief feature on GOF).

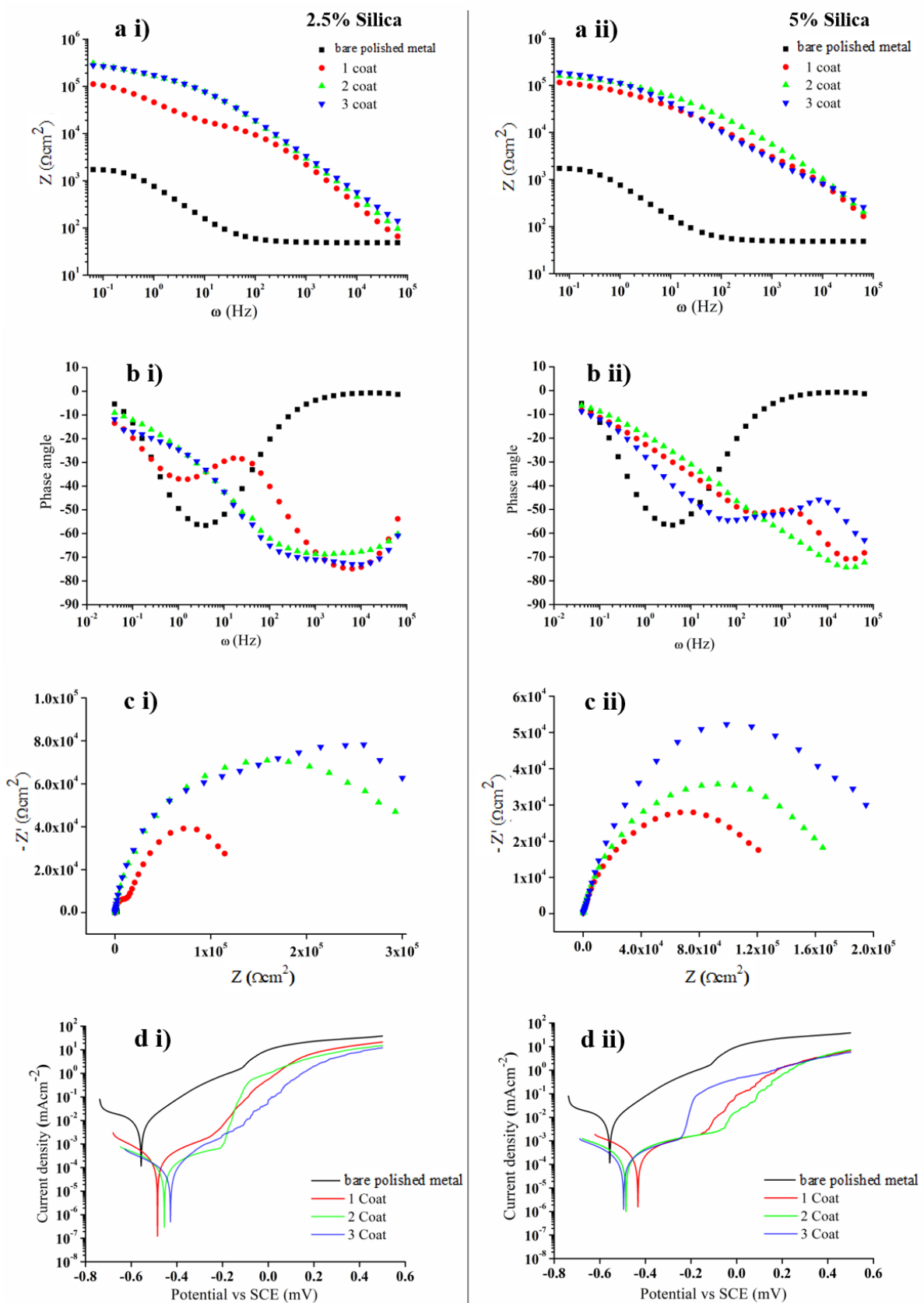


Figure 4.11: Electrochemical plots for MTES:TEOS 60:40 mol% having 2.5% (left) and 5% (right) silica concentrations for single, double and triple coated coupons a) Bode impedance b) Bode phase angle c) Nyquist and d) Potentiodynamic plots.

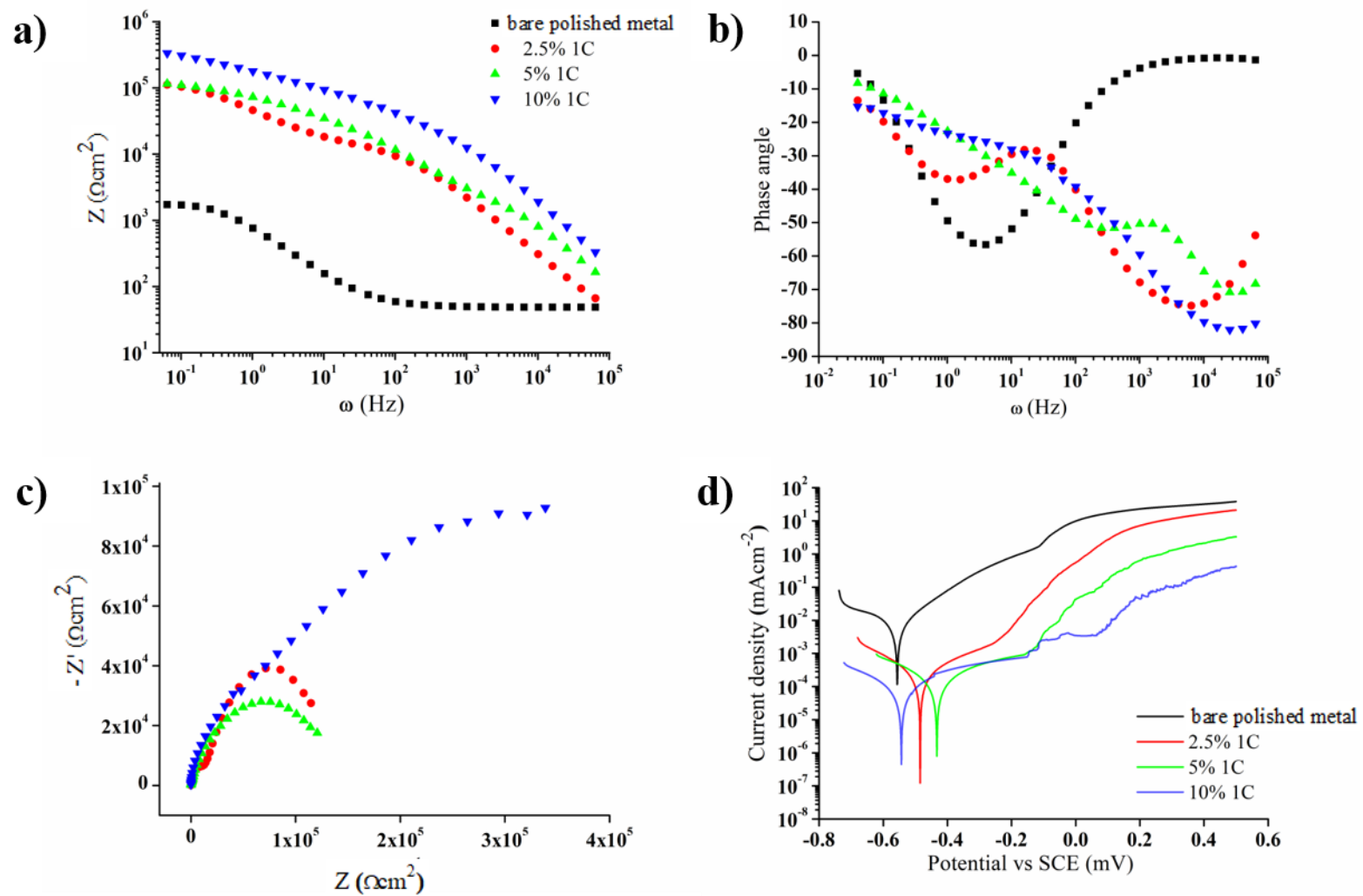


Figure 4.12: Electrochemical plots for MTES:TEOS 60:40 mol% upon increasing SiO₂ concentration from 2.5wt% to 5wt% to 10 wt% SiO₂ for single coatings a) Bode impedance b) Bode phase angle c) Nyquist and d) Potentiodynamic plots.

Table 4.3: EIS parameters and corrosion current values obtained through electrochemical testing of the various coated surfaces investigated. Bare metal values included for comparative purposes.

SiO ₂ conc.	No. of coatings	R_{sol} ($\Omega \text{ cm}^2$)	R_{po} ($\Omega \text{ cm}^2$)	CPE _c		R_t ($\Omega \text{ cm}^2$)	CPE _{dl}		GOF	I_{corr} (mAcm^{-2})
				Y_c ($\Omega^{-1} \text{ cm}^{-2} \text{ s}^\alpha$)	α_c		Y_{dl} ($\Omega^{-1} \text{ cm}^{-2} \text{ s}^\alpha$)	α_{dl}		
	Bare polished metal	59.90 ±8.65	-	-	-	1.15×10 ³ ±1.29×10 ²	1.05×10 ⁻⁴ ±2.63×10 ⁻⁵	0.76 ±0.04	1.37×10 ⁻³ ±2.60×10 ⁻⁴	9.67×10 ⁻³ ±1.434 ×10 ⁻³
2.5%	1	27.23 ±6.81	1.26×10 ⁴ ± 3.79×10 ³	1.93×10 ⁻⁷ ±2.31×10 ⁻⁸	0.88 ±0.11	1.32×10 ⁵ ±1.58×10 ⁴	6.36×10 ⁻⁶ ±7.63×10 ⁻⁷	0.66 ±0.08	5.92×10 ⁻⁴ ±5.33×10 ⁻⁵	8.3×10 ⁻⁵ ±1.43×10 ⁻⁵
	2	27.47 ±6.87	1.01×10 ⁵ ±3.02×10 ⁴	2.96×10 ⁻⁷ ±3.55×10 ⁻⁸	0.79 ±0.09	2.58×10 ⁵ ±3.09×10 ⁴	2.65×10 ⁻⁶ ±3.18×10 ⁻⁷	0.46 ±0.06	1.01×10 ⁻⁴ ±9.08×10 ⁻⁶	3.0×10 ⁻⁵ ±1.48×10 ⁻⁵
	3	19.85 ±4.96	5.93×10 ⁴ ±1.78×10 ⁴	2.35×10 ⁻⁷ ±2.82×10 ⁻⁸	0.83 ±0.10	4.37×10 ⁵ ±5.25×10 ⁴	3.41×10 ⁻⁶ ±4.09×10 ⁻⁷	0.39 ±0.05	8.16×10 ⁻⁴ ±7.34×10 ⁻⁵	2.3×10 ⁻⁵ ±4.34×10 ⁻⁶
5%	1	38.85 ±9.71	9.07×10 ² ±2.72×10 ²	1.51×10 ⁻⁸ ±1.81×10 ⁻⁹	0.89 ±0.12	1.26×10 ⁵ ±1.52×10 ⁴	2.48×10 ⁻⁶ ±2.97×10 ⁻⁷	0.54 ±0.07	2.35×10 ⁻³ ±2.11×10 ⁻⁴	6.0×10 ⁻⁵ ±1.43×10 ⁻⁵
	2	21.49 ±5.37	8.90×10 ² ±2.67×10 ²	2.42×10 ⁻⁸ ±2.90×10 ⁻⁹	0.94 ±0.11	1.86×10 ⁵ ±2.23×10 ⁴	1.78×10 ⁻⁶ ±2.13×10 ⁻⁷	0.46 ±0.06	3.83×10 ⁻⁴ ±3.45×10 ⁻⁵	2.0×10 ⁻⁵ ±7.34×10 ⁻⁶
	3	16.32 ±2.21	7.45×10 ³ ±2.23×10 ³	1.56×10 ⁻⁶ ±1.87×10 ⁻⁷	0.60 ±0.07	1.99×10 ⁵ ±2.39×10 ⁴	8.42×10 ⁻⁸ ±1.01×10 ⁻⁸	0.84 ±0.10	3.21×10 ⁻³ ±2.89×10 ⁻⁴	1.3×10 ⁻⁵ ±4.34×10 ⁻⁶
10%	1	23.21 ±6.24	8.05×10 ³ ±2.4×10 ³	1.38×10 ⁻⁸ ±1.65×10 ⁻⁹	0.95 ±0.11	6.31×10 ⁵ ±7.6×10 ⁴	2.25×10 ⁻⁶ ±2.7×10 ⁻⁷	0.35 ±0.04	4.68×10 ⁻⁴ ±4.21×10 ⁻⁵	2.3×10 ⁻⁵ ±8.84×10 ⁻⁶

4.2.7 Highly protective coatings and irreproducibility issues

Reproducibility was more difficult to achieve for 10% SiO₂ coatings, especially multiple coated samples. Curing of the first coating was carried out prior to the second coating application to obtain an even coat since such coatings form thicker deposits thus do not dry as quickly as their thinner counterparts. Unusual plots were obtained for double and triple-coated coupons with 10% SiO₂ as shown in **Figure 4.13** when coatings do not fail during electrochemical testing. Typically, a coating that has failed forms channels in which solution percolates and leads to the formation of pitting during higher voltage range of the PD scan, which is recorded as a sudden increase in measured current as exemplified through 2.5% SiO₂ coating in Figure 4.13 at around -250 mV. No pitting was observed when coatings remained intact which is reflected in very high Impedance values and the very low I_{corr} for which changes in current were not observed even at higher voltages. This implies that the best corrosion protection is offered by 10% SiO₂ coatings but renders comparison between results impossible using this technique. Therefore the 10% SiO₂ concentration deposited on clean metal was avoided when conducting electrochemical testing in future chapters for this reason.

For a comparable study to be drawn on thicker, more protective coatings such as 10% SiO₂ double coated specimens of Figure 4.13, a more aggressive corrosion test would have to be used such as higher voltage sweep or a more concentrated salt solution during electrochemical testing. However, it is possible that although quantification and comparison results may be achieved for thicker coatings, if such aggressive tests are imposed on thinner coatings, it is predicted that as thinner coatings will succumb to the harsh conditions, (which would represent outdoor uncontrolled environments, therefore beyond the scope of this work). Thus, such testing conditions would lead to the insensitivity towards the thinner coatings. Therefore, there lies an inability to discuss improvements in corrosion protection of both thicker and thinner coatings using the same testing conditions.

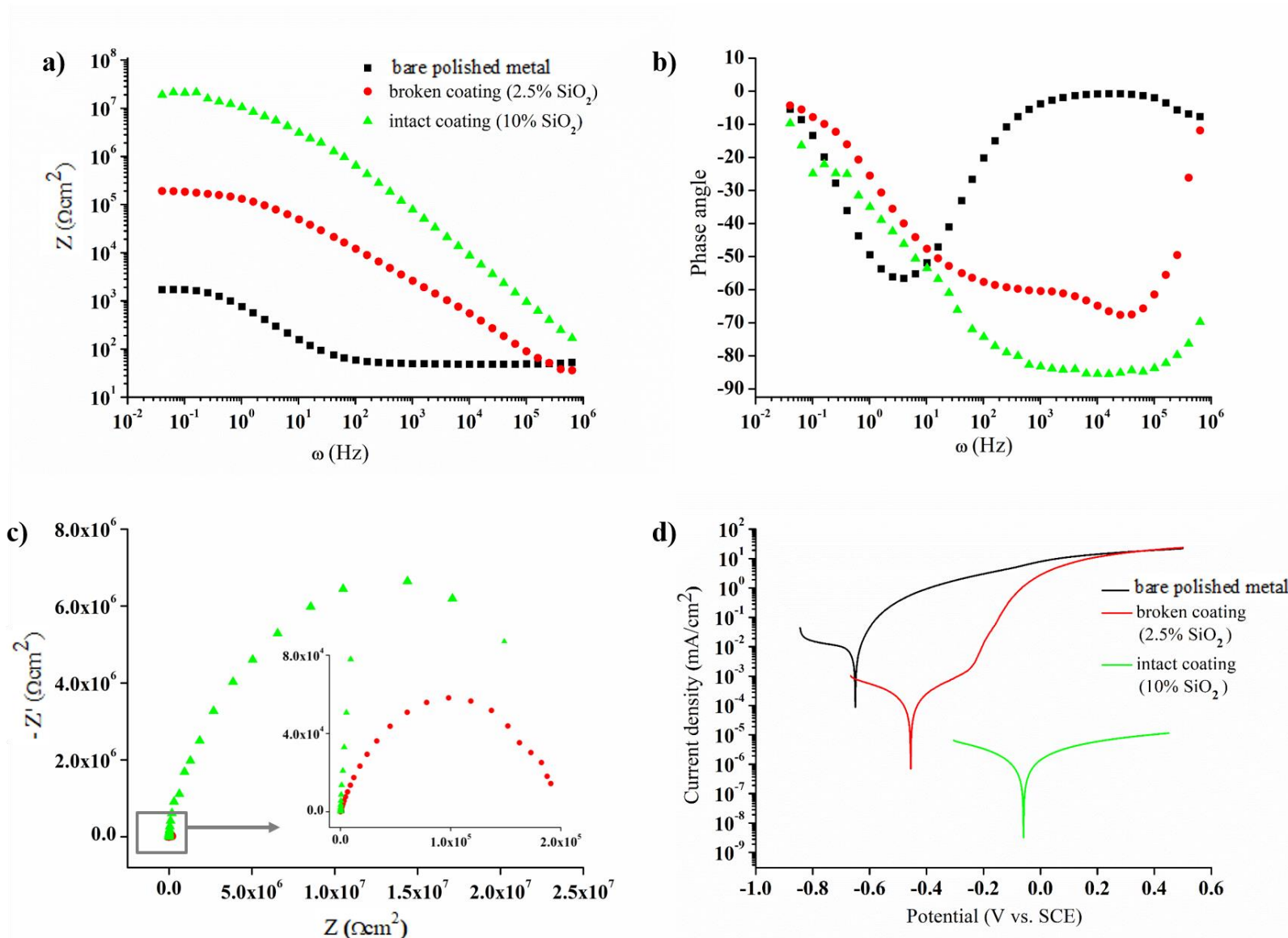


Figure 4.13: a) Bode impedance b) Bode phase angle c) Nyquist and d) Potentiodynamic plots for double-coated MTES:TEOS 60:40 mol% having 2.5% and 10% SiO₂ concentration, the latter do not fail in a regular manner and lead to irreproducibility in results.

4.2.8 Surface pre-treatment using sodium hydroxide solution

Surface pre-treatment using NaOH in different concentrations was investigated as a possible mode of improving corrosion protection. Deflorian *et al* (2006) state that by chemical etching the surface using an alkali solution, an increase in the surface reactivity and polarity is achieved since -OH groups form on the surface, thus providing the surface with more bonding sites for M-O-Si bond formation, leading to the improvement in the coating's adhesion to the surface [209]. Coupons were sonicated in 0.0001 M, 0.01 M and 1M NaOH solution (pH 10, 12 and 14 respectively) for 10 minutes [209] prior to coating. However, no significant improvement was observed over coupons that were left untreated (total Impedance (Z_{tot}) values pH 7= $1.32 \times 10^5 \pm 2.00 \times 10^4 \Omega$, pH10= $3.55 \times 10^5 \pm 1.22 \times 10^4 \Omega$, pH 12= $2.48 \times 10^5 \pm 1.25 \times 10^4 \Omega$ and pH 14= $1.30 \times 10^5 \pm 1.10 \times 10^4 \Omega$) and therefore pre-treatment using NaOH was not considered further. Deflorian *et al* also specifies that this process of surface activation also occurs when the metal surface is coated right after having been freshly polished since polishing also leads to the creation of such bonds. Perhaps, the process of surface polishing renders sufficient surface activation which has not been further improved upon using NaOH.

4.2.9 Effect of silica:water ratio ($\text{SiO}_2:\text{H}_2\text{O}$)

Figure 4.14 illustrates electrochemical testing for coatings obtained from sols produced using different water : silica ratios of 1:2, 1:4 and 1:10 mol. There appears to be a slight improvement in corrosion protection from 1:2 to 1:4 most notable through Nyquist plot showing a wider capacitive arc for 1:4 water:silica ratio coating, whereas results for 1:2 and 1:10 ratios are similar and show lower impedance in Bode impedance and Nyquist plots. Plot of PS (**Figure 4.15**) showing ≈ 5 nm particles vary only slightly with an increase in the water to silica ratio. Significant changes occur in the higher particle size population: as the ratio of silica:water is increased from 1:2 to 1:4, the intensity of particles of 1000 nm decreases substantially and shifts to a smaller size whereas larger particles begin to be detected at around 5000 nm. Further increasing ratio to 1:10 leads to an even greater production of these large particles when considering the % intensity. Presence of already formed large (micro) particles at the sol development

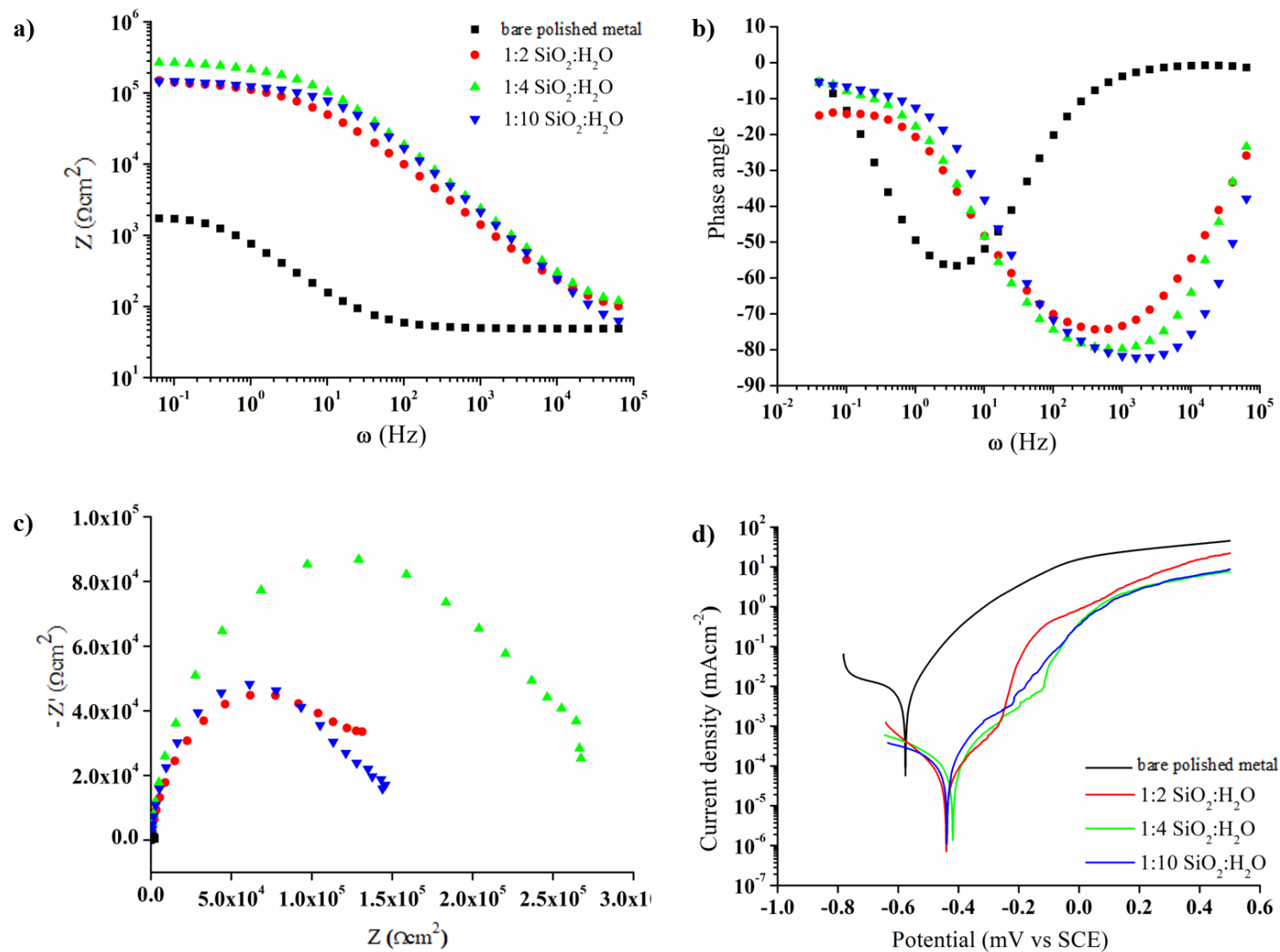


Figure 4.14: a) Bode impedance b) Bode phase angle c) Nyquist and d) Potentiodynamic plots for double coated MTES:TEOS 60:40 mol% having 1:2, 1:4 and 1:10 SiO₂:H₂O ratios for a final silica concentration of 2.5%. Plots include bare metal for comparative purposes.

stage leads to potential problems at the coating and curing stages, especially if the coatings are thinner than the macroparticles. The addition of excessive amounts of water for hydrolysis has been known to cause agglomeration of nanoparticles which could explain the degradation in corrosion protection upon increasing ratio from 1:4 to 1:10 (refer to Figure 4.14). The silica:water 1:4 ratio was thus maintained for the remainder of the work since more protective coating were obtained at this ratio as opposed to the starting 1:2 water:silica ratio.

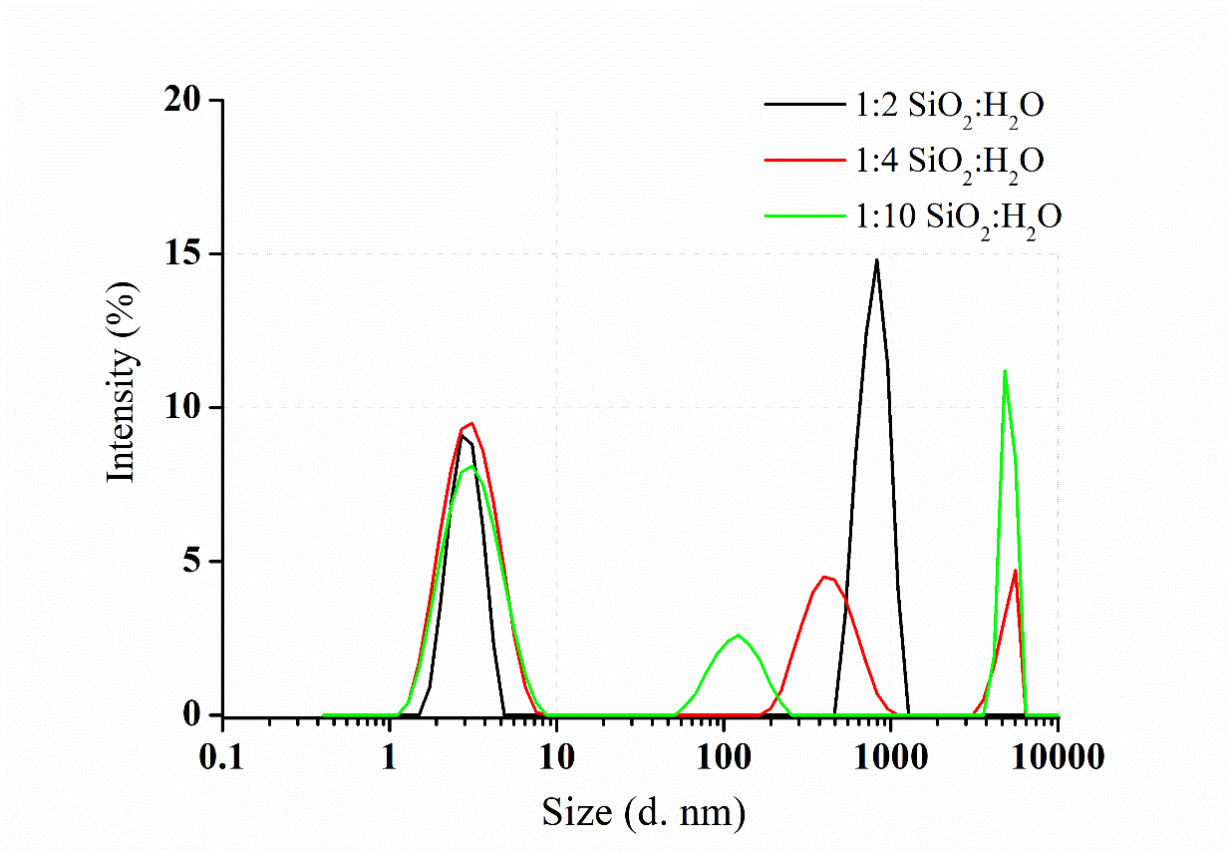


Figure 4.15: Particle size versus Intensity plot for MTES sols having different silica:water ratios.

4.3 Method alterations for OTES:TEOS sol development

When the above 60:40 mol% MTES:TEOS sol development method was applied using octyltriethoxysilane (OTES) instead of MTES precursor, Vella [53] reported the formation of visible microparticles, which was confirmed experimentally by the author herself. Ferri *et al* reported smooth coating formation using OTES:TEOS in various SiO₂ concentration and OTES:TEOS precursor mol% ratios [187]. The main difference in Ferri's sol development and the one developed in this work is that isopropyl alcohol (IPA) was employed as the solvent for the sol development. Apparently a change in solvent was enough to eliminate the formation of microparticles. The development of OTES sols was adapted to include the addition of ethanol solvent after the precursors OTES/TEOS followed by the aqueous HNO₃ and water constituents. The formation of large particles has been explained by Vella who observed an organic rich surface of microparticles whereas the core was entirely silica-based. This observation was attributed to the the slow hydrolysis of OTES, where TEOS hydrolyses at a faster rate forming large particles to which OTES attaches once hydrolysed. The addition of solvent to precursor molecules prevents this sudden agglomeration and allows the two precursors to hydrolyse prior to condensing, leading to smaller particle size.

Longer alkyl chain in OTES would imply a more difficult hydrolysis step [49] even when dispersed in solvent, therefore more time should be allowed for the sol development. **Figure 4.16** shows particle sizing obtained for a 2.5% SiO₂ OTES:TEOS 60:40 mol% system using ethanol as solvent. Particle sizing measurements were taken at various times from the start of the sol development and followed up to 24 hrs. Although results are quite similar, an 8hr development time was allowed when preparing OTES-based coatings due to the small shift in particle size both in the 2 nm range and the 100 nm range. Results for 24 hr are very close to those of 8 hrs, therefore such prolonged periods of development time was avoided.

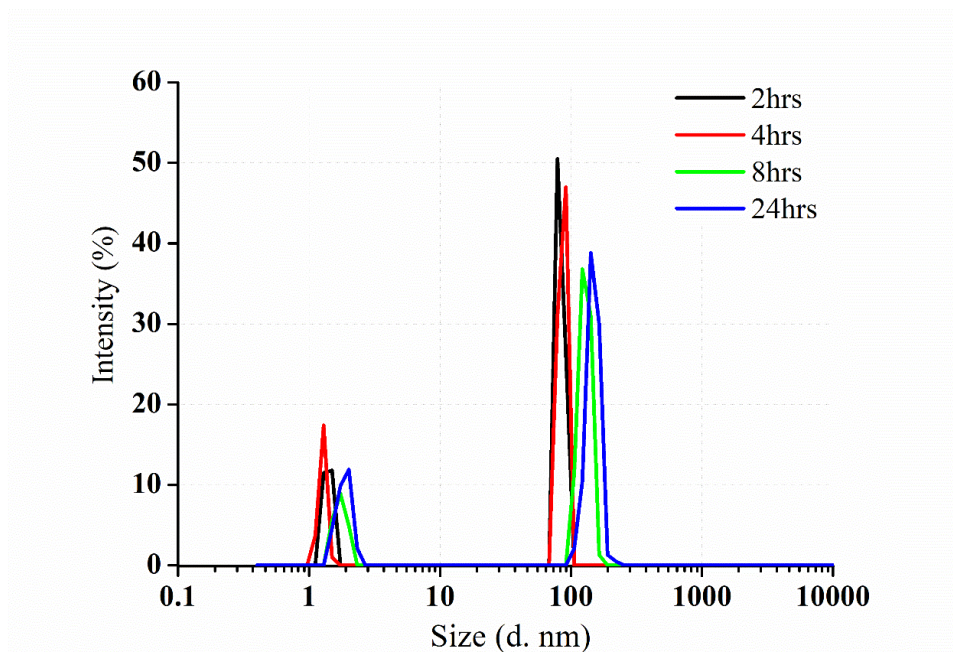


Figure 4.16: Plot of Size versus Intensity for OTES:TEOS 60:40mol% sols allowed to develop at 20 °C. Particle sizing was obtained at various times during the sol development stage.

4.4 Conclusion

In conclusion, the method development for OIH alkoxysilane coatings as established using 60:40 mol% MTES:TEOS coatings was determined to be optimal under the following set of conditions: a 1:4 ratio of silica: water was selected to produce all OIH alkoxysilane coatings and the time for sol development was set to 4 hrs at 20 °C except for OTES-based coatings which were allowed 8hrs. The silica coatings were applied through dip-coating and a double coating deposition was applied, following which coated samples were cured for 1hr at 150 °C.

The next Chapter presents a comparative study of several OIH alkoxysilane based coatings; namely MTES and OTES coatings that have been prepared as specified in this chapter, together with PrTES, HTES and PhTES, in various molar ratios with TEOS (henceforth XTES:TEOS). This work relies heavily on electrochemical testing of OIH alkoxysilane coatings therefore a 2.5% silica concentration was applied to avoid reproducibility issues. Since the latter three precursors do not form macroparticles when developed without the presence of solvent, the only precursor requiring slight modification in method is OTES in terms of solvent inclusion during sol development and longer time allowed for sol development.

CHAPTER 5:

Results

5.1 The effect of alkyl/aryl functional groups on the mechanical and anti-corrosion properties of OIH alkoxy silane coatings

5.1.1 Sol characterisation

5.1.1.1 Particle sizing

It was determined in previous chapter (Figure 4.2) that particle sizing remains unaltered before and after sol neutralisation i.e. neutralisation does not destabilise the system, PS analysis was carried out prior to dip-coating thus assuring that the measurements are representative of the particle size distribution of the sol during the coating application. **Figure 5.1** shows plots of particle size (nm) versus intensity (%) for all 20 XTES:TEOS sols produced. Two particle populations are present in all sols: smaller population which is less than 5 nm and a larger particle size population which is greater than 500 nm.

Figure 5.2 presents the particle size measurements carried out on all sols investigated in this work where the average sol particle sizes falls within a narrow range of 1-3 nm, values have been presented in **Table 5.1** which includes the mean particle size of the smaller particle population (P1) and larger particle population (P2). Polydispersity index (PDI) is also included in the table, values of PDI are relatively high (minimum value of 0.42 ± 0.12 for 20:80 mol% HTES:TEOS) which is expected when two differing particle sizes are present in a dispersion sample; discussion on the larger population (P2) such as shift in particle size of P2 in different sols, should be conducted with caution ($I \propto d^6$, as previously explained in Section 3.3.4.1).

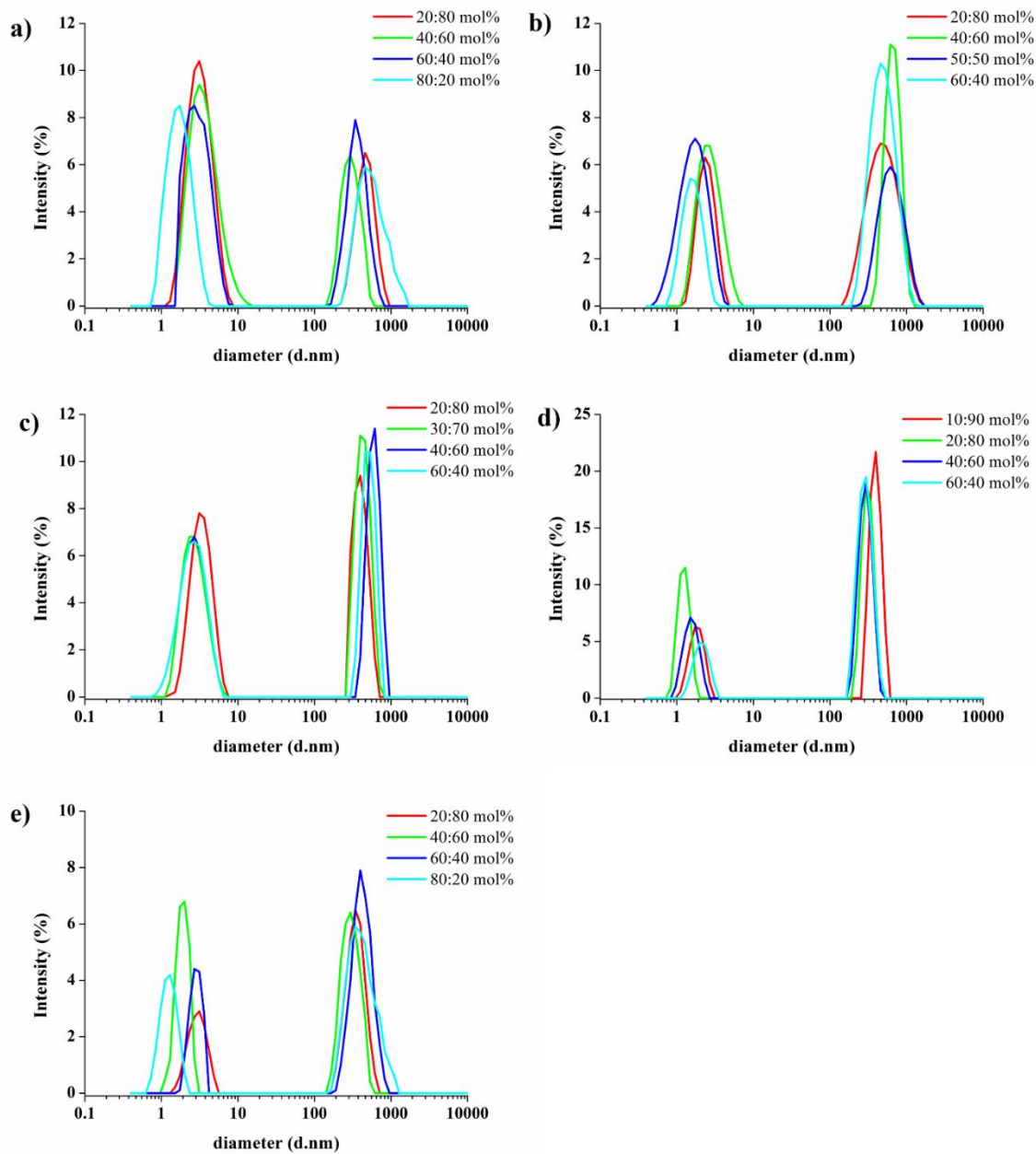


Figure 5.1: Particle sizing for 2.5% SiO₂ sols in ethanol following neutralisation of sol for a) MTES:TEOS b) PrTES:TEOS c) HTES:TEOS d) OTES:TEOS and e) PhTES:TEOS in various XTES concentrations considered in this work.

Table 5.1: Mean particle size values for peaks obtained for XTES:TEOS sols investigated, Table also includes their corresponding values of polydispersity index (PDI).

XTES:TEOS (mol%)		P1		P2		PDI	
		Mean (nm)	± St Error (nm)	Mean (nm)	± St Error (nm)	Mean	± St Error
MTES : TEOS	20:80	3.07	0.14	430.88	32.99	0.54	0.04
	40:60	2.94	0.33	277.39	21.24	0.63	0.10
	60:40	2.98	0.21	378.07	27.05	0.57	0.11
	80:20	1.80	0.12	446.99	55.85	0.52	0.03
PrTES : TEOS	20:80	2.26	0.22	482.87	36.25	0.64	0.09
	40:60	2.41	0.16	587.13	41.95	0.61	0.08
	50:50	1.83	0.14	577.81	44.22	0.62	0.12
	60:40	1.58	0.12	482.87	36.25	0.64	0.08
HTES : TEOS	20:80	2.94	0.33	430.88	32.99	0.42	0.12
	30:70	2.53	0.19	437.83	31.30	0.44	0.08
	60:40	2.19	0.17	559.17	41.95	0.44	0.16
	80:20	2.53	0.19	507.03	36.25	0.59	0.09
OTES : TEOS	10:90	1.93	0.25	378.07	27.05	0.45	0.14
	20:80	1.30	0.14	321.24	24.61	0.53	0.15
	40:60	1.58	0.12	272.91	21.24	0.53	0.11
	60:40	2.12	0.16	277.39	21.24	0.47	0.13
PhTES : TEOS	20:80	3.40	0.26	360.03	27.05	0.53	0.16
	40:60	2.02	0.21	326.43	23.35	0.57	0.10
	60:40	2.58	0.27	437.83	31.30	0.55	0.17
	80:20	1.30	0.17	366.04	28.51	0.57	0.10

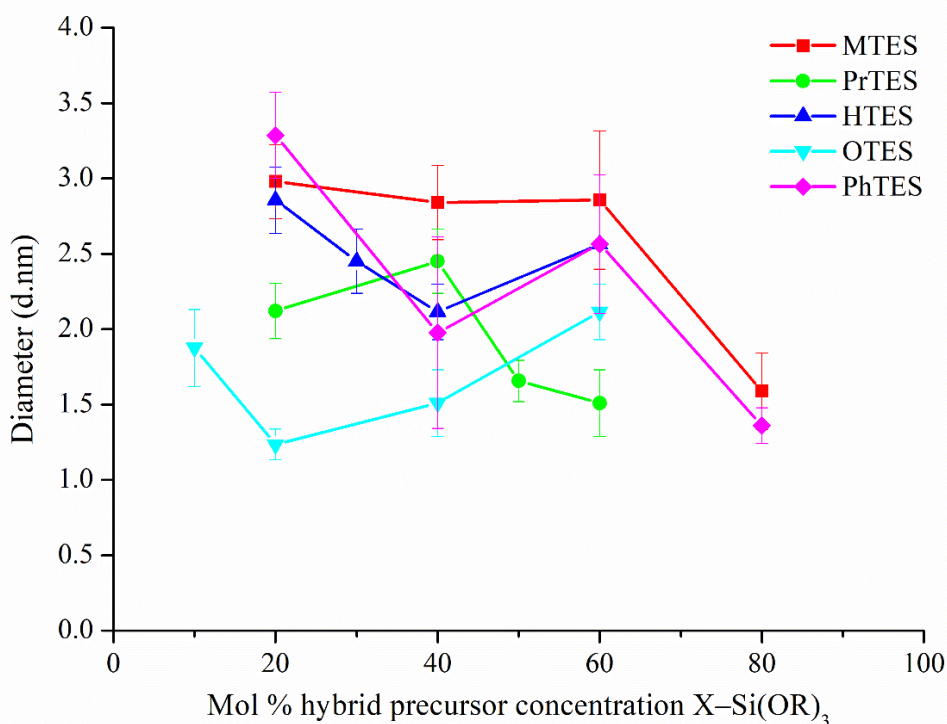


Figure 5.2: Mean particle size and standard deviation (nm) for sols investigated in this work. Data points have been connected with lines for better readability.

5.1.2 Coating characterisation

5.1.2.1 Infra-red spectroscopy

The infra-red (IR) transmission spectra of the cured powders obtained from 20:80 mol% of MTES:TEOS, PrTES:TEOS, HTES:TEOS, OTES:TEOS and PhTES:TEOS sols are shown in **Figure 5.3**. The IR spectra show that the coatings form true hybrids containing a silica network with attached organic groups. The strong absorption band occurring in all spectra between 1200-1000 cm^{-1} arises from asymmetric stretching of the siloxane (Si-O-Si) bridging network which forms the structural backbone of the hybrid material [74]. The neighbouring smaller absorption band appearing at around 750 cm^{-1} in all four spectra, is assigned to the symmetrical vibrational mode of the Si-O-Si . The lower frequency region (500-400 cm^{-1}) of all spectra contain absorption bands that have been attributed to the rocking motions of the oxygen atoms within the silica network [210].

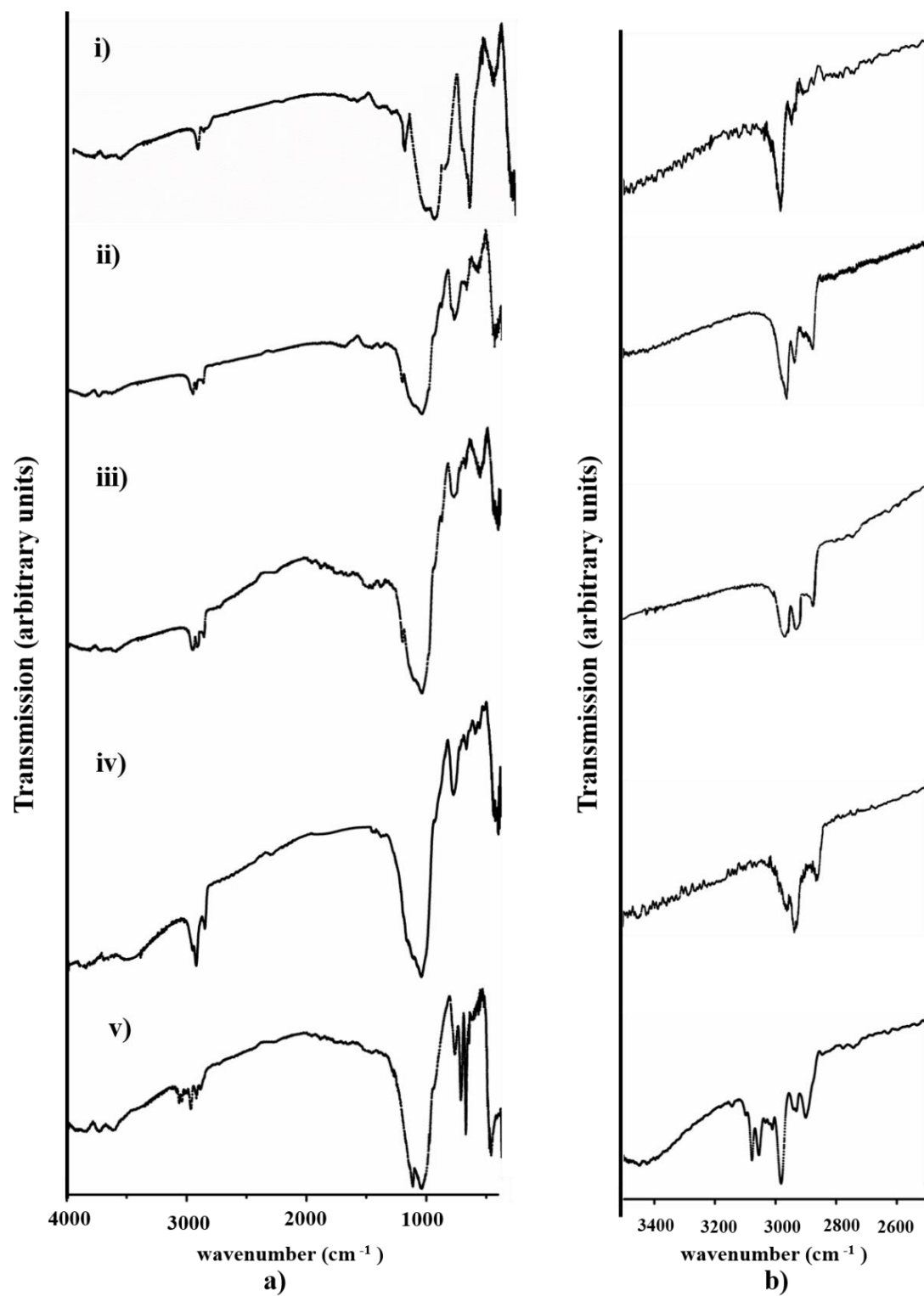


Figure 5.3: Infra-red spectra showing IR window at a) 4000-400 cm^{-1} and b) 3500-2500 cm^{-1} region for 20:80 mol% organic-inorganic alkoxy silane mixtures i) MTES:TEOS ii) PrTES:TEOS iii) HTES:TEOS iv) OTES:TEOS and v) PhTES:TEOS.

Aliphatic alkyl group absorption occurs in a specific region within the IR spectra (3000-2900 cm^{-1}) as can be seen in spectra for silica-networks containing aliphatic groups i.e. MTES, PrTES, HTES and OTES (Figure 5.3 b (i-v)). Absorption peaks in this region are due to the asymmetric and symmetric stretches of the $-\text{CH}_3$ group [211,212]. Moreover, for PrTES, HTES and OTES which possess methylene ($-\text{CH}_2-$) groups, additional absorption bands are observed due to the asymmetric and symmetric $-\text{CH}_2$ stretching. The phenyl group absorbs in the 3100-3000 cm^{-1} region due to $C-H$ stretching which occurs at a higher frequency than the $C-H$ stretching in aliphatic chains. The sharp absorption band at around 700 cm^{-1} is attributed to $C-H$ out of plane bending [58].

IR peak area analysis of OIH alkoxyxilane coatings

In this part of the study, an attempt was made to elucidate the structure of the coatings using infrared spectra. The areas under the IR absorption bands pertaining to Si-O-H and Si-O-Si and C-C bonds were evaluated with increasing mol% hybrid precursor on the overall hybrid silica structure. MTES:TEOS coatings were the only series of coatings that formed a solid that could be ground to a powder thus allowing for the accurate weighing and formation of a KBr disk and it is due to their low organic content, even in an 80:20 mol% ratio.

Table 5.2 shows relative area for 8 absorption bands considered for this analysis, the sum of 8 peaks for each mol% was taken to add up to 100% of the spectrum area. Principle peak that occurs at 1067 cm^{-1} (labelled Peak 4&5) is due to asymmetric stretches of O in Si-O-Si bonds and contributes the most as seen to possess the highest area % in the table for the all of the coatings studied. Peaks 4&5 (1067 cm^{-1}) and Peak 2 (793 cm^{-1}) stem from Si-O-Si framework whereas Peak 3 (951 cm^{-1}) and Peak 1 (600 cm^{-1}) are due to Si-OH bonds. IR spectra analysed in this section are presented in **Appendix A** (CD attached).

Table 5.2: area% for Peaks 1-8 for MTES, PrTES, HTES, OTES and PhTES in concentrations that allowed for IR testing.

X—Si(OR) ₃ : TEOS	mol%	Peak 1: Si—OH/Si—O ⁻ rocking motion (%)	Peak 2: symmetric stretching of the O along the bisector of the Si—O—Si (%)	Peak 3: Si—OH /Si—O ⁻ stretching vibrations (%)	Peaks 4&5: asymmetric stretches of O in Si—O—Si (%)	Peaks 6,7 & 8 due to C—H a/symmetric stretching (%)
MTES:TEOS	20:80	14.84 ± 0.37	23.63 ± 0.69	13.96 ± 0.44	37.17 ± 0.64	10.38 ± 1.14
	40:60	13.59 ± 1.23	29.84 ± 0.06	9.71 ± 0.50	38.66 ± 0.37	8.19 ± 0.90
	60:40	10.02 ± 1.03	34.13 ± 1.5	6.19 ± 0.55	41.21 ± 1.68	8.43 ± 0.92
	80:20	9.25 ± 0.44	38.27 ± 0.33	5.50 ± 0.09	36.50 ± 0.52	10.6 ± 1.16
PrTES:TEOS	20:80	19.24 ± 1.19	22.41 ± 0.89	12.84 ± 1.35	36.04 ± 1.48	9.45 ± 1.03
	40:60	13.30 ± 0.44	23.04 ± 0.32	5.22 ± 0.52	46.69 ± 0.94	11.77 ± 1.27
HTES:TEOS	20:80	10.51 ± 0.82	21.46 ± 0.96	3.99 ± 0.64	48.74 ± 1.27	15.28 ± 1.65
OTES:TEOS	10:90	14.86 ± 0.52	23.71 ± 1.58	6.17 ± 1.20	42.28 ± 0.83	12.97 ± 1.42
	20:80	12.32 ± 1.26	22.14 ± 1.14	5.12 ± 0.35	45.43 ± 2.32	14.98 ± 1.65
PhTES:TEOS	20:80	12.19 ± 0.29	17.15 ± 0.69	12.70 ± 0.79	45.29 ± 0.63	12.56 ± 1.38
	40:60	8.93 ± 0.2	13.96 ± 0.33	13.57 ± 0.93	43.44 ± 1.97	20.06 ± 2.40

The area % of IR peaks for coatings considered was obtained from Table 5.2 and represented in Figures 5.4-5.5. **Figure 5.4** shows relative area for 8 absorption bands considered for this analysis, the sum of 8 peaks for each mol% was taken to add up to 100% of the spectrum area. There is a clear decrease in area % of Peak 3 (951 cm^{-1} due to stretching vibrations of Si–OH /Si–O⁻ groups) and Peak 1 (600 cm^{-1} due to rocking motion Si–OH /Si–O⁻ groups) indicating an overall decrease in Si–OH intensity as the mol% MTES precursor is increased.

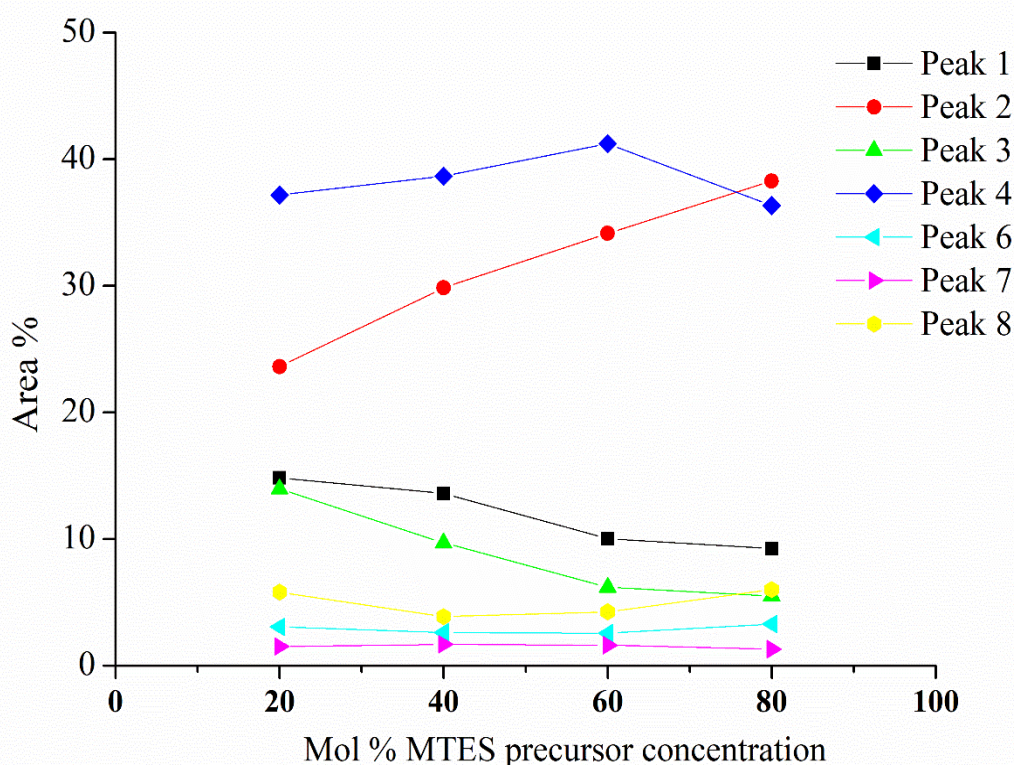


Figure 5.4: Plot of MTES:TEOS hybrid precursor mol% versus percentage area of Peaks (1 to 8) considered. Peak 1 (600 cm^{-1}) is due to the rocking motion Si–OH /Si–O⁻ groups, Peak 2 (793 cm^{-1}) due to the symmetric stretching of the O along the bisector of the Si–O–Si bridging angle, Peak 3 (951 cm^{-1}) due to stretching vibrations of Si–OH /Si–O⁻ groups, Peak 4&5 (1067 cm^{-1}) due to asymmetric stretches of O in Si–O–Si bonds, and Peaks 6-8 due to the asymmetric and symmetric stretches of the –CH₃ group/s.

Results for Si–O–Si peaks shows a significant increase in area % of Peak 2 (793 cm^{-1} due to symmetric stretching of the O along the bisector of the Si–O–Si bridging angle) with increase in MTES content of the sol. Results for the main area Peaks 4&5 (1067 cm^{-1} due to asymmetric stretches of O in Si–O–Si bonds) are less straight forward since a slight increase is obtained up to 60:40 mol% with area then decreasing for 80:20 mol% concentrations leading to a lack of clear trend as observed for Peak 2. Peaks 6-8 are a result of the organic groups (methyl) present in the OIH alkoxy silane powder and contribute the least to the total absorbance area. As expected, there is a slight increase in area as the concentration of MTES is increased since more organic groups are introduced. Since their contribution to the area% is only minor in all results obtained, it can be safely assumed that these peaks do not influence changes occurring in the other more prominent peaks due to silica network.

Figure 5.5 illustrates the variation in Peak areas 1-8 for 20:80 mol% MTES, PrTES, HTES, OTES and PhTES:TEOS. An increase in aliphatic chain length explains the slight increase in area% for Peaks 6-8 which are related to the increasing size of the organic groups. Si-OH related Peaks 1 (Si–OH /Si–O⁻ rocking motion) and Peak 3 (Si–OH /Si–O⁻ stretching vibrations) behave similarly with an increase in chain length: HTES/OTES (longer chains) possess lower areas than those of MTES/PrTES (shorter chains). Si-O-Si related Peak 2 (symmetric stretching of the O along the bisector of the Si–O–Si) exhibit no significant change whereas Peak 4&5 (asymmetric stretches of O in Si–O–Si) illustrates the opposite trend of Peaks 1 and 3 whereby HTES/OTES possess higher area% than those of MTES/PrTES.

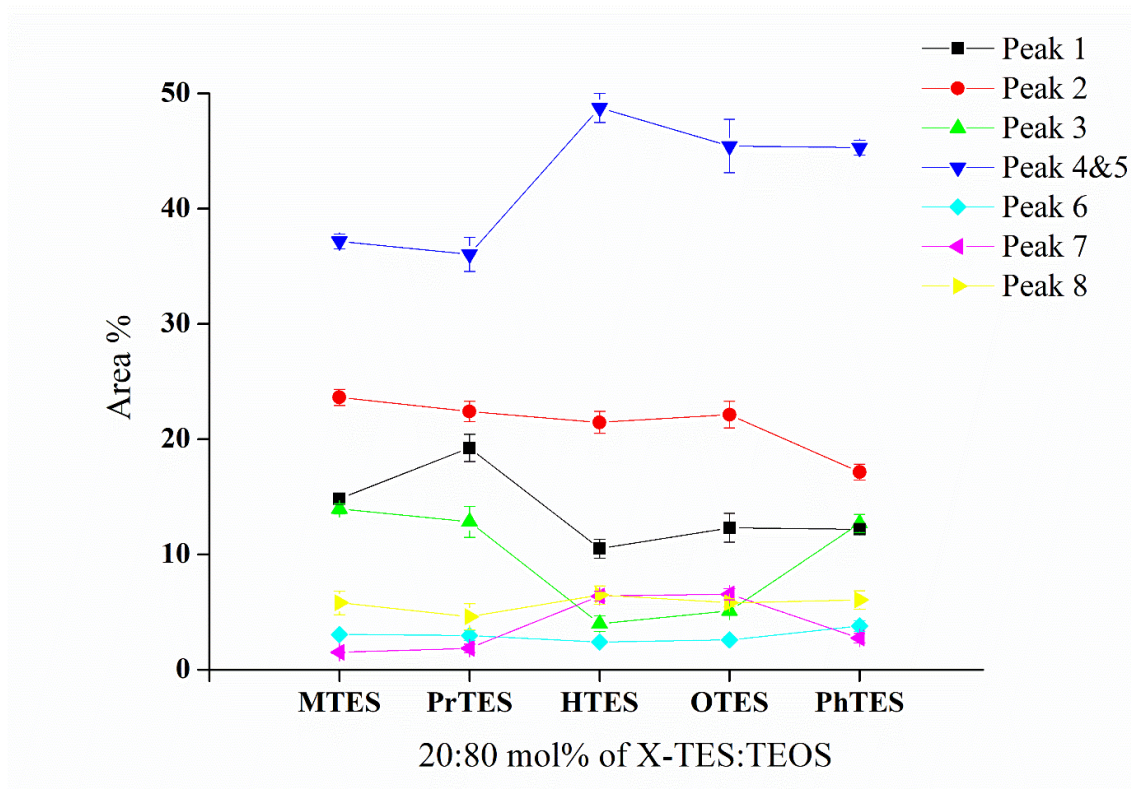


Figure 5.5: Plot of five hybrid precursors in 20:80 mol% versus percentage area for Peaks 1-8 considered. Peak 1 (600 cm^{-1}) is due to the rocking motion Si–OH /Si–O⁻ groups, Peak 2 (793 cm^{-1}) due to the symmetric stretching of the O along the bisector of the Si–O–Si bridging angle, Peak 3 (951 cm^{-1}) due to stretching vibrations of Si–OH /Si–O⁻ groups, Peak 4&5 (1067 cm^{-1}) due to asymmetric stretches of O in Si–O–Si bonds, and Peaks 6-8 due to the asymmetric and symmetric stretches of the –CH₃ group/s.

5.1.2.2 UV-visible spectroscopy

UV-vis transmission spectra for all OIH alkoxysilane coatings deposited on glass are presented in **Figure 5.6**. Coatings have been deposited through dip-coating at 280mm/min speed and double layers having 2.5% SiO₂ concentration were produced for each alkoxysilane coating. The spectrum obtained for uncoated glass is practically identical to the coated glass samples for all five precursor molecules included in this work, i.e. the coatings investigated are transparent to light in the visible region, though it can be stated that OTES:TEOS coatings appear to be slightly less so than the other four precursors considered. This can be attributed to the thickness of OTES: TEOS which deposit thicker coatings when compared to MTES, PrTES, HTES and PhTES:TEOS based coatings.

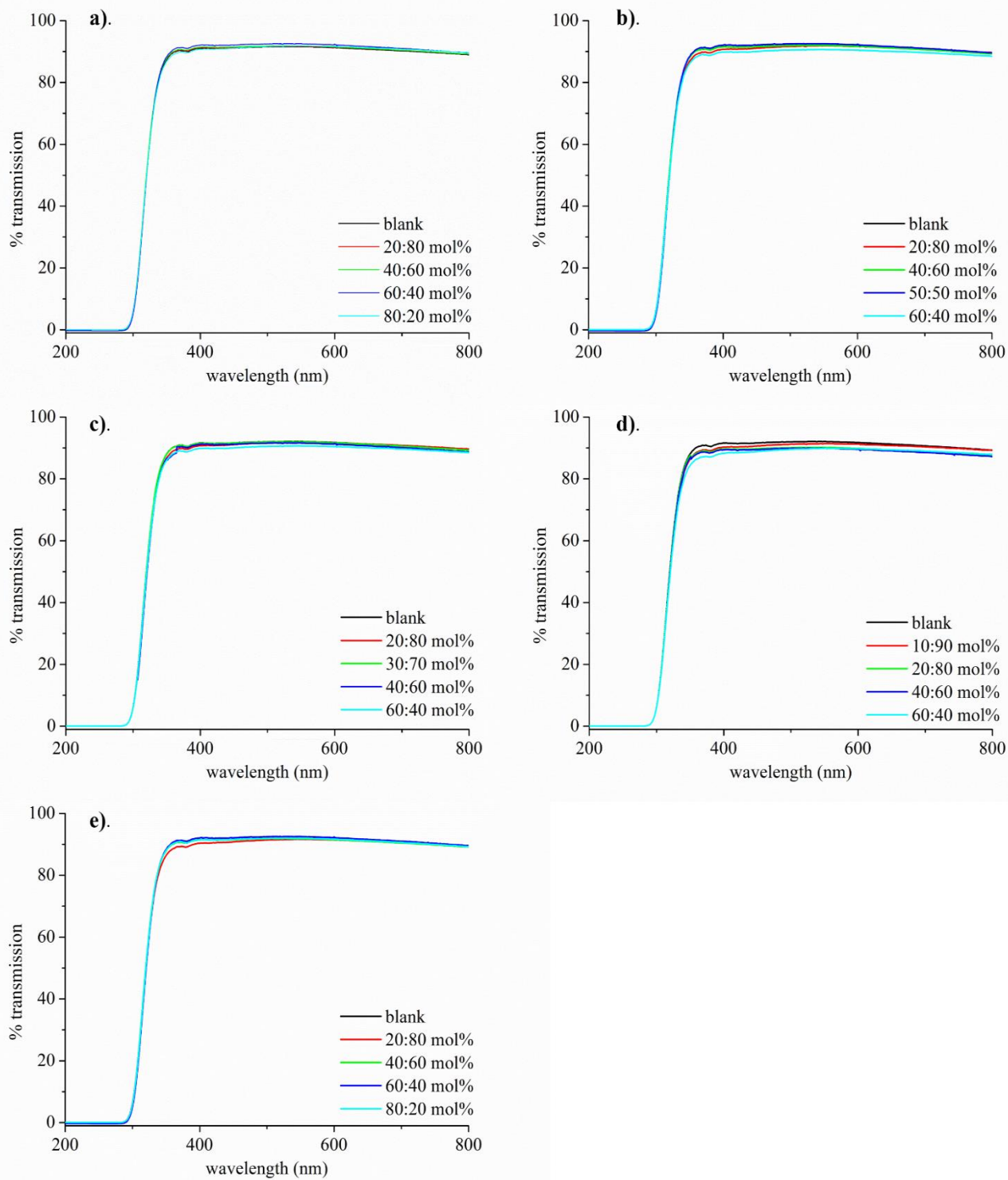


Figure 5.6: Transmission spectra for a) MTES:TEOS, b) PrTES:TEOS, c) HTES:TEOS, d) OTES:TEOS, e) PhTES:TEOS, in several XTES:TEOS mol% ratios. Plots include blank measurement (uncoated glass slide) for comparative reasons.

5.1.2.3 Coating morphology

The electron micrographs of OIH alkoxy silane coatings considered in this study are presented in **Figure 5.7** showing coating surfaces which appear to be smooth with few imperfections noticeable on the surface of the coatings.

5.1.2.4 Coating thickness

Cracks incurred artificially during preparation of the coating cross-section (bending of coated SS strips) are evident in **Figure 5.8** showing 20:80 mol% coatings. The cracks allow for the observation and determination of coating thickness using SEM. It is interesting to note that although the coatings were deposited as a double-film, the interface between the two layers is not evident in the electron micrographs. The lack of a bilayer stems from the manner in which the coatings were deposited and cured. Indeed, no heat treatment was employed between the first and second coating layer, but a single curing process was applied following deposition of the second coat layer. Similar observations were done when measuring the coating thicknesses of other coatings having higher XTES:TEOS ratio, the complete set of images and are shown in **Appendix B** (CD attached).

Figure 5.9 presents a graph of coating thicknesses against increasing XTES precursor concentration for the different coatings prepared in this work, the average double-layer coating thicknesses and their respective standard error have been calculated on the minimum of three similar measurements. Coating thicknesses were found to fall between 500 nm to 1100 nm.OTES:TEOS sols were determined to produce the thickest coatings whereas PhTES:TEOS sols produced the thinnest coatings.

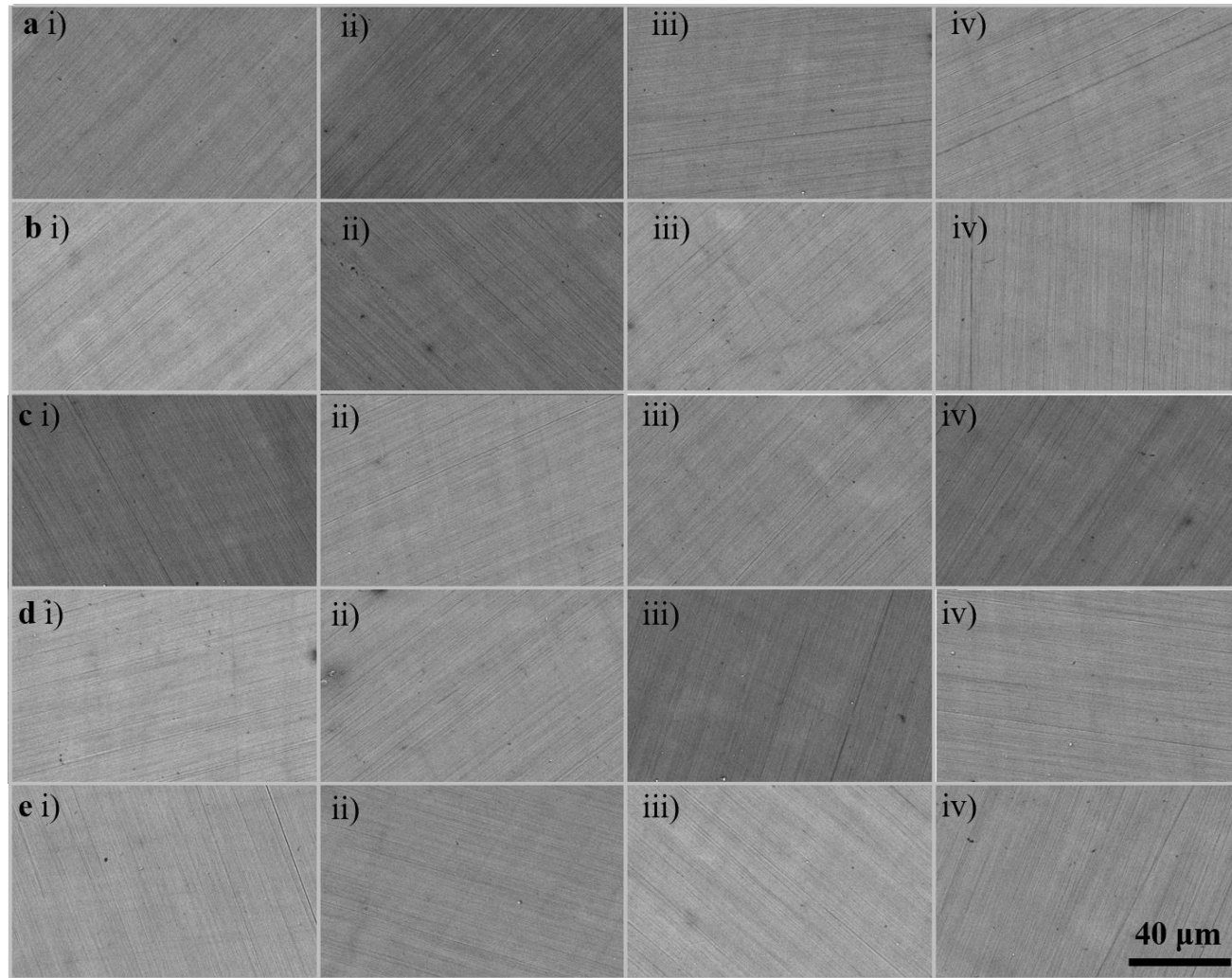


Figure 5.7: Electron micrographs of all OIH alkoxy silane coatings considered (mag $\times 2000$). Double coating application was carried out through dip-coating and a 2.5% SiO_2 concentration was employed: a) MTES:TEOS i) 20:80 ii) 40:60 iii) 60:40 and iv) 80:20 mol%; b) PrTES:TEOS i) 20:80 ii) 40:60 iii) 50:50 and iv) 60:40 mol%; c) HTES:TEOS i) 20:80 ii) 30:70 iii) 40:60 and iv) 60:40 mol%; d) OTES:TEOS i) 10:90 ii) 20:80 iii) 40:60 and iv) 60:40 mol%; and e) PhTES:TEOS i) 20:80 ii) 40:60 iii) 60:40 and iv) 80:20 mol%.

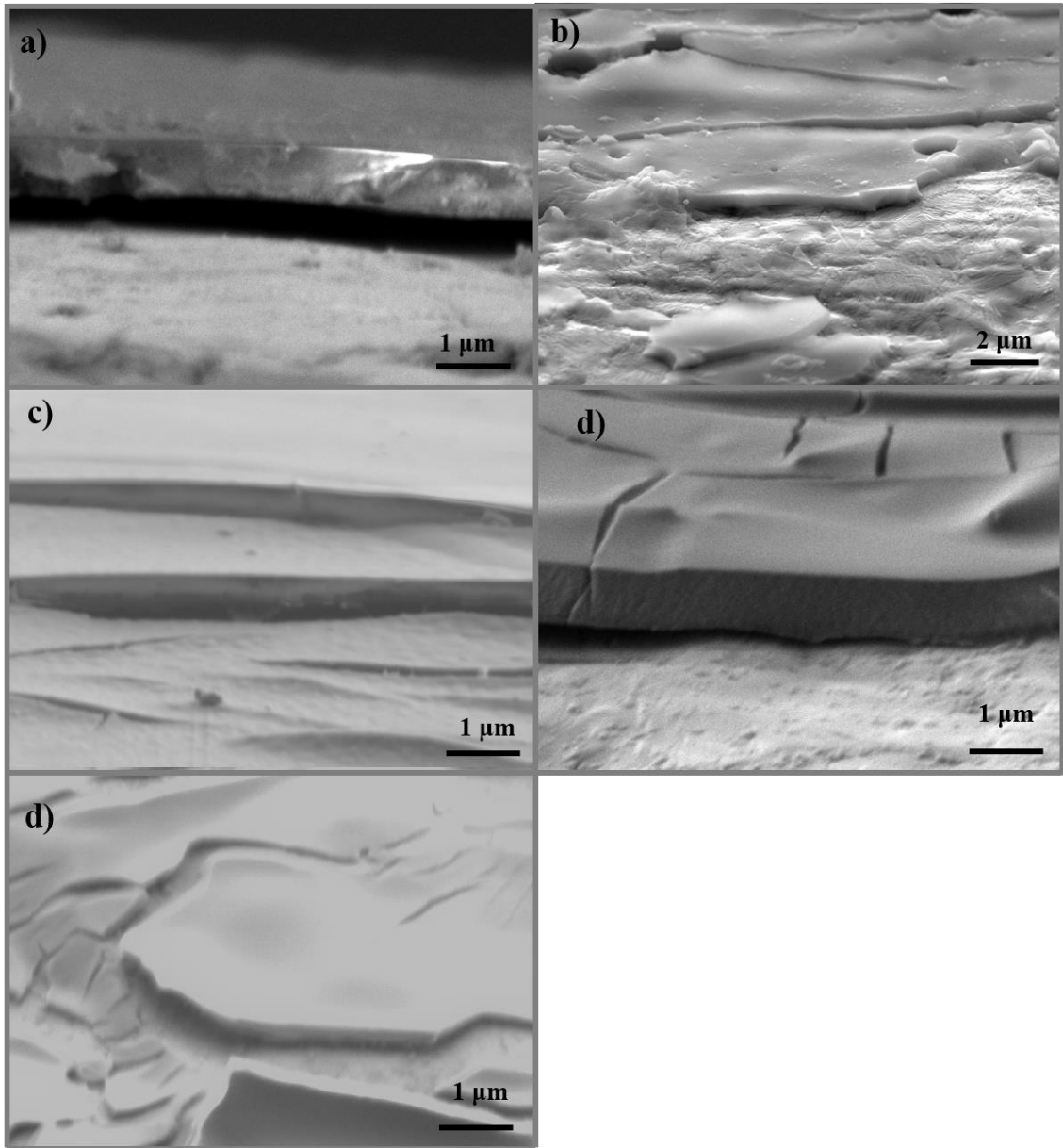


Figure 5.8: SEM showing coated surface of SS strips and a cross-section through 20:80 mol% coatings of a) MTES:TEOS (mag $\times 30k$) b) PrTES:TEOS (mag $\times 5k$) c) HTES:TEOS (mag $\times 30k$) d) OTES:TEOS (mag $\times 30k$) and e) PhTES:TEOS (mag $\times 30k$).

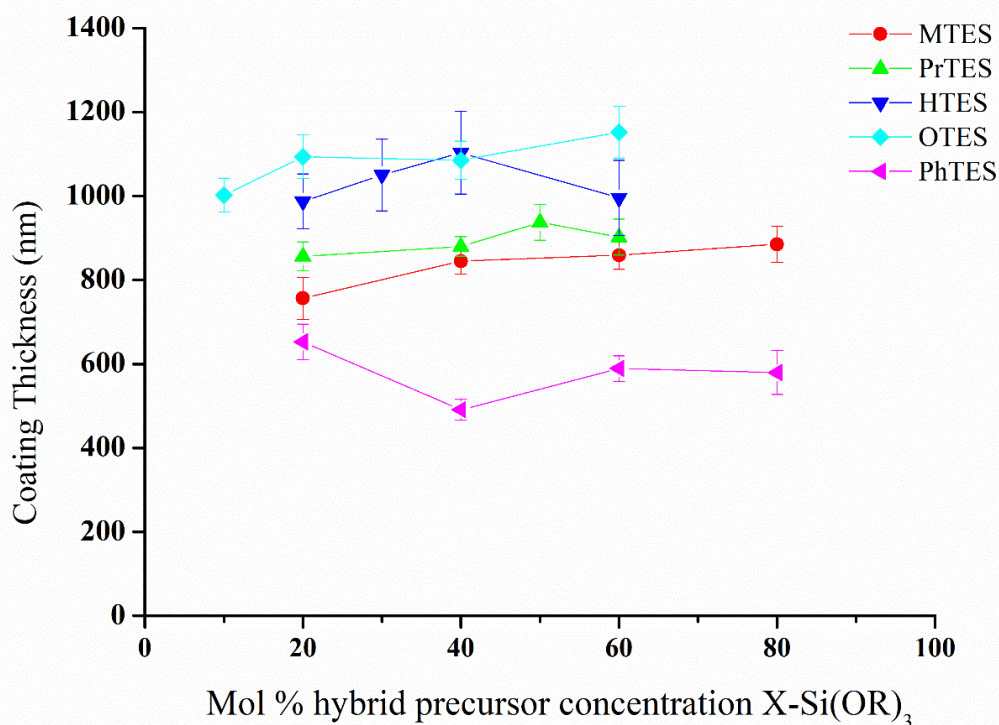


Figure 5.9: Average double-layer coating thicknesses and their respective standard error (nm) for different coatings investigated in this work.

5.1.2.5 Contact angle

Calculations based on contact angle measurements yield the solid surface tension, which quantifies the wetting characteristics of a solid material. Contact angle data indicates the degree of wetting when a solid and liquid interact; in our case, the coating and a water droplet. Small contact angles ($< 90^\circ$) correspond to high wettability and a high interaction between the surface and liquid which leads to a spreading of the liquid along the surface as shown in **Figure 5.10** (a) for bare metal surface. On the other hand, a large contact angle ($> 90^\circ$) corresponds to low wettability due to weak surface interactions. In such cases, the liquid does not spread along the surface but gathers itself in such a way as to minimise contact with the surface. Surfaces that produce a contact angle of $> 90^\circ$ are termed hydrophobic when the liquid is water as seen in Figure 5.10 (b) for OTES: TEOS 40:60 mol% coating. This coating possesses the highest contact angle measured for all coatings investigated, which means that all other coatings produce a droplet which appears in between the two pictured in

Figure 5.10 (see **Appendix C**, CD attached for images of all coatings investigated). The water contact angle measurements of the hybrid coatings deposited onto iron are presented in **Figure 5.11**.

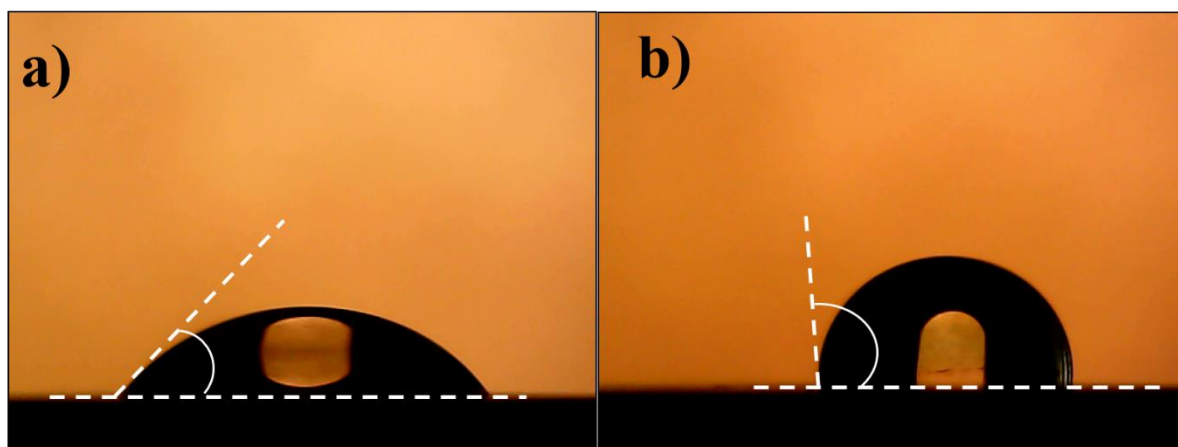


Figure 5.10: Photo-micrographs of sessile water droplets on a) bare metal with the lowest contact angle (left) and b) OTES:TEOS 40:60 mol% having the highest contact angle.

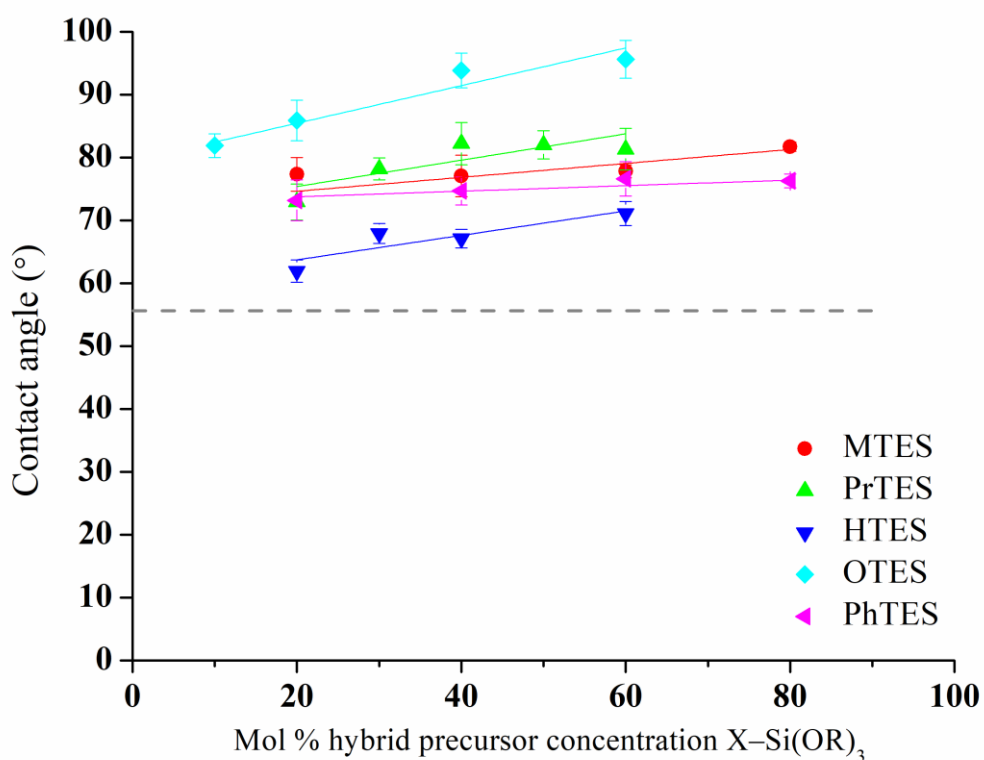


Figure 5.11: Mean contact angle measurements for different organic-inorganic silane coatings prepared in this work. Bare metal contact angle (56°) is represented by dashed line for comparative purposes.

All coatings investigated show a gradual increase in water contact angle with increasing mol% concentration of the alkyl/aryl precursor.OTES:TEOS coatings proved to be possess the highest contact angle whereas HTES:TEOS sols produced the least hydrophobic coatings.

5.1.3 Mechanical testing of coatings

5.1.3.1 Nano-indentation

5.1.3.1.1 Hardness and Young's Modulus determination

During hardness testing, the material surface is indented with a tip loaded with a force, resulting in a penetration depth of the indenter into the coating. During indentation, the force (P) and the penetration depth (h) are recorded as a function of time, through which a load-displacement relationship is attained. The recorded indentation test consists of a single loading-unloading cycle. If plastic deformation occurs, a different curve is followed upon unloading as is the case with OIH alkoxysilane coatings considered in this work and exemplified through result obtained for PrTES:TEOS 20:80 mol% andOTES:TEOS 60:40 mol% shown in **Figure 5.12**.

The concentration of organics present in a coating affects the quality of coatings produced in such a way that low organic concentration leads to the formation of harder and more brittle coatings (high hardness value $H= 0.44$ GPa for PrTES:TEOS 20:80 mol%) whereas high organic concentration leads to coatings that are softer and exhibit more plastic behaviour ($H= 0.02$ GPa forOTES:TEOS 60:40 mol%). The indentation depth increases to a maximum value (h_{max}) due to the application of a maximum force (P_{max}). Upon unloading of the force, a different curve is obtained for which the final depth is not zero (starting position of indenter on surface) but some finite value (h_f) due to the plastic deformation of the coating during indentation.

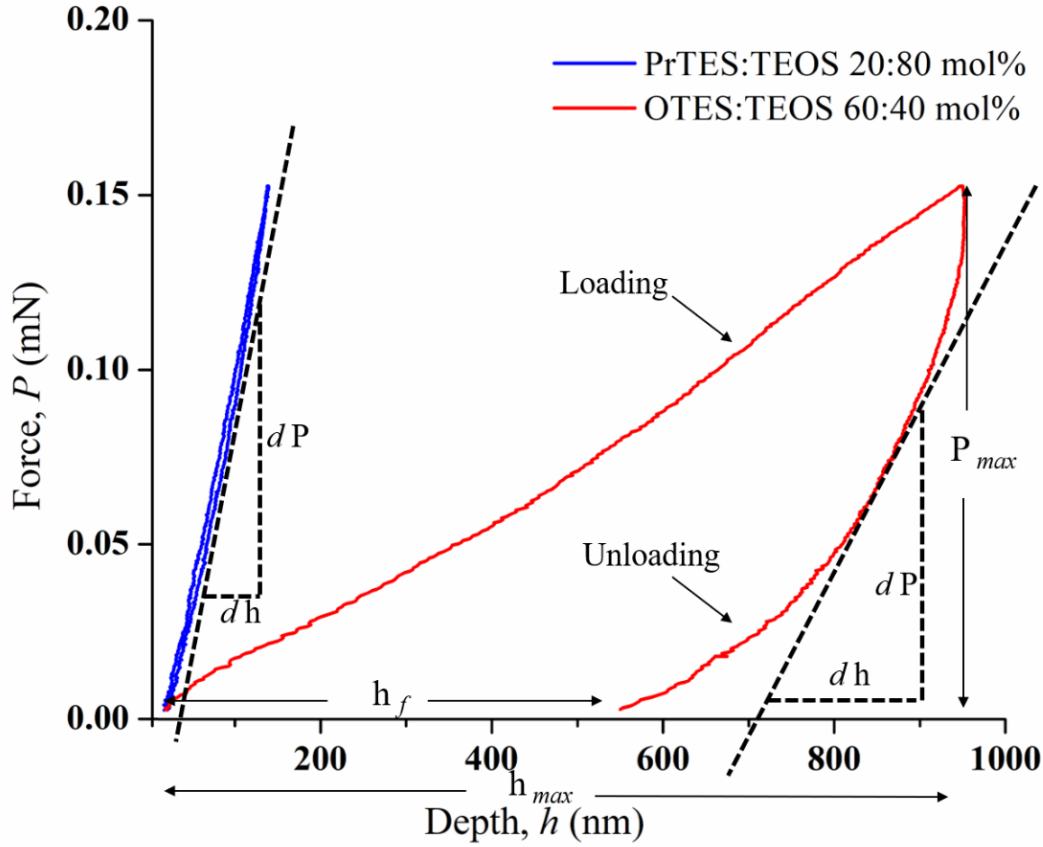


Figure 5.12: Plot of displacement versus load for one of the harder coatings, PrTES:TEOS 20:80 mol% ($H = 0.44$ GPa, left plot) together with the representative for least hard coatings, OTES:TEOS 60:40 mol% coating ($H = 0.02$ GPa, right plot) showing loading-unloading cycle during measurement.

Using the Oliver and Pharr relationship [213], the elastic modulus of the coating material (E_s) can be obtained from the reduced elastic modulus E_r as follows:

$$\frac{1}{E_r} = \frac{(1-\nu_i^2)}{E_i} + \frac{(1-\nu_s^2)}{E_s} \quad \text{Eq 5.1}$$

where E_i is the Elastic Modulus of the diamond Berkovich indenter (1141 GPa) [214], ν_i is the Poisson's ratio of indenter (0.07) [214] and ν_s is the Poisson's ratio of coating which was found to be 0.25 for OIH alkoxy silane coatings [214].

The stiffness S can be obtained as from the following equation [213]:

$$S = \frac{dP}{dh} = \frac{2}{\sqrt{\pi}} E_r \sqrt{A} \quad \text{Eq 5.2}$$

where S (dP/dh) is the experimentally measured stiffness of the upper portion of the unloading data, E_r is the reduced modulus (previously defined), and A is the projected area of the elastic contact. Since dP is similar for both harder and softer coatings due to set maximum force of 0.15 mN, then softer coatings such as OTES in Figure 5.12 would be penetrated to a greater extent, thus possessing a larger dh value than harder coatings such as PrTES. This larger value in dh brings about an increase in area as expected. Hardness is then dependent upon the projected contact area at maximum load and is evaluated through following formula:

$$H = \frac{P_{max}}{A} \quad \text{Eq 5.3}$$

Therefore, the smaller the area, the greater the hardness value of the substrate since P_{max} is set to be constant for all coatings measured. Hardness values of each indentation were outputted once testing was complete. The reduced elastic modulus was not obtained as directly as hardness measurement but calculated as specified in Eq 5.1.

Load-displacement plots for 2.5% SiO₂ OIH alkoxy silane coatings considered are presented in **Figure 5.13**. Softer coatings can be located at the right hand side of the plot, e.g. MTES:TEOS 80:20 mol% coatings in Figure 5.13 (a) since a greater depth has been reached for the same amount of force when compared to MTES:TEOS 20:80 mol% which has been penetrated the least, thus is said to be one of the hardest coatings tested. Greater depths have been obtained with softer coatings, most notable with OTES:TEOS 60:40 mol% (highest organic content) coating in Figure 5.13 (d) for which depth penetrated was over 450 nm. Some degree of sub-surface interference is possible when depth of indentation is greater than 10% of coating thickness. This means that for softer coatings such as OTES:TEOS 60:40 mol%, hardness values measured would in fact be higher due to a hardness contribution from underlying surface.

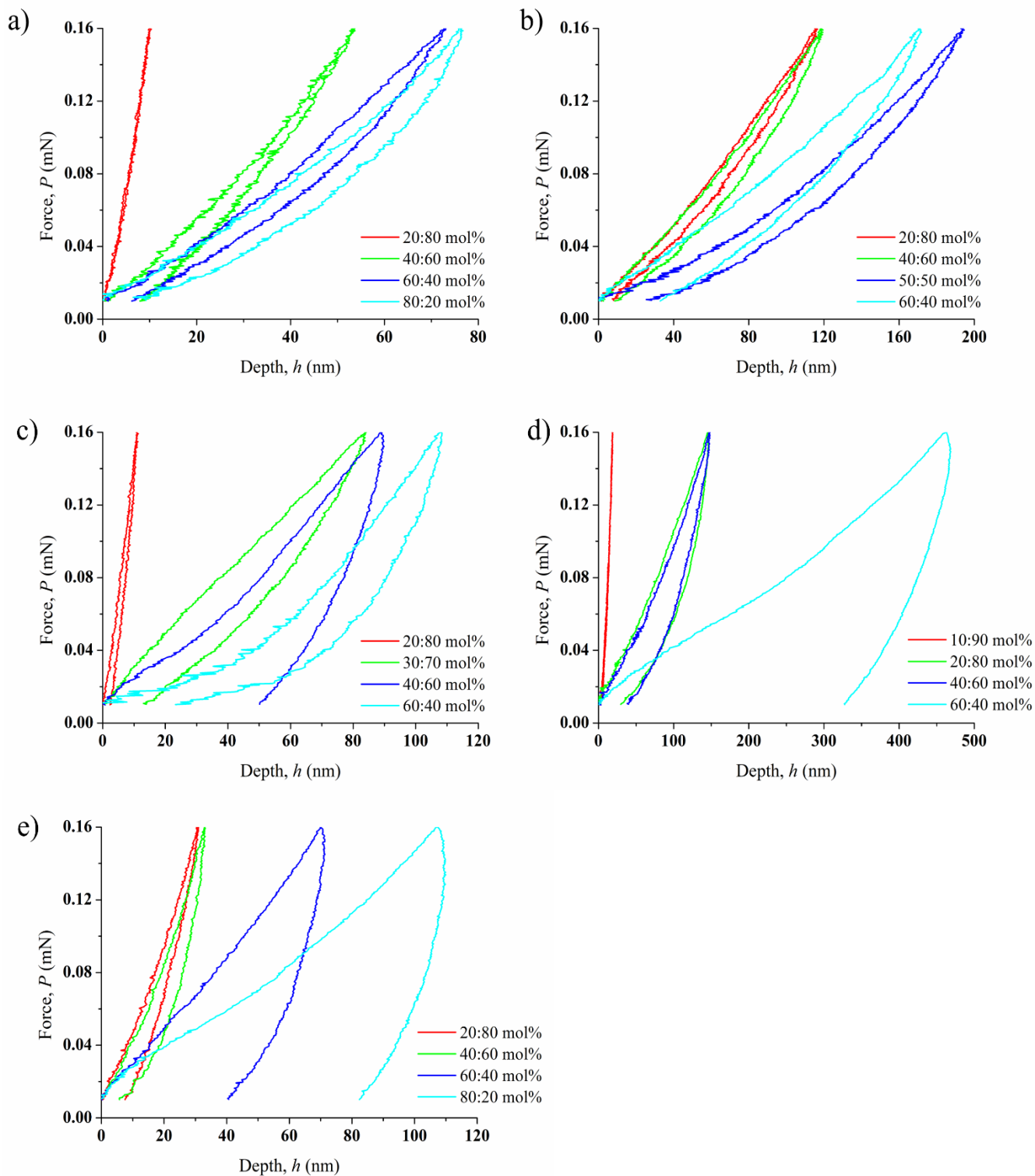


Figure 5.13: Plot of displacement versus load for OIH alkoxy silane coatings considered in this work showing loading-unloading cycle during measurement a) MTES:TEOS b) PrTES:TEOS c) HTES:TEOS d) OTES:TEOS and e) PhTES:TEOS coatings on glass substrate, each plot in several mol% concentrations of precursor molecule.

Results obtained through nano-indentation are presented in **Figure 5.14** showing hardness measurements and Young's moduli which have been calculated for all alkoxy silane coatings considered in this work. The highest hardness values are obtained for coatings having the lowest organic content namely 20:80 mol% for MTES:TEOS, PrTES:TEOS, HTES:TEOS, PhTES:TEOS and 10:90 mol% for OTES:TEOS (see Figure 5.14). An increase in concentration of organic precursor X-Si(OR)₃ leads to a rather sharp decline in the hardness values of the coatings since more organic groups are introduced into the coating which makes for softer, more flexible coatings as shown in Figure 5.13 for which a much greater depth is penetrated with the equivalent force. The Young's Moduli follow the same trends as those of the hardness values where values for E decrease upon increasing the hybrid alkoxy silane precursor concentration.

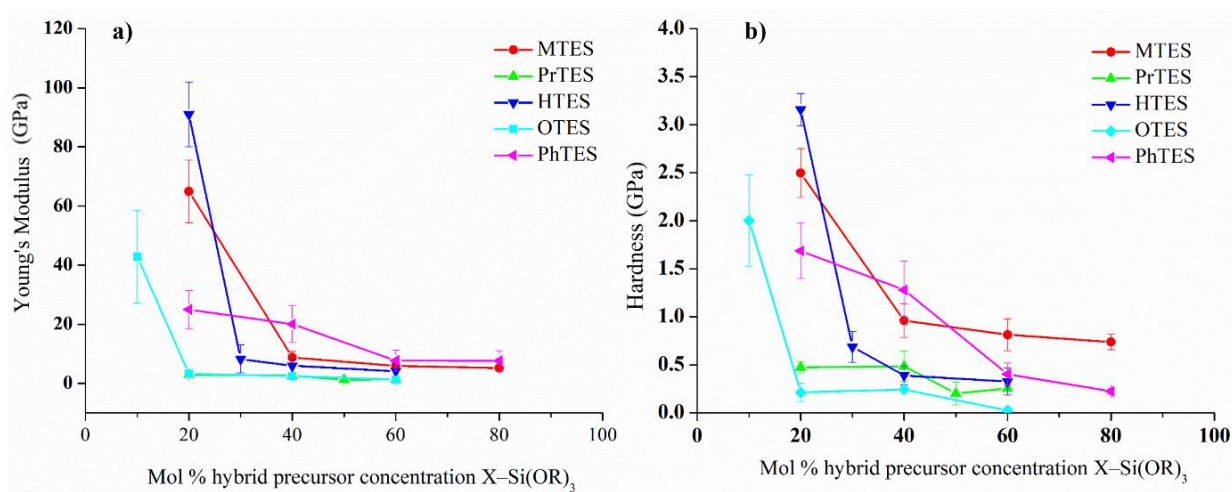


Figure 5.14: a) Calculated Young's Moduli (GPa) and b) Hardness measurements (GPa) for silica-based coatings considered in this work as obtained using nano-indentation.

5.1.3.1.2 Nano-scratch

Nano-scratch testing was carried out so as to study the deformation mechanism of the OIH alkoxy silane coatings considered in this work. The morphology of the scratches are exemplified in **Figure 5.15** which were obtained using an optical microscope for the lowest and highest organic content OIH coatings namely, MTES:TEOS 20:80 mol% having a wt% organics of 4.8% and

OTES:TEOS 80:20 mol% having 55.1% organics. This figure also includes scan distance versus penetration depth plots of these two coated surfaces. The remainder of scan distance versus penetration depth plots can be found in **Appendix D** (CD attached).

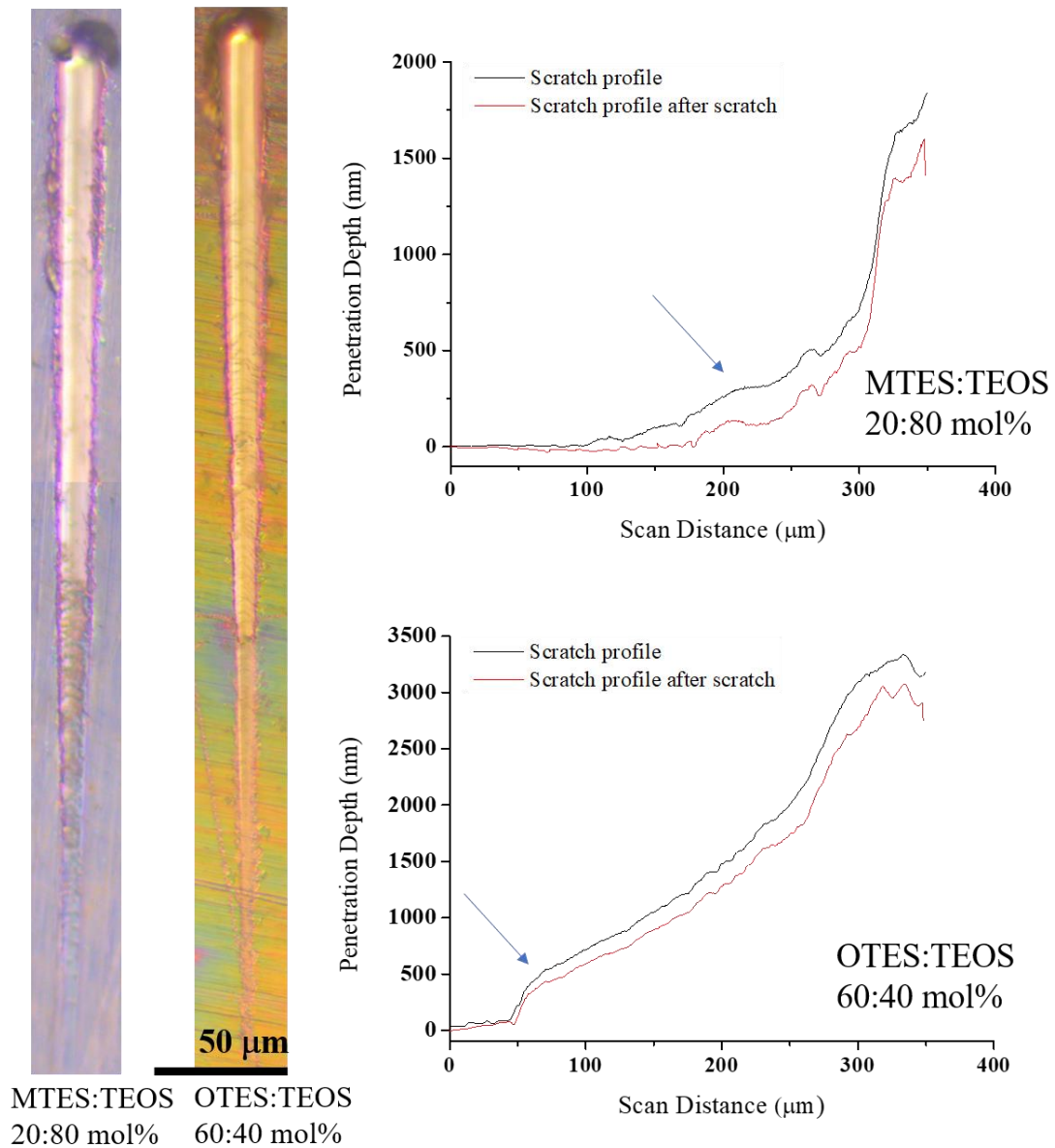


Figure 5.15: Images of scars inflicted onto iron coupons coated with MTES:TEOS 20:80 mol% and OTES:TEOS 60:40 mol%. Plots of scan distance versus penetration depth for during scratch and scratch profile after scratch for two coatings also featured in Figure.

The load at any scan position along the scratch profile is known and therefore critical loads that lead to coating failure can be identified. Three critical loads are typically identified: 1) elastic-to-plastic transition (L_{e-p}) load which is the point at which the scratch profile and the surface profile do not display similar profiles, 2) critical load (L_{c1}) which indicates the first failure seen as the onset of cracking, and 3) the critical load that indicates the beginning of external transverse crack formation (L_{c2}). L_{c1} occurs immediately after L_{e-p} and throughout the scar on both coating and once indenter penetrates through to the metal surface. Coatings appear to be well adhered to the substrate since indenter carries out a clean cut through the material, with only mass accumulation towards the very end of the scratch which features at the higher distance range as a negative depth of the profile after scratch compared to scratch profile. L_{c2} does not apply for these coatings since no localised chipping, adhesive rupture or delamination was witnessed under these set of experimental parameters, which is typical for relatively soft materials due to the organic content of these coatings.

Scars generated through nano-scratch test are rather similar even when considering the most and least organic coatings (Figure 5.15). However, a comparative study can be conducted based on the difference in the distance/force required for indenter to scratch completely through the coating and begin to dig into the metal surface. These locations along the scratch have been estimated visually through the use of microscope and can be seen in the plots where changes in depths are seen, marked with arrows in Figures 5.15 for MTES:TEOS 20:80 mol% and OTES:TEOS 60:40 mol%. The point along which the bare metal begins to be exposed was also confirmed through EDS analysis.

EDS analysis was carried out on scratch of MTES:TEOS 60:40 mol% illustrated in Figure 5.15 to confirm that indenter has indeed reached the surface of the metal as seen through optical microscope and detected as a steeper increase in penetration depth. **Table 5.3** includes the elemental analysis of elements of interest namely: iron, silicon, oxygen and carbon (metal substrate and OIH alkoxy silane coating). Plots of energy (KeV) versus intensity for results obtained in Table 5.3 are shown in **Appendix E** (CD attached). This analysis was conducted along the scratch for which the first reading

was taken at 0 μm i.e. coated region prior to indenter reaching the surface and in increments along the scratch up to 350 μm where the final reading was obtained.

Table 5.3: Elemental analysis along the scratch produced onto MTES:TEOS 60:40 mol% coated iron sample.

Scan Distance (μm)	Fe wt%	Si wt%	O wt%	C wt%
0	69.88 ± 1.4	11.53 ± 0.5	15.46 ± 0.6	3.12 ± 0.6
30	70.66 ± 1.4	11.23 ± 0.4	14.91 ± 0.6	3.20 ± 0.6
70	71.49 ± 1.4	11.00 ± 0.4	14.96 ± 0.6	2.54 ± 0.5
110	70.07 ± 1.4	11.46 ± 0.5	16.08 ± 0.6	2.39 ± 0.5
150	77.58 ± 1.5	8.29 ± 0.3	12.21 ± 0.5	1.92 ± 0.4
190	88.14 ± 1.8	3.57 ± 0.7	6.97 ± 0.3	1.31 ± 0.3
230	87.41 ± 1.7	3.77 ± 0.7	7.28 ± 0.3	1.55 ± 0.3
270	94.79 ± 1.9	0.18 ± 0.2	3.71 ± 0.7	1.32 ± 0.3
310	95.38 ± 1.9	0.42 ± 0.4	3.19 ± 0.6	1.02 ± 0.2
350	95.06 ± 1.9	0.29 ± 0.2	3.39 ± 0.7	1.26 ± 0.3

At 0 μm , Fe wt% is already the main element (69.88 %, Table 5.3) because the coatings are thin and penetrated to some extent with X-rays, thus detecting the underlying metal. As expected, the initial reading is high in Si, O and C elements since indenter has not yet disturbed the coating (Fe = 69.88%, Si = 11.53%, O = 15.46%), whereas at the end of the scratch, a higher Fe content (Fe = 95.06%, Si = 0.29%, O = 3.39%) was recorded since it is evident from microscopic observation that indenter has penetrated not only through the coating but is now ploughing through the metal. At 150 μm there is a significant change in wt % of elements: sharp increase in Fe and a decrease in Si, O and C (Fe content at 150 nm = 77.58 % and at 190 nm = 88.14 %, Si content at 150 nm = 8.29 % and at 190 nm = 3.57 %). This confirms optical microscopy observations of Figure 5.15 for MTES:TEOS 60:40 mol% coating and also indicates that the indenter has reached the underlying metal surface at a distance of 190 nm in accordance with the marked distance (arrow in Figure 5.15) of the scan distance versus penetration depth plot for MTES:TEOS 60:40 mol%.

Figure 5.16 presents the average loads from the beginning of the scratch at which point the indenter reaches the underlying metal surface for all coatings studied. A clear trend is noticeable for all five types of OIH alkoxy silane coatings where the force decreases as the XTES mol% is increased. For instance, metal substrate was reached at a force of 36.7 ± 8.0 mN for OTES:TEOS 10:90 mol% coating whereas indenter reached metal surface at a force of 7.0 ± 8.8 mN along the OTES:TEOS 60:40 mol% surface. This observation also applies for XTES= MTES, PrTES, HTES and PhTES coatings.

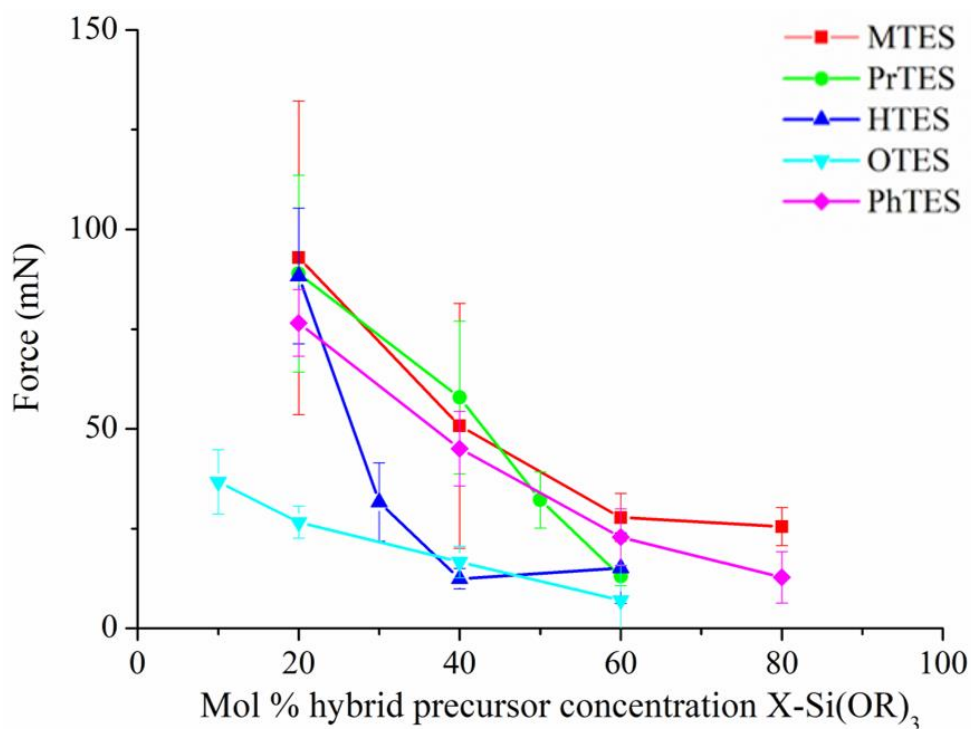


Figure 5.16: Plot of the average loads from the beginning of the scratch at which point the indenter reaches the underlying metal surface for all silica coatings studied.

5.1.3.2 Pull-out test for the study of adhesion of OIH alkoxy silane coatings

The pull-out test was carried out by applying a tensile force on the coating surface via a dolly, held together using an epoxy adhesive. **Figure 5.17** shows images of surface of coupons coated with all OIH alkoxy silane coatings considered in this work following pull-out test. In some cases, adhesive was left behind on the coupon exemplified through the PrTES;TEOS images, fully detached from

the surface of the coated coupon such as PhTES:TEOS 80:20 mol% ,or partially detached from the surface of the coupon as observed with PhTES:TEOS 20:80 mol%.

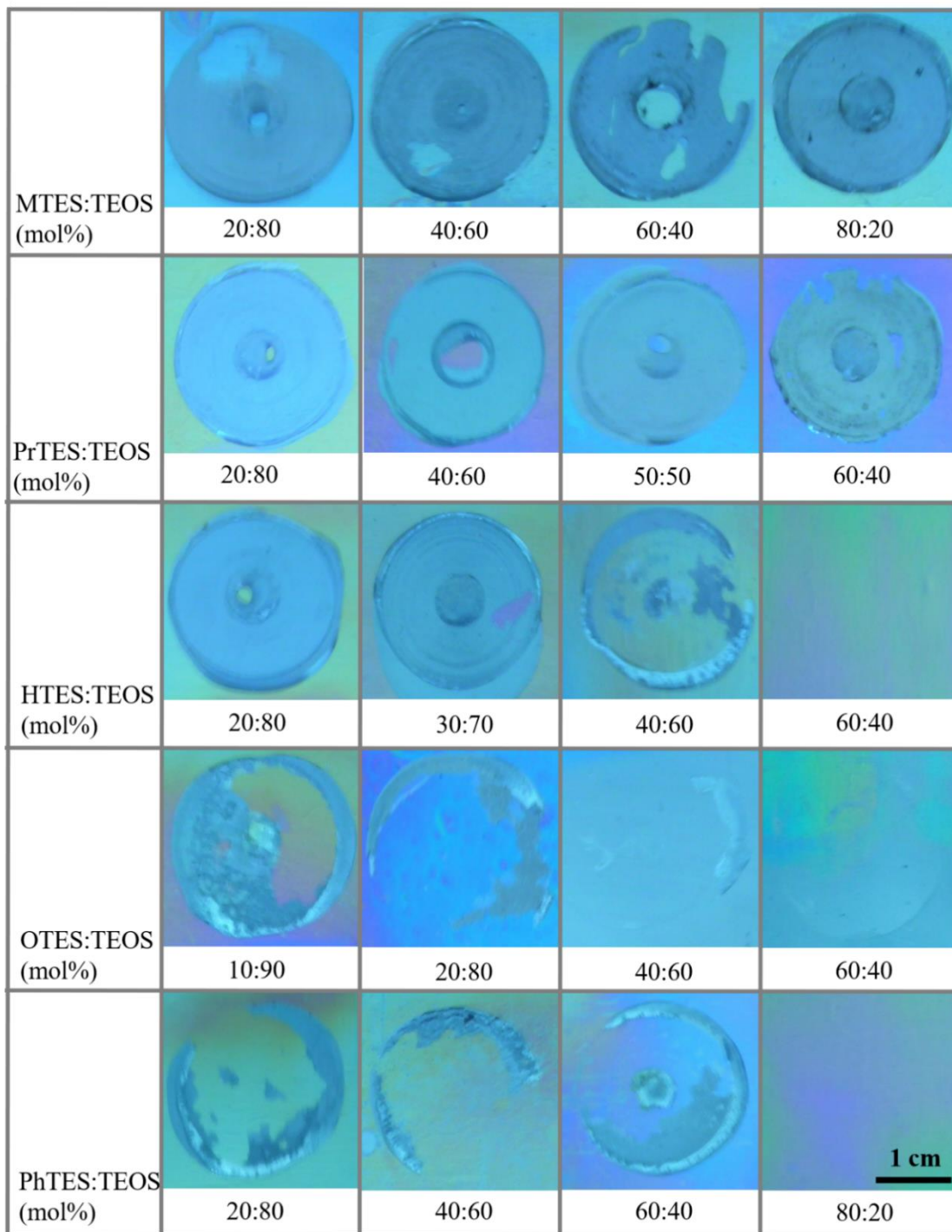


Figure 5.17: Images of coated coupons after pull-out testing where coatings have remained completely intact in all cases. Dolly was pulled away from each of the coated coupons where adhesive was left behind on the coupon (as seen in PrTES;TEOS coatings), fully detached from the surface of the coated coupon (such as PhTES:TEOS 80:20 mol%) or partially detached from the surface of the coupon (such as PhTES:TEOS 20:80 mol%).

Plots of displacement versus load for all alkoxy silane coatings considered in this work are presented in **Appendix F** (CD attached). **Figure 5.18** illustrates the force measured at the point of detachment of dolly from the coated coupon as obtained from plots in Appendix F. As specified in the methodology section, epoxy adhesive was used since it proved to withstand the highest tensile force, thus being the best adhered to the tested coatings. This figure also includes bare metal which produced the highest detachment force.

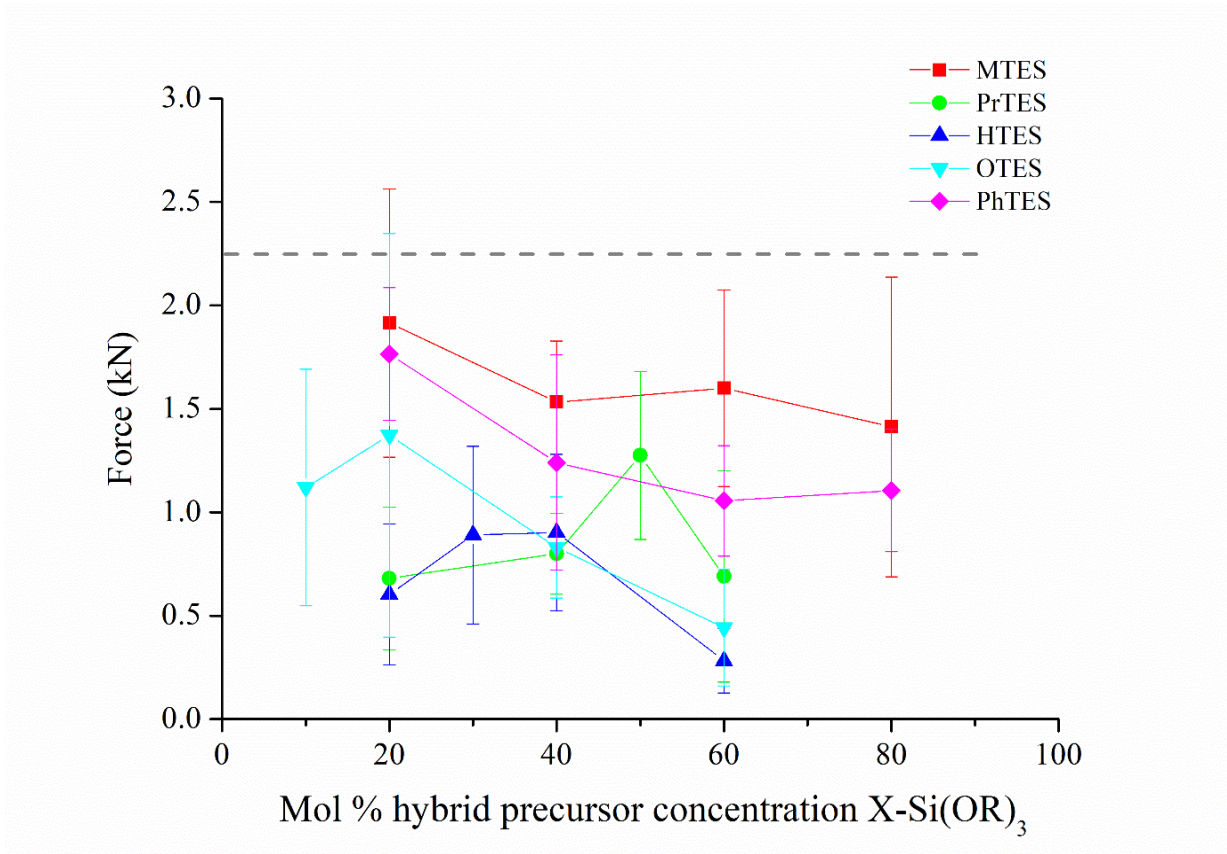


Figure 5.18: Plot of pull-out force required to detach the dolly from the coated coupons.

5.1.4 Electrochemical Evaluation Results

Electrochemical testing was carried out on double coated clean iron surfaces and consists of Electrochemical Impedance Spectroscopy (EIS) and Potentiodynamic scan. **Figures 5.19-5.23** show the Bode, Nyquist and potentiodynamic results obtained for MTES, PrTES, HTES, OTES and PhTES coatings respectively at various X-Si(OR)₃:TEOS ratios. All coatings offer, at least to some extent, corrosion protection which can be immediately seen through the lower frequency range of the Bode Impedance plots (Figure 5.19-23 (a)) for which the impedance modulus is higher for all coated specimens compared to the bare specimen. This observation is most notable in the lower frequencies of the plot. However, the significant improvement in corrosion protection can be observed best through the Nyquist plot where widest arc is obtained showing highest Impedance by 60:40 mol% MTES:TEOS in Figure 5.19 (c), 50:50mol% PrTES:TEOS Figure 5.20 (c), 30:70 mol% HTES:TEOS in Figure 5.21 (c), 20:80mol% OTES:TEOS in Figure 5.22 (c) and 40:60 mol% PhTES:TEOS in Figure 5.23 (c). Potentiodynamic scan (d) in Figures 5.19-5.23 is a plot of log current density (mAcm^{-2}) versus potential (V).

The results complement EIS data in terms of the corrosion current density rather than resistance of the coating, where a shift to a more positive corrosion potential is observed (for example, Figure 5.19 MTES:TEOS 20:80 mol% \approx -500 mV and 60:40 mol% \approx -450 mV) together with an observed drop in current signifying a coating that is more resistant to the voltage applied. Increase in impedance of coating leads to an equal decrease in I_{corr} in potentiodynamic plot ($V=IR$): taking MTES:TEOS 60:40 mol% versus bare polished metal plot where a two order of magnitude improvement in Impedance is observed through the Bode Impedance and Nyquist plots (Figure 5.19 (a) and (c)) together with a two order of magnitude decrease in corrosion current density in Potentiodynamic plot (Figure 5.19 (d)). Impedance phase angle plots Figures 5.19-23 (b) display a two-phase system appearing through two drops in phase angle versus single drop for bare metal. Two phase system does not typically show up in the Nyquist results obtained in Figure 5.19-23 except for Figure 5.20 (c) seen as two semicircles rather than as a single arc.

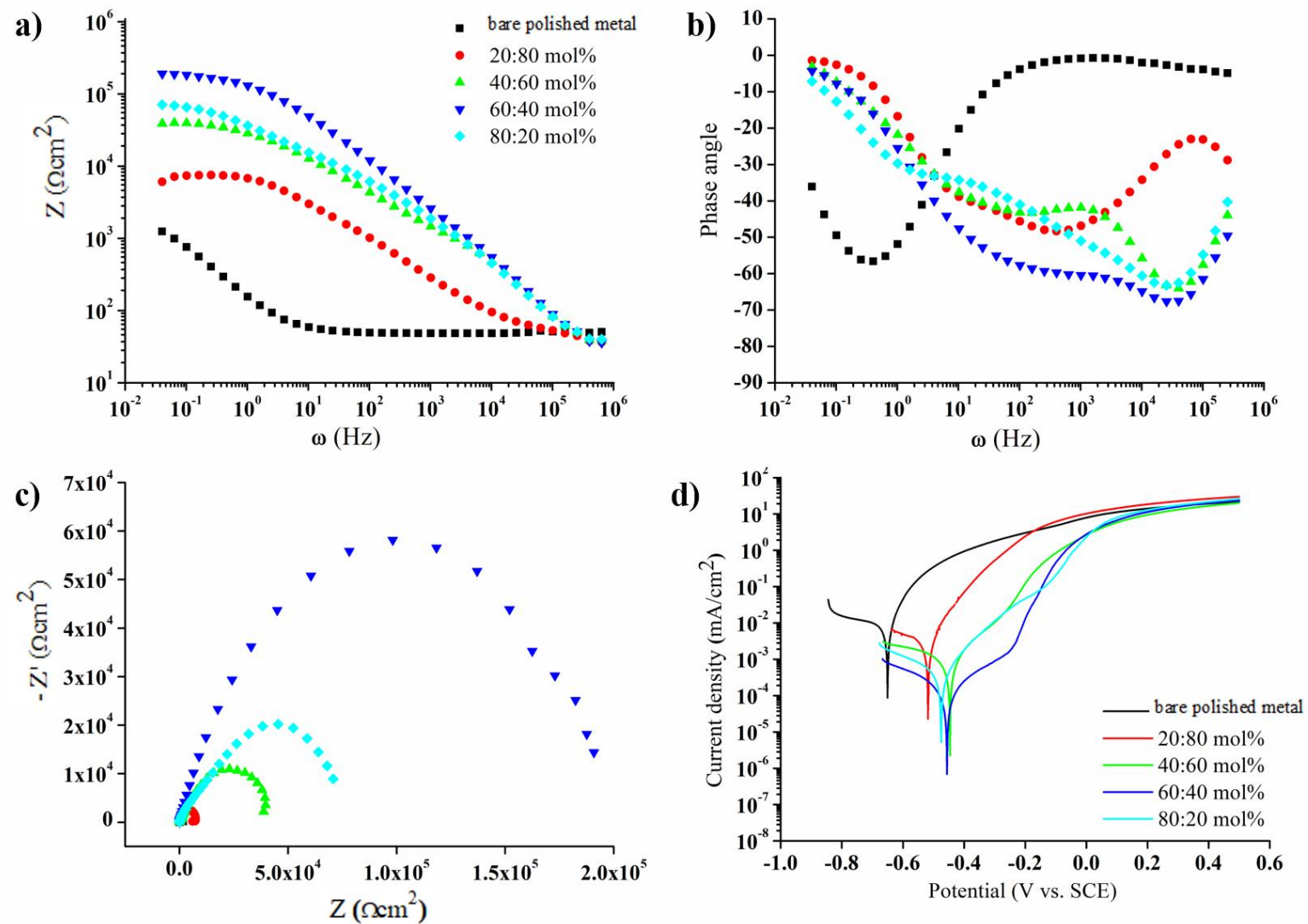


Figure 5.19: a) Bode impedance b) Bode phase angle c) Nyquist and d) Potentiodynamic plots for MTES:TEOS double coatings. The data for bare polished metal is not visually perceivable in Nyquist plot as it is negligible compared to coated coupon data.

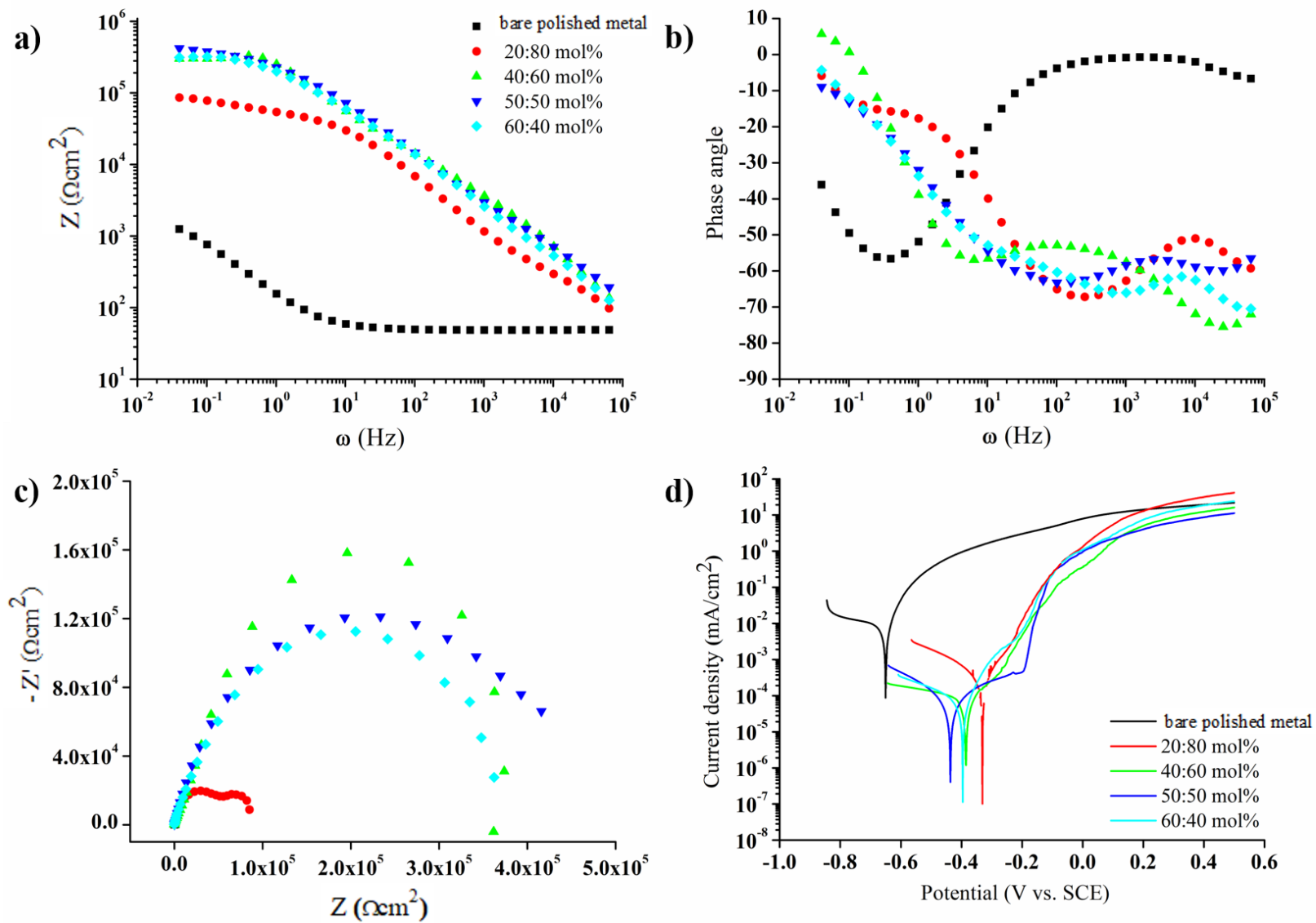


Figure 5.20: a) Bode impedance b) Bode phase angle c) Nyquist and d) Potentiodynamic plots for PrTES:TEOS double coatings. Bare polished metal data is included for comparative purposes.

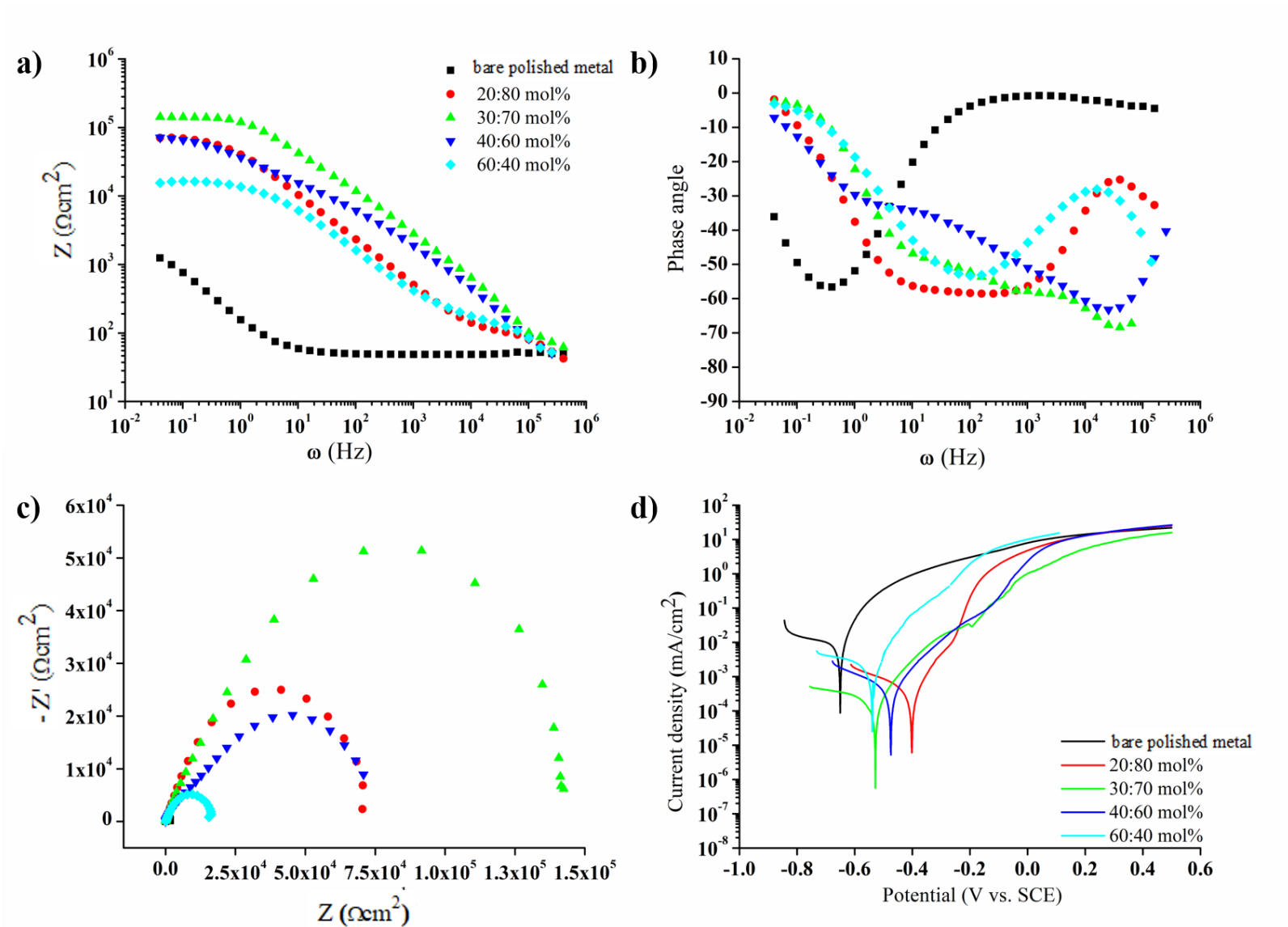


Figure 5.21: a) Bode impedance b) Bode phase angle c) Nyquist and d) Potentiodynamic plots for HTES:TEOS double coatings. Bare polished metal data is included for comparative purposes.

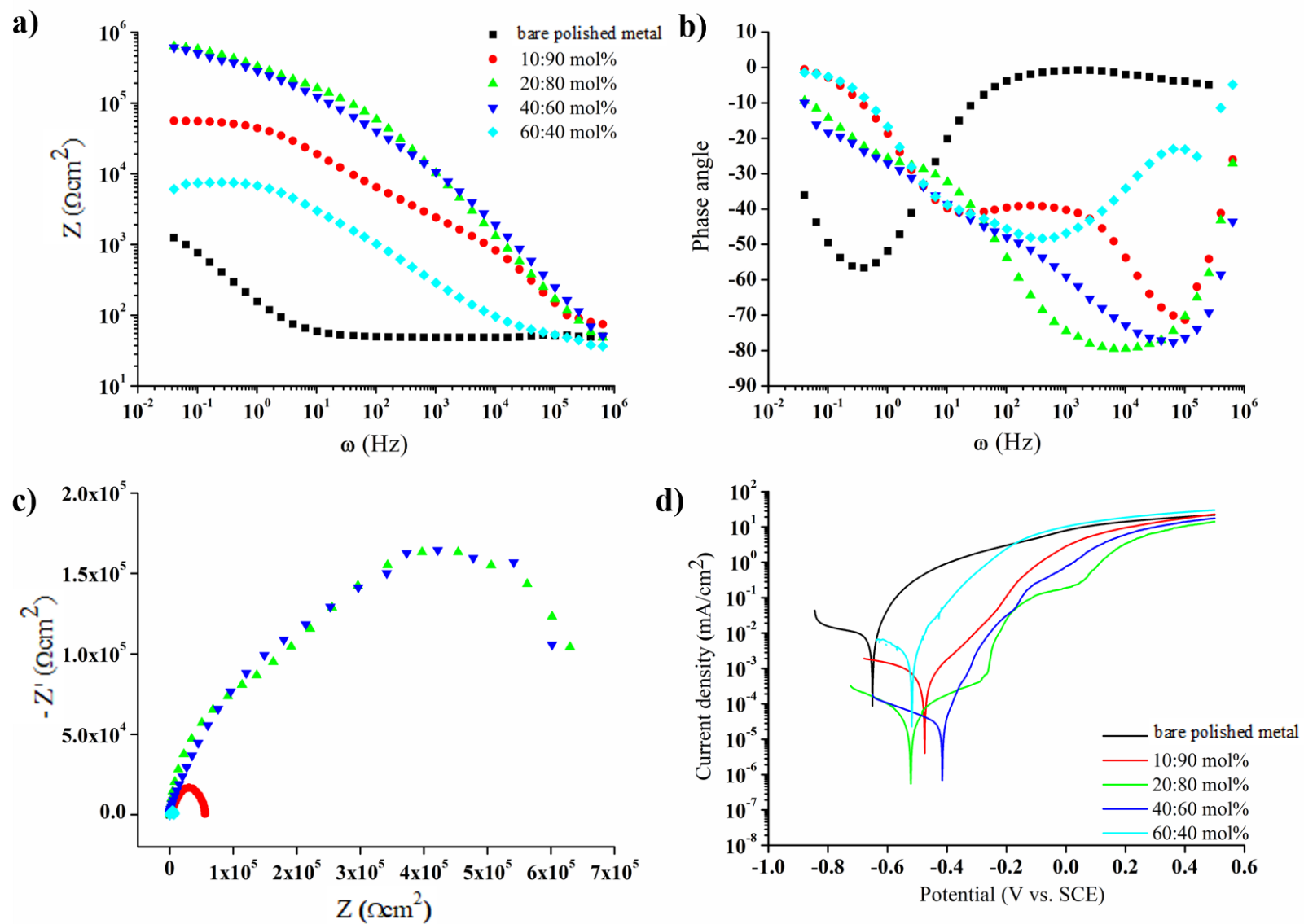


Figure 5.22: a) Bode impedance b) Bode phase angle c) Nyquist and d) Potentiodynamic plots for OTES:TEOS double coatings. Bare polished metal data is included for comparative purposes.

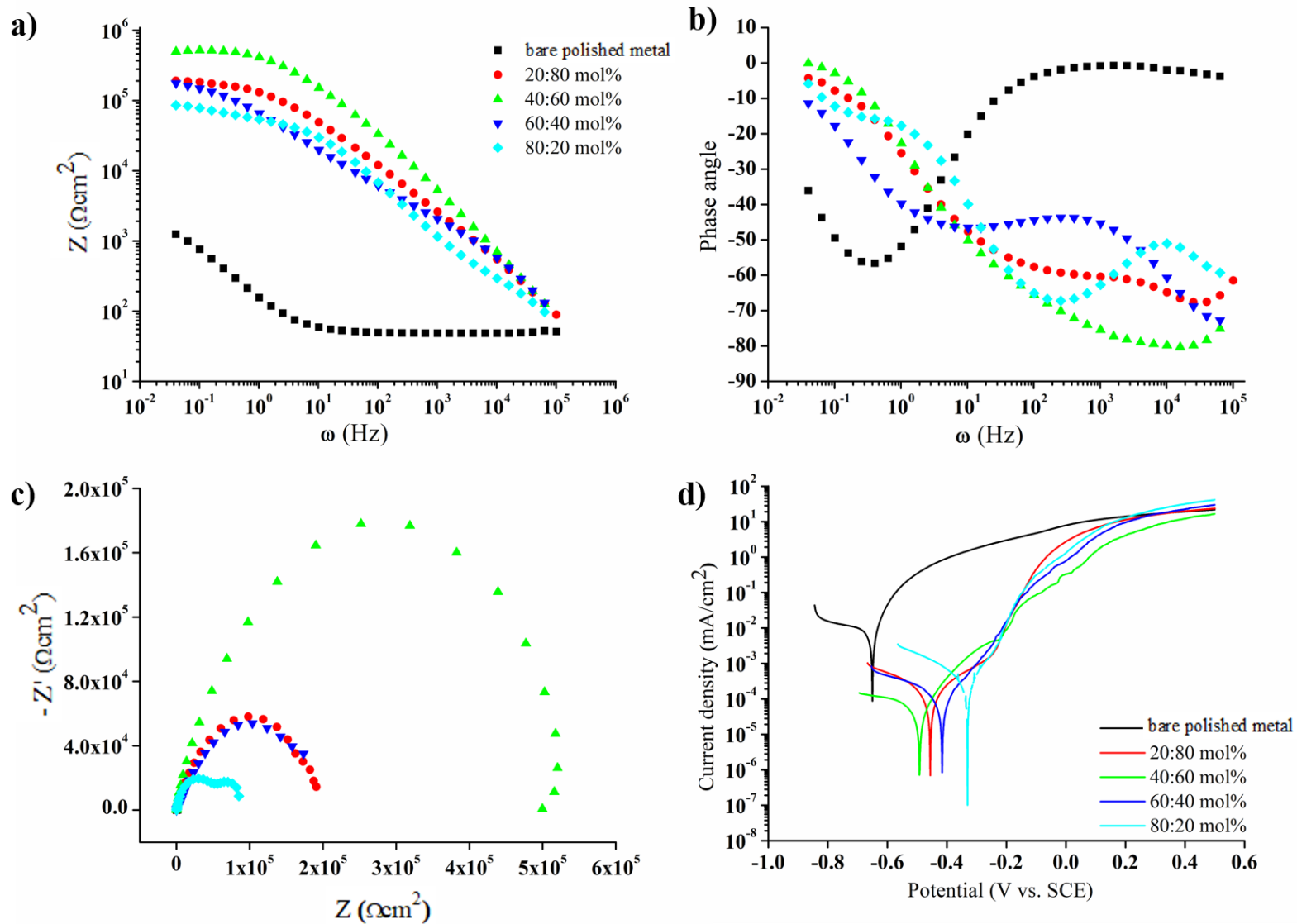


Figure 5.23: a) Bode impedance b) Bode phase angle c) Nyquist and d) Potentiodynamic plots for PhTES:TEOS double coatings. Bare polished metal data is included for comparative purposes.

EIS data was modelled using EEC 1 in Figure 4.5 due to two time constant system appearing in Bode phase angle plots for coated systems of Figures 5.19-23 (c) where two time constant system shown through two drops in phase angle versus single drop for bare metal (modelled using EEC 2 of Figure 4.5). Parameters obtained through modelling of the raw data are shown in **Table 5.4** for the MTES:TEOS series of coatings. These parameters aid the discussion of outputted results since a more accurate analysis of the data can be achieved and a comparative study can be drawn with confidence. Modelling using EEC 1 and 2 (Figure 4.5) carried out lead to low values in goodness of fit (GOF) as presented in Table 5.4 which indicates suitability of these circuits for modelling of EIS data obtained.

Table 5.4: EEC parameters for MTES:TEOS coatings where R_{sol} = uncompensated solution resistance, R_{po} = pore resistance of coating, CPE_c = constant phase element of coating featuring the exponent α_c and Y_c of CPE_c , R_t = charge transfer resistance and CPE_{dl} = constant phase element of the double layer formed at the metal-coating interface featuring the exponent α_{dl} and Y_c of CPE_{dl} and goodness of fit (GOF).

	R_{sol} (Ω cm^2)	R_{po} (Ω cm^2)	CPE_c		R_t (Ω cm^2)	CPE_{dl}		GOF
			Y_c (Ω^{-1} $cm^{-2}s^\alpha$)	α_c		Y_{dl} (Ω^{-1} $cm^{-2}s^\alpha$)	α_{dl}	
Bare polished metal	59.91 ± 8.65	-	-	-	1.15×10^3 $\pm 1.29 \times 10^2$	1.05×10^{-4} $\pm 2.63 \times 10^{-5}$	0.76 ± 0.04	1.37×10^{-3} $\pm 2.60 \times 10^{-4}$
20 80	32.96 ± 9.89	2.54×10^1 $\pm 6.35 \times 10^0$	3.43×10^{-8} $\pm 4.11 \times 10^{-9}$	1.00 ± 0.12	7.87×10^3 $\pm 9.44 \times 10^2$	1.79×10^{-5} $\pm 2.15 \times 10^{-6}$	0.61 ± 0.07	6.48×10^{-3} $\pm 7.78 \times 10^{-4}$
40 60	35.14 ± 10.54	7.11×10^2 $\pm 1.78 \times 10^2$	3.65×10^{-8} $\pm 4.38 \times 10^{-9}$	0.96 ± 0.12	4.41×10^4 $\pm 5.29 \times 10^3$	6.00×10^{-6} $\pm 7.20 \times 10^{-7}$	0.57 ± 0.07	1.81×10^{-3} $\pm 2.17 \times 10^{-4}$
60 40	33.66 ± 10.10	5.78×10^2 $\pm 1.44 \times 10^2$	1.97×10^{-8} $\pm 2.37 \times 10^{-9}$	1.00 ± 0.12	2.02×10^5 $\pm 2.42 \times 10^4$	1.15×10^{-6} $\pm 1.38 \times 10^{-7}$	0.64 ± 0.08	1.69×10^{-3} $\pm 2.03 \times 10^{-4}$
80 20	37.73 ± 11.32	1.28×10^2 $\pm 3.21 \times 10^1$	2.17×10^{-8} $\pm 2.60 \times 10^{-9}$	1.00 ± 0.12	9.77×10^4 $\pm 1.17 \times 10^4$	7.93×10^{-6} $\pm 9.52 \times 10^{-7}$	0.46 ± 0.06	3.02×10^{-3} $\pm 3.62 \times 10^{-4}$

It can be qualitatively concluded, from the Bode and Nyquist plots for MTES:TEOS coatings (Figure 5.19), that as the concentration of hybrid precursor is increased, the coatings become more protective up to a point where the maximum protection is offered by 60:40 mol% MTES:TEOS coatings. Corrosion protection appears to degrade when the MTES concentration is increased further i.e. up to 80:20 mol% MTES:TEOS. This observation is quantitatively manifested through EEC parameters modelled and presented in Table 5.4. The charge transfer resistance (R_t) was found to be $2.02 \times 10^5 \Omega \text{cm}^2$ for 60:40 mol% MTES:TEOS which is approximately 2 orders of magnitude higher than that measured for bare metal $\sim 1.50 \times 10^3 \Omega \text{cm}^2$. On the contrary, values for Y_{dl} will decrease when a coating is applied to the bare metal ($Y_{dl} \text{ bare metal} = 1.45 \times 10^{-4} \Omega^{-1} \text{cm}^{-2} \text{s}^\alpha$ whereas for MTES:TEOS coated metal $Y_{dl} = 1.15 \times 10^{-6} \Omega^{-1} \text{cm}^{-2} \text{s}^\alpha$). Similarly, R_{po} and Y_c will follow the same trend where R_{po} will increase in value and Y_c will decrease with more protective coatings. Additionally, R_{po} is typically $1/10^{\text{th}}$ the value of R_t , has a tendency to shift significantly within repeatable runs, resulting in high standard deviation.

The total Impedance ($Z_{tot} = R_t + R_{po} + R_{sol}$ at the low frequency range) for all coatings investigated in this work is compiled in **Figure 5.24** (a) which also features the calculated corrosion current densities from the potentiodynamic scans of Figures 5.19-5.23. A similar trend in corrosion behaviour for all five X-Si(OR)₃:TEOS hybrid systems is evident : Z_{tot} increases with an increase in the hybrid precursor concentration until it reaches a maximum corrosion protection at a specific concentration. A further increase in the hybrid precursor concentration beyond this point leads to a decrease in the coating resistance and hence a deterioration of the anti-corrosion properties offered by the coating. Potentiodynamic results (Figure 5.24 (b)) follow up on trends observed in EIS in terms of the corrosion current density rather than resistance of the coating.

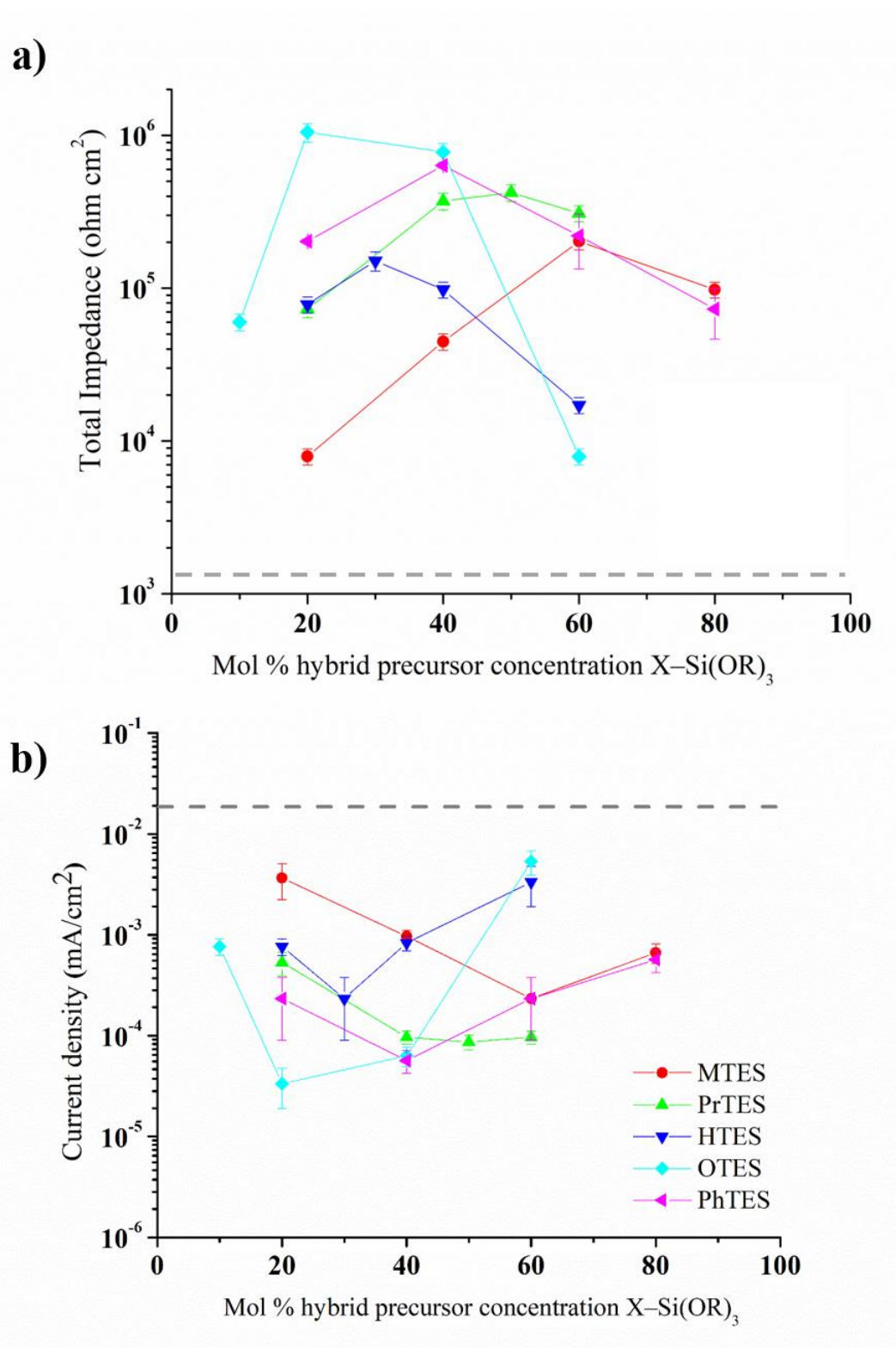


Figure 5.24: Plot showing comparison of a) Total Impedance (Z_{tot}) and b) corrosion current density (I_{corr}) for the five types of OIH silane coatings. Bare polished metal featured as grey dotted line.

Although the coatings investigated provide significant corrosion protection, these thin coatings are expected to fail at some point in time during the potentiodynamic voltage sweep where water penetrates the coating and reaches the surface of the metal thus initiating corrosion processes. An optical microscope was used to observe the surface of the tested specimens following PD scans (**Figure 5.25**). Coating failure occurs due to the high voltage applied through the potentiodynamic scan and is most notable in areas where pitting has occurred. Pitting occurs in a similar way for all coatings tested where pits are approximately 200 μm in diameter and circular. Figure 5.25 also features the surface of bare metal after electrochemical testing where the effect of the potentiodynamic scan can be visualised as a roughened matt grey area (light reflecting off the exposed grain faces) with deposited corrosion products. For coated surfaces, this even corrosion is prevented and corrosion is only able to occur at failure sites i.e. the eventual coating failure by water permeation through the coating leads to the formation of water channels (coating's pores). Therefore, corrosion will occur at the site of these pores leading to the formation of pits (Figure 5.25 a-e).

Figure 5.25 features pits pertaining to the most protective coating for each of the five organic groups i.e. MTES:TEOS in a 60:40 mol% molar ratio, PrTES:TEOS 50:50 mol%, HTES:TEOS 30:70 mol%, OTES:TEOS 20:80 mol% and PhTES:TEOS in a 40:60 mol% molar ratio. For each of these five surfaces, pits appear to be similarly spherical but with a slight variation in size: HTES coatings appear to have the largest pits whereas OTES the smallest which corresponds to electrochemical data where HTES coatings were determined to be the least protective, therefore give rise to larger pits. On the contrary, OTES coatings being the most protective give rise to the smallest pits. Interestingly, pitting is spherical and does not spread beyond the pit outline indicating good adhesion of coating even when coating begins to form pores. Pitting size for all other less protective coatings is similar; however, pits are more frequent.

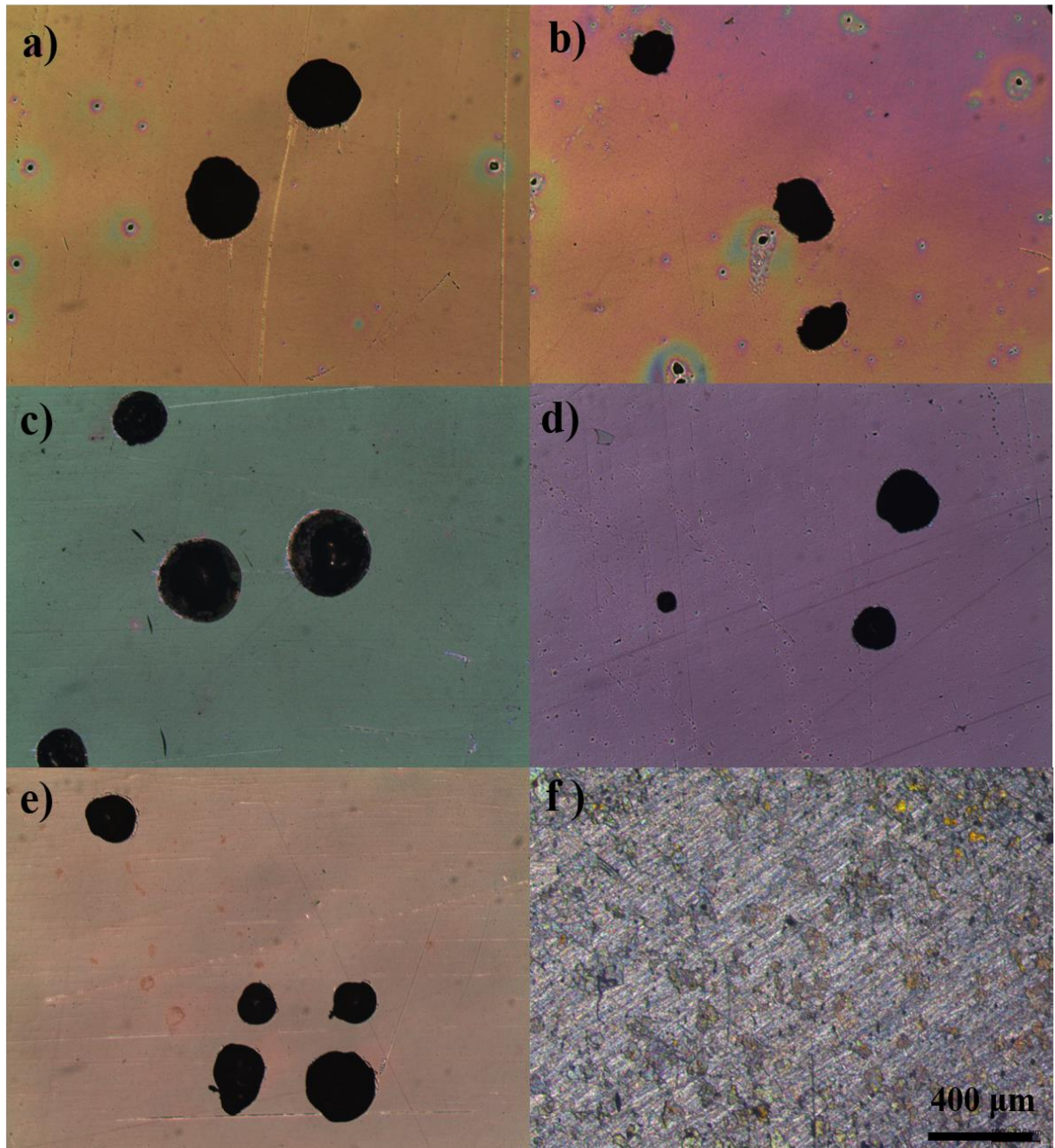


Figure 5.25: Optical micrograph showing pitting formed on (a) 60:40 mol% MTES:TEOS, (b) 50:50 mol% PrTES:TEOS, (c) 30:70 mol% HTES:TEOS, (d) 20:80 mol% OTES:TEOS, (e) 40:60 mol% PhTES:TEOS coated coupons and (f) uncoated (bare) coupon following the potentiodynamic polarisation test at $\times 5$ magnification.

5.2 The corroded iron surface

5.2.1 Iron microstructure

The microstructure of iron utilised in this work is shown in **Figure 5.26**. The etching process revealed a ferritic microstructure as expected for this material.

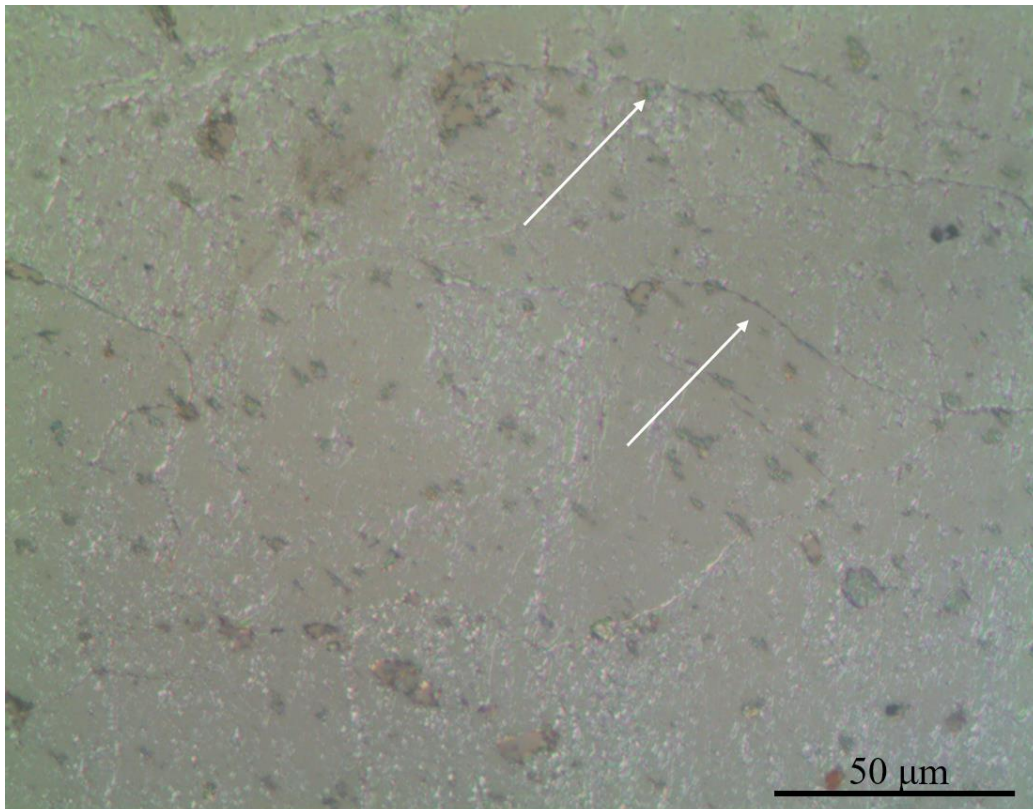


Figure 5.26: Microstructure of iron substrate revealed using Nital solution at a mag x50 taken using a metallographic microscope. Arrows indicate faint grain boundaries.

5.2.2 Clean and corroded iron surface morphology

Figure 5.27 illustrates the surface of coupons that have been polished (a), corroded and left uncleaned with an orange/brown layer of rust (b) and corroded coupons that have been cleaned using Dremel® 3000 Multi-tool followed by gentle manual cleaning using 800 SiC abrasive paper to reveal the underlying even black layer of oxide (c). The scope of applying a cleaning method to corroded coupons is to follow procedure carried out by conservators, the black rust which remains after cleaning is typically aesthetically allowed by conservation practices.

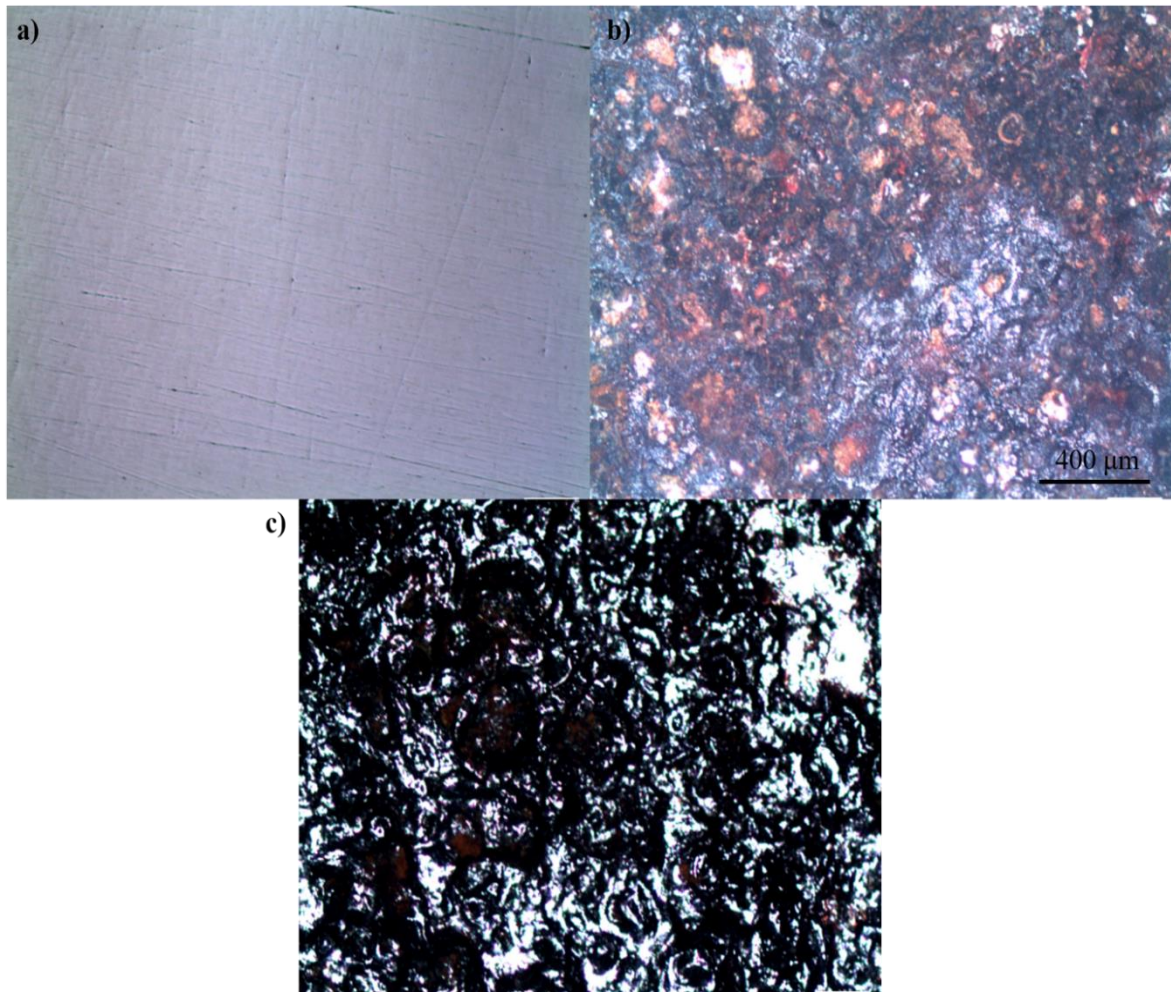


Figure 5.27: Images obtained using stereo microscope using x5 magnification of (a) clean mirror-polished coupon, (b) corroded uncleaned coupon and (c) corroded cleaned coupon.

Figure 5.28 (a) shows cross-sections obtained using SEM through corroded coupons that have been (i) left uncleaned and (ii) after cleaning procedure. Cleaning of corroded surface leads to a remaining black layer of oxide which is more adherent to the surface and difficult to remove. There is an overall decrease in thickness of oxide layer after cleaning process (thickness in (i) $50.23 \pm 5.28 \mu\text{m}$ and (ii) $18.69 \pm 10.87 \mu\text{m}$), the latter layer is present throughout the surface as is also evident in Figure 5.28 (b). The black oxide layer is not uniformly thick due to the build-up of this oxide in some areas more than others (establishment of anodic/cathodic sites). Figure 5.28 (b) shows electron micrographs of clean and uncleaned corroded surfaces where such differences in surface roughness is evident compared to the polished metal surface shown on the bottom of Figures 5.28 (a).

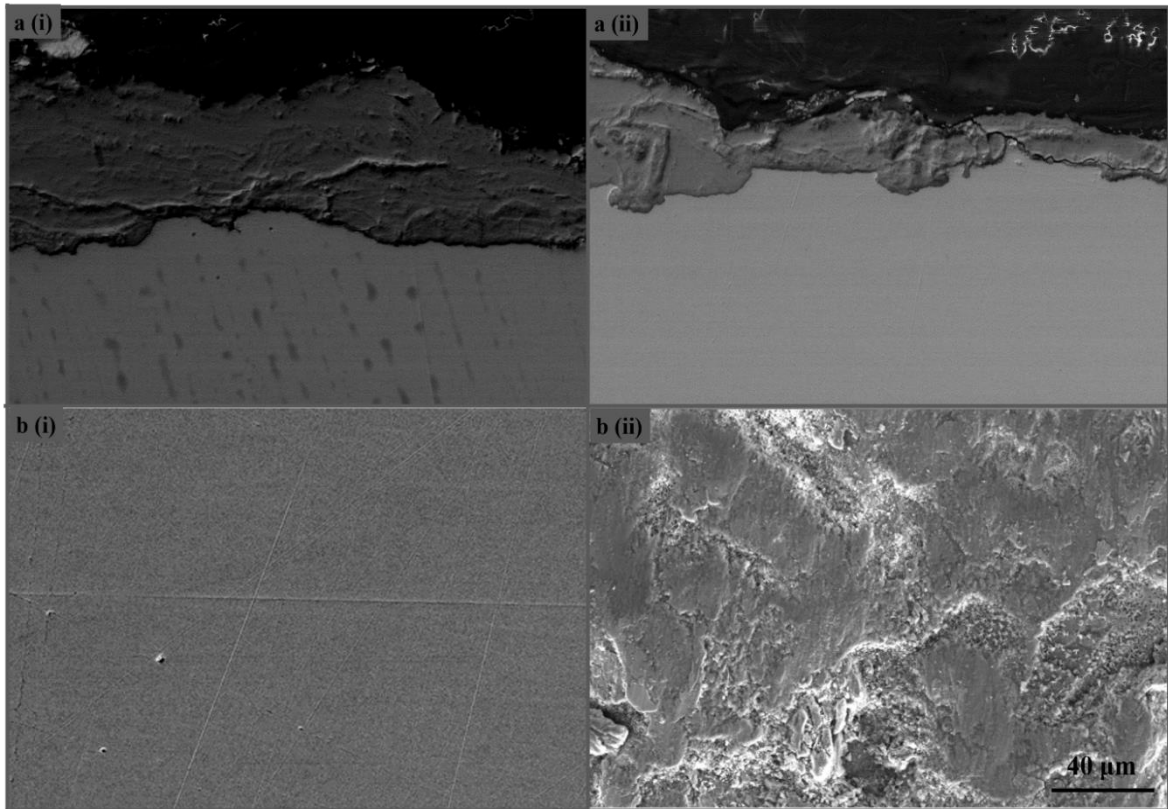


Figure 5.28: Electron micrograph showing a) cross-sections of i) uncleaned and ii) cleaned corroded coupon; b) surface of i) polished and ii) cleaned corroded coupon. All images were taken using x500 magnification.

5.2.3 X-ray Diffraction of iron surface

Figure 5.29 shows diffractograms obtained for polished, uncleaned and cleaned corroded surfaces (shown as black spectrum). Diffractograms for corroded surfaces (Figure 5.29 (b) uncleaned corroded and (c) cleaned corroded) are less even than polished clean surface (Figure 5.29 (a)) due to higher background noise originating from fluorescence of iron oxide emitted when using CuK_α source which in turn results in lower intensity reflection being recorded. The surface crystalline phases of the samples were determined by comparing the X-ray diffraction patterns obtained with those found in the Powder Diffraction Files (red markers). The best fit for the polished surface was obtained with the α -Fe card (00-001-1267), uncleaned corroded iron surface was best represented through the β -Iron (III) oxide card (00-005-0480) whereas the cleaned corroded surface was matched to the magnetite card (01-082-3510).

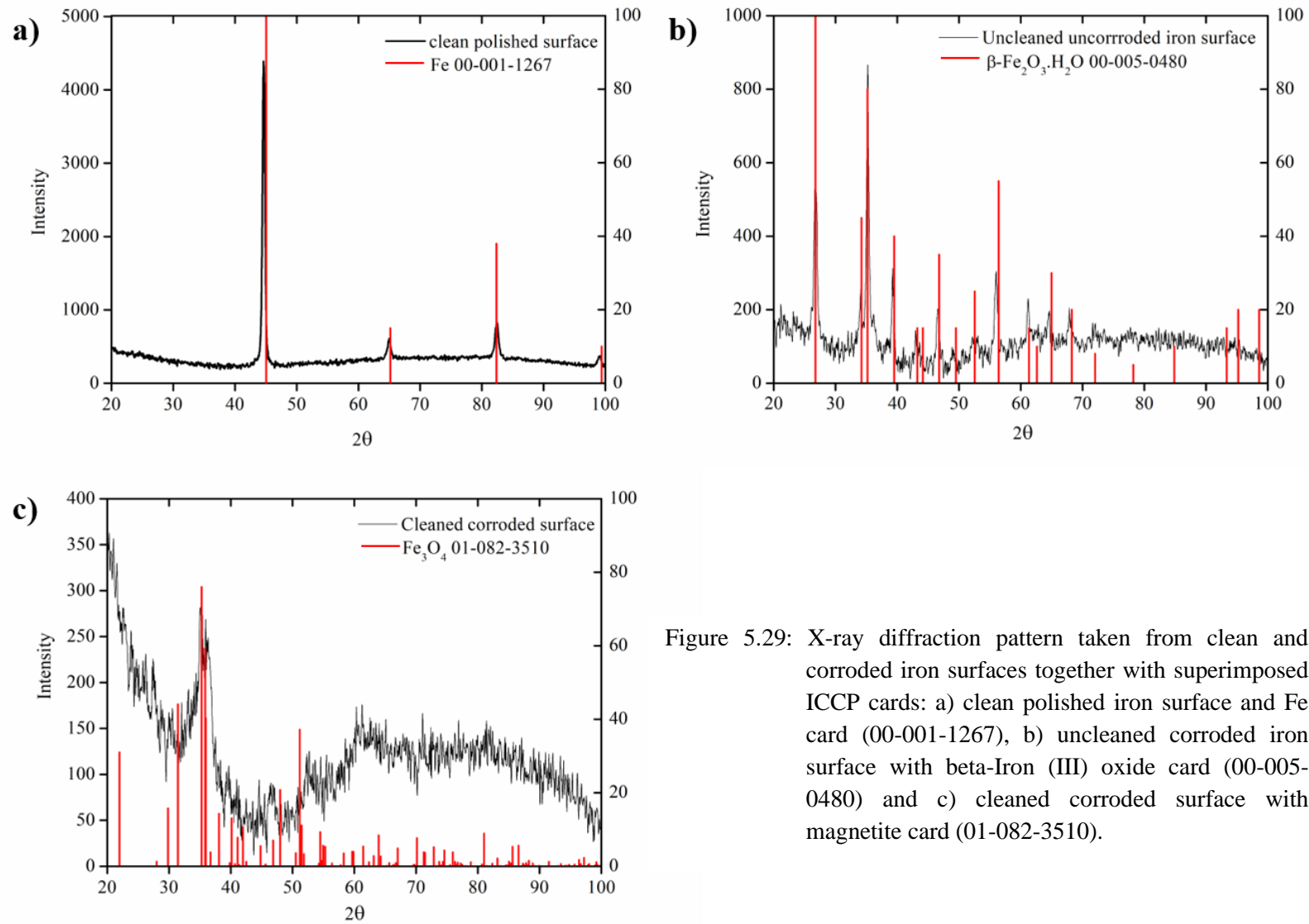


Figure 5.29: X-ray diffraction pattern taken from clean and corroded iron surfaces together with superimposed ICDD cards: a) clean polished iron surface and Fe card (00-001-1267), b) uncleaned corroded iron surface with beta-Iron (III) oxide card (00-005-0480) and c) cleaned corroded surface with magnetite card (01-082-3510).

5.2.4 Electrochemical study on uncoated metal surfaces

Figure 5.30 shows electrochemical data obtained when testing was carried out on a bare iron surface that has been polished (up to 2500 grade grinding paper, followed by mirror finish obtained using 6 nm polycrystalline diamond paste), ground to 180 SiC surface finish, and corroded surface that has been cleaned. Results indicate the effect of surface area on corrosion process: the higher the surface area the lower the resistance metal surface will have to corrosion process seen in the lowering of R_p values (see **Table 5.5**, polished= $1.15 \times 10^3 \pm 1.29 \times 10^2 \Omega \text{ cm}^2$, ground clean metal= $1.03 \times 10^3 \pm 1.46 \times 10^2 \Omega \text{ cm}^2$, corroded-cleaned surface= $1.31 \times 10^2 \pm 2.60 \times 10^1 \Omega \text{ cm}^2$) together with an increase in the Y_{dl} values (polished= $1.05 \times 10^{-4} \pm 2.63 \times 10^{-5} \Omega^{-1} \text{ cm}^{-2} \text{ s}^{\alpha}$, ground clean metal= $6.08 \times 10^{-4} \pm 1.52 \times 10^{-4} \Omega^{-1} \text{ cm}^{-2} \text{ s}^{\alpha}$, corroded-cleaned surface= $2.17 \times 10^{-2} \pm 1.86 \times 10^{-3} \Omega^{-1} \text{ cm}^{-2} \text{ s}^{\alpha}$).

Parameters presented in Table 5.5 were obtained through modelling using EEC 2 (Figure 4.5) since relatively good fits were obtained as shown through low GOF values. Results obtained for polished and ground surface only differ in values in parameters and less so in shape of plots obtained in Figure 5.30; a lower resistance to the corrosion process was obtained with an increase of surface area (less polished substrate). On the other hand, shape of plots obtained for corroded cleaned surface is visibly different from that of the polished and ground surface metal due to the heavy onset of corrosion process on the surface of metal seen as significantly lower impedance in Figure 5.30 (a) (lower frequency range of Bode impedance plot) and Figure 5.30 (c) showing Nyquist plot where the arc for corroded cleaned surface is minute compared to semi-circles pertaining to polished and ground surface. There is also a shift in the minimum phase angle towards a higher frequency (Figure 5.30 (b)) and an increase in I_{corr} seen in PD plot of Figure 5.30 (d) for corroded surface relative to clean surfaces.

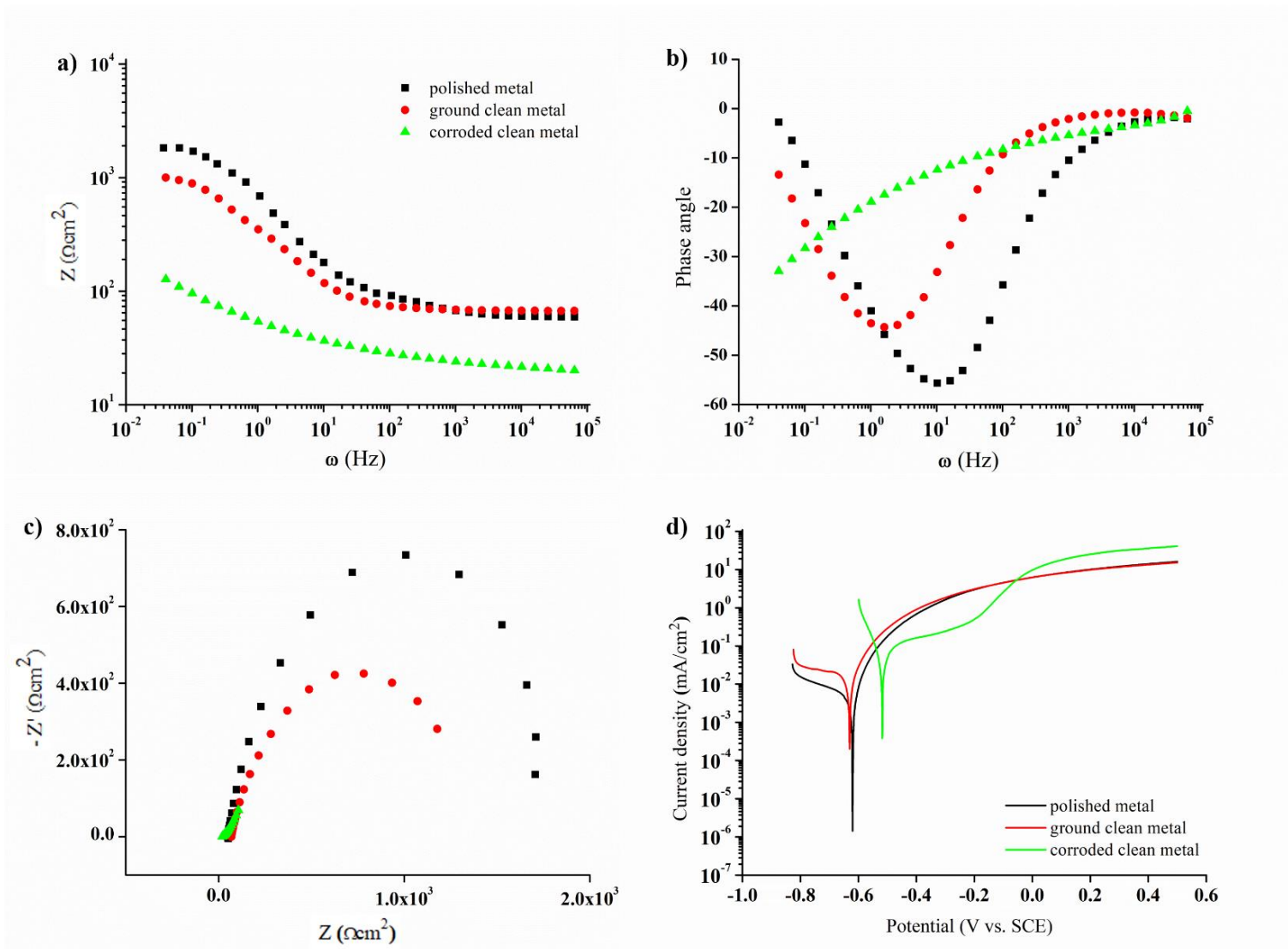


Figure 5.30: a) Bode Impedance b) Bode phase angle c) Nyquist and d) potentiodynamic plots obtained for uncoated polished, ground clean metal and corroded clean metal.

Table 5.5: EIS parameters modelled using EEC 1 and 2 and I_{corr} values for surfaces studied in Figure 5.30.

	R_{sol} (Ω cm^2)	R_t (Ω cm^2)	CPE_{dl}		GOF	I_{corr} ($mAcm^{-2}$)
			Y_{dl} ($\Omega^{-1} cm^{-2}s^\alpha$)	α_{dl}		
Polished surface	59.91 ± 8.65	1.15×10^3 $\pm 1.29 \times 10^2$	1.05×10^{-4} $\pm 2.63 \times 10^{-5}$	0.76 ± 0.04	1.37×10^{-3} $\pm 2.60 \times 10^{-4}$	9.67×10^{-3} $\pm 1.43 \times 10^{-3}$
Ground surface	60.75 ± 6.25	1.03×10^3 $\pm 1.46 \times 10^2$	6.08×10^{-4} $\pm 1.52 \times 10^{-4}$	0.43 ± 0.07	8.62×10^{-4} $\pm 1.64 \times 10^{-4}$	1.33×10^{-2} $\pm 1.43 \times 10^{-3}$
Corroded surface	38.46 ± 9.66	1.31×10^2 $\pm 2.60 \times 10^1$	2.17×10^{-2} $\pm 1.86 \times 10^{-3}$	0.38 ± 0.05	8.42×10^{-5} $\pm 1.60 \times 10^{-5}$	2.33×10^{-1} $\pm 1.43 \times 10^{-1}$

5.2.5 Coated corroded iron surface morphology

Figure 5.31 (a) shows electron micrographs of the surface of cleaned corroded coupons that have been coated with MTES:TEOS 60:40 mol% sols having (i) low and (ii) high silica concentrations (2.5 and 20 % SiO_2). X-ray elemental analysis was carried out to confirm the presence of silica coating on several areas along the coupons. Although the coatings seem to have adhered well to the corroded surfaces, several cracks were observed throughout the surface which is due to the changes in surface topology. However, less cracks were observed to occur when employing 20 % SiO_2 concentration since thicker coatings were confirmed to form as measured from cross-sections shown in Figures 5.31 (b) where 2.5 % SiO_2 coating was measured to be 750.1 ± 62.2 nm and 20 % SiO_2 coating 1536.8 ± 102.6 nm thick.

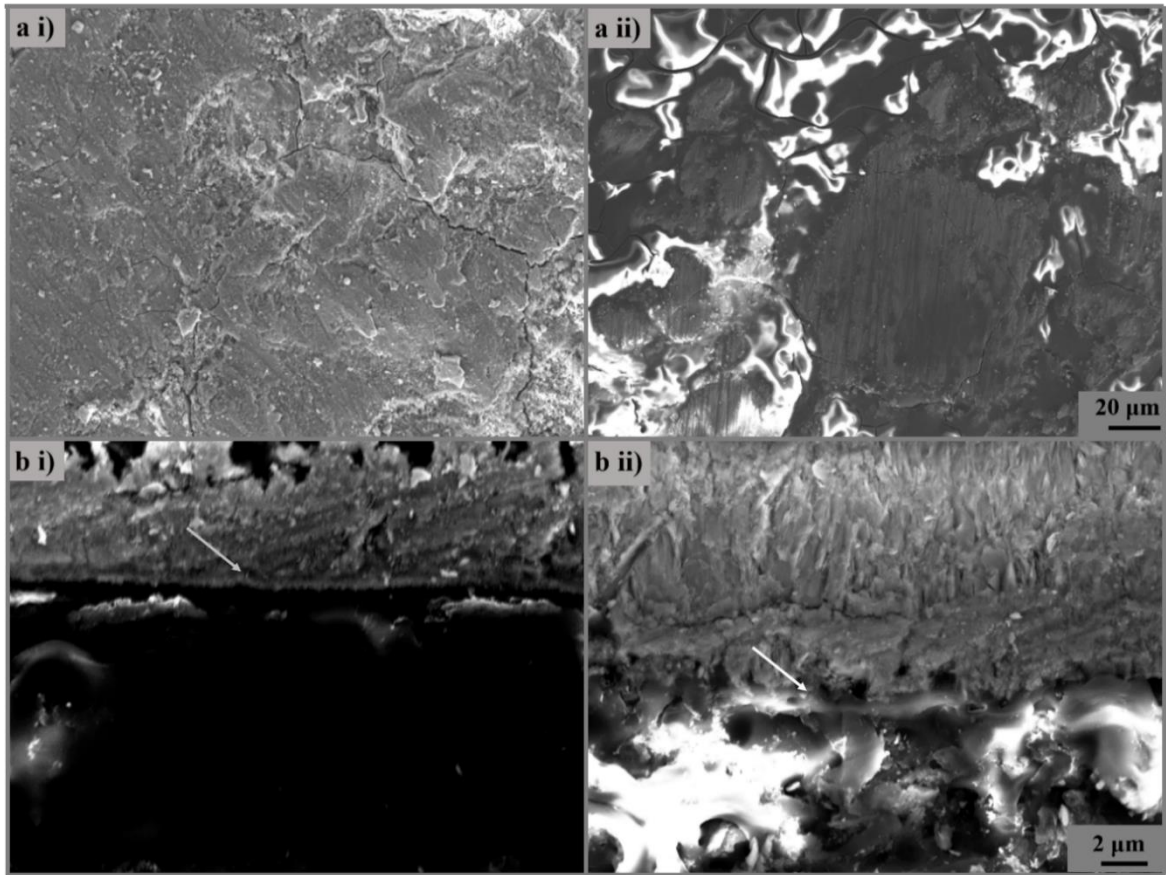


Figure 5.31: Electron micrograph showing (a) corroded-cleaned metal surface that has been coated with MTES:TEOS 60:40 mol% having SiO₂ concentration of (i) 2.5% and (ii) 20% (mag ×500) and (b) cross-section of (i) 2.5% SiO₂ coated coupon and (ii) 20% SiO₂ coated coupon (mag ×10k). Coatings are indicated using arrows.

5.2.6 Surface roughness of un/coated iron surfaces

The absolute roughness values (R_a) for polished, corroded and coated corroded coupons are presented in **Figure 5.32**. Clean bare metal has a negligible roughness value of only 8.0 ± 2.3 nm since it has been polished to an effective mirror finish. As expected, the highest surface roughness was measured for the corroded coupons prior to cleaning at 9618.7 ± 1532.6 nm. The surface roughness decreased significantly, approximately by half to 5640.8 ± 830.8 nm after cleaning. Also included in the Figure are the surface roughness values for clean corroded coupons that have been coated with low and high concentrations of 60:40 mol%. MTES:TEOS. A decrease in surface roughness is measured for clean corroded coupons that have been coated with MTES:TEOS 60:40 mol% for which the lowest roughness value was obtained when using the higher SiO₂ concentration

(20% versus 2.5%). The surface roughness of 20 % and 2.5 % SiO₂ are 2684.1 ± 223.6 nm and 4539.3 ± 598.6 nm respectively.

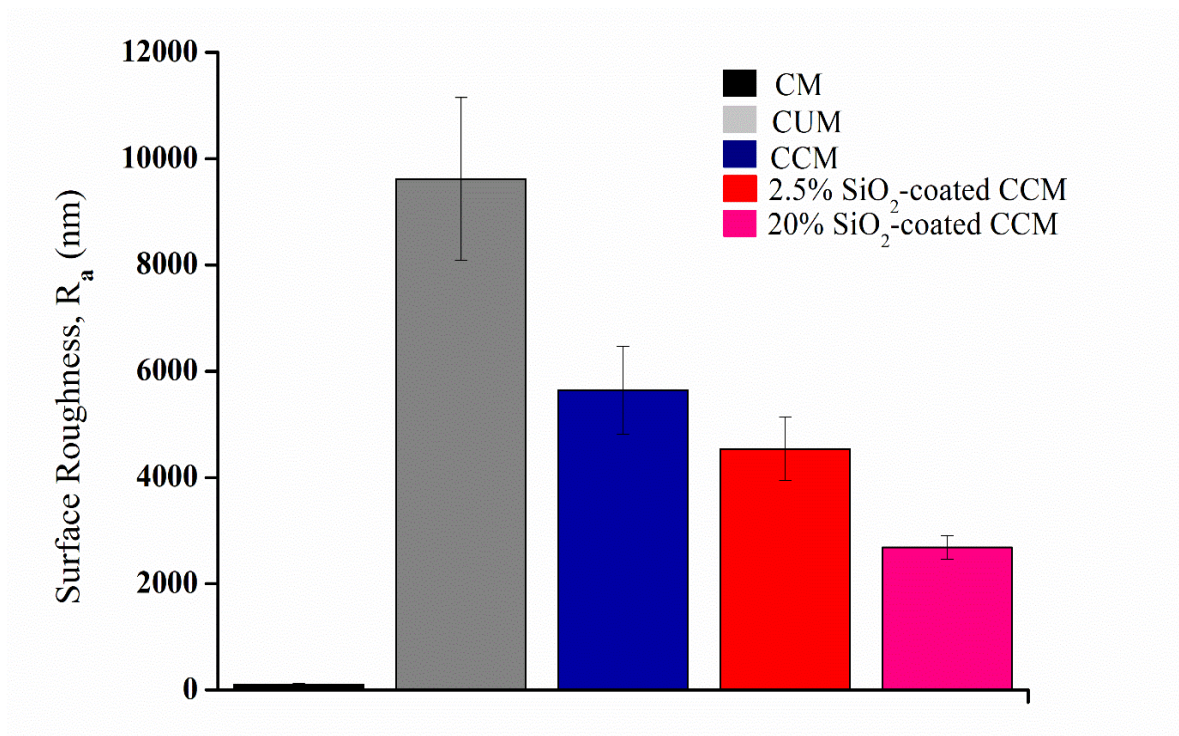


Figure 5.32: Surface roughness plot (R_a (nm)) for several coated and uncoated iron surfaces namely: clean polished metal (CM), corroded uncleaned metal (CUM), corroded-cleaned metal (CCM), 2.5% and 20% SiO₂ MTES:TEOS 60:40 mol%-coated CCM.

5.2.7 MTES and OTES-coated corroded metal surfaces

5.2.7.1 Effect of increasing SiO₂ concentration

The effect of silica concentration for both 60:40 mol% MTES:TEOS and 20:80 mol% OTES:TEOS was investigated as shown through electrochemical plots in **Figure 5.33** and **Figure 5.34** respectively. An initial 2.5% SiO₂ concentration sol was used to coat the corroded coupons as has been done previously to clean iron surfaces (Section 5.1.4). There is only a slight improvement in corrosion protection for MTES:TEOS coatings (Figure 5.33) whereas a more notable improvement was achieved when coating with OTES:TEOS, 2.5% SiO₂ seen as higher impedance obtained in the lower frequency range of Bode plot of Figure 5.34.

Bare and coated corroded metal results of Figures 5.33 and Figure 5.34 were modelled using EEC of Figure 4.5 which differ in shape from coated clean metal data obtained shown through for example, Figure 5.19. The clear two-phase systems shown as two drops in phase angle of Nyquist plot of Figure 5.19 (b) are not as clear in Phase angle plot for coated corroded surface in Figure 5.33 (b) for MTES and Figure 5.34 (b) for OTES coated corroded surfaces. However, the two phases ($R + CPE$) can be distinguished clearly in the Nyquist plot (Figure 5.33 (c)) as two arcs formed. EEC 1 and 2 were deemed suitable for modelling of EIS data obtained in Figure 5.33-5.34 due to good fits obtained using these circuits as shown through very low GOF values presented in **Table 5.6**. Cano *et al* also used EEC 1 to model the coated corroded iron samples and argued that the effect of corrosion products is not visible in the coated samples, where only the response of the coating (R_{po-CPE_c}) and the dissolution of the metal (R_t-CPE_{dl}) can be observed. The EIS response of the corrosion products is concealed by the other processes [170].

There is a general improvement in corrosion protection when increasing the SiO_2 concentration for both MTES (Figure 5.33) and OTES (Figure 5.34) coatings. This can be observed through the higher measured impedance values in Bode (a) and Nyquist (c) plots and decrease in I_{corr} in PD plots (d) upon increasing SiO_2 concentration for both Figures. Much like the results obtained for coatings applied to clean iron surfaces (Table 4.3), there is little improvement when increasing SiO_2 concentration from 2.5% to 5% for MTES and OTES which is reflected in the R_t values obtained and shown in Table 5.6; MTES 2.5% $SiO_2 = 6.18 \times 10^2 \pm 7.41 \times 10^1 \Omega \text{ cm}^2$ and 5% $SiO_2 = 5.33 \times 10^2 \pm 6.39 \times 10^1 \Omega \text{ cm}^2$, OTES 2.5% $SiO_2 = 1.13 \times 10^3 \pm 1.35 \times 10^2 \Omega \text{ cm}^2$ and 5% $SiO_2 = 1.07 \times 10^3 \pm 1.28 \times 10^2 \Omega \text{ cm}^2$).

A pronounced corrosion protection occurs when using $\geq 10\%$ SiO_2 concentrations and can be attributed to the increase in thickness of the coatings when the SiO_2 concentration is increased, see Table 5.6 (20% MTES:TEOS $R_t = 1.86 \times 10^3 \pm 3.86 \times 10^2 \Omega \text{ cm}^2$, 10% OTES:TEOS $R_t = 3.20 \times 10^3 \pm 6.20 \times 10^2 \Omega \text{ cm}^2$). These trends in R_t values showing improvement in corrosion protection are also shown through trends in PD plots where more protective coatings lead to lower I_{corr} values (for values

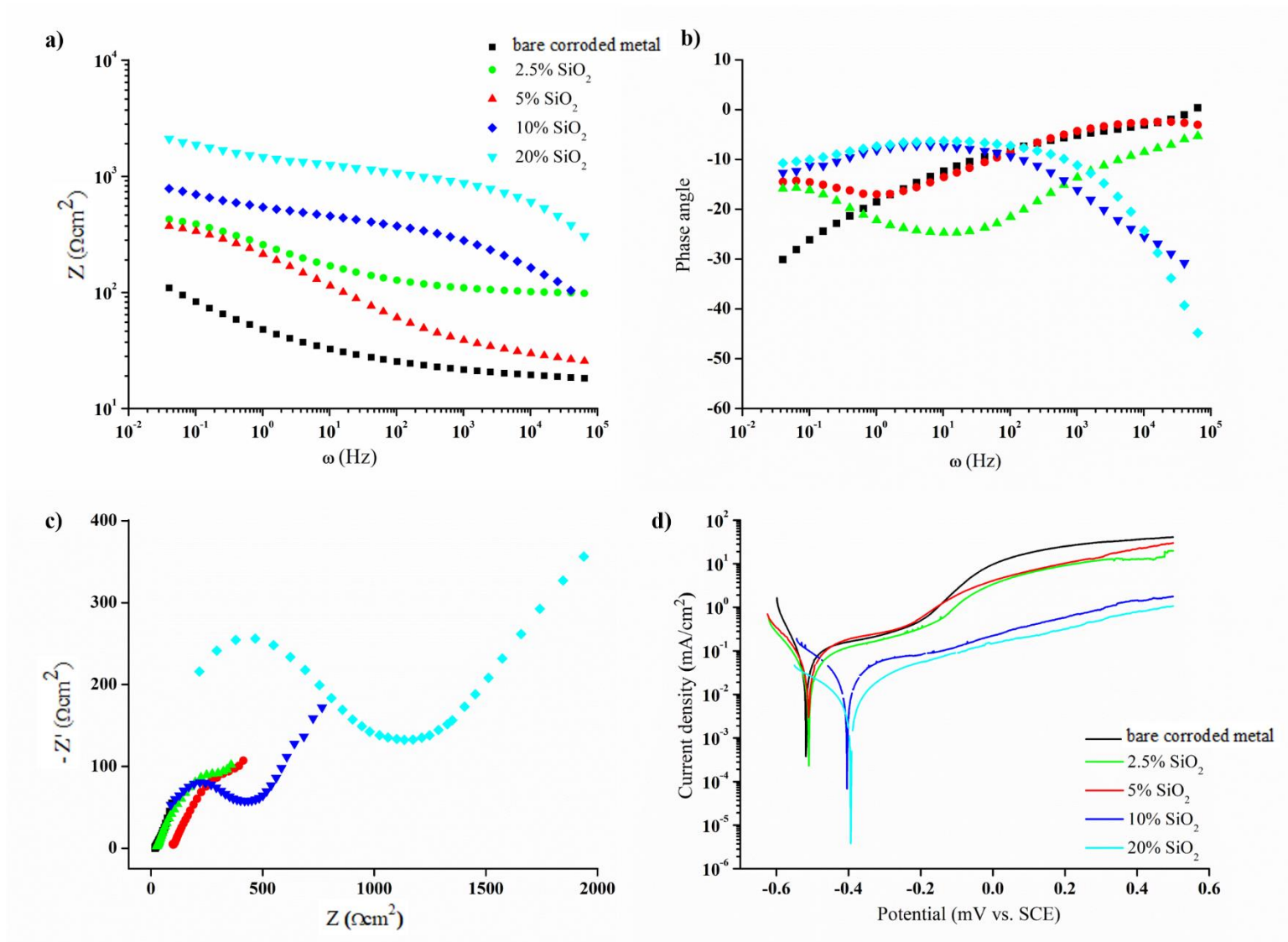


Figure 5.33: a) Bode Impedance b) Bode phase angle c) Nyquist and d) potentiodynamic plots obtained for clean-corroded metal coated with 60:40 mol% MTES:TEOS at several silica concentrations.

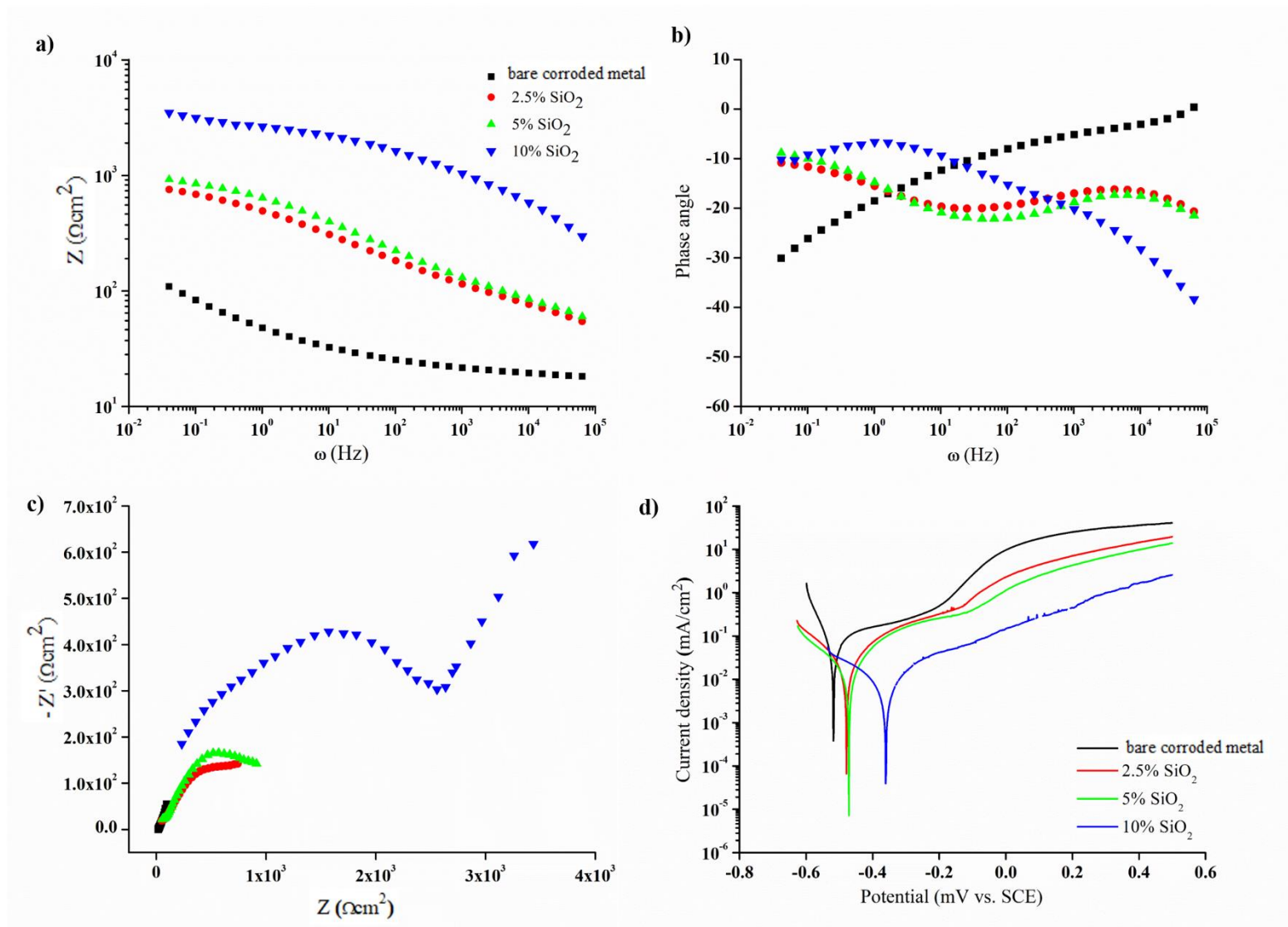


Figure 5.34: a) Bode Impedance b) Bode phase angle c) Nyquist and d) potentiodynamic plots obtained for clean-corroded metal coated with 20:80 mol% OTES:TEOS at several silica concentrations.

Table 5.6: EIS parameters modelled using EEC 1 and 2 and I_{corr} values for coated corroded-cleaned surfaces studied in Figures 5.33 and Figure 5.34.

	SiO ₂ conc	R_{sol} (Ω cm ²)	R_{po} (Ω cm ²)	CPE _c		R_t (Ω cm ²)	CPE _{dl}		GOF	Current Density (mAcm ⁻²)
				Y_c (Ω^{-1} cm ⁻² s ^{α})	α_c		Y_{dl} (Ω^{-1} cm ⁻² s ^{α})	α_{dl}		
Bare corroded metal		38.46 ±9.66	-	-	-	1.31×10 ² ±2.60 ×10 ¹	2.17± ±1.86×10 ⁻³	0.38 ±0.05	8.42×10 ⁻⁵ ±1.60×10 ⁻⁵	2.33×10 ⁻¹ ± 1.43×10 ⁻¹
OTES: TEOS 20:80 %mol	2.5%	22.26 ±6.68	5.00 ×10 ² ±1.25 ×10 ²	3.91 ×10 ⁻⁵ ±4.69 ×10 ⁻⁶	0.60 ±0.07	1.13 ×10 ³ ±1.35 ×10 ²	9.64×10 ⁻⁴ ±1.16×10 ⁻⁴	0.40 ±0.05	1.84×10 ⁻⁴ ±2.21×10 ⁻⁵	3.67×10 ⁻² ± 1.43×10 ⁻²
	5%	12.92 ±3.88	5.03 ×10 ² ±1.26 ×10 ²	8.10 ×10 ⁻⁷ ±9.72 ×10 ⁻⁸	0.72 ±0.09	1.07 ×10 ³ ±1.28 ×10 ²	4.38×10 ⁻⁴ ±5.25×10 ⁻⁵	0.38 ±0.05	1.47×10 ⁻⁴ ±1.76×10 ⁻⁵	2.67×10 ⁻² ± 1.43×10 ⁻²
	10%	21.89 ±6.57	1.21 ×10 ² ±3.02 ×10 ¹	5.01 ×10 ⁻⁶ ±6.01 ×10 ⁻⁷	0.49 ±0.06	4.12 ×10 ³ ±8.54 ×10 ²	2.59×10 ⁻⁴ ±3.10×10 ⁻⁵	0.09 ±0.01	1.22×10 ⁻³ ±1.46×10 ⁻⁴	9.33×10 ⁻³ ± 1.43×10 ⁻³
MTES: TEOS 60:40 %mol	2.5%	52.06 ±15.62	4.46 ×10 ¹ ±1.11 ×10 ¹	1.22 ×10 ⁻⁸ ±1.46 ×10 ⁻⁹	0.92 ±0.11	6.18 ×10 ² ±7.41 ×10 ¹	2.29×10 ⁻³ ±2.75×10 ⁻⁴	0.38 ±0.05	1.86×10 ⁻⁴ ±2.23×10 ⁻⁵	9.33×10 ⁻² ± 1.43×10 ⁻²
	5%	22.46 ±6.74	4.95 ×10 ⁰ ±1.24 ×10 ⁰	2.30 ×10 ⁻⁵ ±2.76 ×10 ⁻⁶	0.67 ±0.08	5.33 ×10 ² ±6.39 ×10 ¹	1.74×10 ⁻³ ±2.09×10 ⁻⁴	0.40 ±0.05	4.64×10 ⁻⁴ ±5.56×10 ⁻⁵	8.67×10 ⁻² ± 1.43×10 ⁻²
	10%	27.68 ±8.30	3.45 ×10 ² ±8.63 ×10 ¹	6.37 ×10 ⁻⁵ ±7.64 ×10 ⁻⁶	0.39 ±0.05	1.49 ×10 ³ ±4.19 ×10 ²	3.87×10 ⁻³ ±4.64×10 ⁻⁴	0.32 ±0.04	2.04×10 ⁻⁴ ±2.44×10 ⁻⁵	6.67×10 ⁻² ± 1.43×10 ⁻²
	20%	32.11 ±9.63	3.65 ×10 ² ±9.1×10 ¹	1.48 ×10 ⁻⁶ ±1.77 ×10 ⁻⁷	0.67 ±0.08	2.97 ×10 ³ ±1.1 ×10 ³	1.05×10 ⁻³ ±1.26×10 ⁻⁴	0.16 ±0.02	5.31×10 ⁻⁴ ±6.37×10 ⁻⁵	1.02×10 ⁻² ± 7.17×10 ⁻⁴

see Table 5.6) most pronounced for higher concentrations of SiO₂ i.e. 10-20%. There is a notable increase in R_{po} as silica concentration is increased for MTES coatings (5% = $4.95 \times 10^0 \pm 1.24 \times 10^0 \Omega \text{ cm}^2$, 10% = $3.45 \times 10^2 \pm 8.63 \times 10^1 \Omega \text{ cm}^2$, 20% = $3.65 \times 10^2 \pm 9.10 \times 10^1 \Omega \text{ cm}^2$). However, relatively large standard errors can only lead to a cautionary discussion especially for OTES coatings where no clear trend can be drawn.

Nyquist plots for coated corroded samples in Figure 5.33 (c) for MTES and Figure 5.34 (c) for OTES coatings show an additional tail in the higher impedance range which is typically attributed to the Warburg impedance. This element models the impedance associated to diffusion (i.e. mass transfer) processes and is frequently used when the diffusion of species through the pores of the coating or corrosion products controls the corrosion rate producing a distinctive 45° tail [178]. This shape is most evident for 10% SiO₂ OTES:TEOS 20:80 mol% Nyquist plot (blue plot of Figure 5.34 (c)); in fact EEC parameter α_c is very close to 0.5 for that coating (see Table 5.6, $\alpha_c = 0.49 \pm 0.06$), indicating that the CPE_c element is a Warburg impedance. However, such data was not modelled using a Warburg element instead of CPE_c element since no improvement in fit and worsening in GOF value was obtained.

5.2.7.2 Effect of dip-coating speed on crack formation

Crack-formation is caused by stress due to changes in pore size during the dip-coating process and by capillary forces arising from evaporation of the solvent [215]. Crack formation was initially suspected to be partially due to curing process which speeds up the evaporation of solvent and capillary forces are therefore greater. However, 20:80 mol% OTES:TEOS coatings still formed an abundance of cracks when heat treatment of 150 °C for 1hr was not applied (**Figure 5.35** (a i)) which meant that cracking arises during the coating deposition process.

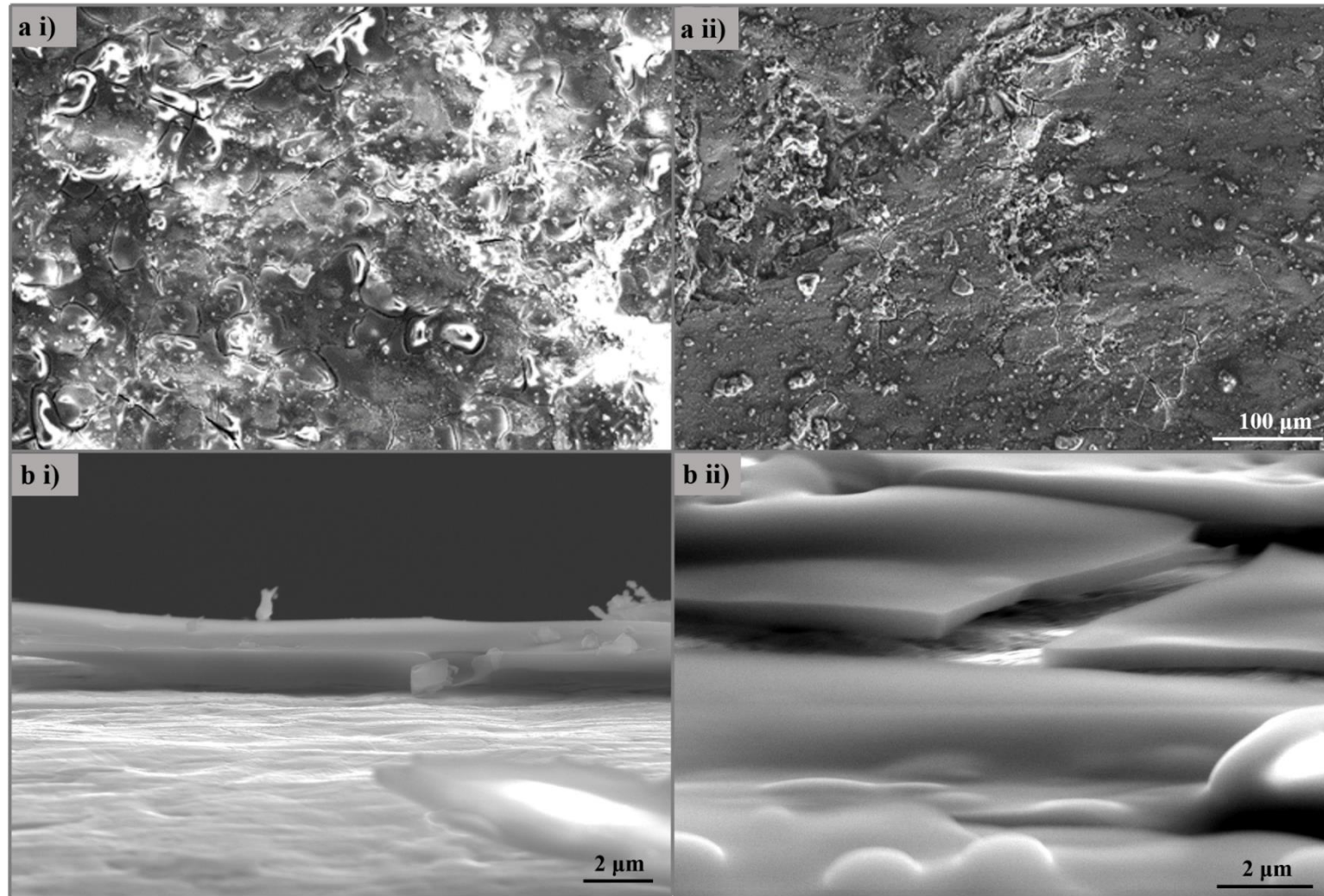


Figure 5.35: a) Electron micrographs (x500 mag) of corroded-cleaned coupon coated with 5% SiO₂ 20:80 mol% OTES:TEOS uncured coatings b) coating cross sections of 5% SiO₂ 20:80 mol% OTES:TEOS deposited using i) 280 mm/min (mag × 10k) and ii) 40 mm/min (mag × 20k) dip-speed.

Following this result, the dip-speed was lowered to 40 mm/min instead of 280 mm/min which is conventionally used in this work. It was anticipated that a lower dip-speed would allow more time for sol penetration into crevices and pores of the corrosion layer leading to a more evenly coated surface along the grooves of the rough surface. However, this was not the case as cracks still occurred (Figure 5.35 (a ii)) and electrochemical testing revealed a less protective coating (total impedance (Z_{tot}) values for coatings applied at a rate of 280mm/min = $3.10 \times 10^2 \pm 3.14 \times 10^1 \Omega \text{ cm}^2$ and 40mm/min = $1.37 \times 10^2 \pm 2.14 \times 10^1 \Omega$). Curing of samples at 150 °C for 1hr was thus maintained since it was not the cause of crack formation. Less protective coatings are postulated to be due to the thinner coating formed at a lower dip-speed. Figure 5.35 b (ii) ($470.63 \pm 52.36 \text{ nm}$) indicates a thinner coating deposition when carried out at 40 mm/min compared to a thicker coating at 280 mm/min ($1146 \pm 97.32 \text{ nm}$) shown in Figure 5.35 b (i).

5.2.7.3 Effect of increase in X-Si(OR)₃

The most protective coatings for each of the five organic precursors (X-Si(OR)₃) studied was related to the organic content of the coatings (see Section 5.1.4). A ratio of 60:40 mol% proved to be the most corrosion resistant for MTES:TEOS systems; a lower hybrid precursor concentration and the coating becomes more brittle whereas an increase in the concentration of MTES:TEOS leads to a softer coating due to the presence of more organic (methyl) groups. However, it is possible that this ratio of 60:40 mol%, which provides optimal protection, is in fact too brittle when applied onto a corroded surface, resulting in crack formation during drying.

In this section, 10% SiO₂ concentrations were used for both MTES and OTES coatings. The dip speed was kept to 280 mm/min followed by a curing time of 1 hr at 150 °C. Figure 5.31 and Figure 5.35 show coated samples for 60:40 mol% MTES and 20:80 mol% OTES:TEOS respectively, for which several cracks are clearly visible. **Figure 5.36** (a) shows an increase in the hybrid precursor concentration of MTES:TEOS to 80:20 mol% concentration resulting in a smoother and more continuous coating with far less cracks compared to MTES:TEOS 60:40 mol% coating as seen in

Figure 5.31 (a). Similarly, OTES:TEOS 40:60 mol% coatings (Figure 3.36 (b i)) show a smooth and crack-free surface coverage compared to OTES:TEOS 20:80 mol% shown in Figure 5.35 (a).

Figure 5.37 presents electron-micrograph of 10% SiO₂ double coating applications of MTES:TEOS in molar ratios 60:40 and 80:20 mol% and OTES:TEOS molar ratios 20:80 and 40:60 mol%. Slightly thicker coatings were obtained upon increasing in organic content of MTES and OTES coatings: MTES:TEOS 60:40 mol% $812.3.5 \pm 102.3$ nm, 80:20 mol% 925.3 ± 98.6 nm; and OTES:TEOS 20:80 mol% 1105.2 ± 156.2 nm, 40:60 mol% 1332.2 ± 216.3 nm which contributes to the formation of smoother coatings over rough surfaces.

Improvement observed in coating deposition on corroded surface with an increase in organic content has also manifested itself in electrochemical results (**Figure 5.38**) for which higher values of impedance were obtained as clearly seen in lower frequency range of the Bode Impedance (a), wider arc in Nyquist plots (c) and lower I_{corr} in PD plots (d) : an increase in hybrid precursor concentration of OTES:TEOS from 20:80 to 40:60 mol% brought about greater corrosion resistance; similarly, MTES:TEOS 80:20 mol% being more protective than 60:40 mol%.

5.2.7.4 Effect of Drying Control Chemical Additives

Formamide (FMA) and ethylene glycol butyl ether (EGBE) were employed as Drying Control Chemical Additives (DCCAs) in order to eliminate or at least reduce the formation of cracks over 10% SiO₂ MTES:TEOS 60:40 mol% and OTES:TEOS 20:80 mol% coatings. **Figure 5.39** shows the effect of solvent on the particle size distribution for MTES (a) and OTES (b) sols. PS results in Section 5.1.1.1 display two particle populations as can be seen for sols dispersed in EtOH in Figure 5.39. Solvents other than EtOH produce additional particle populations where, e.g. 4 populations appear for EGBE and FMA:EtOH solvents.

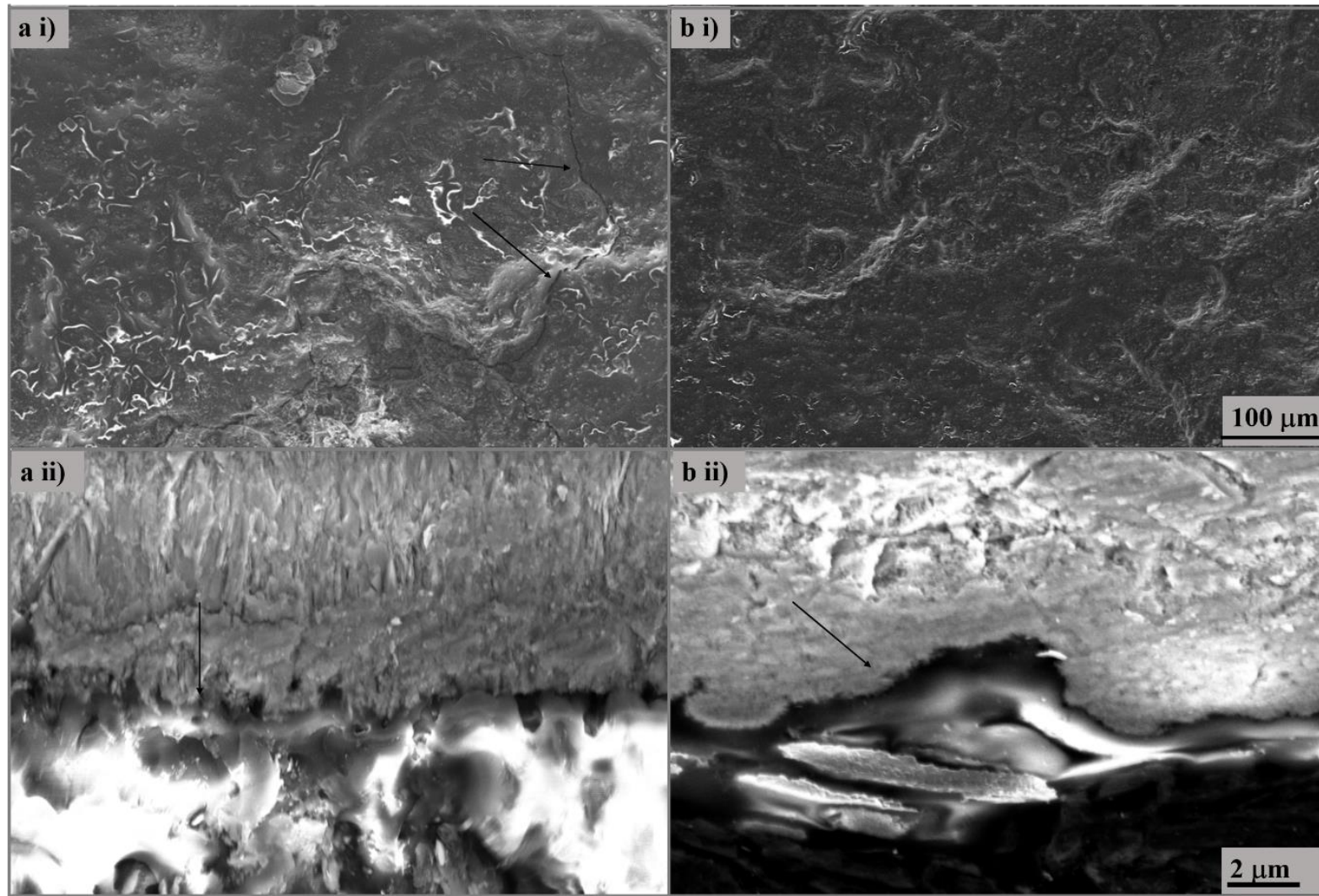


Figure 5.36: electron-micrograph showing (a) surface of coated corroded samples of i) 10% SiO₂ 80:20 mol% MTES:TEOS and ii) 10% SiO₂ 40:60 mol% OTES:TEOS (mag ×500) and (b) cross-section of i) 10% SiO₂ 80:20 mol% MTES:TEOS and ii) 10% SiO₂ 40:60 mol% OTES:TEOS (mag ×10k). Arrows highlight cracks present in Figure (a i) whereas arrows indicate OIH alkoxy silane coatings in Figure b)

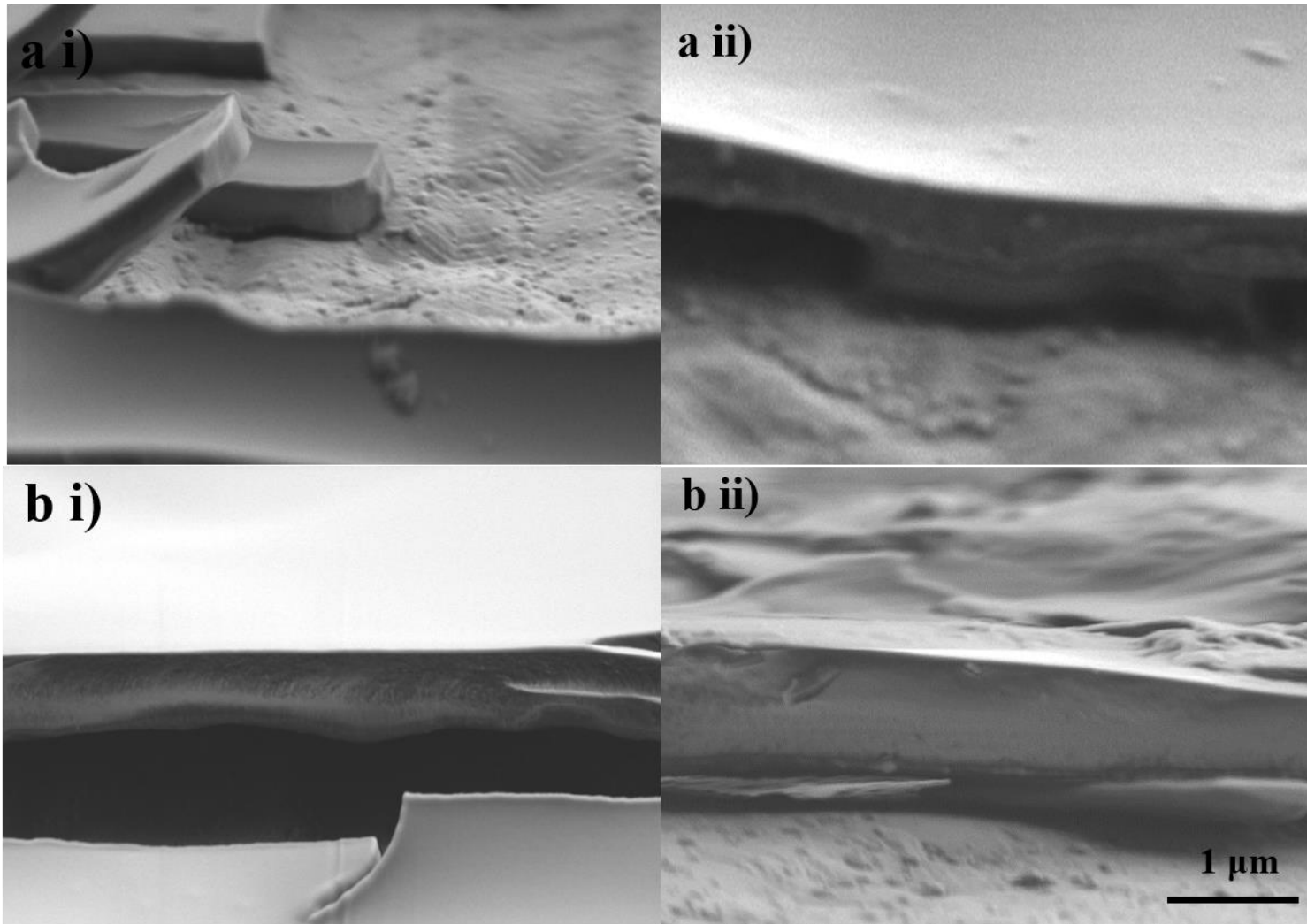


Figure 5.37: electron-micrograph showing 10% SiO₂ double coating applications of (a) MTES:TEOS i) 60:40 mol% ii) 80:20 mol%; b) OTES:TEOS i) 20:80 mol% ii) 40:60 mol%. Images were captured under x10k magnification.

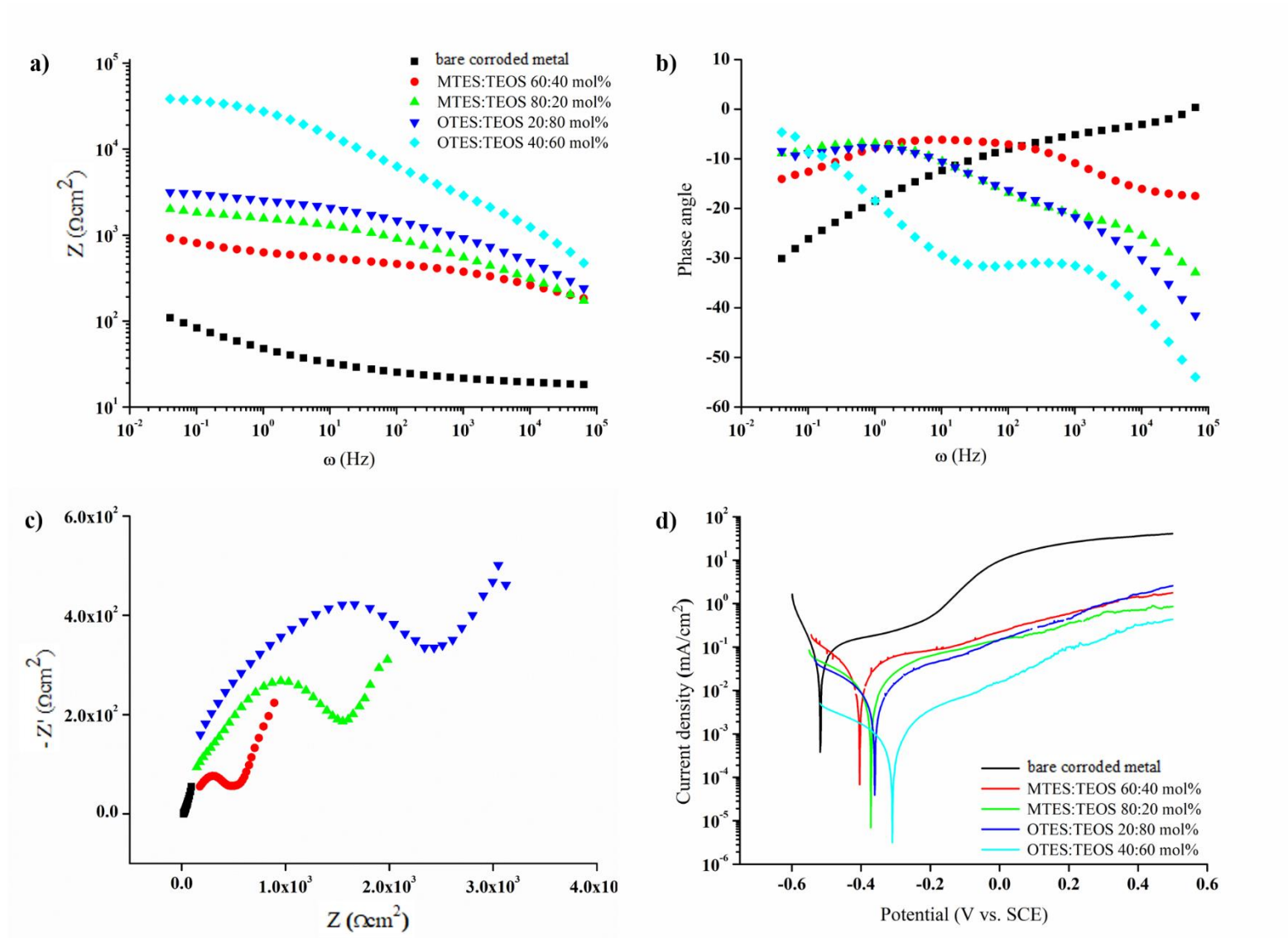


Figure 5.38: a) Bode Impedance b) Bode phase angle c) Nyquist and d) potentiodynamic plots obtained for corroded iron metal coated with 10% SiO_2 20:80 mol% OTES:TEOS, 40:60 mol% OTES:TEOS, 60:40 mol% MTES:TEOS and 80:20 mol% MTES:TEOS

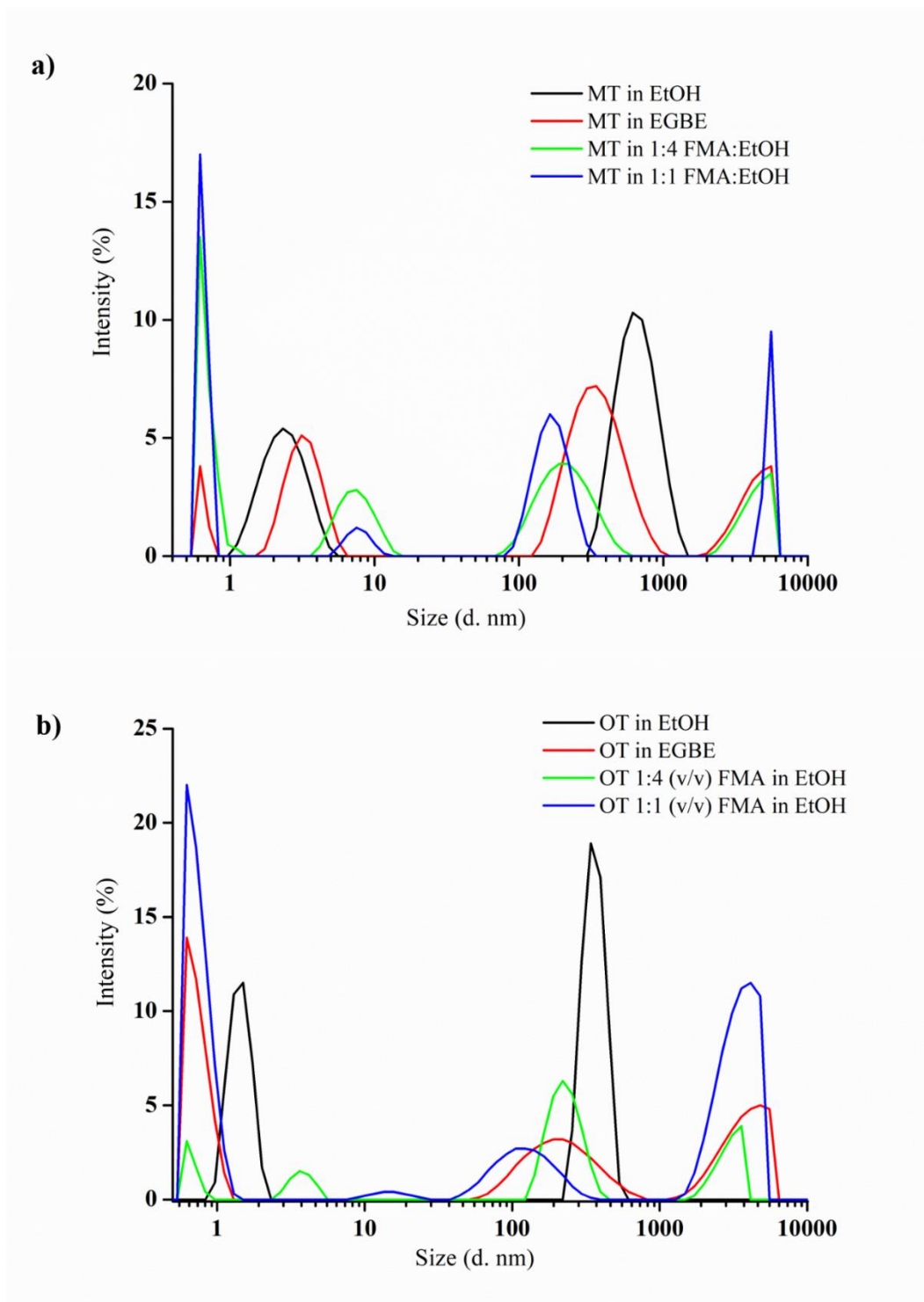


Figure 5.39: Particle size measurements for a) 2.5% SiO₂ 60:40 mol% MTES:TEOS sols b) 2.5% SiO₂ 20:80 mol% OTES:TEOS sols developed in EtOH, FMA:EtOH 1:4 (v/v), FMA:EtOH 1:1 (v/v) and EGBE solvent

Coating thickness determination was carried out using sols that feature in Figure 5.39, the sols were applied onto SS strips through dip-coating at 280mm/min and curing was maintained at 150 °C for 1 hr. **Figure 5.40** shows electron-micrographs of 2.5% SiO₂ double coating applications of MTES:TEOS 60:40 mol% (Figure 5.40 (a)) and OTES:TEOS 20:80 mol% (Figure 5.40 (b)) as procured in several solvents during sol development namely i) ethanol, ii) 20% (vol/vol) FMA in ethanol, iii) 50% (vol/vol) FMA in ethanol and iv) EGBE. Thinner coatings are produced when ethanol solvent is completely substituted by either EBGA or partially substituted with FMA: 20% FMA in ethanol (1:4 FMA in EtOH) and 50% FMA in ethanol (1:1 FMA in EtOH).

Thickness measurements obtained using SEM are presented in **Table 5.7**. The thickest coating (600.93 ± 21.10 nm) was obtained when the sol was procured in ethanol diluent whereas MTES:TEOS sols produced in 1:4 FMA:EtOH presented slightly thinner (542.31 ± 36.98 nm for 20 vol% FMA). On increasing the volume of FMA:EtOH to 1:1 (50 vol% FMA), coating decreases further in thickness (385.34 ± 24.67 nm). MTES:TEOS sols prepared in EGBE gave rise to the thinnest films (290.69 ± 45.87 nm). Similar trends were observed for OTES:TEOS coatings which were overall, slightly thicker than MTES:TEOS 60:40 mol%.

Table 5.7: Thickness measurements obtained using SEM for double coated 2.5% SiO₂ 60:40 mol% MTES:TEOS and OTES:TEOS 20:80 mol% dispersed in different solvents

Solvent	MTES Mean thickness \pm St. Error (nm)	OTES Mean thickness \pm St. Error (nm)
Ethanol	600.93 ± 21.10	712.36 ± 53.21
Formamide: ethanol 1:4 (vol/vol)	542.31 ± 36.98	687.23 ± 42.31
Formamide: ethanol 1:1 (vol/vol)	385.34 ± 24.67	552.78 ± 52.36
ethylene glycol butyl ether	290.69 ± 45.87	419.84 ± 39.87

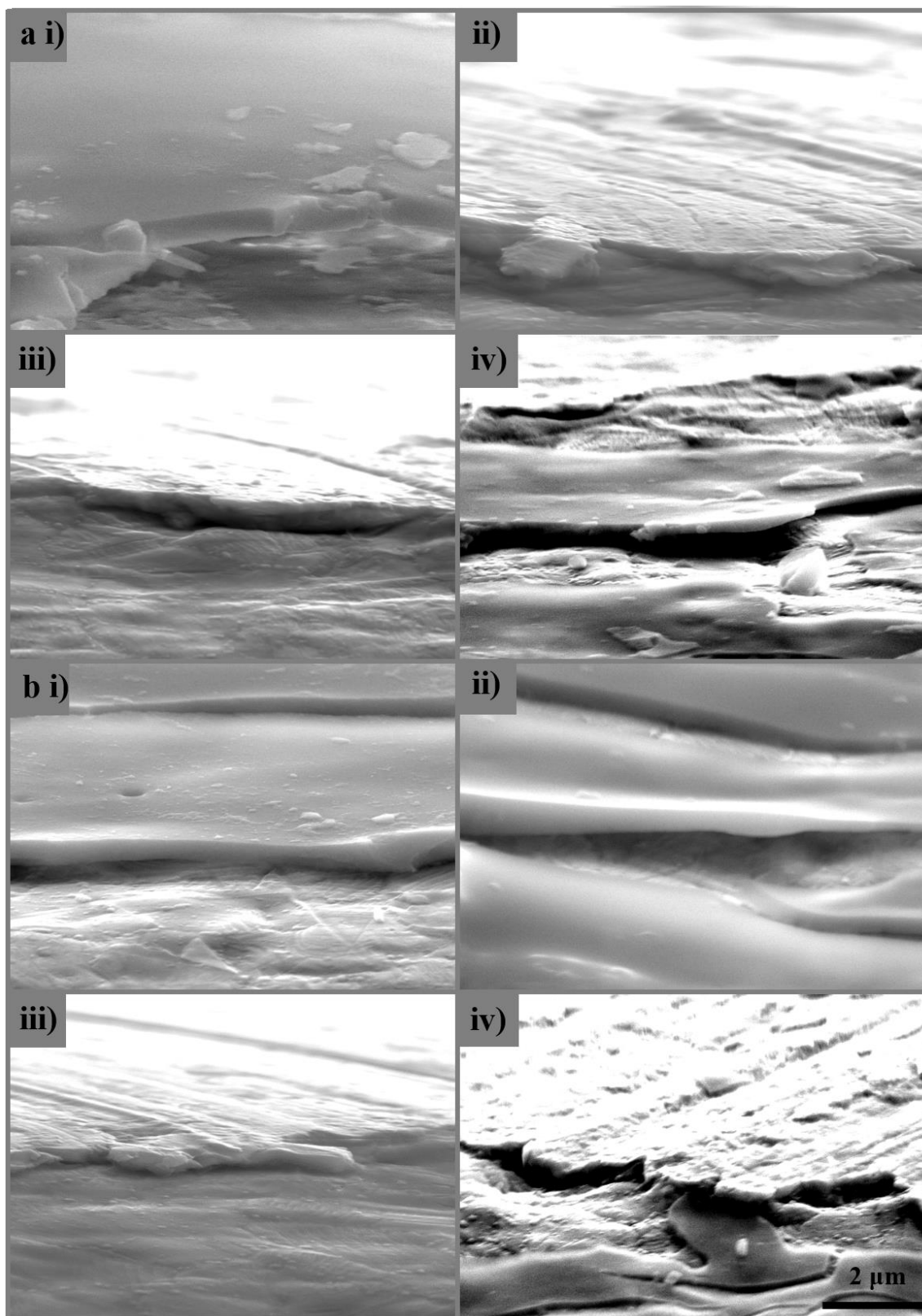


Figure 5.40: Electron-micrograph showing 2.5% SiO₂ double coating applications of a) MTES:TEOS 60:40 mol% b) OTES:TEOS 20:80 mol% in solvent (i) ethanol; ii) 20% (vol/vol) FMA in ethanol; iii) 50% (vol/vol) FMA in ethanol; and iv) EGBE. Images were captured under x10k magnification.

Figure 5.41 (a) and (b) show electron micrographs of coatings deposited from ethanol and EGBE-solvent based MTES:TEOS sols onto corroded surface. The latter appear to have significantly smaller cracks (note the change in scale).

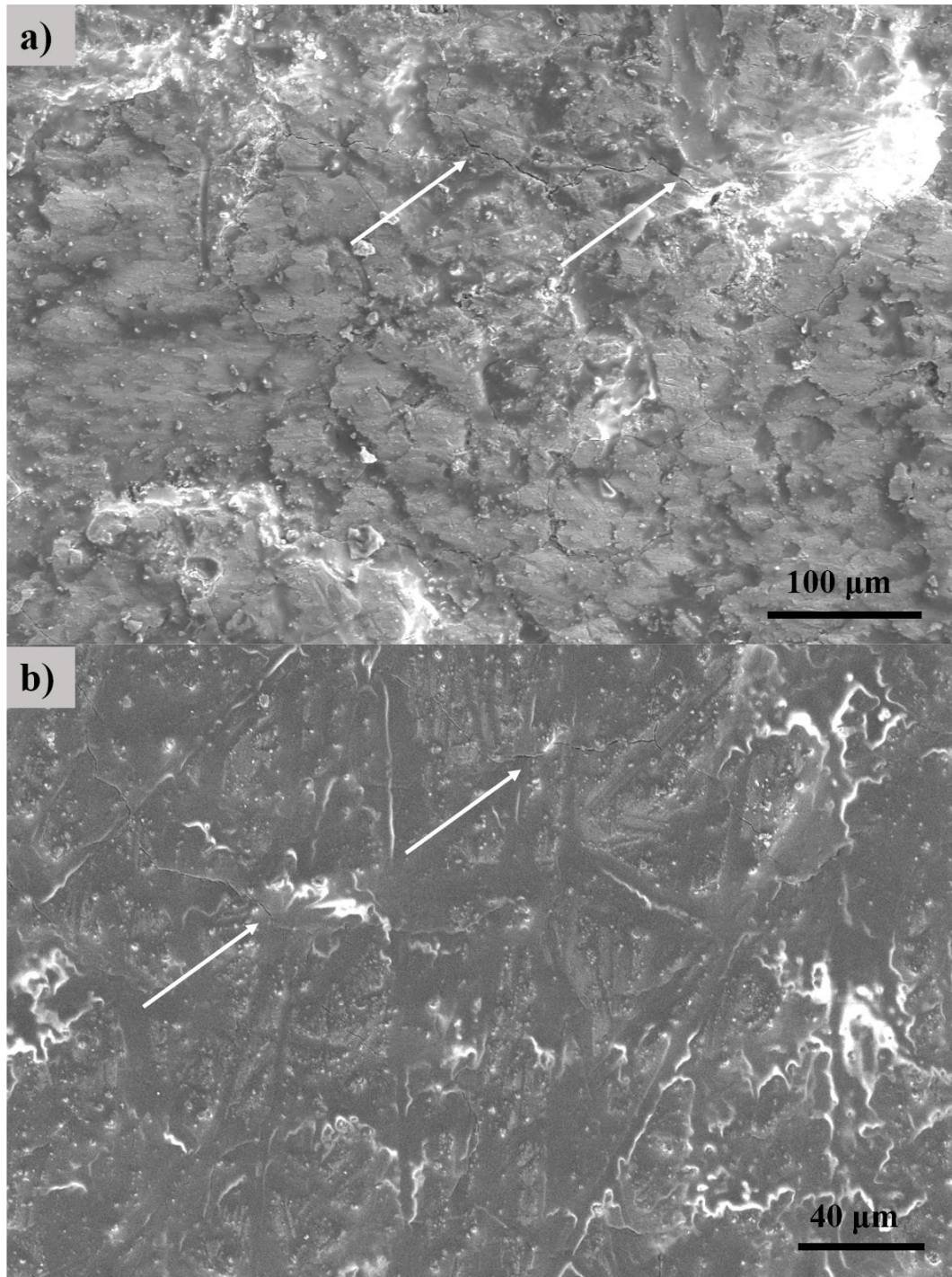


Figure 5.41: Electron micrograph of 10% SiO₂ 60:40 mol% MTES:TEOS coated corroded surface where solvent used as diluent was a) ethanol at mag x500 and b) ethylene glycol butyl ether at mag x1000. Cracks are indicated with arrows.

Figure 5.42 presents a micrograph of the surface of coated corroded metal using 10% SiO₂ 20:80 mol% OTES:TEOS using EGBE as solvent for which crack formation was frequent and clearly visible at low magnification (x500). **Figure 5.43** (a) and (b) shows 60:40 mol% MTES:TEOS coatings formed using 1:1 and 1:4 (v/v) formamide : ethanol (FMA:EtOH) dispersant respectively. The coatings formed are of very poor quality as they are severely cracked and also appear to have formed pockets of air between the coating and underlying surface which have remained following the solidification of the coating during curing (few of these ‘bubbles’ are clear in image and are indicated using arrows).

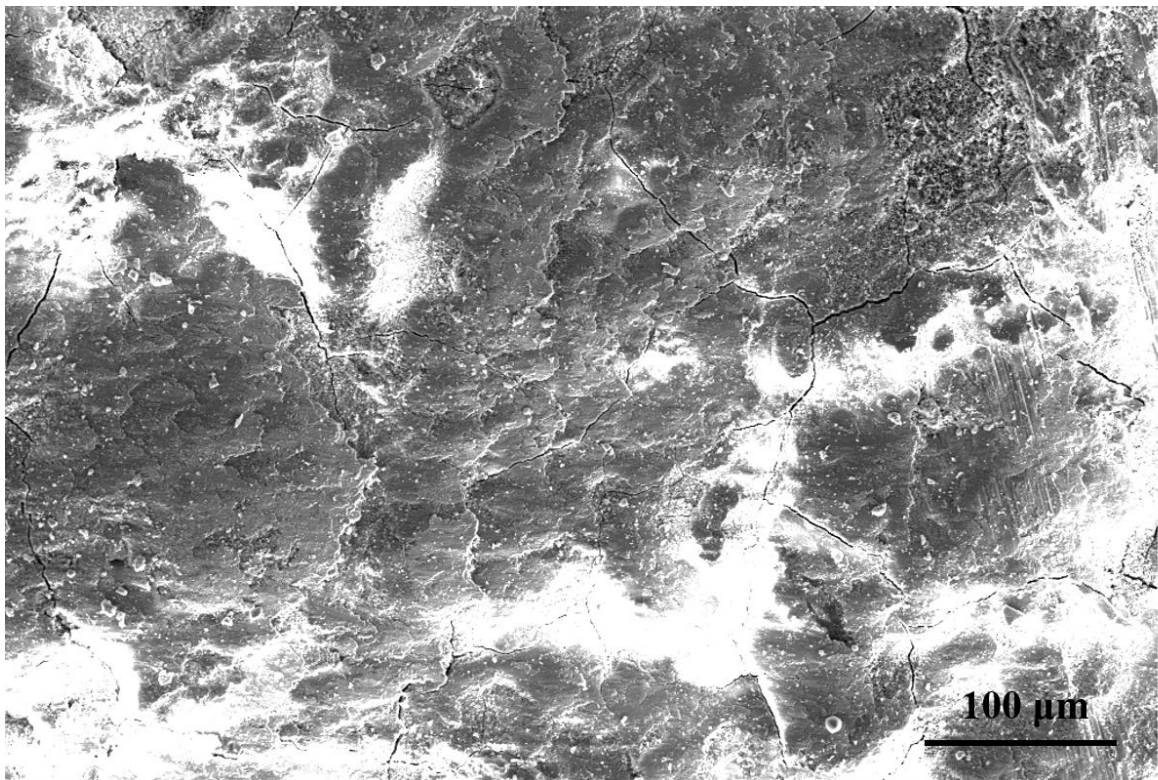


Figure 5.42: Electron micrograph of 10% SiO₂ 20:80 mol% OTES:TEOS coated corroded surface using EGBE as diluent at mag x500.

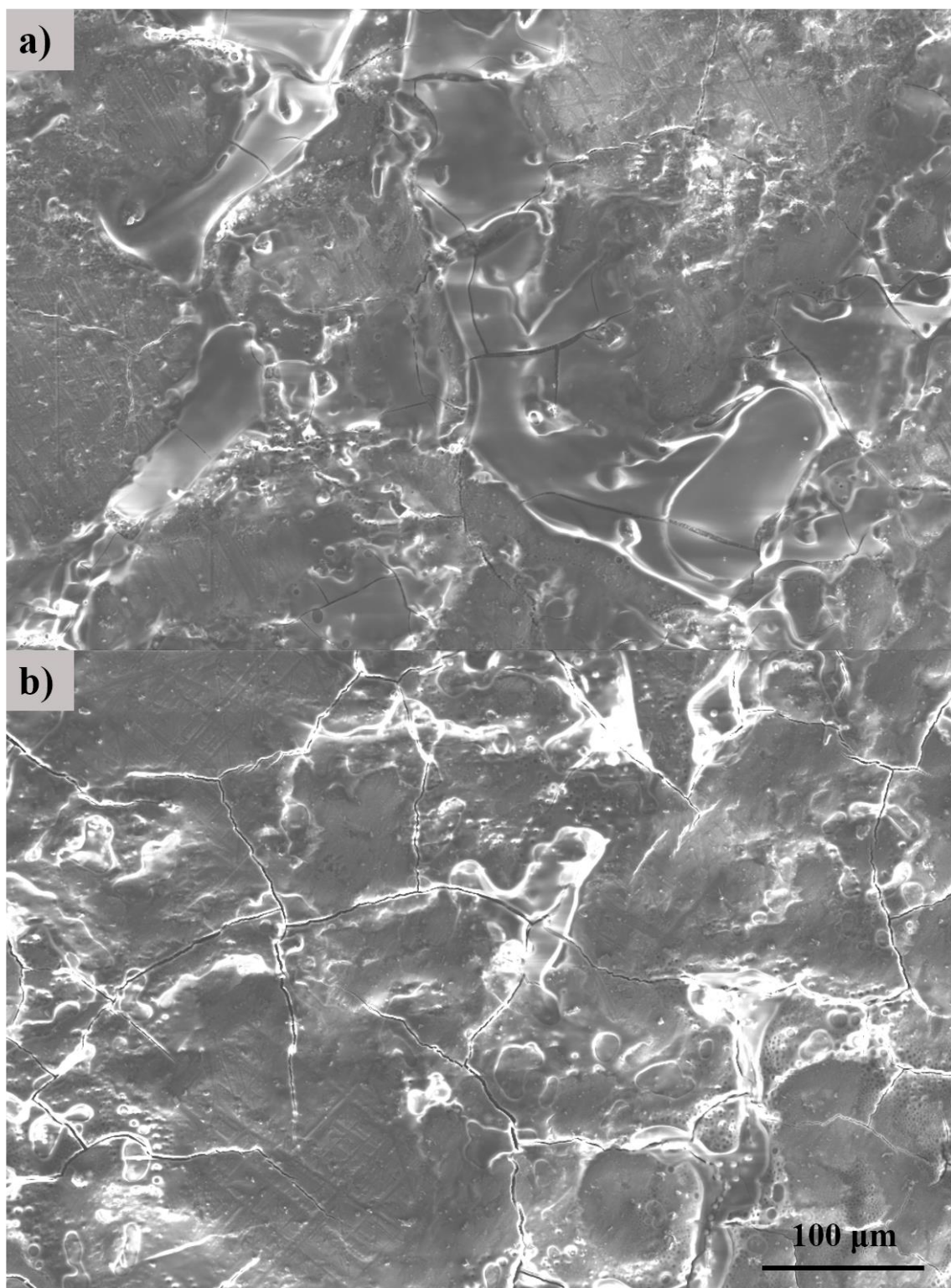


Figure 5.43: Electron micrograph of 10% SiO₂ 60:40 mol% MTES:TEOS coated corroded surface using mixture of FMA:EtOH a) 1:1 (v/v) and b) 1:4 (v/v). images generated at x500 magnification.

Electrochemical data for MTES:TEOS and OTES:TEOS coatings in EtOH, EGBE and FMA:EtOH solvent is presented in **Figure 5.44**, EIS parameters were obtained through modelling using EEC1 and 2 as previously done for un/coated corroded coupons as in e.g. Figure 5.38 and are presented in **Table 5.8**. EEC 1 and 2 were employed in modelling due to two-time constants observed in Nyquist, these circuits fit EIS data obtained well which is indicated through low GOF values in Table 5.8. Despite the visual improvement in the coating (Figure 5.41), the results of electrochemical testing revealed no improvement in the anti-corrosion properties upon changing solvent from EtOH to EGBE for MTES:TEOS 60:40 mol% system as seen through similar Bode impedance, Nyquist and PD plots (Figure 5.44 (a), (c) and (d) respectively).

Less protective 20:80 mol% OTES:TEOS coatings were obtained when using EGBE instead of ethanol as solvent (see plots in Figure 5.44) shown through R_t values in Table 5.8 OTES in EtOH= $5.19 \times 10^3 \pm 4.67 \times 10^2 \Omega \text{ cm}^2$, in EGBE= $1.81 \times 10^3 \pm 1.63 \times 10^2 \Omega \text{ cm}^2$). This has been attributed to the heavy cracking as can be observed in Figure 5.42.

There is a significant reduction in impedance measured (Figure 5.44 low frequency range in Bode impedance (a) and smaller arc in Nyquist (c) plots) when comparing both FMA:EtOH 1:4 and 1:1 (vol/vol) systems with MTES:TEOS coatings (Table 5.8 R_t values for MTES in EtOH= $1.19 \times 10^3 \pm 1.07 \times 10^2 \Omega \text{ cm}^2$, FAM:EtOH 1:4 (v/v) = $2.00 \times 10^2 \pm 1.80 \times 10^1 \Omega \text{ cm}^2$, FAM:EtOH 1:1 (v/v)= $4.53 \times 10^2 \pm 4.08 \times 10^1 \Omega \text{ cm}^2$), which can be visually appreciated through the electron micrographs in Figure 5.43. Since such poor results were obtained for MTES:TEOS systems, the use of FMA was not further applied onto OTES:TEOS systems.

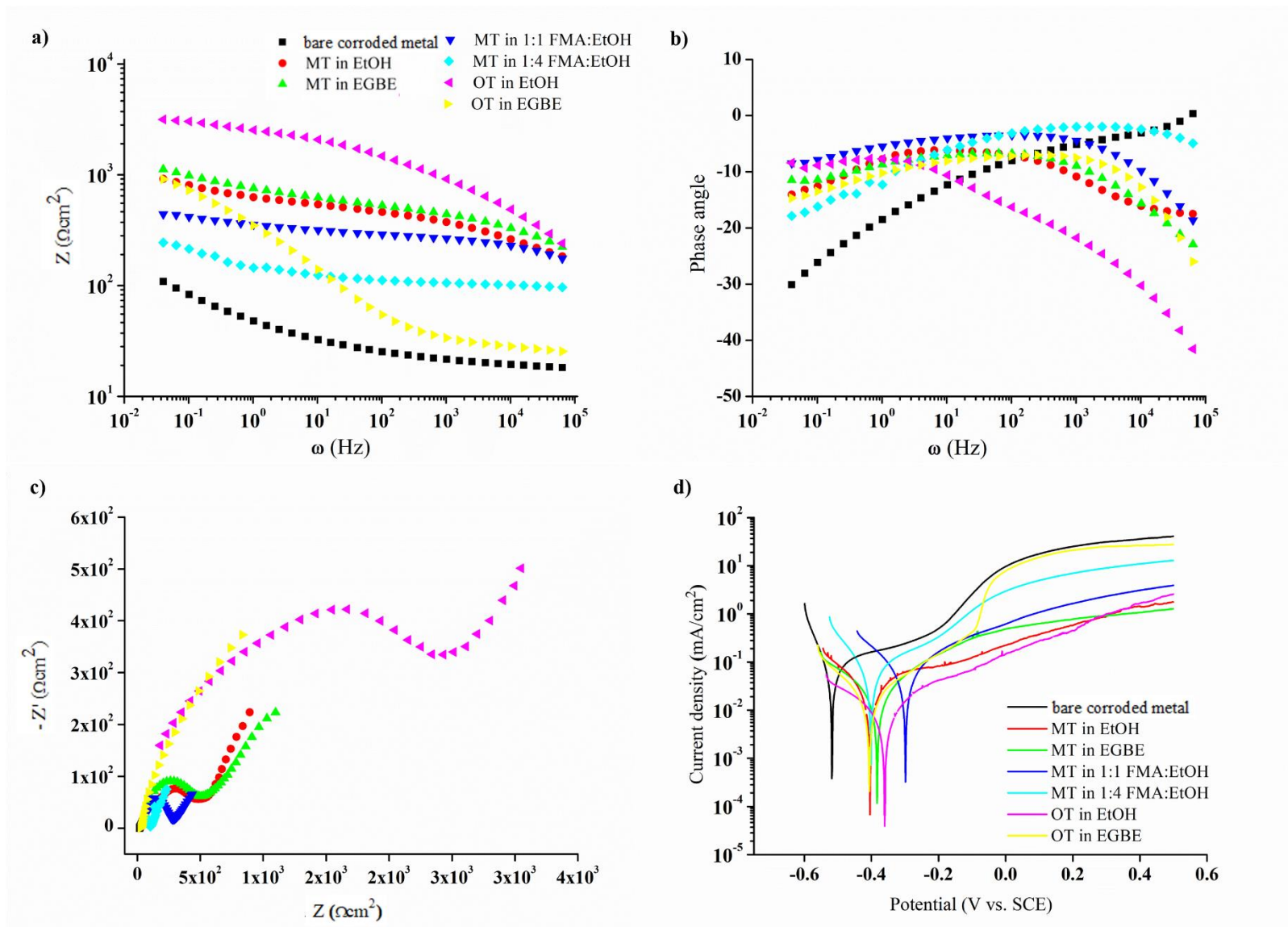


Figure 5.44 a) Bode Impedance b) Bode phase angle c) Nyquist and d) potentiodynamic plots obtained for corroded metal coated with 10% SiO₂ 60:40 mol% MTES:TEOS and 20:80 mol% OTES:TEOS originating from sols that have been dispersed in EtOH, FMA in EtOH, and EGBE solvent.

Table 5.8: EIS parameters modelled using EEC 1 and 2 and I_{corr} values for un/coated corroded surfaces studied in Figure 5.44.

	R_{sol} ($\Omega \text{ cm}^2$)	R_{po} ($\Omega \text{ cm}^2$)	CPEc		R_t ($\Omega \text{ cm}^2$)	CPEdl		GOF	Current Density (mA m^{-2})
			Y_c ($\Omega^{-1} \text{ cm}^{-2} \text{ s}^\alpha$)	α_c		Y_{dl} ($\Omega^{-1} \text{ cm}^{-2} \text{ s}^\alpha$)	α_{dl}		
Bare corroded metal	38.46 ± 9.66	-	-	-	1.31×10^2 $\pm 2.60 \times 10^1$	2.17×10^{-2} $\pm 1.86 \times 10^{-3}$	0.38 ± 0.05	8.42×10^{-5} $\pm 1.60 \times 10^{-5}$	1.02×10^{-1} $\pm 7.17 \times 10^{-3}$
MTES:TEOS in EtOH	65.99 ± 19.13	4.49×10^2 $\pm 1.17 \times 10^2$	3.73×10^{-5} $\pm 3.65 \times 10^{-5}$	0.40 ± 0.04	1.19×10^3 $\pm 1.07 \times 10^2$	3.45×10^{-3} $\pm 3.10 \times 10^{-4}$	0.33 ± 0.03	3.03×10^{-5} $\pm 2.73 \times 10^{-6}$	6.33×10^{-2} $\pm 1.43 \times 10^{-2}$
MTES:TEOS in EGBE	32.93 ± 9.54	3.94×10^2 $\pm 1.02 \times 10^2$	5.03×10^{-6} $\pm 4.93 \times 10^{-6}$	0.50 ± 0.05	1.18×10^3 $\pm 1.06 \times 10^2$	1.92×10^{-3} $\pm 1.72 \times 10^{-4}$	0.21 ± 0.02	8.41×10^{-5} $\pm 7.57 \times 10^{-6}$	4.33×10^{-2} $\pm 1.43 \times 10^{-2}$
MTES:TEOS in 1:4 FA:EtOH	41.57 ± 3.35	9.51×10^1 $\pm 2.47 \times 10^1$	8.50×10^{-6} $\pm 8.33 \times 10^{-6}$	0.41 ± 0.04	2.00×10^2 $\pm 1.80 \times 10^1$	9.71×10^{-3} $\pm 8.74 \times 10^{-4}$	0.40 ± 0.04	1.51×10^{-3} $\pm 1.36 \times 10^{-4}$	7.33×10^{-2} $\pm 1.43 \times 10^{-2}$
MTES:TEOS in 1:1 FA:EtOH	59.53 ± 17.26	1.64×10^2 $\pm 4.25 \times 10^1$	3.39×10^{-6} $\pm 3.32 \times 10^{-6}$	0.72 ± 0.07	4.53×10^2 $\pm 4.08 \times 10^1$	4.47×10^{-3} $\pm 4.02 \times 10^{-4}$	0.18 ± 0.02	5.05×10^{-4} $\pm 4.54 \times 10^{-5}$	7.33×10^{-2} $\pm 1.43 \times 10^{-2}$
OTES:TEOS in EtOH	45.65 ± 10.36	8.01×10^2 $\pm 2.08 \times 10^2$	8.12×10^{-7} $\pm 7.96 \times 10^{-7}$	0.62 ± 0.06	5.19×10^3 $\pm 4.67 \times 10^2$	1.03×10^{-4} $\pm 9.25 \times 10^{-6}$	0.22 ± 0.02	8.85×10^{-4} $\pm 7.97 \times 10^{-5}$	1.02×10^{-2} $\pm 7.17 \times 10^{-4}$
OTES:TEOS in EGBE	46.28 ± 7.62	7.14×10^2 $\pm 1.86 \times 10^2$	7.03×10^{-5} $\pm 6.89 \times 10^{-5}$	0.57 ± 0.05	1.81×10^3 $\pm 1.63 \times 10^2$	2.85×10^{-3} $\pm 2.56 \times 10^{-4}$	0.53 ± 0.05	4.56×10^{-4} $\pm 4.10 \times 10^{-5}$	3.33×10^{-2} $\pm 1.43 \times 10^{-2}$

5.3 Addition of silica nanoparticles for the improvement of corrosion protection of OIH alkoxy silane coatings

5.3.1 Addition of Commercial Nanoparticles (CNPs) to OIH alkoxy silane coatings

5.3.1.1 Dispersion of CNPs studied through PS

The CNPs were dispersed in the ethanol solvent that was then added to prepared 2.5% SiO₂ concentration of MTES:TEOS 60:40 mol% sol. The dispersion of CNP in ethanol proved difficult for 0.01%, 0.1% and 1% (w/v) concentrations by sonication. Particle size measurements of the supernatant dispersions after appropriate sonication showed that the dispersions contained mostly particles in the micro range i.e. nanoparticles of the size specified ~ 10-20 nm were not detected as shown in **Figure 5.45**.

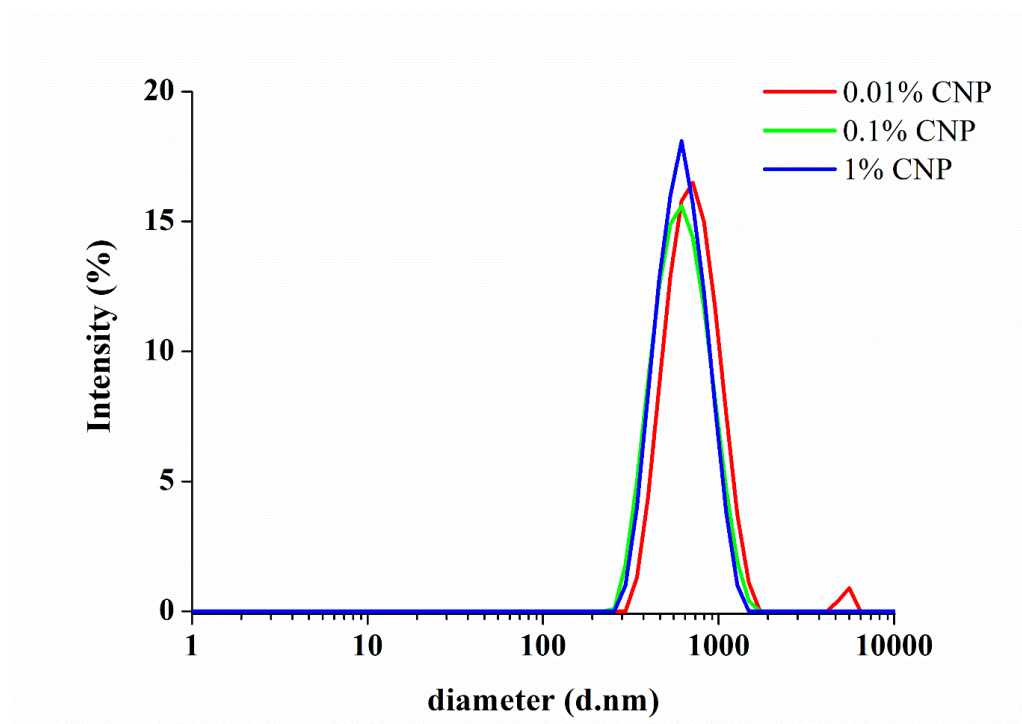


Figure 5.45: Plot of intensity versus particle size (nm) for 0.01, 0.1 and 1 % (w/v) CNP in ethanol dispersion.

Ma *et al* reported an improved dispersed silica NP mixture in ethanol through the use of the cationic surfactant cetyltrimethylammonium bromide (CTAB). CTAB can be adsorbed onto the surface of silica due to the positive charge on the polar portion (head group) of the surfactant onto the negatively

charged silica [216]. Therefore, dispersion was attempted as specified by Ma *et al* by the addition of 1.0 g silica powder to 100ml water, the pH was adjusted to pH 8 by the addition of 0.1 M NaOH. The silica NP were modified under constant stirring by adding CTAB surfactant (0.5, 1.0 and 3.0 wt%) into the system. This method did not lead to a satisfactory dispersion as shown through PS results presented in **Figure 5.46**; therefore, the preparation of a high concentrations of nanoparticles was abandoned.

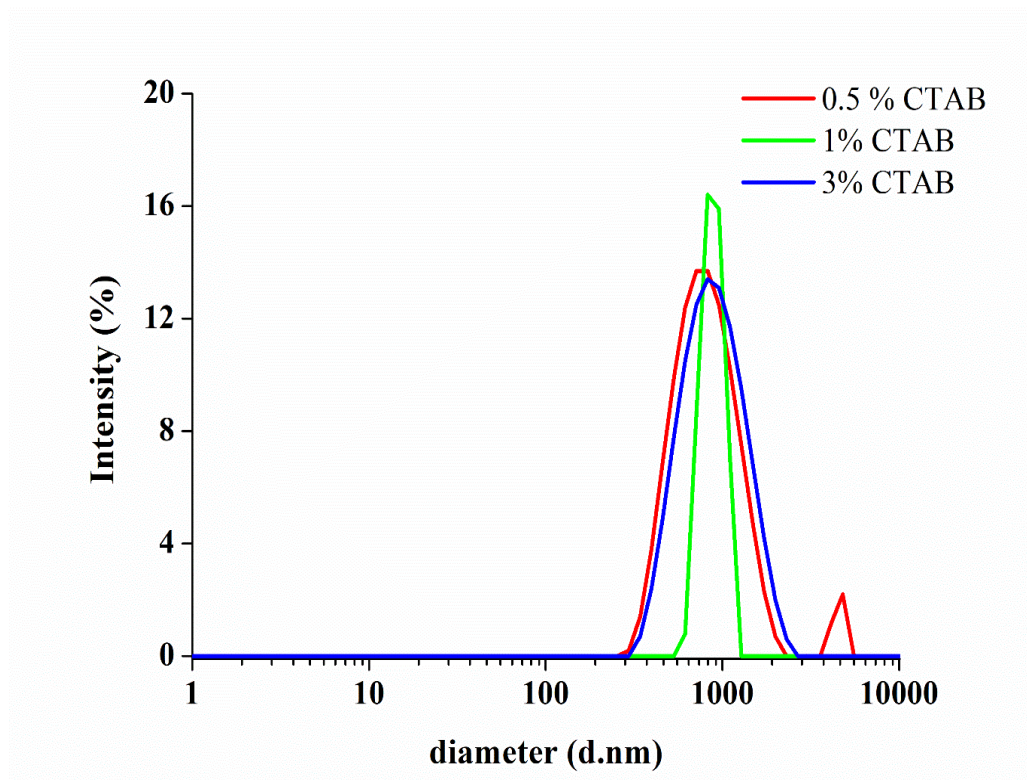


Figure 5.46: Plots of intensity versus particle size (nm) for 1% (wt/vol) CNP in water dispersion having CTAB surfactant added in 0.5, 1.0 and 3% (wt/vol) concentrations.

Instead, lower amounts of CNP were employed (100 up to 500 ppm) for which a 30-minute sonication was allowed to disperse the particles in ethanol solvent. Although the ethanol dispersion appeared clear, PS measurements on 100, 300 and 500 ppm samples showed a single peak in the micro range, indicating the presence of microparticles (**Figure 5.47**). Such a result is not necessarily indicative of the lack of nano-particles but could be due to the overpowering intensity of the larger particles over the smaller ones.

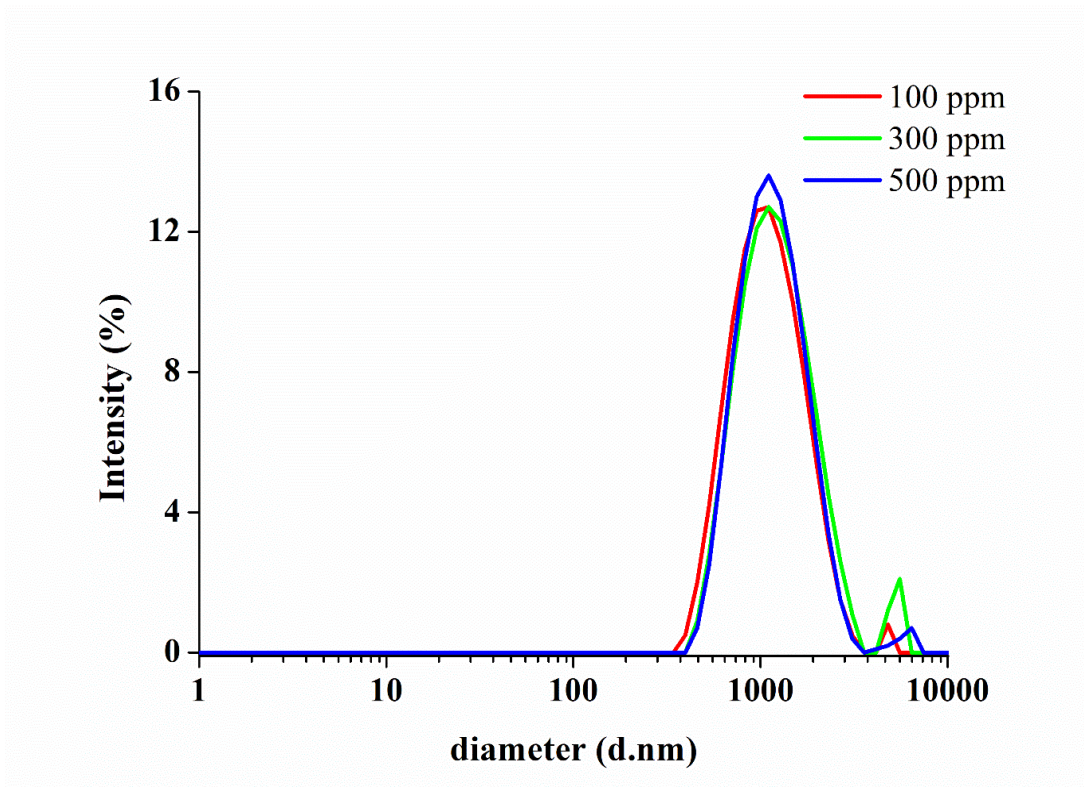


Figure 5.47: Plot of intensity versus particle size (nm) for 100, 300 and 500 ppm CNP in ethanol dispersion.

5.3.1.2 Electrochemical testing on CNP-doped MTES coatings

Electrochemical testing was carried out on MTES:TEOS 60:40 mol% coatings having an SiO₂ concentration of 2.5% that include CNPs in 100, 300 and 500 ppm concentrations (**Figure 5.48**). There is an improvement in impedance for the 100 ppm CNP concentration, which is most evident through the higher impedance obtained in the lower frequency range of the Bode plot (a), the wider arc in the Nyquist plot (c) and visibly lower I_{corr} in PD plot (d).

EEC 1 and 2 were employed to model data obtained due to two-phase system present in Bode Phase angle plot (Figure 5.48 (b)) where two dips in phase angle are clearly seen for 500ppm CNP. EEC1 and 2 fit the raw data well, thus low GOF values obtained for parameters presented in **Table 5.9**.

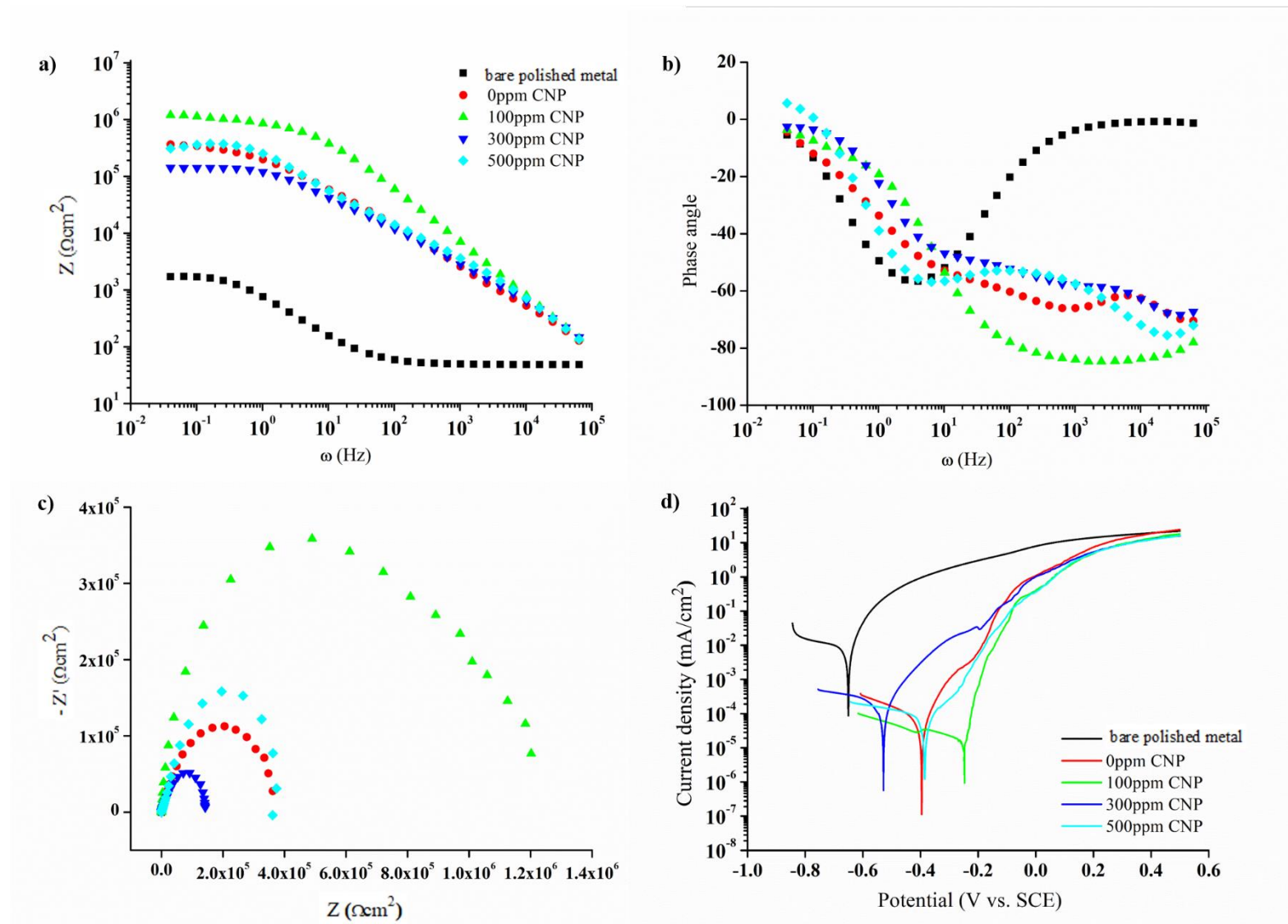


Figure 5.48: a) Bode impedance b) Bode phase angle c) Nyquist and d) Potentiodynamic plots of 2.5% SiO₂ MTES:TEOS 60:40 mol% with CNP in various concentrations. Plots include a blank coating (0 ppm CNP) and bare polished metal for comparative purposes.

Table 5.9: EIS parameters modelled using EEC 1 and 2 and I_{corr} values for CNP-doped MTES coated surfaces studied in Figure 5.48.

CNP (ppm)	R_{sol} (Ω cm ²)	R_{po} (Ω cm ²)	CPE _c		R_t (Ω cm ²)	CPE _{dl}		GOF	I_{corr} (mA cm ⁻²)
			Y_c (Ω^{-1} cm ⁻² s ^{α})	α_c		Y_{dl} (Ω^{-1} cm ⁻² s ^{α})	α_{dl}		
Bare polished metal	59.9 ±8.65	-	-	-	1.15 ×10 ³ ±1.29 ×10 ²	1.05 ×10 ⁻⁴ ±2.63 ×10 ⁻⁵	0.76 ±0.04	1.37 ×10 ⁻³ ±2.60 ×10 ⁻⁴	9.67 ×10 ⁻³ ± 7.17 ×10 ⁻³
0	24.24 ±8.48	3.88 ×10 ² ±9.71 ×10 ¹	2.00 ×10 ⁻⁸ ±2.40 ×10 ⁻⁹	0.99 ±0.12	3.89 ×10 ⁵ ±4.67 ×10 ⁴	9.15 ×10 ⁻⁷ ±1.10 ×10 ⁻⁷	0.66 ±0.08	1.08 ×10 ⁻³ ±1.29 ×10 ⁻⁴	2.33 ×10 ⁻⁴ ± 1.43 ×10 ⁻⁴
100	18.00 ±6.30	1.61 ×10 ⁵ ±4.01 ×10 ⁴	3.48 ×10 ⁻⁸ ±4.18 ×10 ⁻⁹	0.95 ±0.11	1.16 ×10 ⁶ ±1.39 ×10 ⁵	3.70 ×10 ⁻⁷ ±4.44 ×10 ⁻⁸	0.34 ±0.04	1.49 ×10 ⁻⁴ ±1.79 ×10 ⁻⁵	1.02 ×10 ⁻⁴ ± 7.17 ×10 ⁻⁶
300	22.27 ±7.79	1.69 ×10 ⁴ ±4.24 ×10 ³	6.23 ×10 ⁻⁷ ±7.47 ×10 ⁻⁸	0.71 ±0.09	1.24 ×10 ⁵ ±1.49 ×10 ⁴	4.23 ×10 ⁻⁷ ±5.07 ×10 ⁻⁸	0.80 ±0.12	2.34 ×10 ⁻³ ±2.81 ×10 ⁻⁴	2.33 ×10 ⁻⁵ ± 1.43 ×10 ⁻⁵
500	17.65 ±6.18	1.49 ×10 ⁴ ±3.72 ×10 ³	1.83 ×10 ⁻⁷ ±2.20 ×10 ⁻⁸	0.81 ±0.10	3.57 ×10 ⁵ ±4.28 ×10 ⁴	4.04 ×10 ⁻⁷ ±4.85 ×10 ⁻⁸	0.82 ±0.10	9.37 ×10 ⁻³ ±1.12 ×10 ⁻³	3.33 ×10 ⁻⁴ ± 1.43 ×10 ⁻⁴

Values for R_t presented in Table 5.9 show an increase in R_t from $3.89 \times 10^5 \pm 4.67 \times 10^4 \Omega$ cm² for 60:40 mol% MTES-TEOS coating to $1.16 \times 10^6 \pm 1.39 \times 10^5 \Omega$ cm² for 100 ppm CNP doped coatings, which is a significant improvement in corrosion protection. Higher concentrations of CNP however led to the degradation of anti-corrosion properties, 300 ppm CNP doped coatings providing an R_t value of $1.24 \times 10^5 \pm 1.49 \times 10^4 \Omega$ cm² and 500 ppm CNP doped coatings $3.57 \times 10^5 \pm 4.28 \times 10^4 \Omega$ cm², which are similar R_t values to 0 ppm CNP doped (blank MTES) coating. This trend can also be observed for R_{po} values where highest resistance was achieved through 100ppm CNP-doped coatings ($3.89 \times 10^5 \pm 7.78 \times 10^4 \Omega$ cm², Table 5.9).

5.3.1.3 Surface morphology of CNP-doped MTES coatings

Figure 5.49 shows electron micrographs of MTES-TEOS coatings with 100 ppm of CNP (a) at a higher magnification showing coatings that are smooth and defect-free and (b) at a lower magnification (larger area of coating shown) for which large particles ($>1\ \mu\text{m}$) are present and are interfering with the proper deposition of the coatings. A close-up of one of these particles is shown in **Figure 5.50** (a) for which a ring formed around the particle in which coating appears to have drawn away from the particle. EDS analysis was conducted on the areas marked by a cross in the figure, which confirmed that silica is still present (see table in Figure 5.50). This indicates that the micro-particle was deposited over the second coating and only the top coat was affected by this micro particle. The presence of microparticles will therefore increase the likelihood that only one coating is present in turn, leading to less protective areas. The coating appears to be otherwise, smooth and defect free as shown in Figure 5.49 (a) captured at a higher magnification in a region between microparticles.

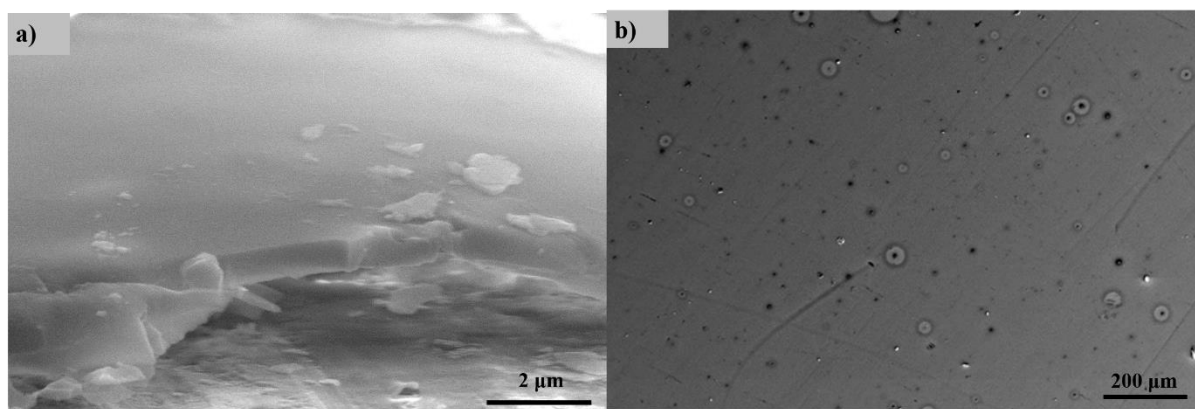


Figure 5.49: Electron micrographs of surface of double coated 2.5% MTES:TEOS 60:40 mol% + 100 ppm CNP a) at high magnification ($\times 20,000$) b) at low magnification ($\times 200$).

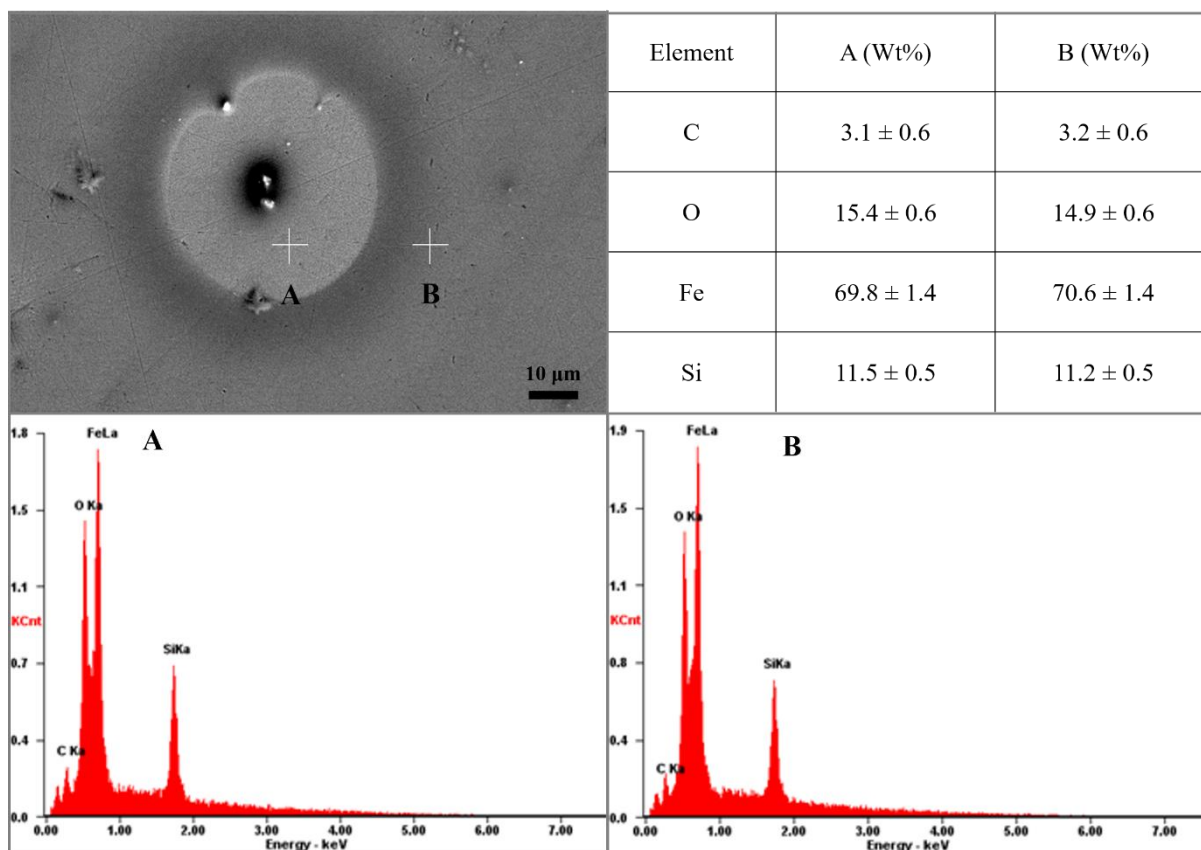


Figure 5.50: EDS analysis on surface of double coated 2.5% MTES:TEOS 60:40 mol% + 100 ppm CNP at magnification x2000 showing microparticle deposit, cross indicating the points of EDS analysis A and B. Figure features EDX analysis at points A and B together with Wt % table of elements of sampled spots A and B.

5.3.2 Addition of Stöber Nanoparticles to MTES coatings

5.3.2.1 SNP Sol characterisation through Particle size measurements

The bottom-up approach was considered as a mode of forming silica particles of the desired particles size (10-20 nm) whilst avoiding issues with dispersion and presence of microparticles in the final coatings as encountered previously with CNPs (Section 5.3.1). For such a sol, the average particle size was determined to be 25 nm which is very close to the particle size of CNPs.

Particle size measurements were carried out at various stages of the 1 M TEOS SNP sol development as shown in **Figure 5.51** (a). An initial PS of 150 nm was obtained and clouding of sol was observed within the first 30 minutes of the reaction, which gradually faded with time resulting in a clear sol nm (see explanation for OTES:TEOS sol in Section 4.2.4 also applicable for Stöber sol which is based on TEOS only as precursor). There is a shift to a lower and final PS of 26 when sampled after 24 hrs, therefore sols were allowed to develop for 24 hrs prior to use. Figure 5.51 (b) shows a shift in particle size when the concentration of TEOS is increased where PS of 20 nm is obtained for 0.22 M TEOS sol (mean PS = 20.45 ± 2.02 nm having PDI of 0.35 ± 0.09 , therefore referred to as 20 nm sol) 26 nm is obtained for 1M TEOS (mean PS = 26.50 ± 2.03 nm having PDI of 0.37 ± 0.08 , 26 nm sol) and a 56 nm PS was measured for 2 M TEOS concentration (mean PS = 56.10 ± 4.01 nm having PDI of 0.38 ± 0.08 , 56 nm sol).

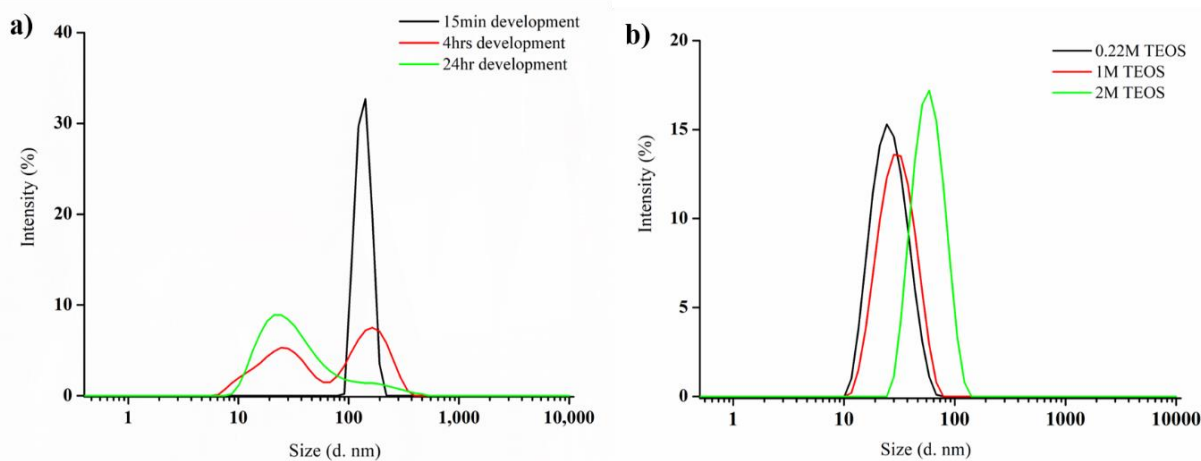


Figure 5.51: PS plots of intensity versus particle size for a) 1 M TEOS SNP at various times during sol development and b) SNP from different TEOS concentrations, conducted after 24hr sol development.

Studying the corrosion protection of coatings doped with Stöber nanoparticles was initiated using 2.5% SiO₂ 60:40 mol% MTES:TEOS sol with 26 nm SNP having the following concentrations: 1.25% SiO₂, 0.25% SiO₂ and 0.025% SiO₂. It was necessary to assess whether a change in PS has occurred when the two sols are mixed where it is assumed that if the system remains stable, then two particle populations (at 2-5 nm from acidic sol and at 26 nm from alkaline sol) should be detected by the instrument.

Particle size for all three of the above chosen concentrations of Stöber NP + MTES:TEOS sol produced a single peak in the PS data at around 34 nm. It was initially suspected that although the two sols are stable, destabilisation and agglomeration was occurring when brought together. However, even in the most concentrated system (1.25% SNP) it has been calculated and estimated that there is 1000 times more of the small nanoparticles from MTES sol than the large SNPs. In the case of the less concentrated 0.025% SNP system, there is 10,000 more small particles and still the 3 nm peak of MTES does not appear. This has been attributed to the effect of particle size on the intensity output of results where intensity is proportional to d^6 which would mean that the smaller particles are not being detected by the instrument due to the intensity generated by the larger ones.

Figure 5.52 includes PS results for when the concentration of acidic sol was unaltered (2.5% SiO₂ MTES:TEOS) whilst adding a more dilute Stöber sol a) 0.025% and b) 0.0025% SNP sol. Peaks belonging to acidified sol and Stöber sol are both evident for 0.0025% SNP sol illustrating that PS measurements conducted on a mixture of sols having different sized particles could render such analysis more difficult. Nevertheless, Figure 5.52 confirms that both nanoparticle populations are able to coexist in final sol mixture.

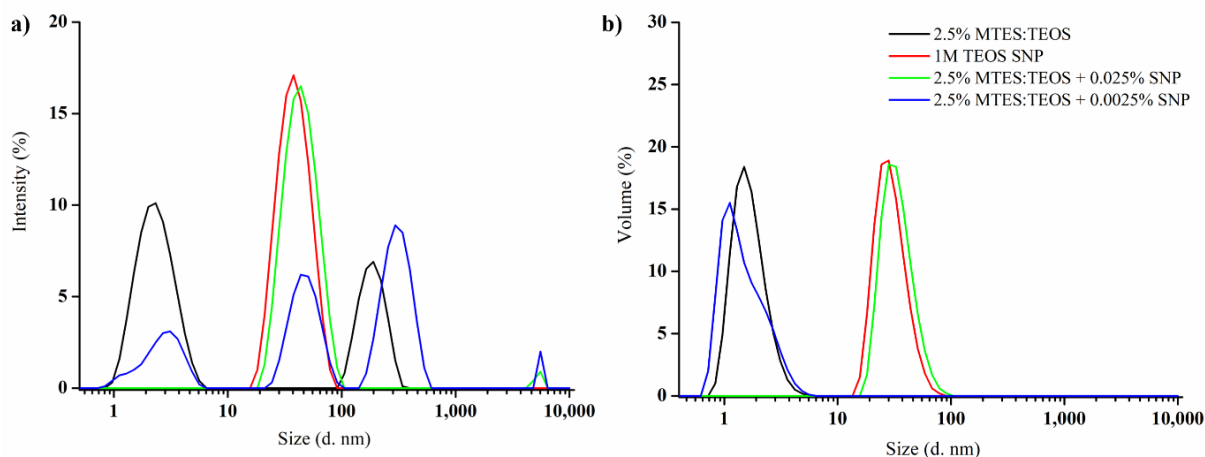


Figure 5.52: Particle size measurements obtained for 2.5% 60:40 mol% MTES:TEOS sol, 1M TEOS SNP sol (26 nm SNP), mixture of 2.5% 60:40 mol% MTES:TEOS with 0.025% SNP and 2.5% 60:40 mol% MTES:TEOS with 0.0025% SNP. Results are represented as a) % intensity and b) % volume versus size plots.

5.3.2.2 Electrochemical evaluation of SNP-doped MTES coatings

Figure 5.53 shows electrochemical results obtained when employing different concentrations of TEOS to produce the SNP under alkaline conditions (for which PS differ as shown in Figure 5.51 (b)). These sols were then introduced into the 2.5% SiO₂ acidic MTES:TEOS 60:40 mol% sol at a concentration of 1% SiO₂.

The inclusion of SNP into MTES systems seem to be producing coatings that are less protective when 56 nm SNP were used, seen as significantly lower impedance values in lower frequency range of the Bode Impedance plot (Figure 5.53 (a)) which also translates to a smaller arc in Nyquist plot (c) and higher I_{corr} in potentiodynamic plot (d) when compared to blank, 20 nm and 26 nm SNP MT coatings. Therefore 56 nm sols were not further considered. The 20 nm (0.22 M TEOS) sols were also not considered since they are too dilute and therefore unable to reach higher concentrations of SiO₂ obtainable by 26 nm (1 M TEOS) sols, which were the only Stöber sols deemed suitable for further analysis.

5.3.3 The origin of SiO₂ in final sol and its effect on deposited coating

In this section, the SiO₂ concentration of MTES:TEOS sol was increased to from 2.5% to 5% so as to deposit thicker coatings, which should lead to better accommodation of the larger SNPs into the coating.

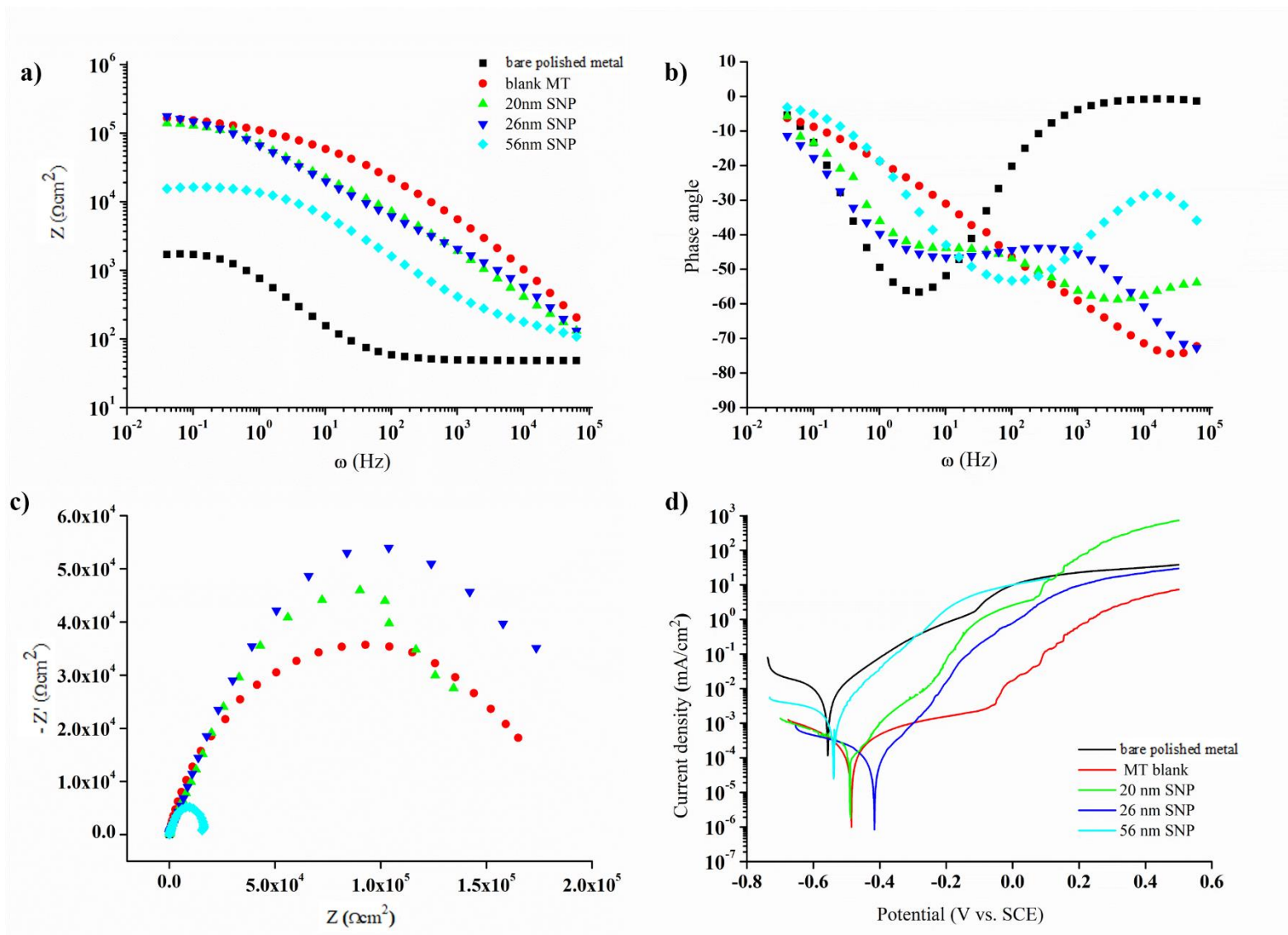


Figure 5.53: a) Bode impedance b) Bode phase angle c) Nyquist and d) Potentiodynamic plots for different sized SNP added to MTES:TEOS 60:40 mol% coatings. SNP sols were then introduced into the 2.5% SiO₂ acidic sol at a concentration of 1% SiO₂. Plots include a blank coating (0 M SNP) and bare polished metal for comparative purposes.

5.3.3.1 Coating topography

Figure 5.54 (a) shows electron micrographs of 5% SiO₂ MTES:TEOS 60:40 mol% (i) without and (ii) with the addition of 1% SiO₂ originating from 26 nm SNP sol. The addition of SNP into the coating does not appear to affect the coating's topography as both coatings are smooth and lacking surface defects. Substituting 1% SiO₂ originating from SNP (1% SNP) with TEOS in the MTES:TEOS 60:40 mol% sol by developing an MTES:TEOS 60:20 mol% sol of 4% SiO₂ to which 1% SNP is added leads to the creation of a 5% SiO₂ 60:20:20 mol% MTES:TEOS:SNP sol; i.e. this coating only differs from 5% SiO₂ MTES:TEOS 60:40 mol% coating in that 20% of the TEOS originated from SNPs. Figure 5.54 (b) illustrates that such a coating is inferior to the even and smooth MTES:TEOS 60:40 mol% coatings.

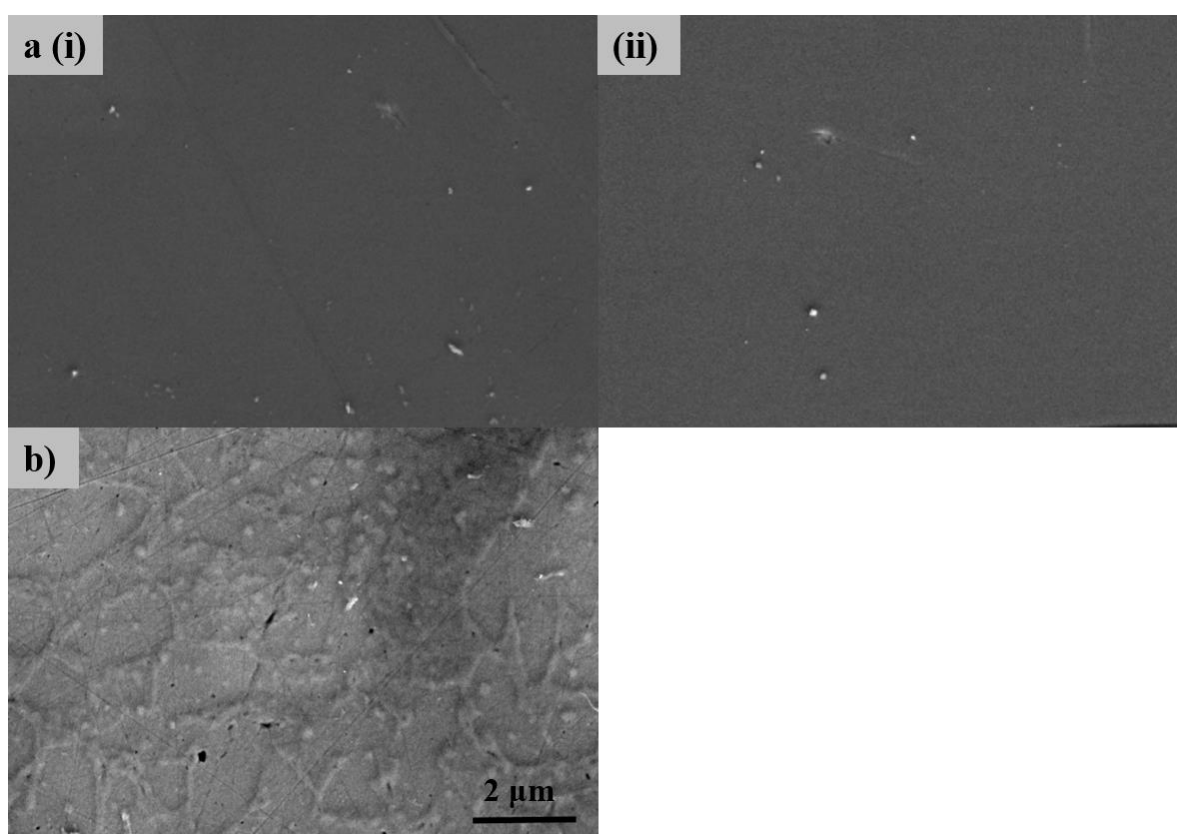


Figure 5.54: Electron micrographs of (a) (i) 5% SiO₂ MTES:TEOS 60:40 mol% (ii) 5% SiO₂ MTES:TEOS 60:40 mol% + 1% SiO₂ 26 nm SNP and (b) MTES:TEOS:SNP 60:20:20 mol% (5% SiO₂ total). Images were obtained using a $\times 2000$ magnification.

5.3.3.2 Electrochemical testing

Figure 5.55 illustrates electrochemical results for coatings presented in Figure 5.54. EIS parameters presented in **Table 5.10** have been extracted by modelling of data in Figure 5.55 using EEC 1 and 2 due to two-time constant system seen in Phase angle plot (b) for coated samples which provide a good fit as shown through low GOF values in table. Addition of 1% SNPs does not produce more protective coatings ($8.21 \times 10^4 \pm 9.85 \times 10^3 \Omega \text{ cm}^2$, see Table 5.10) when compared to the 5% SiO₂ MTES:TEOS coating on clean metal ($1.11 \times 10^5 \pm 1.33 \times 10^4 \Omega \text{ cm}^2$). Even though by adding 1% SNP may be considered as additional TEOS being incorporated (therefore making the coating more brittle due to lower overall organic content) this is not the case. In fact, when the TEOS originating from SNP was considered as part of the organic:inorganic mol% ratio (60:20:20 mol% MTES:TEOS:SNP) the coating performed poorly ($1.08 \times 10^4 \pm 1.29 \times 10^3 \Omega \text{ cm}^2$) when compared to the 60:40 mol% MTES:TEOS with and without SNP (see Table 5.10 for R_t values).

The decrease in R_t values where 5% MTES: TEOS 60:40 mol% > 5% MTES: TEOS 60:40 mol% + 1% SNP > 5% MTES: TEOS: SNP 60:20:20 mol% is accompanied by an increase in Y_{dl} as coatings are less protective. R_{po} values do not follow clear trend as for R_t values and can be attributed to the large standard error obtained. The decrease in R_t is proceeded with an increase in I_{corr} values obtained from PD plot (Figure 5.55 (d)) where 5% MTES: TEOS 60:40 mol% = $5.00 \times 10^{-5} \pm 2.48 \times 10^{-5} \text{ mA cm}^{-2}$, 5% MTES: TEOS 60:40 mol% + 1% SNP = $4.67 \times 10^{-5} \pm 1.43 \times 10^{-5} \text{ mA cm}^{-2}$, 5% MTES: TEOS: SNP 60:20:20 mol% = $1.67 \times 10^{-3} \pm 1.43 \times 10^{-3} \text{ mA cm}^{-2}$. α_c for the 5% MTES: TEOS 60:40 mol% and 5% MTES: TEOS 60:40 mol% + 1% SNP are high (0.87 ± 0.10 and 0.83 ± 0.10 respectively) compared to value for 5% MTES: TEOS: SNP 60:20:20 mol% ($\alpha_c = 0.56 \pm 0.07$). The low alpha for interface EDL might show high dispersion/ limit by diffusion.

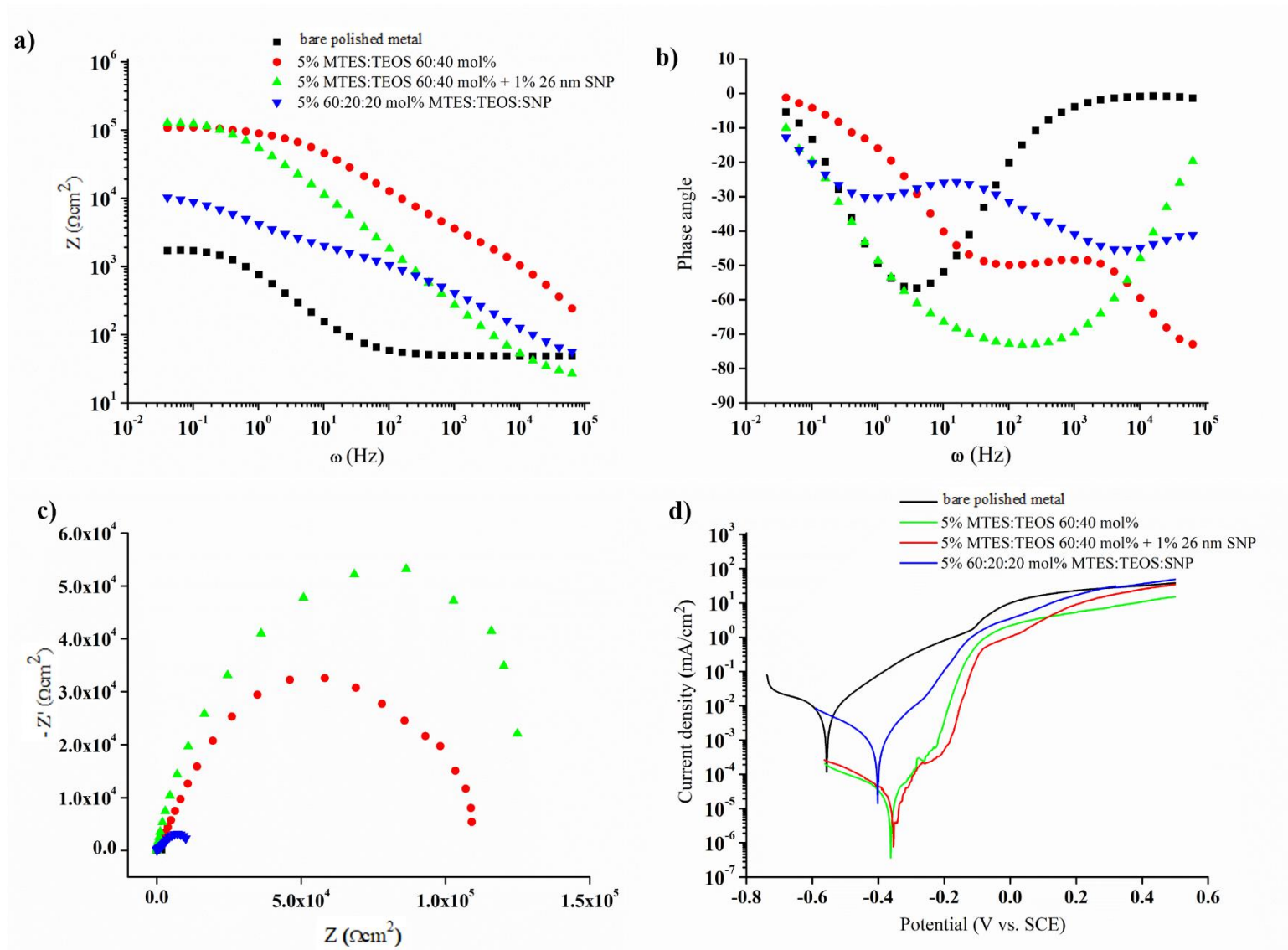


Figure 5.55: a) Bode impedance b) Bode phase angle c) Nyquist and d) Potentiodynamic plots for 5% SiO₂ MTES:TEOS 60:40 mol%, 5% SiO₂ MTES:TEOS 60:40 mol% + 1% 26 nm SNP and MTES:TEOS:SNP 60:20:20 mol% (5% SiO₂ total).

Table 5.10: EIS parameters modelled using EEC 1 and 2 and I_{corr} values for MTES:TEOS coatings with and without the addition of SNPs as obtained from results presented in Figure 5.55.

	R_{sol} (Ω cm^2)	R_{po} (Ω cm^2)	CPE _c		R_t (Ω cm^2)	CPE _{dl}		GOF	I_{corr} ($mAcm^{-2}$)
			Y_c (Ω^{-1} $cm^{-2}s^\alpha$)	α_c		Y_{dl} (Ω^{-1} $cm^{-2}s^\alpha$)	α_{dl}		
Bare metal	59.90 ± 8.65	-	-	-	1.15 $\times 10^3$ ± 1.29 $\times 10^2$	1.05 $\times 10^{-4}$ ± 2.63 $\times 10^{-5}$	0.76 ± 0.04	1.37 $\times 10^{-3}$ ± 2.60 $\times 10^{-4}$	9.67 $\times 10^{-3}$ ± 1.43 $\times 10^{-3}$
5% MTES:TEOS 60:40 mol%	15.61 ± 5.46	2.60 $\times 10^3$ ± 6.51 $\times 10^2$	5.16 $\times 10^{-8}$ ± 6.19 $\times 10^{-9}$	0.87 ± 0.10	1.11 $\times 10^5$ ± 1.33 $\times 10^4$	1.03 $\times 10^{-6}$ ± 1.24 $\times 10^{-7}$	0.65 ± 0.08	3.15 $\times 10^{-4}$ ± 3.78 $\times 10^{-5}$	5.00 $\times 10^{-5}$ ± 2.48 $\times 10^{-5}$
5% MTES:TEOS 60:40 mol% + 1% SNP	23.80 ± 8.33	6.64 $\times 10^4$ ± 1.66 $\times 10^4$	2.65 $\times 10^{-6}$ ± 3.18 $\times 10^{-7}$	0.83 ± 0.10	8.21 $\times 10^4$ ± 9.85 $\times 10^3$	4.16 $\times 10^{-6}$ ± 4.99 $\times 10^{-7}$	0.64 ± 0.08	7.15 $\times 10^{-4}$ ± 8.58 $\times 10^{-5}$	4.67 $\times 10^{-5}$ ± 1.43 $\times 10^{-5}$
5% MTES:TEOS:SNP 60:20:20 mol%	11.16 ± 3.90	2.22 $\times 10^3$ ± 5.56 $\times 10^2$	1.67 $\times 10^{-5}$ $\pm 2.00 \times 10^{-6}$	0.56 ± 0.07	1.08 $\times 10^4$ ± 1.29 $\times 10^3$	7.48 $\times 10^{-5}$ ± 8.97 $\times 10^{-6}$	0.64 ± 0.08	3.21 $\times 10^{-4}$ ± 3.86 $\times 10^{-5}$	1.67 $\times 10^{-3}$ ± 1.43 $\times 10^{-3}$

5.3.4 Effect of 26 nm SNP concentration on corrosion protection of MTES coatings

Given that a 1% SNP concentration inclusion did not produce more protective coatings (see previous Section), a range of SNP concentrations was considered and investigated. **Figure 5.56** features electrochemical data obtained for 5% SiO₂ MTES:TEOS 60:40 mol% coatings with 0% (blank), 0.1%, 1%, 2% and 5% SiO₂ from 26 nm SNP concentrations. From plots presented in Figure 5.56 it is already evident that no visible improvement in corrosion protection is obtained with the addition of SNPs to MTES coating. Similar plots have been obtained for the blank, 0.1% and 1% SNP concentrations; a further increase in SNP leads to the deterioration of impedance seen in low frequency range of the Bode impedance plot (a) and narrower arc (i.e. lower impedance) in the Nyquist plot (c), together with higher I_{corr} in potentiodynamic plots (d).

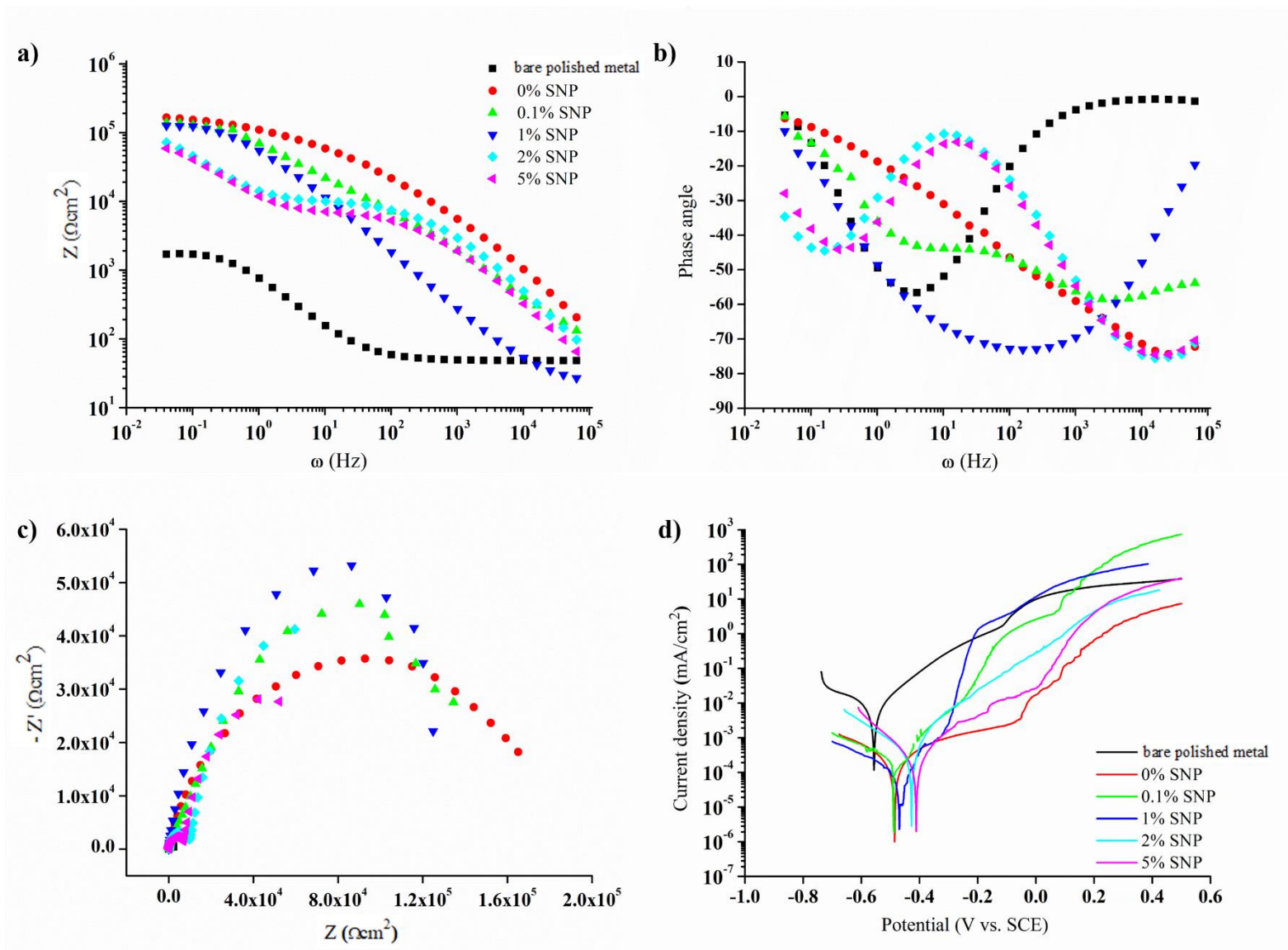


Figure 5.56: a) Bode impedance b) Bode phase angle c) Nyquist and d) Potentiodynamic plots for 5% SiO₂ MTES:TEOS 60:40 mol% with various concentrations of 26 nm SNPs.

EIS parameters (**Table 5.11**) were obtained through modelling of data using EEC1 and 2 since two-phase system is evident through two dipping points in phase angle plot (Figure 5.56 (b)), accentuated in data obtained for 2% and 5% SNPs. This is also manifested in Bode impedance plot (a) for 2% and 5% SNP where an additional slope is obtained which is not evident for 0%, 0.1% or 1% plots. Low GOF were obtained when modelling the data using EEC 1 and 2 as presented in Table 5.11. Values of R_t confirm less protective coatings were obtained upon increasing SNP concentrations (0% = $4.95 \times 10^5 \pm 5.94 \times 10^4 \Omega \text{ cm}^2$, 0.1% = $1.12 \times 10^5 \pm 1.34 \times 10^4 \Omega \text{ cm}^2$, 1% = $8.21 \times 10^4 \pm 9.85 \times 10^3 \Omega \text{ cm}^2$, 2% = $1.01 \times 10^5 \pm 1.21 \times 10^4 \Omega \text{ cm}^2$ and 5% = $8.24 \times 10^4 \pm 9.89 \times 10^3 \Omega \text{ cm}^2$), note a similar decrease in R_{po} values from table, coupled with an increase in I_{corr} values with increasing SNP concentration.

Table 5.11: EIS parameters and I_{corr} values for 5% SiO₂ 60:40 mol% MTES:TEOS coatings with various concentrations of 26 nm of SNPs as obtained from results presented in Figure 5.56.

	$R_{sol} (\Omega \text{ cm}^2)$	$R_{po} (\Omega \text{ cm}^2)$	CPE_c		$R_t (\Omega \text{ cm}^2)$	CPE_{dl}		GOF	$I_{corr} (\text{mAcm}^{-2})$
			$Y_c (\Omega^{-1} \text{ cm}^{-2} \text{ s}^\alpha)$	α_c		$Y_{dl} (\Omega^{-1} \text{ cm}^{-2} \text{ s}^\alpha)$	α_{dl}		
Bare polished metal	59.9 ±8.65	-	-	-	1.15×10^3 ±1.29 $\times 10^2$	1.05×10^{-4} ±2.63 $\times 10^{-5}$	0.76 ±0.04	1.37×10^{-3} ±2.60 $\times 10^{-4}$	9.67×10^{-3} ± 1.434 $\times 10^{-3}$
0% SNP	21.14 ±7.40	2.39×10^4 ±5.98 $\times 10^3$	2.13×10^{-8} ±2.55 $\times 10^{-9}$	0.93 ±0.11	4.95×10^5 ±5.94 $\times 10^4$	1.61×10^{-6} ±1.94 $\times 10^{-7}$	0.26 ±0.03	8.02×10^{-4} ±9.63 $\times 10^{-5}$	2.00×10^{-4} ± 2.48 $\times 10^{-4}$
0.1% SNP	20.81 ±7.28	2.21×10^4 ±5.53 $\times 10^3$	1.55×10^{-6} ±1.85 $\times 10^{-7}$	0.78 ±0.09	1.12×10^5 ±1.34 $\times 10^4$	1.34×10^{-6} ±1.61 $\times 10^{-7}$	0.68 ±0.08	4.21×10^{-3} ±5.05 $\times 10^{-4}$	1.67×10^{-4} ± 1.43 $\times 10^{-4}$
1% SNP	23.80 ±8.33	6.64×10^4 ±1.66 $\times 10^4$	4.16×10^{-6} ±4.99 $\times 10^{-7}$	0.64 ±0.08	8.21×10^4 ±9.85 $\times 10^3$	2.65×10^{-6} ±3.18 $\times 10^{-7}$	0.83 ±0.10	7.15×10^{-4} ±8.58 $\times 10^{-5}$	2.58×10^{-4} ± 1.43 $\times 10^{-4}$
2% SNP	32.21 ±11.27	9.25×10^3 ±2.31 $\times 10^3$	3.05×10^{-5} ±3.65 $\times 10^{-6}$	0.76 ±0.09	1.01×10^5 ±1.21 $\times 10^4$	2.15×10^{-7} ±2.57 $\times 10^{-8}$	0.83 ±0.10	3.10×10^{-3} ±3.72 $\times 10^{-4}$	4.67×10^{-4} ± 1.43 $\times 10^{-4}$
5% SNP	29.58 ±10.35	6.54×10^3 ±1.64 $\times 10^3$	2.95×10^{-5} ±3.54 $\times 10^{-6}$	0.77 ±0.09	8.24×10^4 ±9.89 $\times 10^3$	3.54×10^{-7} ±4.25 $\times 10^{-8}$	0.82 ±0.11	1.98×10^{-3} ±2.37 $\times 10^{-4}$	4.33×10^{-4} ± 1.43 $\times 10^{-4}$

5.3.5 Application of MTES-CNP and MTES-SNP coatings to corroded surfaces

Figure 5.57 shows electron micrographs of corroded coupons coated with 10% SiO₂ 60:40 mol% MTES:TEOS with CNP and SNPs incorporated into the coatings. The 100 ppm-containing coating was determined to be the most protective of all concentrations of CNP studied (Figure 5.48) whereas the 1% SNP was the most protective of all SNP concentrations studied (Figure 5.56), therefore were further considered for application onto corroded surfaces. Given that the micrographs have been captured with the same magnification, it is clear that the coating containing 100 ppm CNP is more cracked than that containing 1% SNP.

These observations also apply to electrochemical data presented in **Figure 5.58** which includes bare corroded metal, corroded metal coated with 100 ppm CNP-, and 1% SNP-doped MTES coatings. EIS data was modelled using EEC 1 and 2 as previously done for corroded surface since two-time constant system is evident as two dips in Bode Phase angle plot (Figure 5.58 (a)) and two arc present indicating two capacitors in Nyquist plot (Figure 5.58 (c)). EIS parameters for data presented in Figure 5.57 is tabulated in **Table 5.12** which also features I_{corr} values obtained from PD plots. There is a slight degradation in coating quality for 100 ppm CNP-containing coatings ($R_t = 5.56 \times 10^2 \pm 9.07 \times 10^1 \Omega \text{ cm}^2$), whereas higher R_t value was obtained for 1% SNP doped MTES coatings ($1.15 \times 10^3 \pm 1.25 \times 10^2 \Omega \text{ cm}^2$) compared to the blank MTES coatings ($6.93 \times 10^2 \pm 7.12 \times 10^1 \Omega \text{ cm}^2$), thus indicating more protective coatings are obtained when doping MTES coatings with 1% SNP over corroded metal surfaces.

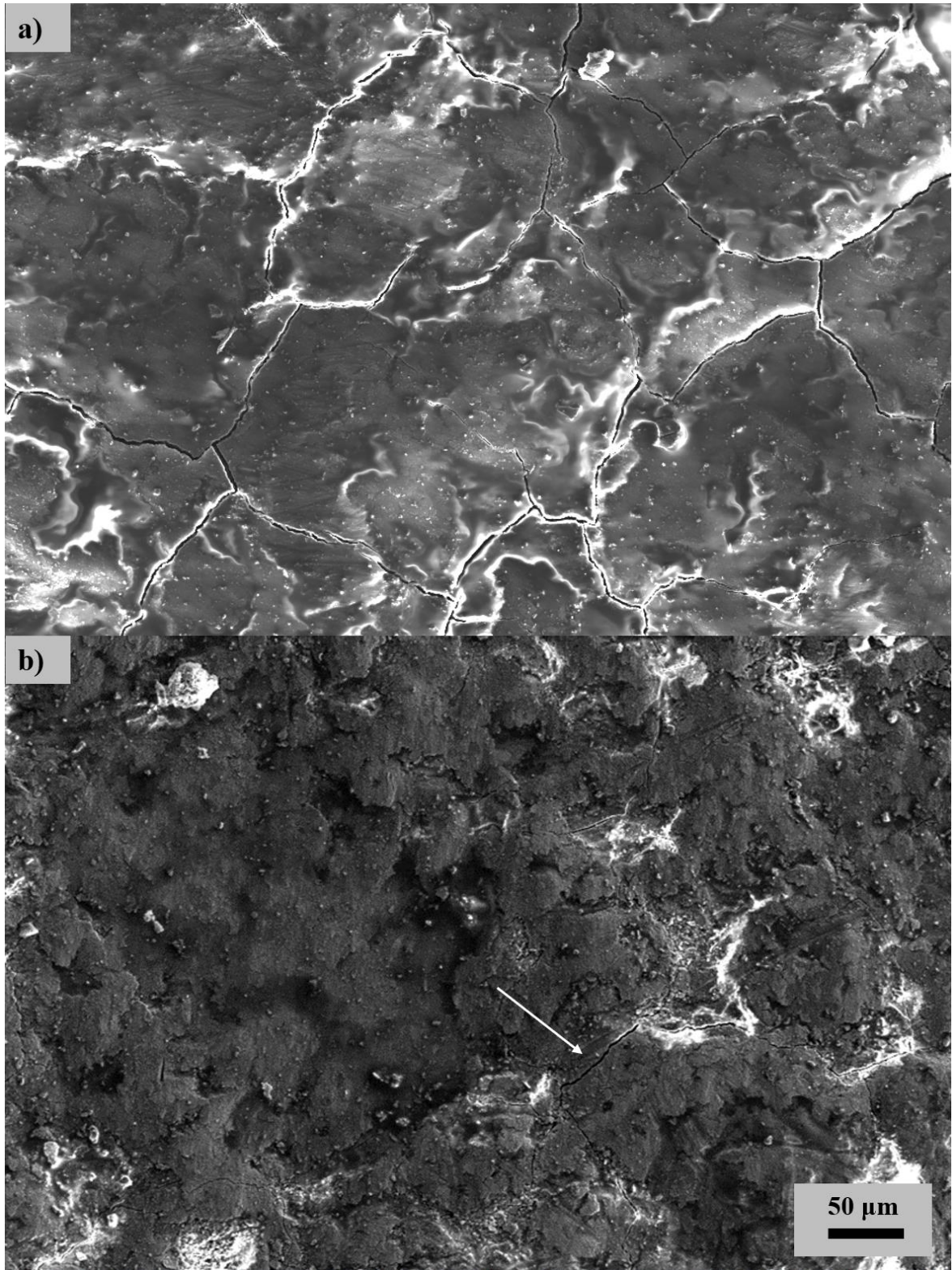


Figure 5.57: Electron micrograph of corroded coupons coated with 10% SiO₂ MTES:TEOS 60:40 mol% double coating including a) 100 ppm CNP and b) 1% SNP. Images were obtained at a $\times 500$ magnification, arrow highlights crack formation.

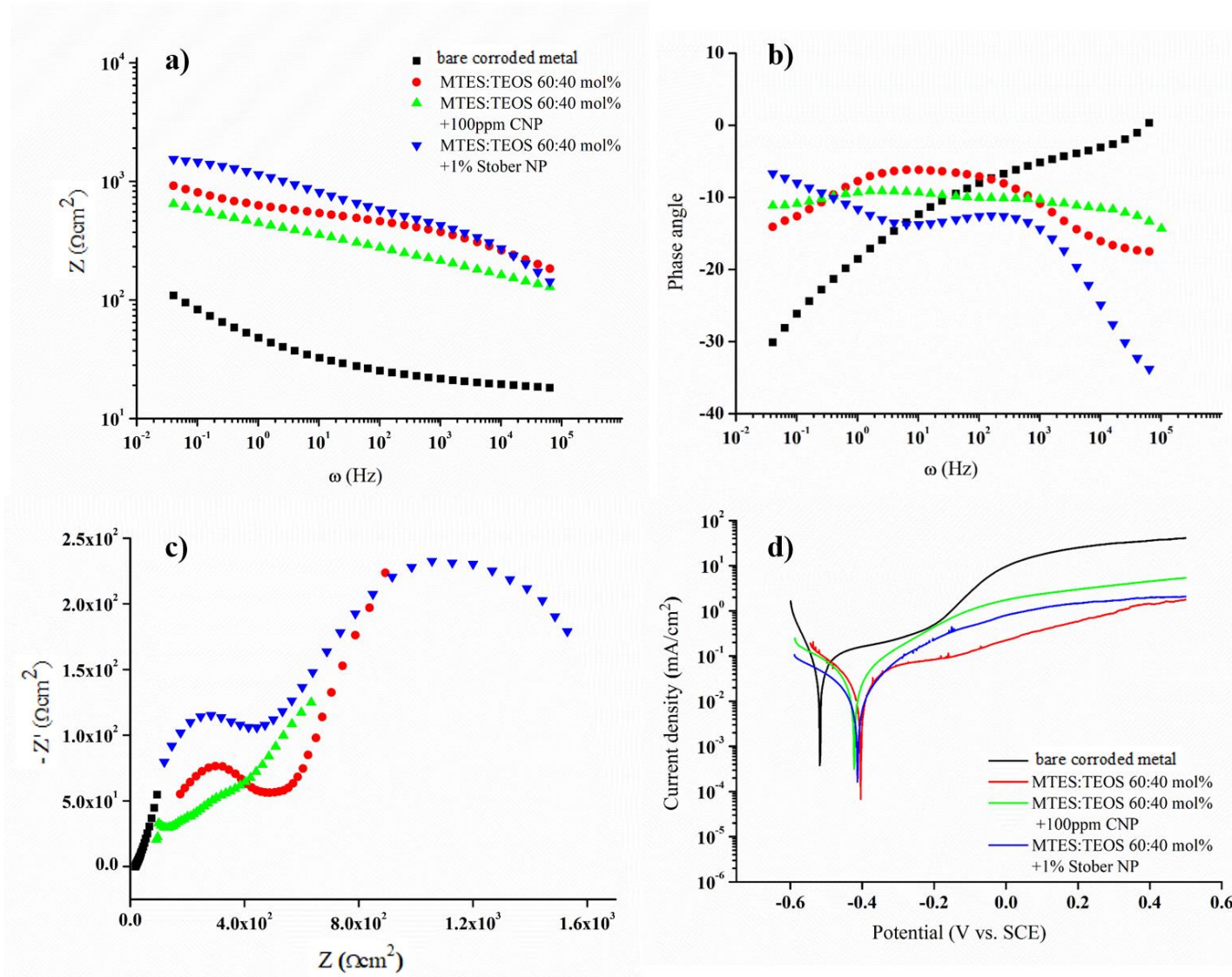


Figure 5.58 a) Bode impedance b) Bode phase angle c) Nyquist and d) Potentiodynamic plots for 10% SiO_2 60:40 mol% MTES:TEOS (blank) together with 100 ppm CNP and 1% SNP on cleaned corroded surface.

Table 5.12: EIS parameters modelled using EEC 1 and 2 and I_{corr} values for 10% SiO₂ 60:40 mol% MTES:TEOS coatings with 1% SNP and 100 ppm CNP obtained from results presented in Figure 5.58.

	R_{sol} (Ω cm ²)	R_{po} (Ω cm ²)	CPE _c		R_t (Ω cm ²)	CPE _{dl}		GOF	I_{corr} (mA cm ⁻²)
			Y_c (Ω^{-1} cm ⁻² s ^{α})	α_c		Y_{dl} (Ω^{-1} cm ⁻² s ^{α})	α_{dl}		
Bare corroded metal	38.46 ±9.66	-	-	-	1.31 ×10 ² ±2.60× 10 ¹	2.17 ×10 ⁻² ±1.86 ×10 ⁻³	0.38 ±0.05	8.42 ×10 ⁻⁵ ±1.60 ×10 ⁻⁵	1.02 ×10 ⁻¹ ± 7.17 ×10 ⁻²
MTES: TEOS 60:40 mol% (MT)	65.99 ±15.18	4.48 ×10 ² ±1.30 ×10 ²	3.73 ×10 ⁻⁵ ±5.59 ×10 ⁻⁶	0.40 ±0.06	6.93 ×10 ² ±7.12 ×10 ¹	3.45 ×10 ⁻³ ±4.14 ×10 ⁻⁴	0.33 ±0.04	3.03 ×10 ⁻⁵ ±3.64 ×10 ⁻⁶	6.33 ×10 ⁻² ± 1.43 ×10 ⁻²
MT + 100 ppm CNP	51.69 ±11.89	5.68 ×10 ² ±1.64 ×10 ²	2.63 ×10 ⁻⁵ ±3.94 ×10 ⁻⁶	0.35 ±0.05	5.56 ×10 ² ±9.07 ×10 ¹	4.45 ×10 ⁻³ ±5.34 ×10 ⁻⁴	0.27 ±0.03	4.03 ×10 ⁻⁵ ±4.84 ×10 ⁻⁶	7.33 ×10 ⁻² ± 1.43 ×10 ⁻²
MT + 1% SNP	26.05 ±5.99	4.91 ×10 ² ±1.42 ×10 ²	2.64 ×10 ⁻⁶ ±3.96 ×10 ⁻⁷	0.60 ±0.09	1.15 ×10 ³ ±1.25 ×10 ²	3.50 ×10 ⁻⁴ ±4.2 ×10 ⁻⁵	0.38 ±0.05	4.31 ×10 ⁻⁵ ±5.17 ×10 ⁻⁶	3.33 ×10 ⁻² ± 1.43 ×10 ⁻²

5.4 Addition of inorganic and organic inhibitor molecules to OIH alkoxy silane coatings for enhanced corrosion protection

In this Section, the addition of several inorganic and organic inhibitor molecules to MTES:TEOS 60:40 mol% and 20:80 mol% OTES:TEOS sols prior to deposition has been carried out so as to determine the extent (if any) of corrosion protection additionally incurred by inhibitor-doped coatings. The molecules considered are the inorganic inhibitor cerium (iii) nitrate hexahydrate (abbreviated to Ce), the organic inhibitor molecules pyrrolidine (Pyr), 1-naphthol (1-N), 1,4-naphthoquinone, 2-hydroxypyridine (2-H) and phenylbenzoate (PhB).

5.4.1 Particle size measurements of inhibitor-doped MTES/OTES sols

Figure 5.59 shows particle size analysis conducted on 60:40 mol% MTES:TEOS based sols having 2.5% SiO₂ concentration that have been doped with inhibitors Ce, Pyr, 1-N, 1,4-N, 2-H and PhB in several concentrations. Each plot presents a single representative measurement captured, the mean particle size (PS) values and polydispersity index (PDI) for which mean was formulated on a total of 9 measurements, are presented in **Table 5.13**. All featured sols produced a bimodal distribution as typical of OIH alkoxy silane sols shown in Figure 5.1, i.e. a peak of lower intensity with average particle size of ~ 2 nm together with a second peak of higher intensity corresponding to an average particle size >100 nm, labelled as P1 for smaller PS population and P2 for the larger PS population, Table 5.13. Ce molecules appear to have the greatest effect on particle sizing of MTES sols especially at higher concentrations where a broader 2 nm particle population was detected. Moreover, there appears to be a slight shift to a larger particle size of the 200 nm sized population with increasing in Ce concentration (P2 for 0 M Ce= 239.53 ± 18.34 nm, 0.0001 M Ce= 286.34 ± 17.77 nm, 0.001 M Ce= 321.24 ± 24.61 nm, and 0.01 M Ce = 372.06 ± 28.51 nm, taken from Table 5.13). Such a clear trend was not observed for organic-inhibitor doped MTES sols.

Similarly, **Figure 5.60** features 20:80 mol% OTES:TEOS coatings doped with inhibitor molecules, the mean particle size (PS) values and polydispersity index (PDI) for plots are presented in **Table**

5.14. The 2 nm population appears to not be significantly affected by the presence of inhibitor in any of the concentrations studied for most inhibitors featured except for PhB doped sols where a broader population was measured with 0.01 M PhB (Figure 5.60). Additionally, a slight shift in the larger population (P2) to a smaller particle size is noticeable with an increase in inhibitor concentration for all inhibitors studied e.g. P2 for PhB-doped OTES having PS values of 0 M = 437.83 ± 31.30 nm, 0.0001M = 384.08 ± 23.86 nm, 0.001M = 175.71 ± 13.65 nm and 0.01M = 206.82 ± 15.86 nm, see Table 5.14. Nevertheless, given the high values of PDI obtained for most measurements in Tables 5.13 and Table 5.14, larger population should be discussed with caution.

Figure 5.61 illustrates the effect of phenyl benzoate on the particle size of MTES and OTES measurements have been taken just after the addition of inhibitor to developed sols (T=0 hrs) and 24 hrs after the addition of inhibitor to developed sols (T=24 hrs) where doped sol was left to mix in flask. The mean particle size (PS) values and polydispersity index (PDI) for plots are presented in **Table 5.15**. This was carried out to determine whether inhibitor molecule such as PhB would eventually alter PS with time. A shift to a larger particle size for the larger population is seen for MTES at T=24 hrs (0M = 321.24 ± 24.61 nm, 0.0001M = 423.92 ± 32.99 nm, 0.001M = 372.06 ± 28.51 nm and 0.01M = 474.81 ± 31.97 nm, see Table 5.15) compared to T=0 hrs (0M = 321.24 ± 24.61 nm, 0.0001M = 175.71 ± 13.65 nm, 0.001M = 366.04 ± 28.51 nm and 0.01M = 252.36 ± 29.19 nm), which is expected since the growth of particles progresses with time.

Interestingly, OTES results at T= 24 hrs are not as stable as those at T=0 hrs but a shift in particle size is evident in the smaller particle population (P1) e.g. for 0.01 M PhB P1 = 1.41 ± 0.11 nm at T=0 hrs and 1.63 ± 0.12 nm at T=24hrs (see Table 5.15) together with the appearance of an additional peak at ≈ 10 nm which means that the organic inhibitor is allowing for particle growth to occur. There is also a shift to larger particle size of the larger particle population (P2) when comparing T= 0 and 24 hrs for all concentrations considered e.g. for 0.01 M PhB P2 = 206.82 ± 15.86 nm at T=0 hrs and 658.34 ± 51.28 nm at T=24hrs (see Table 5.15).

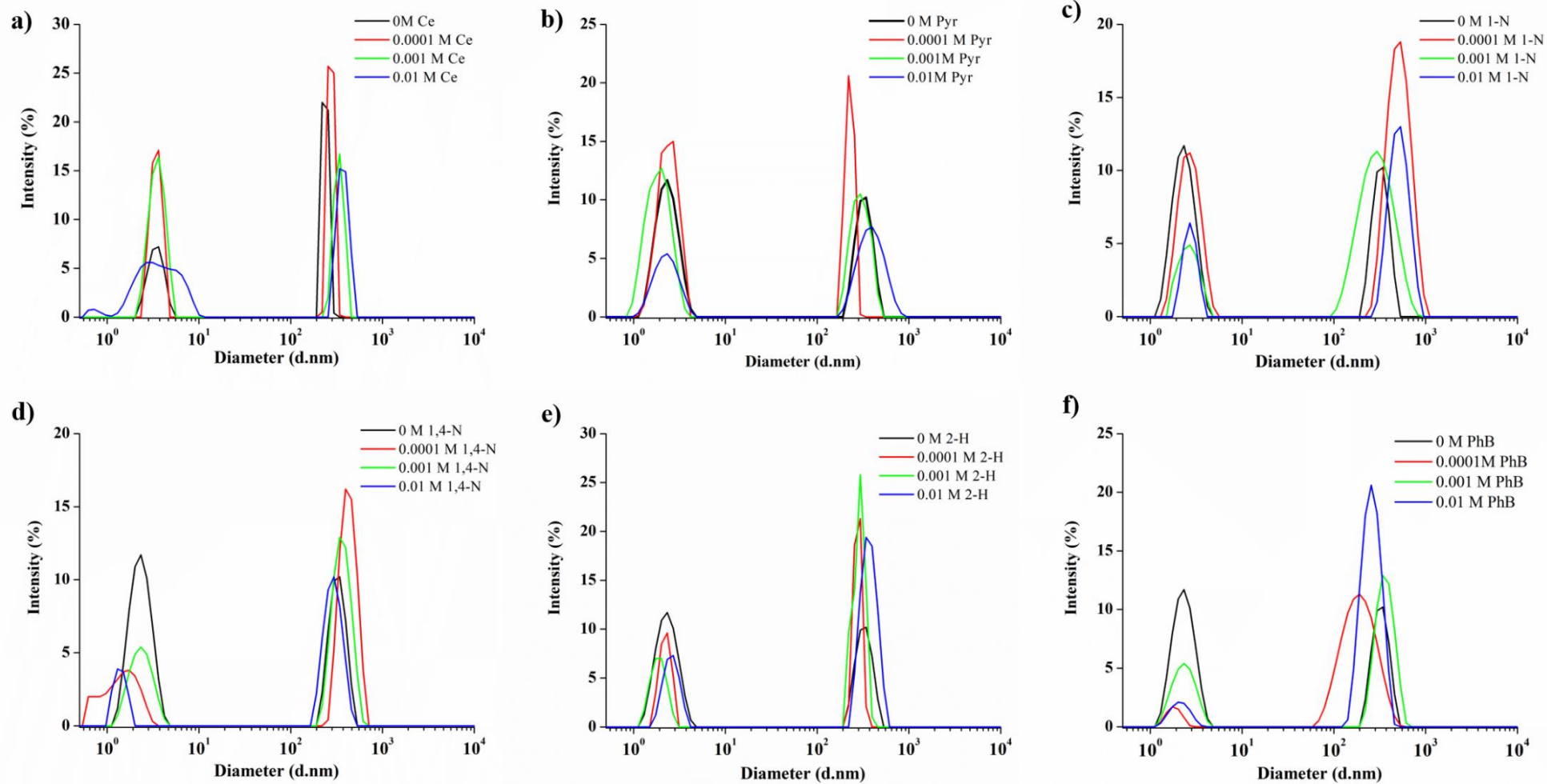


Figure 5.59: Particle size plots for 2.5% SiO₂ MTES:TEOS 60:40 mol% sols doped with a) cerium (iii) nitrate hexahydrate (Ce), b) pyrrolidine (Pyr), c) 1-naphthol (1-N), d) 1,4-naphthoquinone (1,4-N), e) 2-hydroxypyridine (2-H), f) phenylbenzoate (PhB) in 0.0001, 0.001 and 0.01 M concentrations. The measurements have been taken just after the addition of inhibitor to developed sols. Plots also feature 0 M inhibitor concentrations (blank MTES:TEOS 60:40 mol%) for comparative reasons.

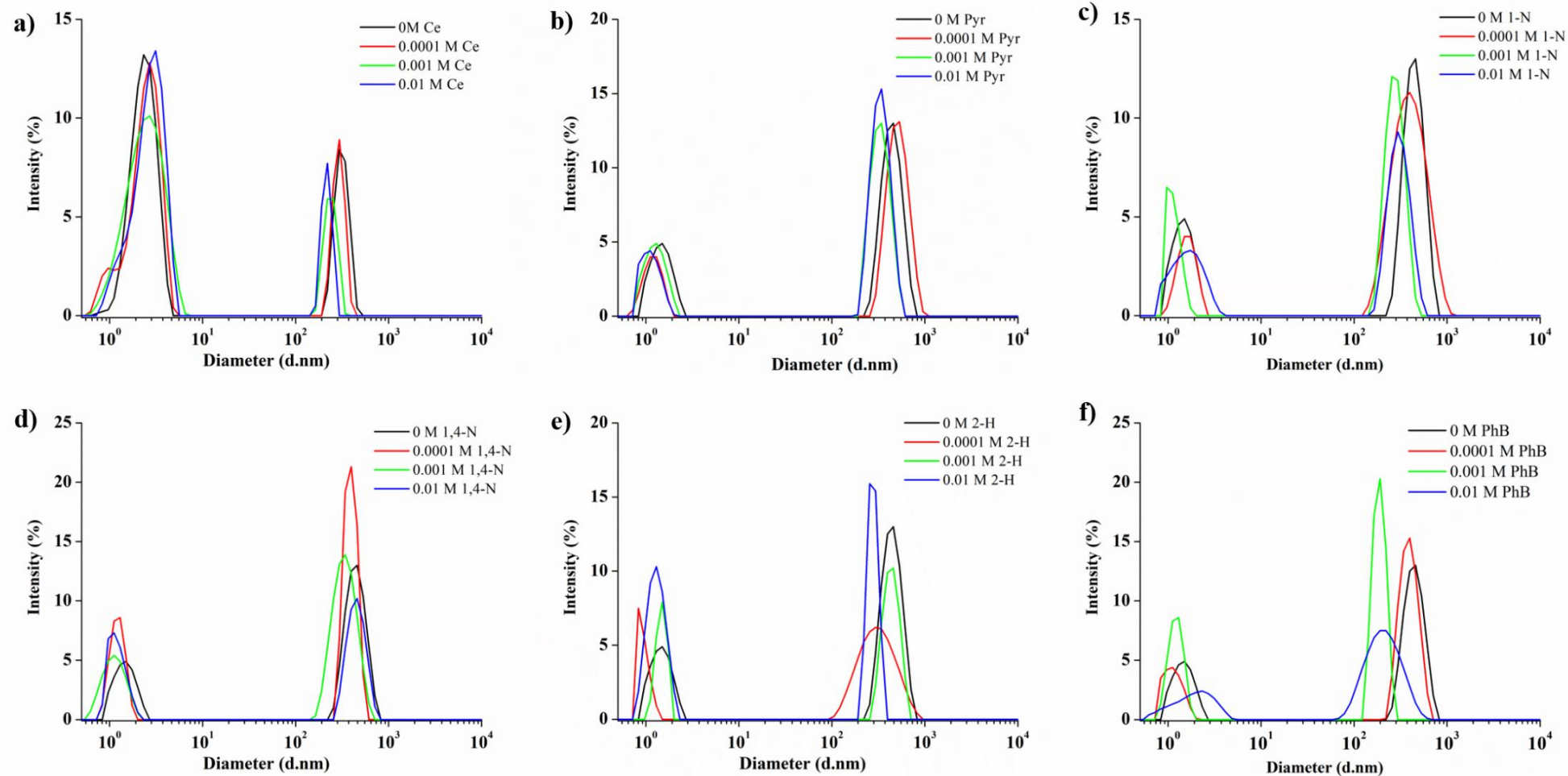


Figure 5.60: Particle size plots for 2.5% SiO₂ OTES:TEOS 20:80 mol% sols doped with a) cerium (iii) nitrate hexahydrate (Ce), b) pyrrolidine (Pyr), c) 1-naphthol (1-N), d) 1,4-naphthoquinone (1,4-N), e) 2-hydroxypyridine (2-H), f) phenylbenzoate (PhB) in 0.0001, 0.001 and 0.01 M concentrations. The measurements have been taken just after the addition of inhibitor to developed sols. Plots also feature 0 M inhibitor concentrations (blank OTES:TEOS 20:80 mol%) for comparative reasons.

Table 5.13: Particle size measurements for 2.5% SiO₂ MTES:TEOS 60:40 mol% sols doped with cerium (iii) nitrate hexahydrate (Ce), pyrrolidine (Pyr), 1-naphthol (1-N), 1,4-naphthoquinone (1,4-N), 2-hydroxypyridine (2-H), phenylbenzoate (PhB) in 0.0001, 0.001 and 0.01 M concentrations. The measurements have been taken just after the addition of inhibitor to developed sols. Plots also feature 0 M inhibitor concentrations (blank MTES:TEOS 60:40 mol%) for comparative reasons.

Inhibitor Concentration (M)		P1		P2		PDI	
		Mean PS (nm)	St Error (nm)	Mean (nm)	St Error (nm)	Mean	St Error
Ce	0	3.74	0.25	239.53	18.34	0.66	0.05
	0.0001	3.56	0.16	286.34	17.77	0.79	0.03
	0.001	3.34	0.26	321.24	24.61	0.69	0.09
	0.01	3.81	0.39	372.06	28.51	0.97	0.02
Pyr	0	2.15	0.17	321.24	24.61	0.85	0.07
	0.0001	2.53	0.19	235.67	18.34	0.71	0.06
	0.001	1.83	0.14	286.34	17.77	0.77	0.09
	0.01	2.22	0.16	366.04	28.51	0.71	0.12
1-N	0	2.22	0.16	316.06	24.61	0.66	0.05
	0.0001	2.84	0.21	490.92	38.21	0.80	0.05
	0.001	3.03	0.19	277.39	21.24	0.69	0.10
	0.01	3.03	0.19	490.92	38.21	0.84	0.08
1,4-N	0	2.12	0.16	310.87	23.35	0.74	0.10
	0.0001	1.63	0.12	430.88	32.99	0.73	0.16
	0.001	2.39	0.32	378.07	27.05	0.76	0.08
	0.01	1.41	0.11	268.43	20.15	0.72	0.08
2-H	0	2.08	0.14	316.06	24.61	0.74	0.09
	0.0001	2.19	0.17	281.87	20.15	0.64	0.02
	0.001	1.86	0.14	263.96	17.77	0.74	0.10
	0.01	2.61	0.16	326.43	23.35	0.84	0.08
PhB	0	2.19	0.17	321.24	24.61	0.76	0.11
	0.0001	1.89	0.14	175.71	13.65	0.78	0.13
	0.001	2.34	0.24	366.04	28.51	0.70	0.10
	0.01	2.26	0.14	252.36	29.19	0.78	0.01

Table 5.14: Particle size measurements for 2.5% SiO₂ OTES:TEOS 20:80 mol% sols doped with cerium (iii) nitrate hexahydrate (Ce), pyrrolidine (Pyr), 1-naphthol (1-N), 1,4-naphthoquinone (1,4-N), 2-hydroxypyridine (2-H), phenylbenzoate (PhB) in 0.0001, 0.001 and 0.01 M concentrations. The measurements have been taken just after the addition of inhibitor to developed sols. Plots also feature 0 M inhibitor concentrations (blank OTES:TEOS 20:80 mol%) for comparative reasons.

Inhibitor Concentration (M)		P1		P2		PDI	
		Mean PS (nm)	St Error (nm)	Mean (nm)	St Error (nm)	Mean	St Error
Ce	0	2.49	0.19	321.24	24.61	0.67	0.10
	0.0001	2.98	0.21	277.39	21.24	0.74	0.12
	0.001	2.53	0.19	243.40	17.40	0.73	0.10
	0.01	2.89	0.22	203.48	15.86	0.81	0.07
Pyr	0	1.41	0.11	416.97	31.30	0.71	0.10
	0.0001	1.20	0.09	482.87	36.25	0.61	0.02
	0.001	1.22	0.09	316.06	24.61	0.71	0.09
	0.01	1.03	0.08	343.64	35.69	0.69	0.07
1-N	0	1.36	0.10	423.92	32.99	0.75	0.01
	0.0001	1.60	0.12	372.06	28.51	0.73	0.07
	0.001	1.05	0.08	277.39	21.24	0.70	0.15
	0.01	1.63	0.18	316.06	24.61	0.71	0.10
1,4-N	0	1.39	0.11	430.88	32.99	0.81	0.07
	0.0001	1.20	0.09	360.03	27.05	0.67	0.10
	0.001	1.12	0.12	321.24	24.61	0.77	0.05
	0.01	1.10	0.05	423.92	32.99	0.63	0.05
2-H	0	1.39	0.11	430.88	32.99	0.68	0.12
	0.0001	0.95	0.04	310.87	23.35	0.74	0.09
	0.001	1.41	0.11	416.97	31.30	0.68	0.06
	0.01	1.25	0.08	286.34	17.77	0.82	0.07
PhB	0	1.41	0.11	437.83	31.30	0.63	0.05
	0.0001	1.08	0.07	384.08	23.86	0.66	0.08
	0.001	1.20	0.09	175.71	13.65	0.76	0.03
	0.01	2.26	0.14	206.82	15.86	0.93	0.02

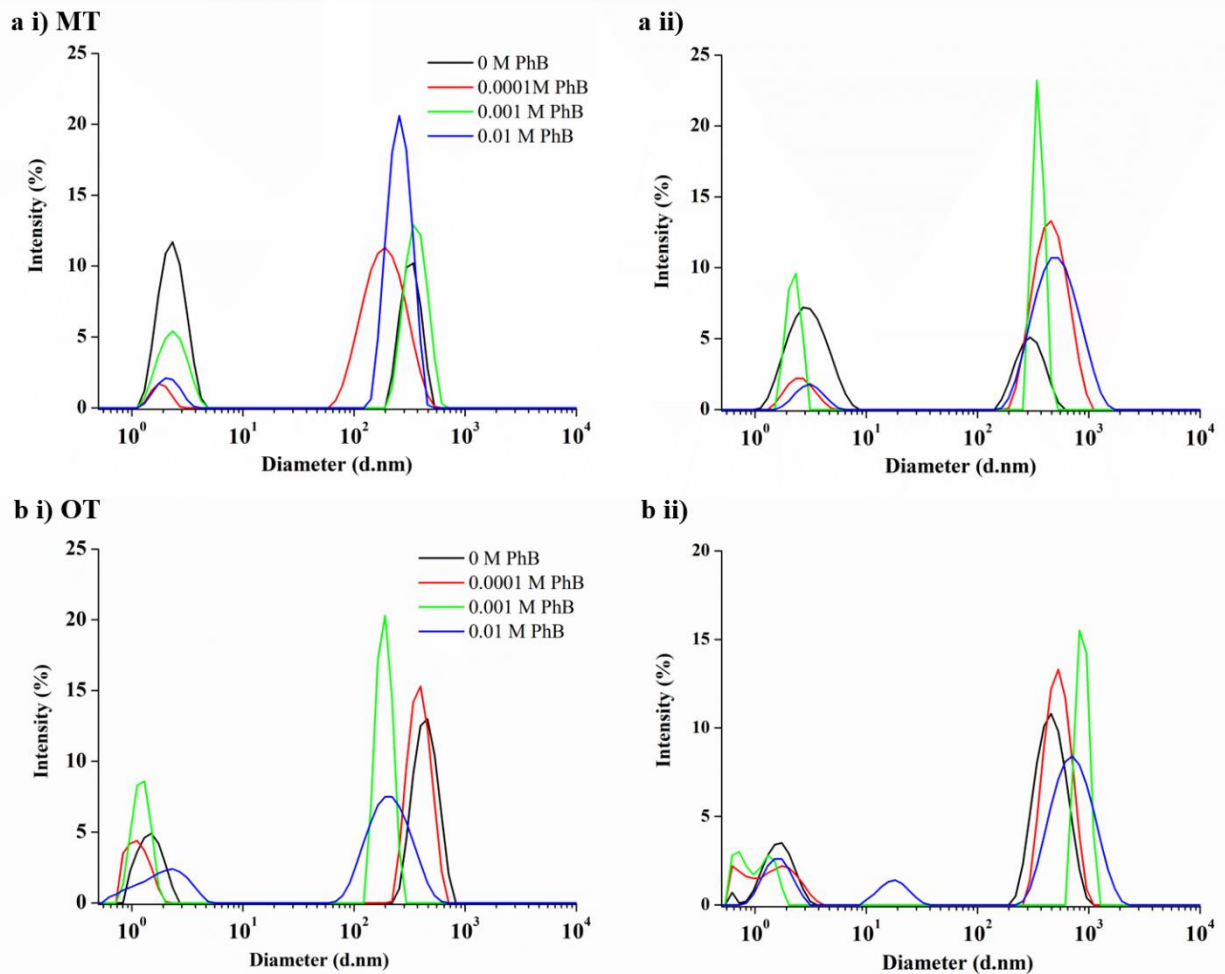


Figure 5.61: Particle size plots obtained for various concentrations of phenylbenzoate in a) MTES:TEOS 60:40 mol% sol and b) OTES:TEOS 20:80 mol% sol i) just after the addition of inhibitor to developed sols (T=0) and ii) 24 hrs after the addition of inhibitor to developed sols (T= 24 hrs).

Table 5.15: Mean particle size measurements obtained for various concentrations of phenylbenzoate in MTES:TEOS 60:40 mol% and OTES:TEOS 20:80 mol% sols just after the addition of inhibitor to developed sols (T=0) and 24 hrs after the addition of inhibitor to developed sols (T= 24 hrs).

Inhibitor Concentration (M)		P1		P2		PDI	
		Mean PS (nm)	St Error (nm)	Mean (nm)	St Error (nm)	Mean	St Error
MTES 0 hrs	0	2.19	0.17	321.24	24.61	0.76	0.11
	0.0001	1.89	0.14	175.71	13.65	0.78	0.13
	0.001	2.34	0.24	366.04	28.51	0.70	0.10
	0.01	2.26	0.14	252.36	29.19	0.78	0.01
MTES 24 hrs	0	2.89	0.22	321.24	24.61	0.76	0.08
	0.0001	2.57	0.18	423.92	32.99	0.77	0.07
	0.001	2.26	0.14	372.06	28.51	0.81	0.07
	0.01	3.24	0.31	474.81	31.97	0.77	0.13
OTES 0 hrs	0	1.41	0.11	437.83	31.30	0.63	0.05
	0.0001	1.08	0.07	384.08	23.86	0.66	0.08
	0.001	1.20	0.09	175.71	13.65	0.76	0.03
	0.01	2.26	0.14	206.82	15.86	0.93	0.02
OTES 24 hrs	0	1.63	0.12	437.83	31.30	0.72	0.06
	0.0001	1.98	0.09	507.03	36.25	0.80	0.09
	0.001	1.41	0.11	853.98	57.50	0.75	0.07
	0.01	1.58	0.12	658.34	51.28	0.94	0.05

5.4.2 IR spectra of inhibitor-doped MTES/OTES sols

Figures 5.62 and **5.63** feature IR spectra of 60:40 mol% MTES:TEOS and 20:80 mol% OTES:TEOS sols that have been doped with a 0.01 M concentration of inhibitors. These sols were cured at 60 °C for 4 hours, following the curing procedure for inhibitor-doped OIH alkoxysilane coatings (see Section 3.3.2.4). The white solids formed after curing were mixed with KBr and made into disks. **Figure 5.64** features standard spectra for six inhibitor molecules studied (taken from [217]).

Figure 5.64 (a) shows IR spectrum for cerium (iii) nitrate hexahydrate for which Ce-O stretch occurs at 550 cm⁻¹[218]. Broad O-H stretch due to water occurs at 3500-3000 cm⁻¹. Two principle peaks belonging to nitrate anion arise: peak at around 1550 cm⁻¹ is due to the characteristic N-O asymmetric stretch and N-O symmetric stretch from 1350 cm⁻¹ [219,220]. These two peaks are also present in MTES and OTES spectra (Figure 5.62 (b) which are absent in the blank spectra (Figure

5.62 (a)), thus indicating the presence of inhibitor following curing of the sols. The intensity of the N-O peaks in OIH alkoxysilane sols will be significantly less than those found in cerium nitrate spectrum since lower amounts of inhibitor is present in sols, for which main peaks are due to Si-O and Si-OH bonds. This also applies for other inhibitor doped XTES:TEOS powders analysed.

The spectrum of pyrrolidine is shown in Figure 5.64 (b). Pyrrolidine, being a secondary amine, shows one characteristic N-H stretch at around 3300 cm^{-1} . An N-H wag occurs at around 700 cm^{-1} whereas the C-N stretch occurs at around 1100 cm^{-1} [220]. Strong groups of peaks occur in the 3000 cm^{-1} region of the spectrum which is due to C-H symmetric and asymmetric stretching. When comparing this spectrum to inhibitor doped XTES:TEOS spectra in Figure 5.62 (c), peaks due to N-H and C-N do not clearly show up since they occur in the same regions as silica peaks. However, a more intense signal was measured in the organic part (3000 cm^{-1}) due to the presence of C-H bonds in pyrrolidine in addition to organics originating from XTES, which is more evident in the OTES:TEOS coating (Figure 5.62 (c ii)) when compared to blank (Figure 5.62 (a ii)).

The spectrum of 1-naphthol is shown in Figure 5.64 (c). Spectrum of 1-naphthol possesses several peaks due to aromatic C-H stretches in the 3000 cm^{-1} region. C-C stretches in the aromatic ring appear at around 1500 cm^{-1} , in-plane C-H bending occur at around 1000 cm^{-1} , whereas out-of-plane C-H bending occur as two sharp peaks at around 700 cm^{-1} . The broad peak at around 3300 cm^{-1} is due to O-H stretch. The sharpest peak pertaining to 1-naphthol occurs in the 700 cm^{-1} region is not clearly visible in XTES spectra in Figure 5.62 (d) due to silica peaks occurring in that region, although OTES plot of Figure 5.62 (d ii) appears to show main peak at 700 cm^{-1} that consists of two peaks rather than just one as in blank (Figure 5.62 (a ii)). Broad characteristic O-H peak at $3500\text{--}3300\text{ cm}^{-1}$ (Figure 5.64 (c)) is especially evident in the 1-naphthol doped MTES spectrum (Figure 5.62 (d i)), less so in Figure 5.62 (d ii) for OTES. Additionally, greater intensity was obtained in 3000 cm^{-1} region due to C-H asymmetric/symmetric stretching originating from both MTES/OTES and naphthol, therefore larger peaks at 3000 cm^{-1} occurred in Figures 5.62 (d) compared to relevant blanks (Figures 5.62 (a)).

Spectrum of 1,4-naphthoquinone shown in Figure 5.64 (d). This spectrum possesses several peaks due to aromatic C-H stretches in the 3000cm^{-1} region. C-C stretches in the aromatic ring appear at around 1500 cm^{-1} , whereas out-of-plane C-H bending occur as a sharp peak at around 700 cm^{-1} . A strong characteristic peak occurs at around 1700 cm^{-1} which is due to the C=O stretch. This peak is in fact, has also risen in the MTES/OTES plots (Figures 5.63 b) and absent in blanks (Figure 5.63 (a)) indicating the presence of the inhibitor in cured MTES/OTES powders. Figures 5.63 (b) also possess more intense peaks in the 3000 cm^{-1} region compared to blanks due to the additional organic contribution from inhibitor molecules.

Spectrum of 2-hydroxypyridine is shown in Figure 5.64 (e). Since 2-hydroxypyridine is a tertiary amine, an N-H stretch at 1100 cm^{-1} will not be produced, nor an N-H wag at 700 cm^{-1} . The C-N stretch occurs at 1250 cm^{-1} (as for pyrrolidine Figure 5.64 (b)). Groups of peaks occur in the 3000 cm^{-1} region of the spectrum which are due to C-H symmetric and asymmetric stretching. C-C stretches in the heteroaromatic ring appear at around 1500 cm^{-1} , in-plane C-H bending occur at around 1000 cm^{-1} , whereas out-of-plane C-H bending occur as two sharp peaks at around 750 cm^{-1} . A broad O-H peak at $3500\text{-}3300\text{ cm}^{-1}$ was not present, and it has been attributed to the ability of 2-hydroxypyridine to exist in its tautomeric form, 2-pyridone; the latter form is known to predominate in polar solvents[221] (see structure in Figure 5.64 (e) marked as '2-pyr'). The presence of this form can be seen through a sharp peak occurring at around 1650 cm^{-1} which has been attributed to C=O stretch of 2-pyridone. This peak can be seen to occur in 2-hydroxypyridine-doped XTES plots (Figure 5.63 (c)) which is absent in their respective blanks (Figure 5.63 (a)).

IR spectrum of phenylbenzoate is shown in Figure 5.64 (f). Several peaks occur in the 3000 cm^{-1} region of the spectrum which are due to C-H symmetric and asymmetric stretching. C-C stretches in the aromatic ring appear at around 1500 cm^{-1} , in-plane C-H bending occur at around 1000 cm^{-1} , whereas out-of-plane C-H bending occur as two sharp peaks at around 700 cm^{-1} . C=O stretch occurs at around 1700 cm^{-1} and C-O stretches at around $1200\text{-}1100\text{ cm}^{-1}$. C=O stretch at 1700 cm^{-1} is small but visible in IR spectra of PhB-doped XTES sols, see Figure 5.63 (d). Also, these spectra have

stronger peaks in the 3000 cm^{-1} region compared to their blanks (Figure 5.63 (a)) due to the presence of PhB organic molecules in the OIH alkoxy silane powders.

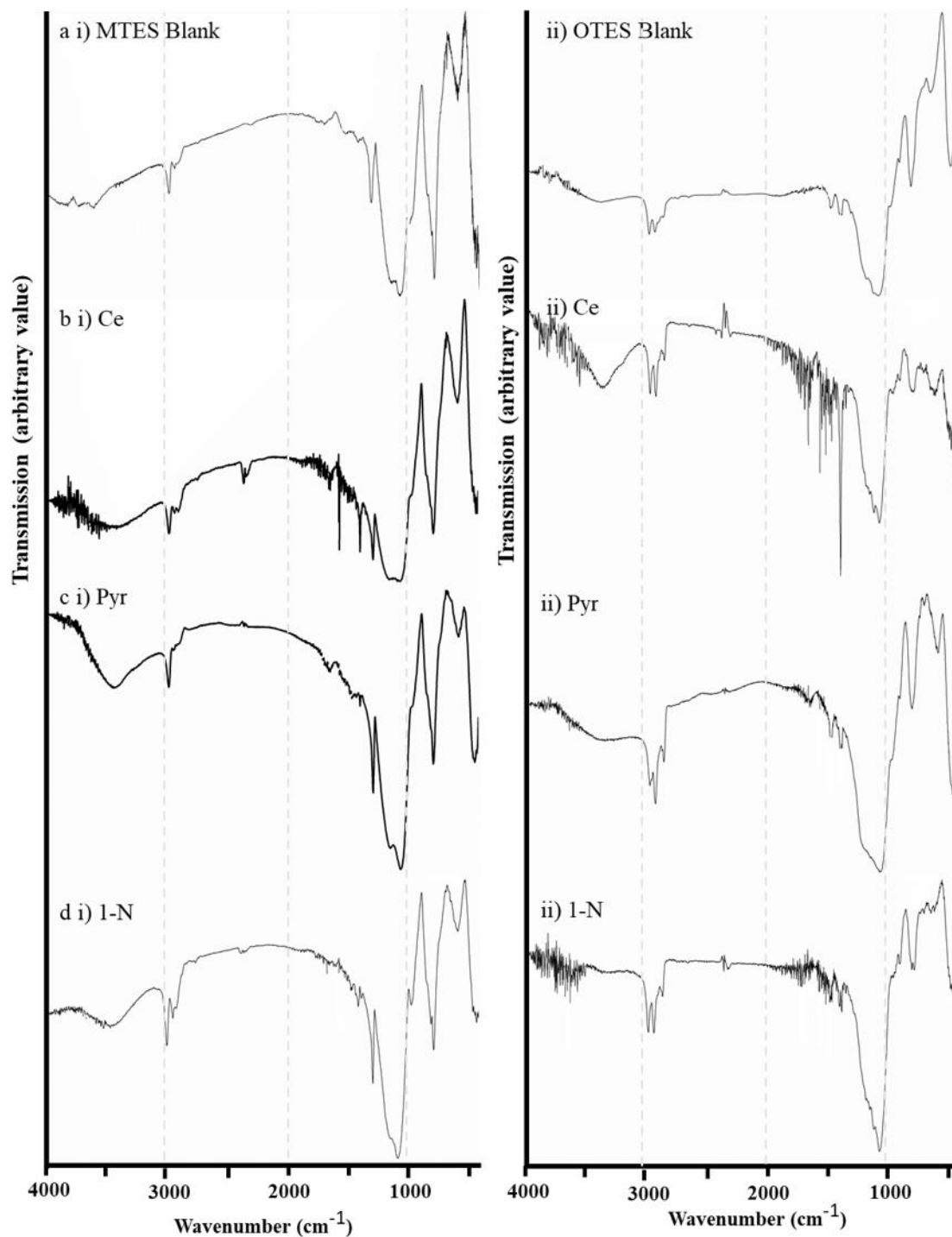


Figure 5.62: Infra-red spectra showing IR window at 4000-400 cm^{-1} region for a) 2.5% SiO_2 60:40 mol% MTES:TEOS and b) 2.5% SiO_2 20:80 mol% OTES:TEOS doped with inhibitors: i) blank coatings, ii) cerium (Ce), iii) pyrrolidine (Pyr), iv) 1-naphthol (1-N).

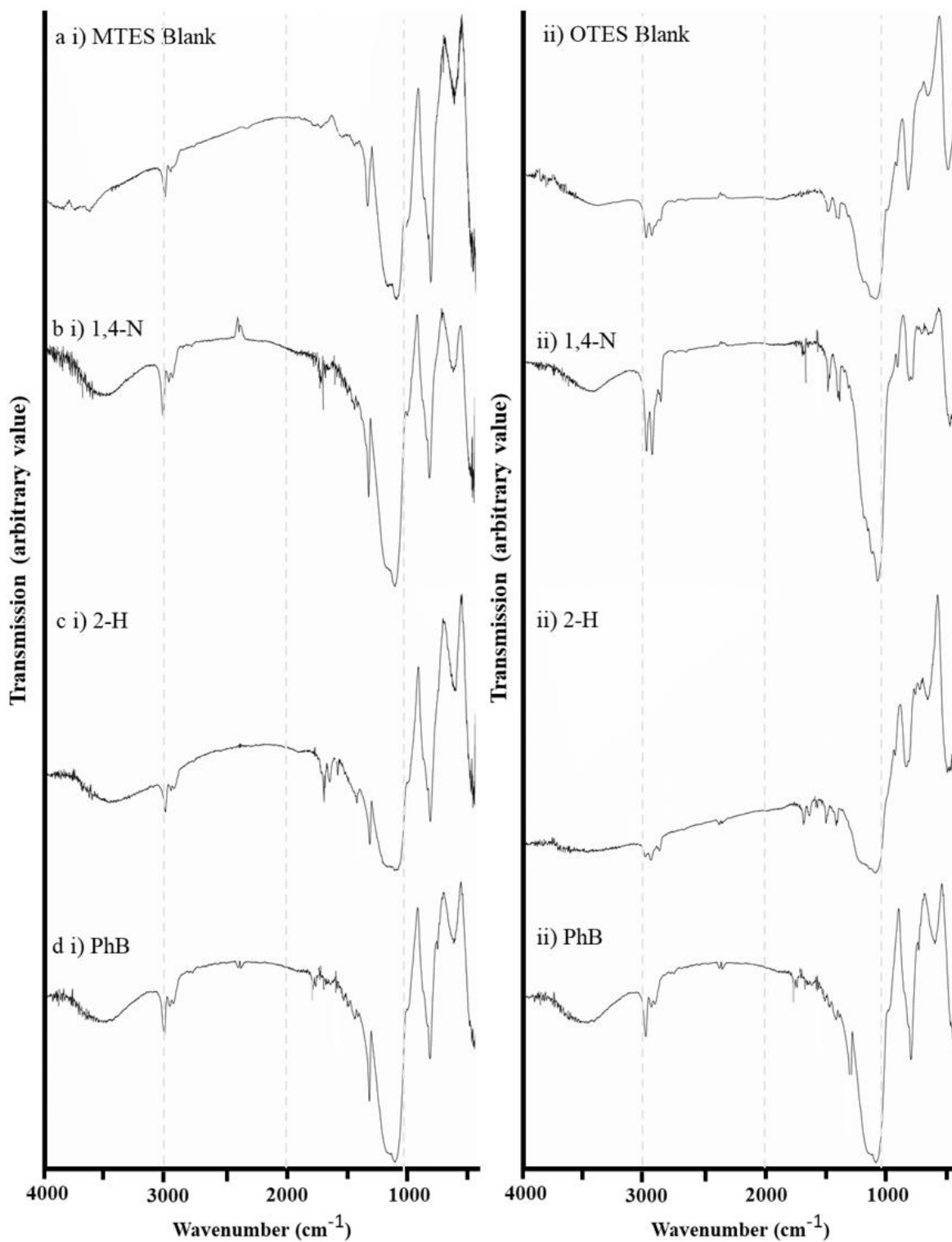


Figure 5.63: Infra-red spectra showing IR window at 4000-400 cm⁻¹ region for a) 2.5% SiO₂ 60:40 mol% MTES:TEOS and b) 2.5% SiO₂ 20:80 mol% OTES:TEOS doped with inhibitors: i) blank coatings, ii) 1,4-naphthoquinone (1,4-N), iii) 2-hydroxypyridine (2-H), iv) phenylbenzoate (PhB).

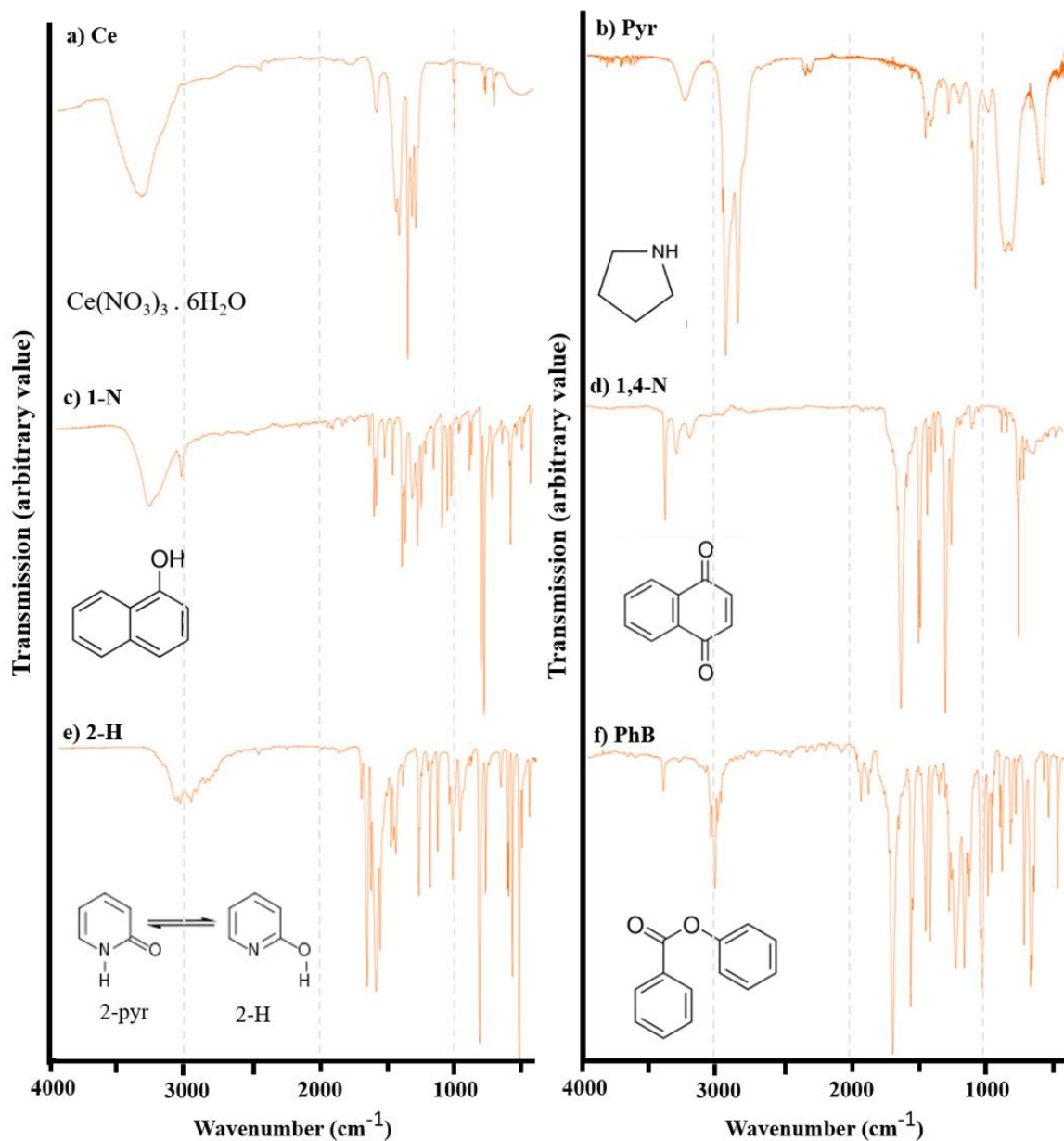


Figure 5.64: Infra-red spectra showing IR window at 4000-400 cm^{-1} region for i) cerium (iii) nitrate hexahydrate, ii) pyrrolidine (Pyr), iii) 1-naphthol (1-N) iv) 1,4-naphthoquinone (1,4-N), v) 2-hydroxypyridine (2-H), vi) phenylbenzoate (PhB). Spectra were obtained from [217].

5.4.3 Scanning Electron Microscopy

5.4.3.1 Surface Coating morphology

The incorporation of inorganic and organic inhibitors into 2.5% SiO₂ MTES:TEOS 60:40 mol% and OTES:TEOS 20:80 mol% had not visible effect on the coating integrity since smooth and defect-free coatings were still obtained at concentrations investigated. These are shown in Appendix Section (CD attached) which features 60:40 mol% MTES:TEOS inhibitor-doped coatings as presented in **Appendix G** and 20:80 mol% OTES:TEOS inhibitor-doped coatings presented in **Appendix H**.

5.4.3.2 EDS analysis

The inorganic (Ce) and organic (Pyr, 1-N, 1,4-N, 2-H and PhB) inhibitor-doped MTES and OTES coatings have been analysed for their chemical composition through EDS analysis. However, only blank and cerium-doped MTES and OTES wt% results are presented in **Table 5.16** which features the wt% of elements of interest (Fe, C, O, Si, Ce, N) for Ce-doped MTES:TEOS 60:40 mol% and OTES:TEOS 20:80 mol% coated iron samples. Only minor discrepancies in wt% of elements was recorded for the organic inhibitor doped coatings compared to blank coatings which is insufficient to warrant discussion especially when considering the lighter elements N, O and C [222]. **Appendix I** (CD attached) contains Energy (KeV) versus intensity plots for both inorganic and organic inhibitor-doped MTES and OTES coatings.

The blank (0 M inhibitor) 60:40 mol% MTES:TEOS coatings show the presence of Si ($21.6 \pm 0.4\%$), O ($54.6 \pm 1.1\%$) and C ($18.1 \pm 0.7\%$) whereas for blank 20:80 mol% OTES:TEOS coatings, higher C value ($29.6 \pm 0.6\%$) was obtained due to its higher organic content relative to MTES. Cerium nitrate-doped coatings at higher concentrations of Ce ($3.7 \pm 0.7\%$ for MTES compared to blank $0.4 \pm 0.08\%$, and $4.4 \pm 0.9\%$ for OTES compared to blank $0.9 \pm 0.2\%$), thus proving the uptake of inorganic inhibitor with sol during the deposition stage.

Table 5.16: Elemental analysis of 0.01 M Ce-doped MTES:TEOS 60:40 mol% and 20:80 mol% OTES:TEOS coated iron sample.

MTES:TEOS 60:40 mol%	C K (wt%)	N K (wt%)	O K (wt%)	Si K (wt%)	Ce L (wt%)
Blank	18.1 ± 0.7	5.0 ± 0.2	54.6 ± 1.1	21.6 ± 0.4	0.4 ± 0.08
Ce	18.6 ± 0.7	5.2 ± 0.2	52.8 ± 1.0	19.5 ± 0.8	3.7 ± 0.7
<hr/>					
OTES:TEOS 20:80 mol%	C K (wt%)	N K (wt%)	O K (wt%)	Si K (wt%)	Ce L (wt%)
Blank	29.6 ± 0.6	2.7 ± 0.6	47.9 ± 0.9	18.5 ± 0.7	0.9 ± 0.2
Ce	29.9 ± 0.6	2.9 ± 0.6	46.9 ± 0.9	19.6 ± 0.8	4.4 ± 0.9

5.4.4 Electrochemical testing

5.4.4.1 Clean metal surface coated with in/organic inhibitor-doped MTES and OTES coatings

All coatings featured in this section (Figures 5.65-5.70 for MTES and Figures 5.71-5.76 for OTES) result in a significant improvement in corrosion protection when compared to bare polished metal as seen through Bode impedance (a) plots as higher impedance values in lower frequency range of the plot, wider arc in the Nyquist plot (c) where bare metal plot is barely visible compared to coated metal, and drop in I_{corr} in potentiodynamic plots (d). Bode phase angle plots (b) show a two-time constant system seen as two dips in phase angle indicating the presence of a coating capacitor together with capacitor due to metal surface which is seen as a single dip in the bare metal phase angle plot. Electrochemical data obtained for inhibitor-doped 2.5% SiO₂ MTES:TEOS 60:40 mol% coatings is shown through Figures 5.65-5.70. Each of these figures includes a blank MTES:TEOS 60:40mol% for comparative purposes.

The Bode Impedance plot for Ce-containing MTES coatings (**Figure 5.65** (a)) illustrates a higher impedance when the inhibitor concentration was set to 0.0001 and 0.001 M, for which the 0.0001 M is slightly more protective due to the wider capacitive arc of the Nyquist plot (Figure 5.65 (c)). This

improvement in corrosion protection is also manifested in the phase angle plot (Figure 5.65 (b)) where the time constant occurring at higher frequency (approx. 10^4 Hz) dips deeper relative to the blank MTES:TEOS data. The Potentiodynamic plot (Figure 5.65 (d)) illustrates the improvement through a decrease in current density as the addition of 0.0001M and 0.001 M Ce render the coating more protective.

A further increase in Ce to 0.01 M leads to a notable decrease in the coating's protective properties compared to the lower Ce concentrations, which is evident in all plots of Figure 5.65 including the phase angle plot where the dip in angle at the higher frequency is milder. The Nyquist plot illustrates similar results for 0.01 M Ce and blank MTES:TEOS coatings. Apart from the obvious decrease in width of the capacitive arc when inhibitor concentration is increased from 0.001 to 0.01 M, it is interesting to note the beginnings of a change in shape of the 0.01 M Ce data which appears to comprise of two arcs rather than a single one. Such a shape in Nyquist plot is indicative of a failed coating which stands to reason since less protective coatings will tend to fail. Potentiodynamic data confirms the decrease in protection through an increase in current density from 0.01 to 0.001 M Ce, comparable to the blank data.

Figure 5.66 illustrates the electrochemical data for 1-naphthol-doped coatings for which a similar trend to that obtained for Ce-doped coatings i.e. an increase in inhibitor concentration leads to an improvement in protection up to a certain point where further increase in inhibitor concentration leads to the degradation of the coating. Results for 0.01 M of 1-N indicate a less protective coating relative to the coating without inhibitor. **Figure 5.67** shows plots for 1,4-naphthoquinone doped coatings where gradual improvement in corrosion protection can be observed when increasing the inhibitor concentration from 0.0001 to 0.001 M up to which point 0.01 M concentration produces the most protective coatings. A similar trend is observed for phenylbenzoate-doped coatings (**Figure 5.68**).

Figure 5.69 shows plots for 2-hydroxypyridine doped coatings where improvement in corrosion protection can be observed in all electrochemical plots, however, more notably for lower concentrations of 0.0001 and 0.001 M inhibitor; a 0.01 M concentration brings about only a slight improvement over coating without inhibitor. **Figure 5.70** illustrates electrochemical data obtained for pyrrolidine-doped coatings where there appears that inhibitor exhibits no effect in smaller inhibitor concentration (0.0001 M). Improvement in corrosion protection relative to the uninhibited coating is achieved at 0.001 M followed by a decrease in corrosion protection when concentration is further increased to 0.01 M, this coating being comparatively protective as the blank coating.

It has been established that 20:80 mol% OTES:TEOS coatings (Figure 5.24) are more protective than 60:40 mol% MTES:TEOS coatings. Therefore, it was deemed necessary to investigate the effect of the in/organic inhibitors on such coatings in the hope of obtaining further improved corrosion protection. Figures 5.71-5.76 show electrochemical data obtained when doping 2.5% SiO₂ OTES:TEOS 20:80 mol% coatings with the six inhibitors considered in this work. **Figure 5.71** presents results obtained for cerium-doped OTES:TEOS coatings which indicates a gradual decline in impedance compared to the blank 20:80 mol% OTES:TEOS coating, the least protective coatings being that containing the highest Ce concentration of 0.01 M. Similar results were obtained with 1-naphthol doped coatings (**Figure 5.72**). 1,4-naphthoquinone doped coatings show a slight increase in impedance which is most evident through the Bode and Nyquist plots (**Figure 5.73** (a) and (c)) for the 0.0001 M concentration. Less protective coatings were formed when the inhibitor concentration was increased to 0.001 M and even less protective for 0.01 M relative to the coating material containing no inhibitor.

Figure 5.74 shows results for phenylbenzoate and **Figure 5.75** for 2-hydroxypyridine doped coatings. Both of these inhibitors display the same trend in results where the impedance is highest for the blank OTES coating as evident in low frequency range of the Bode impedance (a) and Nyquist plots (c), impedance gradually decreases where it is the lowest for the highest concentration of inhibitor (as was also the case for MTES coatings in Figures 5.71 and 5.72). Results for pyrrolidine-

doped coatings (**Figure 5.76**) differ from the other results obtained for OTES:TEOS coatings in that upon increasing the inhibitor concentration a gradual increase in impedance was measured, the most protective being 0.01 M Pyr-doped coatings.

Figure 5.77 shows EIS data obtained when (a) Ce and (b) PhB-doped MTES:TEOS coatings on clean surfaces were monitored at time intervals from the start of OCP; the scope of such work was to determine whether inhibiting effect could be sustained over time. Concentrations of 0.001 M Ce and 0.01 M for PhB were employed since these concentrations proved to produce the most protective coatings (Ce-doped MTES Figures 5.65 and Figure 5.68 for PhB-doped MTES). Results of Figure 5.77 show a clear drop in Impedance values in low frequency range of the Bode impedance plot (i) and narrowing of the capacitive arc in Nyquist plots (iii) with time for MTES coatings that have been doped with Ce (a) and PhB (b) inhibitors.

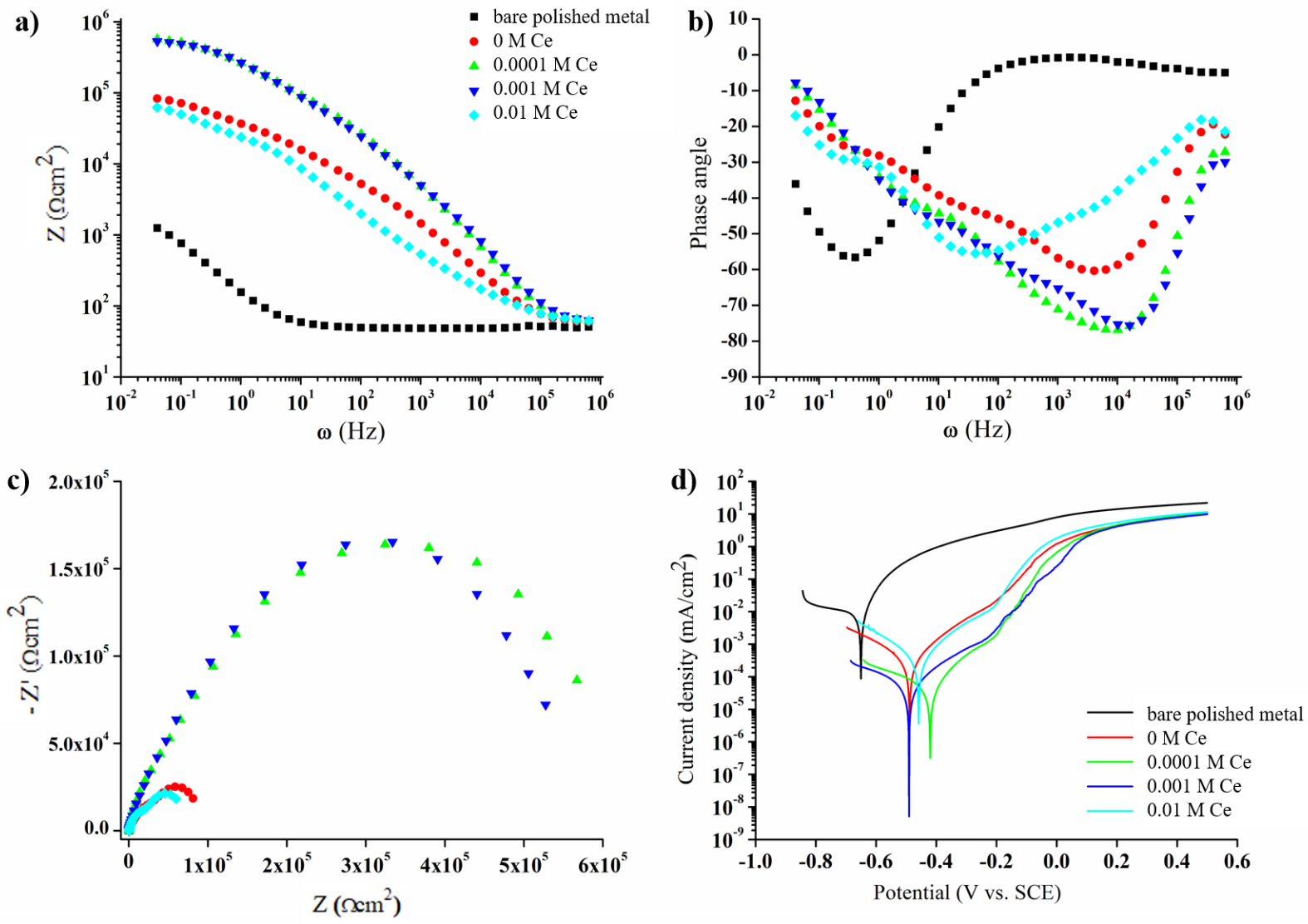


Figure 5.65: a) Bode Impedance, b) Bode Phase angle, c) Nyquist, and d) Potentiodynamic plots for various concentrations of cerium (iii) nitrate hexahydrate (Ce) inhibitor in 2.5% SiO₂ 60:40 mol% MTES:TEOS coatings.

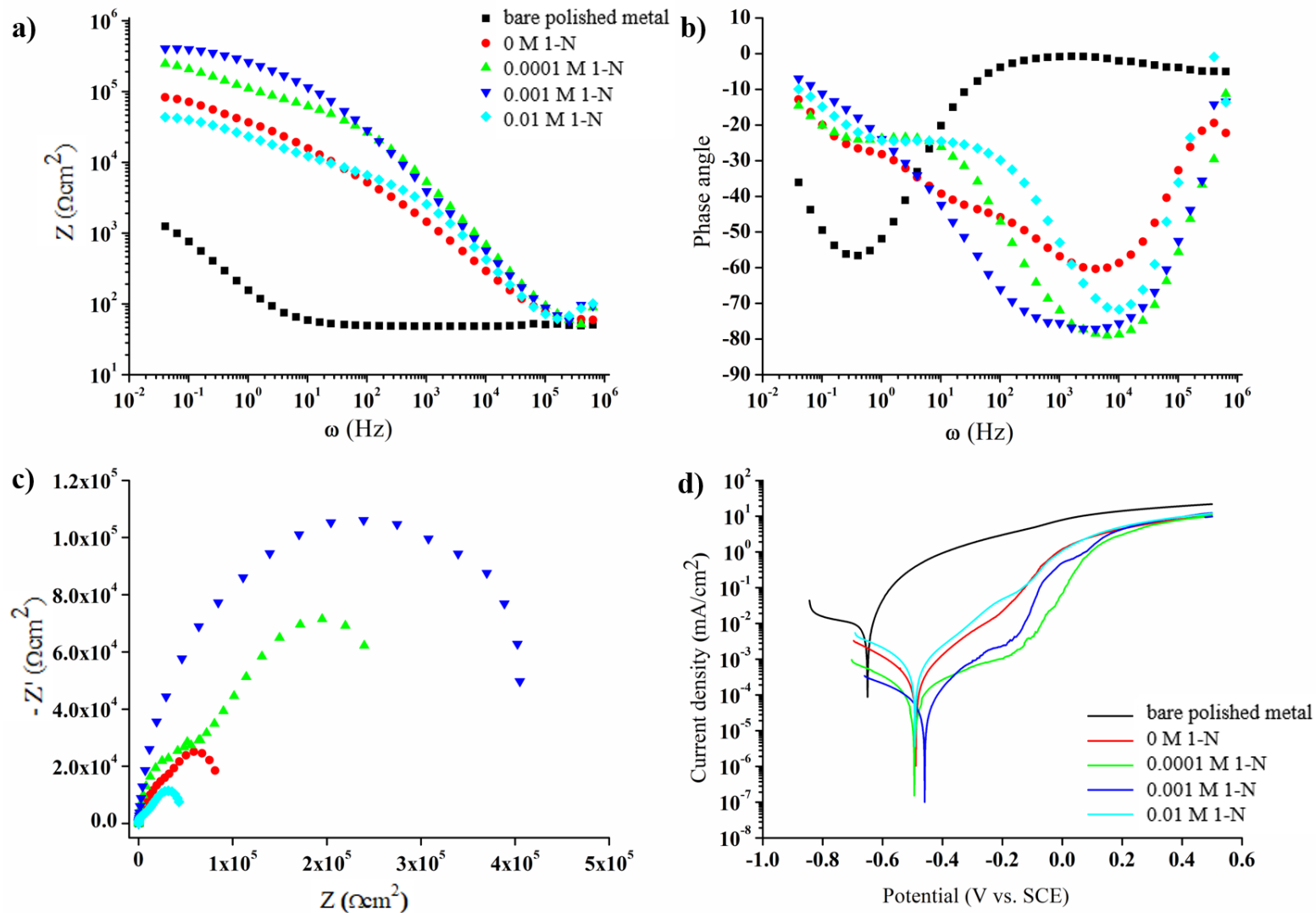


Figure 5.66: a) Bode Impedance, b) Bode Phase angle, c) Nyquist, and d) Potentiodynamic plots for various concentrations of 1-naphthol (1-N) inhibitor in 2.5% SiO₂ 60:40 mol% MTES:TEOS coatings.

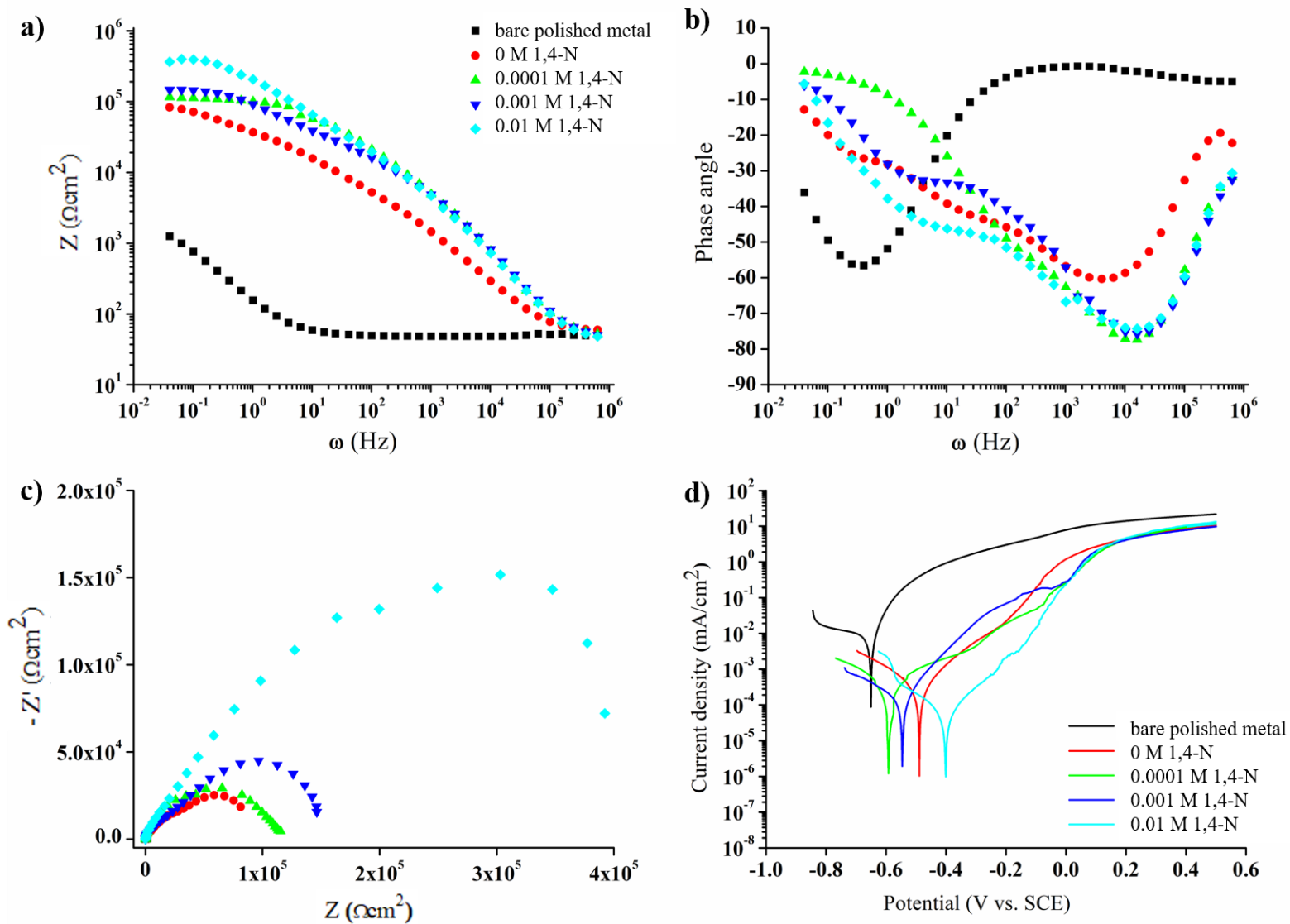


Figure 5.67: a) Bode Impedance, b) Bode Phase angle, c) Nyquist, and d) Potentiodynamic plots for various concentrations of 1,4-naphthoquinone (1,4-N) inhibitor in 2.5% SiO_2 60:40 mol% MTES:TEOS coatings.

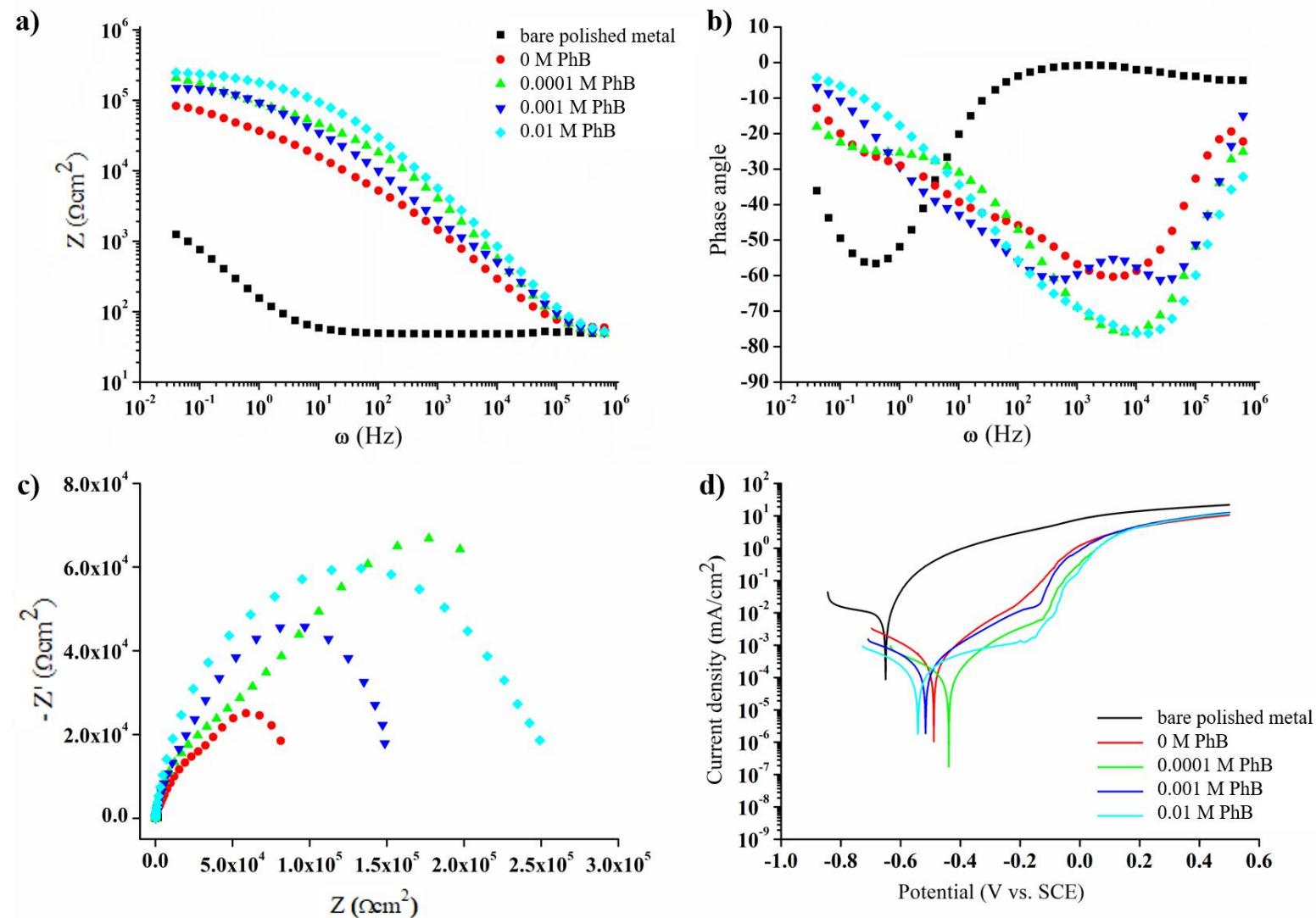


Figure 5.68: a) Bode Impedance, b) Bode Phase angle, c) Nyquist, and d) Potentiodynamic plots for various concentrations of phenylbenzoate (PhB) inhibitor in 2.5% SiO₂ 60:40 mol% MTES:TEOS coatings.

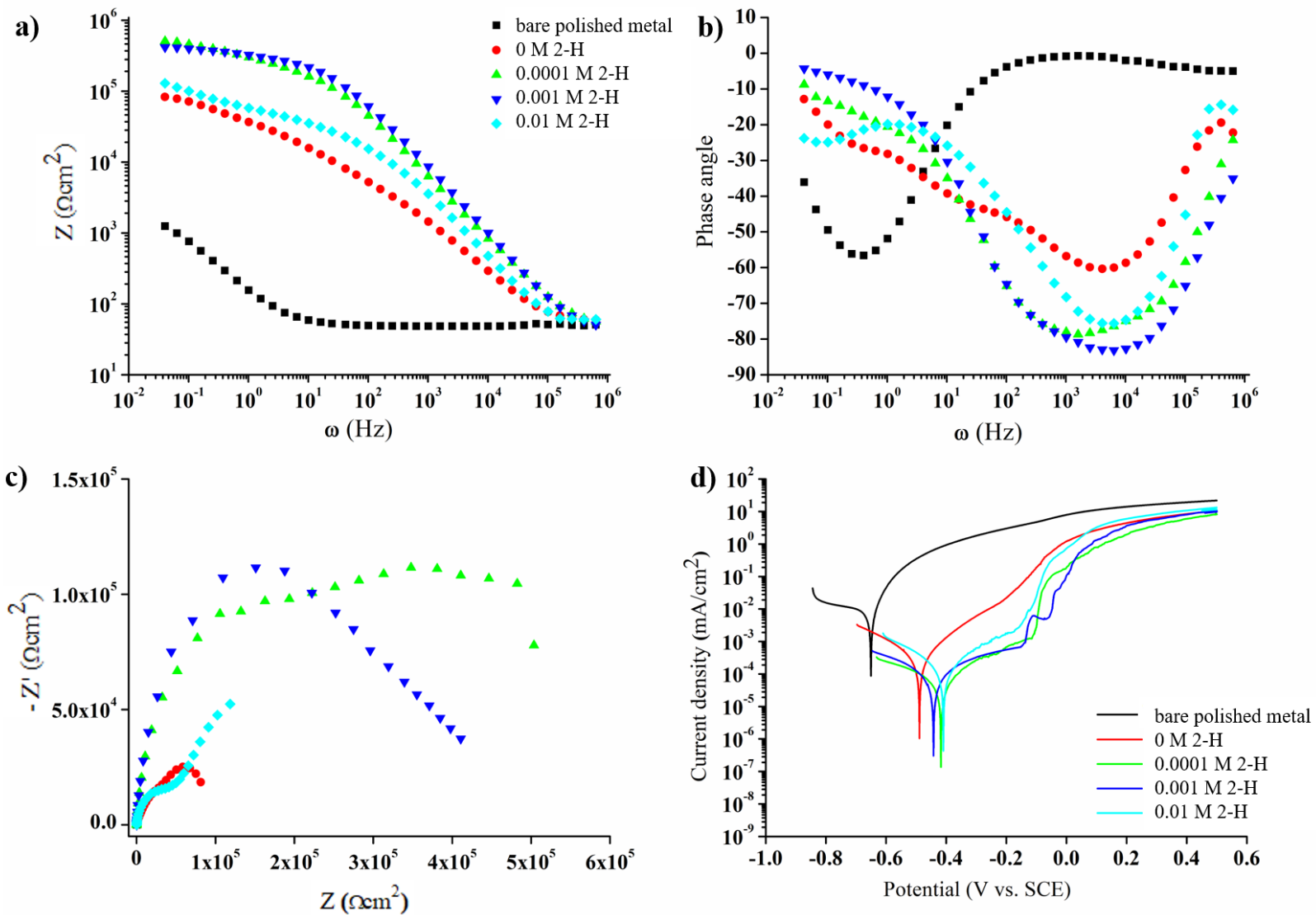


Figure 5.69: a) Bode Impedance, b) Bode Phase angle, c) Nyquist, and d) Potentiodynamic plots for various concentrations of 2-hydroxypyridine (2-H) inhibitor in 2.5% SiO₂ 60:40 mol% MTES:TEOS coatings.

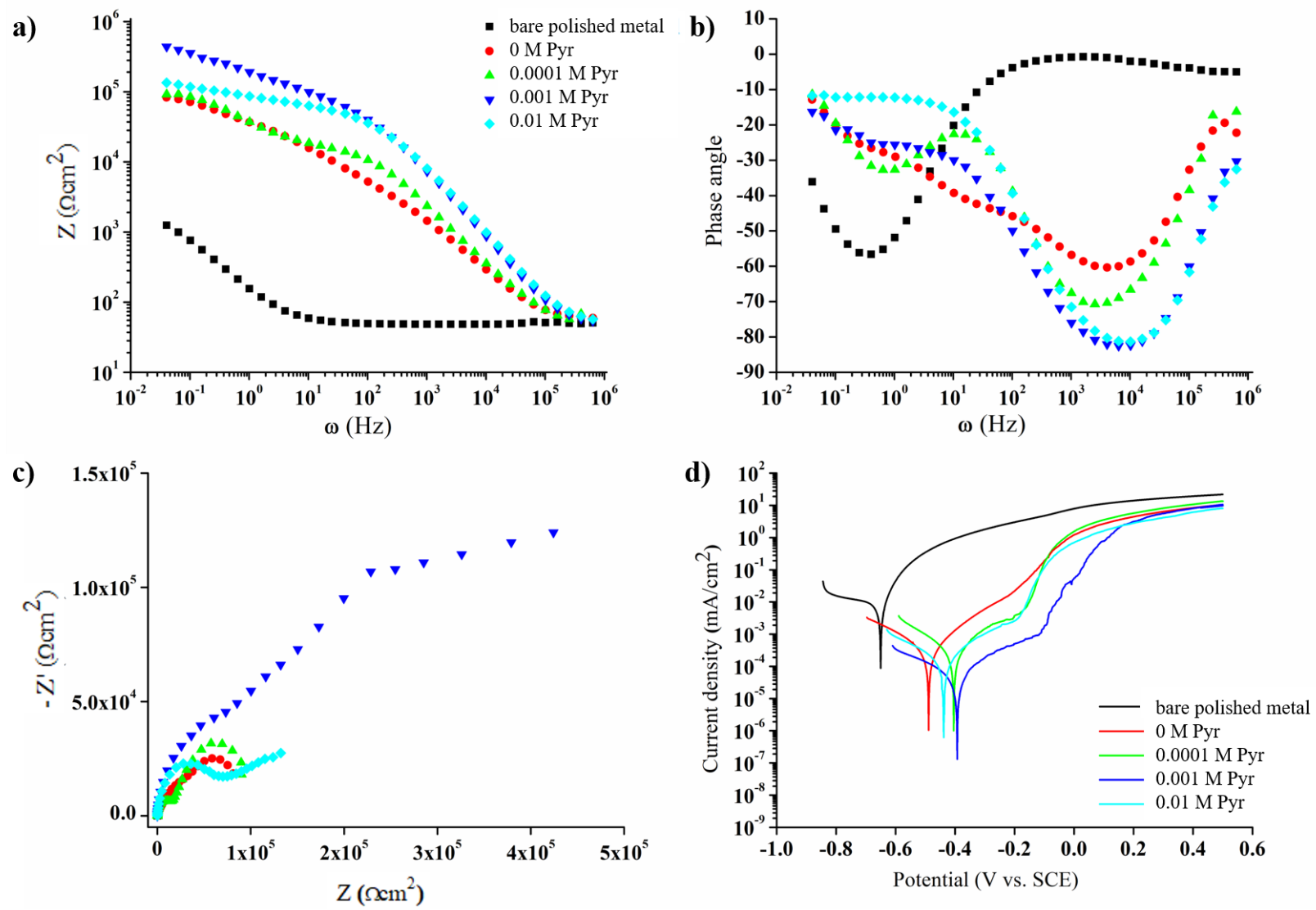


Figure 5.70: a) Bode Impedance, b) Bode Phase angle, c) Nyquist, and d) Potentiodynamic plots for various concentrations of pyrrolidine (Pyr) inhibitor in 2.5% SiO₂ 60:40 mol% MTES:TEOS coatings.

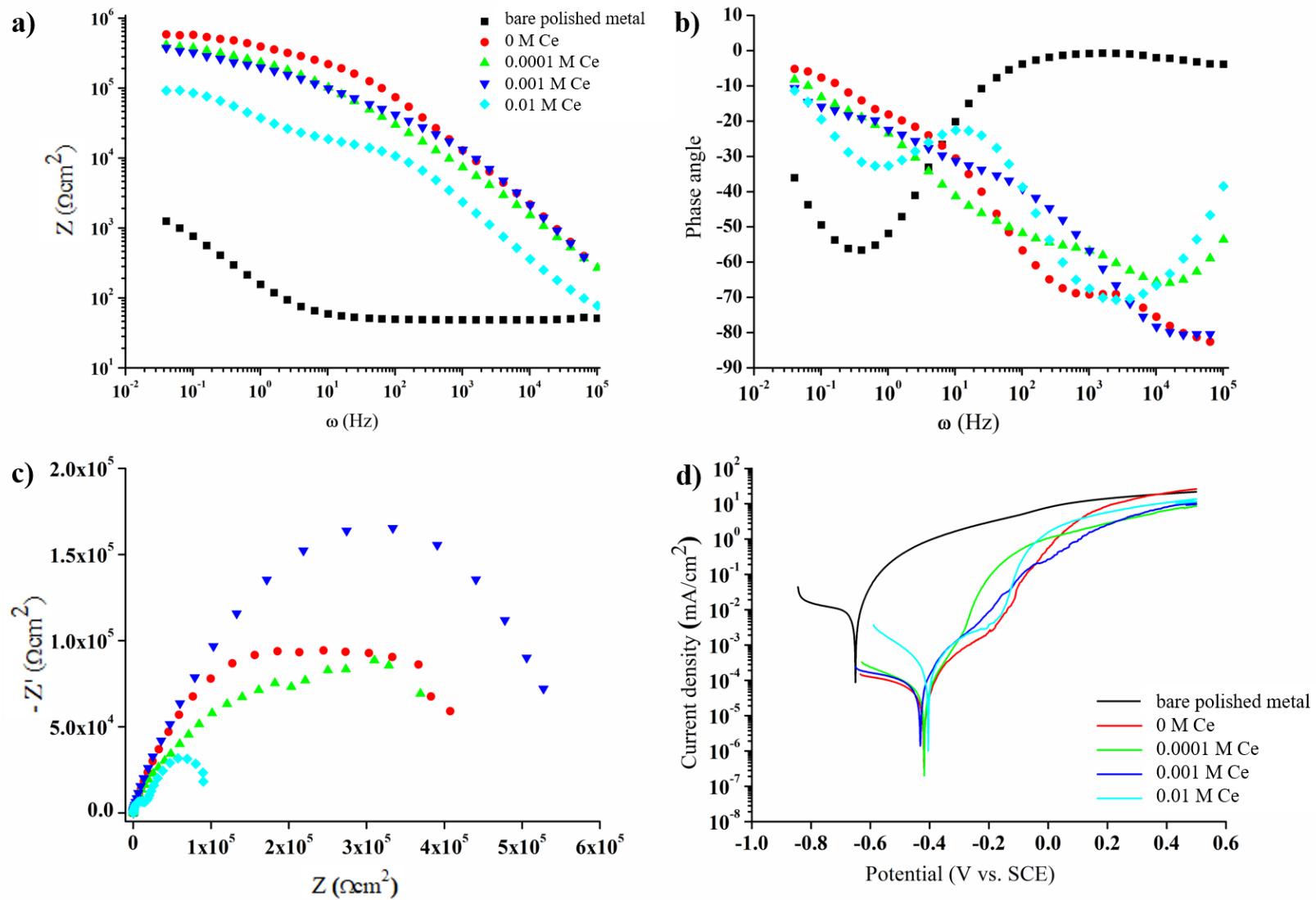


Figure 5.71: a) Bode Impedance, b) Bode Phase angle, c) Nyquist, and d) Potentiodynamic plots for various concentrations of cerium (iii) nitrate hexahydrate (Ce) inhibitor in 2.5% SiO₂ 20:80 mol% **OTES:TEOS** coatings.

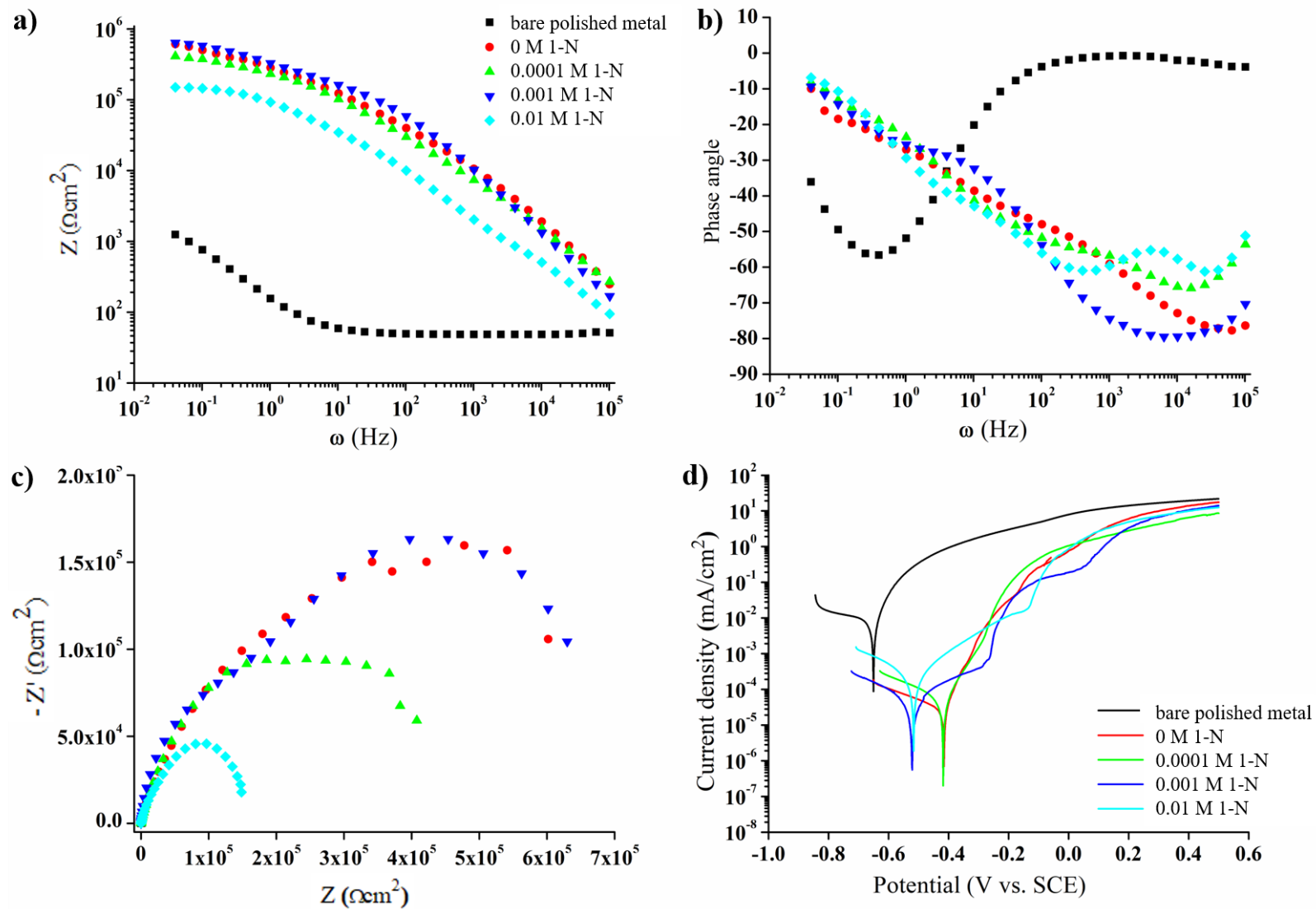


Figure 5.72: a) Bode Impedance, b) Bode Phase angle, c) Nyquist, and d) Potentiodynamic plots for various concentrations of 1-naphthol (1-N) inhibitor in 2.5% SiO₂ 20:80 mol% OTES:TEOS coatings.

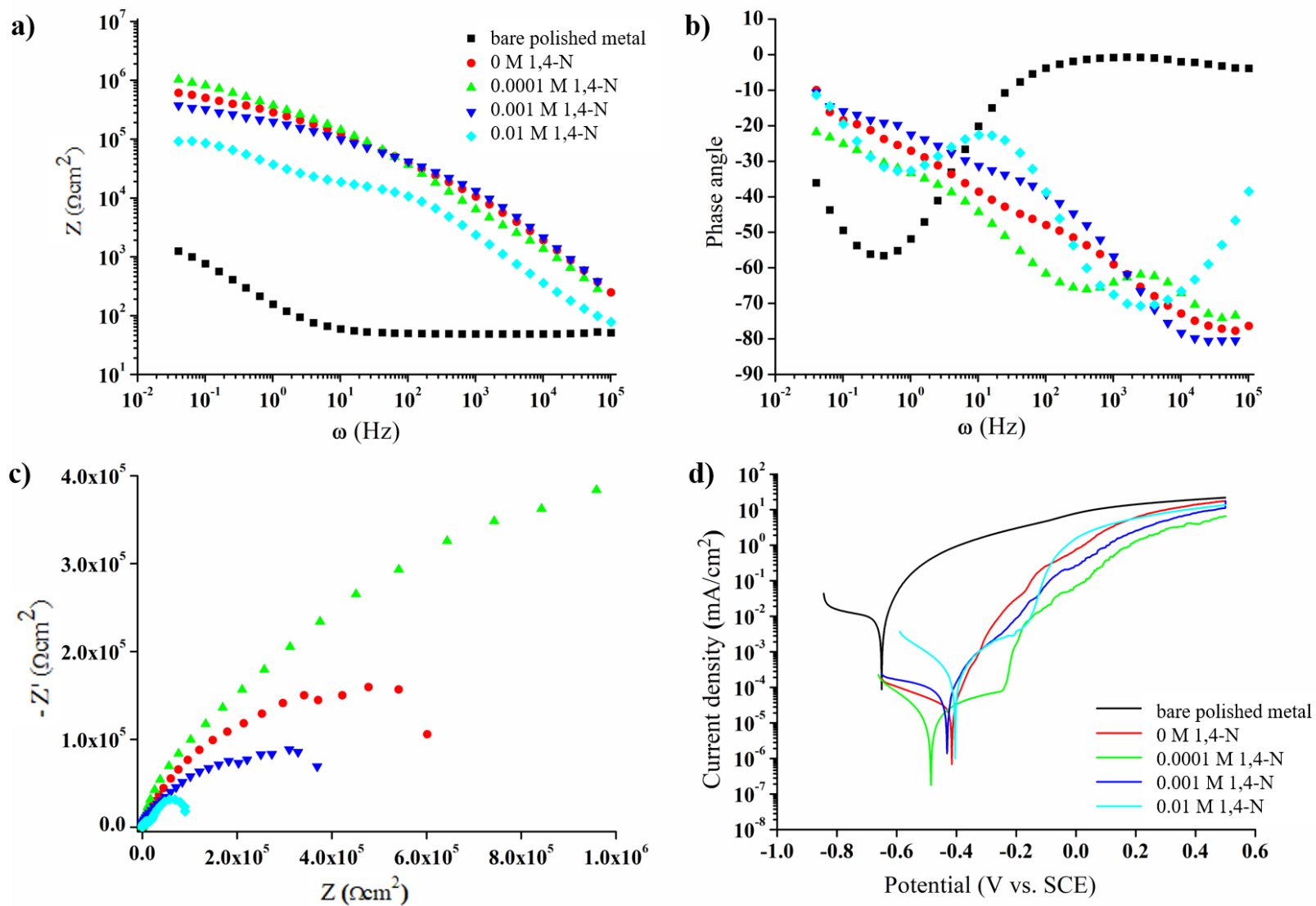


Figure 5.73: a) Bode Impedance, b) Bode Phase angle, c) Nyquist, and d) Potentiodynamic plots for various concentrations of 1,4-naphthoquinone (1,4-N) inhibitor in 2.5% SiO₂ 20:80 mol% OTES:TEOS coatings.

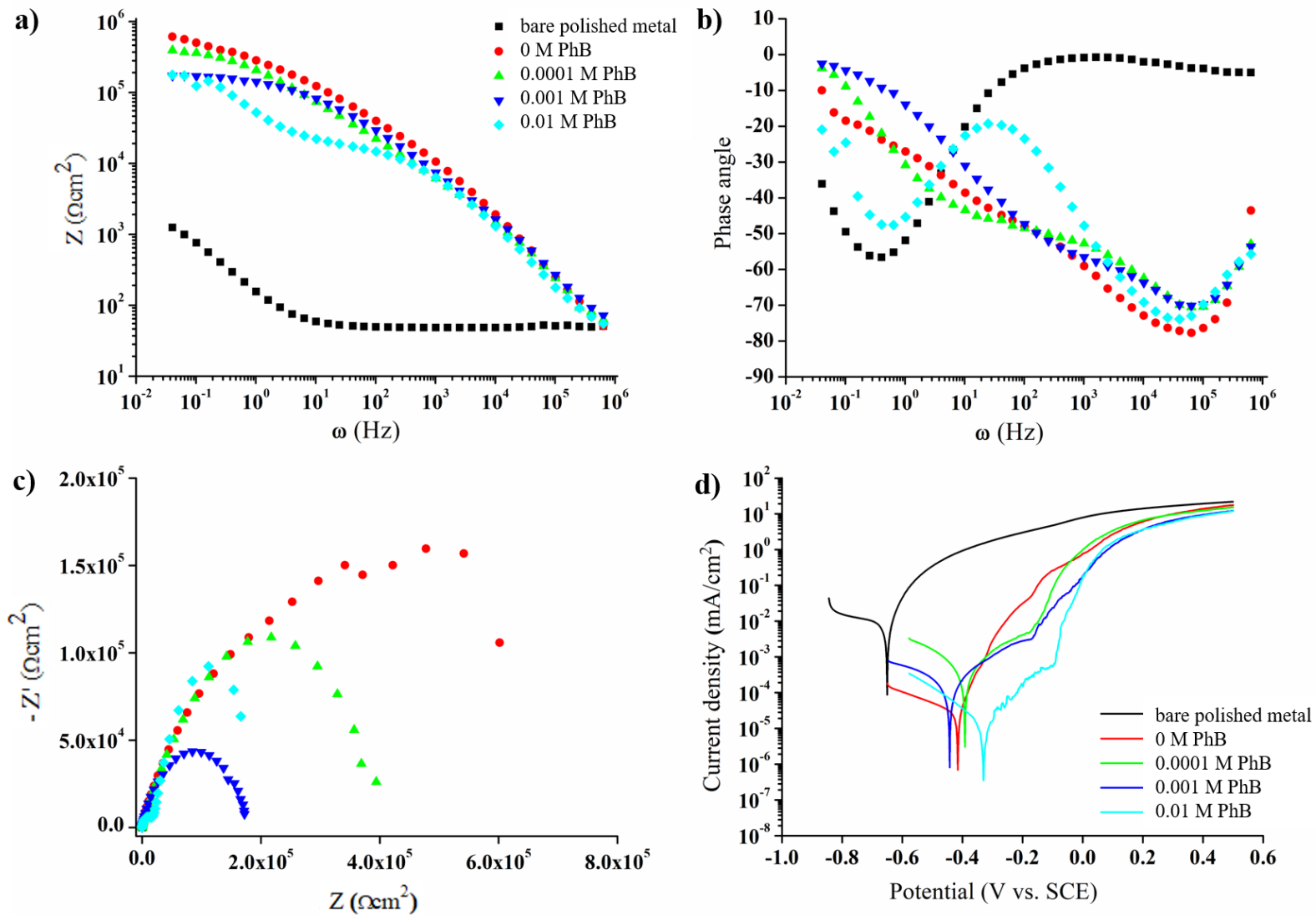


Figure 5.74: a) Bode Impedance, b) Bode Phase angle, c) Nyquist, and d) Potentiodynamic plots for various concentrations of phenylbenzoate (PhB) inhibitor in 2.5% SiO₂ 20:80 mol% OTES:TEOS coatings.

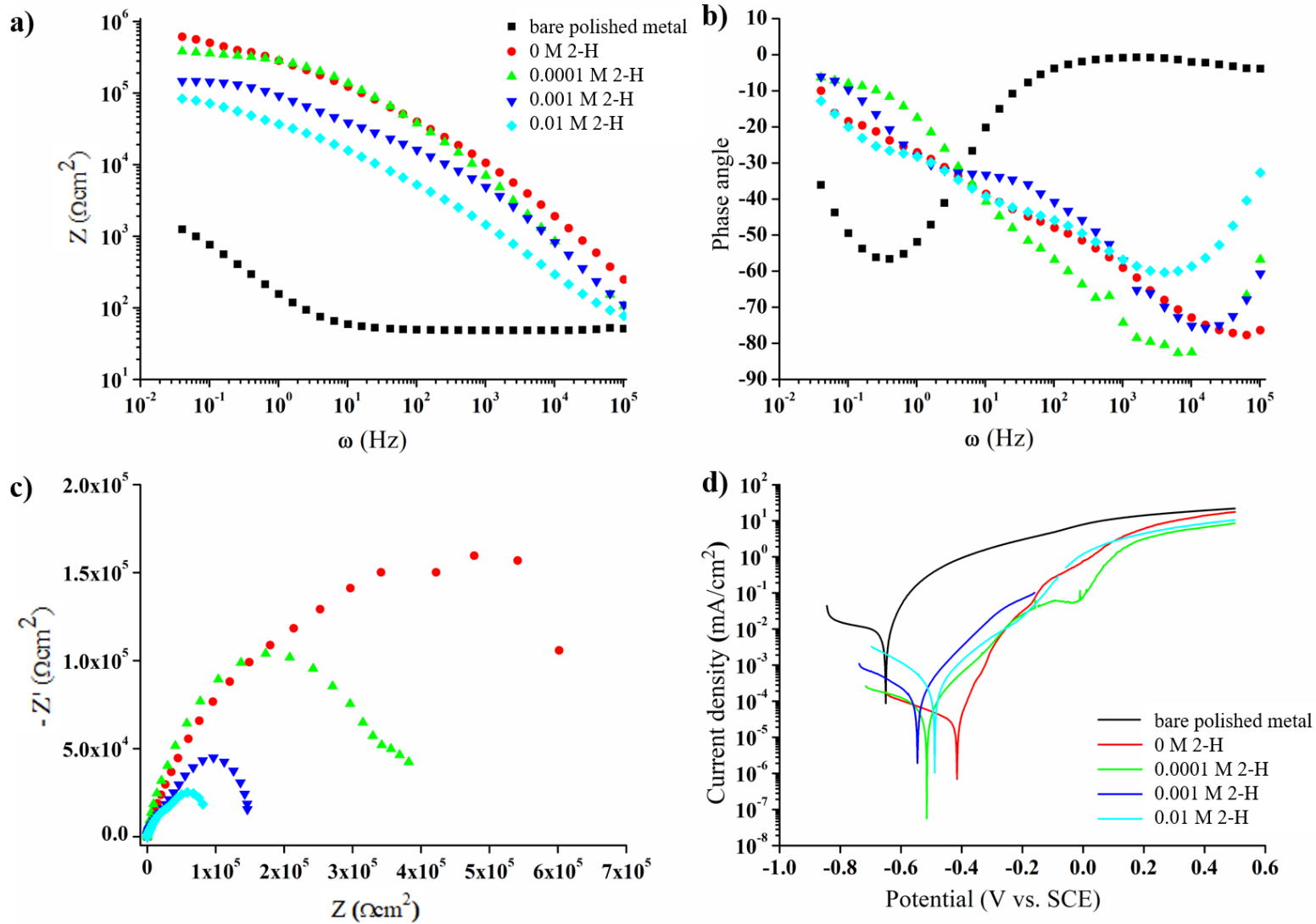


Figure 5.75: a) Bode Impedance, b) Bode Phase angle, c) Nyquist, and d) Potentiodynamic plots for various concentrations of 2-hydroxypyridine (2-H) inhibitor in 2.5% SiO₂ 20:80 mol% OTES:TEOS coatings.

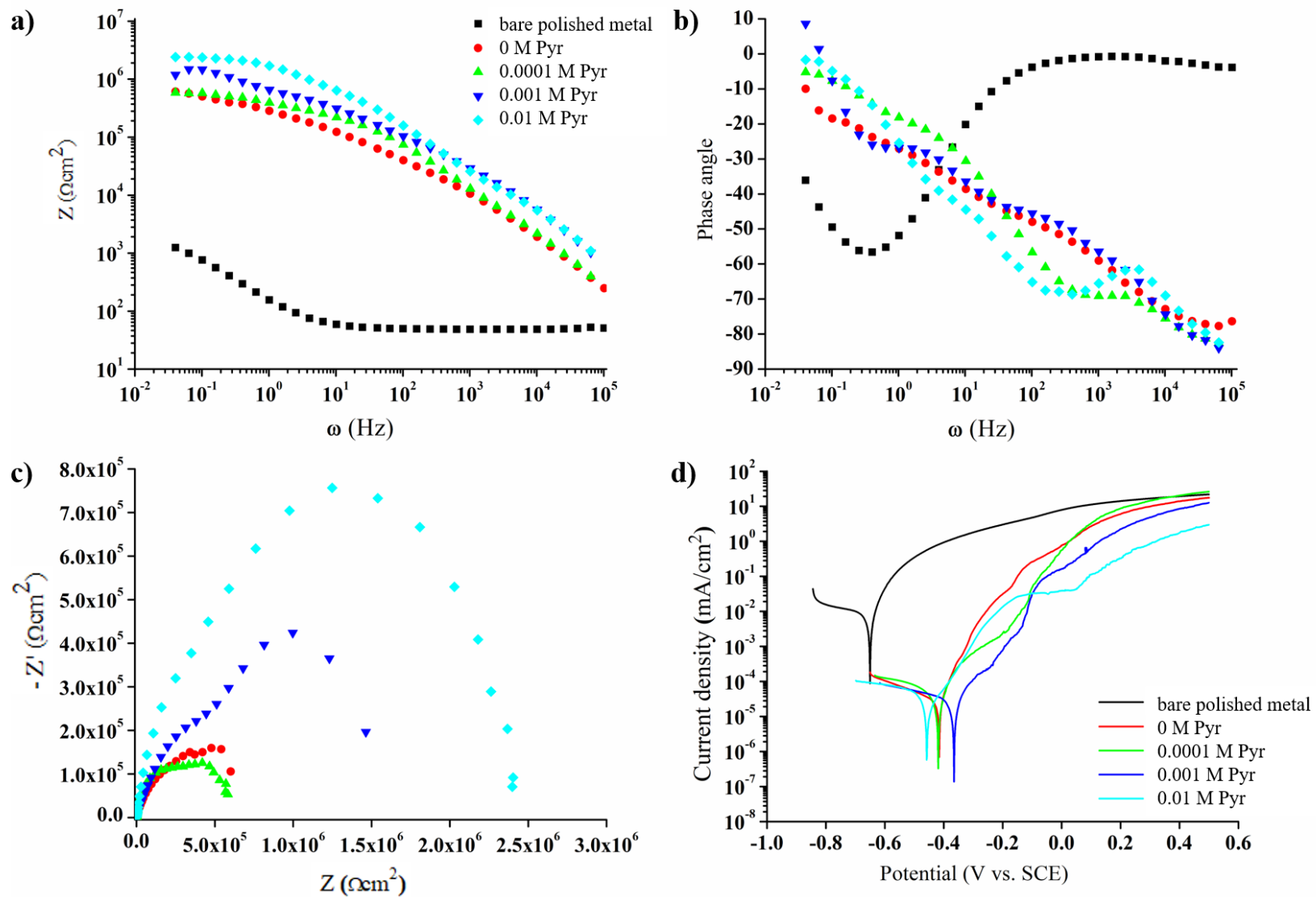


Figure 5.76: a) Bode Impedance, b) Bode Phase angle, c) Nyquist, and d) Potentiodynamic plots for various concentrations of pyrrolidine (Pyr) inhibitor in 2.5% SiO₂ 20:80 mol% OTES:TEOS coatings.

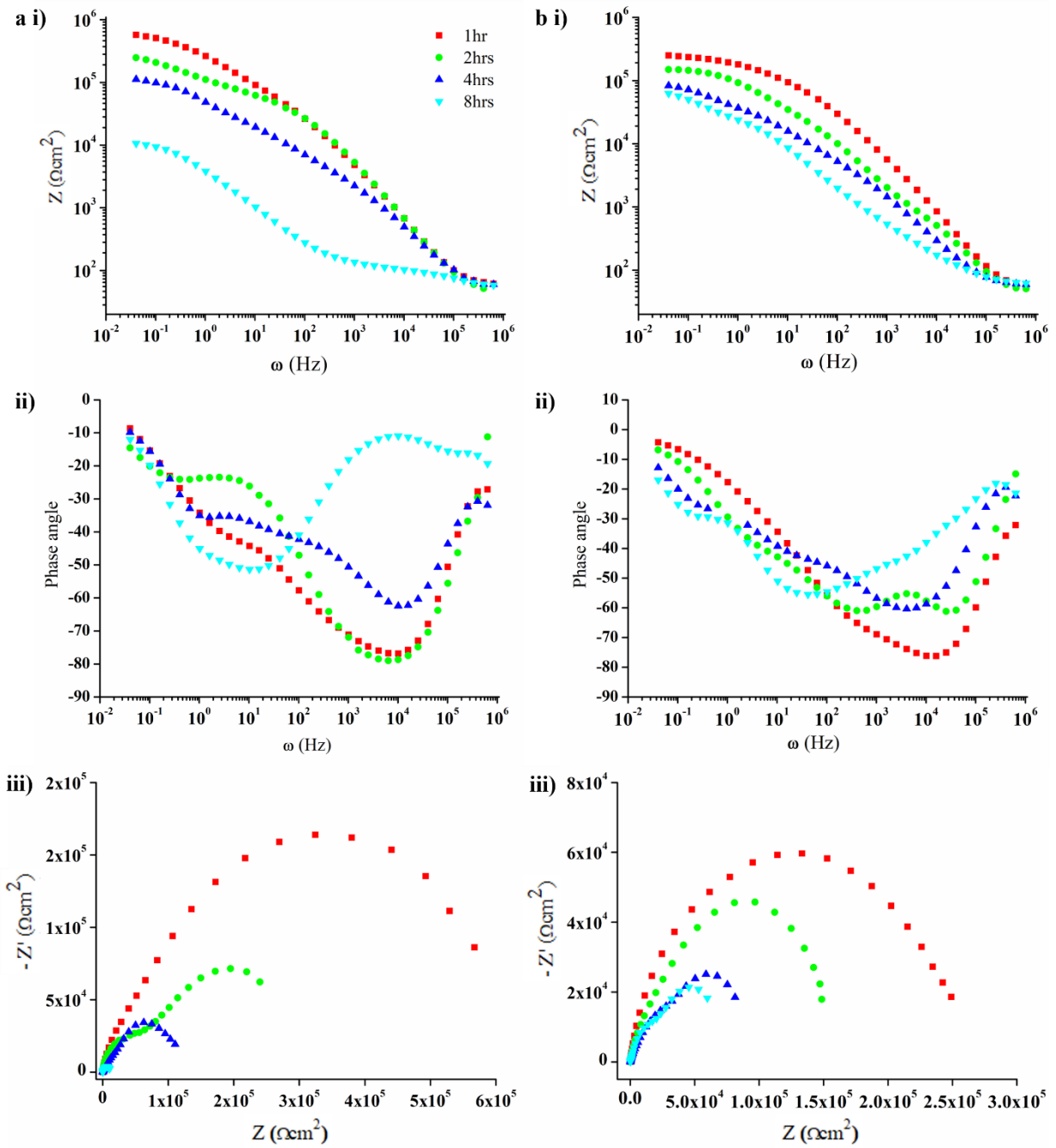


Figure 5.77: EIS results for 2.5% SiO₂ 60:40 mol% MTES:TEOS coating taken at different times from start of OCP doped with a) 0.001 M Ce and b) 0.01 M PhB where i) Bode Impedance, ii) Bode Phase angle and iii) Nyquist plots.

5.4.4.2 Corroded surfaces coated with in/organic inhibitor-doped MTES:TEOS 60:40 mol% coatings

The effect of the incorporation of inhibitors in OIH alkoxy silane coatings deposited onto corroded surfaces was also studied. The concentration of SiO_2 was increased to 10% in order to deposit thicker coatings onto the rough corroded surface as previously done in Section 5.2.7. **Figure 5.78** illustrates electrochemical data obtained for corroded surfaces that have been coated with 10% SiO_2 MTES:TEOS 60:40 mol% coatings that have been doped with various concentrations of cerium (iii) nitrate hexahydrate. It is clear that the coating containing no inhibitor is the most protective, seen as highest impedance obtained in low frequency range of the Bode impedance plot (a), widest capacitive arc in the Nyquist plot (c) and lowest corrosion current density in potentiodynamic plot (d). An increase in inhibitor concentration only leads to lower impedance, indicating less protective coatings.

A higher concentration of Ce was employed, i.e. 0.1 M featured apart from 0.0001, 0.001 and 0.01 M as previously done on clean metal, for such a surface since it was envisaged that more inhibitor would be needed to alter the progress of corrosion reactions occurring on such a surface. Similar results were obtained (not shown) when the organic inhibitor PhB was employed instead of Ce, thus illustrating the inability of both inorganic and organic inhibitors to improve on a coating's protective properties on corroded surfaces.

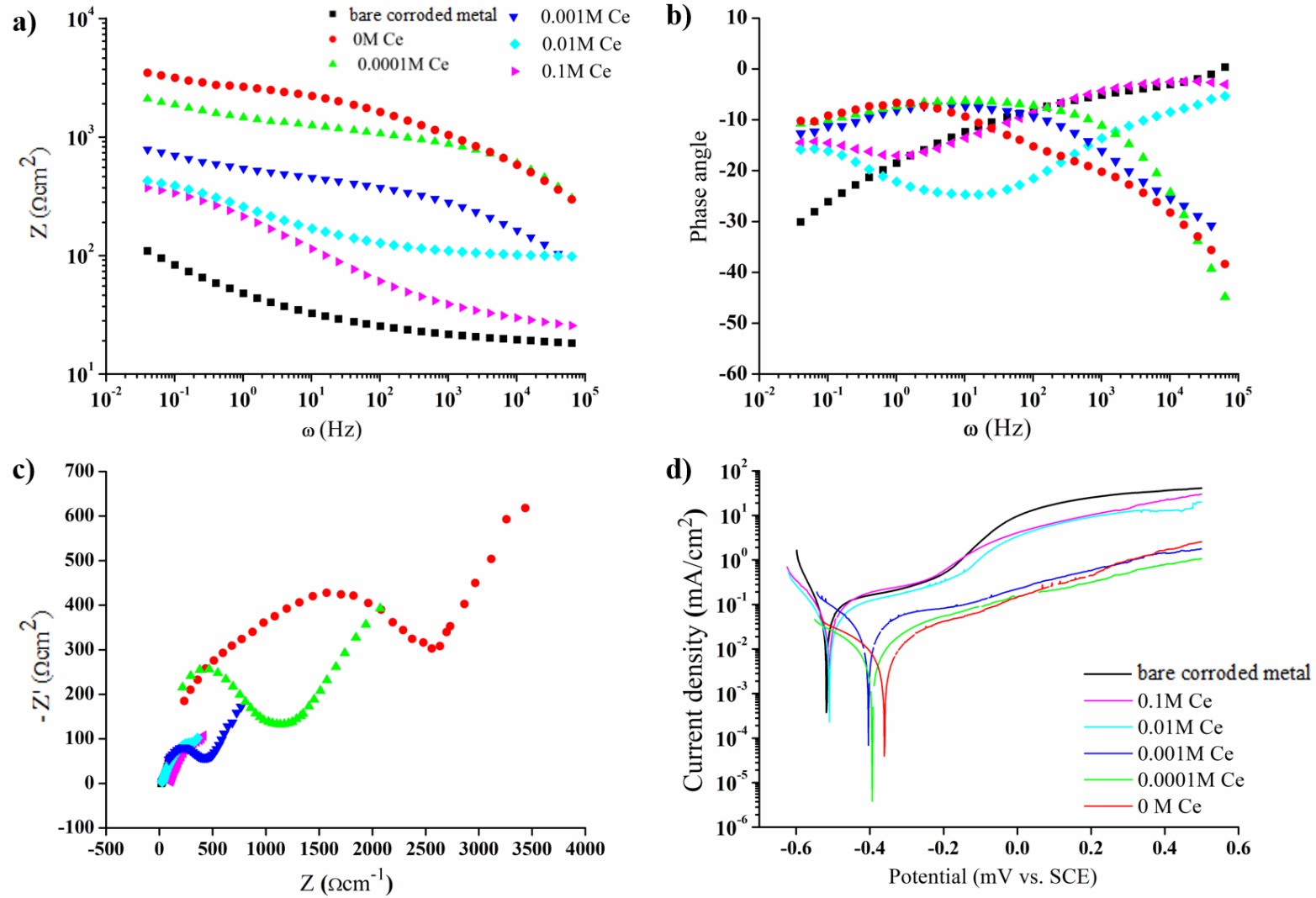


Figure 5.78: a) Bode Impedance, b) Bode Phase angle, c) Nyquist, and d) Potentiodynamic plots for various concentrations of Ce inhibitor in 10% SiO₂ 60:40 mol% MTES:TEOS coatings on corroded surface.

5.5 Performance of OIH coatings relative to Paraloid and Ercalene lacquers

5.5.1 Optical and Scanning Electron Microscopy

5.5.1.1 Coating morphology and thickness on clean metal surfaces

Figure 5.79 shows electron micrographs of cross-sections through double coats of Paraloid B-48, Paraloid B-72 and Ercalene coatings (prepared as double films over SS strips by dipping at 280mm/min speed; Paraloid coatings prepared in acetone solvent as 2.5, 5, 10 and 15% (wt/v) and Ercalene in diluente nitro solvent (3:1 vol/vol). Paraloid coatings were deposited using different lacquer concentrations in acetone whereas only one Ercalene concentration was considered. The Figure also features thicker MTES:TEOS 60:40 mol% deposited achieved through higher silica concentration (20%). The interface between the two coating layers is clearly visible for Paraloid and Ercalene (unlike alkoxy silane OIH coatings) and the coatings appear to be smooth and crack-free which was also observed for lower concentrations of these lacquers. Coating thicknesses are presented in **Table 5.17**.

Table 5.17 indicates an increase in thickness of Paraloid B-48 and Paraloid B-72 as the concentration of acrylate is increased for which a steeper increase occurs once concentration is increased to 10% and beyond. An increase in acrylate concentration leads to an increase in viscosity which in turn results in thicker coatings during the deposition process due to slower drainage as sample exist from the lacquer during dip-coating. B-48 and B-72 coatings increase in thickness similarly as the acrylate concentration is increased. For Paraloid coatings, the acrylate was investigated up to a 15% concentration since it is applied in this concentration by conservators. The nitrocellulose lacquer Ercalene was diluted to 75% of its original volume using the lacquer thinner diluente nitro (mixture of solvents toluene, acetone, methyl acetate, methanol and *n*-butyl acetate) as frequently carried out by conservators. This produced coatings that were thinner than 15% Paraloid coatings but still thicker than silica-based coatings.

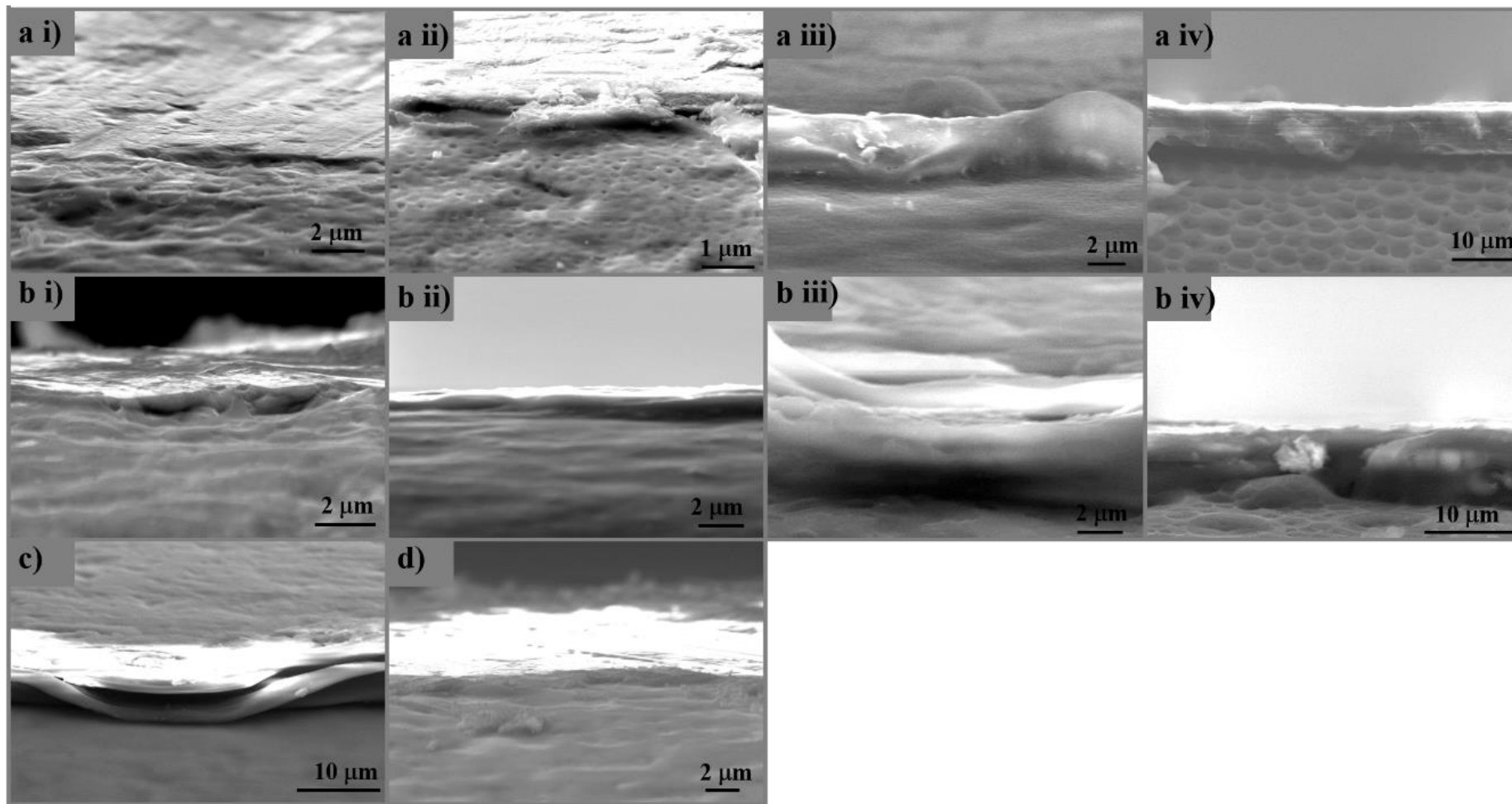


Figure 5.79: Scanning electron micrograph showing cross-section of double layered coatings consisting of (a) Paraloid B-48 i) 2.5% ($\times 20k$ mag) ii) 5% ($\times 20k$ mag) iii) 10% ($\times 10k$ mag) iv) 15% ($\times 5k$ mag); (b) 15% Paraloid B-72 i) 2.5% ($\times 20k$ mag) ii) 5% ($\times 10k$ mag) iii) 10% ($\times 10k$ mag) iv) 15% ($\times 5k$ mag); (c) 75% Ercalene ($\times 5k$ mag) and d) 20% SiO_2 MTES:TEOS 60:40 mol% ($\times 10k$ mag)

Table 5.17: Coating thicknesses for various concentrations of lacquers in their corresponding solvents as applied through dip-coating (280 mm/min). Table features thicknesses for MTES:TEOS 60:40 mol% at several SiO₂ concentrations (* are taken from Table 4.2).

Lacquer conc.	Thickness of coatings (nm)			
	B-48 in acetone	B-72 in acetone	Erc in diluente nitro	SiO ₂ in ethanol
2.5%	220 ± 19	786 ± 33	-	600 ± 211*
5%	430 ± 25	1059 ± 57	-	632 ± 23 *
10%	4292 ± 365	4277 ± 458	-	979 ± 85 *
15%	6584 ± 452	7387 ± 636	-	-
20%	-	-	-	1453 ± 120
75%	-	-	4512 ± 654	-

5.5.1.2 Coating morphology of lacquer coatings on corroded-cleaned iron surfaces

Figure 5.80 shows scanning electron micrographs of corroded-clean surfaces that have been coated with 75% Ercalene, 15% Paraloid B-48 and 15% Paraloid B-72 which appear to provide a continuous coverage over the entire corroded surface. The concentrations applied, namely 15% for Paraloid coatings and 75% for Ercalene were chosen as prepared by conservators which produce fairly viscous lacquers and thicker coating application and thus good surface coverage on corroded surfaces. However, cracks become evident at a higher magnification (Figure 5.80 a-c (ii)) for all three coatings which proves that for these given thicknesses applied through dip-coating, surface roughness does not allow for a completely crack-free coating.

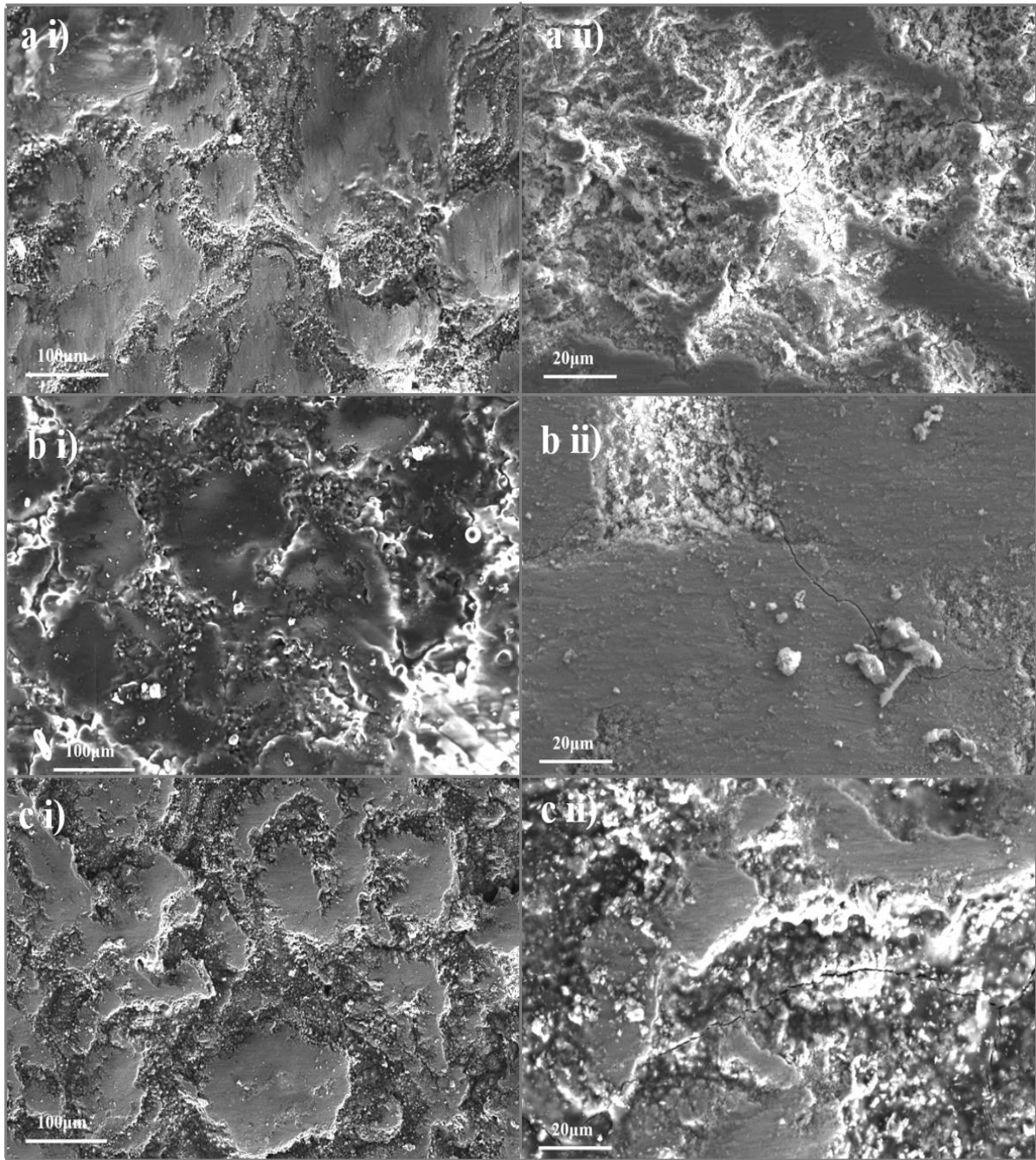


Figure 5.80: Scanning electron micrographs for corroded iron surfaces double coated with a) 15% Paraloid B-48 b) 15% Paraloid B-72 and c) 75% Ercalene at i) $\times 500$ magnification and ii) $\times 2000$ magnification.

5.5.1.3 Coating morphology under different modes of application of coatings onto clean surfaces

In preparation for salt-spray testing, thicker OIH alkoxysilane coatings (10% SiO₂) were deposited and using different modes of application. **Figure 5.81** shows images of clean iron coupon surfaces that have been coated with 10% SiO₂ MTES:TEOS 60:40 mol% through dip, fine brush, coarse brush and sponge application, viewed using a light microscope. It is evident that the smoothest and most defect-free coatings have been obtained through dip-coating. Brush application tends to lead to the formation of silica particles which accumulate in between the bristles of the brush due to the evaporation of solvent resulting in the deposition of silica particles during sol application (Figure 5.81 (b)). This tendency has been observed to occur to a greater extent with coarse brush as a greater volume of sol is taken up.

Apart from the formation of silica particles, brush coated surfaces tend to form troughs in the coating (bristle marks) which shows an uneven thickness along the surface of the coupon, seen as variations in coating colour (fringes) in Figure 5.81 (b). The scope of testing with coarse brush was to be able to deposit the coatings using less strokes per coupon and a greater volume leading to thicker coatings. Coarse brush application also results in silica particles depositing along the coating together with the additional deposition of fragments from the bristles seen as black spots in Figure 5.81 (c). Silica particles have also deposited onto the coated surface when sponge was used. Sponge application lead to the uneven deposition of coating where the surface appears similar to an orange peel due a venous pattern of deposition along the majority of the coupon surface as shown in Figure 5.81 (d ii) under higher magnification.

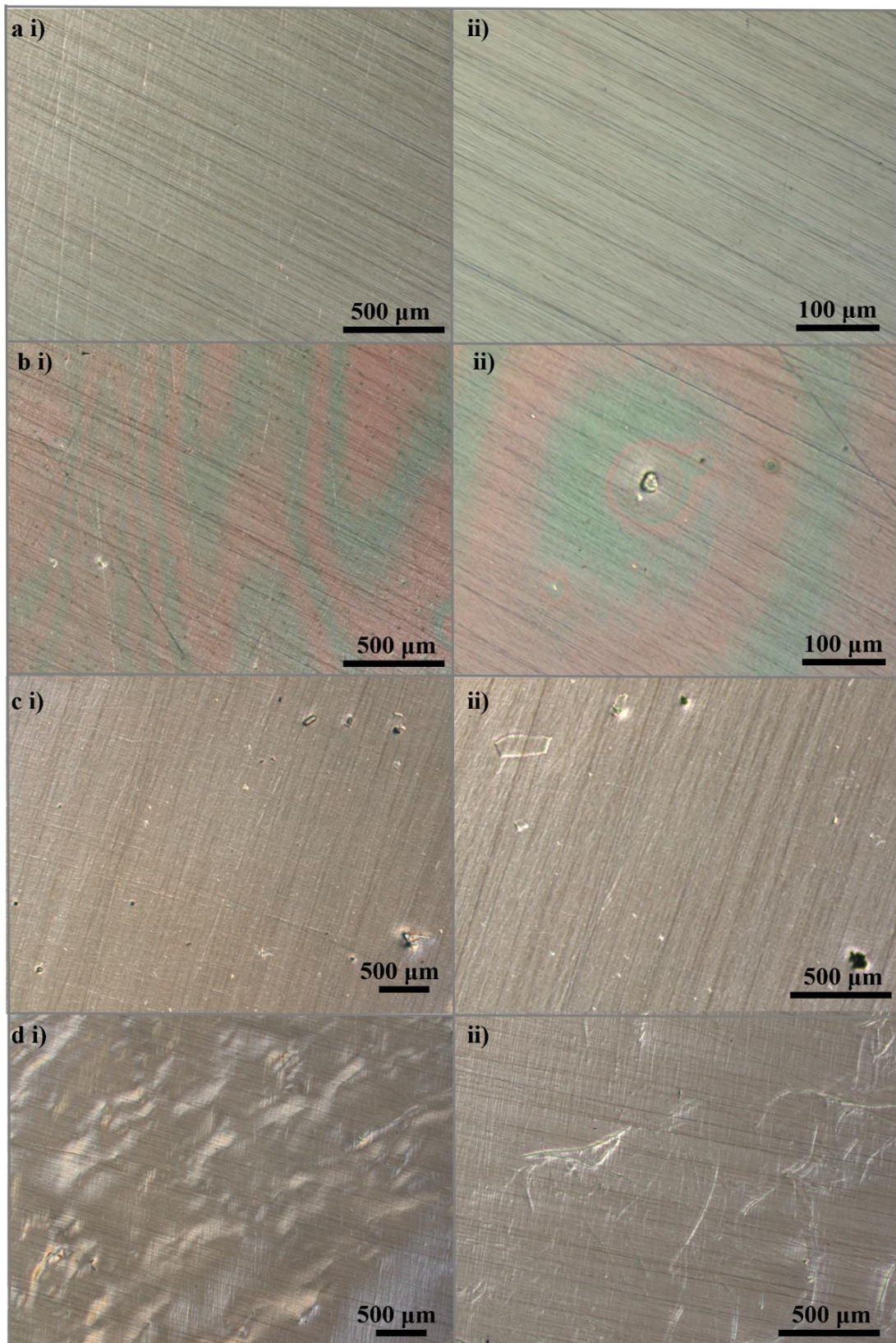


Figure 5.81: Micrographs showing 10% SiO₂ MTES:TEOS 60:40 mol% coated coupons that have been deposited by a) dip coating using i) $\times 5$ and ii) $\times 20$ magnification b) fine brush i) $\times 5$ and ii) $\times 20$ magnification c) coarse brush i) $\times 2.5$ and ii) $\times 5$ magnification and d) sponge application i) $\times 2.5$ and ii) $\times 5$ magnification.

5.5.1.4 Coating thickness determination by fine brush application

Since uneven coating were obtained through thick brush and sponge applications (Figure 5.81), these were not considered further in this Section. The polished coupons were coated with 15% Paraloid B-48, B-72 and 75% Ercalene using fine brush and their thicknesses are listed in **Table 5.18** and their cross-sections are shown in **Figure 5.82**. It also includes the five OIH alkoxysilanes featured in Section 5.1 where only the most protective coatings for each precursor concentration were considered and applied through brush application in a 10% SiO₂ concentration. There is an increase in coating thickness with the length of the alkyl chain (MTES to OTES), PhTES coating having deposited the thinnest of the 5 alkoxysilane coatings considered. The three lacquers form thicker coatings than OIH alkoxysilane coatings where similar values were obtained for Paraloid coatings ($\approx 8 \mu\text{m}$), Ercalene being slightly thinner.

Table 5.18: Thickness determination of double coatings applied using a fine brush.

Coating (two-coat application)	Coating thickness \pm Std Error (μm)
10% MTES:TEOS 60:40 mol%	4.21 ± 0.45
10% PrTES:TEOS 50:50 mol%	4.76 ± 0.80
10% HTES:TEOS 30:70 mol%	5.48 ± 0.08
10% OTES:TEOS 20:80 mol%	5.16 ± 0.30
10% PhTES:TEOS 40:60 mol%	3.27 ± 0.34
15% Paraloid B-48	8.38 ± 0.51
15% Paraloid B-72	8.32 ± 0.29
75% Ercalene	7.47 ± 0.70

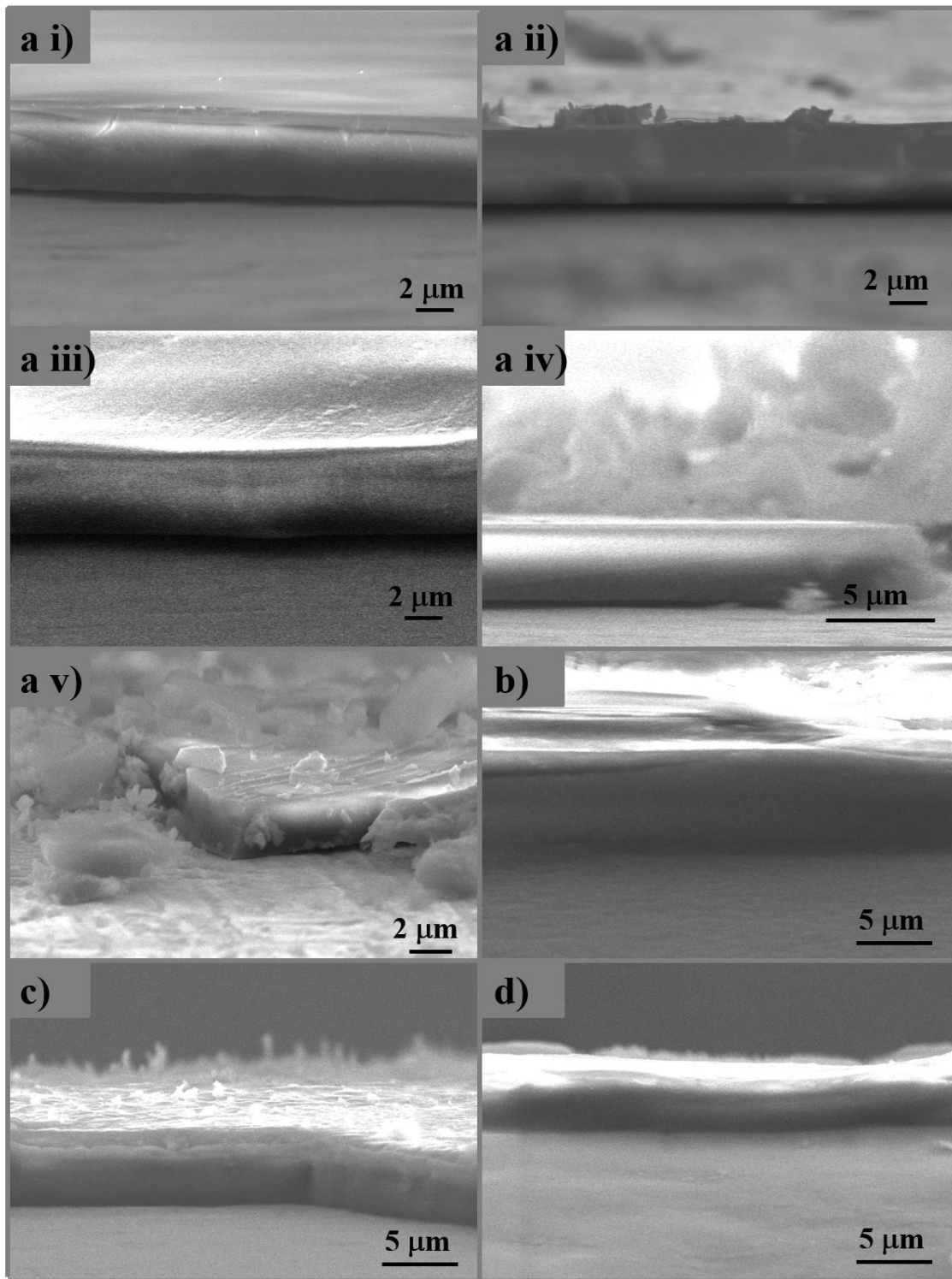


Figure 5.82: Electron micrograph showing the surface and a cross-section through double coatings
 a) 10% SiO₂ of i) MTES:TEOS 60:40 mol% (mag ×10k) ii) PrTES:TEOS 50:50 mol% (mag ×10k) iii) HTES:TEOS 30:70 mol% (mag ×10k) iv) OTES:TEOS 20:80 mol% (mag ×5k) v) PhTES:TEOS 40:60 mol% (mag ×10k); b) 15% Paraloid B-48 (mag ×5k) c) 15% Paraloid B-72 (mag ×5k) and c) 75% Ercalene (mag ×5k). Coatings were applied using a fine brush.

5.5.2 Mechanical testing of lacquers

5.5.2.1 Nano-scratch

Figure 5.83 features scars generated through nano-scratch test for the three lacquer coated surfaces. All three single application coatings were applied through dip-coating at 280mm/min, 2.5% Paraloid in acetone concentrations were used for B-48 and B-72 acrylate coatings whereas a 75% Ercalene in diluente nitro was used to produce nitrocellulose coating.

Scar morphology and plots of scan distance versus penetration depth for the two Paraloid coated surfaces are similar to each other and to the OIH alkoxysilane coatings previously presented in Figure 5.15. A clean-cut scratch is made with some material accumulation on the sides of the scratching path is seen for Paraloid-coated coupons, without significant delamination or cracking of the coatings. However, the effect of the indenter on Ercalene coated surface is different since delamination of the coating is clearly visible from the very start of the scratch which explains the change in plot shape compared to Paraloid coatings where a sudden increase in depth has been recorded early on along the scratch.

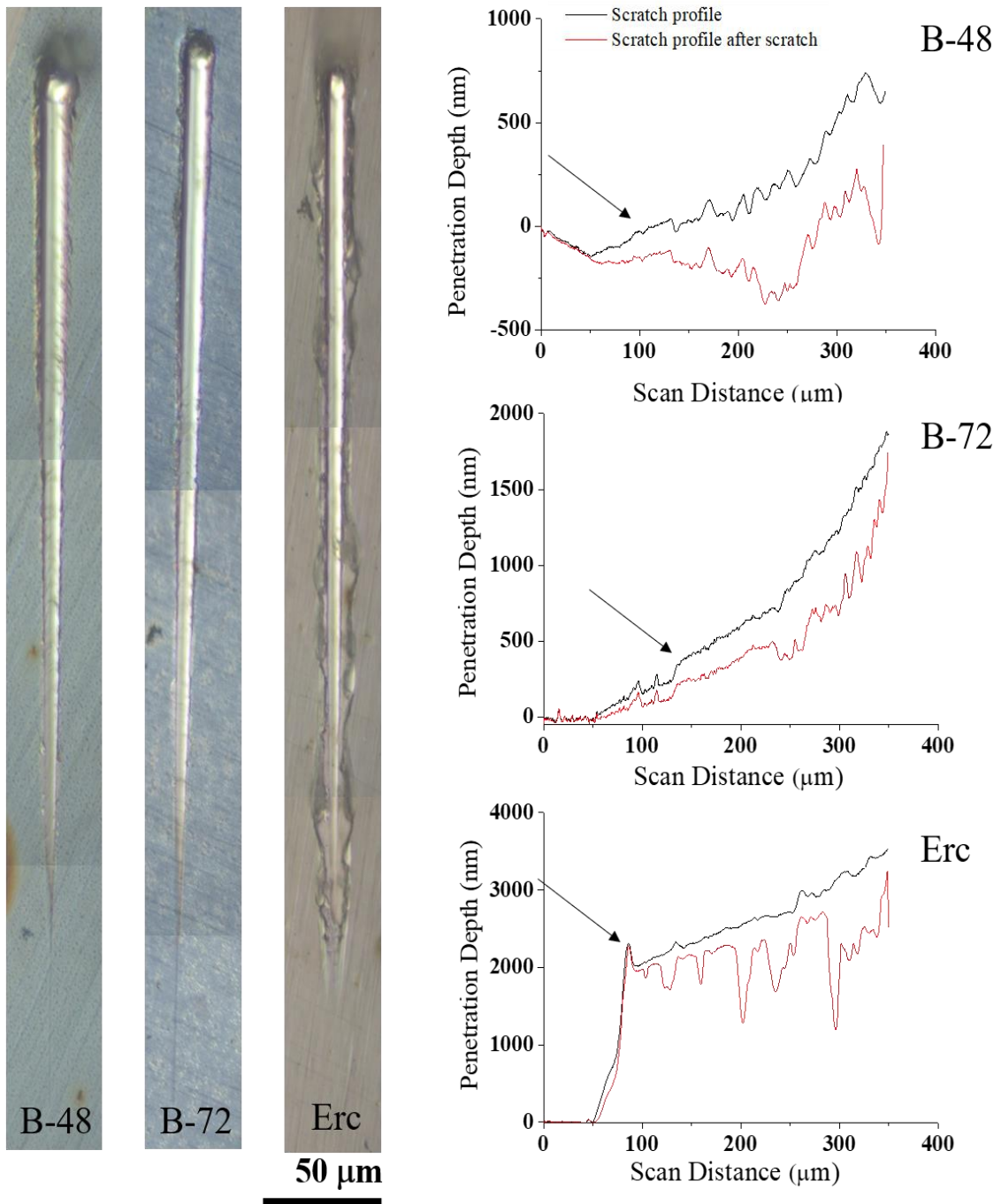


Figure 5.83: Images of scars inflicted onto iron coupons coated with 2.5% Paraloid B48, B72 and 75% Ercalene. Plots of scan distance versus penetration depth for 'during scratch' and scratch profile after scratch for the three coatings also feature in this Figure.

5.5.2.2 Pull-out testing

Plots of displacement versus load for Paraloid B-48, B-72 and Ercalene are presented in **Appendix J** (CD attached). **Table 5.19** the force measured at the point of detachment of dolly from the coated coupon as obtained from plots in Appendix J for single layer coatings that have been applied through dip-coating. The Table also features results obtained previously from Figure 5.18 for OIH alkoxy silane coatings for which most protective precursor concentrations were considered. Following pull-out test, all three lacquer coatings were undamaged since the detachment occurred at the coating-adhesive interface which indicates good adhesion of the coatings to the metal coupon and/or weak adhesion of epoxy resin to alkoxy silane coating.

Table 5.19: Pull-out force measured when pull-out test is conducted on Paraloid B-48, B-72 and Ercalene. Data for OIH silane coatings marked using (*) is taken from Figure 5.18 is included for comparison purposes.

Coating	Pull-out Force \pm St. Error (kN)
2.5% Paraloid B-48 in acetone	1.25 \pm 0.25
2.5% Paraloid B-72 in acetone	2.00 \pm 0.82
75% Ercalene in diluente nitro	1.62 \pm 0.23
2.5% SiO ₂ MTES:TEOS 60:40 mol%	1.60 \pm 0.47*
2.5% SiO ₂ PrTES:TEOS 50:50 mol%	1.27 \pm 0.40*
2.5% SiO ₂ HTES:TEOS 30:70 mol%	0.89 \pm 0.42*
2.5% SiO ₂ OTES:TEOS 20:80 mol%	1.37 \pm 0.97*
2.5% SiO ₂ PhTES:TEOS 40:60 mol%	1.24 \pm 0.51*
Bare metal	2.29 \pm 0.41*

5.5.3 Electrochemical Tests

5.5.3.1 Lacquer coatings on clean polished iron surface

Figures 5.84-5.86 display electrochemical results obtained for Paraloid and Ercalene-coated clean polished surfaces. Both Paraloid coatings display improvement in corrosion protection at all concentrations considered when compared to bare metal seen as higher impedance obtained in low frequency range of the Bode impedance plots (a), wider capacitive arc in Nyquist plot (c) where bare metal arc is barely visible, and lower I_{corr} obtained in potentiodynamic plots (d). However, higher impedance was achieved once concentration was increased to 10% of the acrylate, see Bode impedance and Nyquist plots of Figures 5.84 and 5.85. Bode phase angle plots of Figures 5.84-5.86 (b) indicate a two-time constant system shown as two dips in phase angle.

Through the data displayed in these figures, it is clear that B-48 coatings are more protective than B-72 due to the higher impedance obtained at all concentrations. In fact, 15% B-48 coatings could not be assessed electrochemically on clean surfaces due to very large and irreproducible values for which coatings remained intact following testing. A four order of magnitude improvement over bare metal was achieved by B-48 coatings having 10% acrylate concentration whereas a three order of magnitude improvement was achieved by B-72 having a 15% acrylate concentration. Figure 5.86 shows electrochemical data obtained for Ercalene-coated metal for which a two order of magnitude improvement over bare metal was achieved. It can be said from these three figures, that Paraloid B-48 coatings are the most protective, followed by Paraloid B-72 whereas the nitrocellulose coating is least protective through electrochemical testing. Such a poor performance by the nitrocellulose coating Ercalene was the reason for featuring a single 75% concentration in the study, without considering the more dilute systems.

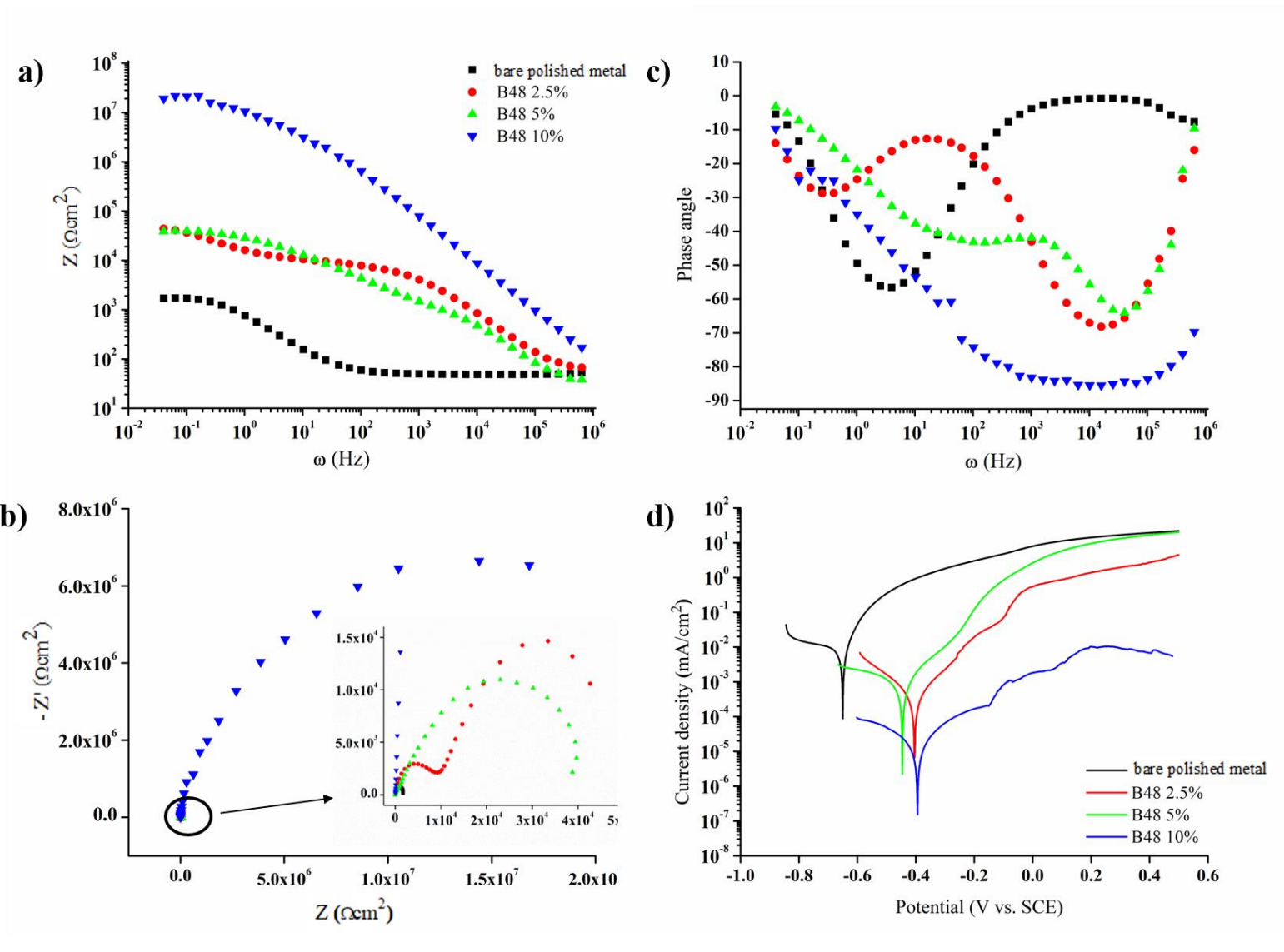


Figure 5.84: Electrochemical data obtained for Paraloid B-48 double-coated clean polished surface where a) Bode Impedance b) Bode Phase angle c) Nyquist and d) Potentiodynamic plots at various acrylate concentrations.

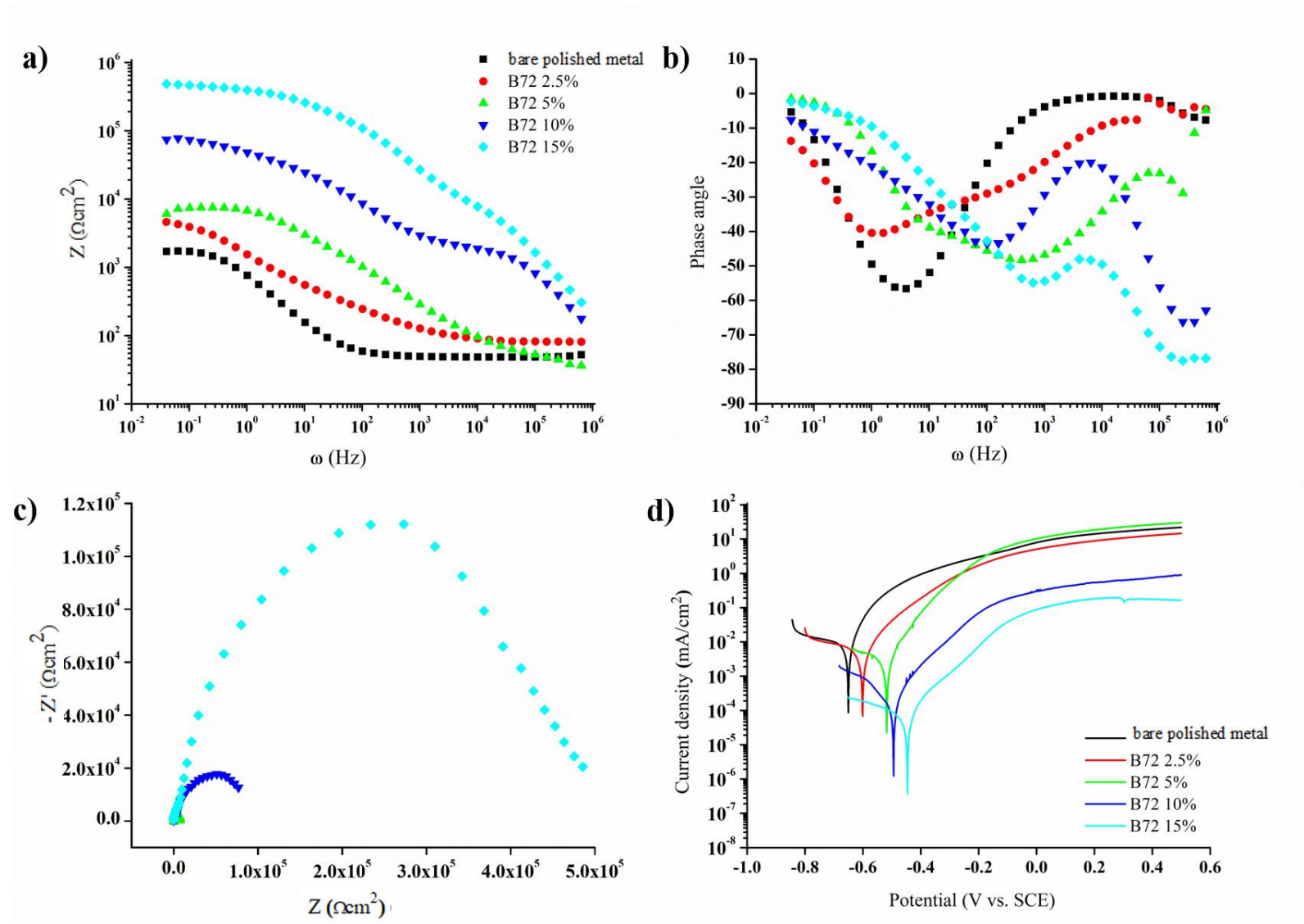


Figure 5.85: Electrochemical data obtained for Paraloid B-72 double-coated clean polished surface where a) Bode Impedance b) Bode Phase angle c) Nyquist and d) Potentiodynamic plots at various acrylate concentrations.

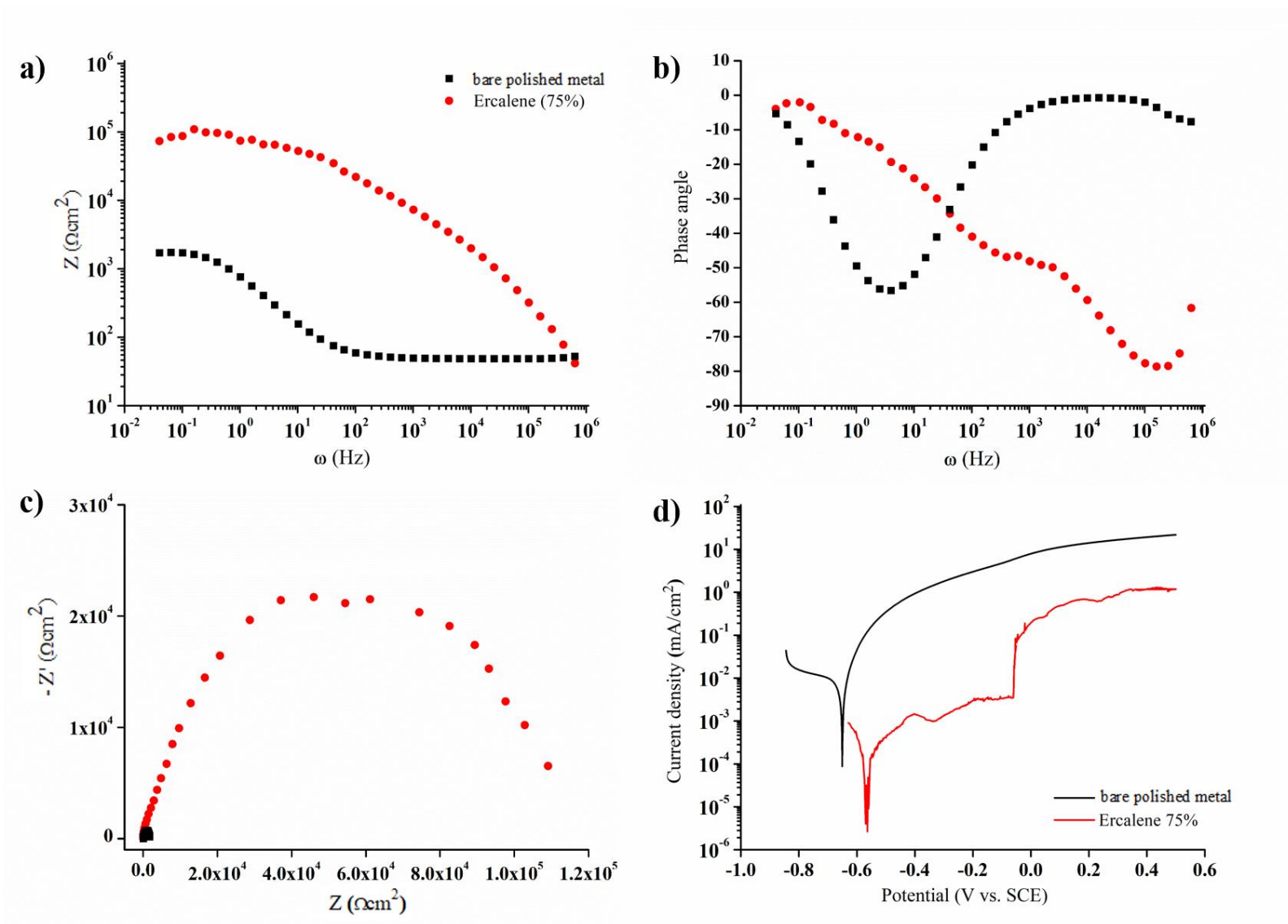


Figure 5.86: Electrochemical data obtained for 75% Ercalene double-coated clean polished surface where a) Bode Impedance b) Bode Phase angle c) Nyquist and d) Potentiodynamic plots.

5.5.3.2 Lacquer coatings on corroded-cleaned iron surfaces

Figures 5.87-5.89 display electrochemical results obtained for Paraloid and Ercalene-coated corroded surfaces. As previously shown in Figure 5.30, Impedance for corroded surface is less than that for a polished clean surface ($\approx 10^2 \Omega$). All coatings included in Figures 5.87-5.89 are protective to some extent seen as higher impedance obtained in low frequency range of the Bode impedance plots (a), wider capacitive arc in Nyquist plot (c) where bare metal arc is barely visible, and lower I_{corr} obtained in potentiodynamic plots (d). A higher impedance is obtained upon increasing acrylate concentration for Paraloid-based coatings, seen in Figures 5.87 and 5.88. An approximate two order of magnitude improvement over bare metal was obtained when a 10% Paraloid B-48 and B-72 concentration was used. Interestingly, a further increase in concentration for B-72 to 15% acrylate does not improve protection significantly.

15% B-48 coatings which had proven difficult to assess due to their inability to fail on clean metal (Figure 5.84), have been assessed on corroded metal surface in Figure 5.87 which shows a higher impedance value for 15% relative to 10% acrylate concentration. A 2.5 order of magnitude improvement has been obtained using 15% B-48 coatings on corroded surface which indicates their impressive corrosion protection even on a rougher corroded surface. B-72 coatings are also deemed protective, however to a lesser extent due to their ability to obtain a two order of magnitude improvement over bare corroded metal when applied in a 15% concentration (Figure 5.88). Results for Ercalene (Figure 5.89) illustrate a 1.5 order of magnitude improvement over bare metal which indicates that the nitrocellulose lacquer is the least protective lacquer on corroded surfaces as determined through electrochemical testing.

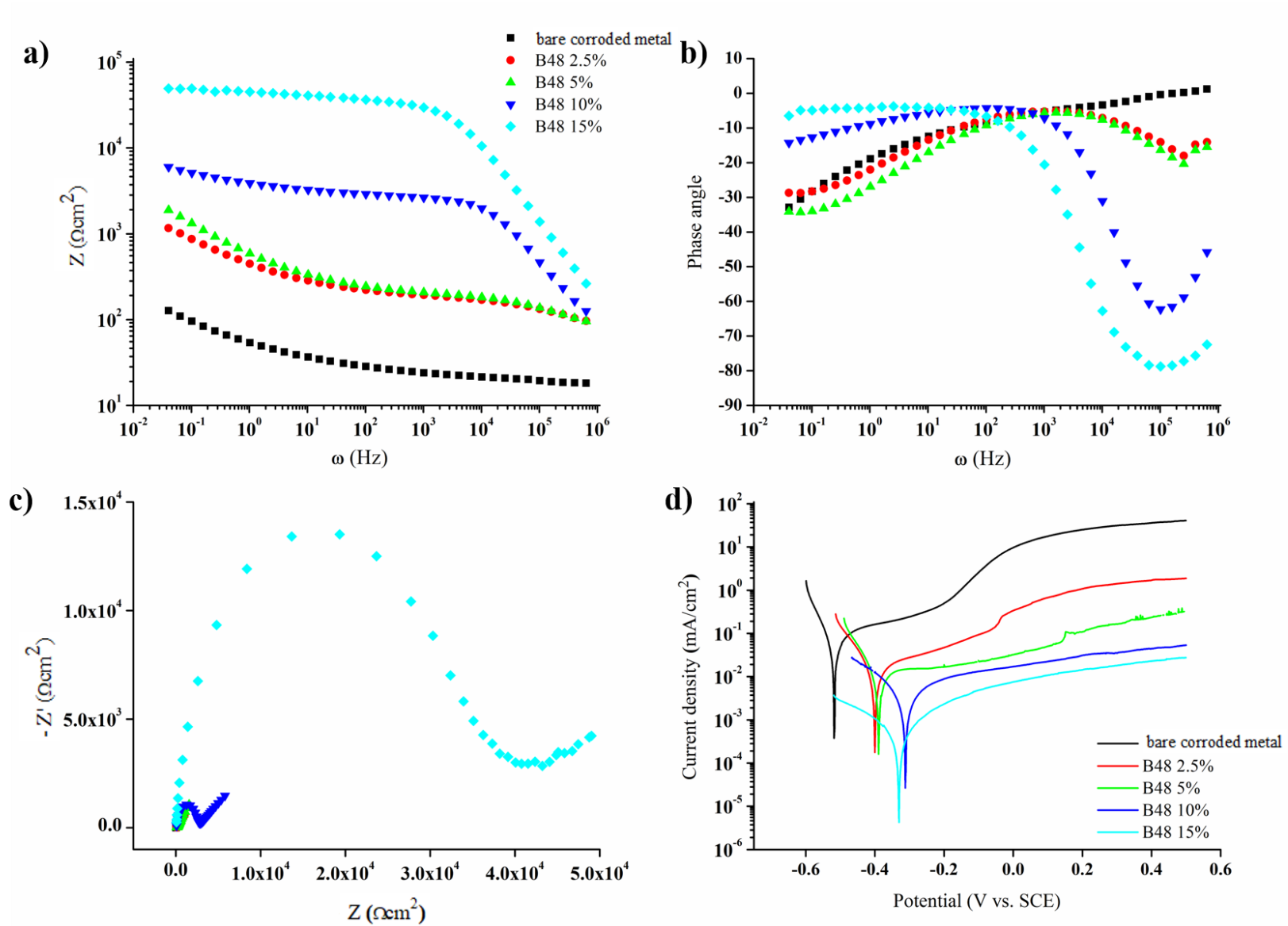


Figure 5.87: Electrochemical data obtained for Paraloid B-48 double-coated corroded surface where a) Bode Impedance b) Bode Phase angle c) Nyquist and d) Potentiodynamic plots at various acrylate concentrations.

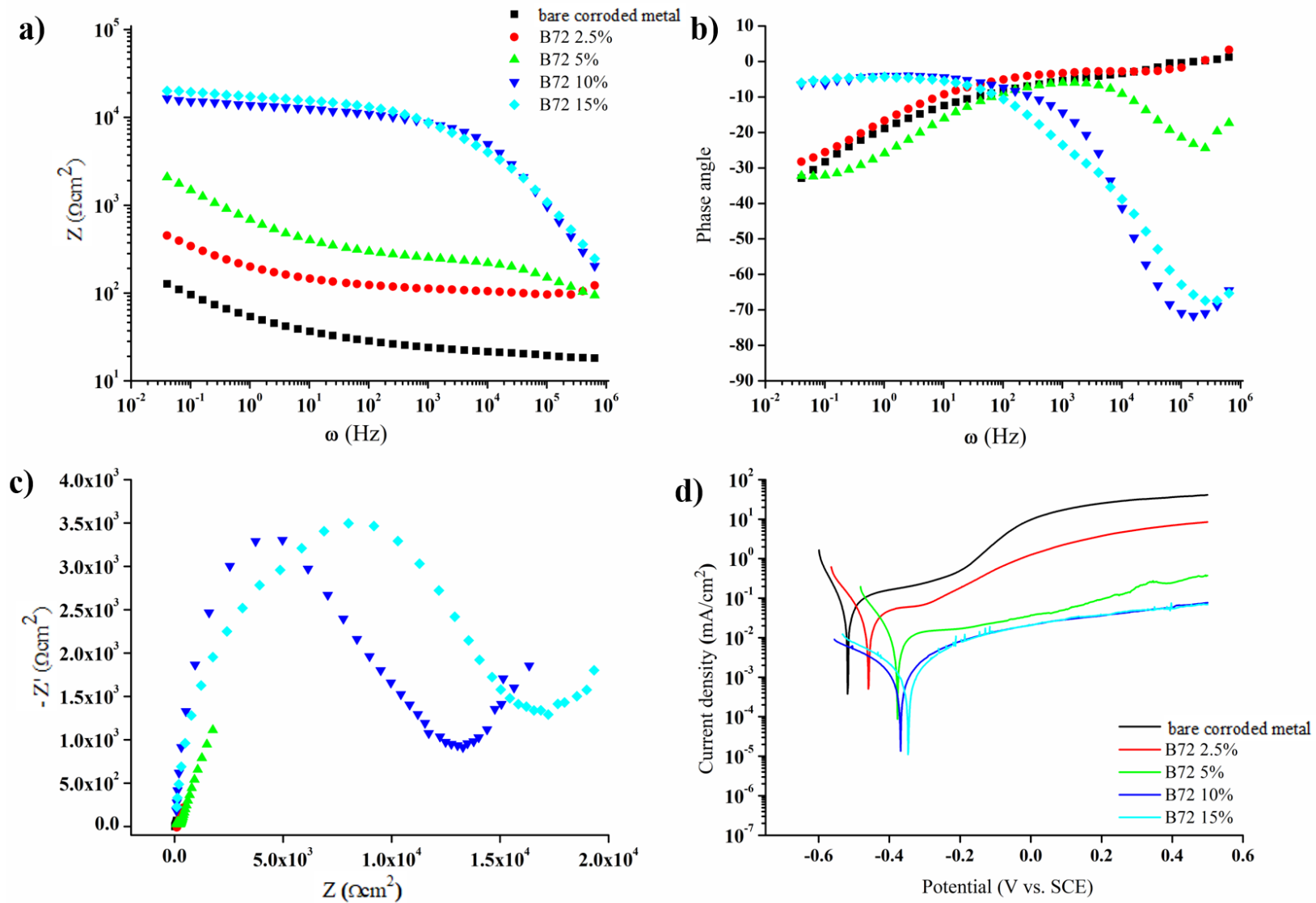


Figure 5.88: Electrochemical data obtained for Paraloid B-72 double-coated corroded surface where a) Bode Impedance b) Bode Phase angle c) Nyquist and d) Potentiodynamic plots at various acrylate concentrations.

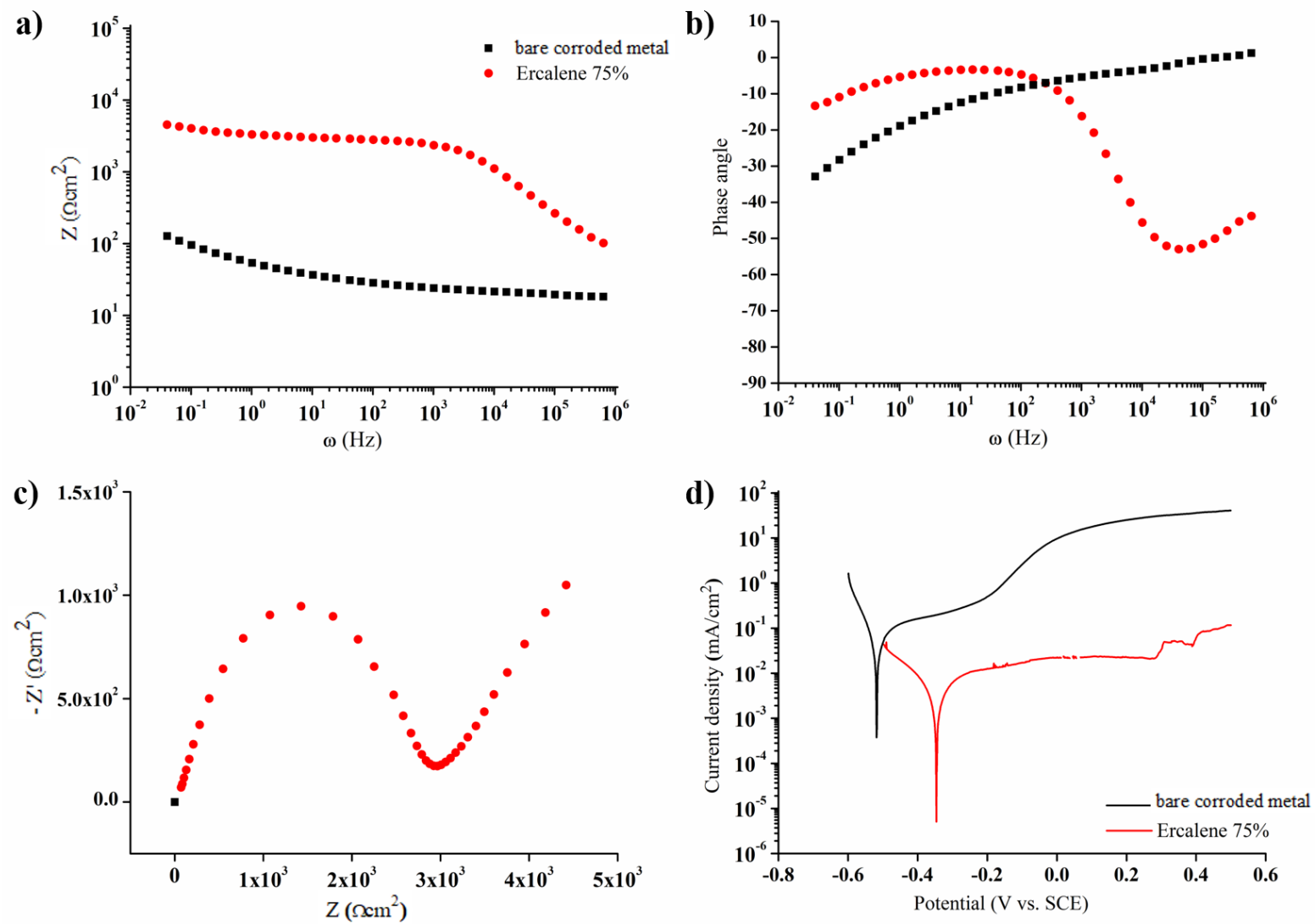


Figure 5.89: Electrochemical data obtained for 75% Ercalene lacquer double-coated corroded surface where a) Bode Impedance b) Bode Phase angle c) Nyquist and d) Potentiodynamic plots.

5.5.4 Accelerated corrosion (salt spray) testing

5.5.4.1 OIH alkoxysilane coatings applied through dip, fine brush, coarse brush and sponge applications

The results for the salt spray test are presented in **Figures 5.90-5.94** which feature clean metal surfaces that have been coated with a 10% SiO₂ concentration of MTES:TEOS 60:40 mol%, PrTES:TEOS 50:50 mol%, HTES:TEOS 30:70 mol%, OTES:TEOS 20:80 mol% and PhTES:TEOS 40:60 mol%. Several modes of coating application were considered for this testing; coatings were deposited using either dip (D), fine brush (FB), coarse brush (CB) and sponge (S) application. Unprotected iron coupons were also included as controls for which corrosion occurred immediately after cycle 1, most of the surface of coupon was already corroded. The metal composition contains a low percentage of microelements which translates into a relatively reactive surface which will corrode readily when subjected to an elevated temperature and humidity as carried out during the accelerated corrosion testing described in Section 3.4.

All coatings subjected to the accelerated corrosion testing protect the metal surface against corrosion to some extent when compared to uncoated surface. Corrosion deposits begin appearing on the coated coupons in the form of distinct corrosion spots. These spots show up following the first cycle, which are barely visible for dip-coated and fine-brush applications, but more conspicuous for coarse-brush and sponge-applied coatings. As cycling progresses, the number of spots increase and their size becomes larger, until the point is reached where the surface is mostly covered with corrosion products. The cycling process was halted after cycle 10.

Percentage area coverage of corrosion products over surface analysis was carried out by adjusting the threshold colour of images acquired for which 'Thresholding Method' was set to default, Threshold Colour was chosen to be indicated in red (**Figure 5.95**, right image) and Color Space was set to HSB (Hue, Saturation, Brightness). By manually adjusting the Brightness, whilst the Hue and Saturation are kept constant, the corroded spots begin to be highlighted in red. Special care was taken with each image not to adjust the brightness past the point where corrosion product staining is also highlighted (see Figure

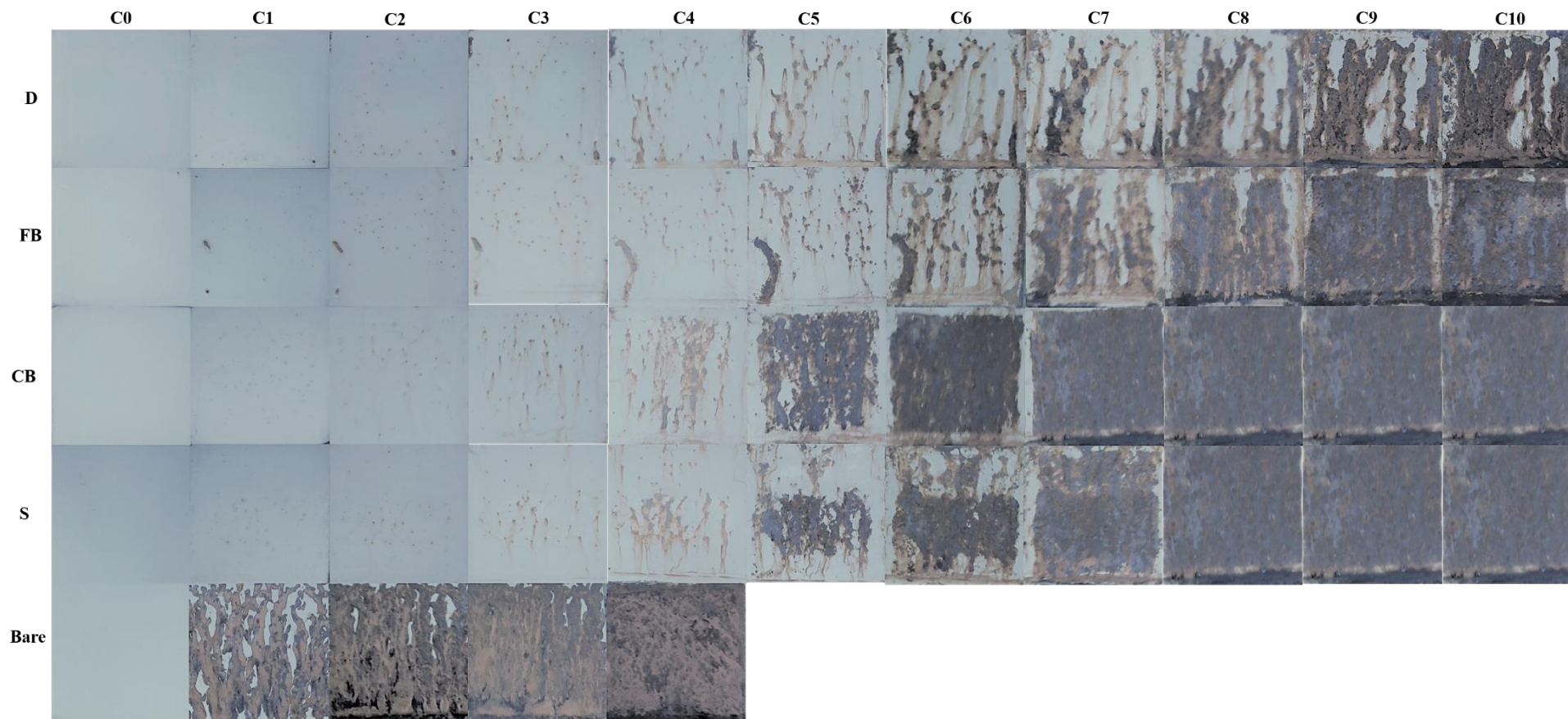


Figure 5.90: Photographs of clean iron coupons (38 mm x 38 mm) before (cycle 0) and after several cycles (cycle 1-10) in 0.6% (wt/wt) NaCl solution for polished iron coupons (bare metal) as comparison for coated coupons. Coupons have been double-coated with 10% SiO₂ MTES:TEOS 60:40 mol% and deposited via dip coating (D), fine-brush (FB), coarse-brush (CB) and sponge application (S).

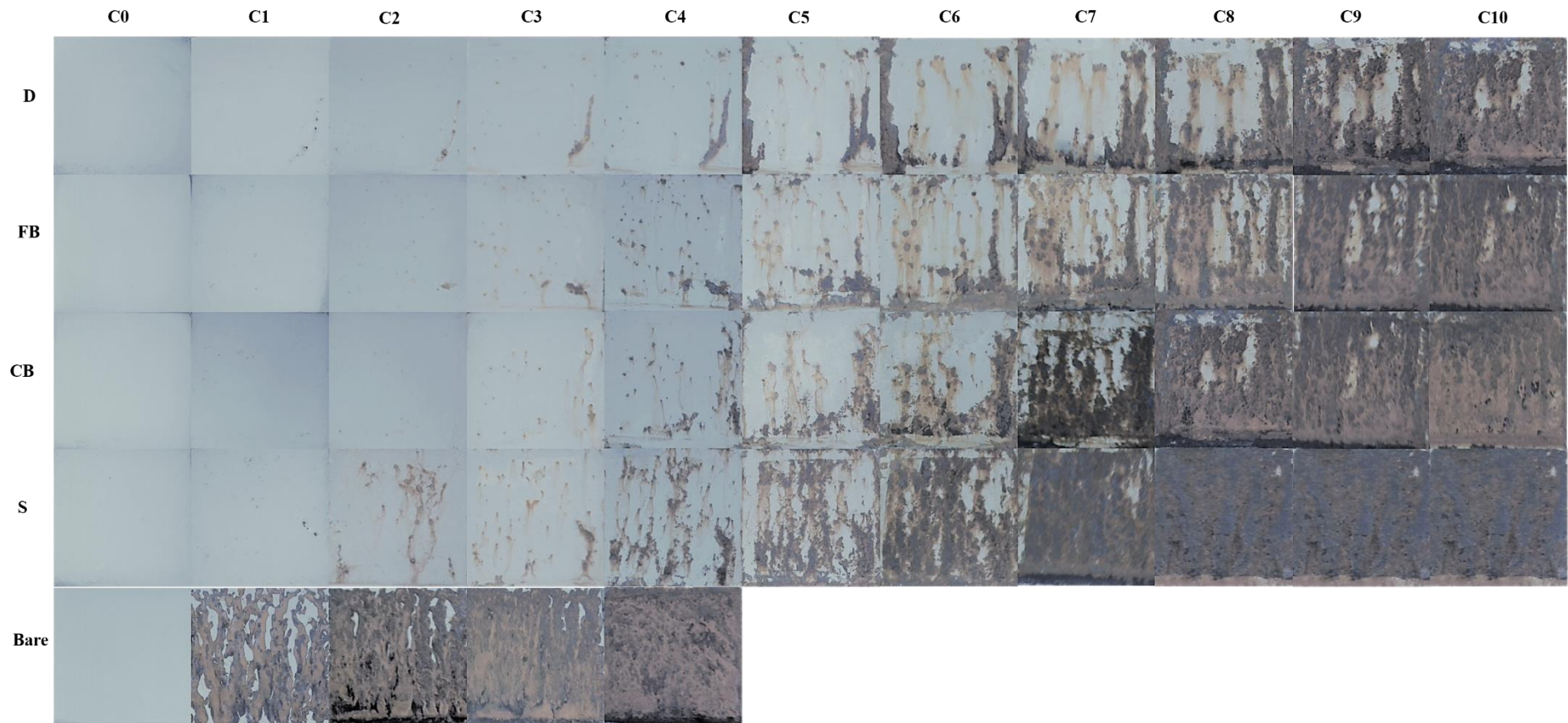


Figure 5.91: Photographs of clean iron coupons (38 mm x 38 mm) before (cycle 0) and after several cycles (cycle 1-10) in 0.6% (wt/wt) NaCl solution for polished iron coupons (bare metal) as comparison for coated coupons. Coupons have been double coated with 10% SiO₂ PrTES:TEOS 60:40 mol% and deposited through dip coating (D), fine brush (FB), coarse brush (CB) and sponge application (S).

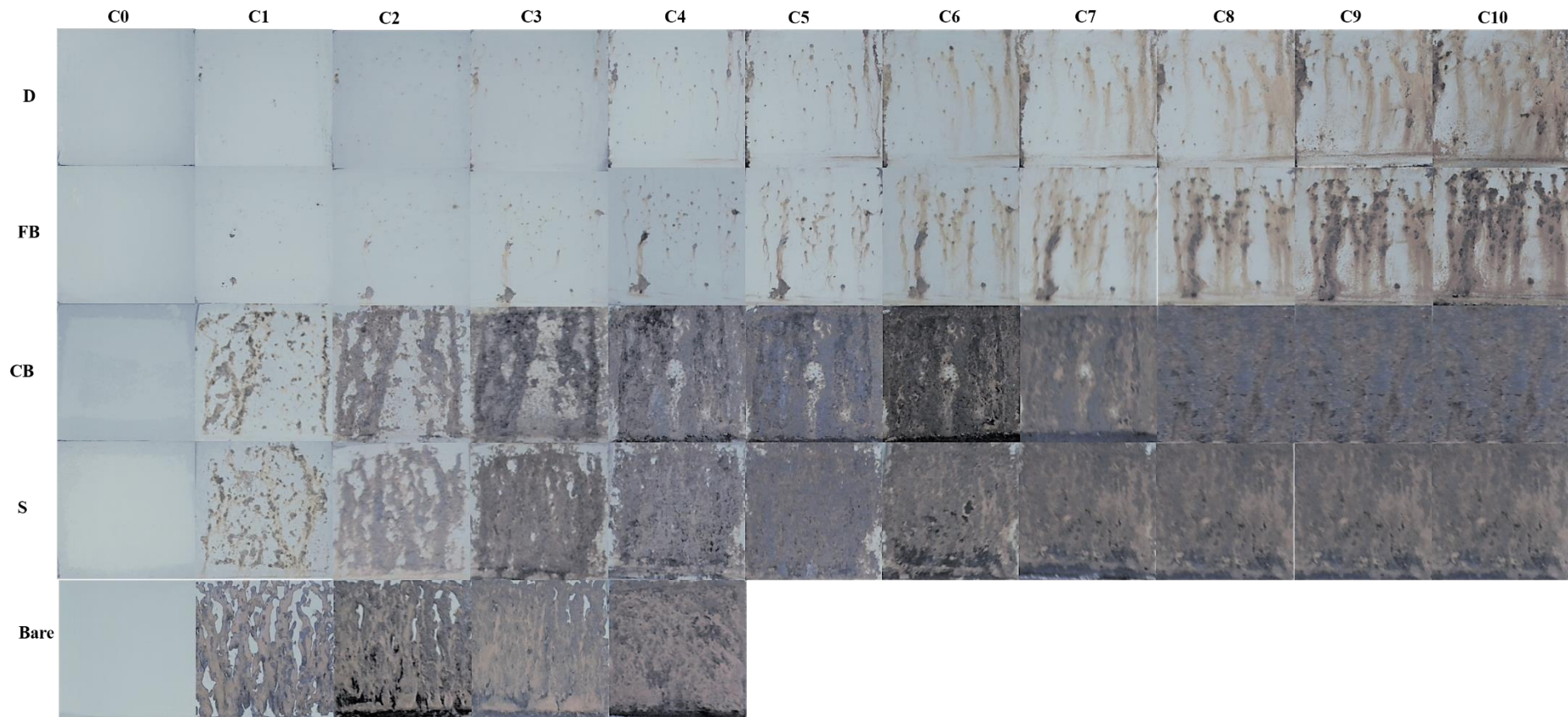


Figure 5.92: Photographs of clean iron coupons (38 mm x 38 mm) before (cycle 0) and after several cycles (cycle 1-10) in 0.6% (wt/wt) NaCl solution for polished iron coupons (bare metal) as comparison for coated coupons. Coupons have been double coated with 10% SiO₂ HTES:TEOS 60:40 mol% and deposited through dip coating (D), fine brush (FB), coarse brush (CB) and sponge application (S).

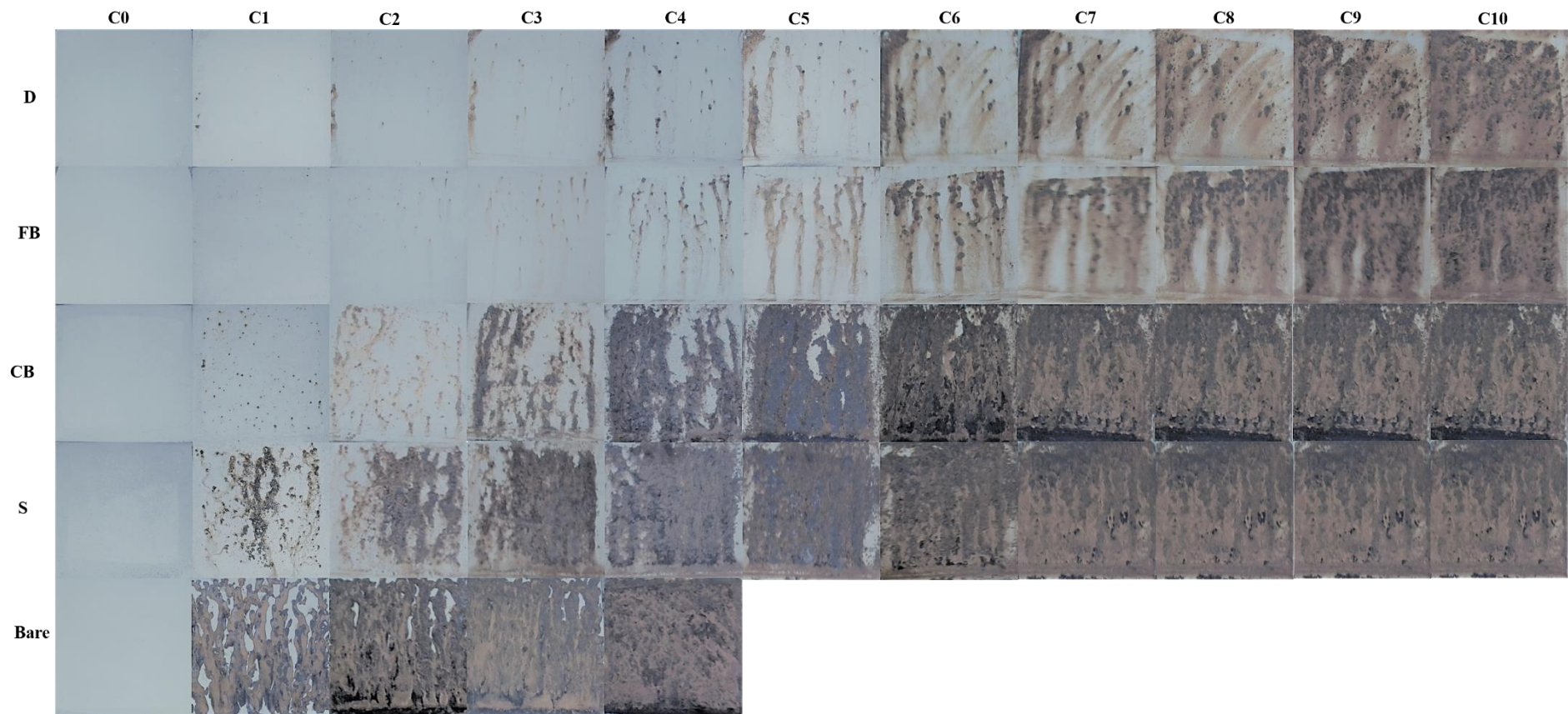


Figure 5.93: Photographs of clean iron coupons (38 mm x 38 mm) before (cycle 0) and after several cycles (cycle 1-10) in 0.6% (wt/wt) NaCl solution for polished iron coupons (bare metal) as comparison for coated coupons. Coupons have been double coated with 10% SiO₂ OTES:TEOS 60:40 mol% and deposited through dip coating (D), fine brush (FB), coarse brush (CB) and sponge application (S).

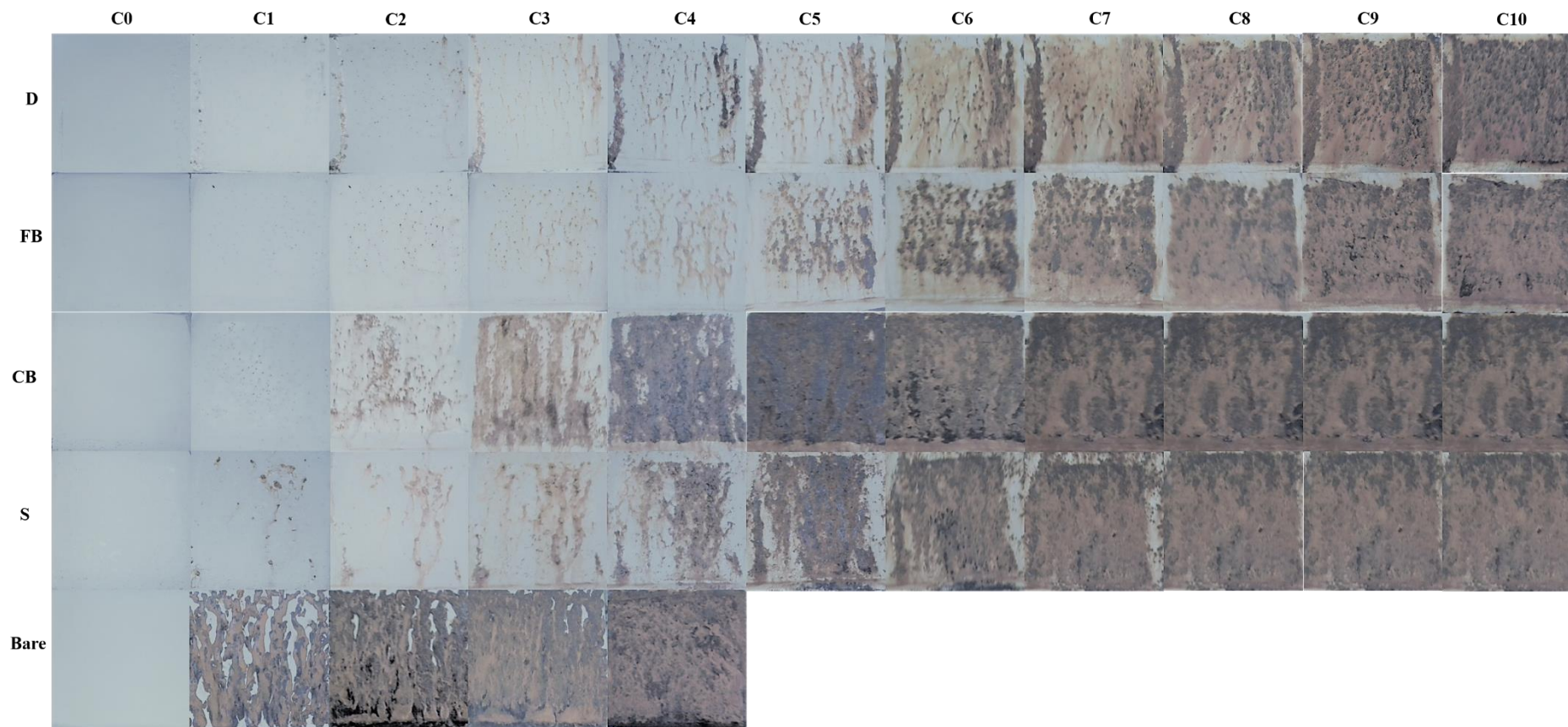


Figure 5.94: Photographs of clean iron coupons (38 mm x 38 mm) before (cycle 0) and after several cycles (cycle 1-10) in 0.6% (wt/wt) NaCl solution for polished iron coupons (bare metal) as comparison for coated coupons. Coupons have been double coated with 10% SiO₂ PhTES:TEOS 60:40 mol% and deposited through dip coating (D), fine brush (FB), coarse brush (CB) and sponge application (S).

5.95 right image). The software then calculates the total percentage coverage of the highlighted red areas which was carried out for all images recorded.

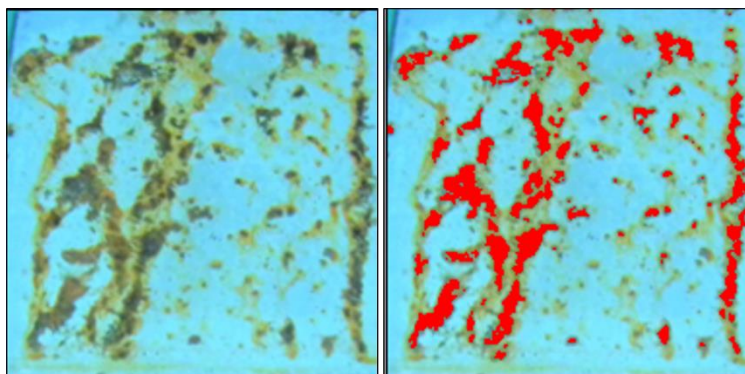


Figure 5.95: Photograph of HTES:TEOS 30:70 mol% coated coupon following first cycle (left image). Right image shows the covering of corrosion spots in red when the brightness of the image is adjusted accordingly using image J.

5.5.4.2 Paraloid and Ercalene lacquers applied through dip and fine brush applications

The results for salt spray test are presented in **Figure 5.96** which features clean metal surfaces that have been coated with 15% Paraloid B-48, B-72 and 75% Ercalene. Since coarse brush and sponge applications were ruled out as suitable modes of application for OIH alkoxysilane coatings, the lacquers were applied using dip (D) and fine brush (FB) application. All lacquers tested during the cycling process protect the metal surface against corrosion to some extent when compared to uncoated surface. Corrosion products began appearing by the end of the 2nd cycle on all lacquers. Both acrylates and nitrocellulose coatings appear to delaminate with relative ease and over a great part of the coupon surface which leads to an unprotected surface unhindered from the corrosion process. The delamination of coatings can be clearly exemplified with Paraloid coated coupon (see Figure 5.96, B-72 FB Cycle 2). Ercalene appears to fail through filiform manner (see Figure 5.96, Erc FB Cycle 2) initially followed by delamination of the coating as cycling progresses. Percentage area coverage of corrosion products over surface analysis was carried out as exemplified through Figure 5.95 above. Detailed discussion on percentage area coverage for results obtained in through salt spray testing i.e. Figures 5.90-5.94 and Figure 5.96, has been outlined in Chapter 10.

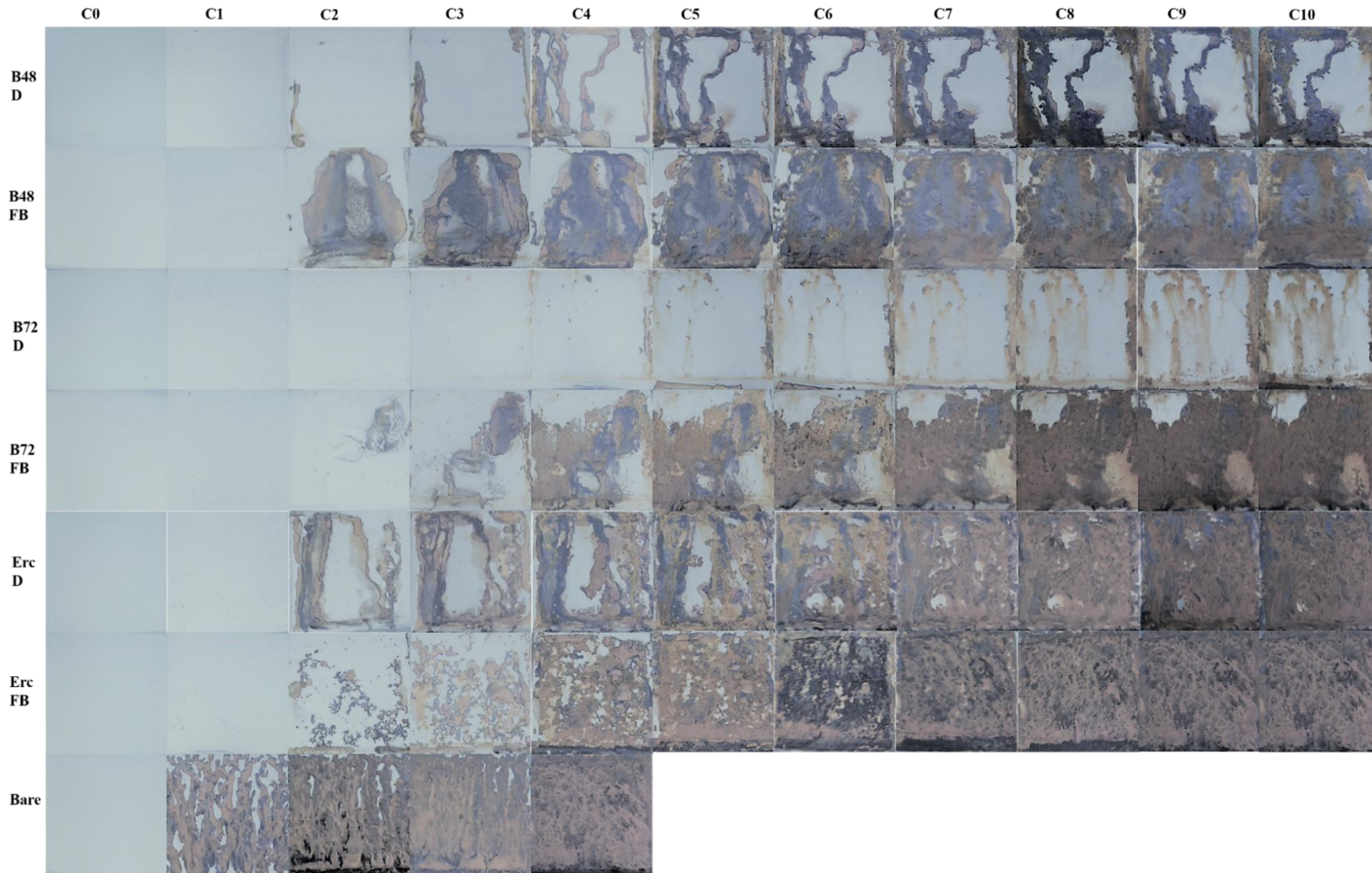


Figure 5.96: Photographs of clean iron coupons (38 mm x 38 mm) before (cycle 0) and after several cycles (cycle 1-10) in 0.6% (wt/wt) NaCl solution for polished iron coupons (bare metal) as comparison for coated coupons. Coated coupons shown have been double coated with 15% Paraloid B-48, Paraloid B-72 and 75% Ercalene lacquer by dip-coating (D) and fine brush (FB) application.

5.6 Reversibility of OIH alkoxy silane coatings

5.6.1 Immersion tests

Single coatings of OIH alkoxy silane coatings have been applied onto clean iron coupons through dip-coating, having a 2.5% SiO₂ concentration. The immersion test was carried out by immersing the coated coupons into each of the following: isopropyl alcohol (IPA 100%), NaOH solutions having pH 12 (0.01 M NaOH), 13 (0.1 M NaOH) and 14 (1 M NaOH). Immersion time results for all coatings investigated are presented in **Figure 5.97**. All coatings were removed successfully using pH 14 NaOH solution after just one hour of immersion. **Figure 5.98** presents a representative optical micrograph of a surface of coupon coated with OTES:TEOS 10:90 mol% , the right side of the image indicates the immersed part of the coupon on which coating has been fully removed after 1h of immersion in 1 M NaOH (pH~ 14).

A decrease to pH 12 lead to a significant increase in immersion time in most coatings relative to pH 13 and pH 14, drastic increases were recorded most notably for PhTES:TEOS and PrTES:TEOS coatings. Immersion testing at pH 12 required several days for coating material dissolution, at which point coupons began to develop black corrosion spots on sites where coating was partially removed/damaged as shown in **Figure 5.99**. Immersion testing was therefore halted after 10 days of testing (240 hrs) for which coatings marked with an asterisk in Figure 5.97 were still well adhered to the surface of the coupon. The longest immersion testing was carried out using IPA solvent; coatings having a high organic content such as OTES:TEOS 60:40 mol% were removed after a few hours, whereas coating having a low organic content remained intact for 10 days beyond which the testing was halted. The strength of these coatings was confirmed when two coupons coated with 20:80 mol% MTES and 20:80 mol% PrTES:TEOS were allowed to soak in IPA, and although the metal surface formed more corroded spots, undamaged coated sites still remained intact after one month of immersion.

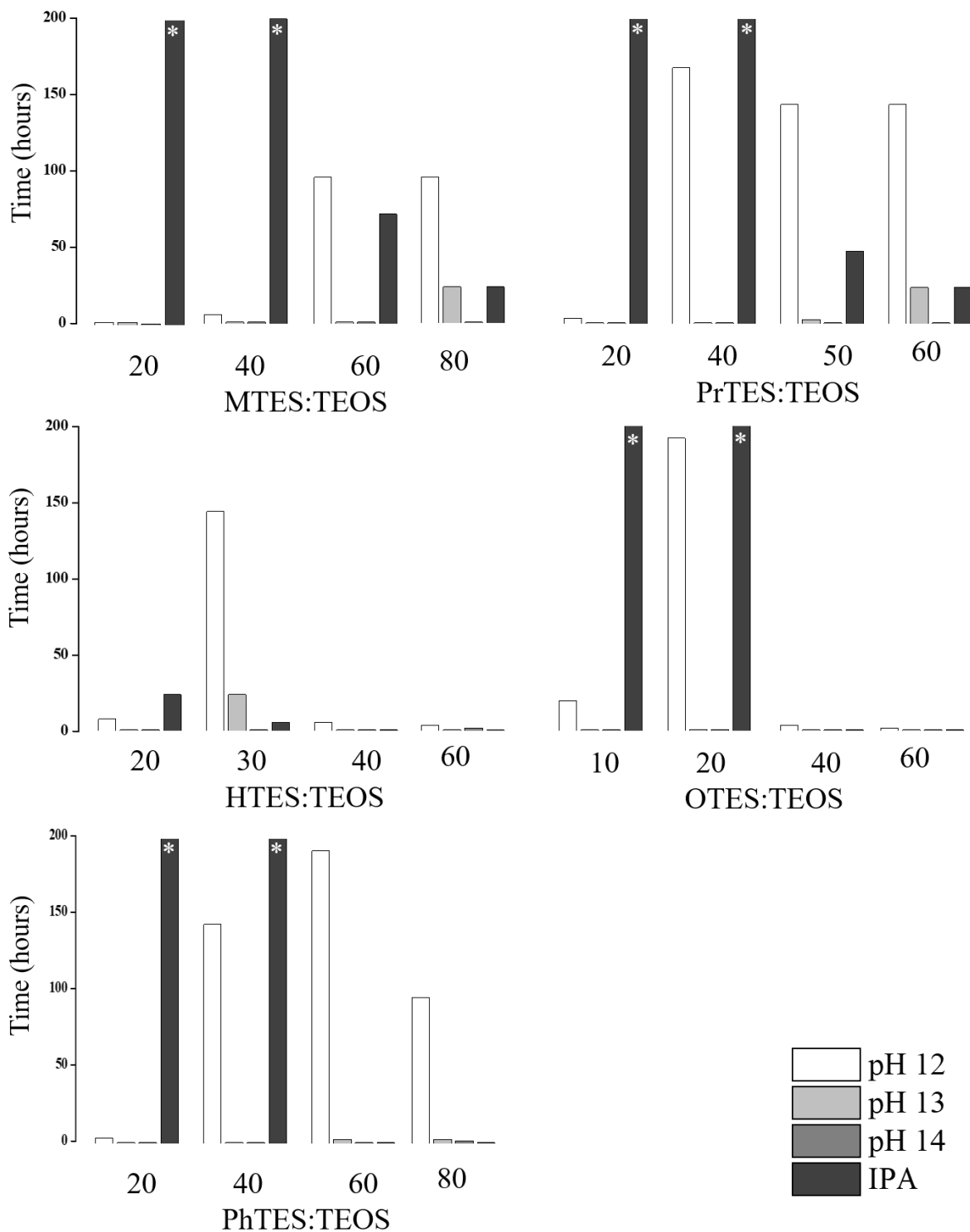


Figure 5.97: Plot showing immersion time (hrs) required to remove coatings. Coatings that remained intact beyond 240 hrs are marked with (*). Immersion liquids featured in this testing are IPA, NaOH solutions at pH12,13 and 14.

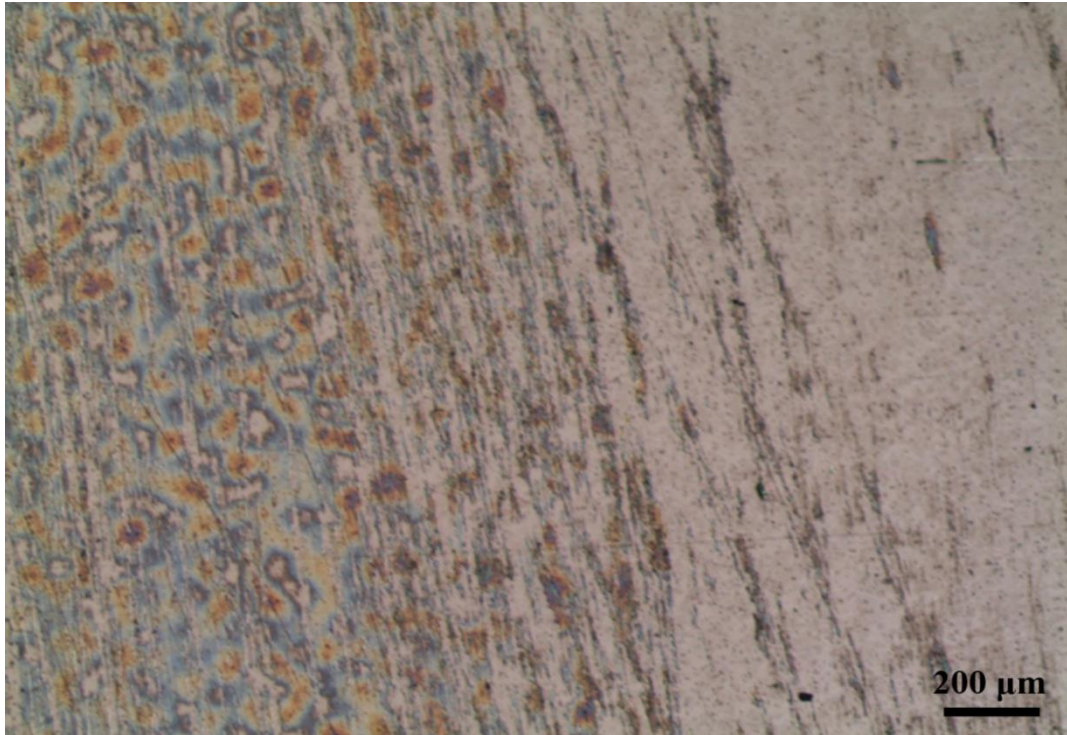


Figure 5.98: Optical micrograph of polished iron coupon that has been coated with 2.5% SiO₂ 10:90 mol% OTES:TEOS and immersed in pH 14 solution.

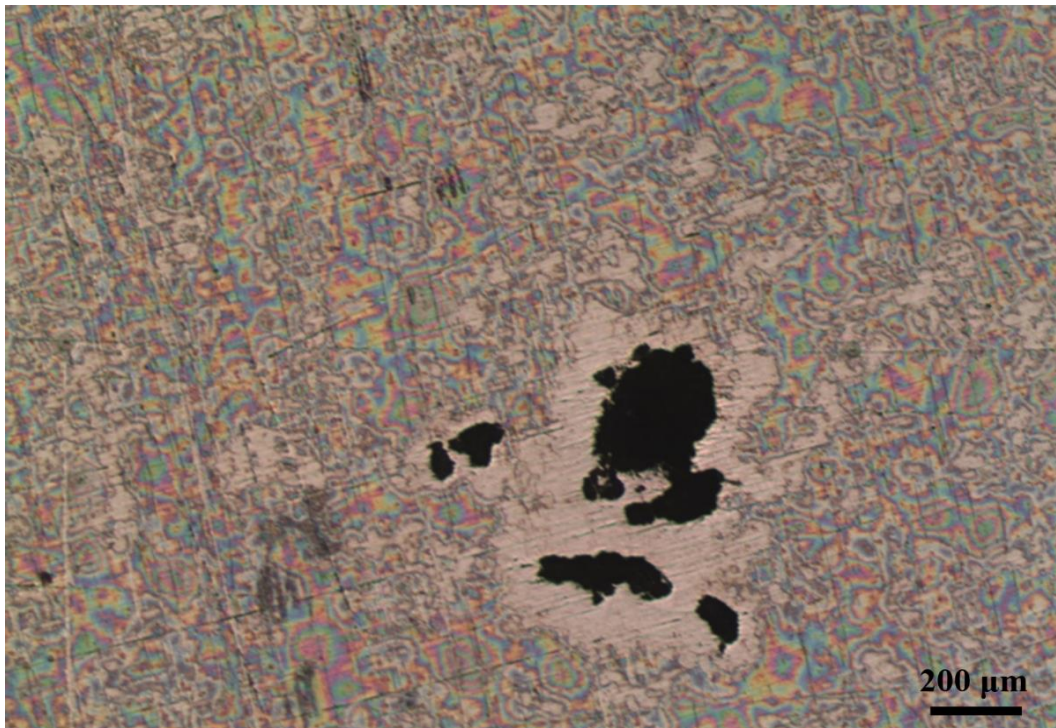


Figure 5.99: Optical micrograph of polished iron coupon that has been coated with 2.5% SiO₂ 60:40 mol% PhTES:TEOS and immersed in pH 12 solution which required 96 hrs for removal of coating. Image was acquired after 48hrs from beginning of immersion testing and showing formation of corrosion spots over exposed metallic surface.

5.6.2 Removal of coatings by manual cleaning

The removal of coatings by manual cleaning was carried out since it is not only a more realistic mode of removal of coatings from HM but avoids lengthy times and issues with corrosion products as shown in Figure 5.99. From immersion results it is clear that all OIH alkoxy silane coatings are easily removed using NaOH pH 14 solution. However, the more organic coatings (such as OTES:TEOS 60:40 mol%) were removed after an equally short time using IPA, which is a safer cleaning fluid than NaOH solution. Thus, it stands to reason that most coatings could be removed with a mixture of these two solutions; the solutions featured in this section were pH 14 NaOH solution (abbreviated as 100% N), IPA pure solvent (100% I) and ratios of the two (25:75% N/I, 50:50% N/I, 75:20% N/I).

Figure 5.100 presents the number of strokes required to completely remove coatings manually from the metal surface.

Overall, it can be said that HTES, OTES and PhTES coatings require less effort to be removed, when compared with MTES and PrTES-based coatings. Most coatings were easily removed using either 100% NaOH solution or a mixture of NaOH:IPA. The least organic coatings (20:80 mol% MTES/PrTES/HTES/PhTES:TEOS and 10:90 mol% OTES:TEOS) proved to be very difficult to remove using IPA solvent.

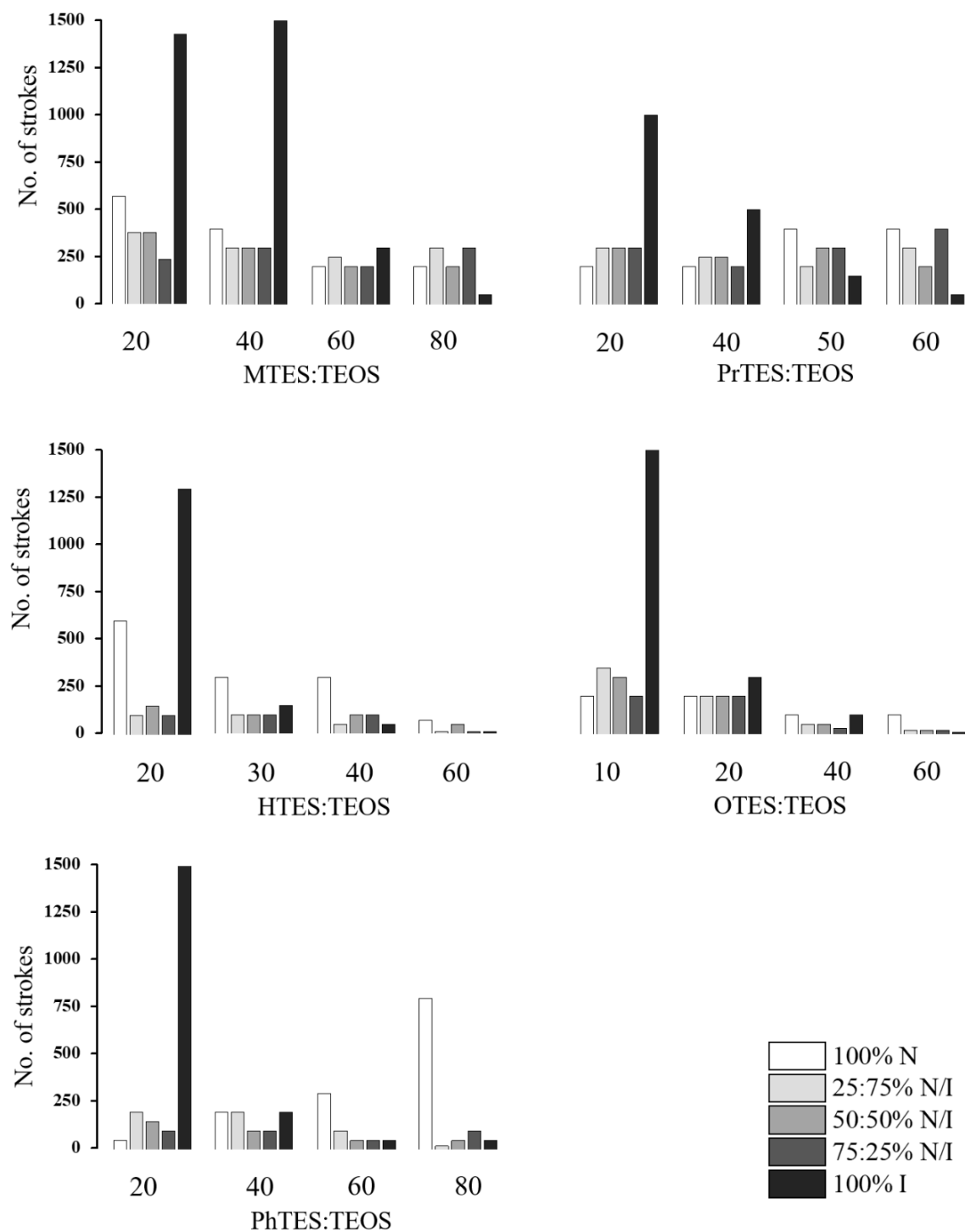


Figure 5.100: Number of strokes required to remove coating from the metal surface for all five precursors investigated. The solutions used were pH 14 NaOH solution (100% N), IPA pure solvent (100% I) and mixtures of the two (25:75% N/I, 50:50% N/I, 75:20% N/I).

CHAPTER 6:

The effect of alkyl/aryl functional groups on the mechanical and anti-corrosion properties of OIH alkoxy silane coatings

6.1 Introduction

The scope of this Chapter is to conduct a detailed comparative study into a set of OIH alkoxy silane coatings, namely X-Si(OR)₃ silane precursor molecules, where X= methyl-, *n*-propyl-, *n*-hexyl-, *n*-octyl- and phenyl-) in various proportions with TEOS. The study includes several mechanical tests which are utilised to explain trends observed in corrosion testing. The determination of the extent of corrosion protection offered by this set of OIH alkoxy silane coatings will feature as a backdrop to the remaining chapters within this work. The chapter has been sectioned to feature with characterisation of the developed sol, the characterisation of the coating and electrochemical testing carried out on coated coupons.

6.2. Sol characterisation

Figure 5.1 presents the particle size measurements carried out on all sols investigated in this work where the average sol particle sizes were measured to be within a narrow range of 1-3 nm. These values are in general agreement with measurements carried out by others on similar sols [223]. Figure 5.2 features the average particle size of the smaller population for each OIH alkoxy silane sol considered, where there appears to be no clear trend of particle size with varying concentration of hybrid precursor molecule for all five types of precursors investigated.

Particle size measurements of the sols used to prepare the coatings suggest that nanometrically sized particles with a very narrow size range as the coating building blocks. Such small particles can pack tightly to form relatively dense coatings with smooth surfaces as seen through SEM scans of surface of coatings (Figure 5.7). Such results can be collectively explained as follows: The longer alkyl chains have a tendency to position themselves on the outer surfaces of the forming sol particles leaving a silica-rich networks forming at their cores. Low organic-containing particles are therefore more free to form fractals whereas high organic-containing particles are sterically restricted from doing so. This can be corroborated through PS results of Figure 5.1 where OTES:TEOS coatings possess the smallest PS.

6.3 Coating characterisation

6.3.1. *Infra-red spectroscopy*

This section discusses results obtained in Chapter 5 Section 5.1.2.1, which begins with the evaluation of the peaks within the MTES precursor group as presented in Figure 5.4 which shows the relative area for 8 absorption bands considered for this analysis. As illustrated in Figure 5.4, there is a clear decrease in area % of Peak 3 (951 cm^{-1} due to stretching vibrations of Si–OH /Si–O⁻ groups) and Peak 1 (600 cm^{-1} due to rocking motion Si–OH /Si–O⁻ groups) indicates an overall decrease in Si–OH intensity as the mol% MTES precursor is increased. Yang *et al* has also reported a decrease in O–H absorption Peak 3 with an increase in MTES:TEOS ratio [223]. Results for Si–O–Si peaks shows a significant increase in area % of Peak 2 at 793 cm^{-1} which is due to symmetric stretching of the O along the bisector of the Si–O–Si bridging angle, with increase in MTES content of the sol. Results for the main area Peaks 4&5 (1067 cm^{-1} due to asymmetric stretches of O in Si–O–Si bonds) are less straight forward since a slight increase is obtained up to 60:40 mol% with area then decreasing for 80:20 mol% concentrations leading to a lack of clear trend as observed for Peak 2. This observation cannot be explained through the set of data obtained using IR analysis solely and could be explored further perhaps with the aid of ^{29}Si solid state NMR.

Table 5.2 features Peaks 1 to 5 (Si-O and O-Si-O related peaks) which are of particular interest for this discussion for all OIH alkoxy silane coatings that have been analysed using IR spectroscopy. The decrease in the area% for Si-OH related Peaks 1 and 3 coupled with an increase in area% for Si-O-Si related Peaks 2 and 4 (trends witnessed for MTES samples of Figure 5.4) are also evident when mol% of PrTES, OTES and PhTES: TEOS are increased. Only one mol% HTES:TEOS sol was applicable for sample preparation and therefore the effects of increasing the organic concentration remains unknown. However, this coating can still be compared to other OIH alkoxy silane coatings as shown in Figure 5.5 where all of the five organic group-containing powders feature in a 20:80 mol% ratio.

Figure 5.4 shows a decrease in the area % for Si-OH related Peaks 1 and 3 coupled with an increase in area % for Si-O-Si related Peaks 2 and 4 as the MTES (organic) content is increased. In Figure 5.5, when considering the aliphatic-containing organics MTES, PrTES, HTES and OTES; it is noticeable HTES/OTES:TEOS having a lower Si-OH and higher Si-O-Si intensity compared to MTES and PrTES which are similar in value. Therefore, a decrease in Si-OH coupled with an increase in Si-O-Si areas is a phenomenon that is occurring as a result of an increase in organic content of a coating, irrespective of the identity of the organic group. However, sharper changes in Area % were obtained in Figure 5.5 than Figure 5.4 due to more pronounced increase in organics as the chain is elongated (Figure 5.5) compared to an increase in methyl group concentration (Figure 5.4) as highlighted in **Table 6.1**.

Table 6.1: Percentage organic content (wt%) calculated for coatings investigated.

Mixture of XTES: TEOS	mol%						
	10:90	20:80	30:70	40:60	50:50	60:40	80:20
MTES:TEOS		5		10		14	18
PrTES:TEOS		13		23	28	32	
HTES:TEOS		23	31	37		48	
OTES:TEOS	16	28		44		55	
PhTES:TEOS		21		35		46	53

6.3.2 Coating thickness

Figure 5.9 presents thicknesses for every coating considered in this work. For the same hybrid precursor, there is a general slight increase in thickness with increasing hybrid precursor concentration which was also reported by Metroke *et al* [54]. However, coating thickness increases more significantly with increasing chain length in the following manner: MTES < PrTES < HTES < OTES for the same X-Si(OR)₃:TEOS molar ratio. PhTES containing phenyl groups produced the thinnest coatings, their coating thickness being comparable to that of MTES:TEOS coatings. It is postulated that thickness of coatings is related to the viscosity of sols upon deposition where more viscous sols will bring up more sol (slower drainage of sol during dip-coating process) thus leaving behind thicker layer of sol on the metal's surface. In fact, Kumar *et al* [56] reported similar viscosity measurements for 80:20 mol% MTES:TEOS and PhTES;TEOS sols which lead to similar coating thicknesses in the study of Kumar *et al*, and as shown in Figure 5.9.

6.3.3 Contact angle

The water contact angle measurements of the OIH alkoxy silane coatings as presented in Figure 5.11 show a gradual increase in water contact angle with increasing mol% concentration of the alkyl/aryl precursor. Such trends also reflect an increase in the population of organic moieties on the surface of the coatings. As the organic loading increases, surfaces become more hydrophobic, reducing interaction between coating surface and water droplet. All coatings except those of OTES:TEOS with OTES < 40 mol% concentration show contact angles below 90°. Water contact angles for 40:60, 60:40 and 80:20 mol% OTES:TEOS were respectively 93.8°, 95.7° and 93.1° which is attributed to their high organic content). Another general trend can be observed in which higher contact angles are obtained when the length of the organic moiety is increased, for example OTES:TEOS coatings are significantly more hydrophobic at a given OTES:TEOS mol% when compared to MTES:TEOS coatings. HTES:TEOS do not follow this trend, low contact angle measurements for this set of coatings has been difficult to corroborate.

Ferri *et al* [187] reported a water contact angle of 101° for 10:90 mol% OTES:TEOS and 105° for a 20:80 mol% ratio of OTES:TEOS, higher than those recorded in this work. Metroke *et al* [54] on the other hand, measured a water contact angle of 95° for 60:40 mol% OTES:TEOS coating which is close to the measurement obtained in this work. Nonetheless, all coatings deposited provided a significant increase in water contact angle (by approximately 20°) over the bare uncoated iron surface which shows that coatings not only act as physical barriers to corrosion, but also repel water molecules making it more difficult for corrosive species to penetrate the coating. All contact angle measurements featured in this work were conducted under static conditions. A more detailed study on contact angle using Dynamic measurements can be featured in future work using volume changing method (advancing and receding angles) and/or tilting cradle modes of determination.

6.4 Mechanical testing

6.4.1 Hardness and elastic modulus measurement using Nano-Indentation

Results obtained through nano-indentation presented in Figure 5.13 which demonstrate an increase in organics concentration in coatings that results in lower hardness measurements and hence less rigid coatings which undergo a greater extent of deformation (e.g. 60:40 mol% OTES:TEOS hardness value = 0.025 GPa) than the stiffer coatings containing low organic content (e.g. 10:90 mol% OTES:TEOS hardness value = 2.00 GPa). MTES:TEOS systems in 60:40 mol% ratios was featured in the work by Ballarre for which Young's modulus was calculated to be 6.5 and Hardness of 0.92 GPa [214] which is similar to values obtained in this work (5.9 and 0.81 GPa respectively). Mizuta *et al*, worked on PhTES:TEOS systems and have also reported a slight decrease in hardness with an increase in the organic content originating from PhTES. This observation has been attributed to the organic phenyl-silane part undergoing less cross-linking than the inorganic TEOS resulting in Hardness and Young's modulus being lower when the organic content increases [224]. Kalidindi also attributes the presence of chemical bonds of high strength (Si-O-Si network) to greater hardness of the coating [225].

Ferchichi studied MTES:TEOS and PhTES:TEOS systems in 30:70 mol% ratios and has reported Hardness of 2.1 GPa and Young's Modulus of 11.6 GPa for MTES systems, together with Hardness of 0.5 GPa and Young's Modulus of 5.2 GPa for PhTES systems. The author indicates that a decrease in hardness is due to the larger organic group size [226]. In fact, it is also observable in results of Figure 5.13 for 20:80 mol% coatings where an increase in size of organic group generally leads to a decrease in hardness where OTES:TEOS coatings are the least hard. HTES:TEOS coatings appear to be the exception to the trend and have shown to be the hardest at that concentration. This instance does not follow through at higher HTES concentrations i.e. HTES:TEOS concentration of greater than 20:80 mol% results in hardness values similar to that of OTES coatings.

6.4.2 Pull-out test for the study of adhesion of OIH alkoxy silane coatings

Coating adhesion to the substrate could result from a purely mechanical bond held together due to anchoring as a result of increased effective surface area or a chemical bond, or a combination of both. It is always assessed by the amount of force required to separate the coating from the substrate. The coating could fail at the interface between the coating and substrate, if the adhesion to the substrate is poor, or in the coating, if coating cohesion is poor [225].

The pull-out test was carried out by applying a tensile force on the coating surface via a dolly, held together using an epoxy adhesive. Figure 5.17 shows images of surface of coupons following pull-out test whereas Figure 5.18 illustrates the force measured at the point of detachment of dolly from the coated coupon. As specified in the methodology section, epoxy adhesive was used since it proved to withstand the highest tensile force, thus being the best adhered to the OIH alkoxy silane coatings. Nevertheless, even when employing the epoxy adhesive, failure during pull-out appears to happen at the dolly-adhesive interface for lower organic % coatings (such as PrTES/MTES:TEOS 20:80 mol%) and at the coating-adhesive interface for coatings with higher organic content such as 60:40 mol% HTES/OTES:TEOS and 80:20 mol% PhTES:TEOS (Figure 5.17). No failure was observed at the coating-iron substrate interface for any of the coatings studied which indicates that all of these

coatings are very well adhered to the metal surface, so much so that an appropriate adhesive has yet to be found that is capable of forming stronger dolly-adhesive and adhesive-coating bonding compared to metal-OIH alkoxy silane coatings considered.

Through images of Figure 5.17 it can be said that coatings having a higher organic content tend to have the adhesive-to-coating interface as the weakest interface, which indicates poor adhesion of the adhesive to the coating. This observation is quantitatively described in Figure 5.18 where epoxy adhesive endures less tensile forces when applied onto OTES-based coatings. This can be confirmed through the force measured for bare metal which is the highest value tested and adhesive remains attached completely to the dolly, leaving behind no residue on the coupon surface. Less organic coatings such as MTES and PrTES endure higher forces before failure at the dolly-adhesive interface which indicates better adhesion of the adhesive to the more silica-rich MTES and PrTES coatings. Even though a quantitative analysis was possible in determining the extent of adhesion of coatings, results obtained in Figure 5.18 should be considered with caution since the failure mode of more organic-containing coatings is not the same as that of coatings having lower organics percentage.

Pull-off testing for the determination of adhesion of coatings did not lead to the desired force required to detach the coatings from the metal substrate since the coating-metal bonding proved to be superior to the coating-adhesive and adhesive-dolly interfaces. This in itself is a positive result, however the comparative study shown in Figure 5.18 shows the force of detachment at the undesired interfaces. Thus, it can be stated that the coatings are capable of withstanding a minimum force as shown in Figure 5.18. Published work on adhesion testing through the pull-out method for OIH coatings is scarce. The most relevant papers are those by Ramezanzadeh *et al* [227] and Yuan *et al* [228] for which OIH coatings were used as primers to improve adhesion of the top coat (epoxy) to metal surfaces.

Ramezanzadeh *et al* studied mixtures of 3-aminopropyltriethoxysilane (APS) and TEOS in molar ratios of 0:100, 30:70, 50:50, 70:30 and 100:0 mol% which were deposited on mild steel surfaces. An epoxy top coat was then applied over the various OIH coatings for which pull-off testing was carried out to investigate the effects of the silane pre-treatment on the adhesion properties of the epoxy coating. The methodology used was similar to that employed in our work where aluminium dollies were glued on the surface of the silane-epoxy coated samples using a two-part Araldite adhesive. Samples were allowed to dry for 24 hrs at ambient temperature to ensure that the adhesive was properly cured. The dolly was pulled at a speed of 10 mm/min normal to the coating surface until the epoxy coating was detached from the steel substrate. The authors reported adhesive failure on the bare steel indicating poor adhesion of the epoxy coating on the sample when no silane pre-treatment was applied. The application of 70:30 and 100:0 mol% APS:TEOS led to the enhanced adhesion of the epoxy coating to the steel surface for which cohesive failure had occurred. An adhesive strength of up to 5.5 MPa was documented [227] for 0:100 TEOS:APS (550 N/cm² compared to 1,356 N/cm² for the highest pull-out force recorded for 20:80 mol% MTES:TEOS coatings in this work) compared to epoxy-coated samples without silane pre-treatment (3.4 MPa).

Yuan *et al* reported a 9.3 MPa pull-out strength when an OIH coating consisting of a mixture of silanes namely GPTMS, TEOS and MTES [228] was employed as pre-treatment to an epoxy topcoat on 2024 Al-alloy substrate. The adhesion strength of the coatings on the samples with and without OIH pre-treatment was evaluated using pull-off adhesion tests before and after immersion in a NaCl solution where values of 9.3 MPa before immersion and 6.6 MPa after immersion are reported. This publication could inspire future work for adhesion strength determination using the OIH coatings from this work: since adhesion strength of a coating decreases upon immersion in a solution, then it may become possible to determine the force required to detach the coatings from the metal surface, assuming that all coatings considered would degrade in a similar manner thus allowing for a comparative study.

6.4.3 Nano-scratch

A clear trend is noticeable in scratch test results presented in Figure 5.16 for all five types of OIH alkoxy silane coatings in which force required to reach surface of underlying metal substrate decreases as XTES mol% is increased.OTES coatings, having the highest organic content and thus being the softest coatings as determined through nano-hardness testing, are penetrated the quickest.HTES plots are similar to those ofOTES whereas the shorter chained OIH alkoxy silane coatings withstand a greater force along the scar since they are harder thanOTES coatings.

6.5 Electrochemical Evaluation

The *U*-shaped trends in Z_{tot} at low frequency and I_{corr} versus mol% composition of coating (see Figure 5.24) has previously been reported in potentiodynamic results for the MTES:TEOS system on steel [53]. The current work demonstrates that this trend also holds true for the other four organic precursors investigated, for both EIS and electrochemical polarisation testing. Moreover, the ratio of X-Si(OR)₃:TEOS that produces a maximum resistance was found to be different for the different coatings tested: 60:40 mol% for MTES:TEOS, 50:50 mol% for PrTES:TEOS, 30:70 mol% for HTES:TEOS 40:60 mol% for PhTES:TEOS and 20:80 mol% forOTES:TEOS. Furthermore, from the five aforementioned coatings, 30:70 mol% HTES:TEOS exhibits the lowest Z_{tot} value $\sim 1.24 \times 10^5 \Omega \text{ cm}^2$, followed by 60:40 mol% MTES:TEOS with a Z_{tot} value of $2.02 \times 10^5 \Omega \text{ cm}^2$, $4.08 \times 10^5 \Omega \text{ cm}^2$ for 50:50 mol% PrTES:TEOS, $4.56 \times 10^5 \Omega \text{ cm}^2$ for 40:60 mol% PhTES:TEOS, whereas 20:80 mol%OTES:TEOS provides the highest corrosion protection $\sim 8.53 \times 10^5 \Omega \text{ cm}^2$ i.e. close to three orders of magnitude improvement over bare metal.

Very few electrochemical studies have been conducted that feature the two precursors X-Si(OR)₃ and TEOS in various ratios. Base-catalysed MTES:TEOS 80:20 mol% coatings were produced by Subarsi and co-workers for the protection of aluminium substrate with coating thickness range of 1-5 μm by varying the dip-coating speed. Corrosion testing involved the use of EIS and

electrochemical polarisation measurements in a 3.5% NaCl solution for a 1 hr exposure time [44]. A potentiodynamic scan revealed a two-order of magnitude decrease in I_{corr} compared to the bare metal. This improvement is higher than what was obtained in this current work. These authors [44] also show R_{po} values between $2.6-7.6 \times 10^3 \Omega \text{ cm}^2$ for coating thicknesses of between (1-5 μm), whereas 80:20 mol% MTES:TEOS coatings produced in this work presented an R_{po} value of $128.2 \Omega \text{ cm}^2$, such significantly lower values can be attributed to the thinner coatings used in this work (Figure 5.9). Kumar *et al* [56] studied the corrosion protection of organic-inorganic hybrid sol-gel based coatings deposited on SS-316 grade stainless steel substrate using dip-coating technique. The coatings investigated included PhTES: TEOS and MTES:TEOS in a 80:20 mol% which were tested for their corrosion protection through a potentiodynamic scan. Similar results were obtained where the I_{corr} for PhTES: TEOS and MTES:TEOS were one order of magnitude lower than bare metal which is in agreement with results obtained in this work.

6.6 General discussion

Analysis of the infra-red spectra belonging to MTES-coatings (Figure 5.4) shows a decrease in the area % for Si–OH related Peaks 1 and 3 coupled with an increase in area % for Si–O–Si related Peaks 2 and 4&5 as the organic content is increased. This is also true when considering the aliphatic-containing organics MTES, PrTES, HTES and OTES (Figure 5.5). Therefore, a decrease in Si-OH coupled with an increase in Si-O-Si areas is a phenomenon that is occurring as a result of an increase in organic content of a coating, irrespective of the identity of the organic group. This may explain PS of 20:80 mol% OTES (C8) being smaller than of 20:80 mol% MTES (C1) (Figure 5.1), since more discrete spherical particles would be formed (OTES) compared to longer chain-like particles for MTES. However, a clear decrease in particle sizing (see Figure 5.1) has not been reported when increasing MTES:TEOS ratio from 20:80 up to 80:20 mol% even though the organic content is being increased. This could be due to the instrument not being sensitive enough, or the increase in Si–O–Si formation from 20:80 to 80:20 mol% MTES:TEOS is insufficient for producing a measurable change in particle sizing. In fact, a more modest increase in organic content is obtained when MTES

concentration is increased (see Table 6.1 for wt% of organics) compared to increase in chain length MTES to OTES in a 20:80 mol% ratio.

Results obtained through nano-indentation and nano-scratch can be joined in discussion since a greater hardness and elastic modulus increases the resistance of coatings to plastic deformation, leading to resistance to the entry of the scratch tip [229]. The relationship between results of nano-indentation and nano-scratch can be appreciated through Figures 5.13 and 5.16 respectively, where an increase in silica content led to harder coatings, which in turn require a greater force to be scratched by the tip. Nanoindentation on relevant alkyl-silane sol-gel coatings literature review typically feature a mixture of the alkyl-silane with metacrylate- [230,231] epoxy- [232-234] vinyl-silanes [233,235] or amino-silanes [236]. The decrease in hardness with a decrease in silica concentration has also been reported by Palanivel *et al* on bis-sulfur silane films with different silica amounts were deposited on mirror-like stainless steel surfaces [43].

Low wt% organic containing coatings (such as 20:80 mol% MTES:TEOS, PrTES:TEOS, HTES:TEOS, PhTES:TEOS and 10:90 mol% OTES:TEOS) have been shown to be harder and more resistant to scratch compared to their higher XTES:TEOS counterparts, however, they did not produce the most corrosion resistant coatings as shown through electrochemical data obtained (Figure 5.24). Moreover, the ratio of $X_n\text{-Si(OR)}_{4-n}$: TEOS that produces the most protective coating was found to be different for the five types of organic coating systems investigated: 60:40 mol% for MTES:TEOS, 50:50 mol% for PrTES:TEOS, 30:70 mol% for HTES:TEOS, 20:80 mol% for OTES:TEOS and 40:60 mol% for PhTES:TEOS. Interestingly, the larger the organic molecule (X) the less of the organosilicon precursor concentration will be required to produce a protective coating i.e. a 60:40 mol% ratio produces the best protective coating when employing MTES as the precursor whereas only 20:80 mol% ratio is sufficient for creating the most protective coating when using OTES precursor molecules.

Following these promising trends, the total percent organic content present in the coatings that gave rise to the highest corrosion protection was calculated and presented in **Table 6.2**. It appears that for the case of alkyl-containing precursors, excluding MTES, the organic content that gives rise to the most protective coatings per hybrid group was 27-30 wt%. The % by weight organic content for the MTES:TEOS 60:40 mol% system was found to be less, at 14 wt%. It can be said that weight% organics could be used to gauge the mol% of precursor required to give a good coating when a new precursor is used (for instance, pentyl triethoxysilane).

Table 6.2: Percentage organic content (wt%) calculated for the five precursors investigated

X-Si(OR) ₃ :TEOS	mol% ratio	Organic content (wt%)	Z _{tot} (Ω cm ²)
MTES:TEOS	60:40	14	2.01×10 ⁵ ± 2.52 ×10 ⁴
PrTES:TEOS	50:50	28	4.08×10 ⁵ ± 5.10×10 ⁴
HTES:TEOS	30:70	30	1.24×10 ⁵ ± 1.55×10 ⁴
OTES:TEOS	20:80	28	8.12×10 ⁵ ± 1.01×10 ⁴
PhTES:TEOS	40:60	35	4.56×10 ⁵ ± 5.7×10 ⁴

From the five coating systems tested, 30:70 mol% HTES:TEOS was the least protective while 20:80 mol% OTES:TEOS the most protective of all coatings tested based on the increase in Z_{tot} and decrease in corrosion current density values measured (Z_{tot} values shown in Table 6.2). In the process of forming sol particles, organic groups are more likely to locate themselves on the outer surface of the said particles rather than be incorporated in the silica network, that is inside the growing particle [237]. This leads to the formation of sol particles with organic-rich surfaces. 50:50 mol%, PrTES:TEOS and 30:70 mol% HTES:TEOS have a similar organic wt% content to OTES:TEOS 20:80 mol% and yet the latter produces more protective coatings; the contact angle values for 20:80 mol% OTES:TEOS are also higher, see Figure 5.11.

It is possible that in the formation of the coating, the longer chain octyl chains fill interstitial spaces between the deposited sol nanoparticles more effectively than the shorter chain propyl and hexyl groups resulting in overall more hydrophobic and protective coatings. It is also possible that 20:80 mol% OTES:TEOS coatings were the most protective due to the thicker deposition (Figure 5.9) compared to other alkyl silanes together with the smaller particle sizing (Figure 5.2) which leads to more compact coatings. Ni and co-workers have also investigated the effect of alkyl chain length (n=4, 8, 10, 16) using EIS measurements and identified octyl-containing silane coatings as the one offering the highest corrosion protection [238].

Mechanical properties obtained through nano-scratch, nano-indentation, and pull-out testing show how an increase in silica content of a coating leads to harder, more well-adhered coatings. However, if the silica content is too high then coatings will tend to be more brittle and porous which in turn leads to less protective coatings as revealed through electrochemical testing. On the other hand, if the coatings contain a large portion of organics, then coatings will be softer, verging on tacky and show poor adhesion, even though contact angle is improved. Therefore, a right balance must be developed in which coating must possess sufficient silica for strength and adhesion together with an appropriate organic content to form water-repellent and more flexible coatings. Similar conclusions have been drawn by Seok *et al* who studied inorganic-organic GPTMS hybrid precursors for corrosion protective coatings on galvanized iron [52].

CHAPTER 7:

The corroded iron surface

7.1 Introduction

The previous chapter was intended to study a number of mechanical properties of the five types of OIH coatings and to determine the extent of corrosion protection offered by these coatings on highly polished iron surfaces. The most protective coatings from each of the five precursors used are in ratio with TEOS as follows: MTES:TEOS in a 60:40mol%, PrTES:TEOS 50:50 mol%, HTES:TEOS 30:70 mol%, OTES:TEOS 20:80 mol% and PhTES:TEOS 40:60 mol%. From these five coatings, OTES:TEOS 20:80 mol% proved to be the most protective whereas HTES:TEOS 30:70 mol% the least and therefore these two coatings can be viewed as a bracket of corrosion protection without the need of conducting testing using all five optimal coatings. However, since HTES coatings have shown to behave anomalously, MTES:TEOS 60:40mol% was chosen to represent the lower end of corrosion protection since a similar electrochemical output was obtained to that of HTES:TEOS 30:70 mol%.

This Chapter features a discussion of surface characterisation of both polished and corroded iron surfaces which differ greatly, therefore the performance of the OIH coatings on corroded surfaces will be assessed. Furthermore, several alterations to the coating material were made in an attempt to improve the corrosion protection, which is envisaged to be a challenge due to the uneven surface and more chemically diverse nature of the corroded surface compared to previously studied clean polished surface. Nevertheless, it is worth determining the extent of protection that these coatings have to offer since a principle scope of the thesis is to determine the extent of protection offered by OIH alkoxysilane coatings onto clean as well as corroded iron as a representative of the best and worst-case scenarios respectively on Heritage Metals.

7.2 Characterisation of uncoated iron surfaces

XRD analysis (Figure 5.29) confirms the presence of two types of iron oxides, the top layer is cleaned off during cleaning procedure prior to coating. The corroded surface is vastly different from the clean polished surface studied in previous chapters, both in terms of topology and surface chemistry. Two kinds of oxides have been characterised: Figure 5.27 (b) shows the orange-brown iron (III) oxide which forms due to high oxygen and water exposure whereas Figure 5.27 (c) shows the underlying layer of black rust which forms in limited oxygen and low moisture environments due to the presence of an upper layer. Since the coupons were allowed to heavily corrode through a slow cycling process the black coloured corrosion layer was evenly built up and distributed over the metal surface. XRD analysis confirms the presence of at least one layer of iron (III) oxide namely $\beta\text{-Fe}_2\text{O}_3$ ($\text{Fe}^{\text{III}+}$) on the surface of the uncleaned corroded surface and an interlayer of Magnetite Fe_3O_4 ($\text{Fe}^{\text{II/III}+}$) when coupon surface was cleaned from iron (III) oxide layer. Magnetite contains both $\text{Fe}^{\text{II}+}$ and $\text{Fe}^{\text{III}+}$ ions and is sometimes better represented as $\text{FeO} \cdot \text{Fe}_2\text{O}_3$.

7.3 The variation of surface roughness on polished, corroded and coated surfaces

Surface roughness results presented in Figure 5.32 indicate that the cleaning process leads to a smoothening of the corroded surface, though surface still remains rough as shown in cross-sections of Figure 5.28 (a ii). A high roughness value of the cleaned corroded surfaces is the main challenge presented in this chapter for which several attempts to compensate for this problem have been carried out. The metal surface resistance to corrosion differs according to the surface finish and more drastically if oxides are already present (Figure 5.30).

Even though the iron used in this work is of high purity i.e. contains negligible amounts of impurities that act as corrosion inhibitors (elements such as Mn, Mo)[239], a high degree of surface polishing initially inhibits the corrosion process [240] shown through the high R_p value obtained. A low polished surface will possess a greater surface area compared to a highly polished surface thus presenting more corrosion initiating sites. The dependence in resistance of the bare metal on surface finish has been reported by Wallinder *et al* on stainless steel [240]. Impedance of corroded surface will be significantly lower than for polished metal for two reasons: corroded surface has the highest surface area due to black iron (III) oxide deposits which not only increase the surface area but corrosion reactions have already been established, thus the resistance to the corrosion reactions is low.

The deposition of coatings as carried out in previous chapter onto clean metal (2.5% concentration) leads to the formation of thin coatings with ample cracks visible on the surface, e.g. 2.5% SiO₂ MTES:TEOS 60:40 mol% Figure 5.31 a) which do not lead to a significant decrease in roughness values of uncoated and 2.5% SiO₂ coated surfaces (Figure 5.32). A more significant decrease in surface roughness is obtained when using higher silica concentrations (Figure 5.32 for MTES 20% SiO₂), however, even though thicker and smoother coatings are obtained as observed in Figure (5.31), cracks were still evident, though to a lesser extent.

7.4 Corrosion protection on corroded surface using MTES:TEOS and OTES:TEOS coatings

It is still evident, as determined from coated polished surfaces in Chapter 6, that the OTES:TEOS 20:80 mol% coatings offer greater corrosion protection when compared to MTES:TEOS 60:40 mol% coatings on corroded surfaces; applicable to all SiO₂ concentrations tested (see Table 5.6 for MTES:TEOS 60:40 mol% and OTES:TEOS 20:80 mol% R_t and I_{corr} values). As seen in Figure 5.30, the surface roughness and onset of corrosion present on corroded samples results in a change in shape of electrochemical results compared to clean polished iron surface which is quantified as a decrease in R_t value (Table 5.5). Nyquist plots for coated corroded samples coatings show a tail in the higher impedance range which may indicate a diffusion process happening through accumulated corrosion products inside cracks in the coating. However, such data was not modelled using a Warburg element instead of CPE_c element since no improvement in fit and worsening in GOF value was obtained. Cano *et al* [170] have also studied corroded surfaces as previously discussed in Section 2.8.3.1 of Chapter 2, however, Bode plot (Figure 2.8) indicate a higher impedance than that presented in Figure 5.30 since the surface was only partially allowed to develop corrosion products[170].

The improvement in corrosion protection of MTES and OTES-based coatings having a 2.5% SiO₂ concentration that has been documented in Chapter 6 for which a 2.5 order of magnitude improvement over bare polished metal for OTES:TEOS 20:80 mol% coating was achieved (Figure 5.24 (a)) together with a two order of magnitude improvement for MTES:TEOS 60:40 mol% coatings. This level of improvement was not achieved on the corroded surface, instead a mere one order of magnitude in improvement is shown in Table 5.6 for OTES:TEOS coatings (R_t bare metal = $1.31 \times 10^2 \pm 2.60 \times 10^1 \Omega \text{ cm}^2$, 2.5% OTES:TEOS = $1.13 \times 10^3 \pm 1.35 \times 10^2 \Omega \text{ cm}^2$) and even less protection offered by MTES:TEOS coatings (R_t bare metal = $1.31 \times 10^2 \pm 2.60 \times 10^1 \Omega \text{ cm}^2$, 2.5% MTES:TEOS = $6.18 \times 10^2 \pm 7.41 \times 10^1 \Omega \text{ cm}^2$). More protective coatings were obtained by increasing the SiO₂ concentration to 20% for MTES:TEOS 60:40 mol% ($2.97 \times 10^3 \pm 1.10 \times 10^3 \Omega \text{ cm}^2$) and 10%

for OTES:TEOS 20:80 mol% ($4.12 \times 10^3 \pm 8.54 \times 10^2 \Omega \text{ cm}^2$), R_f values prove to be similar for these two coatings. It is interesting to note that OTES:TEOS coatings are once again proving to be more protective than MTES:TEOS coating at the same silica concentration as has been the case on clean metal surfaces (Figure 5.24 (a)), even when using higher SiO_2 concentrations on corroded surfaces.

OIH coatings that have featured in Chapter 6 ($\text{X-Si(OR)}_3 = \text{MTES, PrTES, HTES, OTES, PhTES}$ in various ratios with TEOS) are smooth and crack-free after curing when deposited on polished metal which lead to the significant improvement in corrosion protection. Crack formation is evident when applying these coatings onto cleaned corroded surfaces, even with an increase in SiO_2 concentration (see Figure 5.31 (a ii)). Surface roughness is drastically increased due to iron oxide deposits along the entire surface of the coupon which leads to improper coating in certain areas along the surface: cracks are frequently formed at the base of clumps of corrosion material that appear to jut out of the surface, it is in these crevices that thicker coatings are deposited, which exceed the critical coating thickness [241] (defined as the maximum thickness without cracks[242]), thus leading to crack formation during drying process as shown through schema presented in **Figure 7.1**.

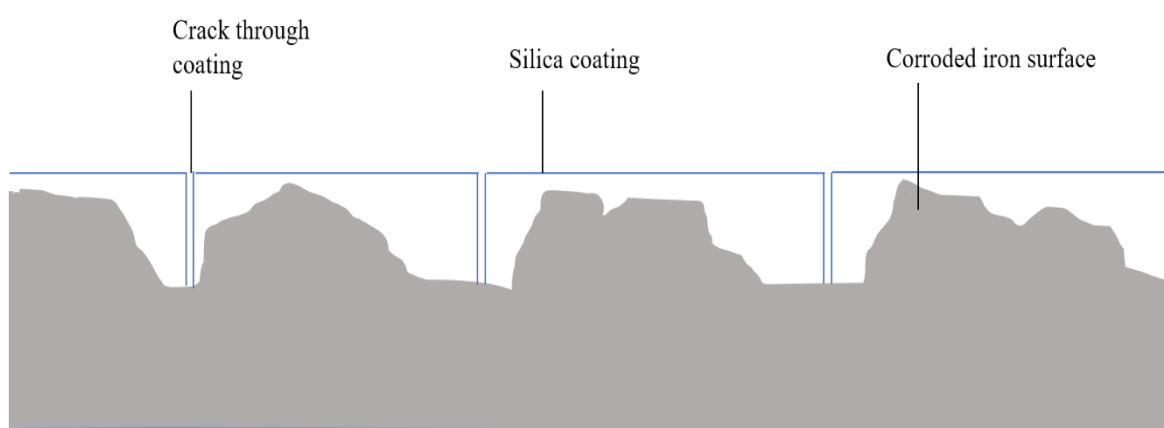


Figure 7.1: Schematic presentation of cross-section through coated corroded metal surface. Cracks tend to form where thicker coating deposition occurs.

The dip-coating speed was reduced so as to allow the crevices on the rough surface to be immersed at a slower rate thus leaving behind a more even layer of coating (minimise thickness variation along the rough surface) thus attempting to avoid scenario illustrated in Figure 7.1. However, coating thicknesses for 5% SiO₂ 20:80 mol% OTES:TEOS determined to be 470 nm for 40 mm/min and 1.146 μm for 280 mm/min dip speed (Figure 5.35 cross sections through coatings). Slower dip-speeds are known to form thinner coatings due to better sol drainage as the coupon emerges from sol. Such an attempt produced an even more cracked coating (Figure 5.35 (a ii)) and was not considered further.

Apart from increasing the silica concentration, another effective method that lead to the further improvement in coating quality was found to be through an increase in the organic precursor used. Innocenzi *et al* also reported that a higher content of MTES (MTES:TEOS molar ratios of 20:80, 40:60 and 60:40 mol% were featured) was found to enhance the maximum thickness of the coatings free of cracks [243]. Although both MTES and OTES coatings became more protective upon increasing in XTES concentration as shown in electrochemical data in Figure 5.38, an increase in OTES leads to a more significant improvement in impedance than for MTES. This can be quantified and confirmed through **Table 7.1** which features Z_{tot} and I_{corr} values for MTES and OTES coated samples, the table includes their relevant weight percent of organic content.

There is a more drastic change in organic content increase for OTES:TEOS (20:80 mol% = 28 wt%, 40:60 mol% = 44 wt%) than for MTES:TEOS coatings (60:40 mol% = 14 wt%, 80:20 mol% = 18 wt%). The higher organic-containing OTES:TEOS 40:60 mol% coatings produce smoother and less cracked coatings (Figure 5.36 (b i)) compared to MTES:TEOS 80:20 mol% (Figure 5.36 (a i)), thus providing the metal surface with better protection of up to 2.5 orders of magnitude improvement over bare corroded metal (Table 7.1: Z_{tot} OTES:TEOS 20:80 mol% = $5.39 \times 10^3 \pm 1.05 \times 10^3 \Omega \text{ cm}^2$, 40:60 mol% = $6.23 \times 10^4 \pm 7.57 \times 10^3 \Omega \text{ cm}^2$). Increasing the organic content for MTES:TEOS from 60:40 to 80:20 mol% produced an increase in Z_{tot} values less significantly to OTES:TEOS

(MTES:TEOS 60:40 mol% = $2.04 \times 10^3 \pm 3.95 \times 10^2 \Omega \text{ cm}^2$, 80:20 mol% = $3.94 \times 10^3 \pm 6.49 \times 10^2 \Omega \text{ cm}^2$)

which can be attributed to its lower wt% organics content.

Table 7.1: Mean total Impedance, Z_{tot} ($R_{sol}+R_t+R_{po}$) and I_{corr} values for un/coated corroded surfaces considered in Figure 5.38. Table includes weight % organics present in coatings.

	Mean Z_{tot} ($\Omega \text{ cm}^2$)	Current Density (mAcm^{-2})	Wt% organics
Bare corroded metal	$1.32 \times 10^2 \pm 2.52 \times 10^1$	$1.02 \times 10^{-1} \pm 7.17 \times 10^{-3}$	–
MTES:TEOS 60:40 mol%	$2.04 \times 10^3 \pm 3.95 \times 10^2$	$6.33 \times 10^{-2} \pm 1.43 \times 10^{-2}$	14
MTES:TEOS 80:20 mol%	$3.94 \times 10^3 \pm 6.49 \times 10^2$	$2.33 \times 10^{-2} \pm 1.43 \times 10^{-2}$	18
OTES:TEOS 20:80 mol%	$5.39 \times 10^3 \pm 1.05 \times 10^3$	$1.02 \times 10^{-2} \pm 7.17 \times 10^{-4}$	28
OTES:TEOS 40:60 mol%	$6.23 \times 10^4 \pm 7.57 \times 10^3$	$9.67 \times 10^{-4} \pm 1.43 \times 10^{-4}$	44

An attempt to reduce crack-formation was carried out by employing drying control chemical additives (DCCAs) such as conducted by other authors using formamide [244,245], dimethylformamide [246,245] and acetonitrile [245]. Physical properties of such solvents differ from ethanol, namely, a higher boiling point, high viscosity, large dielectric constant and the ability to form strong hydrogen bonds to the silica system [245]. This leads to the creation of larger particles and therefore results in larger pore size. This was reported by Katagiri when using ethylene glycol and ethylene glycol monomethyl ether [247]. Due to the larger pore size, the capillary forces will be weaker and hence the stress exerted on the coating during drying will be decreased and thus reducing crack formation.

Some of the physical parameters of solvents utilised are shown in **Table 7.2**. As the boiling point of the solvent increases the volatility decreases, e.g. formamide has a higher boiling point than ethanol and hence is less volatile. Volatility is directly related to the solvent's vapor pressure where more volatile ethanol will possess a high vapor pressure whereas FMA and EGBE will possess low vapor pressures. The solvents were chosen due to their lower vapour pressure compared to ethanol, which should lead to slower drying and larger pore formation, both attributing to lower capillary forces during drying stage thus minimising crack formation.

Table 7.2: Solvents employed and their physical properties.

Solvent	RMM (g/mol)	Boiling Pt. (°C)	Density at 25°C (g/ml)	Chemical Formula	Vapour pressure (Pa)
Ethanol	46.07	78.5	0.816	CH ₃ -CH ₂ -OH	5866 [248]
Formamide	45.04	210	1.134	CH ₃ -NO	8.13 [249]
Ethylene glycol butyl ether	118.17	171	0.902	CH ₃ (CH ₂) ₄ -O-(CH ₂) ₂ -OH	101 [250]

Although smaller cracks were formed when EGBE was used as solvent for MTES coatings (Figure 5.41), no significant improvement in electrochemical testing was achieved (Table 5.8 R_t values for MTES:TEOS in EtOH= $1.19 \times 10^3 \pm 1.07 \times 10^2 \Omega \text{ cm}^2$, MTES:TEOS in EGBE= $1.18 \times 10^3 \pm 1.06 \times 10^2 \Omega \text{ cm}^2$) which can be due to the formation of larger pores during the drying process. More visibly cracked coatings were formed for OTES (Figure 5.42) and less protective coatings were obtained (Table 5.8 R_t values for OTES:TEOS in EtOH= $5.19 \times 10^3 \pm 4.67 \times 10^2 \Omega \text{ cm}^2$, OTES:TEOS in EGBE= $1.81 \times 10^3 \pm 1.63 \times 10^2 \Omega \text{ cm}^2$).

The use of FMA led to the formation of inferior coatings as seen in Figure 5.43 leading to poor electrochemical data in Table 5.8 (MTES:TEOS in EtOH= $1.19 \times 10^3 \pm 1.07 \times 10^2 \Omega \text{ cm}^2$, 1:1 FMA:EtOH= $4.53 \times 10^2 \pm 4.08 \times 10^1 \Omega \text{ cm}^2$, 1:4 FMA:EtOH= $2.00 \times 10^2 \pm 1.80 \times 10^1 \Omega \text{ cm}^2$). The pockets of air that are formed between the coating and metal surface, which remain present after curing for FMA-based coatings, was not observed with EGBE-based coatings and has been attributed to the unequal evaporation rates of the solvents FMA and EtOH. In the case of FMA:EtOH mixtures, ethanol will evaporate at a faster rate than FMA which leads to pockets of gaseous ethanol in the silicate-FMA layer, the FMA undergoing evaporation more gradually. This process severely damages the integrity of the coatings as shown in Figure 5.43. In fact, higher FMA content in 1:1 FMA:EtOH coating appears to be more damaged than 1:4 to the extent where coating appears to not be well-adhered to the metal surface. This effect was initially anticipated to occur and therefore a 4 hr timeframe was allowed prior to curing. However, resultant coatings were still formed notable defects.

FMA-based coatings are less protective than EGBE-based coatings, however, both did not produce more protective coatings compared to ethanol -based coatings even though EGBE-based coatings appear to provide acceptable surface coverage (Figures 5.41 and 5.42). This has been explained through coating thickness determinations where substituting EtOH with EGBE or FMA leads to thinner coatings. The variation in boiling point and vapour pressure of the solvent employed feature in **Table 7.3** for vapour pressure values of solvents Ethanol/EGBE and solvent mixtures (EtOH:FMA 1:1 and 1:4 (v/v) calculated using Raoult’s law for ideal mixtures [251]). Vapour pressure for ethanol is the highest value whereas the vapor pressure decreases as the amount of formamide is increased due to the introduction of a significantly less volatile solvent. This translates to the solvent evaporating at a slower rate off the surface of the coupon as it emerges from the sol, therefore less silica material is left behind on the surface i.e. better sol drainage occurs with less volatile solvents.

Table 7.3: Thickness measurements obtained from electron micrographs for double coated 2.5% SiO₂ 60:40 mol% MTES:TEOS dispersed in different solvents and their respective vapour pressure in Pa. Values for FMA:EtOH were calculated using Raoult’s law.

Solvent	MTES Mean thickness ± St. Error (nm)	OTES Mean thickness ± St. Error (nm)	Vapour pressure (Pa)
Ethanol	600.93 ± 21.10	712.36 ± 53.21	5866 [248]
Formamide: ethanol 1:4 (v/v)	542.31 ± 36.98	687.23 ± 42.31	4278
Formamide: ethanol 1:1 (v/v)	385.34 ± 24.67	552.78 ± 52.36	2644
ethylene glycol butyl ether	290.69 ± 45.87	419.84 ± 39.87	101 [250]

Table 7.3 also provides thickness measurements for 60:40 mol% MTES:TEOS and 20:80 mol% OTES:TEOS coatings prepared using different solvents investigated. The thickest coating 600.93 ± 21.10 nm was obtained when the sol was procured in ethanol diluent whereas MTES:TEOS sols produced in 1:4 FMA:EtOH presented slightly thinner (542.31 ± 36.01 nm for 20 vol% FMA). On increasing the volume of FMA:EtOH to 1:1 (50 vol% FMA), coating decreases further in thickness (385.34 ± 24.67 nm). Considering the set of solvents listed in Table 7.3, MTES:TEOS sols prepared

in EGBE gave rise to the thinnest films (290.69 ± 45.87 nm). Similar trends were obtained with OTES coatings in Table 7.3, only that OTES coatings deposited slightly thicker than MTES coatings. This decrease in thickness is linked to the vapor pressure of the solvent where a decrease in vapor pressure results in a decrease in coating thickness) which, as explained in previous paragraph, is attributed to better draining of sol for less volatile solvents such as EGBE from metal surface as coupons emerge from sol. Such thinning of coating can be contributing to the decline in corrosion protection. This problem could be eliminated through changing the mode of application, e.g. through spray coating.

The decline in corrosion protection could also be caused by the changes in particle size. Both MTES and OTES sols (Figure 5.39) become more polydisperse as the number of peaks increases from 2 for EtOH sols to 4 for EGBE and FMA-based sols. Although the PS of the nano-sized particle populations do not change drastically, PS data includes the formation of larger micron-sized ($\approx 4,000$ nm) particles in EGBE and FMA-based sols which are not present with ethanol-based sols. Therefore, larger particles are being deposited in thinner coatings due to the mode of application (faster draining with less volatile solvents). This could be contributing to the coatings' quality even though their intensity in the PS plots are not large. Further work may include employing a different mode of application such as brush or spray coating in an attempt to avoid crack formation as illustrated in Figure 7.1 with the hope of obtaining more evenly deposited coatings.

CHAPTER 8:

Addition of silica nanoparticles for the improvement of corrosion protection of OIH alkoxysilane coatings

8.1 Introduction

The scope of this chapter is to enhance corrosion protection of OIH alkoxysilane coatings through the use of silica nanoparticles as corrosion inhibitors [43]. The presence of inhibitors in the coating actively delays chemical reactions that bring about corrosion of metal surface once the coating has been penetrated by the corrosive medium as described in Section 2.6.1.1. Both top-down and bottom-up approaches to obtaining such particles was investigated; top-down through the addition of 10- 20 nm commercial nanoparticles (CNP) and bottom-up through the production of Stöber nanoparticles (SNP) over which control over particle size can be exerted.

8.2 Addition of commercial nanoparticles (CNPs)

Initial difficulties with the dispersion of the CNPs in ethanol led to their use in small amounts (≤ 500 ppm) as carried out by Suegama *et al* [110]. These authors stated that the addition of silica nanoparticles improved corrosion protection of alkoxy silane films by way of the formation of thicker films and/or increased hardness [110]. In this work, an improvement in corrosion protection was indeed obtained with the simple addition of commercial NP at a concentration of 100 ppm, higher concentrations leading to the deterioration in electrochemical results (Table 5.9). However, agglomerated nanoparticles which form microparticles as shown in Figure 5.49 are interfering with the coating which become more problematic as the concentration of CNPs increased, thus leading to the formation of inferior coatings. Future work may include filtering out these particles so as to minimise their presence in the coating, which may lead to further improvement in coating's protective properties.

8.3 Addition of Stöber nanoparticles (SNPs)

Silica nanoparticles produced through the Stöber method where relatively larger nanoparticles (20 nm and over, see Figure 5.51 (b)) were formed under basic conditions compared to the 2-5 nm nanoparticles in acidic conditions (Figure 5.1). By altering the concentration of water, ammonia and TEOS, several particle sizes have been achieved. Wang *et al* [115] reported a particle size of 30 nm using molar ratios TEOS : H₂O : NH₄OH 0.22 : 1.375 : 0.1782 M in ethanol solvent. In fact, The NP formed when using the above ratios of reactants (where TEOS= 0.22 M) yielded particles having an average diameter of 20 nm (Figure 5.51 (b)) which is in close agreement with Wang [2]. A 1 M TEOS concentration lead to the formation of 26 nm sized particles whereas a 2 M TEOS concentration produced a 56 nm particle diameter.

Clouding observed at the beginning of the formation of the NP dispersion, as was previously reported in Chapter 4 for acidic sols, was also observed. Particle size measurements are highest (100-200 nm, see Figure 5.51 (a)) at the beginning of the reaction and a gradual formation of a clear sol can be explained through the decrease in particles size measurements taken after 4 hrs and 24 hrs of sol development. Stöber *et al* stated that by maintaining the ratios of water and alkali the same whilst increasing the concentration of TEOS will bring about an increase in particle size [112] which has been confirmed through Figure 5.51 (b). Electrochemical results (Figure 5.53) show less protective coatings when 56 nm SNPs were employed compared to 26 nm SNPs and it is probably due to the increased particle sizing which is interfering with the packing of the coating on clean surface. Therefore, 26 nm SNPs were further considered.

It is difficult to explain observations in Figure 5.54 for which electrochemical data shown in Figure 5.55 confirms that 5% SiO₂ 60:20:20 mol% MTES:TEOS:SNP are less protective than 5% SiO₂ MTES:TEOS 60:40 mol% with or without 1% SNP. It is possible that the addition of SNP to a more organic 60:20 mol% sol compared to 60:40 mol% MTES:TEOS leads to a different interaction of SNP with MTES nanoparticles resulting in a lower quality coating which appears to be not well-adhered to the surface. Moreover, in the case of 60:20:20 mol% MTES:TEOS:SNP coatings, less TEOS present compared to 60:40 mol% MTES:TEOS based coatings leads to the growth of a more loosely connected material which eventually forms a less continuous coating.

Nevertheless, such results confirm that a 1% SNP addition to an MTES:TEOS coating does not negatively affect the morphology or corrosion protection of the coating. A desirable improvement in corrosion protection was investigated by doping MTES:TEOS coatings with several concentrations of SNP as shown in Figure 5.56. Unfortunately, no improvement in corrosion protection was recorded whether SNP concentration is reduced to 0.1% or increased beyond 1% for which less protective coatings were obtained as clearly visible through decrease in total impedance in low frequency range of the Bode impedance plot and smaller capacitive arc in the Nyquist plot with increasing SNP concentration (see R_t and R_{po} values in Table 5.11).

Coatings remain smooth when viewed under SEM, therefore the addition of Stöber nanoparticles acts as a filler and does not affect the coating deposition and properties as corrosion protection is not compromised either, until higher concentrations are used, resulting in slightly less protective coatings. The addition of 2% and 5% SiO₂ originating from SNP is significant and comparable to the amount of silica originating from the 5% MTES:TEOS 60:40 mol% that forms the bulk of the coating, therefore these coating consist of a large portion of these filler particles. Palanivel *et al* report the formation of porous films upon the heavy loading of OIH coatings with nanoparticles which lead to an increase in electrolyte uptake causing coating delamination [43], thus such high concentrations of nanoparticle addition should be avoided.

Several authors [74,109,110,252] report an improvement in corrosion protection of the alkoxy silane coating upon the addition of CNPs which is also applicable for the results obtained when employing CNPs, even when considering the defects created due to larger particles present. On the other hand, when smaller monodisperse SNPs were used, corrosion protection remains unchanged at best comparable to the coating without NP. This could be due to the fact that CNP are spherical and solid whereas the nanoparticles developed through the Stöber process are still underdeveloped and have not formed well enough, instead forming part of the silica network when curing, rather than remaining as solid particles within the coating which can then act as inhibitors [43] during corrosion testing.

8.4 Application of CNP and SNP-doped MTES:TEOS coatings to corroded surfaces

100 ppm CNP doped coatings which proved to be more protective compared to blank MTES coatings (Figure 5.48) did not perform well on corroded surfaces (Figure 5.58) since crack formation (Figure 5.57 (a)) was still obtained and influenced the coating's protective properties. It could be due to the microparticles that are present which are promoting the propagation of cracks which were ample and clearly seen in Figure 5.57 (a). When employed on corroded surfaces, SNPs have proven to bring about a slight improvement of the R_t value (Table 5.11) which can be visually appreciated through

the less cracked surface shown in Figure 5.57 (b) and has been attributed to the difference in particle sizes which leads to deposition of larger particles that are more capable of blocking crevices and filling empty pockets created through the corrosion process than the smaller MTES-based nanoparticles.

Zheludkevich has studied OIH coatings that have been impregnated with ZrO_2 nanoparticles [252] and the author states these particles may lead to an important effect of pore blocking, thus corrosion protection is a result of enhanced barrier effects rather than through a chemical inhibition, which is also suspected to be the case with results obtained for the corroded surface. Future work on corroded surfaces may include the creation of SNPs having a larger particle size that could block pockets created on the surface more effectively. Stober *et al* have stated that larger particles are formed using long chain silanes instead of TEOS [112] as the starting silane precursor, OTES could be a good candidate for such work.

CHAPTER 9:

Addition of inorganic and organic inhibitor molecules to OIH alkoxysilane coatings for enhanced corrosion protection

9.1 Introduction

This chapter discusses the effect of the addition of several in/organic molecules on corrosion properties of sol-gel coatings, namely cerium (III) nitrate hexahydrate (Ce), 1,4-naphthoquinone (1,4-N), pyrrolidine (Pyr) and 2-hydroxypyridine (2-H), 1-naphthol (1-N), phenylbenzoate (PhB). These molecules are postulated to behave as corrosion inhibitors, for which the latter two are not featured in any known work for their use as corrosion inhibitors. The effect that these corrosion inhibitors have on corroded surfaces was also assessed and featured MTES:TEOS 60:40 mol% and OTES:TEOS 20:80 mol% were considered as valid representatives of OIH coatings studied in earlier chapters as already carried out in Chapter 7 for corroded surfaces.

9.2 Effect of inhibitor molecules on OIH alkoxysilane sols

Inhibitor-doped 60:40 mol% MTES:TEOS sols are presented in Figure 5.59 whereas inhibitor-doped 20:80 mol% OTES:TEOS sols are presented in Figure 5.60. Although slight shifts in particle populations occur, no drastic changes are measured when different concentrations and inhibitors are added to MTES/OTES sols. This result holds true for sols that are utilised immediately after sol development i.e. dip-coating is carried out as soon as the inhibitor is added to developed sol (realistically within the first hour). In fact, Figure 5.61 proves that larger particles begin to form if measurements are taken 24 hrs following the addition of inhibitor to sols.

9.3 Inhibitor-doped MTES/OTES coating characterisation

IR (Figures 5.62-5.64) analysis on cured inhibitor-doped MTES/OTES sols together with EDS analysis on inhibitor-doped MTES/OTES coatings (Table 5.16) confirmed the presence of inhibitor molecules in coatings following coating and curing processes. All inhibitor-doped sols produced coatings that were smooth and defect-free even with higher inhibitor concentrations (0.01 M), refer to Appendix G for inhibitor-doped MTES coatings and Appendix H for inhibitor-doped OTES coatings.

9.4 Effect of inhibitor molecules on corrosion protection OIH alkoxysilane coatings

Improvement in corrosion resistance for MTES/OTES coatings was achieved through the addition of inhibitors after sol development. Each inhibitor was introduced with varying concentrations for which every one of the inhibitors showed improvement in corrosion protection for MTES:TEOS coatings at one or more than one concentrations of inhibitor. **Figure 9.1** includes total impedance ($Z_{tot} = R_t + R_{po} + R_{sol}$ at low frequency range) values for MTES:TEOS 60:40 mol% (EEC 1 and 2 used to model data presented in Figures 5.65-5.70) and OTES:TEOS 20:80 mol% (Figures 5.71-5.76) coated clean surfaces that have been doped with each of the six inhibitors considered, coatings

that do not contain inhibitor molecules have been plotted as 0 M inhibitor concentration (blank). Total impedance (Z_{tot}) is relevant to this discussion since it is a clear indication of the inhibiting effect these chemical additives have on the corrosion process occurring once water begins to penetrate through the coatings' defects and initiates the corrosion process on the underlying metal surface. A higher Z_{tot} value for inhibitor-containing coatings compared to that of inhibitor-free coatings signifies that inhibitor molecules are indeed delaying the corrosion process occurring at the metal surface.

9.4.1 Inhibitor-doped 60:40 mol% MTES:TEOS coatings

As previously discussed in the Result Section 5.4.4.1, for MTES:TEOS inhibitor-doped coatings (Figures 5.65-5.70) some conclusions had already been established without the need of EEC and parameter acquisition: all of the six inhibitors studied improve coating's ability to protect the metal surface from corrosion at a given concentration/s of inhibitor. By considering the MTES: TEOS doped coatings, two trends can be observed through Figure 9.1 (a); the first trend applies to coatings containing Ce, 1-N, 2-H and Pyr where Z_{tot} values increases with increasing inhibitor concentration only to decrease to blank value or lower in the case of Ce. The other trend applies to 1,4-N and PhB-containing coatings where a significant increase in Z_{tot} value is finally obtained at highest concentrations of inhibitor. The first trend has been reported elsewhere [128,253-255] for which an increase in inhibitor concentration has been documented to degrade the quality of the sol-gel matrix. Even though increasing in concentration leads to more inhibitor molecules on the surface of the metal, inhibitor molecules begin to interfere significantly in a two-fold manner [128]: i) following addition of inhibitor to developed sol where molecules destabilise the silica nanoparticle dispersion as seen through particle size results (see Figure 5.59 (a) 0.01M Ce shows wider particle distribution of 2 nm particles compared to lower Ce concentrations) and ii) once deposited, a high concentration of inhibitor can interfere with the formation of silica framework during curing [128].

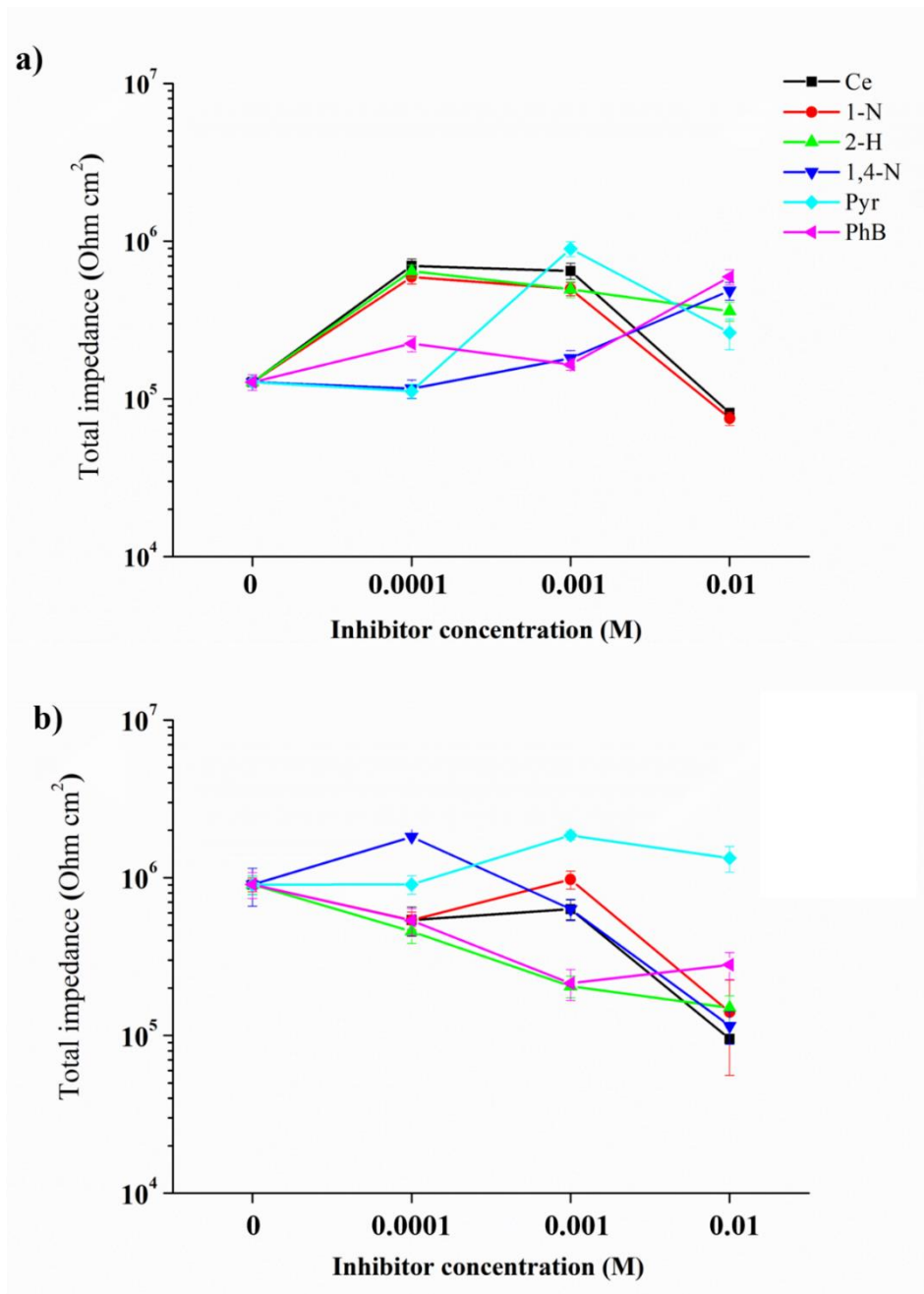


Figure 9.1: Inhibitor concentration for the six inhibitors studied versus total Impedance (Z_{tot}) at low frequency for a) MTES:TEOS 60:40 mol% and b) OTES:TEOS 20:80 mol% coatings. Bare metal values indicated through grey line.

Cambon *et al* [128] have studied the effect of sol-gel films consisting of GPTMS and aluminum *tri-sec*-butoxide that have been impregnated with cerium nitrate inhibitor on 2024-T3 aluminum alloy. EIS results revealed that the addition of a low concentration of cerium (0.005 M) into the hybrid films increases the resistance of the protective coatings. Once concentration exceeded 0.01 M, a strong decrease of the resistance of the coating was recorded and the higher the cerium content, the

greater the degradation of the barrier properties. The authors have postulated that this behaviour is due to the incorporation of bigger cations into the hybrid network inducing the partial destabilisation of the system at the highest cerium concentrations [128]. Voevodin *et al* [256] also witnessed coating degradation with high levels of sodium metavanadate and sodium molybdate inhibitors which has been associated with the formation of inhibitor molecules crystallising during coating formation. Upon contact with NaCl electrolyte solution, the crystallised salts dissolve to produce defects that contribute to delamination of the film [256]. Therefore, apart from the issue of osmotic pressure discussed above for the soluble inhibitors, leaching of these inhibitors further contributes to coating deterioration by leaving behind empty volumes within the coating.

Through nano-hardness testing, Cambon *et al* have also determined that cerium addition leads to harder structures by increasing the rigidity of the systems which values then decrease above a cerium content of 0.01 M [128]. The authors associate the increase in hardness for Ce concentrations lower than 0.01 M to an increase of the organic polymerisation (GPTMS) and the moderate increase of the inorganic polymerisation (alumina) leading to a higher stiffness of the coating, with an increase in the hardness values relative to coatings without inhibitor. With [Ce] higher than 0.01 M, the rise of the inorganic polymerisation leads to a higher condensation rate which could cause a destabilisation of the Si–O–Si (Ce atomic radius are higher than the one of Si) with a possible creation of free volumes into the hybrid and involves a collapse of the coating performances.

In our case, the inhibitor was added after sol development which would mean that the sol particles have already been established. However, such free volumes may still be formed during the curing process as large cerium ions interfere with the packing of silica particles. Zheludkevich [254] attributes the failure in the quality of coating to the inhibitor's solubility which leads to its rapid leaching and increase in concentration of cerium ions in pores (which is desirable). However, the osmotic pressure created can encourage water to be transported through the coating, which acts as a semipermeable membrane, resulting in an influx of more water and the destruction of the barrier layer [254], this effect being enhanced with higher concentrations of inhibitor molecules.

The difference in the electrochemical plots (Figure 9.1 (a)) for Ce, 1-N, 2-H, Pyr compared to PhB and 1,4-N can be explained using their solubilities in water as listed in **Table 9.1**. All six inhibitors are soluble in ethanol thus allowing for their incorporation into the sol with ease followed by the deposition into OIH alkoxy silane coatings. However, phenyl benzoate is insoluble in water and 1,4-N is only sparingly soluble (0.09 g/L). Once water begins penetrating through the coating, a water-soluble inhibitor such as Ce, will readily dissolve into the water-containing pores of the coating thus actively inhibiting metal corrosion at a lower concentration. When inhibitor molecules are less soluble, a greater concentration of inhibitor will be necessary to obtain the same amount of ions in solution which leads to the protective effect as seen in increasing Z_{tot} values for PhB and 1,4-N as concentration is increased (Figure 9.1 (a)). Also, a high concentration of insoluble inhibitor results in far less leaching compared to, for example Ce inhibitor, there being sufficient inhibitor at the coating/metal barrier to retard corrosion reactions whilst keeping the coating integrity by not succumbing to the osmotic effect [254,257] as created by soluble inhibitor molecules.

Table 9.1: List of inhibitors used in this study and their solubilities in water (g/L) at 25 °C.

Inhibitor	Solubility (g/L)	Inhibitor	Solubility (g/L)
1,4-Naphthoquinone	0.09 [258]	2-Hydroxypyridine	1000 [259]
Phenyl benzoate	Insoluble [260]	Pyrrolidine	1000 [261]
1-Naphthol	1.35 [262]	Cerium (III) nitrate hexahydrate	1754 [263]

9.4.2 Inhibitor-doped 20:80 mol% OTES:TEOS coatings

Figure 9.1 (b) illustrates Z_{tot} values obtained for 20:80 mol% OTES:TEOS coatings impregnated with six of the in/organic inhibitor molecules, for which it is evident that the inhibitors did not improve the corrosion properties as well as for MTES:TEOS coatings. To begin with, OTES coatings are more protective than MTES coatings (see blanks in Figure 9.1 (a) and (b)), and it was hoped that inhibitor molecule would further improve on these already very protective coatings. This was only observed for the inhibitor pyrrolidine (see Z_{tot} plot of Figure 9.1 (b)) whereas the other five inhibitors

showed no improvement or indeed worsening over coatings without inhibitors. Pyrrolidine-doped OTES coatings showed a gradual increase in corrosion protection upon increasing the inhibitor concentration, the most protective thus being 0.001 M Pyr-doped coatings.

9.4.3 Inhibitor-doped MTES coatings on corroded surfaces

The effect of inhibitor on corroded iron surfaces was also considered, though no improvements were witnessed. Figure 5.78 includes results obtained for Ce-doped MTES coatings where it is clear that the coating becomes increasingly less protective as the inhibitor concentration is increased. The result is not surprising since corrosion processes are far too developed at that stage for cerium ions to affect these processes in a significant manner. At low concentrations, the inhibitor has no effect on the extent of corrosion protection whereas at high concentrations, less protective coatings are produced due to the high inhibitor content leading to the formation of an inferior coating. Nevertheless, these results are satisfactory since, practically speaking, if Ce-doped MTES coatings had to be applied onto surfaces featuring both clean and corroded areas, then the corroded areas will still be protected through the barrier effect of the coating, whereas the clean surfaces will be better protected through barrier and chemical inhibiting effects (at low Ce concentration of 0.001M).

9.5 General Discussion

The scope of introducing the inhibitor molecules into the sol after the sol has been allowed to develop was to prevent the interference of these molecules with the formation of silica-network and growth of the nanoparticles during sol development. However, the inhibitor molecules may still impart some form of change to the sol even when added after the sol has formed, this effect can be seen in Figure 5.59 (a) for MTES sols. Even though particle size measurement was carried out a short time after the addition of Ce inhibitor to developed sol, a shift to larger PS was observed most clearly for the higher concentrations of Ce for both small and larger particle populations. On the other hand, this was resisted by OTES containing sols (Figure 5.60 (a)) where the smaller sized population appears to not be affected by the presence of cerium in any of the concentrations studied. This result was initially

surprising; however, OTES-based nanoparticles formed are more stable in suspension due to longer chained octyl group and are thus less likely to agglomerate in the presence of salt ions compared to shorter methyl-containing MTES sol particles which are more likely to extend their silica network to other particles in the absence of long-chained interfering organic groups [264].

Another interesting detail that can be discussed is the increase in particle size of the larger populations for MTES (Figure 5.59 (a)) which is expected and indicative of agglomeration and the slight decrease in particle size of the larger population of OTES particles (Figure 5.60 (a)) which is counterintuitive. The explanation being proposed by the author is that OTES:TEOS nanoparticles are more stable and repulsive to one another when dispersed in sol compared to MTES:TEOS particles, and the addition of cerium ions (Ce^{3+}) leads to the 'salting out' effect in MTES sols (particles aggregation [85]). This process is avoided in OTES:TEOS sols due to the stability of individual particles [264] and the unfavourable process of agglomeration perhaps to the extent that separation of clumped up particles may even be possible and favourable. This observation holds true for the other inhibitors considered.

Following the discussion on the effect of inhibitors on OTES and MTES sols it was deemed necessary to carry out further particle size testing using an organic inhibitor namely, phenyl benzoate, since it is a good representative of the improvement in corrosion protection for PhB-doped MTES coatings and the decline in corrosion protection for PhB-doped OTES coatings. Figure 5.61 illustrates the effect of phenylbenzoate on the particle size of MTES and OTES sols immediately after inhibitor addition to developed sol and 24 hrs after inhibitor addition to developed sol. PS was measured at $T=24$ hrs to detect and evaluate any changes occurring that are not measurable at $T=0$ hrs. MTES results (Figure 5.61 (a)) display a shift to a larger particle size for ~ 200 nm population, which was already measured at $T=0$ hrs, this shift being more pronounced at $T=24$ hrs which is expected since agglomeration of particles progresses with time.

For OTES sols, a significant shift of the ~200 nm population to larger particle size is also measured, together with the addition of a third population at ~10 nm for 0.01 M PhB. It is possible that the presence of such an organic molecule is interacting with the organic groups present on the surface of the nanoparticles through Van der Waal interactions thus encouraging the proximity of nanoparticles and their eventual aggregation, such an effect being more pronounced for the longer-chained octyl- versus methyl-containing sols. Moreover, organic molecules such as phenyl benzoate may also preferentially reside in the longer octyl organic chains present in OTES coatings as opposed to leaching to the surface of the metal when coating is damaged. The coating formed is therefore based on larger, more uneven particles with organic inhibitor molecules favourably remaining in organic coating. This results in PhB-doped OTES coatings offering inferior corrosion protection compared to PhB-doped MTES coatings.

One observation remains to be discussed and that is the fact that Pyrrolidine produces the most protective coatings in both OTES and MTES coatings. The most protective coatings produced for each inhibitor studied are listed in **Table 9.2** for both MTES and OTES coatings. The greatest improvement was obtained using pyrrolidine in a 0.001 M concentration ($8.60 \times 10^5 \pm 9.66 \times 10^4 \Omega \text{ cm}^2$) compared to Z_{tot} value of $1.25 \times 10^5 \pm 1.47 \times 10^4 \Omega \text{ cm}^2$ for blank MTES:TEOS 60:40 mol% coating which is almost an order of magnitude improvement in corrosion resistance.

For OTES coatings, the most protective coating was also obtained using 0.001 M pyrrolidine ($1.54 \times 10^6 \pm 9.65 \times 10^4 \Omega \text{ cm}^2$) compared to Z_{tot} value of $7.54 \times 10^5 \pm 1.46 \times 10^4 \Omega \text{ cm}^2$ for blank OTES:TEOS 20:80 mol%. Pyrrolidine, being the smallest molecule considered in this set of inhibitors, will interfere the least with the coating deposition and curing, thus is capable of resulting in an improvement in corrosion protection in OTES coatings. Electrochemical data presented in Table 9.2 can be summed up and explained as follows: since OTES coating is based on sol particle size that is smaller than that of MTES coating, more compact coatings will be formed for which inhibitors will interfere with the OTES silica matrix more effectively than for MTES particles. MTES

particles are larger and will therefore also possess larger interstitial spaces for the accommodation of inhibitor molecules.

The efficiency of an inhibitor is dependent not only on its solubility but also on its structure [152]. Relatively planar molecules have been used in this study ensuring maximum surface area contact with metal surface. Interestingly, pyrrolidine provided the greatest protection which is rather unexpected since it is the smallest molecule and is incapable of delocalisation of lone pairs on its nitrogen atom like the other organic inhibitors considered (Table 9.2). It is possible that a smaller molecule such as pyrrolidine is better accommodated in the silica matrix during the deposition stage, thus interfering minimally with the coating's integrity.

Table 9.2: Z_{tot} values for six inhibitor molecules that produce the most protective coatings in MTES and OTES and in their respective concentrations

Inhibitor	$Z_{tot} \pm$ St. Error (Ω cm ²) MTES	Concentration (mol)	$Z_{tot} \pm$ St. Error (Ω cm ²) OTES	Concentration (mol)	Solubility (g/L)
XTES (blank)	$1.25 \times 10^5 \pm 1.47 \times 10^4$	0	$7.54 \times 10^5 \pm 1.46 \times 10^4$	0	-
Ce	$6.68 \times 10^5 \pm 7.42 \times 10^4$	0.0001	$5.27 \times 10^5 \pm 7.61 \times 10^4$	0.001	1754 [263]
1,4-N	$4.69 \times 10^5 \pm 6.25 \times 10^4$	0.01	$9.13 \times 10^5 \pm 1.54 \times 10^4$	0.0001	0.09 [258]
2-H	$4.85 \times 10^5 \pm 6.07 \times 10^4$	0.0001	$3.80 \times 10^5 \pm 6.06 \times 10^4$	0.0001	1000 [259]
1-N	$5.71 \times 10^5 \pm 5.71 \times 10^4$	0.0001	$8.12 \times 10^5 \pm 1.07 \times 10^5$	0.001	1.35 [262]
PhB	$5.83 \times 10^5 \pm 6.56 \times 10^4$	0.01	$4.46 \times 10^5 \pm 8.53 \times 10^4$	0.0001	Insoluble [260]
Pyr	$8.60 \times 10^5 \pm 9.66 \times 10^4$	0.001	$1.54 \times 10^6 \pm 9.65 \times 10^4$	0.001	1000 [261]

The extent of inhibition of Ce and PhB in MTES coatings was further studied by measuring impedance at various time intervals during an OCP as shown in Figure 5.77. The decrease in impedance over time was expected for 0.001 M Ce-doped MTES coatings since cerium nitrate is highly soluble and will leach out of the pores and coating, thus leaving behind a coating which can only become more porous and damaged with time. Results for 0.01M PhB-doped MTES coatings were similar. It was anticipated that PhB molecules being insoluble will dissolve slowly with time and therefore sustain a concentration of inhibitor molecules in the pores of the coating. However, it has been realised that once the few solubilised molecules are in the pore's solution, they are also likely to leach out.

Palanivela *et al* state that it is difficult to control leaching of the entrapped inhibitors out of the coating, especially when they are poorly soluble [156]. For a slow release of inhibitors and long-term protection, several authors [103,120,134,155,160,265-269] report the development of nano-reservoirs to isolate an inhibitor inside and prevent its direct interaction with the sol-gel matrix. For instance, Zheludkevich *et al* used zirconium nanoparticles as both reinforcement of coating matrix and as reservoirs for cerium nitrate [270]. These so-called self-healing coatings do not come without their set of limitations in that the nano-reservoirs should be homogeneously distributed in the film matrix [270]. Nevertheless, this topic merits future work.

CHAPTER 10:

Performance of OIH alkoxysilane coatings relative to Paraloid and Ercalene lacquers

10.1 Introduction

This Chapter features corrosion testing and characterisation of Paraloid B-48, Paraloid B-72 which are acrylate-based lacquers that have been extensively used in the past by conservators on several metals[1,271-273]. Paraloid B-72 is a methyl acrylate/ethyl methacrylate co-polymer having a glass transition temperature (GTT) of 40 °C whereas Paraloid B-48 is a butyl methacrylate/ methyl methacrylate co-polymer having a GTT of 50 °C, which forms a harder coating with a higher adhesion to metal surface[273].

Ercalene also features in this comparative study, which is a nitro-cellulose-based lacquer. This lacquer was included in this study since it is currently being used by conservators to preserve metal armour artefacts at the Palace Armoury, Valletta. The scope of the chapter is to gauge and compare the performance of OIH alkoxysilane coatings to the more conventionally used lacquers, thus determining their suitability for such an application. The lacquers have been applied onto both clean and corroded iron surfaces through dip-coating in a range of concentrations as was carried out for OIH alkoxysilane coatings in previous chapters. In addition to electrochemical testing, salt-spray testing was conducted for which thicker coatings were deposited through increasing the lacquer/SiO₂ concentration and the mode of application was altered to also include brush and sponge application.

10.2 Coating morphology and thicknesses of OIH alkoxysilanes in comparison with Paraloid and Ercalene coatings

OIH alkoxysilane, Paraloid and Ercalene coatings were applied via dip coating having concentrations of 2.5, 5 and 10% SiO₂ in ethanol for OIH alkoxysilane coatings, 2.5, 5, 10 and 15% (wt/v) acrylate in acetone for Paraloid lacquers and 75% (v/v) nitrocellulose for Ercalene lacquer. The coating procedure was also carried out on SS strips to determine the thickness of such coatings, coating thicknesses are listed in Table 5.17 for dip-coating. Thickness increases as the concentration of lacquer is increased, which is the case for Paraloid B-48, B-72 and OIH alkoxysilane coatings. Paraloid lacquers produce similar thicknesses at the same concentration (e.g. at 15% B-48 = 6584 ± 452 μm and B-72 = 7387 ± 636 μm from Table 5.17) whereas Ercalene coatings produced thinner coatings (4512 ± 654 μm). OIH alkoxysilane coatings deposit the thinnest (1453 ± 120 μm) even at a higher SiO₂ concentration of 10%.

OIH alkoxysilane, Paraloid and Ercalene coatings were applied via fine brush, coarse brush and sponge application; however, fine brush application was studied further since it proved suitable for the deposition of OIH alkoxysilane coatings (Figure 5.81) and thickness determination was carried out and presented in Table 5.18. Thicker coatings were utilised when applying using fine brush (intended for salt-spray testing), thus a 10% SiO₂ concentration in ethanol was used with OIH alkoxysilane coatings, 15% (wt/v) acrylate in acetone for Paraloid lacquers and 75% (v/v) nitrocellulose for Ercalene lacquer. As the chain length of the organic part of the X-TES precursor is increased, a slight increase in thickness is achieved (MTES:TEOS = 4.21 ± 0.45 μm, OTES:TEOS = 5.16 ± 0.30 μm, see Table 5.18). This trend has been previously observed in Figure 5.9 for 2.5% SiO₂ coatings that have been applied through dip-coating. However, since application has been changed to feature a higher SiO₂ concentration (10%) and applied using a brush, thicker coatings are obtained i.e. in the micron range. Thickness value for double-coated 60:40 mol% MTES:TEOS (10% SiO₂) applied through dip-coating was determined to be 0.97 ± 0.08 μm (Chapter 4 Table 4.2)

whereas a fine brush application (Table 5.18) gives rise to a four-fold increase in thickness, $4.21 \pm 0.45 \mu\text{m}$.

Thickness for 15% Paraloid B-48 and B-72 coatings is similar, however, deposition by brush did not produce significantly thicker coatings compared to those produced by dip-coating. For example, dip-coating 15% (wt/vol) Paraloid B-48 produces thicknesses of $6.58 \pm 0.45 \mu\text{m}$ (Table 5.17) whereas brushing produces coatings with a thickness of $8.38 \pm 0.51 \mu\text{m}$ (Table 5.18). It is postulated that the reason for this is due to more efficient uptake of lacquer during the dip-coating process as acylate lacquers are more viscous compared to nitrocellulose and alkoxy silane-based coatings. Ercalene produced slightly thinner coatings ($7.47 \pm 0.70 \mu\text{m}$, Table 5.18) compared to Paraloid which was also the case with dip-coating application (Table 5.17). Paraloid and Ercalene coatings have deposited thicker layers than for OIH alkoxy silane coatings (Tables 5.17 for dip-coating and 5.18 fine brush application), where thicknesses for B-48 and B-72 are similar; $8.38 \pm 0.51 \mu\text{m}$ for B-48, $8.32 \pm 0.29 \mu\text{m}$ for B-72 (Table 5.18) whereas Ercalene coatings are slightly thinner $\sim 7.47 \pm 0.70 \mu\text{m}$.

10.3 Electrochemical testing

Electrochemical results presented in Figures 5.84-5.86 on clean metal and Figures 5.87-5.89 on corroded metal dip-coated with Paraloid B-48, B-72, 75% Ercalene and MTES:TEOS 60:40 mol% (representing silica coatings) can be summarised and discussed with ease through **Figure 10.1**. From Figure 10.1 (a) it can be said that the total impedance ($Z_{tot} = R_t + R_{po} + R_{sol}$ at lower frequency range) values do not vary significantly when lacquer concentration is increased from 2.5% to 5% for Paraloid and SiO_2 coatings. Changes in Z_{tot} occur when the concentration is increased to 10%. In fact, coatings improve drastically for SiO_2 which was not always reliable using this method. The same was obtained for B-48 coatings at a 15% concentration which was also deemed unquantifiable. B-72 coatings displayed an increase in Z_{tot} with lacquer concentration up to 15%, however lower than values obtained for B-48 and SiO_2 at any given concentration. Ercalene coatings provided sufficient corrosion protection which is slightly less than that obtained for SiO_2 coatings.

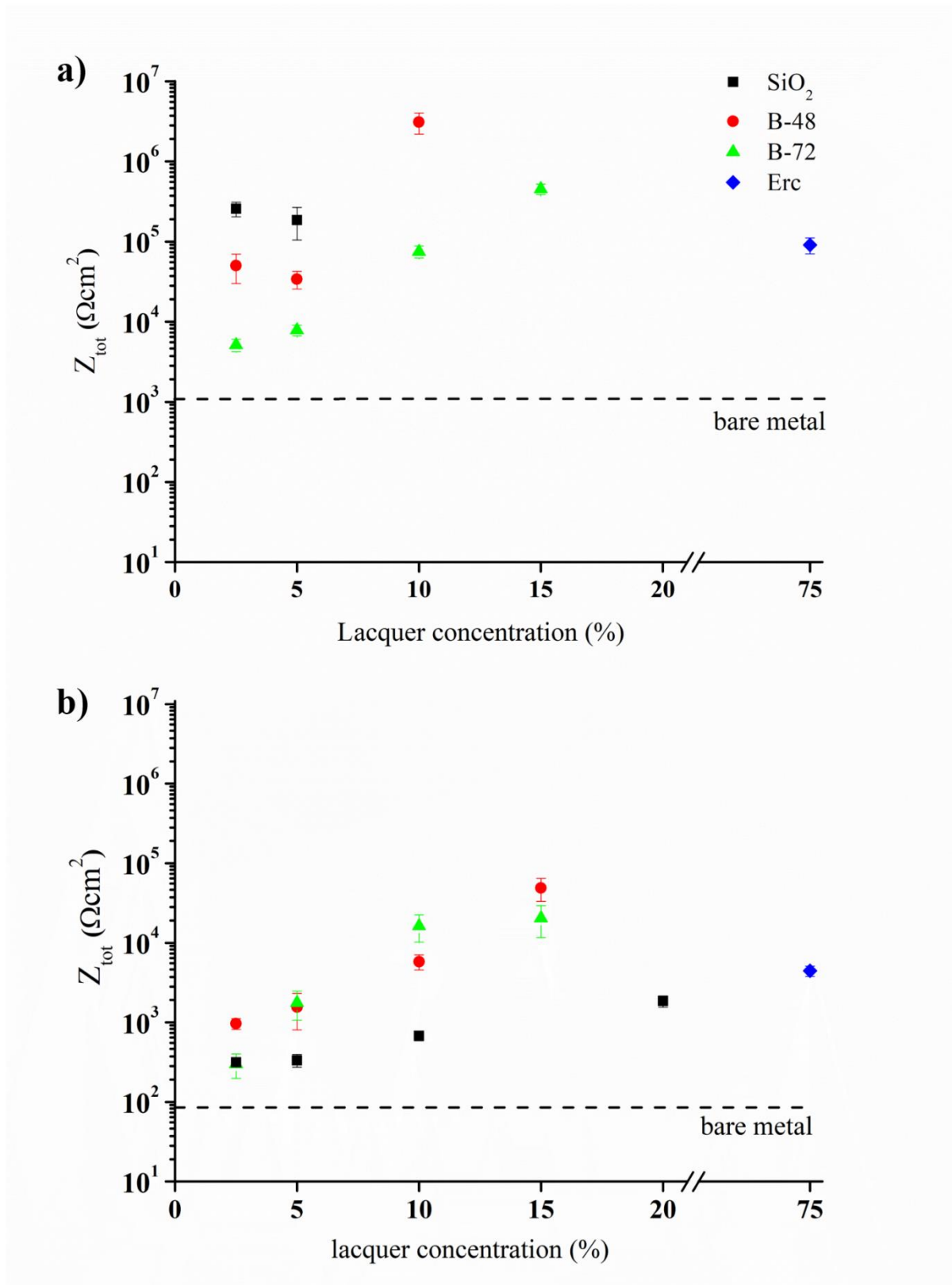


Figure 10.1: Plot of lacquer concentration (%) versus total Impedance (Z_{tot}) for 15% Paraloid B-48, B-72, 75% Ercalene and 10% MTES:TEOS 60:40 mol% (labelled as SiO₂) on a) clean polished iron surface and b) corroded cleaned iron surface applied through dip-coating.

A wider range of lacquer concentration could be studied on corroded surfaces (Figure 10.1 (b)) since less improvement in Z_{tot} is obtained on such rough surfaces. An overall increase in Z_{tot} values is obtained as the concentration is increased for all lacquers. However, SiO₂ coatings fared worse compared to Paraloid and Ercalene coatings. B-72 coatings plateau at 10% whereas B-48 coatings exhibited the highest Z_{tot} value at 15% concentration in acetone which produced the most protective coatings not only on clean but also on corroded metal. Ercalene coatings provided a relatively good impedance to corrosion as higher values were obtained than those for SiO₂ at all concentrations. Thus, it can be stated that silica coatings are best suited for protecting clean surfaces, however, these coatings do not perform as well on corroded surfaces. Although silica coatings have produced the most protective coatings on clean metal, Paraloid B-48 have also fared well on clean surfaces and have been proven to provide the most protection on corroded surfaces.

The coating's ability to protect the underlying surface can be discussed in terms of coating thicknesses, Table 5.17 lists thicknesses obtained for different concentrations of lacquers used through dip-coating application. B-48 coatings are slightly thinner than B-72 at any given concentration and yet produce more protective coatings on clean metal. This is not so on corroded surfaces probably due to the surface roughness which equates to similar Z_{tot} values for B-48 and B-72 on the corroded surface (B-48 are slightly more protective than B-72 still). Surface roughness of corroded metal appears to be an issue with thinner coatings since SiO₂ coatings which are thinnest of all lacquers perform very poorly (Figure 10.1 (b)). Thicker coatings become a requirement on corroded surfaces for improved protection as has been already concluded in Chapter 7. Therefore, since Paraloid coatings have deposited the thickest, they are able to best protect the corroded surface. Although 75% Ercalene, 15% Paraloid B-48 and 15% Paraloid B-72 appear to provide a continuous coverage over the entire corroded surface (Figure 5.80) surface roughness does not allow for a completely crack-free coating which are evident at higher magnification.

As listed in Table 5.17, 75% Ercalene coatings are 4.51 ± 0.65 μm thick which is the approximate thickness for 10% Paraloid coatings (4.29 ± 0.37 μm for B-48 and 4.28 ± 0.46 μm for B-72). Z_{tot}

values for Ercalene are comparable to those of 10% Paraloid B-72 on clean surface, however, 10% B-48 coatings performed significantly better which has been attributed to the adhesion promoters present in B-48 which are known to result in strong adhesion of coating with clean metal surfaces [274,275]. In fact, 10% B-48 does not perform any better than 10% B-72 or 75% Ercalene on corroded surface since the improvement attributed to adhesion promoters no longer occurs on the oxide layer. The highest concentration of SiO₂ used was that of 20% which produced much thinner coatings ($1.45 \pm 0.12 \mu\text{m}$) and resulted in Z_{tot} values that are indeed lower than that for Ercalene and 10% Paraloid coatings on corroded surfaces as expected.

Cano *et al* [170] report a 1.5 order of magnitude improvement compared bare polished metal (see Specimen 3 in Bode plot of Figure 2.6, Chapter 2) when Paraloid B-72 is applied through brush coating having thickness of $7 \pm 4 \mu\text{m}$ [170]. Although the mode of application is different since Figure 10.1 displays results obtained for dip-coated specimens, this thickness obtained by Cano through brush application is comparable to thickness of dip-coated samples (15% B-72 having thickness of $7.3 \pm 0.6 \mu\text{m}$, see Table 5.17) for which a 2.5 order of magnitude was obtained as shown for 15% B-72 in Figure 10.1 (a). Higher impedance can be attributed to the mode of application even though similar thicknesses were deposited. Cano *et al* have stated that a non-uniform layer was obtained due to brush strokes which left behind weak points where thickness of the coating is lower.

Electrochemical results obtained for alkyl trialkoxysilanes, acrylates and nitrocellulose-based coatings have generated a detailed comparative account of the extent of corrosion protection incurred by these coatings. However, as previously explained in Chapter 4, repeatability issues arise when coatings are very protective which leads to the inability to quantify and compare such coatings to coatings that fail to at least some extent during testing. Had there been no such issues with reproducibility, electrochemical testing is perhaps not sufficient to reach conclusions on coating quality since the mode of testing involves immersion in salt solution for an hour prior to testing. Electrochemical testing, although a comparable and accurate study, was enriched with accelerated

corrosion (salt spray) testing which is arguably closer to a real-life study of the degradation of the coatings. Furthermore, it was used to draw a comparison between higher concentrations of lacquer which rendered electrochemical testing problematic as previously stated in Chapter 4 for 10% SiO₂ concentrations and in 15% B-48 results of Figure 10.1 (not shown due to irreproducibility). The mode of application was also changed from dip-coating to brush coating to mimic more closely the method employed by conservators, which in turn brings about thicker, more protective coatings.

10.4 Accelerated corrosion (salt-spray) tests

10.4.1 OIH alkoxysilane coatings deposited through dip, fine brush, coarse brush and sponge application

As shown in Figure 5.81, the cleanest and most evenly coated surface was obtained when OIH alkoxysilane coatings are applied through dip-coating. Brush application leads to the inevitable brush strokes which are deeper when a coarser brush is used. Brush application also lead to the deposition of silica particles which are visually observable, which was more evident when a coarse brush was used. Additionally, coarse brush application lead to the deposition of black particles originating from the brush bristles. Although the scope of testing with coarse brush was to be able to deposit the coatings using less strokes per coupon and a greater volume i.e. thicker coatings, silica particle deposits together with brush debris deposition occurring during sol deposition lead to the poor coating performance compared to coatings that have been applied using a fine brush.

This is evident visually through Figures 5.90-5.94 where brush-applied coated coupons formed more corrosion products compared to dip- and fine-brush applied coated coupons during the same cycle. Brush strokes are reduced when a finer brush is used which partially explains the more protective coatings obtained through fine brush compared to coarse brush application. Also, fewer silica deposits were observed for such an application. OIH alkoxysilane coating preformed very poorly when applied through sponge as seen in Figure 5.81 (d). Coatings did not deposit in an even manner,

since a rougher surface was obtained compared to coatings deposited through dip-coating. Also, the majority of the surface appeared where venous pattern of coating deposition was observed.

Images of coupons presented in Figures 5.90-5.94 have been processed using ImageJ software and the percentage corroded area of coupon surface was calculated and presented in **Figure 10.2** for the five alkyl trialkoxysilane coatings considered for salt spray test. Each alkoxy silane has been applied using dip-coating, fine brush, coarse brush and sponge application as two layers. The four modes of application were considered for silica-based coatings and can be compared with ease through Figure 10.2. Clean uncoated metal will be mostly covered by corrosion products by the end of the first cycle, also evident in Figure 10.2 as having the largest % area coverage from the 1st cycle. All coatings are expected to fail at some point during the cycling process, however, more protective coatings will maintain a low corroded area% even after several cycles have been applied to the coupons.

It is clear for all five silane coatings that dip-coating and fine brush applications lead to longer lasting coatings when compared to sponge and coarse brush application. This observation being most prominent in OTES and HTES-based coatings where coarse brush and sponge applications lead to an increase in area% coverage already by the 1st cycle (Figures 5.92 for HTES and 5.93 for OTES). Therefore, coarse brush and sponge applications were not further considered as a satisfactory mode of application of these silanes.

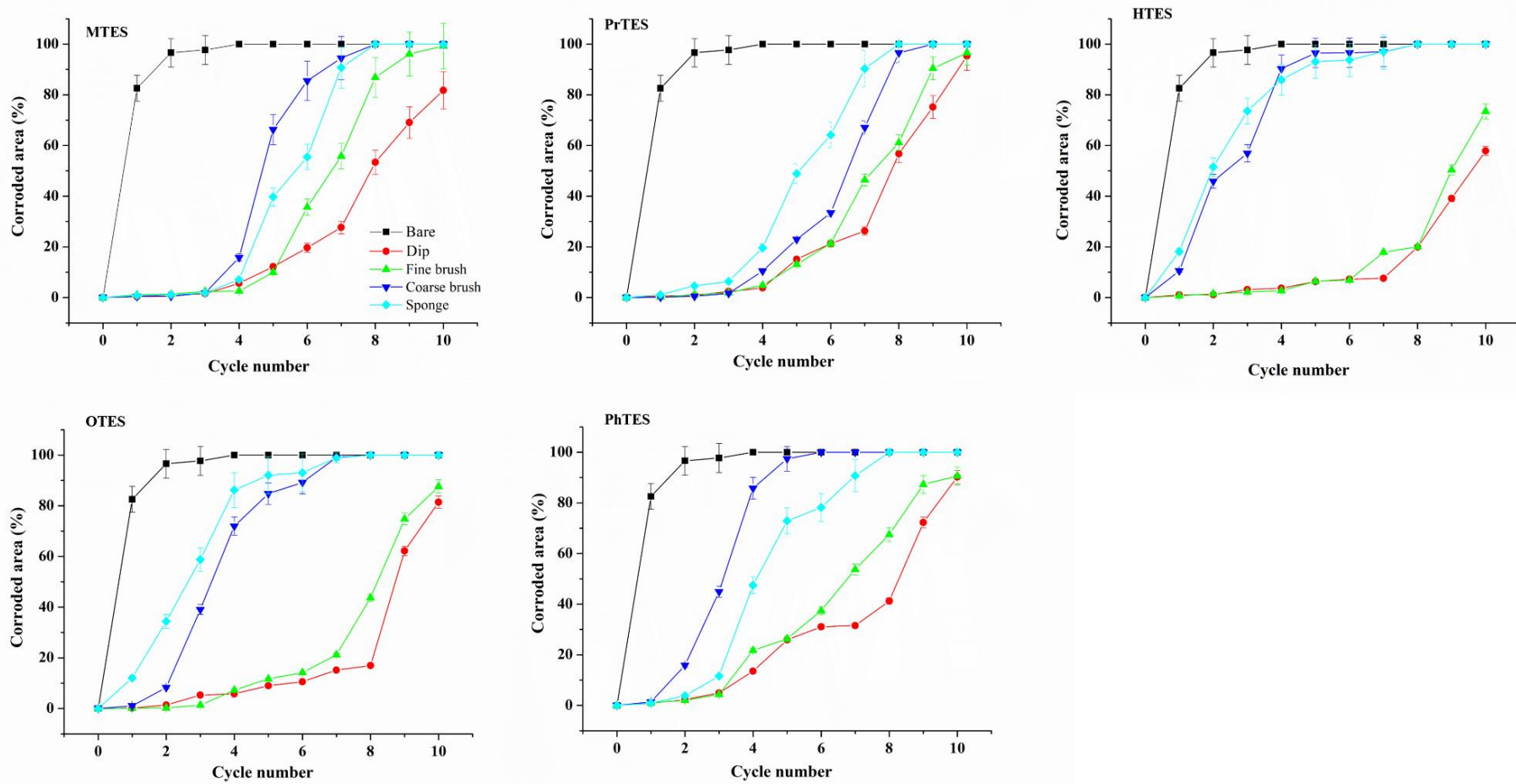


Figure 10.2: corroded area percentage coverage of coupon surface for the five alkyl alkoxy silane-based coatings considered for salt spray testing conducted over 10 cycles. Each coating system was applied using four methods: dip-coating, fine-brush, coarse-brush and sponge application. Plots include bare metal results for comparative reasons.

10.4.2 Comparison of OIH alkoxy silane coatings to Paraloid and Ercalene coatings deposited through dip and fine brush applications.

Figure 10.3 shows corroded area percentage coverage of coupon surface calculated for the five silane-based coatings (obtained from Figure 5.96) together with Paraloid and Ercalene coatings for the duration of salt-spray testing. The scope of Figure 10.2 was to determine the best mode of application for OIH coatings whereas Figure 10.3 was compiled to compare the extent of corrosion protection offered by these coatings to Paraloid and Ercalene lacquers. Figure 10.3 (a) shows results for dip-coating where silanes perform very similarly up to cycle number 4, beyond which PhTES coatings begin to degrade at a faster rate than the aliphatic silane coatings. From cycle 5 onwards it becomes clear that the least corroding coupons are those coated with OTES and HTES. B-72 coating performance is comparable to the most protective silanes (HTES and OTES). Ercalene performed poorly and was in fact deemed the least protective coating of all coatings considered, B-48 fared better than Ercalene but still not as well as OIH alkoxy silane coatings. Fine brush results for silanes (Figure 10.3 (b)) are similar to those obtained through dip-coating. On the other hand, fine brush application for acrylate and nitrocellulose lacquers are clearly worse off than those obtained through dip-coating.

In Chapter 6 it was determined that most protective coatings were MTES:TEOS in a molar ratio of 60:40 mol%, PrTES:TEOS 50:50 mol%, HTES:TEOS 30:70 mol%, OTES:TEOS 20:80 mol% and PhTES:TEOS 40:60 mol% through electrochemical testing on coupons that have been dip-coated in 2.5% SiO₂ concentration sols; the most protective coating was determined to be OTES:TEOS whereas the least being HTES:TEOS. These results are not entirely reflected in salt-spray testing (Figure 10.3 (a)) where, although the most protective coating was determined to also be OTES:TEOS, HTES:TEOS coating was second best rather than being the least protective as one would expect. In fact, it is clear through Figure 10.3 (a) that coatings containing longer aliphatic chains (OTES, HTES) maintain a lower corrosion area% coverage than the shorter aliphatics (MTES, PrTES), PhTES:TEOS coatings revealed to be the least protective.

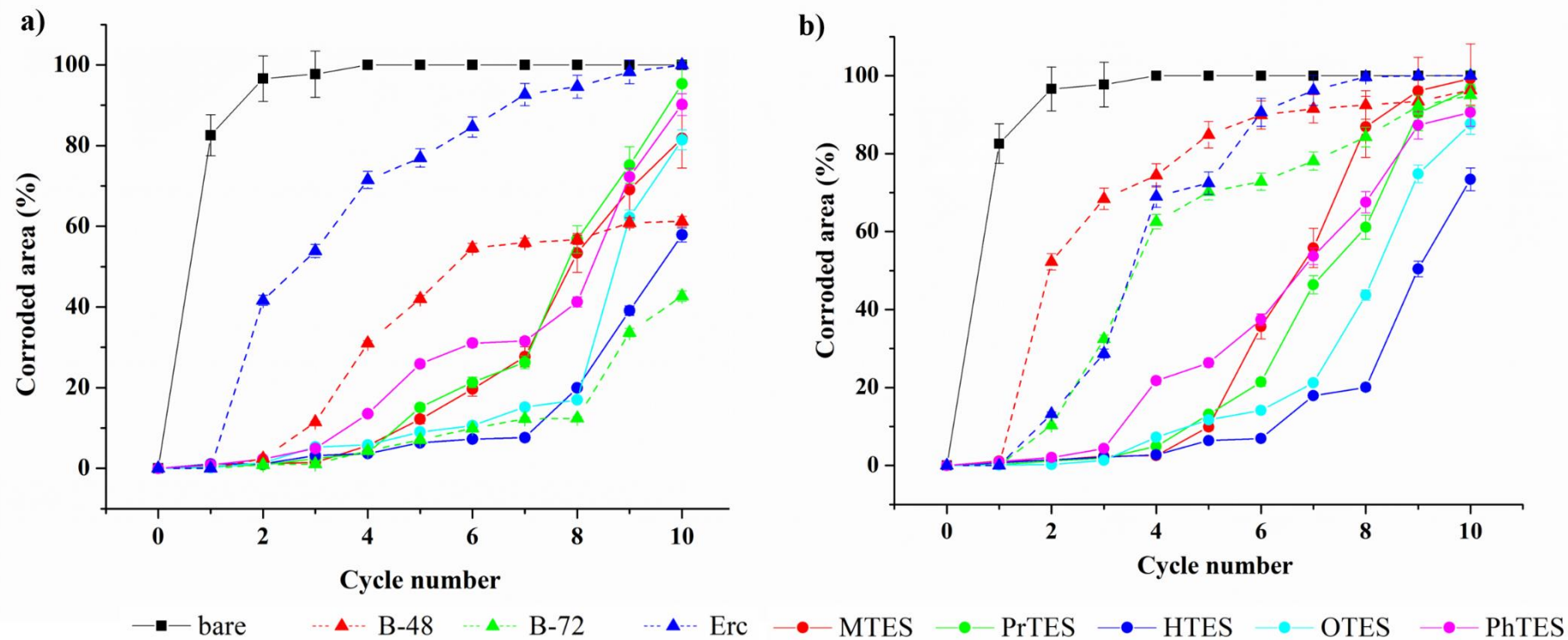


Figure 10.3: corroded area percentage coverage of coupon surface calculated through ImageJ software for the five alkyl alkoxy silane-based coatings together with Paraloid and Ercalene lacquers. Each alkyl trialkoxy silane/lacquer was applied through a) dip-coating and b) fine brush. Plots include bare metal results for comparative reasons.

Perhaps it may not be possible to compare the two modes of testing since thicker coatings and the mode of application was changed for salt spray testing. Salt spray testing involved subjecting the coated coupons to a wet cycle consisting of 8 hrs at 100% RH and 35 ± 3 °C followed by the dry cycle consisting of 16 hrs of laboratory climatic conditions (20-25 °C at 50-60% RH). Unlike electrochemical testing, accelerated corrosion testing involves changes in temperature, where HTES and OTES coatings appear to resist failure more effectively than MTES, PrTES and PhTES coatings. Figure 10.3 (b) features results for OIH alkoxysilanes which have been applied using fine-brush for which trend observed with dip-coating (Figure 10.3 (a)) are also applicable.

Through Figure 10.3 it can be stated that OIH alkoxysilane, Paraloid and Ercalene coatings are less prone to corrosion when applied through dip-coating compared to fine-brush and it is due to the even coating (lack of brush-strokes) obtained when dip-coating is carried out. Paraloid and Ercalene lacquers fare significantly worse when applied using fine-brush compared to dip-coating. Although the brush used possessed fine bristles, brush application is known to produce coatings varying in thickness[276], thus increasing likelihood of solution penetration, see Figure 5.96 showing B-48 and B-72 for which corrosion is significantly more widespread for brush application relative to dip-coated coupons at any given cycle. Brush-applied OIH alkoxysilane coatings protect almost as well as when dip-coating is carried out.

It is interesting to note plot for B-48 shown in Figure 10.3 (a) where a plateau is reached at Cycle 6 beyond which increase in corrosion area% coverage is minimal. This was already noticeable during testing where a pocket of solution would form due to a defect in coating, beyond which no further spreading occurred unlike for Ercalene where spreading was effective from the start of the testing and can be seen as rapid increase in area% coverage throughout the cycling process. When water penetrates through the Paraloid coatings, the contained solution will lead to the corrosion of the exposed metal area even after the coupons are drained as well as possible after being removed from salt-spray chamber and since the acrylate film remains intact, the solution remains contained and does not evaporate completely. Therefore, the corrosion process is sped up in such solution-

containing pocketed areas. This does not occur in the case of OIH alkoxysilane-based coatings, for which defects in the coating leads to a very localised area of exposure and corrosion (spotted pattern of corrosion) due to excellent coating adhesion. Nevertheless, unaffected areas of Paraloid coated metal remain intact which accounts for the low areas of corrosion in later cycles.

Paraloid B-72 coatings have performed better than B-48 coatings (Figure 10.3) for both dip- and brush- applications. This is not in agreement with electrochemical data where B-48 coatings were significantly more protective than B-72 coatings (Figure 10.1 (a)). Paraloid B-72 is an ethyl methacrylate co-polymer having a glass transition temperature (GTT) of 40 °C [170] whereas Paraloid B-48 is a methyl methacrylate copolymer having glass transition temperature of 50 °C [277]. The GTT is the temperature range where an amorphous thermoplastic polymer changes from its hard, rigid (glassy) state to a more pliable, compliant state. Therefore, B-72 would be close to its GTT during salt-spray testing since temperature was set to alternate between 35 ± 3 °C (upper limit being 38 °C) and 25 ± 2 °C. This shift in temperature brings about a greater change in coating hardness properties for B-72 than for B-48 that has a higher GTT.

B-48 is in fact preferred by conservators over B-72 for application onto HM for hotter climates since B-48 is more durable at higher temperatures relative to B-72 [278]. Therefore, it was expected that B-48 coatings will perform better than B-72 coatings, which makes results even more contradictory at first thought since B-48 coatings proved to be less protective when applied through fine brush and dip-coating (see Figure 10.3). When Paraloid coatings are damaged, underfilm corrosion occurs which aids in explaining these odd observations. It is postulated that since B-48 coatings are softer than B-72 coatings at higher temperature, then underfilm corrosion would be more prominent with the more rigid B-48 coatings which do not alter in their hardness during cycling process. Such observations due to temperature alterations cannot be made from electrochemical testing.

Nano-scratch testing (Figure 5.83) conducted on the three lacquers can explain the poor performance of Ercalene coatings obtained through both dip- and brush- applications. Although pull-out testing

(Table 5.19) is indicative of good adhesion of Paraloid and Ercalene coatings (tensile strength), nano-scratch testing reveals the ease at which delamination of Ercalene occurs when a shearing force is applied which does not occur for Paraloid or OIH alkoxy silane coatings. Material accumulation on the sides of the scratch are registered as a decrease in depth of the scratch profile after scratch relative to scratch profile and is evident for Paraloid plots (Figure 5.83). The delamination of Ercalene shows up as changes in depth following a wave-like pattern of the scratch profile after scratch relative to the scratch profile. The distances from the beginning of the scratch at which point the indenter reaches the underlying metal surface for the three lacquers studied are marked by arrows in Figure 5.83 having values of $132.2 \pm 31.3 \mu\text{m}$, $138.0 \pm 29.3 \mu\text{m}$ and $85.2 \pm 12.6 \mu\text{m}$ for B-48, B-72 and Ercalene respectively. Larger distances and loads are obtained for Paraloid coatings compared to Ercalene which is softer and was penetrated quicker.

As seen in Figure 5.83, force and distance required for the indenter to penetrate through the Ercalene coating and reach to the metal surface is similar to that measured for softer coatings such as OTES:TEOS 60:40 mol% (Figure 5.16); however even when considering the softest of OIH alkoxy silane coatings, a sharp cut through the coating occurs during scar development. In the case of Ercalene, the cut generates the additional formation of shear lips from the very start of the scar development. This shearing weakness could explain the poor results obtained in electrochemical testing and especially salt-spray where penetration of water would lead to the immediate spreading of solution between the coating and underlying metal surface, thus affecting the coating's ability to offer significant protection against corrosion of underlying metal.

Chapter 11:

Reversibility of OIH alkoxysilane coatings

11.1 Introduction

Coatings applied onto Heritage Metal require to be removed with relative ease for the re-application of a fresh coating once it no longer fulfils its protective function. Typically, lacquers are wiped off the surface of the artefact using cotton dampened with solvent; for instance, acetone is typically used to re-dissolve and remove Paraloid coatings. Since OIH alkoxysilane coatings consist of an extensive silica network, a strong alkaline solution ($\text{pH} > 10$) would be required to break apart the siloxane -O-Si-O- bonds i.e. reverse the condensation reactions that occurred during sol development and curing. Therefore, solvents such as acetone are not capable of removing OIH silane coatings, or do so to a limited extent.

Kachurina *et al* [169] have conducted a reversibility study of alkoxysilane coatings on aerospace aluminium alloys. The alcohols and ketones, which are polar organic solvents, were found to affect the integrity of the coatings through the solvents' ability to solubilise the organic portions of the coating thus degrading the integrity of the coating. Hexane, which is a non-polar organic solvent, did not affect the integrity of the deposited films. Isopropyl alcohol and sodium hydroxide solution were therefore selected to conduct the work presented in this Chapter, the scope being to identify the solvents/solutions that are able to remove such coatings with relative ease.

The chapter comprises of two parts due to the two methods of testing employed. The first method consists of immersion testing where coupons were immersed in several solvent/solutions and monitored over several weeks until coating was easily dislodged. The second method involves the manual cleaning of coatings until no longer visible on the metal surface for which the number of strokes required to remove the coating using solvent/solution-soaked cotton swabs was recorded. Although immersion testing reveals the most suitable solvents for removal of coatings and is a typical mode of assessment of coating removal[169], the scope of manual cleaning was to obtain results through the application of a more hands on method of coating removal.

11.2 immersion testing versus manual cleaning

Figure 5.97 presents data obtained for immersion testing for coatings considered in this study. It is clear that all coatings require less than 24 hrs to be completely removed from the metal surface in NaOH solutions at pH 14 and 13. Although pH 12 NaOH solution is safer to handle, immersion testing was prolonged and is most evident for PrTES and PhTES-based coatings, therefore was not considered as a suitable mode of removal of coatings for which a higher alkalinity is necessary. Immersion in pH 13 caustic solution did not significantly increase the time required to remove coatings when compared to pH 14, therefore it is a safer option for the removal of coatings. Low organic precursor-containing coatings are difficult to remove using IPA which is reflected in the lengthy time required to dislodge the coating such as 240+ hours for MTES:TEOS 20:80 mol% in IPA, whereas 80:20 mol% coatings require a short amount of time to be removed (24 hrs).

Low organic precursor-containing coatings i.e. 20:80 mol% MTES/ PrTES/ HTES/ PhTES:TEOS and 10:90 mol% OTES:TEOS, are the most difficult to remove using IPA solvent which is due to the presence of more inorganic entities originating from TEOS which lead to the formation of more metal to O-Si bonding responsible for the good adhesion of coating. Such strong adhesion can only be reversed using high concentrations of NaOH. On the other hand, high organic precursor-containing coatings such as 80:20 mol% MTES/PhTES:TEOS, PrTES/HTES/OTES:TEOS 60:40 mol%, are

removed with relative ease using IPA, which was also reported by Kachurina et al [169]. The organic molecules tend to orient themselves outwardly to the particle's surface, therefore as the organic content in the coating is increased, lower levels of Si-O-M bonds formed leading to less efficient adhesion. Higher organic content leads to more efficient removal of coatings using IPA due to the solvent's degreasing and destabilising ability on the softer, tackier organic coatings.

It is interesting to note that MTES:TEOS 60:40 mol%, PrTES:TEOS 50:50 mol%, HTES:TEOS 30:70 mol%, OTES:TEOS 20:80 mol% and PhTES:TEOS 40:60 mol% coatings which have been deemed as most protective in Chapter 6, require the most immersion time in pH 12 solution. NaOH solution at pH 12 seems to be too dilute to carry out effective reversibility of these silicate coatings which are able to resist the process, thus the most protective coatings will take the longest to dislodge from the coupon surface. Taking into consideration MTES:TEOS coatings to explain the trend, 20:80 mol% coating have the lowest organic content therefore should be more difficult to remove using NaOH. However, since NaOH in a lower concentration, the MTES:TEOS 20:80 mol% coatings are less hydrophobic than 60:40 mol% therefore are seeped through at a faster rate. On the other hand, 80:20 mol% coatings are softer and easier to dislodge even using NaOH solution.

As already evident in immersion testing, manual cleaning of low organic precursor-containing coatings (20:80 mol% MTES/PrTES/HTES/PhTES:TEOS and 10:90 mol% OTES:TEOS) are the most difficult to remove using IPA (Figure 5.100). The coatings' strong adhesion can only be reversed using 100% N solution (pH 14 NaOH solution without IPA) for which substantially less strokes were required to dislodge the coatings. As the percentage organic precursor is increased, less effort is required to remove the coating using IPA (for instance, MTES:TEOS number of strokes using IPA drastically reduces from 3500 for 20:80 mol% down to 50 strokes for 80:20 mol%). This trend applies for the other precursors used. On the other hand, high organic precursor-containing coatings (as exemplified through MTES/PrTES/PhTES:TEOS 80:20 mol% and HTES/OTES:TEOS 60:40 mol%) are removed with ease using 100% I (IPA solvent without NaOH) and not so quickly removed using 100% N.

It is interesting to note how higher organic precursor-containing coatings of MTES:TEOS, HTES:TEOS and OTES:TEOS are still removed when using 100% NaOH (for example OTES:TEOS 60:40 mol% 100 strokes NaOH, 10 strokes IPA). Even though the IPA removes the coating instantly, it is still dislodged using NaOH solution due to poor adhesion and tackiness of the coating. Similar results were obtained for OTES:TEOS 40:60 mol% and HTES:TEOS 60:40 mol%. The ease by which these coatings can be removed is reflected in the electrochemical testing in Chapter 6 which revealed these coatings to be the least protective of the coatings considered.

PrTES:TEOS and PhTES:TEOS coatings actually require more strokes to remove coating using NaOH as the organic-precursor concentration is increased, for example, PhTES:TEOS 20:80 mol% requires 50 strokes using 100% NaOH and 80:20 mol% requires 800 strokes. The trend is clearly exhibited in PhTES:TEOS coatings for which an increase in organic precursor concentration would lead to an ease in removal of coating using IPA and an ease of removal with NaOH with a decrease in organic precursor concentration; such a trend was initially anticipated from such testing. However, such opposing trends were not followed by all precursors due to poor adhesion and tackiness of coatings at higher organic precursor concentration namely for OTES and HTES-based coatings which leads to the dislodging of the coating with any cleaning solution as described in previous paragraph. Oddly, MTES-based coatings appear to behave similarly to OTES and HTES coatings rather than PrTES and PhTES coatings where an increase in organics leads to the decrease in strokes using not only IPA but NaOH as well, which is difficult to explain.

Coatings that have mid-way XTES concentrations are expected to require least effort to be removed using a mixture of IPA and NaOH solutions. The most protective coatings obtained for the five precursors investigated in Chapter 6 are not easily removed and can be exemplified through **Table 11.1** where PhTES:TEOS 40:60 mol% is removed using a minimum of 100 strokes whereas PhTES:TEOS 60:40 mol% requires 50 strokes (taken from Figure 5.100). Table 11.1 lists the solution that requires the least strokes to remove these five protective coatings which shows that HTES and

PhTES coatings are the coatings requiring the least effort to remove whereas OTES and MTES required more strokes to be removed completely.

Table 11.1: List of mixtures of NaOH and IPA (N/I v/v) that lead to the quickest removal (least strokes) of most protective coatings.

Coating identity	Solution (relative % v/v NaOH/IPA)	No. of strokes
60:40 mol% MTES:TEOS	50:50%, 75:25%	200
50:50 mol% PrTES:TEOS	0:100%	150
30:70 mol% HTES:TEOS	25:75%, 50:50%, 75:25%	100
20:80 mol% OTES:TEOS	25:75% , 50:50%, 75:25%, 100:0%	200
40:60 mol% PhTES:TEOS	50:50%, 75:25%	100

All coatings listed in Table 11.1, with the exception of PrTES:TEOS 50:50 mol%, require a mixture of NaOH and IPA to be removed with the least effort. These coatings have proven to be the most corrosion resistant and it is due to both hydrophobicity obtained through sufficient concentration of organic groups (percentage organic content) and adhesion originating from sufficient Si-O-M bond formation. Thus, it follows that the removal of these coatings would be done most efficiently using a solution that can break Si-O-M bonds (NaOH) whilst destabilising the coating by dissolving organic groups (IPA). For when the same effort is required to remove a coating, e.g. 20:80 mol% OTES:TEOS removed equally well using 100% NaOH solution or 25:75% NaOH:IPA solution (Table 11.1), the author recommends the use of 25:75% N/I solution to remove the coating since it contains far less alkaline solution and more IPA solvent making it a safer cleaning agent. As shown in Table 11.1 which features the most protective OIH alkoxysilane coatings, none of the coatings require 100% NaOH solution to be removed.

Removal of coatings through immersion has advantages over manual cleaning since conservators would simply allow artefacts to soak in pH 13/14 NaOH solution for some time. However, this may not always be feasible since object may be too large/ bulky for immersion. Leather is sometimes present in HM artefacts which, if immersed in pH >10, will cause the leather to harden, darken, and weaken its structure[279]. Therefore, in such cases the manual cleaning should be implemented.

11.3 Further work

Reversibility is perhaps the most difficult aspect of OIH alkoxy silane coatings for their intended application since the most protective coatings are not as easily removed as acrylate coatings are using acetone solvent. Preliminary studies were conducted using 2.5% B-72 which was applied as a base coat followed by the application of 2.5% SiO₂ MTES:TEOS 60:40 mol% top coat. The coupon was not cured but allowed to dry overnight prior to testing since acrylate coatings form extensive cracks when cured above their GTT. Electrochemical testing revealed no difference between a coupon that has been coated with two coats of MTES:TEOS (no cure) compared to that having a top coat of MTES and a base coat of B-72. However, a crucial difference between two such coated coupons is that the one having a base coat of acrylate can easily be removed using acetone. Although MTES:TEOS coatings perform similarly to B-72 coatings as determined in Chapter 10, it is worth investigating methods of improving on such a concept where protective properties of OIH alkoxy silanes can be maintained whilst having the ability to remove them as easily as acrylate coatings using acetone as the cleaning fluid.

CHAPTER 12:

Conclusion

12.1 Effect of alkyl/aryl functional groups on anti-corrosion properties of OIH alkoxy silane coatings

Investigations into OIH alkoxy silane coatings for corrosion protection of iron was initiated following the established method for sol development and coating deposition optimisation. Alkyl/aryl precursors featured in various mol% ratios with TEOS namely: MTES, PrTES, HTES, OTES and PhTES, were characterised for their mechanical properties and their extent of corrosion protection was studied using electrochemical testing. Particle size measurements on sols showed that all coatings are based on nanoparticles in the size range 1-3 nm. The thicknesses of the deposited coatings were measured to be 0.5-1.1 μm which shows that double coatings are thinly applied through dip-coating at the chosen silica concentration of 2.5%. The presence of organic alkyl/aryl groups in the coatings originating from XTES precursor was confirmed by infrared spectroscopy whereas UV-vis spectroscopy confirmed the coating's transparency. An increase in the size and concentration of the organic alkyl group generally led to the increase in hydrophobicity of the coating.

Electrochemical corrosion tests showed that coatings involving mixtures of X-Si(OR)_3 : TEOS displayed similar *U*-shaped trends in their corrosion behaviour as seen through the corrosion current density and charge transfer resistance profiles. Corrosion resistance was found to be optimal for the

following XTES:TEOS ratios: 60:40 mol% for MTES:TEOS coatings, 50:50 mol% PrTES:TEOS, 40:60 mol% PhTES:TEOS, 30:70 mol% HTES:TEOS and 20:80 mol% for OTES:TEOS coatings. The longer the alkyl chain length, the less hybrid precursor was required to obtain the most protective coating. From these, the most protective was determined to be 20:80 mol% OTES:TEOS, whereas 30:70 mol% HTES:TEOS was the least protective.

The coating's mechanical properties obtained through IR analysis, Nano-scratch, Nano-indentation and pull-out testing, show how an increase in silica content of a coating leads to harder, more well-adhered coatings. However, if the silica content is too high then coatings will tend to be more brittle which in turn leads to less protective coatings as revealed through electrochemical testing. On the other hand, if the coatings contain a large portion of organics, then coatings will be softer, verging on tacky and show poor adhesion, even though hydrophobicity is improved. Therefore, a protective coating is achieved when it possesses sufficient silica for strength and adhesion together with an appropriate organic content to form water-repellent and flexible coatings.

12.2 Application of OIH alkoxy silane coatings onto corroded surfaces

OTES;TEOS 20:80 mol% and MTES:TEOS 60:40 mol% coatings were chosen to represent results obtained on clean surfaces as the most and least protective coatings respectively. These coatings are able to offer significant corrosion protection when applied onto corroded surfaces especially when the silica concentration was increased. An increase in silica concentration lead to the formation of thicker coatings that are less cracked due to a more even deposition over the rough surface. The alkoxy silane coatings appear to have adhered well onto the oxide layer, however, crack formation has been proven to be inevitable and problematic which was partially resolved though the increase in XTES:TEOS ratio. It has also been established that OTES coatings are more protective than MTES coatings even when applied on corroded surfaces for which OTES:TEOS 40:60 mol% having a 10% SiO₂ concentration were the most protective coatings produced.

The effect of surface morphology on the coating's performance on polished and corroded surface can be compared: 2.5% SiO₂ OTES:TEOS 20:80 mol% provides a 2.5 orders of magnitude improvement over bare metal whereas a one order of magnitude improvement over bare metal was attained for corroded surfaces. This concept can be applied onto surfaces that contain both uncorroded and corroded areas, thus the extent of corrosion protection will fall somewhere in between the one to 2.5 orders of magnitude in improvement, depending on the extent of oxide area coverage.

12.3 Addition of inhibitors to OIH alkoxy silane coatings

12.3.1 Silica nanoparticles

The scope of incorporating nanoparticles was to further improve upon the corrosion protection offered by OIH alkoxy silane coatings. The addition of 100 ppm CNPs to MTES:TEOS 60:40 mol% sols lead to an improvement in corrosion protection of clean iron surface, even though defects created due to larger particles were evident. Improved control over the size of incorporated particles was achieved through the production and addition of SNPs to OIH alkoxy silane coatings, however, corrosion protection was not enhanced. CNPs and SNPs were also applied onto corroded surfaces and examined similarly. Less protective coatings were obtained relative to the blank MTES coating when 100 ppm CNPs were applied onto corroded surfaces as it has been speculated that the presence of microparticles promotes the propagation of cracks, which were ample. SNPs did bring about a slight improvement R_t values which was visually appreciated through the less cracked surfaces compared to the blank MTES coatings. This observation has been attributed to the difference in particle sizes (3 nm MTES vs. 26 nm SNP) which leads to deposition of larger particles that are more capable of blocking crevices and filling empty pockets created through the corrosion process than the smaller MTES-based nanoparticles.

12.3.2 Organic and inorganic inhibitor molecules

Several in/organic molecules were incorporated with MTES:TEOS 60:40 mol% and OTES:TEOS 20:80 mol% coatings; namely, cerium (III) nitrate hexahydrate (Ce), 1-naphthol (1-N), 1,4-naphthoquinone (1,4-N), phenylbenzoate (PhB), pyrrolidine (Pyr) and 2-hydroxypyridine (2-H). An improvement in corrosion protection was achieved successfully for the most part with MTES coatings in which all six inhibitors produced a desired improvement over the blank coating at some inhibitor concentration. This was unfortunately not the case with OTES coatings for which only pyrrolidine inhibitor molecules produced an improvement over the blank coating. This has been attributed to the differences in size and nature of the nanoparticles for OTES:TEOS 20:80 mol% and MTES:TEOS 60:40 mol%. OTES form more protective coatings than MTES due to the more compact and hydrophobic coatings formed. The introduction of inhibitors into the silica matrix does very little and even brings about a decay in the coating's protective properties, improvement only being seen with the presence of the smallest and least interfering organic molecule pyrrolidine.

MTES coatings, on the other hand, behaved more protectively with the inclusion of inhibitor molecules both through low concentrations of soluble inhibitors and high concentrations of insoluble inhibitors. Soluble molecules brought about inhibition at a low concentration (0.001 M or less), whereas a high concentration (0.01M) leads to the infiltration of water through pores present/forming together with the interference of such molecules with the matrix formation during coating deposition. Although the water influx issue is avoided with the water insoluble organic molecules at high inhibitor concentrations, these molecules are likely to still interfere with the silica matrix formation at the deposition stage. The extent of these effects cannot be evaluated; however, it can be said that an overall improvement was still obtained thus any matrix interference effect is not significant enough to outweigh the inhibiting effect of the molecules.

The effect of inhibitor on corroded iron surfaces was also considered in this work, though no improvements were witnessed when using Ce-doped MTES coatings onto corroded surfaces, where it is clear that the coating becomes increasingly less protective as the inhibitor concentration is increased. Low Ce concentrations did not bring about an improvement as achieved on clean metal since corrosion processes are far too developed at that stage for cerium ions to alter these processes in a significant manner. At high concentrations, less protective coatings are produced due to the interference of cerium ions with the coating's integrity.

It can be concluded that the addition of inhibitor molecules does not guarantee an improvement in corrosion protection as was initially expected. An inhibitor will not necessarily result in a more protective coating since a coating may already be at or close to its optimum as is the case for OTES coatings to which additives can have interfering effects. Even with less protective coatings (MTES), improvement is attainable but is greatly influenced by the solubility of inhibitor, its concentration and the size of the inhibitor for which it is clear that a larger more delocalised system (ex. 1,4-naphthoquinone) will not necessarily translate into more protection since it may be interfering with the silica matrix formation to a greater extent than a smaller pyrrolidine molecule.

12.4 Comparative study of OIH alkoxy silane coatings with acrylate/nitrocellulose lacquers

Electrochemical testing carried out on clean metal coupons that have been dip-coated with silica, Paraloid and Ercalene lacquers revealed OIH alkoxy silane coatings to be more protective than the lacquers. This was not the case on corroded surfaces where OIH alkoxy silane coating were found to be less protective than the lacquers which has been attributed to the thickness of coatings. Accelerated corrosion testing was also carried out for which the first set of salt spray testing was carried out on OIH alkoxy silane coated coupons that have been applied through dip-coating, fine brush, coarse brush and sponge application. Coupons that have been coated using coarse brush or sponge corroded at a

visibly faster rate than fine brush or dip-coated coupons, thus eliminating sponge and coarse-brush application as suitable modes of application of OIH alkoxy silane coatings.

A second set of accelerated corrosion testing featured Paraloid and Ecalene lacquers applied using dip-coater and fine brush which were compared to alkoxy silane coated coupons. Dip-coating was deemed as producing more protective coatings compared to fine-brush application of OIH alkoxy silane sols, and especially for Paraloid or Ecalene lacquers. Protective coatings were obtained using both dip and fine brush applications for OIH alkoxy silane coatings relative to lacquers and can be attributed to the better adhesion of these coatings brought about through strong M-O-Si chemical bonding.

OTES:TEOS 20:80 mol% coatings which have been proven to be the most protective through electrochemical testing at lower SiO₂ concentrations (2.5% SiO₂), have also been determined to be the most protective of the OIH alkoxy silane coatings through salt-spray testing when applied using both dip- and fine brush-application at a 10% SiO₂ concentration. Accelerated corrosion testing also revealed OTES coatings to be significantly more protective than lacquers through brush application, which means that OIH alkoxy silane coatings retain their protective properties even when applied using a fine brush. Brushing as a suitable mode of application of OIH alkoxy silane coatings is a crucial finding since it is the typical application of lacquers employed by conservator-restorers.

12.5 Reversibility of OIH alkoxy silane coatings

Immersion testing revealed that all alkoxy silane coatings under study were removed within an hour of immersion using pH 14 NaOH solution. Coatings containing a higher organic content required short immersion times and could be removed using IPA solvent instead of NaOH solution. On the other hand, coatings having a low organic content could not be easily removed using IPA but required the application of NaOH solution. Medium ranges of XTES:TEOS mol% ratios took significantly more time to be removed in pH 12, 13 NaOH and IPA since coatings are well-adhered (SiO₂ network) and possess sufficient organic groups that brings about the formation of protective coatings. Mechanical

cleaning of coatings revealed similar conclusions to immersion testing; however, additional details have emerged from this testing. Most coatings can be removed with relative ease using a mixture of NaOH and IPA thus creating a cleaning solution that is safer to use compared to pure pH 14 NaOH solution, which is caustic. However, the most protective coating from each X-TES:TEOS group of coatings (MTES:TEOS 60:40 mol%, PrTES:TEOS 50:50 mol%, HTES:TEOS 30:70 mol%, OTES:TEOS 20:80 mol%, PhTES:TEOS 40:60 mol%) are not as easily removed using any solution mixture, which is expected from such protective coatings.

12.6 General conclusion

The most protective OIH alkoxy silane coatings were found possess a balance of inorganic component, TEOS which provides strong adhesion and hard silicate network together with an organic component, XTES which contributes to flexibility and hydrophobicity of the coating. These coatings have been proven to be more protective compared to the more conventionally used lacquers on clean metal, less so on corroded surfaces, even though significant corrosion protection is still achieved on such surfaces. OIH alkoxy silane coatings are in compliance with CR guidelines for the protection of metal artefacts since they have proven to provide sufficient protection, are transparent, are applied at low curing temperatures and can be removed without imparting changes to the metal surface.

References:

1. Watkinson D (2010) Preservation of metallic cultural heritage, , vol 4. Shreir's Corrosion. Elsevier, London
2. Scott DA (1991) Metallography and Microstructure of Ancient and Historic Metals The J. Paul Getty Trust Singapore
3. D. Wang, Bierwagen GP (2009) Sol–gel coatings on metals for corrosion protection. *Progress in Organic Coatings* 64:327-338
4. Jackson JE (2017) Cost of Corrosion Annually in the US Over \$1.1 Trillion in 2016. <http://www.g2mtlabs.com/corrosion/cost-of-corrosion/>.
5. Wang D, Bierwagen GP (2009) Sol-gel coatings on metals for corrosion protection. *Progress in Organic Coatings* 64 327-338
6. Wright JD, Sommerdijk NA (2001) *Sol-Gel Materials Chemistry and Applications*. CRC Press, United States of America
7. D. Teoli, L. Parisi, N. Realdon, N. Guglielmi, A. Rosato, Morpurgo M (2006) Wet sol-gel derived silica for controlled release of proteins. *Journal of Control Release* 116:295-303
8. U. Tiringer, I. Milošev, A. Durán, Castro Y (2018) Hybrid sol–gel coatings based on GPTMS/TEOS containing colloidal SiO₂ and cerium nitrate for increasing corrosion protection of aluminium alloy 7075-T6. *Journal of Sol-Gel Science and Technology* 85:546–557
9. S. Tabesh, F. Davar, M. Rez, Estarki L (2018) Preparation of γ -Al₂O₃ nanoparticles using modified sol-gel method and its use for the adsorption of lead and cadmium ions. *Journal of Alloys and Compounds* 730:441-449
10. H. Rashidi Nodeha, W. Ibrahim, M. Kamboh, Sanagi M (2017) New magnetic graphene-based inorganic–organic sol-gel hybrid nanocomposite for simultaneous analysis of polar and non-polar organophosphorus pesticides from water samples using solid-phase extraction. *Chemosphere* 166:21-30
11. M. Catauro, F. Bollino, F. Papale, M. Gallicchio, Pacifico S (2015) Influence of the polymer amount on bioactivity and biocompatibility of SiO₂/PEG hybrid materials synthesized by sol–gel technique. *Materials Science and Engineering: C* 48:548-555
12. R. Lorenzi, A. Paleari, Golubev N (2015) Non-aqueous sol–gel synthesis of hybrid rare-earth-doped γ -Ga₂O₃ nanoparticles with multiple organic–inorganic-ionic light-emission features. *Journal of Materials Chemistry: C* 3:41-45
13. M. Pilz, Römich H (1997) Sol-gel derived coating for outdoor bronze conservation. *Journal of Sol-Gel Science and Technology* 8:1071-1075
14. Maleki H (2016) Recent advances in aerogels for environmental remediation applications: A review. *Chemical Engineering Journal* 300:98-118
15. Pagliaro M (2009) *Silica-Based Materials for Advanced Chemical Applications*. RSC Publishing, United Kingdom
16. Guglielmi M (1997) Sol-Gel Coatings on Metals. *Journal of Sol-Gel Science and Technology* 8:443–449
17. D. Balgude, Sabnis A (2012) Sol–gel derived hybrid coatings as an environment friendly surface treatment for corrosion protection of metals and their alloys. *Journal of Sol-Gel Science & Technology* 64:124–134
18. R. Ciriminna, A. Fidalgo, V. Pandarus, F. Béland, L. M. Ilharco, Pagliaro M (2013) The Sol–Gel Route to Advanced Silica-Based Materials and Recent applications. *Chemical Review* 113 6592–6620
19. A. Durán, Y. Castro, M. Aparicio, A. Conde, Damborenea JJd (2007) Protection and surface modification of metals with sol–gel coatings. *International Materials Reviews* 52 175-192
20. Figueira RB, Silva CJ, Pereira EV (2015) Organic–inorganic hybrid sol–gel coatings for metal corrosion protection: a review of recent progress. *Journal of Coatings Technology and Research* 12:1–35

21. T. L. Metroke, R. L. Parkhill, Knobbe ET (2001) Passivation of metal alloys using sol–gel-derived materials — a review. *Progress in Organic Coatings* 41:233-238
22. A. M. Mohamed, A. M. Abdullah, Younana NA (2015) Corrosion behavior of superhydrophobic surfaces: A review. *Arabian Journal of Chemistry* 8:749-765
23. Montemor MF (2014) Functional and smart coatings for corrosion protection: A review of recent advances. *Surface and Coatings Technology* 258:17-37
24. M. L. Zheludkevich, I. Miranda Salvado, Ferreira MG (2005) Sol–gel coatings for corrosion protection of metals. *Journal of Materials Chemistry* 15:5099-5111
25. S. X. Zheng, Li JH (2010) Inorganic–organic sol gel hybrid coatings for corrosion protection of metals. *Journal of Sol-Gel Science and Technology* 54:174–187
26. Sinapi F, Forget L, Delhalle J, Mekhalif Z (2003) Self-assembly of (3-mercaptopropyl) trimethoxysilane on polycrystalline zinc substrates towards corrosion protection. *Applied Surface Science* 212–213:464–471
27. Li Y, Lu W, Wang Y, Tran T (2009) Studies of (3-mercaptopropyl) trimethoxysilane and bis(trimethoxysilyl)ethane sol–gel coating on copper and aluminium. *SpectrochimicaActa Part A: Molecular and Biomolecular Spectroscopy* 73:922–928
28. Chou TP, Chandrasekaran C, Limmer S, Nguyen C, Cao GZ (2002) Organic-inorganic sol-gel coating for corrosion protection of stainless steel. *Journal of Materials Science Letters* 21:251–255
29. Liu Y, Sun D, You H, Chung JS (2005) Corrosion resistance properties of organic–inorganic hybrid coatings on 2024 aluminum alloy. *Applied Surface Science* 246 82–89
30. B. Mahltig, H. Haufe, Bottcher H (2005) Functionalisation of textiles by inorganic sol–gel coatings. *Journal of Materials Chemistry* 15:4385–4398
31. Shen GX, Chen YC, Lin CJ (2005) Corrosion protection of 316 L stainless steel by a TiO₂ nanoparticle coating prepared by sol–gel method. *Thin Solid Films* 489:130–136
32. L. Bamoulid, M. T. Maurette, D. De Caro, A. Guenbour, A. B. Bachir LA, S. El Hajjaji, F. Benoît-Marquié, Ansart F (2008) An efficient protection of stainless steel against corrosion: Combination of a conversion layer and titanium dioxide deposit. *Surface and Coatings Technology* 202:5020-5026
33. A. Shanaghi, A. R. Sabour , T. Shahrabi, Aliofkhaeze M (2009) Corrosion protection of mild steel by applying TiO₂ nanoparticle coating via sol-gel method. *Protection of Metals and Physical Chemistry of Surfaces* 45:305-311
34. S. T. Döşlü, B. D. Mert, B.Yazıcı (2013) Polyindole top coat on TiO₂ sol–gel films for corrosion protection of steel. *Corrosion Science* 66:51–58
35. Atik M, Neto P, Avaca LA, Aegerter MA (1995) Sol-gel thin films for corrosion protection. *Ceramics International* 21:403-406
36. F. L. Perdomo, P. De Lima-Neto, M. A. Aegerter, Avaca LA (1999) Sol-Gel Deposition of ZrO₂ Films in Air and in Oxygen-Free Atmospheres for Chemical Protection of 304 Stainless Steel: A Comparative Corrosion Study. *Journal of Sol-Gel Science and Technology* 15:87–91
37. L. Fedrizzi, F. J. Rodriguez, S. Rossi, F. Deflorian, Maggio RD (2001) The use of electrochemical techniques to study the corrosion behaviour of organic coatings on steel pretreated with sol–gel zirconia films. *Electrochimica Acta* 46:3715-3724
38. H. Li, K. Liang, L. Mei, S. Gu, Wang S (2001) Corrosion protection of mild steel by zirconia sol-gel coatings. *Journal of Materials Science Letters* 20:1081-1083
39. A. Nazeri, P. P. Trzaskoma-Paulette, Bauer D (1997) Synthesis and Properties of Cerium and Titanium Oxide Thin Coatings for Corrosion Protection of 304 Stainless Steel. *Journal of Sol-Gel Science and Technology* 10:317–331
40. G. R. Salazar-Banda, S. R. Moraes, A. J. Motheo, Machado SA (2009) Anticorrosive cerium-based coatings prepared by the sol–gel method. *Journal of Sol-Gel Science and Technology* 52:415-423

41. S. Acosta, R. J. Corriu, D. Leclercq, P. Lefèvre, P. H. Mutin, Vioux A (1994) Preparation of alumina gels by a non-hydrolytic sol-gel processing method. *Journal of Non-Crystalline Solids* 170 234-242
42. J. Masalski, J. Gluszek, J. Zabrzewski, K. Nitsch, Gluszka P (1999) Improvement in corrosion resistance of the 316l stainless steel by means of Al₂O₃ coatings deposited by the sol-gel method. *Thin Solid Films* 349:186-190
43. V. Palanivel, D. Zhu, Ooij WJv (2003) Nanoparticle-filled silane films as chromate replacements for aluminum alloys *Progress in Organic Coatings* 47:384–392
44. G. J. Owens, R. K. Singh, F. Foroutan, Alqaysi M (2016) Sol-gel based materials for biomedical applications. *Progress in Materials Science* 77:1-79
45. Veerarahavan B, Haran B, Slavkov D, Prabhu S, Popov B, Heimann B (2006) Development of an Electroless Method to Deposit Corrosion-Resistant Silicate Layers on Metallic Substrates. *Journal of Electrochemical and Solid-State Letters* 153:253-259
46. Parkhill RL, Knobbe ET, Donley MS (2001) Application and evaluation of environmentally compliant spray-coated ormosil films as corrosion resistant treatments for aluminum 2024-T3. *Progress in Organic Coatings* 41:261–265
47. Ramezani M, Vaezi MR, Kazemzadeh A (2014) Preparation of silane-functionalized silica films via two-step dip coating sol-gel and evaluation of their superhydrophobic properties. *Applied Surface Science* 317:147-153
48. Norouzi M, Garekani AA (2014) Corrosion protection by zirconia-based thin films deposited by a sol-gel spin coating method. *Ceramics International* 40: 2857–2861
49. Brinker C, Scherer G (1990) *Sol-Gel Science: The Physics and Chemistry of Sol-Gel Processing*. Academic Press, United States of America
50. Sakka S (1989) Formation of Particles in Sol-Gel Process. *KONA Powder and Particle Journal* 7:106-118
51. Ono S, Tsuge H, Nishi Y, Hirano S (2004) Improvement of Corrosion Resistance of Metals by an Environmentally Friendly Silica Coating Method. *Journal of Sol-Gel Science and Technology* 29:147–153
52. Seok SL, Kim JH, Choi KH, Hwang YY (2006) Preparation of corrosion protective coatings on galvanized iron from aqueous inorganic-organic hybrid sols by sol-gel method. *Surface & Coatings Technology* 200:3468-3472
53. Vella D (2013) Inorganic and hybrid transparent protective coatings for clean and corroded steel surfaces: A conservation approach alignment. *Univeristy of Malta, Malta*
54. Metroke TL, Gandhi JS, Apblett A (2004) Corrosion resistance properties of Ormosil coatings on 2024-T3 aluminum alloy. *Progress in Organic Coatings* 50:231–246
55. Ni L, Moreau N, Chemtob A, Croutxe-Barghorn C (2012) Organic-inorganic tandem route to polymer nanocomposites: kinetic products versus thermodynamic products. *Journal of Sol-Gel Science and Technology* 64:500-509
56. Kumar N, Jyothirmayi A, Raju KRS, Subasri R (2012) Effect Of Functional Groups (Methyl, Phenyl) on Organic- Inorganic Hybrid Sol-Gel Silica Coatings on Surface Modified SS 316. *Ceramics International* 38:6565–6572
57. Sheffer M, Groysman A, Mandler D (2003) Electrodeposition of sol-gel films on Al for corrosion protection. *Corrosion Science* 45:2893–2904
58. Seifzadeh D, Golmoghani-Ebrahimi E (2012) Formation of novel and crack free nanocomposites based on sol gel process for corrosion protection of copper. *Surface and Coatings Technology* 210:103–112
59. Jothi KJ, Palanivelu K (2013) Synergistic effect of silane modified nanocomposites for active corrosion protection. *Ceramics International* 39:7619–7625

60. Hollamby MJ, Fix D, Dönch I, Borisova D, Möhwald H, Shchukin D (2011) Hybrid Polyester Coating Incorporating Functionalized Mesoporous Carriers for the Holistic Protection of Steel Surfaces. *Advanced materials* 23:1361–1365
61. Ni L, Chemtob A, Croutxé-Barghorn C, Moreau N, Boudier T, Chanfreau S, Pébère N (2014) Direct-to-metal UV-cured hybrid coating for the corrosion protection of aircraft aluminium alloy. *Corrosion Science* 89:242–249
62. Calabrese L, Bonaccorsi L, Caprì A, Proverbio E (2014) Effect of silane matrix on corrosion protection of zeolite based composite coatings. *La Metallurgia Italiana*
63. X. Pan, J. Wu, Y. Ge, K. Xiao, H. Luo, S. Gao, Li X (2014) Preparation and characterization of anticorrosion Ormosil sol–gel coatings for aluminum alloy. *Journal of Sol-Gel Science & Technology* 72:8–20
64. Subasri R, Malathi R, Jyothirmayi A, Hebalkar NY (2012) Synthesis and Characterization of CuO-Hybrid Silica Nanocomposite Coatings on SS 304. *Ceramics International* 38:5731–5740
65. T. P. Chou, C. Chandrasekaran, S. J. Limmer, S. Seraji, Y. Wu, M. J. Forbess, C. Nguyen, Cao GZ (2001) Organic–inorganic hybrid coatings for corrosion protection. *Journal of Non-Crystalline Solids* 290:153–162
66. Chou TP, Chandrasekaran C, Cao GZ (2003) Sol-Gel-Derived Hybrid Coatings for Corrosion Protection. *Journal of Sol-Gel Science and Technology* 26:321–327
67. Gallardo J, Durán A, Damborenea JJ (2004) Electrochemical and in vitro behaviour of sol–gel coated 316L stainless steel. *Corrosion Science* 46 795–806
68. Castro Y, Ferrari B, Moreno R, Durán A (2005) Corrosion behaviour of silica hybrid coatings produced from basic catalysed particulate sols by dipping and EPD. *Surface and Coatings Technology* 191:228–235
69. Pepe A, Galliano P, Cere S, Aparicio M, Duran A (2005) Hybrid Silica Sol–Gel Coatings on Austempered Ductile Iron (ADI). *Materials Letters* 59:2219–2222
70. L. Mascia, L. Prezzi, G. D. Wilcox, Lavorgna M (2006) Molybdate Doping of Networks in Epoxy–Silica Hybrids: Domain Structuring and Corrosion Inhibition. *Progress in Organic Coatings* 56:13–22
71. L. Jianguo, G. Gaoping, Chuanwei Y (2006) Enhancement of the Erosion–Corrosion Resistance of Dacromet with Hybrid SiO₂ Sol–Gel. *Surface & Coatings Technology* 200:4967–4975
72. Pepe A, Galliano P, Aparicio M, Duran A, Cere S (2006) Sol–Gel Coatings on Carbon Steel: Electrochemical Evaluation. *Surface & Coatings Technology* 200 3486–3491
73. W. Xing, B. You, Wu L (2008) Chemical and Anticorrosion Characterization of Polysilsesquioxane Coatings Catalyzed by Different Acids. *Journal of Coatings Technology and Research* 5:65–72
74. Phanasgaonkar A, Raja VS (2009) Influence of Curing Temperature, Silica Nanoparticles and Cerium on Surface Morphology and Corrosion Behaviour of Hybrid Silane Coatings on Mild Steel. *Surface and Coatings technology* 203:2260–2271
75. M. A. Espinosa-Medina, G. Carbajal-De la Torre, Liu HB (2009) Study of Ceramic and Hybrid Coatings Produced by the Sol–Gel Method for Corrosion Protection. *The Open Corrosion Journal* 2:197–203
76. Sarmiento VH, Schiavetto MG, Hammer P, Benedetti AV, Fugivara CS, Suegama PH, Pulcinelli SH, Santilli CV (2010) Corrosion Protection of Stainless Steel by Polysiloxane Hybrid Coatings Prepared Using the Sol–Gel Process. *Surface and Coatings Technology* 204:2689–2701
77. S. M. Hosseinalipour, A. Ershad-langroudi, A. N. Hayati, Nabizade-Haghighi AM (2010) Characterization of Sol-Gel Coated 316L Stainless Steel for Biomedical Applications. *Progress in Organic Coatings* 67:371–374
78. P. Hammer, M. G. Schiavetto, F. C. dos Santos, A. V. Benedetti, S. H. Pulcinelli, Santilli CV (2010) Improvement of the corrosion resistance of polysiloxane hybrid coatings by cerium doping. *Journal of Non-Crystalline Solids* 356:2606–2612
79. P. H. Suegama, V. H. Sarmiento, M. F. Montemor, A. V. Benedetti, H. G. de Melo, I. V. Aoki, Santilli CV (2010) Effect of Cerium(IV) Ions on the Anticorrosion Properties of Siloxane-Poly(methyl methacrylate) Based Film Applied on tin Coated Steel. *Electrochimica Acta* 55:5100–5109

80. P. Kiruthika, R. Subasri, A. Jyothirmayi, K. Sarvani, Hebalkar NY (2010) Effect of Plasma Surface Treatment on Mechanical and Corrosion Protection Properties of UV-Curable Sol–Gel Based GPTS-ZrO₂ Coatings on Mild Steel. *Surface & Coatings Technology* 204:1270–1276
81. A. G. Kannan, N. R. Choudhury, Dutta NK (2010) Electrochemical Performance of Sol–Gel Derived Phospho-silicate–Methacrylate Hybrid Coatings. *Journal of Electroanalytical Chemistry* 641:28–34
82. M. Hernández-Escolano, M. Juan-Díaz, M. Martínez-Ibáñez, A. Jimenez-Morales, I. Goñi, M. Gurruchaga, Suay J (2010) The Design and Characterisation of Sol–Gel Coatings for the Controlled-Release of Active Molecules. *Journal of Sol-Gel Science and Technology* 64:442–451
83. S. Ahmad, F. Zafar, E. Sharmin, N. Garg, Kashif M (2012) Synthesis and Characterization of Corrosion Protective Polyurethanefattyamide/Silica Hybrid Coating Material. *Progress in Organic Coatings* 73:112–117
84. H. Kim, Hwang T (2012) Corrosion Protection Enhancement Effect by Mixed Silica Nanoparticles of Different Sizes Incorporated in a Sol–Gel Silica Film. *Journal of Sol-Gel Science & Technology* 63:563–568
85. J. B. Cambon, F. Ansart, J. P. Bonino, Turq V (2012) Effect of Cerium Concentration on Corrosion Resistance and Polymerization of Hybrid Sol–Gel Coating on Martensitic Stainless Steel. *Progress in Organic Coatings* 75:486–493
86. K. Joncoux-Chabrol, J. P. Bonino, M. Gressier, M. J. Menu, Pebere N (2012) Improvement of Barrier Properties of a Hybrid Sol–Gel Coating by Incorporation of Synthetic Talc-Like Phyllosilicates for Corrosion Protection of a Carbon Steel. *Surface & Coatings Technology* 206 2884–2891
87. R. T. Sakai, F. M. da Cruz, H. G. de Melo, A. V. Benedetti, C. V. Santilli, Suegama PH (2012) Electrochemical study of TEOS, TEOS/MPTS, MPTS/MMA and TEOS/MPTS/MMA films on tin coated steel in 3.5% NaCl solution. *Progress in Organic Coatings* 74:288-301
88. Zandi-Zand R, Verbeken K, Adriaens A (2012) Corrosion resistance performance of cerium doped silica sol-gel coatings on 304L stainless steel. *Progress in Organic Coatings* 75:463–473
89. D. del Angel-López, M. A. Domínguez-Crespo, A. M. Torres-Huerta, A. Flores-Vela, J. Andraca-Adame, Dorantes-Rosales H (2013) Analysis of Degradation Process During the Incorporation of ZrO₂:SiO₂ Ceramic Nanostructures into Polyurethane Coatings for the Corrosion Protection of Carbon Steel. *Journal of Materials Science Letters* 48:1067–1084
90. E. Certhoux, F. Ansart, V. Turq, J. P. Bonino, J. M. Sobrino, J. Garcia, Reby J (2013) New sol-gel formulations to increase the barrier effect of a protective coating against the corrosion of steels. *Progress in Organic Coatings* 76:165-172
91. S. Peng, W. Zhao, Z. Zeng, H. Li, Q. Xue, Wu X (2013) Preparation of Anticorrosion Hybrid Silica Sol–Gel Coating Using Ce(NO₃)₃ As Catalyst. *Journal of Sol-Gel Science and Technology* 66:133–138
92. D. Balgude, K. Konge, Sabnis A (2014) Synthesis and Characterization of Sol–Gel Derived CNSL Based Hybrid Anti-corrosive Coatings. *Journal of Sol-Gel Science & Technology* 69:155–165
93. Santana I, Pepe A, Jimenez-Pique E, Pellice S, Ceré S (2013) Silica-Based Hybrid Coatings for Corrosion Protection of Carbon Steel. Part I: Effect of Pretreatment with Phosphoric Acid. *Surface and Coatings Technology* 236:476-484
94. M. Hernandez, A. Barba, J. Genesca, A. Covelo, E. Bucio, Torres V (2013) Characterization of Hybrid Sol-Gel Coatings Doped with Hydrotalcite-like Compounds on Steel and Stainless Steel Alloys. *ECS- The Electrochemical Society* 47:195-206
95. B. Ramezanzadeh, M. Akbariana, M. Ramezanzadeh, Mahdavian M (2017) Corrosion Protection of Steel with Zinc Phosphate Conversion Coating and Post-Treatment by Hybrid Organic-Inorganic Sol-Gel Based Silane Film. *Journal of The Electrochemical Society* 164 224-230
96. H. Sayilkan, S. Sener, Sener E (2003) The Sol–Gel Synthesis and Application of Some Anticorrosive Coating Materials. *Journal of Materials Science* 39:106–110
97. C. Arunchandran, S. Ramya, R. P. George, Mudali UK (2012) Self-Healing Corrosion Resistive Coatings Based on Inhibitor Loaded TiO₂ Nanocontainers. *Journal of the Electrochemical Society* 159:552–559

98. S. Rahoui, V. Turq, Bonino JP (2013) Effect of Thermal Treatment on Mechanical and Tribological Properties of hybrid Coatings Deposited by Sol–Gel Route on Stainless Steel. *Surface & Coatings Technology* 235:15–23
99. M. Fedel, E. Callone, S. Diré, F. Deflorian, M. G. Olivier, Poelman M (2014) Effect of Na-Montmorillonite sonication on the protective properties of hybrid silica coatings. *Electrochimica Acta* 124:90-99
100. K. JeevaJothi, Palanivelu K (2013) Synergistic Effect of Silane Modified Nanocomposites for Active Corrosion Protection. *Ceramics International* 39:7619–7625
101. P. Hammer, F. C. dos Santos, B. M. Cerrutti, S. H. Pulcinelli, Santilli CV (2012) Highly Corrosion Resistant Siloxane–Polymethyl Methacrylate Hybrid Coatings. *Journal of Sol-Gel Science & Technology* 63:266–274
102. T. Gunji, Y. Iizuka, K. Arimitsu, Abe Y (2004) Preparation and Properties of Alkoxy(methyl)silsesquioxanes as Coating Agents. *Journal of Polymer Science Part A* 42:3676–3684
103. H. Wang, Akid R (2008) Encapsulated Cerium Nitrate Inhibitors to Provide High-Performance Anti-corrosion Sol–Gel Coatings on Mild Steel. *Corrosion Science* 50:1142–1148
104. G. Chawada, Dholakiya BZ (2015) Organic–Inorganic Hybrid Sol–Gel Pretreatments for Corrosion Protection of Mild Steel in Neutral and Acidic Solutions. *Research on Chemical Intermediates* 41:3659–3674
105. M. Aparicio, A. Jitianub, G. Rodriguez, A. Degnah, K. Al-Marzoki, J. Mosa, Klein LC (2016) Corrosion Protection of AISI 304 Stainless Steel with Melting Gel Coatings. *Electrochimica Acta* 202:325-332
106. D. A. López, N. C. Rosero-Navarro, J. Ballarre, A. Durán, M. Aparicio, Ceré S (2008) Multilayer silica-methacrylate hybrid coatings prepared by sol–gel on stainless steel 316L: Electrochemical evaluation. *Surface and Coatings Technology* 202:2194-2201
107. C. G. Dariva, Galio AF (2014) Corrosion Inhibitors – Principles, Mechanisms and Applications. InTech,
108. M. F. Montemor, A. M. Cabral, M. L. Zheludkevich, Ferreira MG (2006) The corrosion resistance of hot dip galvanized steel pretreated with Bis-functional silanes modified with microsilica. *Surface & Coatings Technology* 200:2875 – 2885
109. L. Liu, J. Hu, J. Zhang, Cao C (2006) Improving the formation and protective properties of silane films by the combined use of electrodeposition and nanoparticles incorporation. *Electrochimica Acta* 52:538-545
110. Suegama PH, Recco AA, Tschiptschin AP, Aoki IV (2007) Influence of silica nanoparticles added to an organosilane film on carbon steel electrochemical and tribological behaviour. *Progress in Organic Coatings* 60 90-98
111. I. Ab Rahman, Padavettan V (2010) Synthesis of Silica Nanoparticles by Sol-Gel: Size-Dependent Properties, Surface Modification, and Applications in Silica-Polymer Nanocomposites— A Review. *Journal of Nanomaterials* 8:1-15
112. Stober W, Fink A (1968) Controlled Growth of Monodisperse Silica Spheres in the Micron Size Range *Journal of Colloid and Interface Science* 26:62-69
113. Castro Y, Ferrari B, Moreno R, Duran A (2004) Coatings produced by electrophoretic deposition from nano-particulate silica sol–gel suspensions. *Surface and Coatings Technology* 182:199–203
114. G. H. Bogush, M. A. Tracy, Zukoski CF (1988) Preparation of Monodisperse Silica Particles: Control of Size and Fraction. *Journal of Non-Crystalline Solids* 104:95–106
115. Wang XD, Shen ZX, Sang T, Cheng XB, Li MF, Chen LY, Wang ZS (2010) Preparation of spherical silica particles by Stöber process with high concentration of tetra-ethyl-orthosilicate. *Journal of Colloid Interface Science* 341:23–29
116. Ibrahim IA, Zikry AA, Sharaf MA (2010) Preparation of spherical silica nanoparticles: Stober silica. *Journal of American Science* 6:985-989
117. N. Plumere, A. Ruff, B. Speiser, V. Feldmann, Mayer HA (2012) Stober Silica Particles as Basis for Redox Modifications: Particle Shape, Size, Polydispersity and Porosity. *Journal of Colloid and Interface Science* 368:208-219

118. R. Sato-Berru, J. M. Saniger, J. Flores-Flores, Sanchez-Espindola M (2013) Simple Method for the Controlled Growth of SiO₂ spheres. *Journal of Materials Science and Engineering* 3:237-242
119. Singh LP, Bhattacharyya SK, Mishra G, Ahalawat S (2011) Functional role of cationic surfactant to control the nano size of silica powder. *Applied Nanoscience* 1 117–122
120. K. A. Yasakau, M. L. Zheludkevich, O. V. Karavai, Ferreira MG (2008) Influence of Inhibitor Addition on the Corrosion Protection Performance of Sol–Gel Coatings on AA2024. *Progress in Organic Coatings* 63:352–361
121. B. E. Rani, Basu BB (2011) Green Inhibitors for Corrosion Protection of Metals and Alloys: An Overview. *International Journal of Corrosion* 2012:1-15
122. K. S. Bokati, C. Dehghanian, Yari S (2017) Corrosion inhibition of copper, mild steel and galvanically coupled copper-mild steel in artificial sea water in presence of 1H-benzotriazole, sodiummolybdate and sodium phosphate. *Corrosion Science* 126:272-285
123. K. A. Yasakau, M. L. Zheludkevich, S. V. Lamaka, Ferreira MG (2006) Mechanism of Corrosion Inhibition of AA2024 by Rare-Earth Compounds. *Journal of Physical Chemistry B* 110:5515-5528
124. M. F. Montemor, Ferreira MG (2007) Electrochemical study of modified bis-[triethoxysilylpropyl] tetrasulfide silane films applied on the AZ31 Mg alloy. *Electrochimica Acta* 52:7486-7495
125. S. Bernal, F. J. Botana, J. J. Calvino, M. Marcos, J. A. Pérez-Omil, H. Vidala (1995) Lanthanide salts as alternative corrosion inhibitors. *Journal of Alloys and Compounds* 225:638-641
126. R. G. Buchheit, H. Guan, S. Mahajanam, Wong F (2003) Active corrosion protection and corrosion sensing in chromate-free organic coatings. *Progress in Organic Coatings* 47:174-182
127. P. H. Suegama, H. G. de Melo, A. V. Benedetti, Aoki I (2009) Influence of cerium (IV) ions on the mechanism of organosilane polymerization and on the improvement of its barrier properties. *Electrochimica Acta* 54:2655-2662
128. J. B. Cambon, J. Esteban, F. Ansart, J. P. Bonino, V. Turq, S. H. Santagneli, C. V. Santilli, Pulcinelli SH (2012) Effect of cerium on structure modifications of a hybrid sol–gel coating, its mechanical properties and anti-corrosion behavior. *Materials Research Bulletin* 47:3170-3176
129. F. Deflorian, S. Rossi, M. Fedel, Motte C (2010) Electrochemical investigation of high-performance silane sol–gel films containing clay nanoparticles. *Progress in Organic Coatings* 69:158-166
130. M. E. Druart, I. Recloux, T. T. Thai, S. Ershov, R. Snyders, Olivier MG (2016) Impact of the addition of cerium salts (Ce(III) and Ce(IV)) on formation and ageing of a silica sol-gel layer. *Surface & Coatings Technology* 304:40–50
131. T. Lampke, S. Darwich, D. Nickel, Wielage B (2008) Development and characterization of sol-gelcomposite coatings on aluminum alloys for corrosion protection. *Materialwissenschaft und Werkstofftechnik* 39:914-919
132. N. C. Rosero-Navarro, S. A. Pellice, A. Durán, Aparicio M (2008) Effects of Ce-containing sol–gel coatings reinforced with SiO₂ nanoparticles on the protection of AA2024. *Corrosion Science* 50:1283-1291
133. M. L. Zheludkevich, R. Serra, M. F. Montemor, K. A. Yasakau, I. M. Miranda Salvado, Ferreira MG (2005) Nanostructured sol–gel coatings doped with cerium nitrate as pre-treatments for AA2024-T3 Corrosion protection performance. *Electrochimica Acta* 51:208–217
134. E. D. Mekeridis, I. A. Kartsonakis, Kordas GC (2012) Multilayer Organic–Inorganic Coating Incorporating TiO₂ Nanocontainers Loaded with Inhibitors for Corrosion Protection of AA2024-T3. *Progress in Organic Coatings* 73:142–148
135. S. A. El-Maksoud, Fouda AS (2005) Some pyridine derivatives as corrosion inhibitors for carbon steel in acidic medium. *Materials Chemistry and Physics* 93:84–90
136. M. Yadav, S. Kumar, R. R. Sinha, I. Bahadurb, Ebenso EE (2015) New pyrimidine derivatives as efficient organic inhibitors on mild steel corrosion in acidic medium: Electrochemical, SEM, EDX, AFM and DFT studies. *Journal of Molecular Liquids* 211:135-145

137. N. Anusuya, J. Saranya, P. Sounthari, A. Zarrouk, Chitra S (2017) Corrosion inhibition and adsorption behaviour of some bis-pyrimidine derivatives on mild steel in acidic medium. *Journal of Molecular Liquids* 225:406-417
138. Q. Ma, S. Qi, X. He, Y. Tang, Lu G (2017) 1,2,3-Triazole derivatives as corrosion inhibitors for mild steel in acidic medium: Experimental and computational chemistry studies. *Corrosion Science* 129:91-101
139. W. Li, Q. He, S. Zhang, C. Pei, Hou B (2008) Some new triazole derivatives as inhibitors for mild steel corrosion in acidic medium. *Journal of Applied Electrochemistry* 38:289–295
140. S. Kertit, Hammouti B (1996) Corrosion inhibition of iron in 1M HCl by 1-phenyl-5-mercapto-1,2,3,4-tetrazole. *Applied Surface Science* 93:59-66
141. Gomma GK (1998) Corrosion of low-carbon steel in sulphuric acid solution in presence of pyrazole—halides mixture. *Materials Chemistry and Physics* 55:241-246
142. M. Elayyachy, M. Elkodadi, A. Aouniti, A. Ramdani, B. Hammouti, F. Malek, Elidrissi A (2005) New bipyrazole derivatives as corrosion inhibitors for steel in hydrochloric acid solutions. *Materials Chemistry and Physics* 93:281-285
143. H. Zarrok, H. Oudda, A. El Midaoui, A. Zarrouk, B. Hammouti, M. Ebn Touhami, A. Attayibat, S. Radi, Touzani R (2012) Some new bipyrazole derivatives as corrosion inhibitors for C38 steel in acidic medium. *Research on Chemical Intermediates* 38:2051–2063
144. Khaled KF (2008) Application of electrochemical frequency modulation for monitoring corrosion and corrosion inhibition of iron by some indole derivatives in molar hydrochloric acid. *Materials Chemistry and Physics* 112:290-300
145. A. Chetouani, A. Aouniti, B. Hammouti, N. Benchat, T. Benhadda, Kertit S (2003) Corrosion inhibitors for iron in hydrochloride acid solution by newly synthesised pyridazine derivatives. *Corrosion Science* 45:1675-1684
146. A. Ghazoui, N. Benaht, S. S. Al-Deyab, A. Zarrouk, B. Hammouti, M. Ramdani, Guenbour M (2013) An Investigation of Two Novel Pyridazine Derivatives as Corrosion Inhibitor for C38 Steel in 1.0 M HCl. *International Journal of Electrochemical Science* 8:2272 - 2292
147. A. Popova, E. Sokolova, S. Raicheva, Christov M (2003) AC and DC study of the temperature effect on mild steel corrosion in acid media in the presence of benzimidazole derivatives. *Corrosion Science* 45:33-58
148. Khaled KF (2003) The inhibition of benzimidazole derivatives on corrosion of iron in 1 M HCl solutions. *Electrochimica Acta* 48:2493-2503
149. L. Tang, X. Li, L. Li, G. Mu, Liu G (2006) The effect of 1-(2-pyridylazo)-2-naphthol on the corrosion of cold rolled steel in acid media: Part 2: Inhibitive action in 0.5 M sulfuric acid. *Materials Chemistry and Physics* 97:301-307
150. L. Tang, X. Li, L. Li, Q. Qu, G. Mu, Liu G (2005) The effect of 1-(2-pyridylazo)-2-naphthol on the corrosion of cold rolled steel in acid media: Part 1: Inhibitive action in 1.0 M hydrochloric acid. *Materials Chemistry and Physics* 94:353-359
151. M. J. Bahrami, S. M. Hosseini, Pilvar P (2010) Experimental and theoretical investigation of organic compounds as inhibitors for mild steel corrosion in sulfuric acid medium. *Corrosion Science* 52:2793-2803
152. E. E. Ebenso, I. B. Obot, Murulana LC (2010) Quinoline and its Derivatives as Effective Corrosion Inhibitors for Mild Steel in Acidic Medium *International Journal of Electrochemical Science* 5: 1574 - 1586
153. D. Wang, D. Yang, D. Zhang, K. Li, L. Gao, Lin T (2015) Electrochemical and DFT studies of quinoline derivatives on corrosion inhibition of AA5052 aluminium alloy in NaCl solution. *Applied surface science* 357:2176-2183
154. E. Slavcheva, E. Sokolova, Raicheva S (1993) Temperature and concentration dependence of the activity of quinones of presumed inhibiting action *Journal of Electroanalytical Chemistry* 360:271-282
155. D. Raps, T. Hack, J. Wehr, M. L. Zheludkevich, A. C. Bastos, M. G. Ferreira, Nuyken O (2009) Electrochemical study of inhibitor-containing organic–inorganic hybrid coatings on AA2024. *Corrosion Science* 51:1012-1021

156. V. Palanivela, Y. Huang, Ooij WJv (2005) Effects of addition of corrosion inhibitors to silane films on the performance of AA2024-T3 in a 0.5 M NaCl solution. *Progress in Organic Coatings* 53:153-168
157. A. F. Galio, S. V. Lamaka, M. L. Zheludkevich, L. F. Dick, I. L. Müller, Ferreira MG (2010) Inhibitor-doped sol-gel coatings for corrosion protection of magnesium alloy AZ31. *Surface and Coatings Technology* 204:1479-1486
158. H. Shi, F. Liu, Han E (2009) Corrosion protection of AZ91D magnesium alloy with sol-gel coating containing 2-methyl piperidine. *Progress in Organic Coatings* 66:183-191
159. S. Peng, W. Zhao, H. Li, Z. Zeng, Q. Xue, Wu X (2013) The enhancement of benzotriazole on epoxy functionalized silica sol-gel coating for copper protection. *Applied Surface Science* 276:284-290
160. A. N. Khramov, N. N. Voevodin, V. N. Balbyshev, Mantz RA (2005) Sol-Gel-Derived Corrosion-Protective Coatings with Controllable Release of Incorporated Organic Corrosion Inhibitors. *Thin Solid Films* 483:191-196
161. Voevodin NN, V. N. Balbyshev, M. Khobai, Donley MS (2003) Nano structured coatings approach for corrosion protection *Progress in Organic Coatings* 47:416-423
162. S. A. El-Maksoud, Fouda AS (2005) Some pyridine derivatives as corrosion inhibitors for carbon steel in acidic medium *Materials Chemistry and Physics* 93:84-90
163. M. D. Gurudatt, Mohana KN (2014) Synthesis of new pyridine based 1,3,4-oxadiazole derivatives and their corrosion inhibition performance on mild steel in 0.5 M hydrochloric acid. *Industrial & Engineering Chemistry Research* 53:2092-2105
164. A. Ghazoui, R. Saddik, N. Benchat, M. Guenbour, B. Hammouti, S. S. Al-Deyab, Zarrouk A (2012) Comparative study of pyridine and pyrimidine derivatives as corrosion inhibitors of C38 steel in molar HCl. *International Journal of Electrochemical Science* 7:7080-7097
165. O. Krim, A. Elidrissi, B. Hammouti, A. Ouslim, Benkaddour M (2009) Synthesis, characterization, and comparative study of pyridine derivatives as corrosion inhibitors of mild steel in HCl medium. *Chemical Engineering Communications* 196 1536-1546
166. K. R. Ansari, M. A. Quraishi, Singh A (2015) Pyridine derivatives as corrosion inhibitors for N80 steel in 15% HCl: Electrochemical, surface and quantum chemical studies. *Measurement* 76:136-147
167. Lucas HR (1988) Curable compositions and corrosion resistant coatings prepared therefrom. USA Patent,
168. E. M. Sherif, Park S (2006) Effects of 1,4-naphthoquinone on aluminum corrosion in 0.50 M sodium chloride solutions. *Electrochimica Acta* 56:1313-1321
169. O. Kachurina, T. L. Metroke, Knobbe ET (2003) Technique for the removal of organic-inorganic hybrid coatings from 2024-T3 aluminum alloy. *Progress in Organic Coatings* 47:55-60
170. Cano E, Bastidas DM, Argyropoulos V, S. Fajardo AS, Bastidas JM, Degryny C (2010) Electrochemical characterization of organic coatings for protection of historic steel artefacts. *Journal of Solid State Electrochemistry* 14:453-463
171. D. Hallam, D. Thorrowgood, V. Otieno-Alego, D. Creagh, A. Viduka, Heath G (2001) Studies of commercial protective petrochemical coatings on ferrous surfaces of historical and museum objects. *Metal*:279-303
172. H. Otmačić Ćurković, T. Kosec, K. Marušić, Legat A (2012) An electrochemical impedance study of the corrosion protection of artificially formed patinas on recent bronze. *Electrochimica Acta* 83:28-39
173. E. Rocca, Mirambet F (2010) The electrochemical techniques for the diagnosis and restoration treatments of technical and industrial heritage: three examples of metallic artefacts. *Journal of Solid State Electrochemistry* 14:415-423
174. N. Swartz, Clare TL (2015) On the protective nature of wax coatings for culturally significant outdoor metalworks: microstructural flaws, oxidative changes, and barrier properties. *Journal of the American Institute for Conservation* 54:181-201

175. Letardi P (ed) (2013) *Electrochemical measurements in the conservation of metallic heritage artefacts: an overview Corrosion and conservation of cultural heritage metallic artefacts*. Woodhead Publishing Limited, United Kingdom
176. G. Cicileo, M. Crespo, Rosales B (2004) Comparative study of patinas formed on statuary alloys by means of electrochemical and surface analysis techniques. *Corrosion Science* 46:929-953
177. Letardi P (2004) Laboratory and field tests on patinas and protective coating systems for outdoor bronze monuments *Proceedings of Metal 2004* 379-387
178. E. Cano, D. Lafuente, Bastidas DM (2010) Use of EIS for the evaluation of the protective properties of coatings for metallic cultural heritage: a review. *Journal of Solid State Electrochemistry* 14:381–391
179. Tait ST (1994) *Introduction into Electrochemical Testing for Practicing Engineers and Scientists*. Pair O Docs Publications, USA
180. H. Otmacic Curkovic, T. Kosec, A. Legat, Stupnisek-Lisac E (2010) Improvement of corrosion stability of patinated bronze. *Corrosion Engineering* 45:327-333
181. Letardi P (2000) Electrochemical impedance measurements in the conservation of metals. In: D. C. Creagh, Bradley DA (eds) *Radiation in Art and Archeometry*. Elsevier Science,
182. B. Mahltig, C. Swaboda, A. Roessler, Böttcher H (2008) Functionalising wood by nanosol application, *Journal of Materials Chemistry*. *Journal of Materials Chemistry* 18:3180-3192
183. B. Bianco, Bertocello R (2008) Sol–gel silica coatings for the protection of cultural heritage glass. *Nuclear Instruments and Methods in Physics Research B* 266:2358–2362
184. B. Bianco, R. Bertocello, A. Bouquillon, J. Dran, L. Milanese, S. Roehrs, C. Sada, J. Salomon, Voltolina S (2008) Investigation on sol–gel silica coatings for the protection of ancient glass: Interaction with glass surface and protection efficiency. *Journal of Non-Crystalline Solids* 354:2983–2992
185. R. Bertocello, L. Milanese, R. Negro, L. Saragoni, Barison S (2003) Sol–gel preparation of non-hygroscopic siliceous thin films enriched with alkaline-earth ions. *Journal of Non-Crystalline Solids* 324:73–78
186. N. Carmona, M. A. Villegas, Fernandez-Navarro JM (2004) Protective silica thin coatings for historical glasses. *Thin Solid Films* 458 121–128
187. Ferri L, Lottici PP, Lorenzi A, Montenero A, Vezzalini G (2013) Hybrid sol–gel based coatings for the protection of historical window glass. *Journal of Sol-Gel Science & Technology* 66:253–263
188. L. Ferri, P. P. Lottici, A. Lorenzi, A. Montenero, Salvioli-Mariani E (2011) Study of silica nanoparticles – polysiloxane hydrophobic treatments for stone-based monument protection. *Journal of Cultural Heritage* 12:356–363
189. Tarasov VI (2001) New Colloid Silicate Solutions for Restoration and Conservation of Stone Facades. *Russian Journal of Applied Chemistry* 74:1985–1989
190. E. K. Kim, J. Won, J. Do, S. D. Kim, Kang YS (2009) Effects of silica nanoparticle and GPTMS addition on TEOS-based stone consolidants. *Journal of Cultural Heritage* 10:214–221
191. P. N. Manoudis, I. Karapanagiotis, A. Tsakalof, I. Zuburtikudis, B. Kolinkeová, Panayiotou C (2009) Superhydrophobic films for the protection of outdoor cultural heritage assets. *Applied Physics A* 97:351–360
192. Kiele E (2014) Methyl–modified hybrid organic-inorganic coatings for the conservation of copper. *Journal of Cultural Heritage* 15:242–249
193. E. Bescher, Mackenzie JD (2003) Sol-Gel Coatings for the Protection of Brass and Bronze. *Journal of Sol-Gel Science and Technology* 26:1223–1226
194. E. Joseph, P. Letardi, R. Mazzeo, S. Prati, Vandini M (2007) Innovative treatments for the protection of outdoor bronze monuments. *Metal, Protection of metal artefacts* 5:71-77
195. B. Seipelt, M. Pilz, Kieseberg J (1998) Transparent coatings- suitable corrosion protection for industrial heritage made of iron? *Metal* 98:291-296

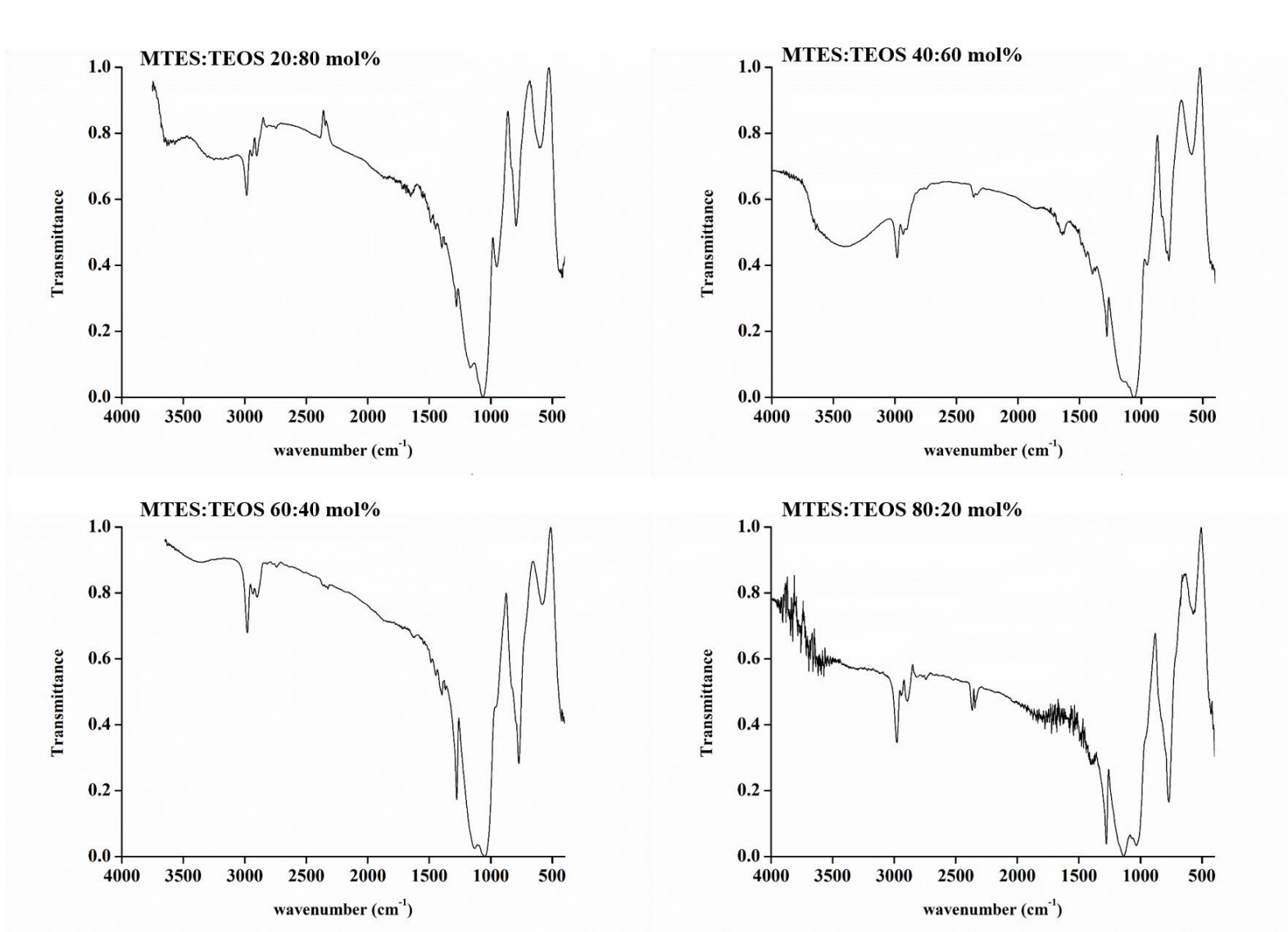
196. Degriigny C (2010) Use of artificial metal coupons to test new protection systems on cultural heritage objects: manufacturing and validation. *Corrosion Engineering* 45:367-374
197. D. Vella, J. Ashton, Hallam D (2004) Metallurgy of armour exhibited at the Palace Armoury, Valletta, Malta. *Metal 04 : proceedings of the International Conference on Metals Conservation : Canberra, Australia*:215-231
198. D. Vella, C. Degriigny, M. Grech, Williams A (2004) Metallurgy of armour exhibited at the Palace Armoury Valletta, Malta. *Proceedings of Metal 2004*
199. Haynes WM (2016) *CRC Handbook of Chemistry and Physics*. 97th Edition edn. CRC Press, USA
200. T. Lan, Y. Fang, W. Xiong, Kong C (2007) Automatic baseline correction of infrared spectra. *20 5* 613-616
201. R. M. Almeida, Marques AC (2005) Characterization of Sol–Gel Materials by Infrared Spectroscopy. In: Almeida RM (ed) *Characterization of Sol–Gel Materials and Products*, vol 2. Kluwer Academic Publishers, United States, pp 65-90
202. R. M. Almeida, Pantano CG (1990) Structural investigation of silica gel films by infrared spectroscopy. *Journal of Applied Physics* 68:4225-4232
203. Rasband W (1997) *ImageJ*.
204. 1951 ESB (1951) Three-faceted diamond pyramid for micro-hardness testing. *Industrial Diamond Review* 127 129-133
205. Galliano P, Damborenea JJd, Pascual MJ, Duran A (1998) Sol-Gel Coatings on 316L Steel for Clinical Applications. *Journal of Sol-Gel Science and Technology* 13:723–727
206. Z. Zhang, Y. Tanigami, R. Terai, Wakabayashi H (1995) Preparation of transparent methyl-modified silica gel *Journal of Non-Crystalline Solids* 189:212-217
207. A. L. Tan, A. M. SoutaraI, F. Annergren, Liu YN (2005) Multilayer sol-gel coatings for corrosion protection of magnesium. *Surface and Coatings Technology* 198:478-482
208. A. Franquet, H. Terryn, Vereecken J (2003) Composition and Thickness of Non-Functional Organosilane Films Coated on Aluminium Studied by Means of IRSE. *Thin Solid Films* 441:76-84
209. F. Deflorian, S. Rossi, Fedrizzi L (2006) Silane pre-treatments on copper and aluminium. *Electrochimica Acta* 51:6097–6610
210. Galeener FL (1979) Band limits and the vibrational spectra of tetrahedral glasses. *Physical Review B* 19:4292
211. Silverstein RM, Webster FX, Kiemle DJ (2005) *Spectrometric Identification of Organic Compounds*. Wiley & Sons United States of America
212. Cai S, Zhang Y, Zhang H, Yan H, Lv H, Jiang B (2014) Sol–Gel Preparation of Hydrophobic Silica Antireflective Coatings with Low Refractive Index by Base/Acid Two-Step Catalysis. *ACS Applied Materials & Interfaces* 6:11470–11475
213. B. D. Fabes, Oliver WC (1990) MECHANICAL PROPERTIES OF SOL-GEL COATINGS *Journal of Non-Crystalline Solids* 121:348-356
214. J. Ballarre, D. A. López, Cavalieri AL (2008) Nano-indentation of hybrid silica coatings on surgical grade stainless steel. *Thin Solid Films* 516:1082–1087
215. Wright JD, Sommerdijk NA (2001) *Sol-Gel Materials: Chemistry and Applications*. Advanced Chemistry Texts. CRC Press, USA
216. Ma X, Lee N, Oh H, Kim J, Rhee C, Park K, Kim S (2010) Surface modification and characterization of highly dispersed silica nanoparticles by a cationic surfactant. *Colloids and Surfaces A: Physicochemical and Engineering Aspects* 358:172–176
217. *SpectraBase™* (2019) Bio-Rad Laboratories, Inc.

218. M. Chelliah, J. B. Rayappan, Krishnan UM (2012) Synthesis and Characterization of Cerium Oxide Nanoparticles by Hydroxide Mediated Approach *Journal of Applied Sciences* 12:1734-1737
219. F. A. Miller, Wilkins CH (1952) Infrared Spectra and Characteristic Frequencies of Inorganic Ions. *Journal of Analytical Chemistry* 8:1253–1294
220. R. M. Silverstein, F. X. Webster, Kiemle D (2005) *Spectrometric Identification of organic compounds*. 7th edn. Wiley, United States of America
221. Y. Matsuda, T. Ebata, Mikami N (2001) IR-UV Double-Resonance Spectroscopic Study of 2-Hydroxypyridine and Its Hydrogen-Bonded Clusters in Supersonic Jets. *Journal of Physical Chemistry (A)* 105:3475-3480
222. Miler M, Mirtic B (2013) Accuracy and precision of EDS analysis for identification of metal-bearing minerals in polished and rough particle samples. *Geologija* 56:5-18
223. J. Yang, Chen J (2009) Surface free energies and steam stability of methyl-modified silica membranes. *Journal of Porous Materials* 16:737-744
224. Y. Mizuta, Y. Daiko, A. Mineshige, M. Kobune, Yazawa T (2011) Phase-separation and distribution of phenyl groups for PhTES-TEOS coatings prepared on polycarbonate substrate. *Journal of Sol-Gel Science & Technology* 58:80–84
225. R. S. Kalidindi, Subasri R (2015) Sol-gel nanocomposite hard coatings. In: Aliofkhazraei M (ed) *Anti-Abrasive Nanocoatings*. Woodhead publishing, United States,
226. A. Ferchichi, S. Calas-Etienne, M. Smaïhi, Etienne P (2008) Study of the mechanical properties of hybrid coating as a function of their structures using nanoindentation. *Journal of Non-Crystalline Solids* 354:712-716
227. B. Ramezanzadeh, E. Raeisi, Mahdavian M (2015) Studying various mixtures of 3-aminopropyltriethoxysilane (APS) and tetraethylorthosilicate (TEOS) silanes on the corrosion resistance of mild steel and adhesion properties of epoxy coating. *International Journal of Adhesion and Adhesives* 63:166-176
228. X. Yuan, Z. F. Yue, X. Chen, S. F. Wen, L. Li, Feng T (2016) The protective and adhesion properties of silicone-epoxy hybrid coatings on 2024 Al-alloy with a silane film as pretreatment. *Corrosion Science* 104:84–97
229. H. Yahyaei, Mohseni M (2013) Use of nanoindentation and nanoscratch experiments to reveal the mechanical behavior of sol–gel prepared nanocomposite films on polycarbonate. *Tribology International* 57:147-155
230. X. Zhang, L. Hu, Sun D (2006) Nanoindentation and nanoscratch profiles of hybrid films based on (γ -methacrylopropyl)trimethoxysilane and tetraethoxysilane. *Acta Materialia* 54:5469-5475
231. G. Carbajal-de la Torre, M. A. Espinosa-Medina, A. Martinez-Villafañe, J. G. Gonzalez-Rodriguez, Castaño VM (2009) Study of Ceramic and Hybrid Coatings Produced by the Sol-Gel Method for Corrosion Protection *The Open Corrosion Journal* 2:197-203
232. A. Tiwari, J. Zhu, Hihara LH (2008) The development of low-temperature hardening silicone ceramer coatings for the corrosion protection of metals. *Surface and Coatings Technology* 202:4620-4635
233. Z. Chan, L. Ai'mei, Z. Xiao, F. Miao, H. Juan, Hongbing Z (2007) Microstructures and properties of ORMOSIL comprising methyl, vinyl, and γ -glycidoxypropyl-substitued silica. *Optical Materials* 29:1543-1547
234. R. Suleiman, H. Dafallab, Alic BE (2015) Novel hybrid epoxy silicone materials as efficient anticorrosive coatings for mild steel. *Royal Society of Chemistry* 5:39155-39167
235. A. R. Ainuddin, T. Ishigaki, N. Hakiri, H. Muto, M. Sakai, Matsuda A (2012) Influence of UV irradiation on mechanical properties and structures of sol–gel-derived vinylsilsesquioxane films. *Journal of the Ceramic Society of Japan* 120:442-445
236. X. Chen, S. Zhou, B. You, Wu L (2012) Mechanical properties and thermal stability of ambient-cured thick polysiloxane coatings prepared by a sol–gel process of organoalkoxysilanes. *Progress in Organic Coatings* 74:540-548

237. J. Esquena, R. Pons, N. Azemar, J. Caelles, Solans C (1997) Preparation of monodisperse silica particles in emulsion media *Colloids and Surfaces A: Physicochemical and Engineering Aspects* 123-124:575-586
238. L. Ni, A. Chemtob, C. Croutxé-Barghorn, N. Moreau, T. Bouder, S. Chanfreau, Pébèr N (2014) Direct-to-metal UV-cured hybrid coating for the corrosion protection of aircraft aluminium alloy. *Corrosion Science* 89:242-249
239. U. Eugene, S. P. O'Donnell, J. V. Ifeoma, Feyisayo VA (2016) The effect of corrosion inhibitors on stainless steels and aluminium alloys: A review. *African Journal of Pure and Applied Chemistry* 10: 23-32
240. D. Wallinder, J. Pan, C. leygraf, Delblanc-Bauer A (1999) EIS and XPS study of surface modification of 205LVM stainless steel after passivation. *Corrosion Science* 41:275-289
241. Sakka S (1994) Preparation and Properties of Sol-Gel Coating Films *Journal of Sol-Gel Science and Technology* 2:451-455
242. S. Pellice, P. Galliano, Y. Castro, Duran A (2003) Hybrid Sol-Gel Coatings Produced from TEOS and γ -MPS. *Journal of Sol-Gel Science and Technology* 28:81-86
243. P. Innocenzi, M. O. Abdirashid, Guglielmi M (1994) Structure and Properties of Sol-Gel Coatings from Methyltriethoxysilane and Tetraethoxysilane. *Journal of Sol-Gel Science and Technology* 3:47-55
244. Orcel G, Hench L (1986) Effect of formamide additive on the chemistry of silica sol-gels Part I: NMR of silica hydrolysis *Journal of Non-Crystalline Solids* 79:177-194
245. Artaki I, Zerda TW, Jonas J (1986) Solvent effects on the condensation stage of the sol-gel process *Journal of Non-Crystalline Solids* 81:381-395
246. Adachi T, Sakka S (1988) The role of n,n-dimethylformamide, a DCCA, in the formation of silica gel monoliths by sol-gel method *Journal of Non-Crystalline Solids* 99:118-128
247. Katagiri T, Maekawa T (1991) Influence of solvents on the structure of SiO₂ gel from hydrolysis of tetramethylorthosilicate. *Journal of Non-Crystalline Solids* 134:183-190
248. C. B. Kretschmer, Wiebe R (1949) Liquid-Vapor Equilibrium of Ethanol-Toluene Solutions. *Journal of the American Chemical Society* 71:1793-1797
249. Daubert TE, Danner RP (1989) *Physical and Thermodynamic Properties of Pure Chemicals Data Compilation*. Taylor and Francis, Washington, D.C.
250. Company DC (1990) *The Glycol Ethers Handbook*.97
251. P. Atkins, J. de Paula, Keeler J (2017) *Atkins' Physical Chemistry*. Oxford Press, United kingdom
252. M. L. Zheludkevich, R. Serra, M. F. Montemor, I. M. Miranda-Salvado, Ferreira MG (2006) Corrosion protective properties of nanostructured sol-gel hybrid coatings to AA2024-T3. *Surface and Coatings Technology* 200:3084-3094
253. D. G. Shchukin, M. Zheludkevich, K. Yasakau, S. Lamaka, M. G. Ferreira, Möhwald H (2006) Layer-by-Layer Assembled Nanocontainers for Self-Healing Corrosion Protection. *Advanced materials* 18:1672-1678
254. M. L. Zheludkevich, D. G. Shchukin, K. A. Yasakau, H. Mohwald, Ferreira MG (2007) Anticorrosion Coatings with Self-Healing Effect Based on Nanocontainers Impregnated with Corrosion Inhibitor. *Chemistry of Materials* 19:402-411
255. OSHA Occupational Chemical DB The National Institute for Occupational Safety and Health – NIOSH.
256. N. N. Voevodin, N. T. Grebasch, W. S. Soto, F. E. Arnold, Donley MS (2001) Potentiodynamic evaluation of sol-gel coatings with inorganic inhibitors. *Surface and Coatings Technology* 140:24-28
257. D. G. Shchukin, Möhwald H (2007) Self-Repairing Coatings Containing Active Nanoreservoirs. *Small* 6:926 – 943
258. Budavari S (1989) *The Merck Index : an encyclopedia of chemicals, drugs, and biologicals*.6315

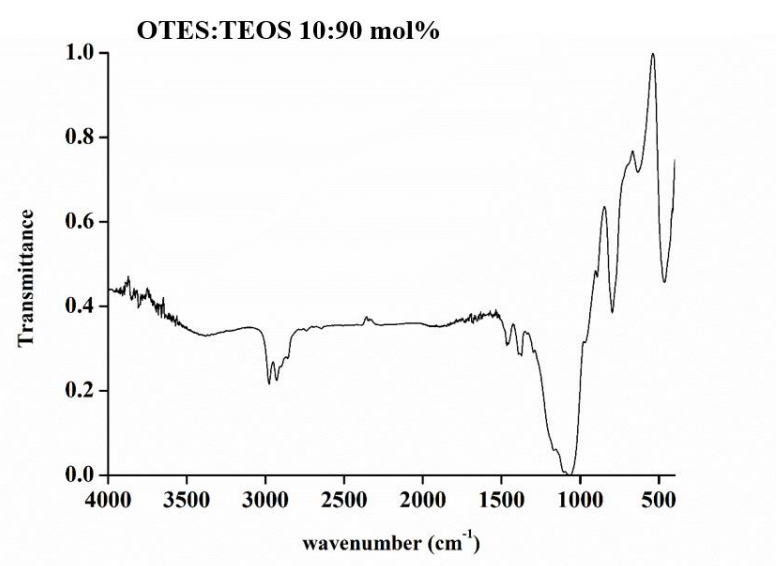
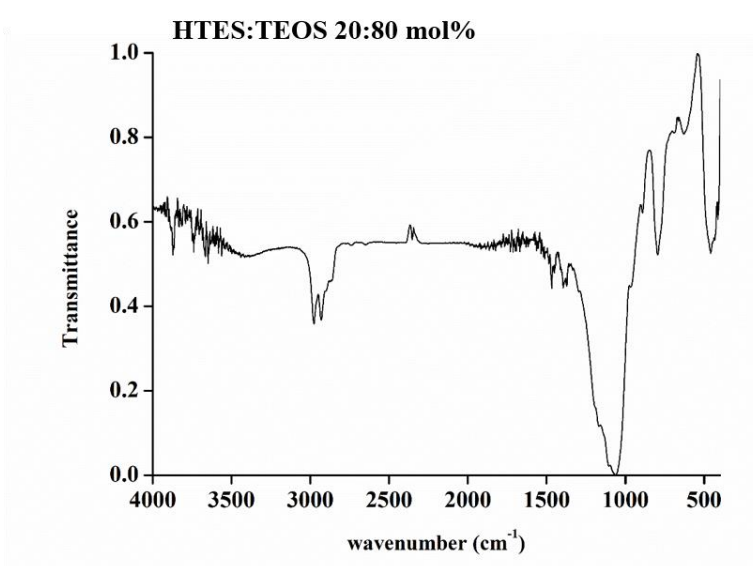
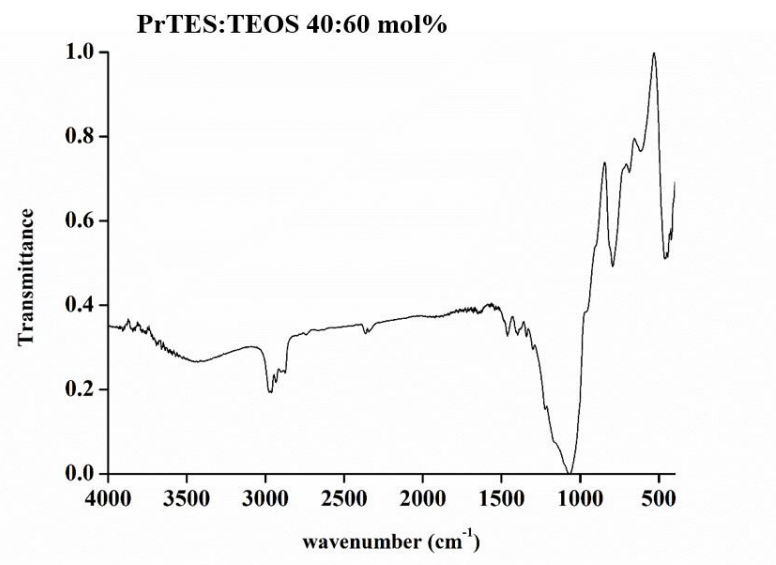
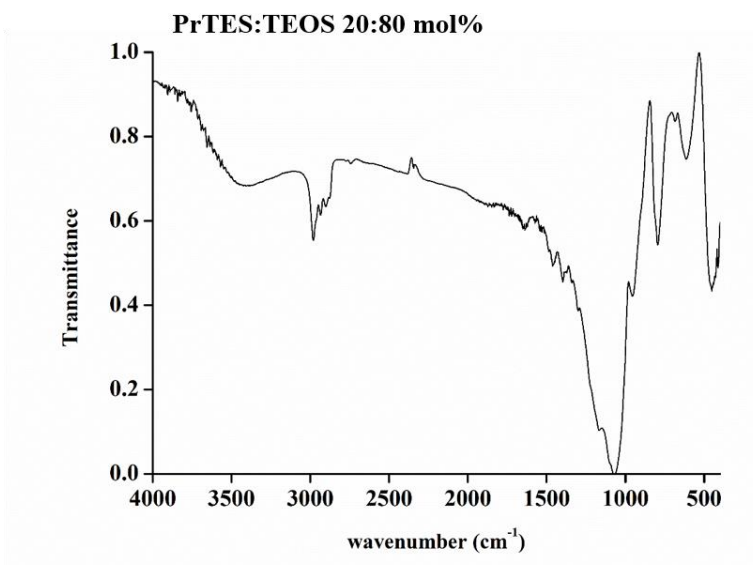
259. Huq F, Yu J (2002) Molecular modeling analysis: “Why is 2-hydroxypyridine soluble in water but not 3-hydroxypyridine?”. *Journal of Molecular Modelling* 8:81–86
260. Wallace WE (2019) NIST Chemistry WebBook, vol 69. NIST Standard Reference Database. Gaithersburg, MD, USA
261. Yalkowsky SH, Dannenfelser RM (1992) The AQUASOL dATABaSE of Aqueous Solubility. 5
262. A. Guiseppi-Elie, Maharajh DM (1984) The solubility of 1-naphthol in water at different temperatures. *Thermochimica Acta* 73:187-191
263. Quill LL, Robey RF (1937) The Rare Earth Metals and their Compounds. III. The Ternary Systems Cerium Group Nitrates-Nitric Acid-Water at 25 and 50°. *Journal of the American Chemical Society* 59:2591-2595
264. S. Das, T. K. Jain, Maitra A (2002) Inorganic–Organic Hybrid Nanoparticles from n-Octyl Triethoxy Silane. *Journal of Colloid and Interface Science* 252:82–88
265. S. Kozhukharov, V. Kozhukharov, M. Schem, M. Aslan, M. Wittmar, A. Wittmar, Veith M (2012) Protective ability of hybrid nano-composite coatings with cerium sulphate as inhibitor against corrosion of AA2024 aluminium alloy. *Progress in Organic Coatings* 73:95-103
266. A. Wittmar, M. Wittmar, H. Caparrotti, Veith M (2011) The Influence of the Inhibitor Particle Sizes to the Corrosion Properties of Hybrid Sol–Gel Coatings. *Journal of Sol–Gel Science & Technology* 59:621–628
267. E. Roussi, A. Tsetsekou, A. Skarmoutsou, C. A. Charitidis, Karantonis A (2013) Anticorrosion and Nanomechanical Performance of Hybrid Organo-silicate Coatings Integrating Corrosion Inhibitors. *surface & Coatings Technology* 232:131–141
268. M. L. Zheludkevich, S. K. Poznyak, L. M. Rodriguesa, D. Raps, T. Hack, L. F. Dick, T. Nunes, Ferreira MG (2010) Active protection coatings with layered double hydroxide nanocontainers of corrosion inhibitor. *Corrosion Science* 52:602-611
269. M. L. Zheludkevich, D. G. Shchukin, K. A. Yasakau, H. Mohwald, Ferreira MG (2007) Anticorrosion Coatings with Self-healing Effect Based on Nanocontainers Impregnated with Corrosion Inhibitor. *Chemistry of Materials* 19:402–411
270. M. L. Zheludkevich, J. Tedim, Ferreira MG (2012) “Smart” coatings for active corrosion protection based on multi-functional micro and nanocontainers. *Electrochimica Acta* 82:314–323
271. P. Kotlik, K. Doubravova, J. Horalek, L. Kubac, J. Akerman (2014) Acrylic copolymer coatings for protection against UV rays. *Journal of Cultural Heritage* 15:44–48
272. O. Chiantore, Lazzari M (1996) Characterization of Acrylic Resins. *International Journal of Polymer Analysis and Characterization* 2:395–408
273. J. Švadlena, Stoulil J (2017) Evaluation of protective properties of acrylate varnishes used for conservation of historical metal artefacts. *Koroze a ochrana materiálu* 61:25-31
274. Boston MoFA (2016) Paraloid B48-N. http://cameo.mfa.org/wiki/Paraloid_B-48N
275. LLC. CRI (2018) Acryloid B48N. http://www.conservationresources.com/Main/section_40/section_40_02.htm.
276. Coatings WI (2010) Coating application guide. <https://wattyindustrial.com.au/documents/industrial/information/3%20COATING%20APPLICATION%20GUIDE%20v2.pdf>.
277. Olender J, Wantuch-Jarkiewicz K (2019) Extraction of Zinc Corrosion from Beneath a Paint Layer: A Case Study. *Studies in Conservation* 64:146-158
278. Licari J (2016) personal communication. Palace Armoury conservator
279. Hutchins R (2014) Saddle Soap and Its dangers for leather cleaning. <https://www.linkedin.com/pulse/20140903064140-69098650-saddle-soap-and-its-dangers-for-leather-cleaning>.

Appendix A

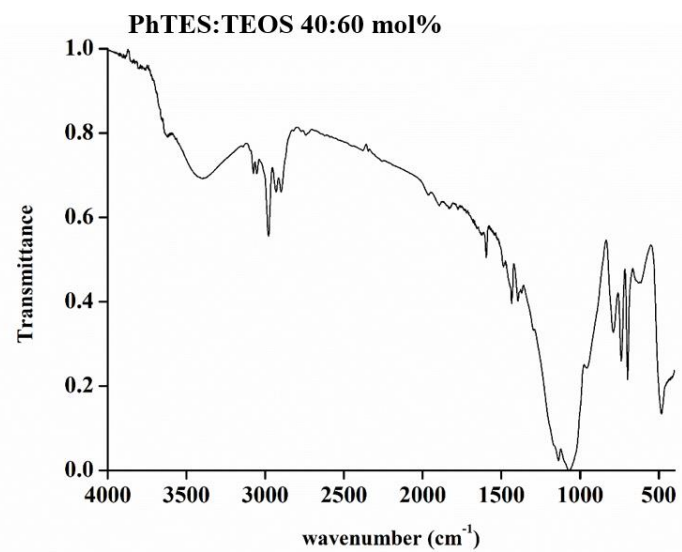
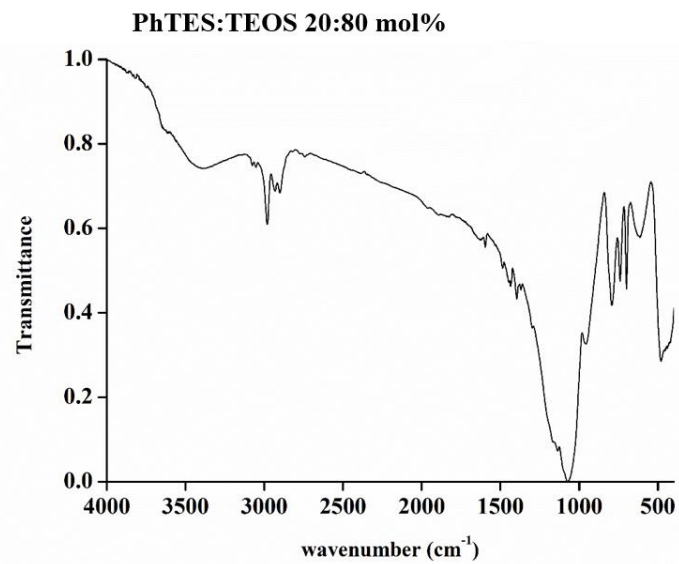
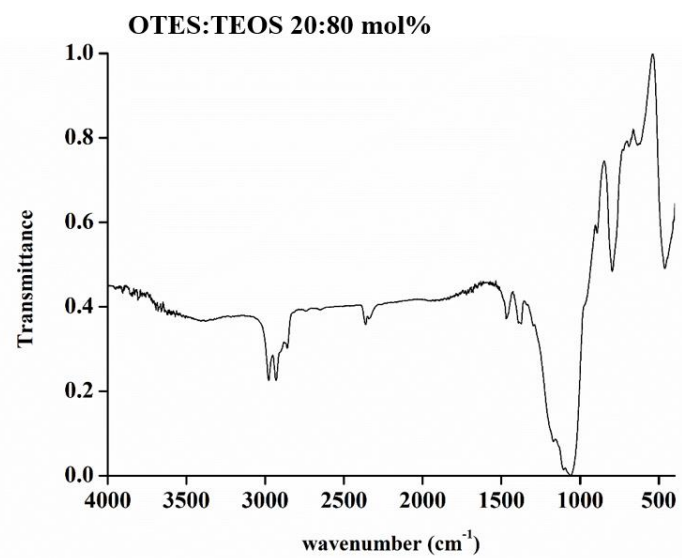


Normalized plots of transmittance versus wavenumber (cm^{-1}) for 2.5% SiO_2 MTES:TEOS sols in molar ratios of 20:80, 40:60, 60:40 and 80:20 mol%; PrTES:TEOS 20:80 and 40:60 mol%; HTES:TEOS 20:80 mol%; OTES:TEOS 10:90 and 20:80 mol%; PhTES:TEOS 20:80 and 40:60 mol%

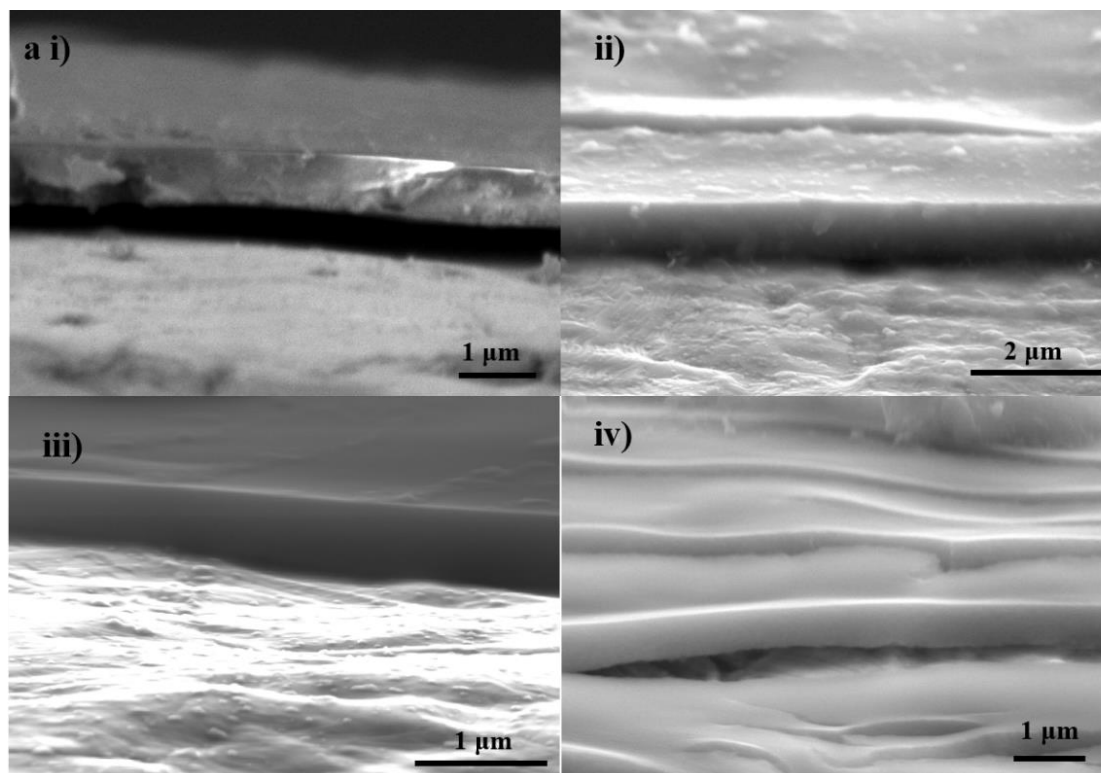
Appendix A (continued)



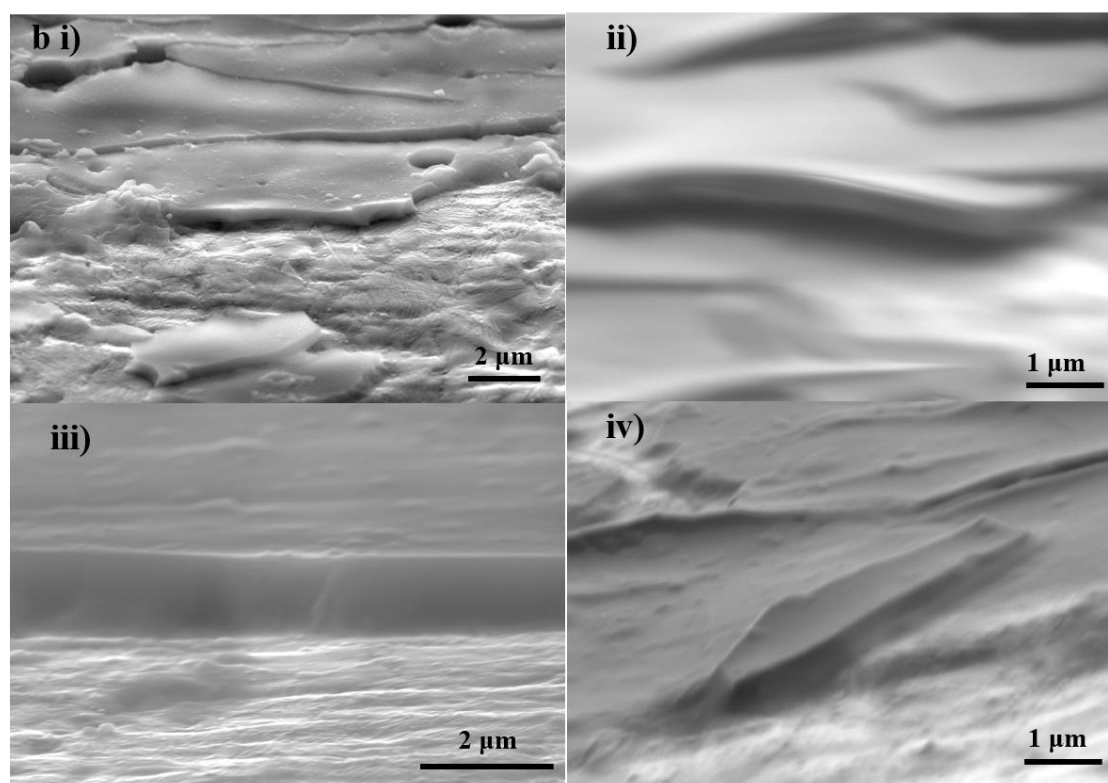
Appendix A (continued)



Appendix B

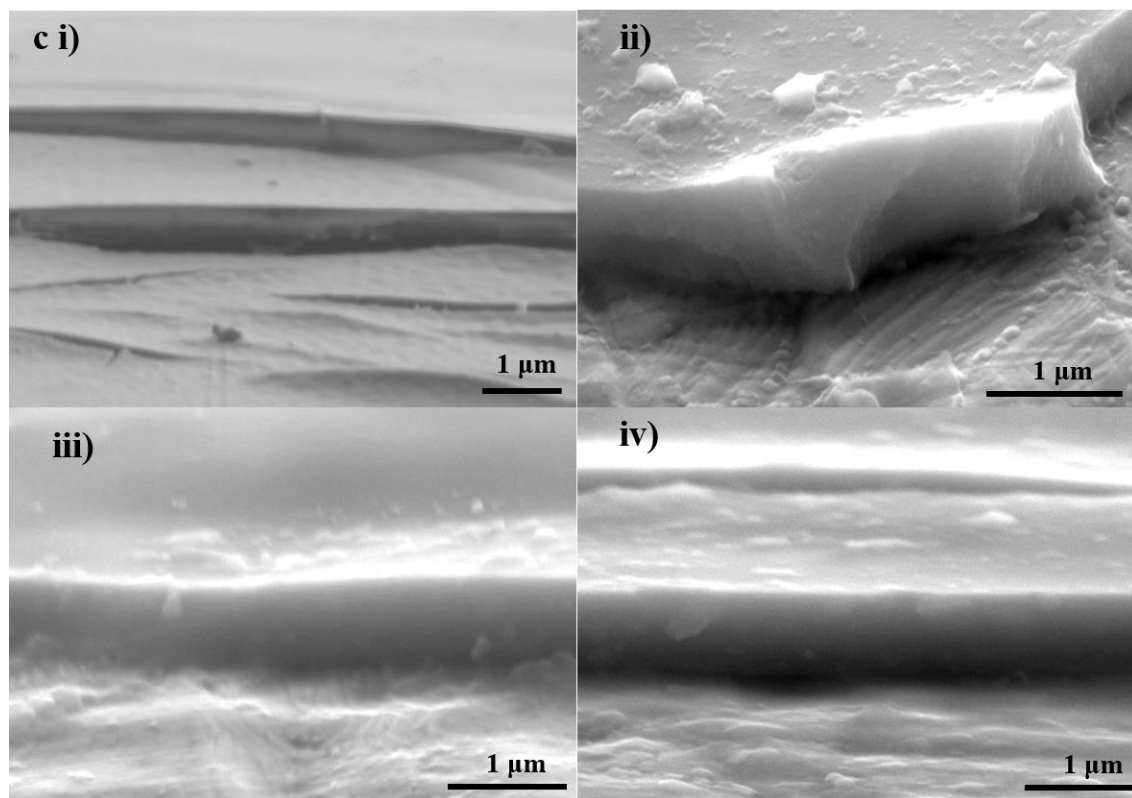


a) Electron micrograph showing the surface and a cross-section through MTES:TEOS coatings of i) 20:80 mol% (mag $\times 30$ k), ii) 40:60 mol% (mag $\times 10$ k), iii) 60:40 mol% (mag $\times 50$ k), and iv) 80:20 mol% (mag $\times 10$ k).

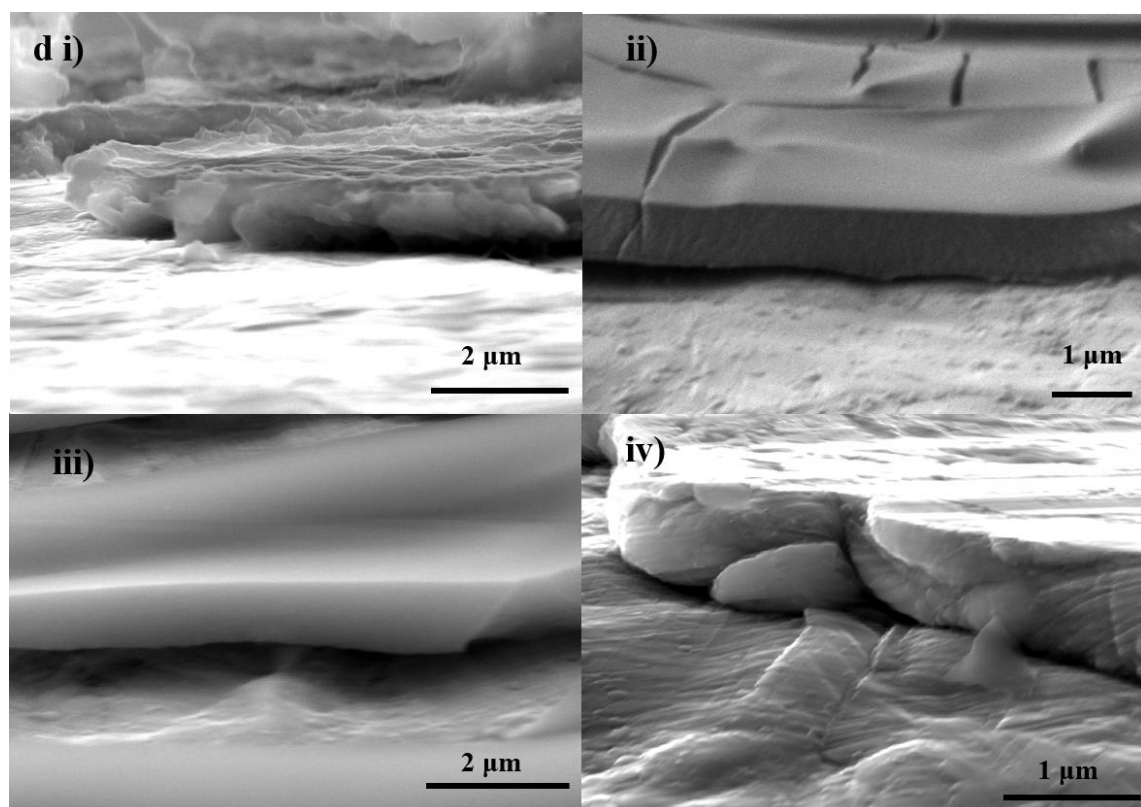


b) Electron micrograph showing the surface and a cross-section through PrTES:TEOS coatings of i) 20:80 mol% (mag $\times 5$ k), ii) 40:60 mol% (mag $\times 30$ k), iii) 50:50 mol% (mag $\times 10$ k), and iv) 60:40 mol% (mag $\times 30$ k).

Appendix B (*continued*)

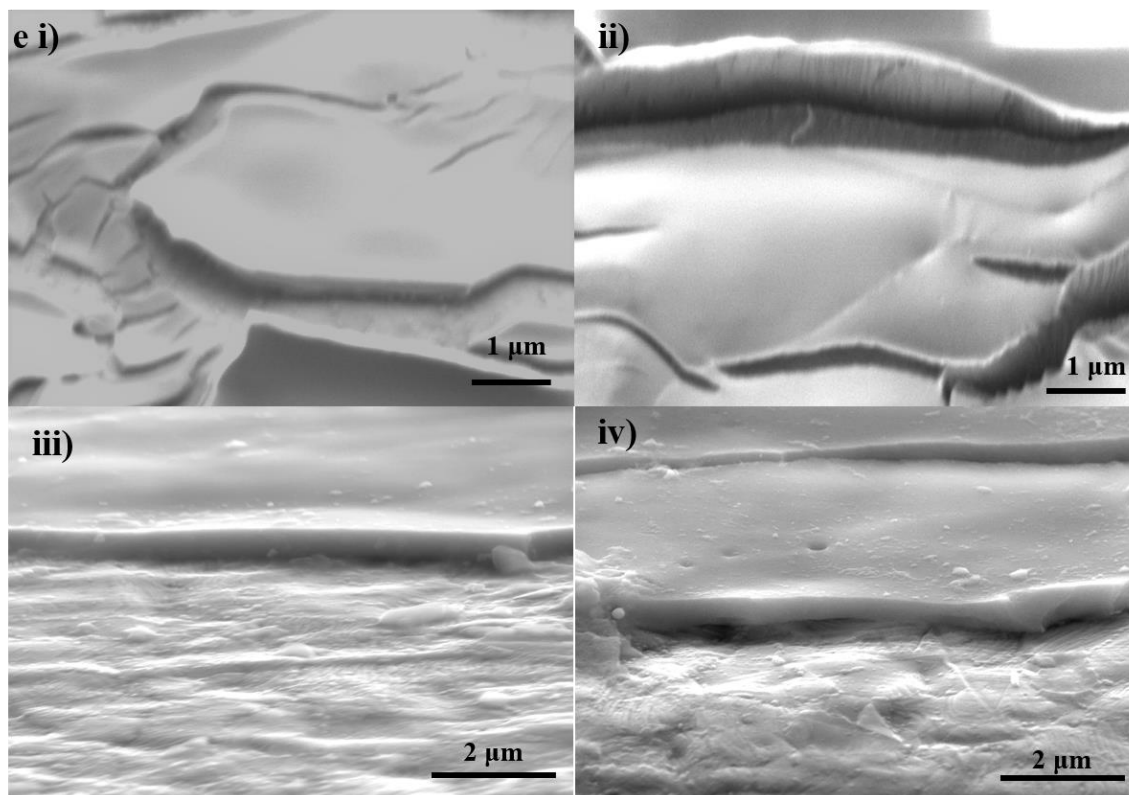


c) Electron micrograph showing the surface and a cross-section through HTES:TEOS coatings of i) 20:80 mol% (mag $\times 30$ k), ii) 30:70 mol% (mag $\times 20$ k), iii) 40:60 mol% (mag $\times 10$ k), and iv) 60:40 mol% (mag $\times 10$ k).



d) Electron micrograph showing the surface and a cross-section through OTES:TEOS coatings of i) 10:90 mol% (mag $\times 10$ k), ii) 20:80 mol% (mag $\times 30$ k), iii) 40:60 mol% (mag $\times 10$ k), and iv) 60:40 mol% (mag $\times 50$ k).

Appendix B (*continued*)



e) Electron micrograph showing the surface and a cross-section through PhTES:TEOS coatings of i) 20:80 mol% (mag $\times 30$ k), ii) 40:60 mol% (mag $\times 30$ k), iii) 60:40 mol% (mag $\times 10$ k), and iv) 80:20 mol% (mag $\times 10$ k).

Appendix C

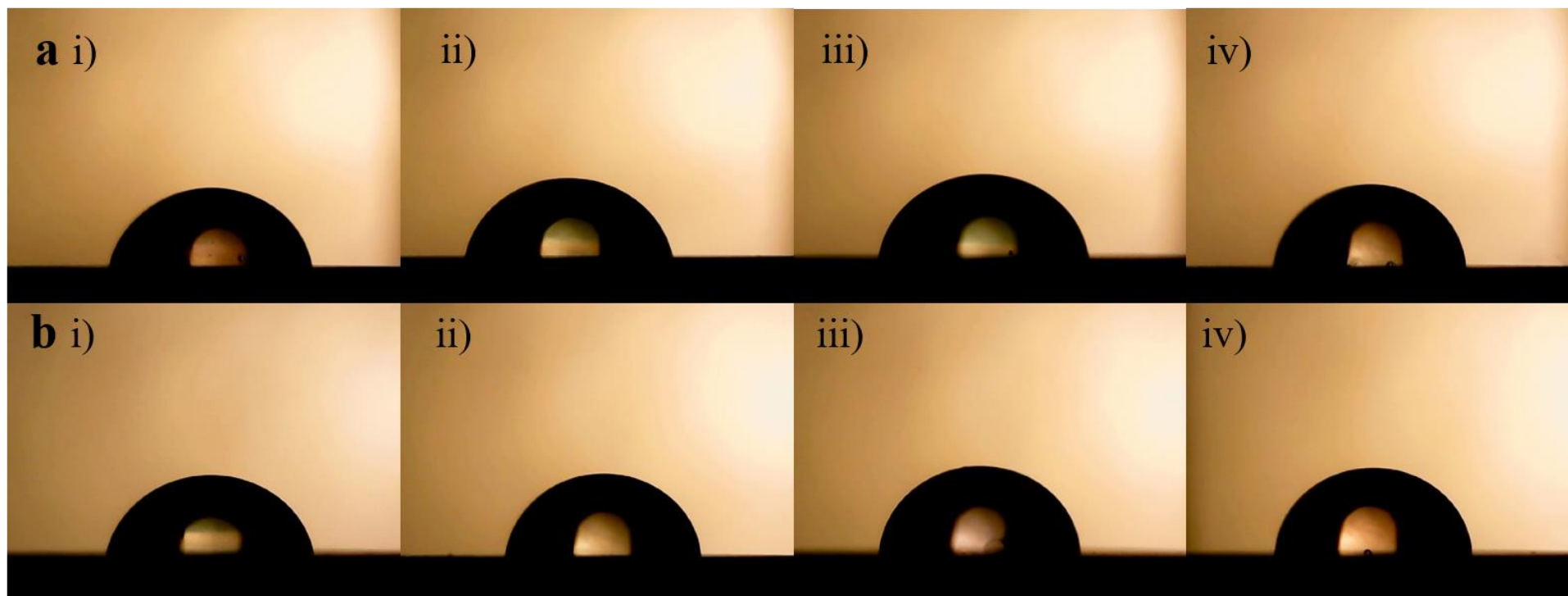
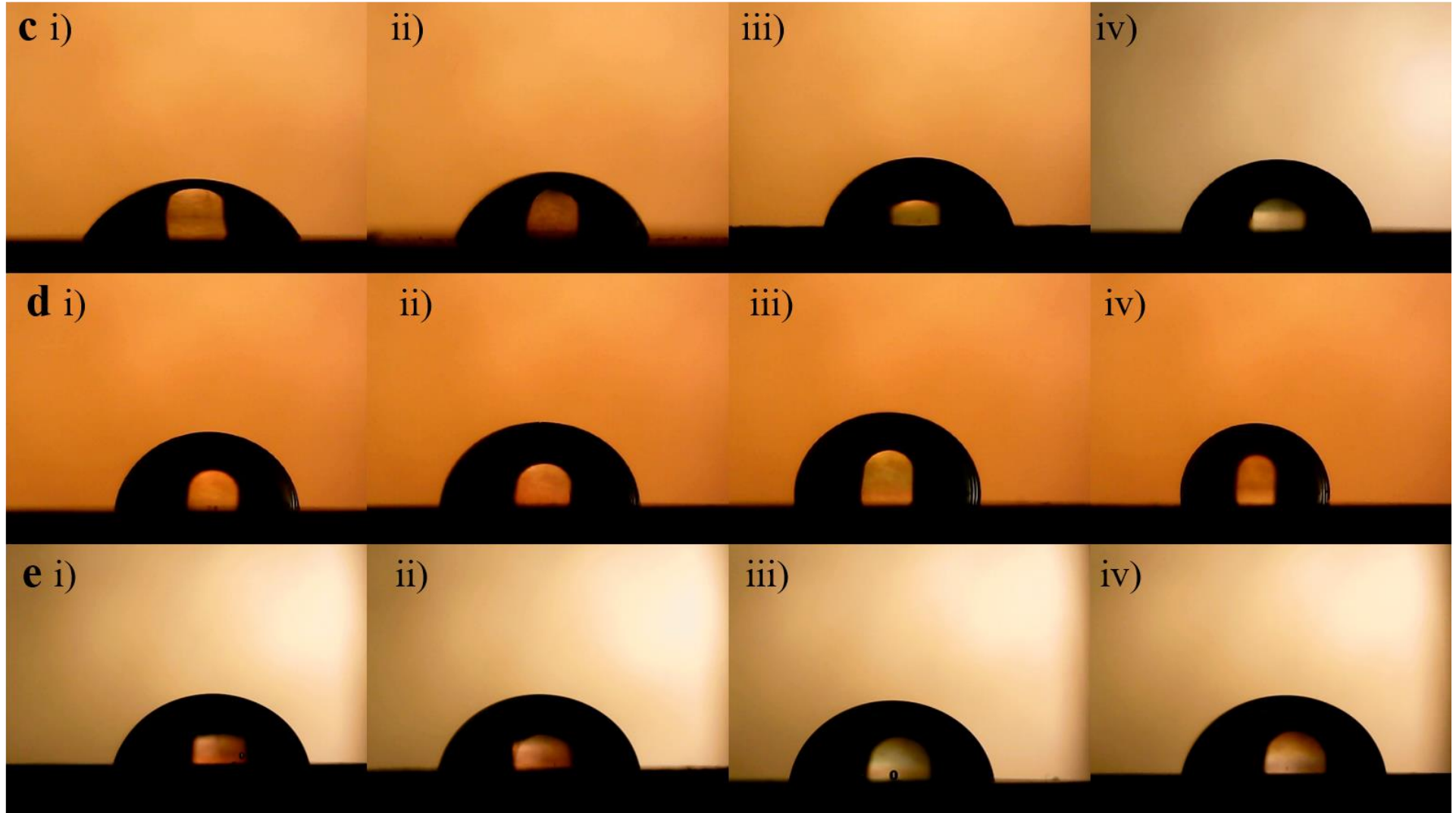
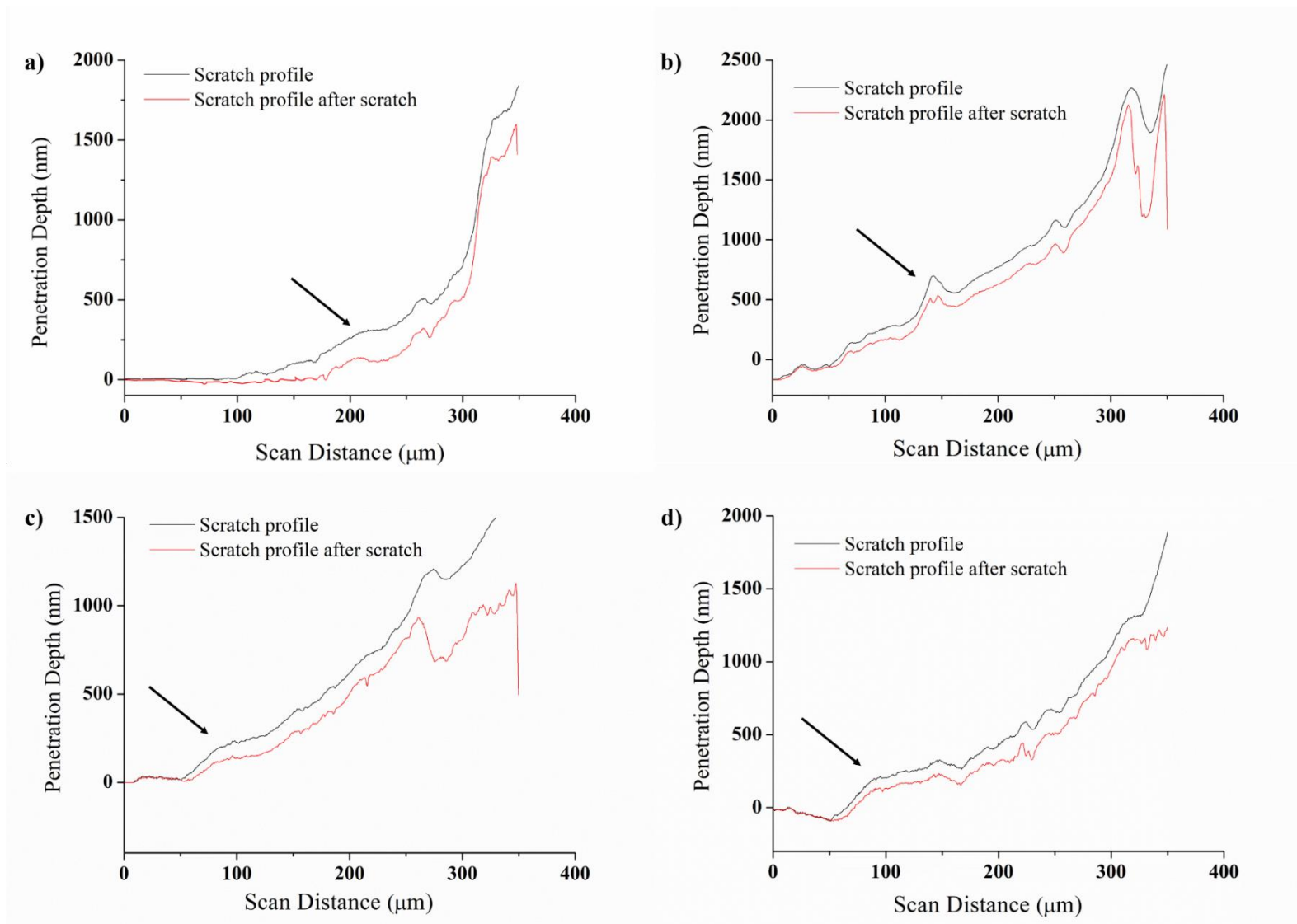


Photo-micrographs of sessile water droplets on a) MTES:TEOS i) 20:80 ii) 40:60 iii) 60:40 and iv) 80:20 mol%, b) PrTES:TEOS i) 20:80 ii) 40:60 iii) 50:50 and iv) 60:40 mol%, c) HTES:TEOS i) 20:80 ii) 30:70 iii) 40:60 and iv) 60:40 mol%, d) OTES:TEOS i) 10:90 ii) 20:80 iii) 40:60 and iv) 60:40 mol%, e) PhTES:TEOS i) 20:80 ii) 40:60 iii) 60:40 and iv) 80:20 mol%.

Appendix C (*continued*)

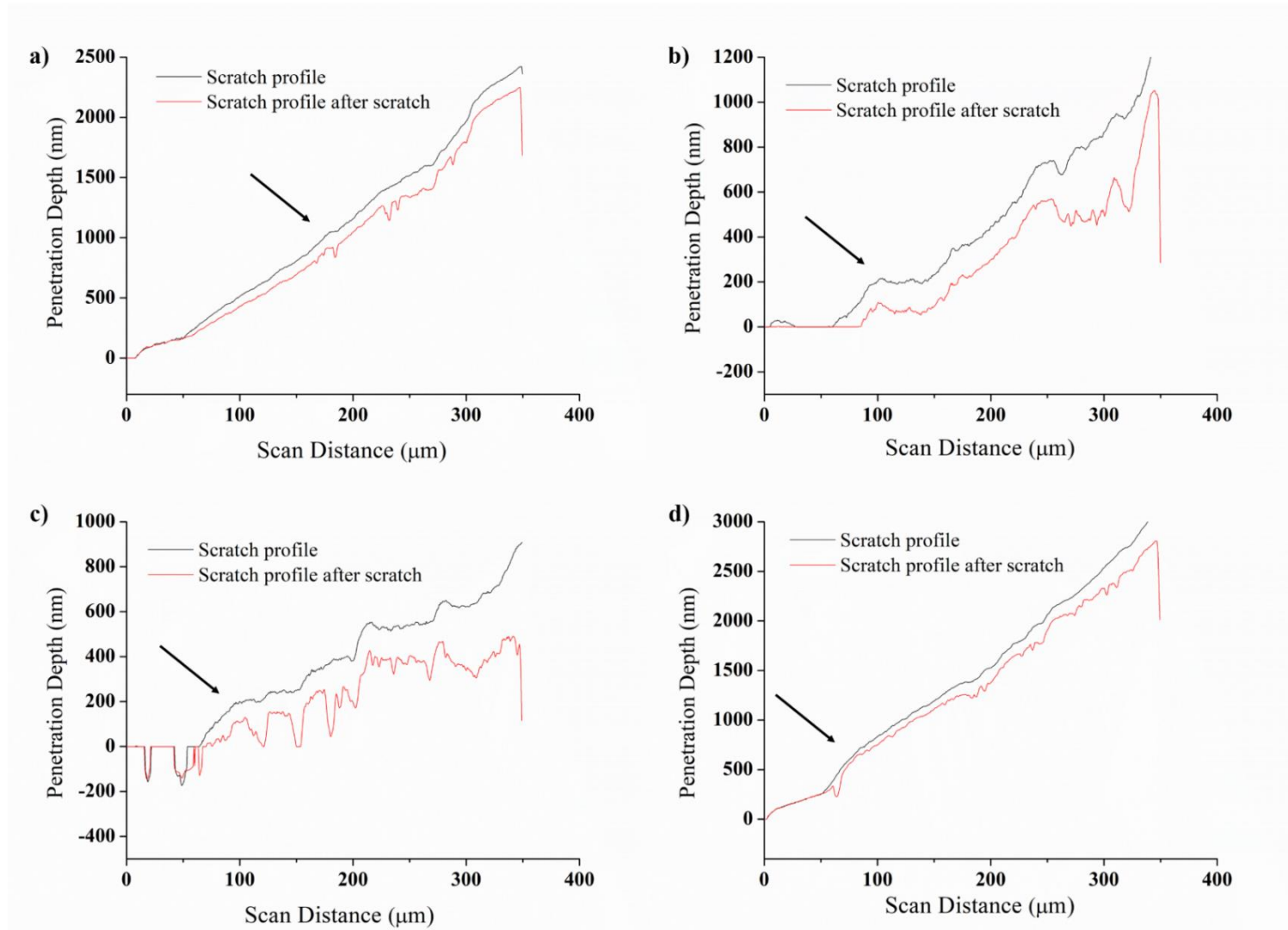


Appendix D



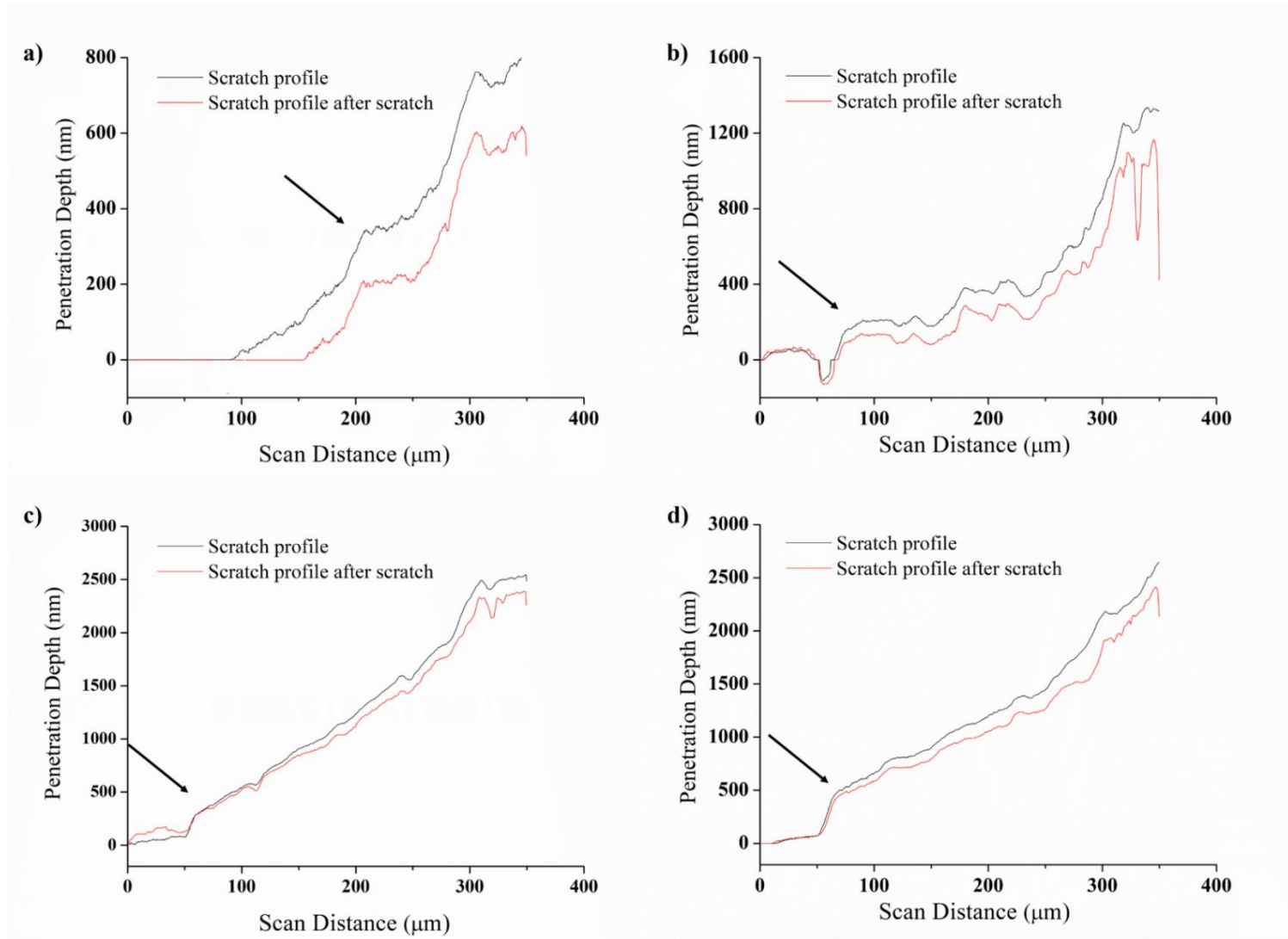
Plots of scan distance (μm) versus penetration depth (nm) for during scratch and scratch profile after scratch for MTES:TEOS having molar ratios of a) 20:80 mol% b) 40:60 mol% c) 60:40 mol% and d) 80:20 mol%.

Appendix D (continued)



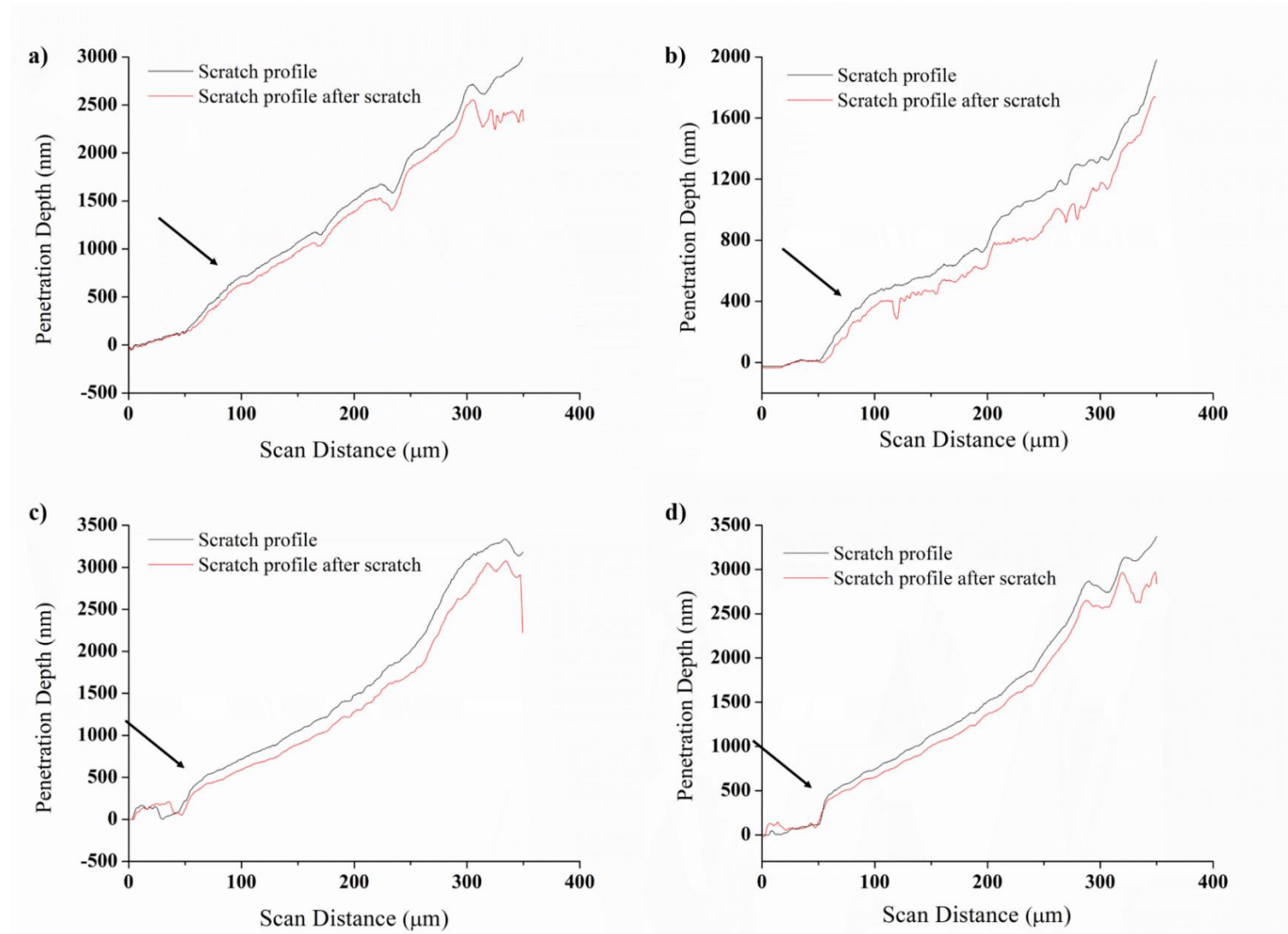
Plots of scan distance (μm) versus penetration depth (nm) for during scratch and scratch profile after scratch for PrTES:TEOS having molar ratios of a) 20:80 mol% b) 40:60 mol% c) 50:50 mol% and d) 60:40 mol%.

Appendix D (continued)



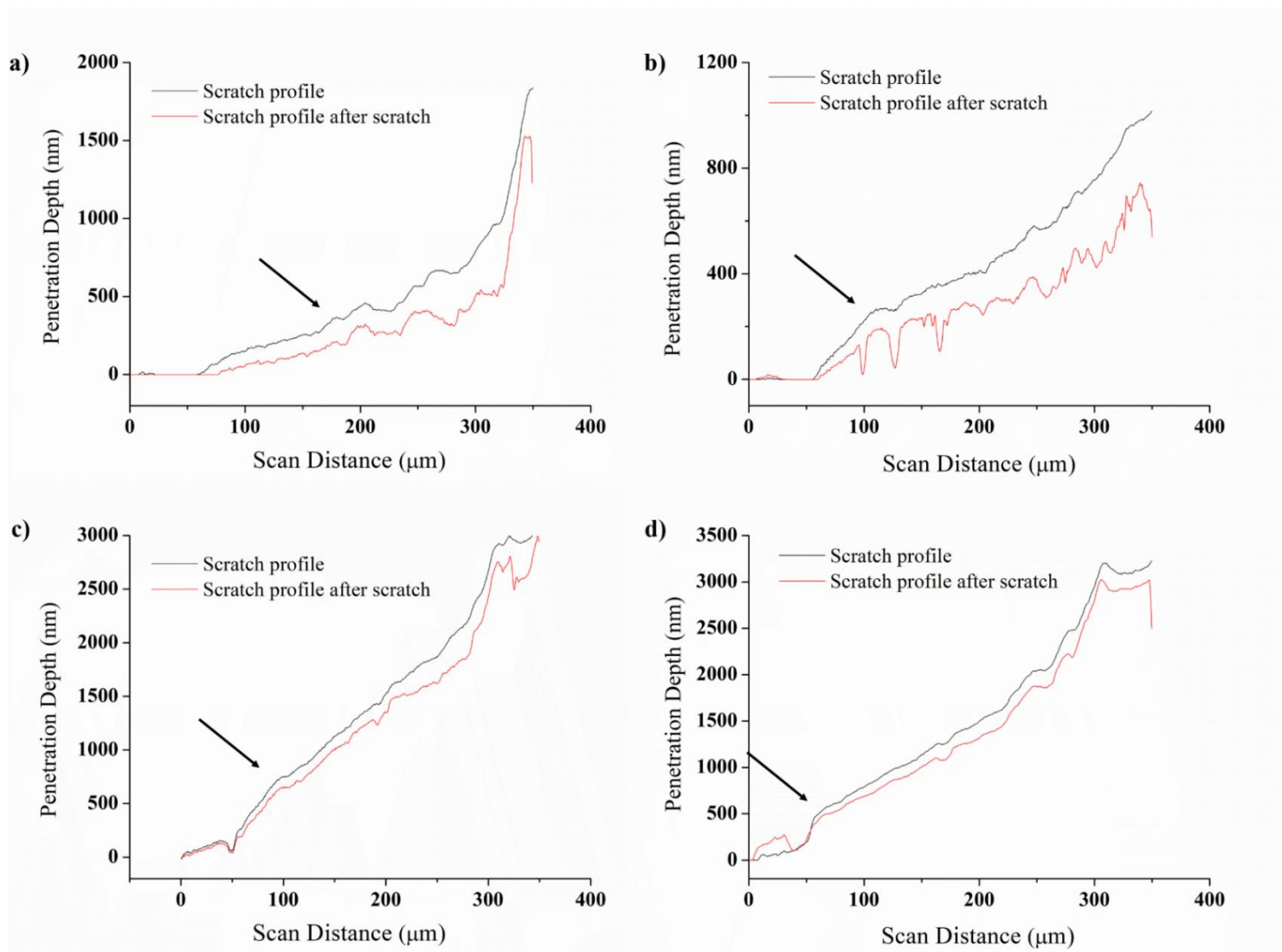
Plots of scan distance (μm) versus penetration depth (nm) for during scratch and scratch profile after scratch for HTES:TEOS having molar ratios of a) 20:80 mol% b) 30:70 mol% c) 40:60 mol% and d) 60:40 mol%.

Appendix D (continued)



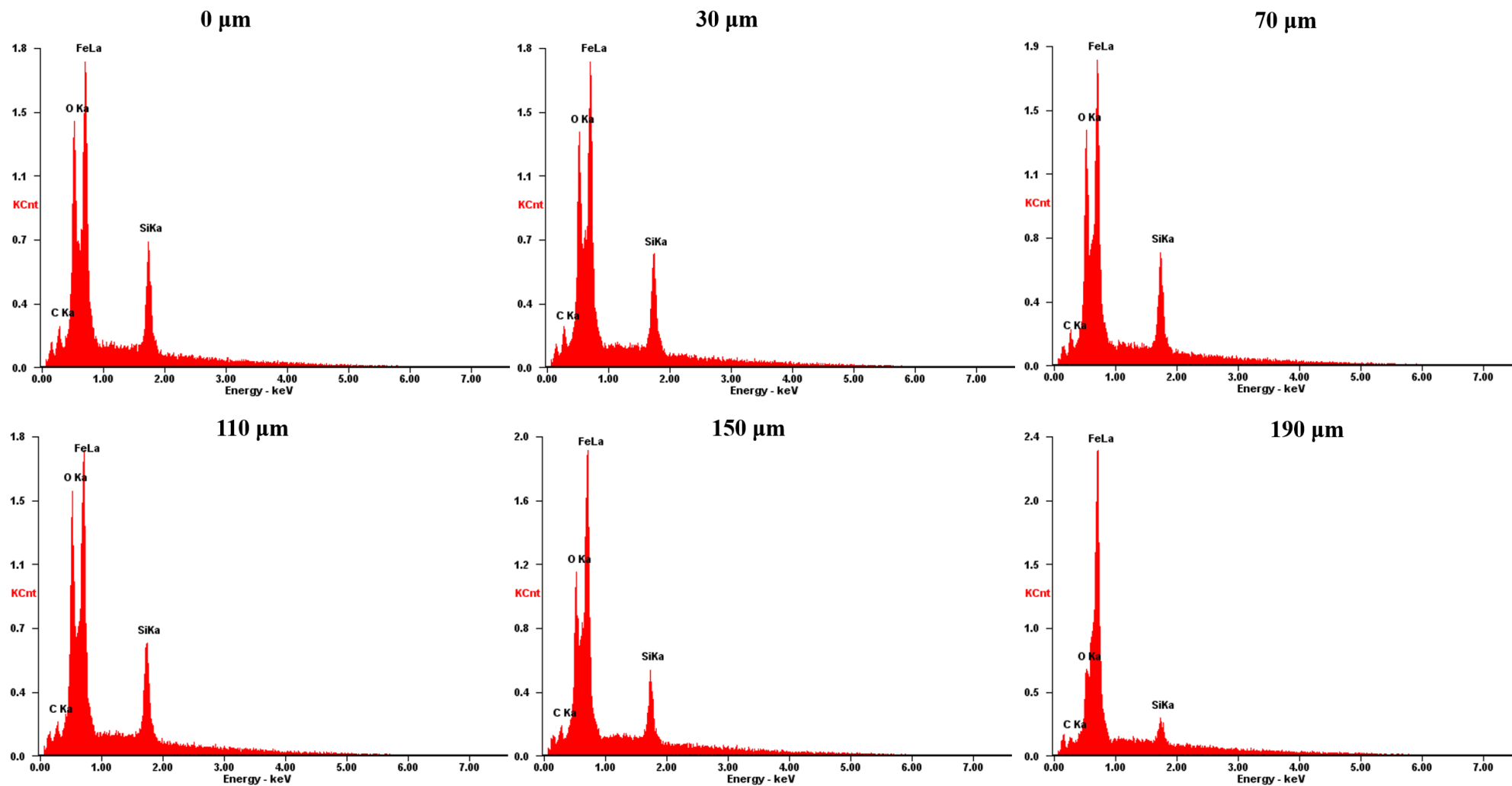
Plots of scan distance (μm) versus penetration depth (nm) for during scratch and scratch profile after scratch for OTES:TEOS having molar ratios of a) 10:90 mol% b) 20:80 mol% c) 40:60 mol% and d) 60:40 mol%

Appendix D (continued)



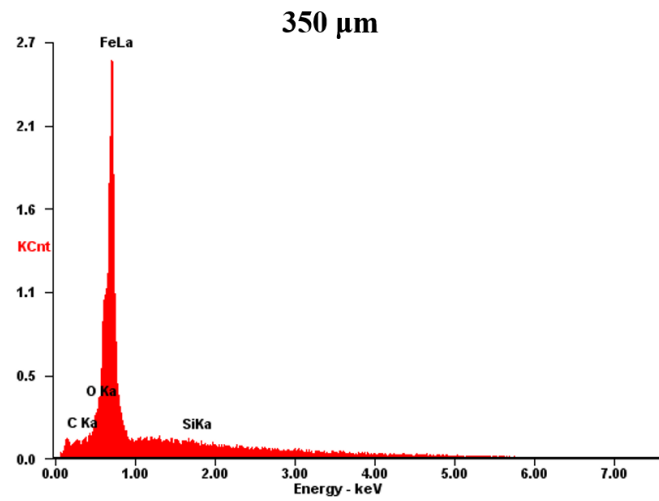
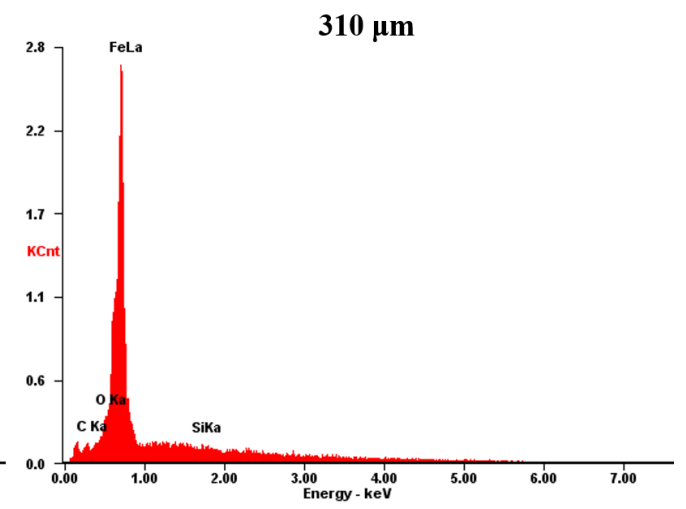
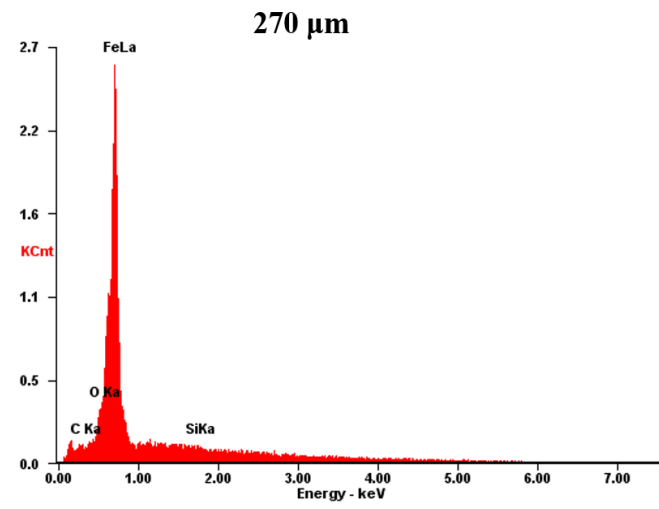
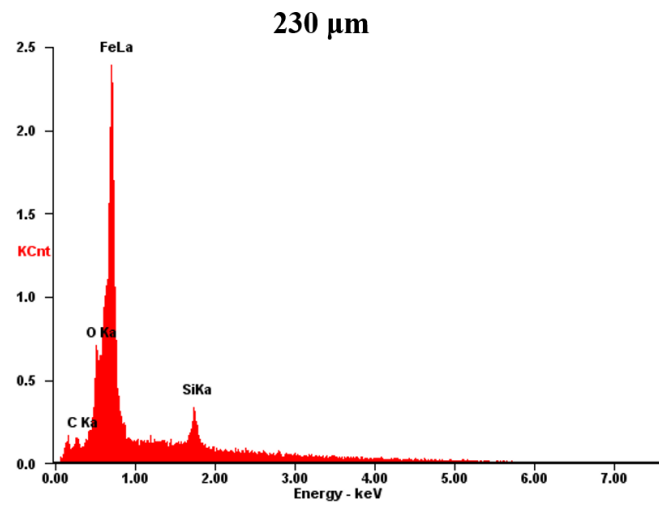
Plots of scan distance (μm) versus penetration depth (nm) for during scratch and scratch profile after scratch for PhTES:TEOS having molar ratios of a) 20:80 mol% b) 40:60 mol% c) 60:40 mol% and d) 80:20 mol%

Appendix E

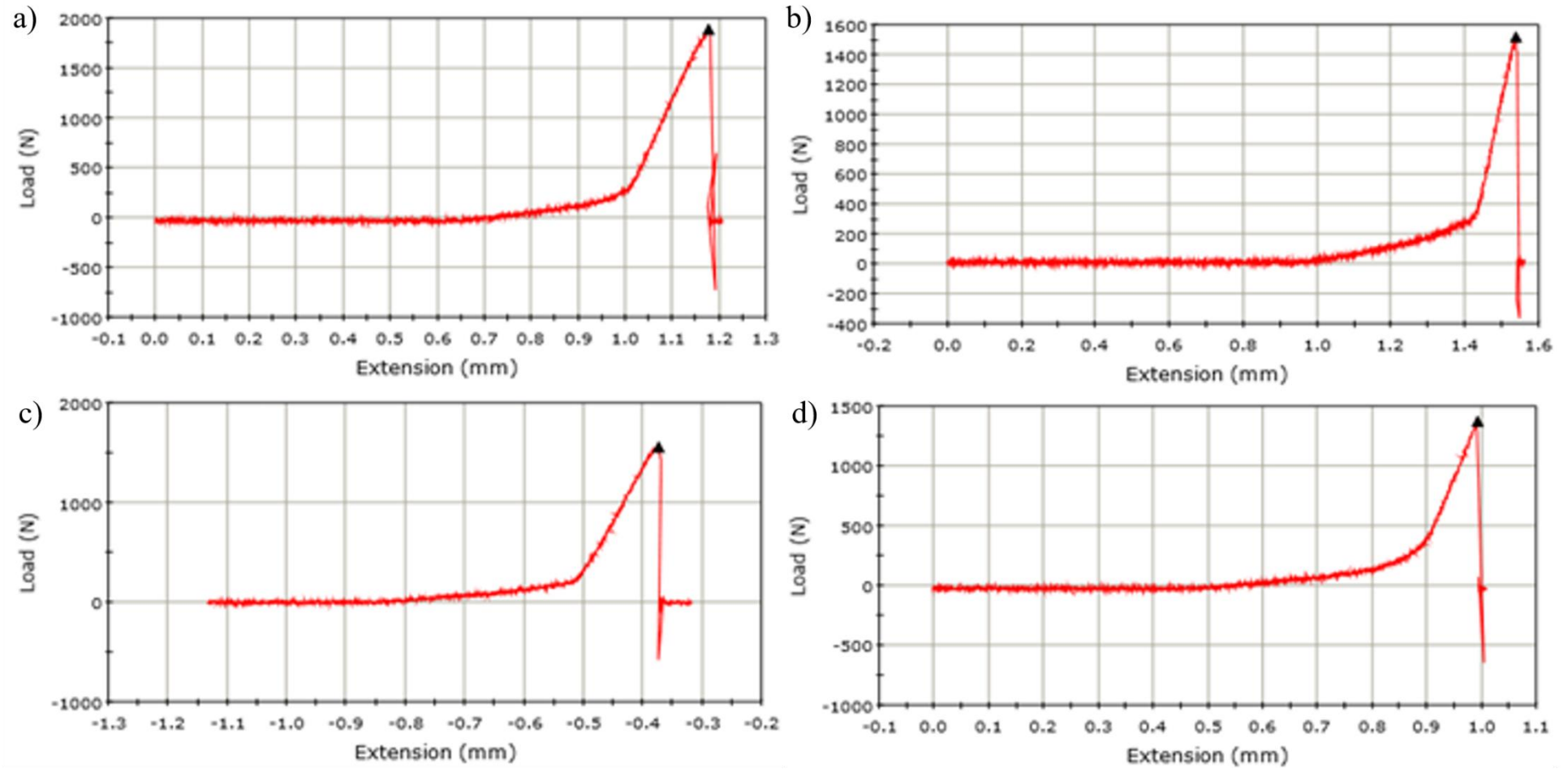


Energy (KeV) versus intensity plots for 2.5% SiO₂ 60:40 mol% MTES:TEOS single coated iron sample along scratch generated through nano-scratch test. Elemental analysis was carried out at several distances (μm) from the starting point (0 μm scratch tip touches surface of coating) up to 350 μm (end of scratch).

Appendix E (continued)

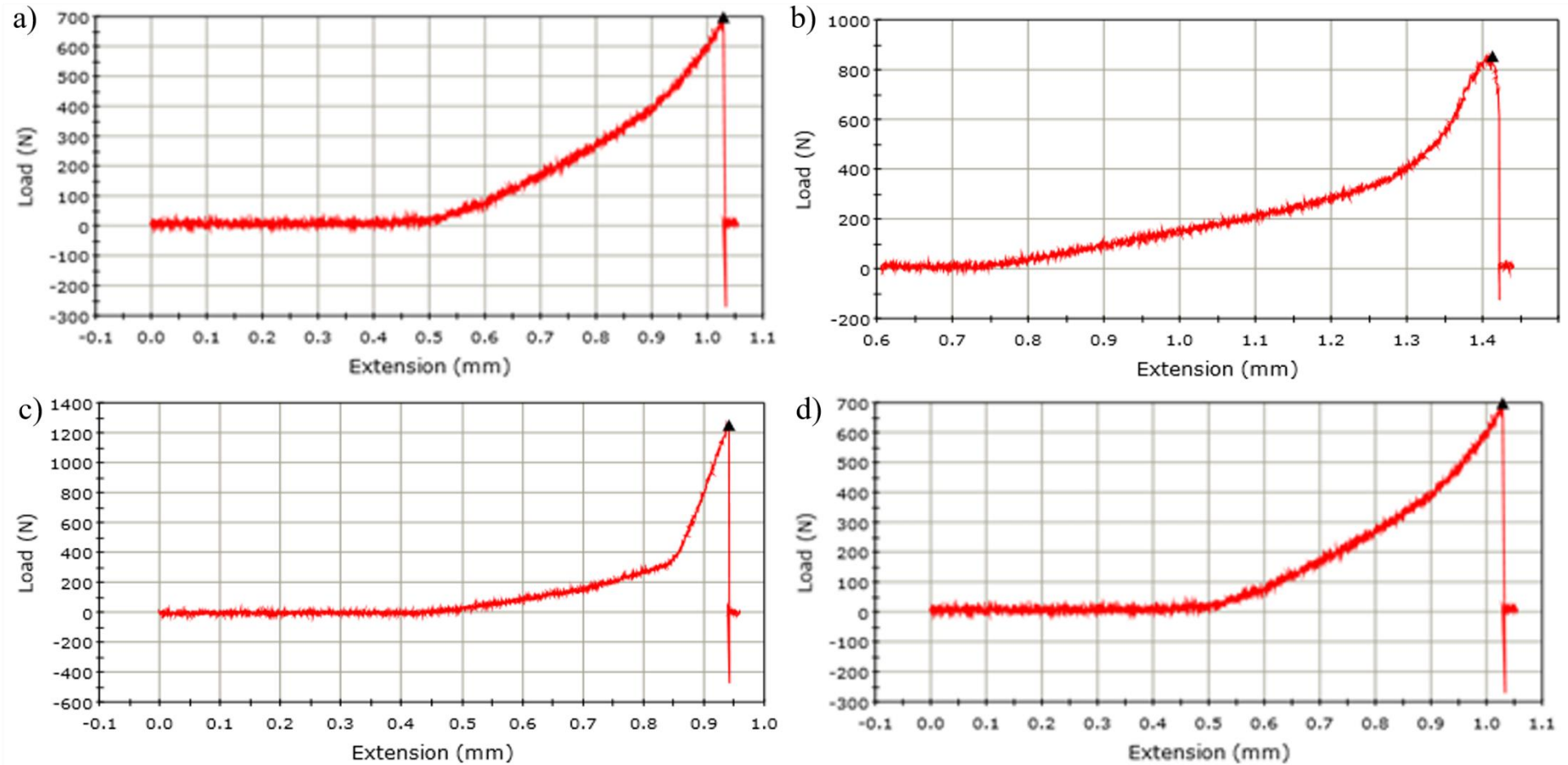


Appendix F



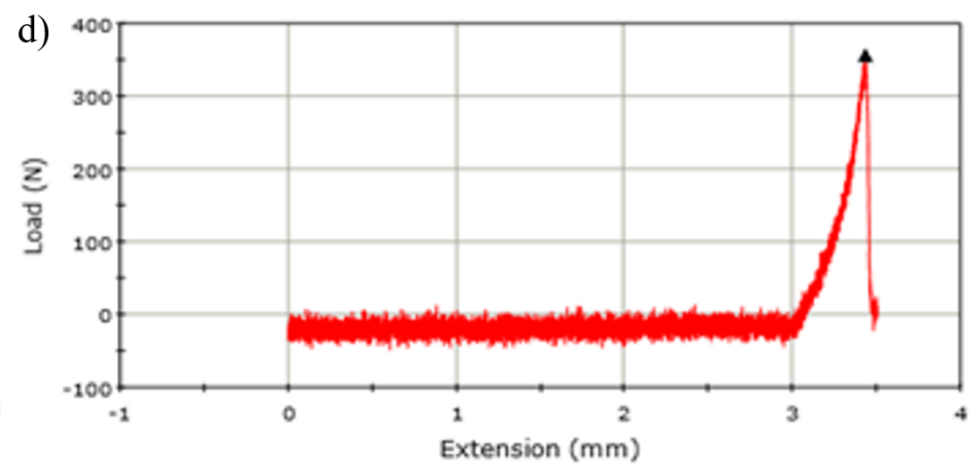
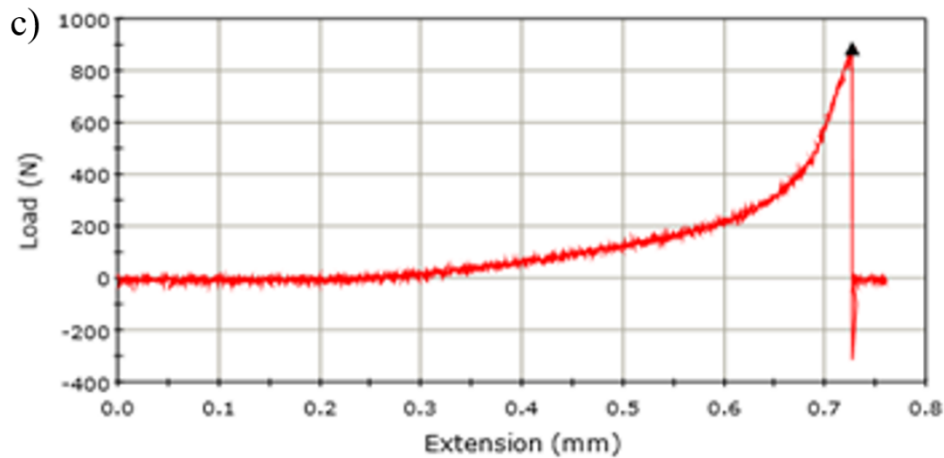
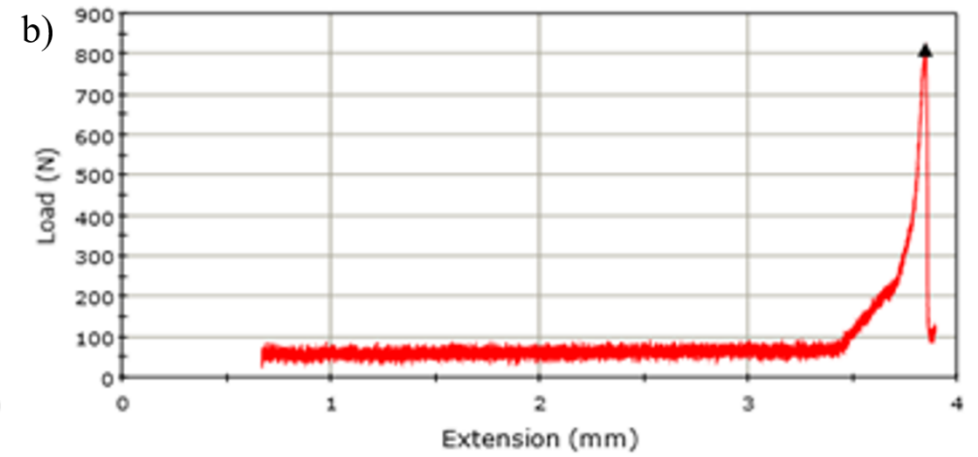
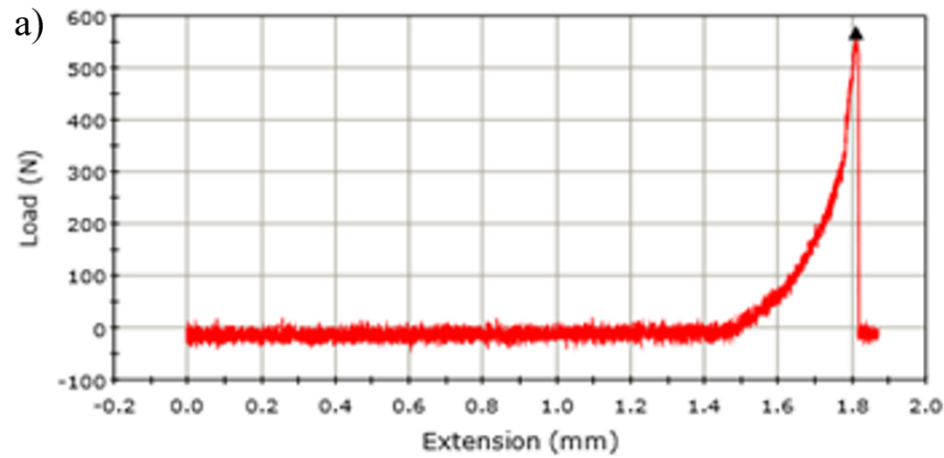
Plot of extension (mm) versus pull-out force required to detach the dolly from the coated coupons for 2.5% SiO₂ MTES:TEOS coatings in a) 20:80 mol% b) 40:60 mol% c) 60:40 mol% and d) 80:20 mol% ratios.

Appendix F (continued)



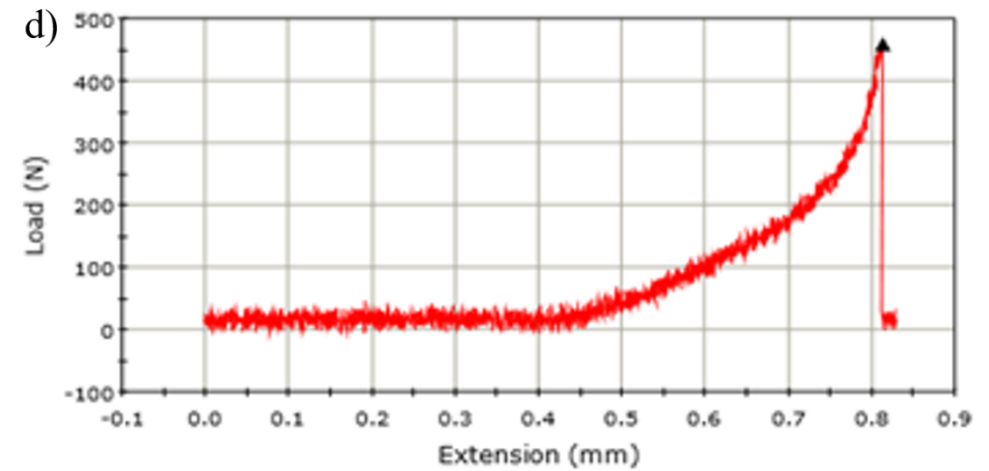
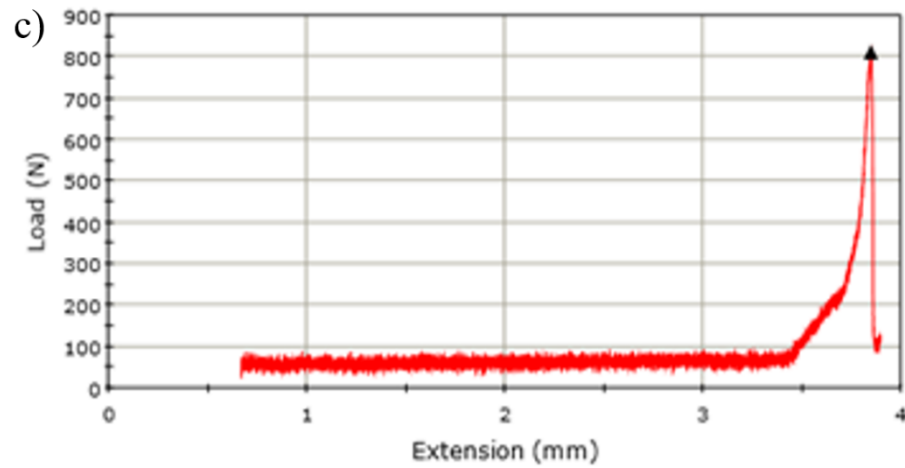
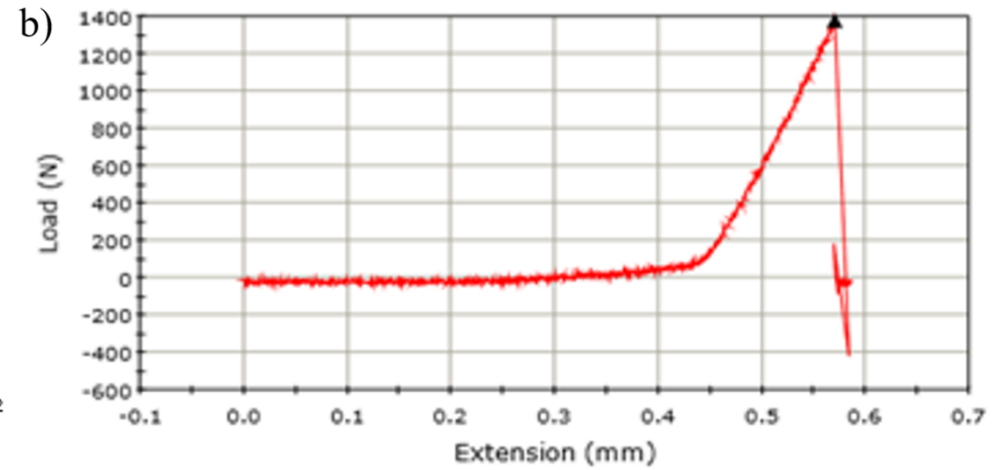
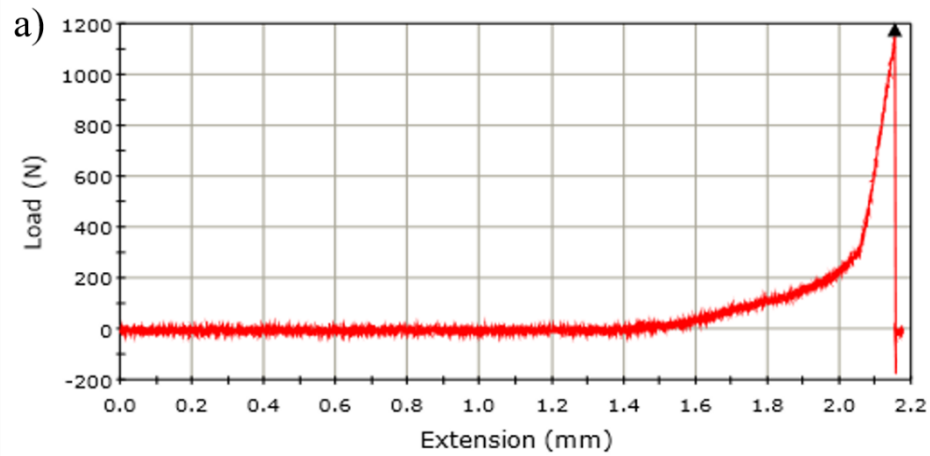
Plot of extension (mm) versus pull-out force required to detach the dolly from the coated coupons for 2.5% SiO₂ PrTES:TEOS coatings in a) 20:80 mol% b) 40:60 mol% c) 50:50 mol% and d) 60:40 mol% ratios.

Appendix F (continued)



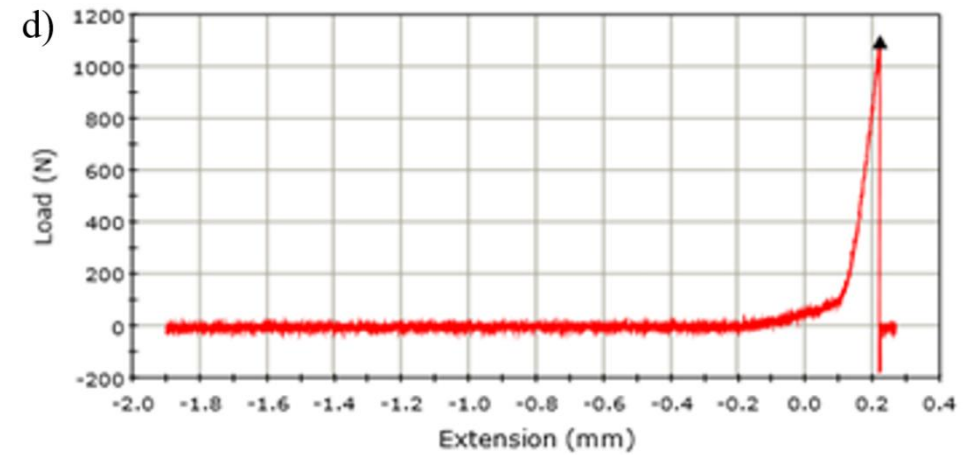
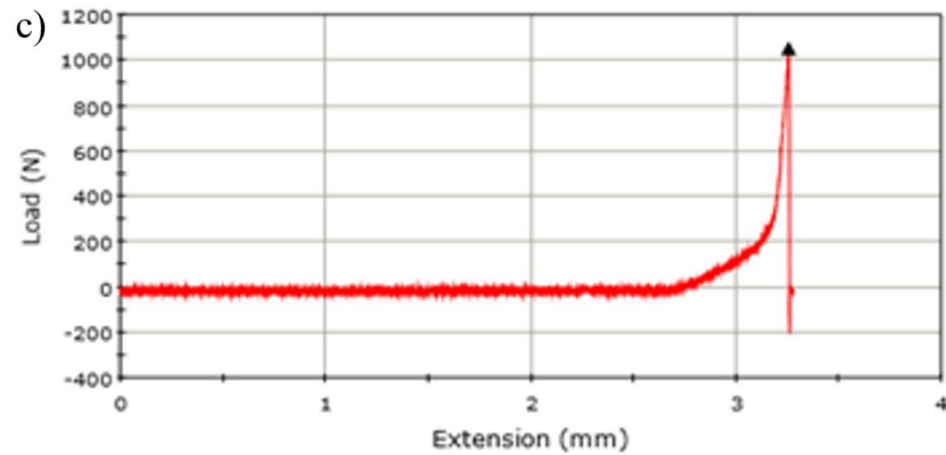
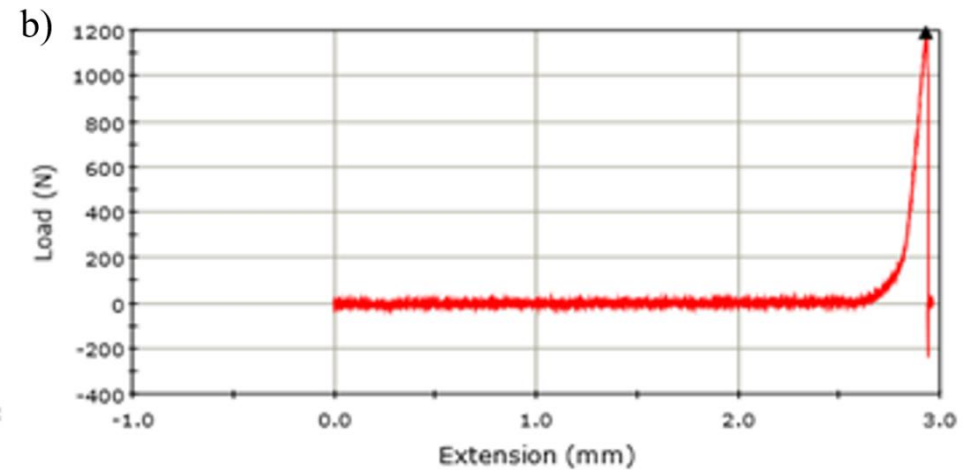
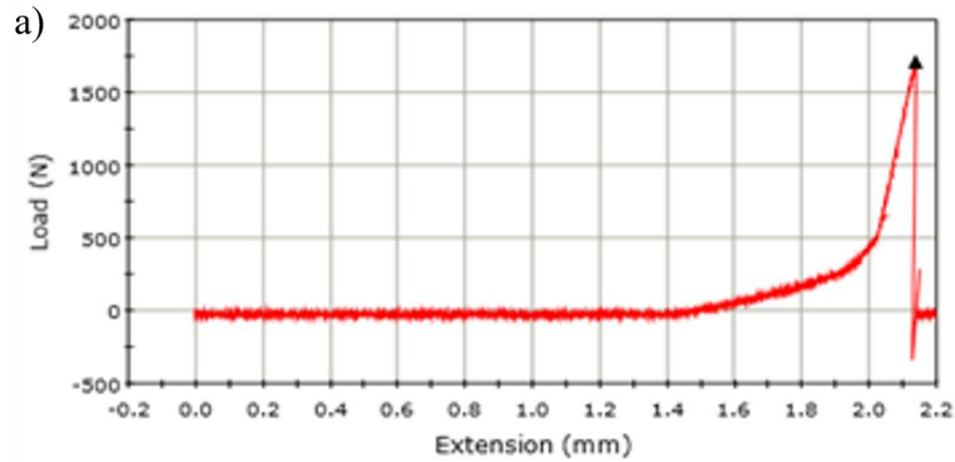
Plot of extension (mm) versus pull-out force required to detach the dolly from the coated coupons for 2.5% SiO₂ HTES:TEOS coatings in a) 20:80 mol% b) 30:70 mol% c) 40:60 mol% and d) 80:20 mol% ratios.

Appendix F (continued)



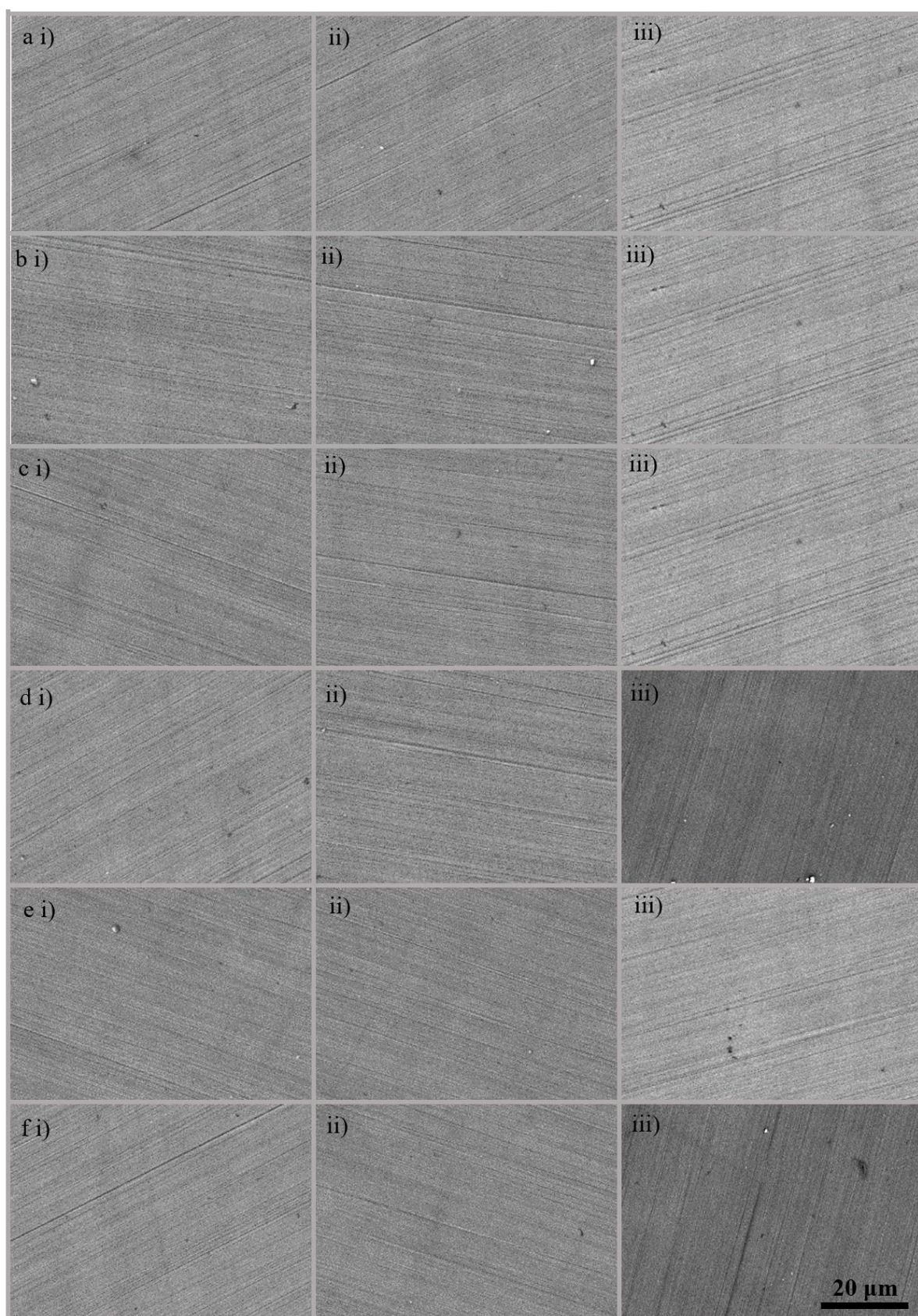
Plot of extension (mm) versus pull-out force required to detach the dolly from the coated coupons for 2.5% SiO₂ OTES:TEOS coatings in a) 10:90 mol% b) 20:80 mol% c) 40:60 mol% and d) 60:40 mol% ratios.

Appendix F (continued)



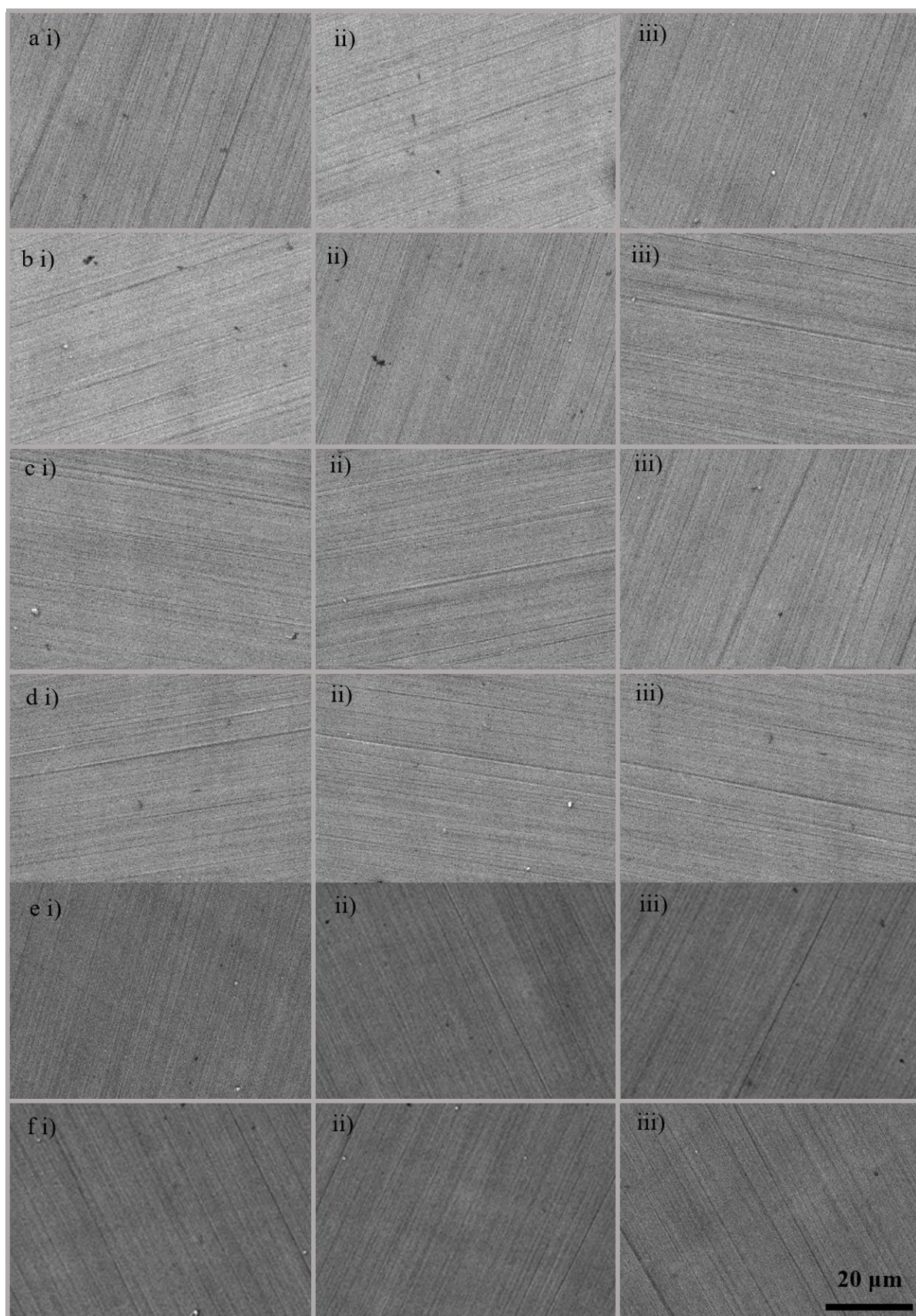
Plot of extension (mm) versus pull-out force required to detach the dolly from the coated coupons for 2.5% SiO₂ PhTES:TEOS coatings in a) 20:80 mol% b) 40:60 mol% c) 60:40 mol% and d) 80:20 mol% ratios.

Appendix G



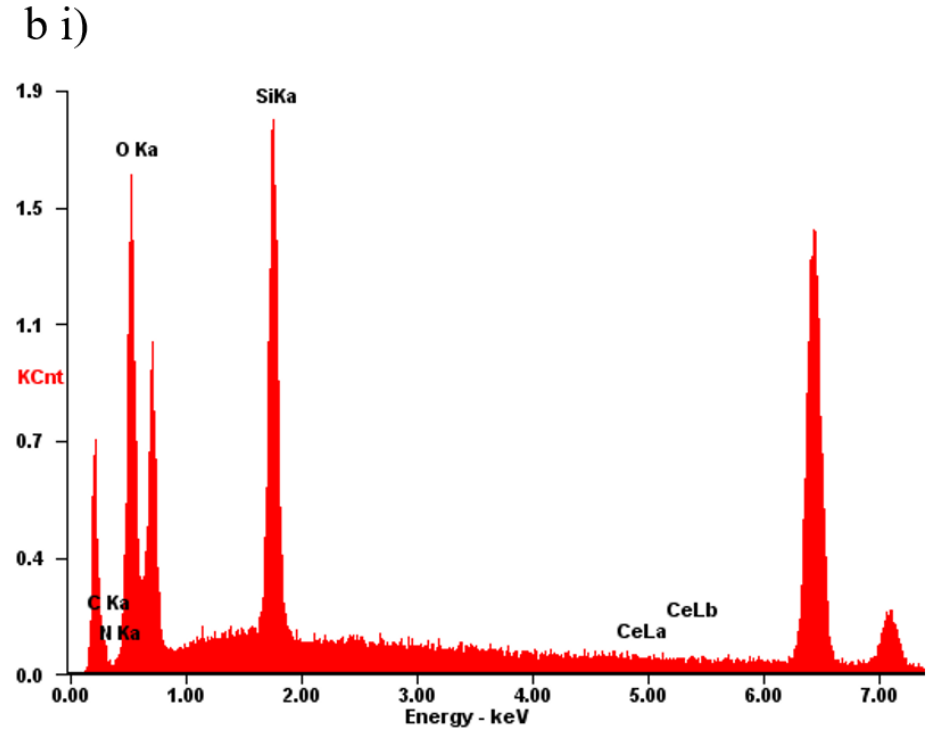
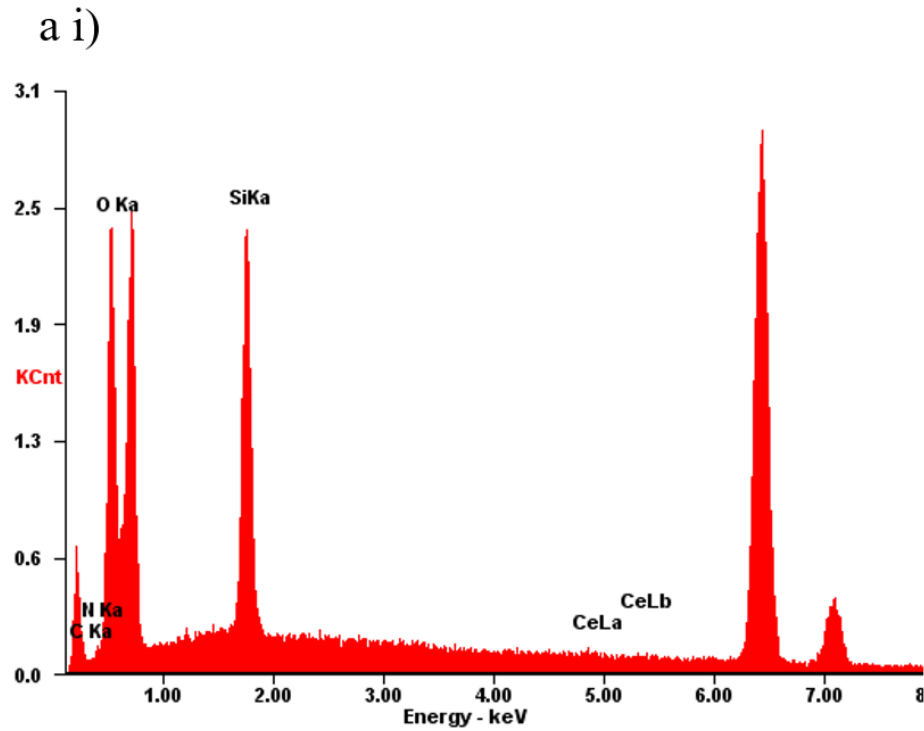
Electron micrographs of MTES:TEOS 60:40 mol% coatings applied through dip-coating and having a 2.5% SiO₂ concentration doped with a) Ce, b) Pyr, c) 1-N, d) 1,4-N, e) 2-H, and f) PhB; having inhibitor concentration of i) 0.0001M ii) 0.001M and iii) 0.01M (mag ×4000).

Appendix H



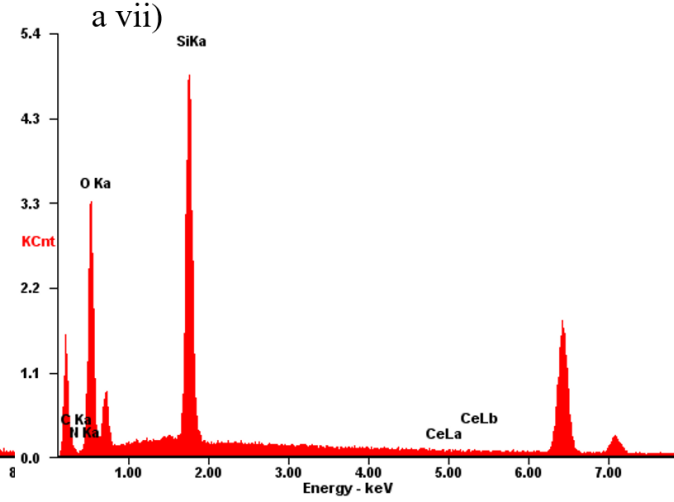
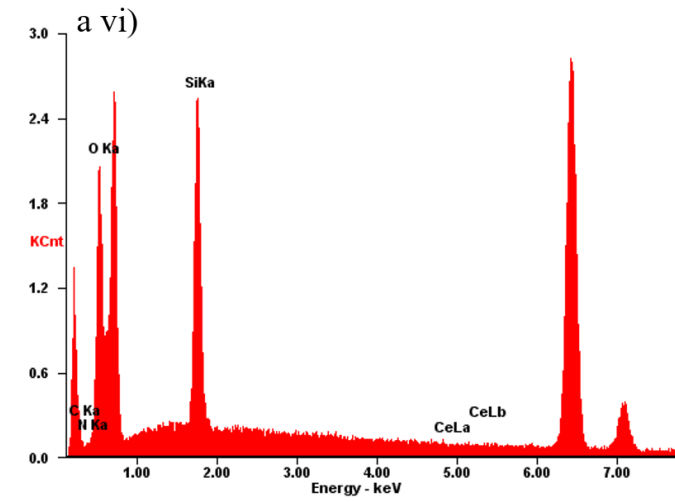
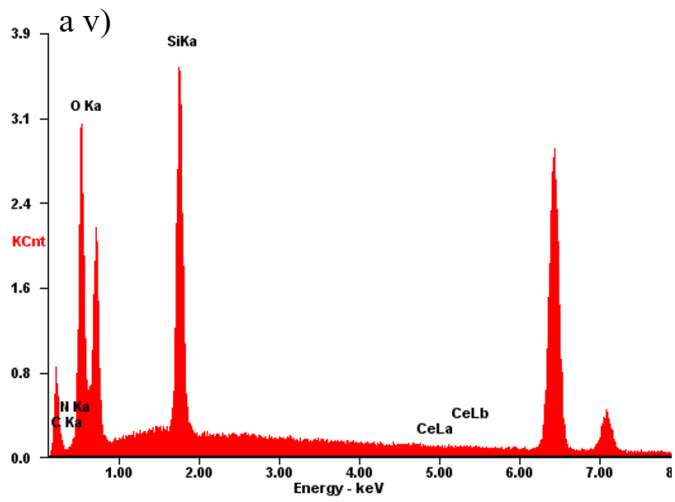
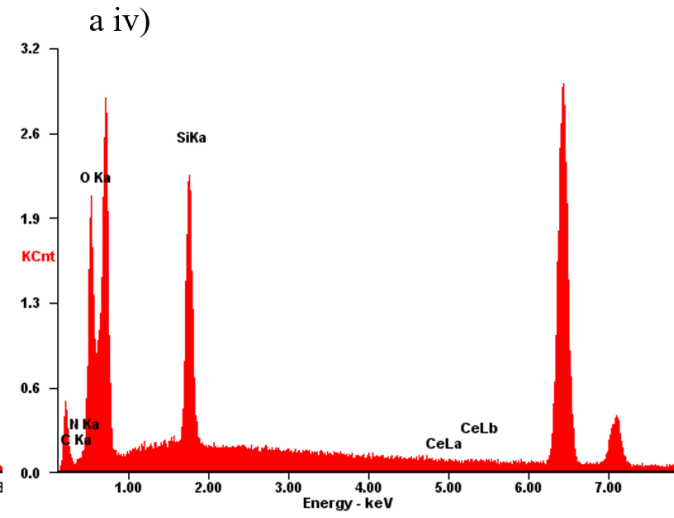
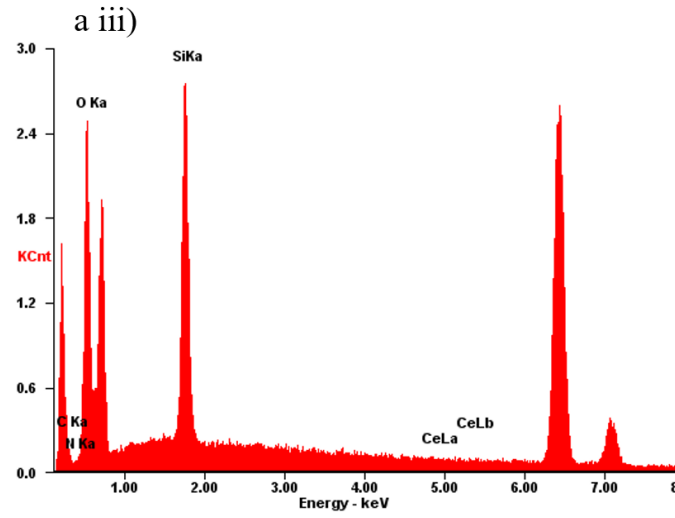
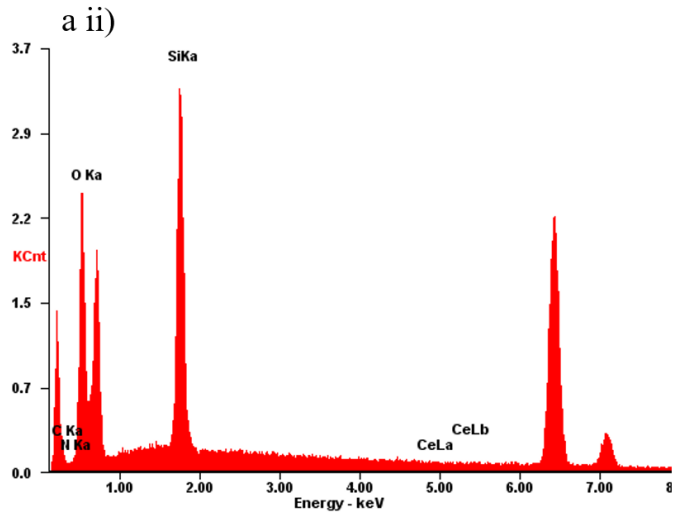
Electron micrographs of OTES:TEOS 20:80 mol% coatings applied through dip-coating and having a 2.5% SiO₂ concentration doped with a) Ce, b) Pyr, c) 1-N, d) 1,4-N, e) 2-H, and f) PhB; having inhibitor concentration of i) 0.0001 M ii) 0.001 M and iii) 0.01 M (mag ×4000).

Appendix I

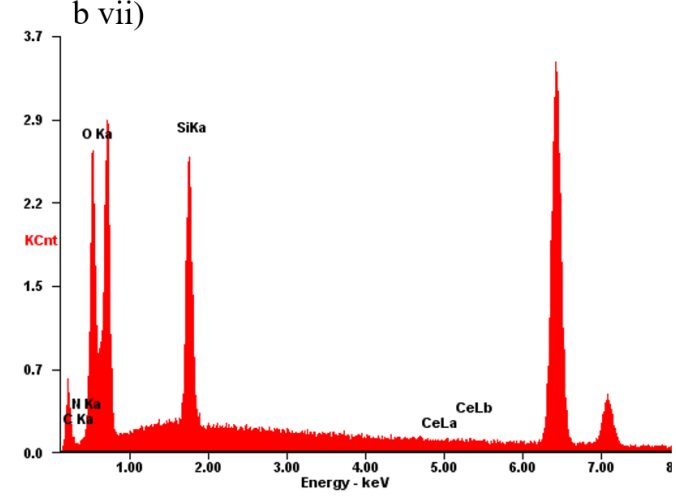
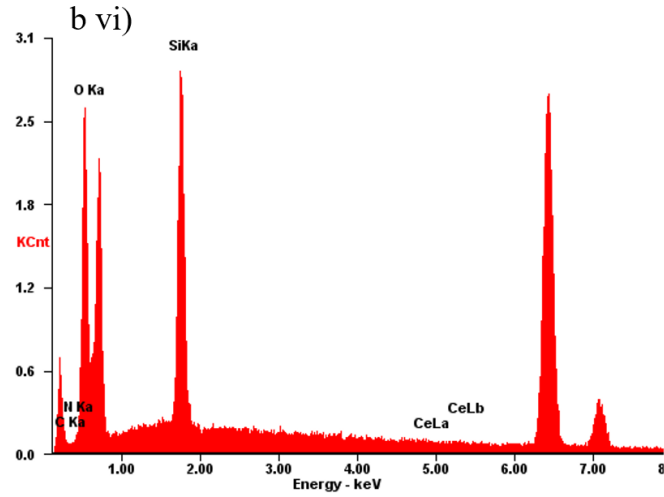
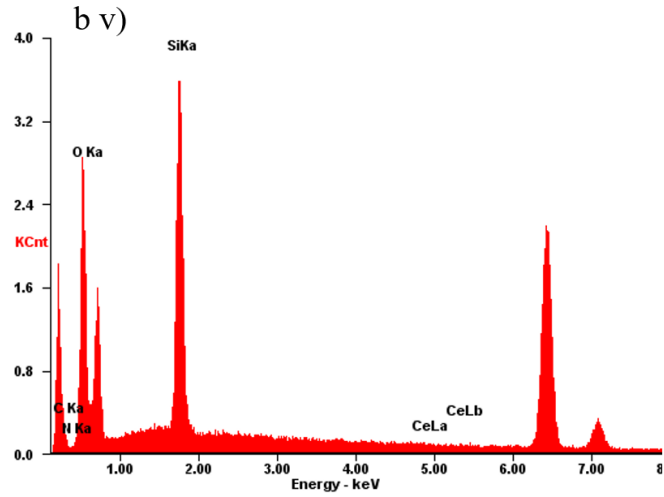
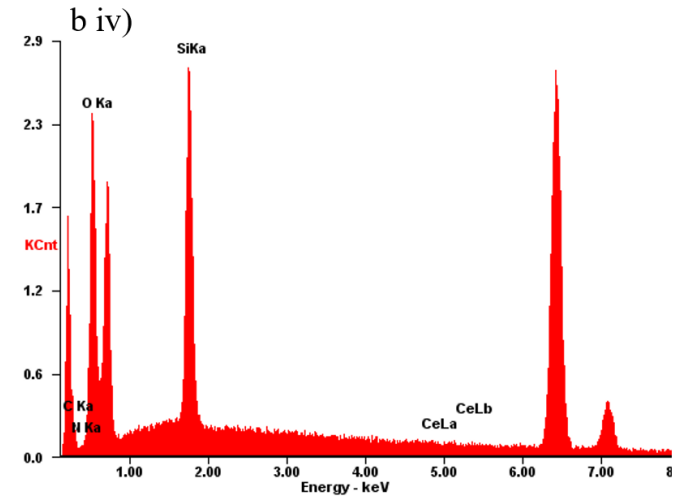
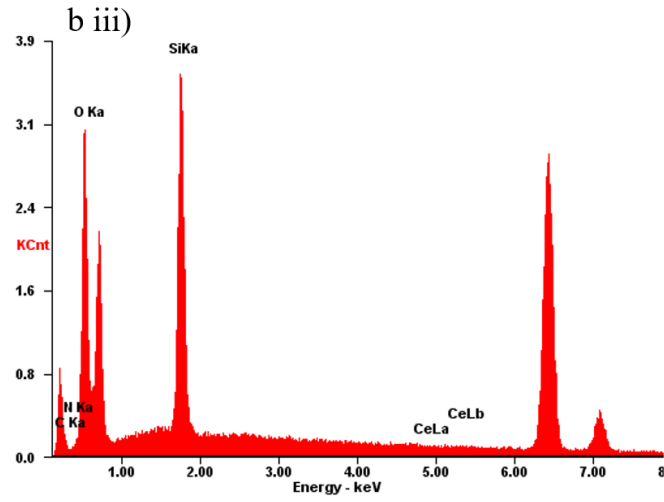
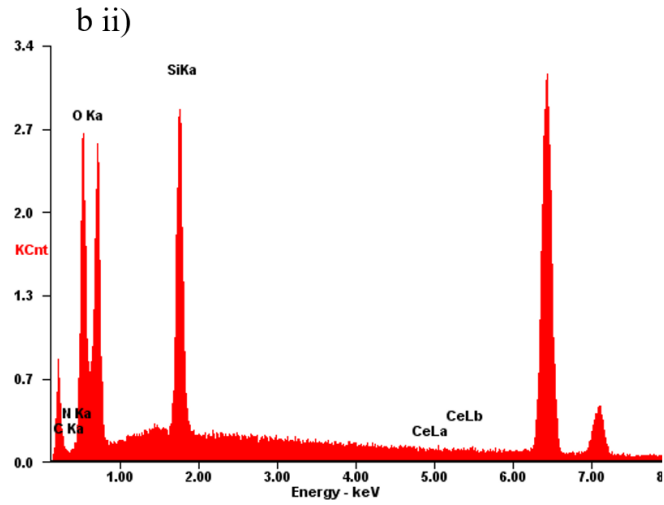


Elemental analysis shown through Energy (KeV) versus intensity plots for a) 2.5% SiO₂ 60:40 mol% MTES:TEOS and b) 2.5% SiO₂ 20:80 mol% OTES:TEOS doped with inhibitors: i) blank coatings, ii) cerium (iii) nitrate hexahydrate (Ce), iii) pyrrolidine (Pyr), iv) 1-naphthol (1-N), v) 1,4-naphthoquinone (1,4-N), vi) 2-hydroxypyridine (2-H), vii) phenylbenzoate (PhB).

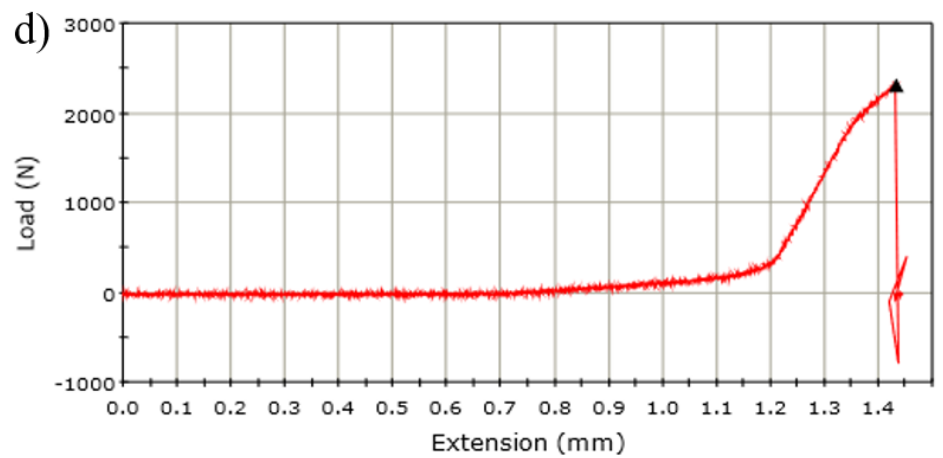
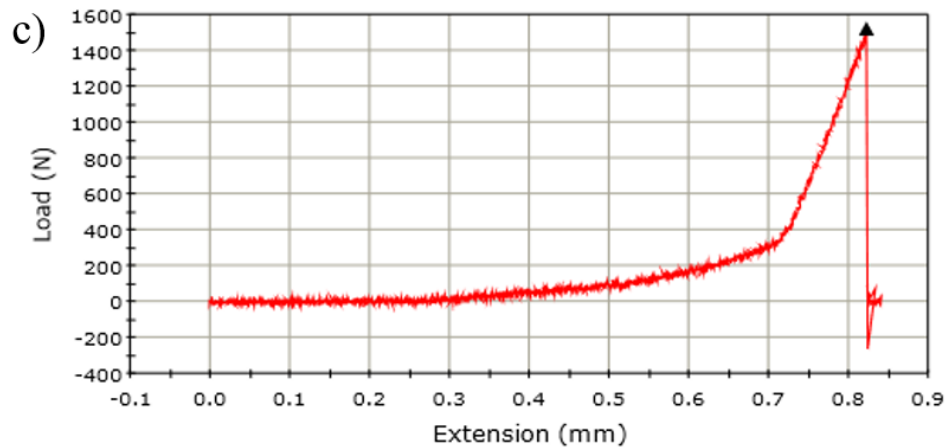
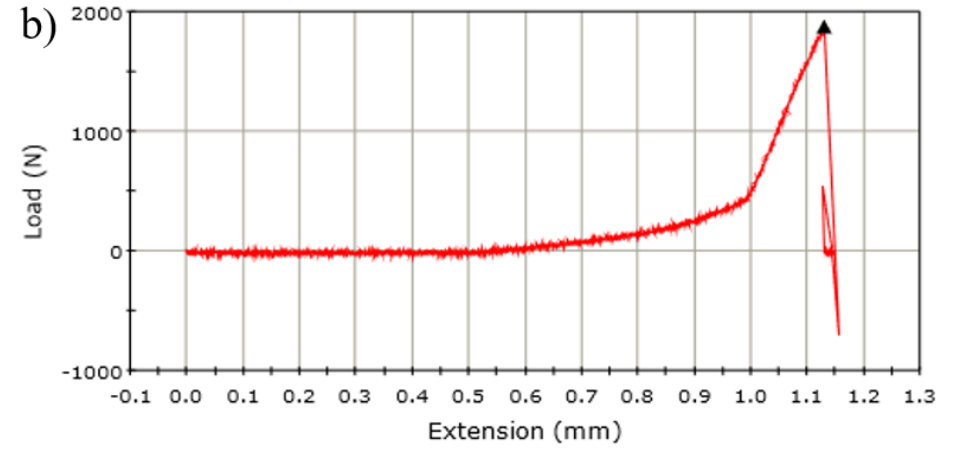
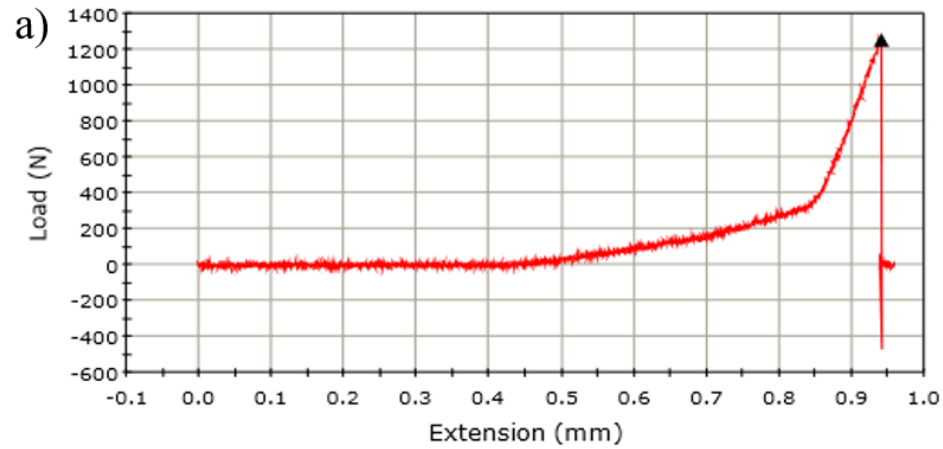
Appendix I (continued)



Appendix I (continued)



Appendix J



Plot of extension (mm) versus pull-out force required to detach the dolly from the coated coupons for a) 2.5% (wt/vol) B-48 in acetone coatings, b) 2.5% (wt/vol) B-72 in acetone coatings c) 75% (vol/vol) Ercalene in diluente nitro solvent d) uncoated (bare) metal